Lecture Notes in Chemistry 87

Zhan-Ting Li
Li-Zhu Wu *Editors*

Hydrogen Bonded Supramolecular Structures

Springer

Lecture Notes in Chemistry

Volume 87

The Lecture Notes in Chemistry

The series Lecture Notes in Chemistry (LNC) reports new developments in chemistry and molecular science-quickly and informally, but with a high quality and the explicit aim to summarize and communicate current knowledge for teaching and training purposes. Books published in this series are conceived as bridging material between advanced graduate textbooks and the forefront of research. They will serve the following purposes:

- provide an accessible introduction to the field to postgraduate students and nonspecialist researchers from related areas,
- provide a source of advanced teaching material for specialized seminars, courses and schools, and
- be readily accessible in print and online.

The series covers all established fields of chemistry such as analytical chemistry, organic chemistry, inorganic chemistry, physical chemistry including electrochemistry, theoretical and computational chemistry, industrial chemistry, and catalysis. It is also a particularly suitable forum for volumes addressing the interfaces of chemistry with other disciplines, such as biology, medicine, physics, engineering, materials science including polymer and nanoscience, or earth and environmental science.

Both authored and edited volumes will be considered for publication. Edited volumes should however consist of a very limited number of contributions only. Proceedings will not be considered for LNC.

The year 2010 marks the relaunch of LNC.

More information about this series at http://www.springer.com/series/632

Zhan-Ting Li · Li-Zhu Wu
Editors

Hydrogen Bonded Supramolecular Structures

Springer

Editors
Zhan-Ting Li
Department of Chemistry
Fudan University
Shanghai
China

Li-Zhu Wu
Technical Institute of Physics
and Chemistry
Chinese Academy of Sciences
Beijing
China

ISSN 0342-4901 ISSN 2192-6603 (electronic)
Lecture Notes in Chemistry
ISBN 978-3-662-45755-9 ISBN 978-3-662-45756-6 (eBook)
DOI 10.1007/978-3-662-45756-6

Library of Congress Control Number: 2014956715

Springer Heidelberg New York Dordrecht London

Printed on acid-free paper

Springer-Verlag GmbH Berlin Heidelberg is part of Springer Science+Business Media (www.springer.com)

Preface

Hydrogen bonding is the electrostatic attraction between the hydrogen atom of a molecule or molecular fragment and an atom or group of higher electronegativity. Since its establishment as a non-covalent force in the 1920s and 1930s by Pauling and others, hydrogen bonding has been continuously intensively studied and applied in chemistry, biology, and materials science. Fundamental studies on hydrogen bonding have continuously provided insights into its inherent electronic property and factors that affect it. However, for most researchers, hydrogen bonding is mainly a versatile tool for controlling or tuning the structure and property of molecules, macromolecules, and supramolecules and a non-covalent interaction for explaining or rationalizing experimental phenomena, properties or functions at molecular and supramolecular levels.

Due to its low electronegativity, hydrogen atoms connected to O, N, and C are partially positively charged. Therefore, organic molecules and macromolecules containing hydrogen atoms all have the possibility of forming hydrogen bonding. Hydrogen bonding formed by single groups, such as hydroxyl, carboxylic acid, amide, and urea, is strong and has been well established. In recent years, weak hydrogen bonding concerning carbon-connected hydrogen atom(s) has received increasing attention. Although there have been few quantitative studies reported in solution, this weak intermolecular interaction motif has been frequently observed in the solid state. Because most organic molecules contain hydrogen atom(s), hydrogen bonding plays a central role in the investigation of many intermolecular binding affairs.

Single hydrogen bonding motif is relatively weak for enhanced recognition and self-assembly in solution. To achieve specific binding in water, Nature has evolved nucleic acid–base pairs, which are stabilized by two or more integrated hydrogen bonds and work in a cooperative manner to drive, together with hydrophobic interaction, the formation of double helix. This simple, but useful strategy has inspired chemists to design artificial triply, quadruply, and more complicated hydrogen bonding motifs for fundamental and practical applications.

Supramolecular chemistry refers to chemistry beyond molecules and focuses on chemical systems consisting of assembled molecular subunits or components.

Intermolecular forces that hold molecular subunits or components together may be hydrogen bonding, coordination, solvophobicity, and electrostatic (ion pair or donor–acceptor) interaction. Among other interactions, hydrogen bonding has several advantages. It is relatively strong and directional. Quantitative evaluation of its stability or strength is relatively easy. The strength can be further enhanced by creating multiple hydrogen bonding motifs, and in this way the stability can be regulated, to a great extent, for different purposes. No transition metal ions are involved, which is a prerequisite for many biologically related researches. As a result, hydrogen bonding has, to a great extent, seized the central position not only in constructing new supramolecular structures, but also in modulating or improving supramolecular functions.

The two volumes, *Hydrogen Bonded Supramolecular Structures* and *Hydrogen Bonded Supramolecular Materials*, belonging to the series of *Lecture Notes in Chemistry*, are aimed at providing undergraduates, graduates, and young researchers of the field with an overview of the important role of hydrogen bonding in supramolecular chemistry. In the first volume, *Hydrogen Bonded Supramolecular Structures*, recent progresses in the construction and assessment of new hydrogen bonding patterns, which is the foundation for future design of new supramolecular structures and supramolecular approaches to creating new scientific phenomena and technological applications, are first summarized. It then introduces several kinds of important recognition phenomena in solution and the solid state. Moreover, it further describes several aspects in the construction of macrocyclic systems and advanced supramolecular architectures, many of which exhibit interesting properties or functions. The second volume, *Hydrogen Bonded Supramolecular Materials*, mainly presents topics on the utility of hydrogen bonding in creating functional architectures and supramolecular materials. Given the breadth of supramolecular chemistry, the book is also of interest to researchers already involved in the field, because it offers references of pioneering contributions, representative researches, as well as inspiring review articles on many specific aspects.

We would like to express our gratitude to all the authors of the chapters, whose great efforts made the publication of this book a reality.

August 2014

Zhan-Ting Li
Li-Zhu Wu

Contents

Chapter 1
Hydrogen Bonding Motifs: New Progresses

Dan-Wei Zhang, Hui Wang and Zhan-Ting Li

Abstract This chapter summarizes the important and typical intramolecular and intermolecular hydrogen bonding motifs. The capacities of hydrogen bonding donors and acceptors are first discussed. Representative and new single hydrogen bonding motifs, particularly those formed by weak hydrogen bonding acceptors and hydrocarbon hydrogen bonding donors reported in the last decade, are then described. In the last section, intermolecular double, triple, quadruple, sextuple, heptuple, and octuple hydrogen bonding motifs are presented.

1.1 Hydrogen Bonding: The Basic Aspects

1.1.1 Definition

A hydrogen bond is an attractive electrostatic interaction between polar molecules or within a polar molecule or group, in which the involved hydrogen (H) is bound to an electronegative atom, such as nitrogen (N), oxygen (O), or fluorine (F). It was conceptually developed in the first 30 years of the twentieth century and finally accepted by the chemical community with the publication of the book *The Nature of the Chemical Bond* by Pauling in 1939 [1]. In 2011, an IUPAC task group defined hydrogen bonding as "an attractive interaction between a hydrogen atom from a molecule or a molecular fragment X–H in which X is more electronegative than H, and an atom or a group of atoms in the same or a different molecule, in which there is evidence of bond formation" [2]. Since its establishment as an important non-covalent interaction, hydrogen bonding has been continuously

D.-W. Zhang (✉) · H. Wang · Z.-T. Li
Department of Chemistry, Fudan University, 220 Handan Road, Shanghai 200433, China
e-mail: zhangdw@fudan.edu.cn

Z.-T. Li
e-mail: ztli@fudan.edu.cn

Z. Li and L. Wu (eds.), *Hydrogen Bonded Supramolecular Structures*,
Lecture Notes in Chemistry 87, DOI 10.1007/978-3-662-45756-6_1

intensively studied in physics, chemistry, and biology, both experimentally and theoretically [3–7].

As one of the major non-covalent forces, hydrogen bonding has played a central role in supramolecular chemistry. The nature of hydrogen bonding, its classification, and the strength of a single hydrogen bond have been summarized in a previous book [7]. This book is specifically dedicated to the structures and functions or material properties of supramolecular systems which are held together with hydrogen bonding. This chapter provides a summary of various hydrogen bonding patterns. Before this, several important aspects affecting the formation of hydrogen bonding, including the nature of donors and acceptors, factors that affect the stability, the role of solvents, and the basic binding patterns of important functional groups, are described. The crystal structures, except those with indicated references, were all obtained from Crystallography Open Database or CCDC. The theoretical study and experimental characterization of hydrogen bonding and the applications of hydrogen bonding for the construction of supramolecular architectures will not be included.

1.1.2 Hydrogen Bonding Donors and Acceptors

In principle, any atom or group whose electronegativity is higher than a connected H atom could induce a dipolar moment for the H atom to act as a donor (D) to form a hydrogen bond with another atom of higher electronegativity. However, when the difference is not large enough, this bonding may be very weak and is usually considered as van der Waals interaction. Thus, among others, O and N atoms have been the most typical and strongest hydrogen bonding acceptors (A) due to their high electronegativity and polarity [8], and in organic supramolecular chemistry, amide and urea derivatives have received the greatest attention for their robust ability to form hydrogen bonding [9, 10]. For organic crystal engineering, amide, carboxylic acid, and phenol derivatives have been investigated most extensively [11–15]. Other heteroatoms, including S, Cl, Br, I, or even C atoms, have been demonstrated to serve as hydrogen bonding donors in organic molecules [16–20]. Electron-rich π-electron systems, including aromatic rings and C=C and C≡C multiple bonds, can also behave as acceptors to form N–H···π (**HB-1–3**) [21–23] and C–H···π H-bonds (**HB-4–6**) [24], and transition metals can serve as both donors (**HB-7**) and acceptors (**HB-8**) for intramolecular hydrogen bonding [25, 26]. However, these kinds of hydrogen bonds are usually relatively weak. As expected, highly electronegative O and N atoms are also the most typical strong hydrogen bonding acceptors [9, 10, 14], and hydrogen bonds formed by them have been widely applied to assemble stable supramolecular structures. In particular, the carbonyl O atom of amide may be the most common hydrogen bonding acceptor.

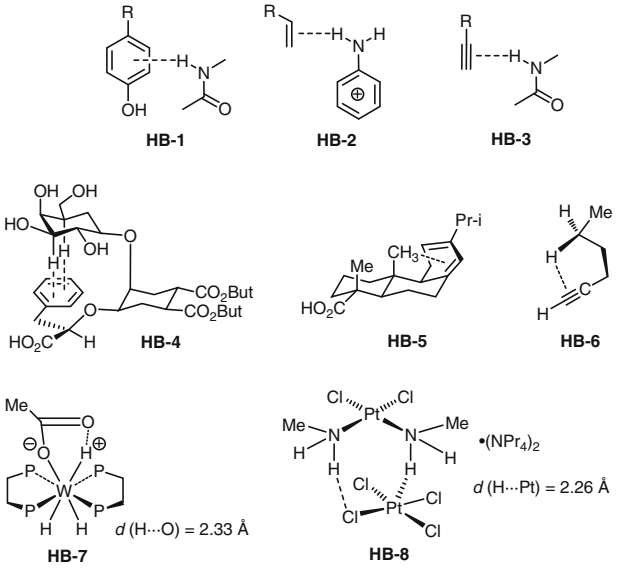

Fluorine (F) atom possesses the highest electronegativity. Although hydrogen fluoride forms probably the strongest H-bonding with F^- anion and the latter may be the strongest hydrogen bonding acceptor, it has been demonstrated that the F atom in organic molecules is a very weak acceptor, which has been attributed to its low polarizability and tightly contracted lone pairs [27]. Moreover, the F atom of hexafluorophosphate and tetrafluoroborate anions also hardly serves as hydrogen bonding acceptor. Nevertheless, five- and six-membered intramolecular hydrogen bonding formed between F and aromatic amides or even 1,4-diphenyl-1,2,3-triazole C^5–H have been confirmed [28, 29].

1.1.3 The Strength of the Hydrogen Bond

The strength of a hydrogen bond is normally defined in terms of bond energy. More exactly, it should be expressed by enthalpy. Depending on the enthalpy, a hydrogen bond may be defined as strong (14–40 kcal M^{-1}), moderate (5–15 kcal M^{-1}), or weak (0–5 kcal M^{-1}) [4]. In solution, the strength of an intermolecular hydrogen bond is most frequently reflected by the value of the association constant, K_a, and the related free energy:

$$\Delta G = \Delta H - T\Delta S = -RT \ln K_a$$

Because the formation of any hydrogen bond is a process of losing degrees of freedom, the standard entropy, ΔS, is always negative and increased with the

tightening of the two interacting molecules or groups. For the formation of a hydrogen bond by two molecules, three translational and three rotational degrees of freedom will be lost. It was reported that this loss can produce a decrease of entropy of 29–36 cal mol^{-1} K^{-1} for translations and of 10–30 cal mol^{-1} K^{-1} for rotations in the gas-phase or 1 M solution [30]. This loss is only partially compensated by the new vibration as a result of the formation of the H-bond, which may contribute significantly (1–4 cal mol^{-1} K^{-1}) for low-frequency vibrational modes (400–100 cm^{-1}).

For supramolecular chemists, most of researches are conducted in solution or in the solid state. In solution, the strength of hydrogen bonding is remarkably affected by the solvent because the solvent molecules are remarkably excessive compared to the hydrogen bonded solutes and can form hydrogen bonding by themselves. For example, polar aprotic solvents, such as dimethyl sulfoxide (DMSO), *N′N*-dimethyl formamide (DMF) or acetonitrile, are strong hydrogen bonding acceptors and can strongly weaken or completely destroy strong hydrogen bonding. Polar protic solvents, like water, methanol, and ethanol, behave as both donors and acceptors and thus also compete with any studied solute molecules or ions. The polarity of the most widely used solvents, chloroform and dichloromethane, is relatively low. However, both of them are also weak hydrogen bonding acceptors and the former is also a weak hydrogen bonding donor. The trace of water or hydrochloride in these solvents can substantially change the hydrogen bonding behavior of studied molecules or ions. Thus, the choice of the solvent is crucially important for any solution-phase investigation of hydrogen bonding and related binding events.

In molecular crystals, to a great extent, weak van der Waals interactions control the aggregation or packing of the molecules in the absence of other stronger interactions. If the molecules are able to form stronger hydrogen bonds, the hydrogen bonds will make a greater contribution to the lattice energy of the crystal. When both hydrogen bonding and van der Waals interaction can be formed, the formation of the former is preferential if geometric matching is allowed. When there are available acceptors, all acidic H atoms in a molecule may be engaged in hydrogen bonding [31]. If the molecules are able to form different hydrogen bonds, their formation is expected to be in order of decreasing strength [32]. When crystals are grown from a solvent that can behave as donors and/or acceptors, the solvent molecules may be trapped in the crystal through hydrogen bonding to the target molecule or to fill a space formed due to the rigidity of the molecule. In such crystals, very weak C–H···X or C–H···π hydrogen bonding may be observed [5].

For intramolecular hydrogen bonding in crystals, the strength can be roughly reflected by the distance between the bonded H atom and the acceptor. When the distance is shorter than the sum of their van der Waals radii, we may say that a hydrogen bond is formed. Currently, there is not a general method available to evaluate the strength of hydrogen bonding in the solid state, even though infrared (IR) spectroscopy may be used to establish if a hydrogen bond exists and the relative strength of different hydrogen bonds [14]. For aromatic molecules of the same backbone, theoretical calculations can give valuable information for the relative strength of different donors in bonding to H atom. For example, molecular

dynamics simulations in the gas phase revealed that compounds **1** (**HB-9**) and **2** (**HB-10**) are primarily engaged in hydrogen bonding, whereas for **3** (**HB-11**), only about 29 % of all calculated conformations are intramolecularly hydrogen bonded [33]. In methanol, the number of other flexible conformations increases for all three compounds. In more polar aqueous solution, the percentage of the hydrogen bonded conformations is reduced to 52, 43, and 3.7 %, respectively. These results are consistent with the strength of O, F, and S atoms as hydrogen bonding acceptor.

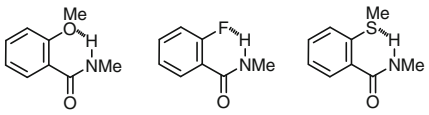

1 (**HB-9**) **2** (**HB-10**) **3** (**HB-11**)

In solution, ^{1}H NMR spectroscopy is the most important tool for studying hydrogen bonding. If intermolecular interactions are absent, the formation of intramolecular hydrogen bonding should be concentration-independent. However, the stability of intermolecular hydrogen bonding highly depends on the concentration. The formation of intermolecular hydrogen bonding can cause the signals of NH and OH protons to shift downfield to a large range in ^{1}H NMR. Diluting the solution may weaken the hydrogen bonding and consequently cause the signal to shift upfield. When the dilution is allowed in a large range of concentration, the chemical shift-concentration correlation can be used to determine the equilibrium constant of the hydrogen bonding by non-linear regression [34]. For hydrogen bond formed by two different components, increasing the concentration of the acceptor component can also force the signal of the proton to shift downfield, which has also been frequently used for evaluating its equilibrium constant [35].

1.1.4 Hydrogen Bonding Formed by a Single Functional Group

Although many weak hydrogen bonds can be observed in crystals, in solution strong hydrogen bonds formed by the NH and OH groups are most common for controlling the formation of supramolecular architectures. In the crystal of ice, one H atom forms one hydrogen bond, while one O atom accepts two H atoms. Thus, one molecule is engaged in four H-bonds. In liquid water, one molecule forms about 3.5 H-bonds. Alcohols have an apolar aliphatic group that is not able to interact with the OH group. The crystal structures of methanol (**HB-12**) and ethanol (**HB-13**) show that one molecule forms only two hydrogen bonds. The data, throughout the chapter, represent the distance (in Å) between the H and the H-bonded atom. That is, OH, as both the donor and acceptor, is hydrogen bonded to

two neighboring OHs [36]. Considering the movement of the molecules, in liquid phase, they and other longer alcohols should not be able to form more hydrogen bonds in the solid state. In co-crystals with water, their OH unit exclusively behaves as donor to form hydrogen bonding with water O atom.

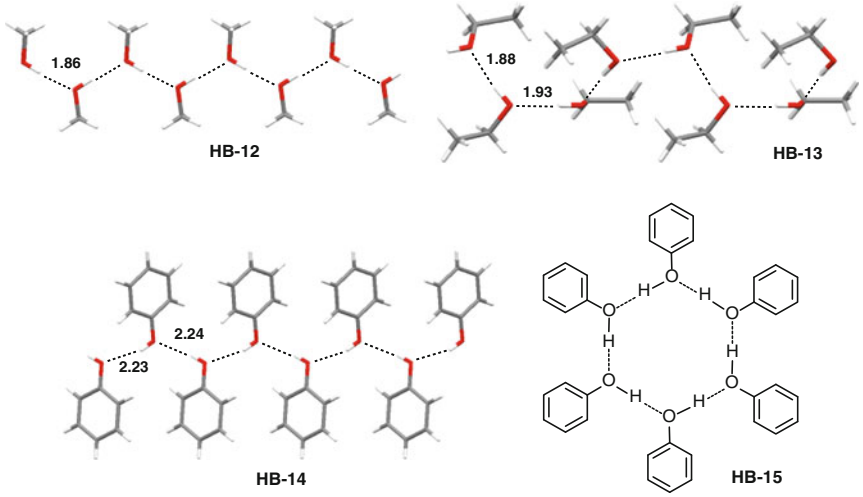

In crystals, phenol also forms a linear packing pattern in which the one molecule is hydrogen-bonded to two neighboring molecules (**HB-14**) [37]. Although a cyclic hexameric hydrogen bonding pattern (**HB-15**) was proposed [38], the pattern has not been confirmed experimentally. Thus, for hydroxyl compounds, it is general that one molecule forms two hydrogen bonds, although the geometry of the hydrogen bonds may be changed depending on the size and shape of the molecules and if other non-covalent interactions exist.

Acids typically form dimers which are stabilized by two O–H···O=C hydrogen bonds. The eight-membered dimer (**HB-16**) is planar and thus, for rigid aromatic acids, the two aromatic rings are forced to stay in a straight line. This directionality is the key for the self-assembly of ordered supramolecular structures from aromatic acids. For dicarboxylic acid, such as terephthalic acid (**HB-17**), it would lead to the formation of infinite repeating packing structures. For benzene-1,3,5-tricarboxylic acid and its analogues, it would drive them to produce porous honeycomb-styled networks (**HB-18**) [39]. When acetic acid is present, a heterodimer may be formed [40], implying that their ability of dimerizing is comparable. Although the eight-membered hydrogen bonding dimer is robust, it has been reported that water (**HB-19**), alcohol, DMSO, or phenol (**HB-20**) can disrupt it by forming expanded hydrogen bonding rings [41].

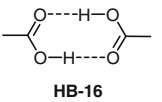

HB-16

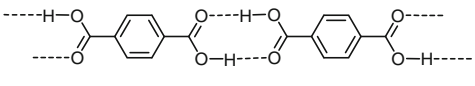

HB-17

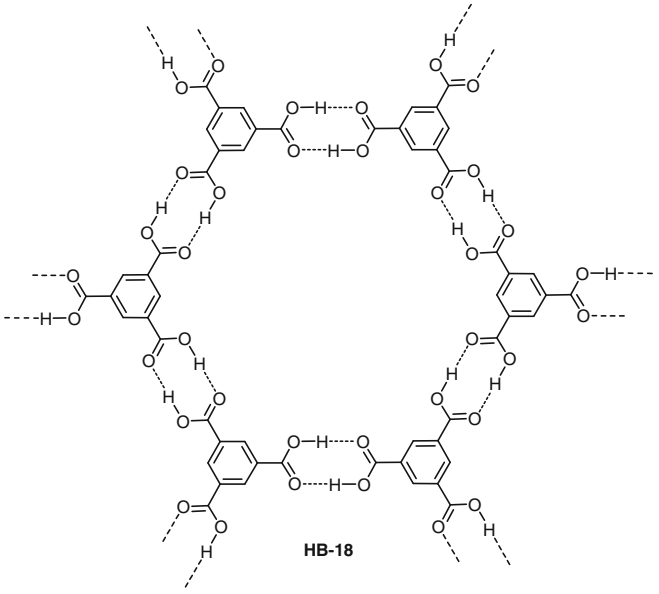

HB-18

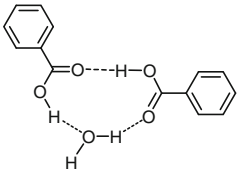

HB-19

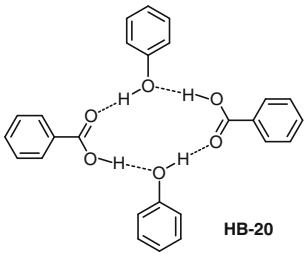

HB-20

Amides are the most important compounds for hydrogen bonding-related studies. For both aliphatic and aromatic amides, it is common that the amide unit prefers to form an eight-membered dimer which is stabilized by two N–H···O=C H-bonds, as evidenced by the crystal structures of acetamide (**HB-21**), butamide (**HB-22**), and benzamide (**HB-23**). Another amide H atom is further hydrogen bonded to the O atom of neighboring molecules to produce a hydrogen bonding chain. For diamides, hydrogen bonding patterns are more complicated in the solid state. The molecules of malonamide pack through successive trimeric eight-membered hydrogen bonding ring (**HB-24**), while 2-methylmalonamide (**HB-25**) gives rise to the typical eight-membered dimer pattern, as observed for the simple amides.

We may expect that the conformation, shape, and substituents of the molecules can all impose an important influence on the packing.

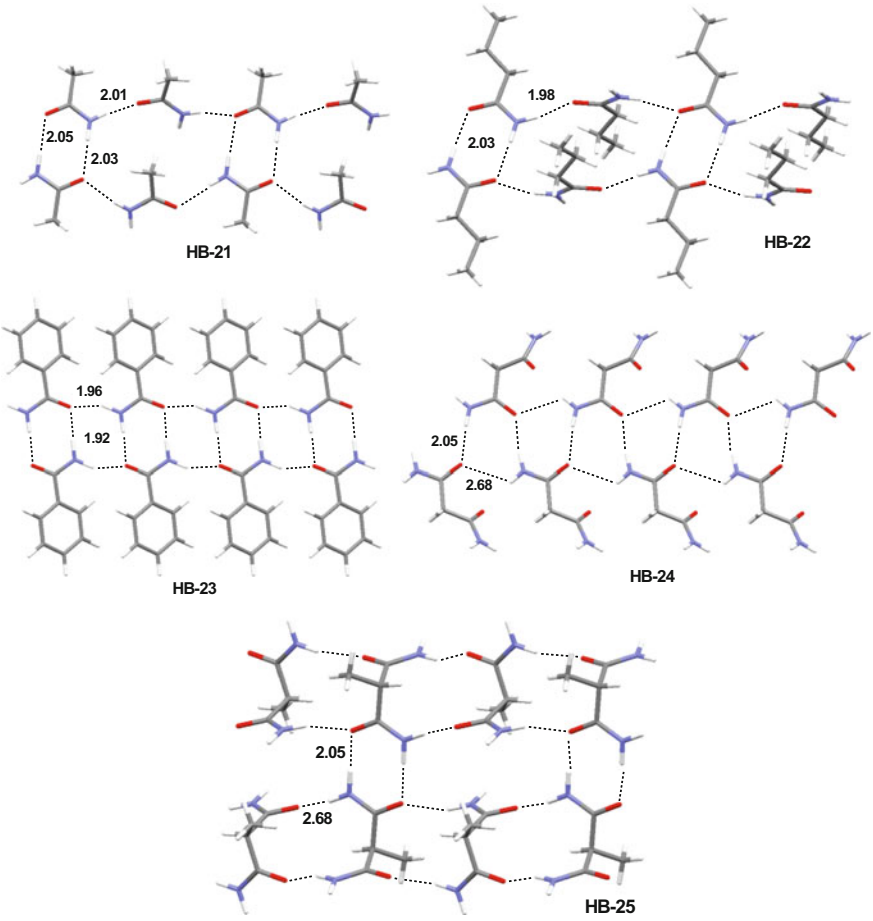

Generally, for secondary amides, the amide unit can form two N–H···O=C hydrogen bonds, with the H and O atoms acting as donor and acceptor, respectively. However, the hydrogen bonding patterns are different. Most typically, a linear hydrogen bonding chain is formed, as observed in the crystal structures of *N*-phenylacetamide (**HB-26**), *N*-benzylformamide (**HB-27**), and *N*-phenylbenzamide (**HB-28**). However, other binding patterns may exist. For example, *N*-phenylformamide gives rise to a cyclic tetramer (**HB-29**), which is stabilized by intermolecular N–H···O=C H-bonds [42].

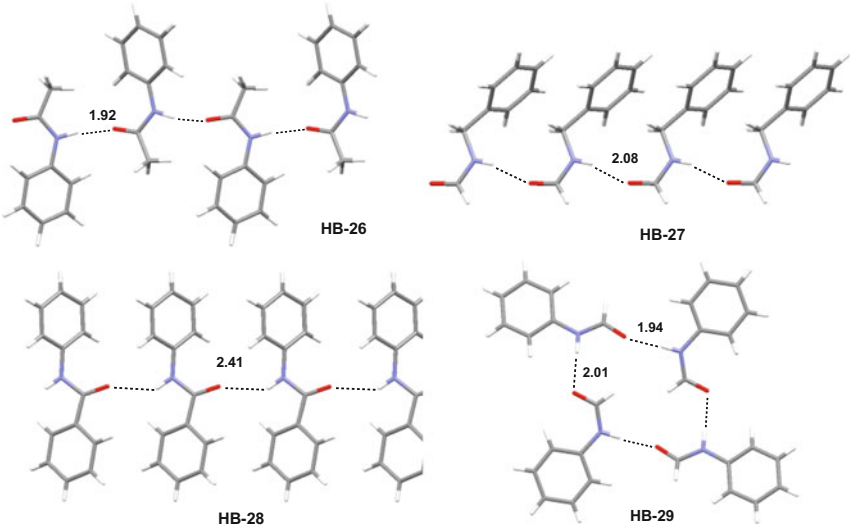

Urea has four H atoms and one O atom. In single crystals, all the H atoms are engaged in intermolecular hydrogen bonding. As a result, one O atom accepts four H atoms (**HB-30**). In the plane defined by the molecule, the O atom forms bifurcated hydrogen bonds with the two inner H atoms of another molecule. This three-center interaction induces the molecules to pack into a planar band. The neighboring bands are perpendicular and held by another two H-bonds formed between the two outer H atoms and the O atoms of two molecules in the two neighboring bands. For *N*-methyl (**HB-31**), *N*-ethyl (**HB-32**), and *N*-phenyl (**HB-33**) ureas, the typical bifurcated hydrogen bonds are also formed, but the hydrogen bonded molecules are not located in one plane and for the ethyl derivative, the neighboring molecules are nearly perpendicular to each other. Again, their outer H atom forms another hydrogen bond with the neighboring molecule. Thus, generally one molecule can form three hydrogen bonds for such mono-substituted ureas. The NH···O distances of the ethyl derivative are generally longer than those of the methyl derivative, reflecting the larger size of ethyl. Both *N*,*N*′-dimethyl (**HB-34**) and *N*,*N*′-diphenyl (**HB-35**) ureas also form the bifurcated hydrogen bonding. All these results demonstrate the robustness of this hydrogen bonding pattern. Because all the NH atoms are engaged in hydrogen bonding and there is only one O atom available, the O atom accepts all the H atoms to form up to four hydrogen bonds. However, in the presence of strong hydrogen bonding acceptors, such as water, carboxylate, and pyridine (**HB-36**), this hydrogen bonding may be disrupted to produce other stronger hydrogen bonding [43].

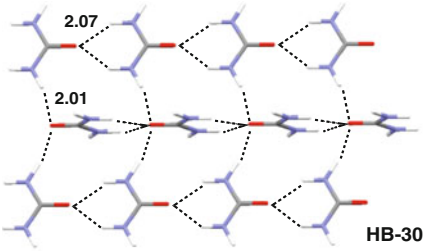

HB-30

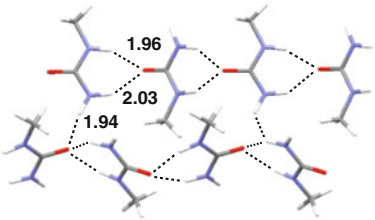

HB-31

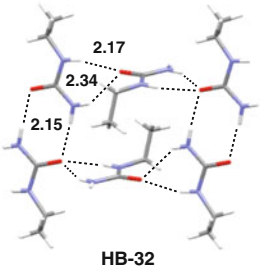

HB-32

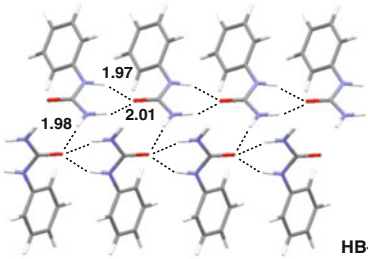

HB-33

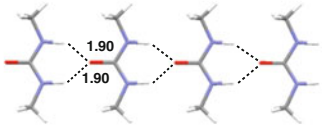

HB-34

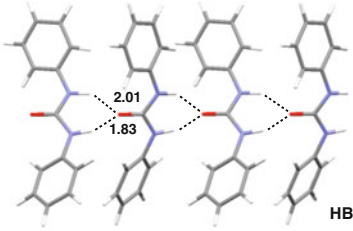

HB-35

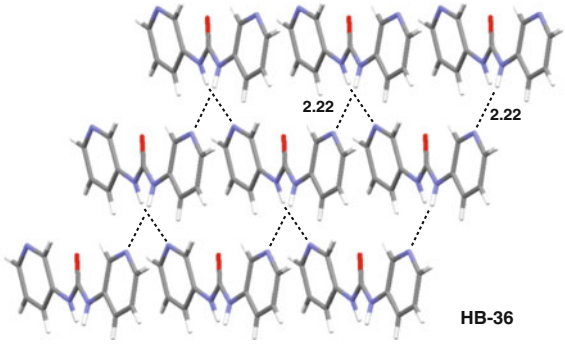

HB-36

Thioureas can also form strong N–H···S=C hydrogen bonding. This character has been utilized for the development of a variety of organocatalysts on the basis of the fact that thiourea H is strong hydrogen bonding donor [44]. In crystals, thiourea displays a complicated packing pattern (**HB-37**). The two outer H atoms form two eight-membered hydrogen bonds with the neighboring molecules. The hydrogen bonding drives the molecules to form a planar zigzag band. The S atom is further

engaged in symmetric bifurcated hydrogen bonds with another molecule which is located on the top of its molecule backbone and thus these two bonds have a very large angle (93°). In the crystal of methyl thiourea (**HB-38**), from the two sides of the C=S double bond, two pairs of eight-membered H-bonds are generated, while the *trans* H atom is further hydrogen bonded to the S atom of another molecule, with an angle of 85°. For *N*,*N*-dimethyl thiourea (**HB-39**), the *cis* H atoms of two molecules form a pair of eight-membered H-bonds, and the *trans* H atom is engaged in another hydrogen bond to hold the molecules together with the neighboring molecules which are nearly perpendicular to each other. For both *N*,*N*′-diethyl (**HB-40**) and *N*,*N*′-diisopropyl (**HB-41**) thiourea, in crystals, one R alkyl group is located on the side of the C=S double bond. Thus, the bifurcated hydrogen bonding is not observed. The two molecules pack similarly. Two molecules dimerize by forming an eight-membered hydrogen bonding ring and another H atom forms a single hydrogen bond with another molecule from the top of its C=S double bond. *N*,*N*′-diphenyl thiourea does exhibit the bifurcated hydrogen bonding pattern (**HB-42**), which drive the molecules to arrange in a zigzag style. Different from the urea analogue (**HB-36**), for which the bifurcated hydrogen bonding occurs in a co-planar manner, the H atoms approach the S atom from the direction perpendicular to the thiourea plane. Such a large tendency of thiourea derivatives may be rationalized by considering the large size of the S atom and its hexavalent nature.

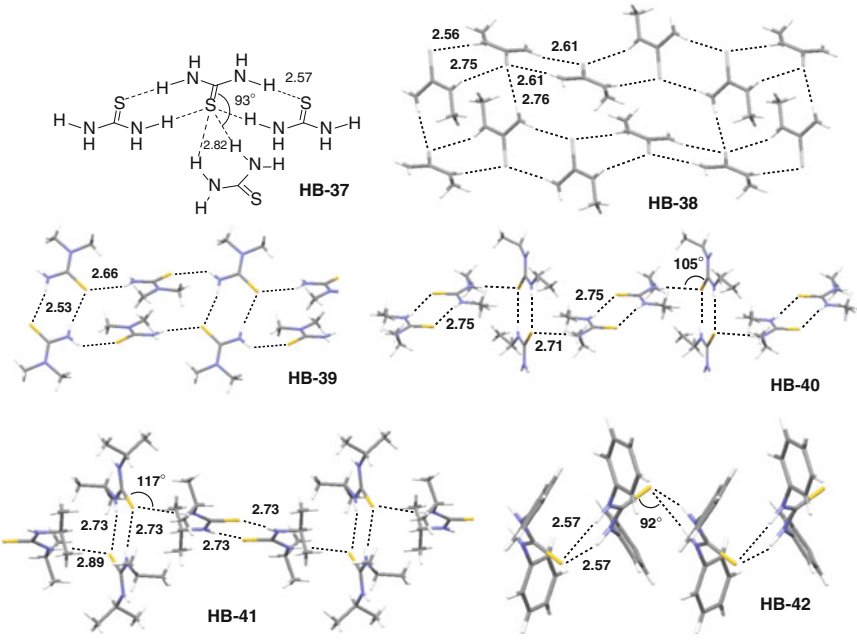

In the presence of electron-withdrawing atoms or groups, the polarity of the C–H bond may be strengthened and its ability to behave as a hydrogen bonding donor

increased. For example, compared to dichloromethane, chloroform is a much stronger hydrogen bonding acceptor. 1,2,3-Triazole is planar and has a strong dipole moment of approximately 5 D, which is even higher than that of amide (~ 3.3–4.0 D). Thus, its C^5–H atom is able to engage in varying hydrogen bonds in the solid state [19]. For example, 4-phenyl-1,2,3-triazole gives rise to both C^5–H···N^3 and N^2–H···N^1 hydrogen bonds (**HB-43**) [45]. Both 1,4-(**HB-44**) [46] and 2,4-disubstituted (**HB-45**) [47] 1,2,3-triazole can also form an intermolecular C^5–H···N^3 hydrogen bond. For 4-anthracenyl 1,2,3-triazole (**HB-46**) [48], C^5–H···π interaction has been observed [49]. In the crystal structure of a tetrahedronal compound, intermolecular C^5–H···F hydrogen bonding has been revealed (**HB-47**). In the presence of a CHF_2 group, the F atom may serve as hydrogen bonding acceptor to form C^5–H···F hydrogen bonding (**HB-48**), while the N^2 and N^3 atoms of triazole are engaged in bifurcated N···HCF_2— hydrogen bonding [50]. It is expected that the F atoms increase the acidity of the difluoromethyl H atom and the two different hydrogen bonds promote each other.

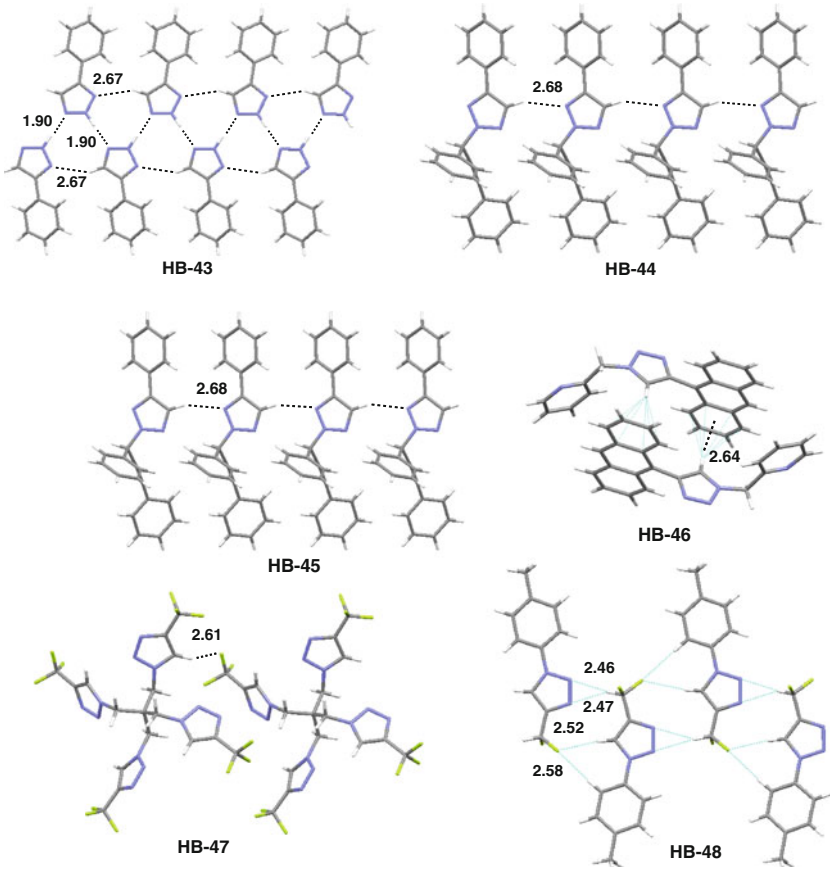

1.2 Intramolecular Hydrogen Bonding

1.2.1 The O–H···X Hydrogen Bonding

The OH unit is strong as hydrogen bonding donor and acceptor. As demonstrated in the previous section, intermolecular hydrogen bonding is common for alcohols, phenols, and carboxylic acids. In the solid state, linear aliphatic alcohols and acids containing two OH groups or one OH group and another hydrogen bonding acceptor tend to form intermolecular hydrogen bonding, as observed for ethanediol, propane-1,3-diol, malonic acid, and succinic acid. For rigid or preorganized molecules, intramolecular H-bonding may be favored. For example, in the crystal structures of 1,2-dimethyl cyclobutane-1,2-diol (**HB-49**) and cyclohexane-1,2-diol (**HB-50**), intramolecular O–H···OH hydrogen bonding is observed, in addition to the normal intermolecular ones. For phenols and analogues, when a hydrogen bonding acceptor exists at the ortho-position, an intramolecular O–H···X (mainly O) hydrogen bonding is formed, as exhibited by the crystal structures of maleic acid (**HB-51**), 2-nitro-5-chlorophenol (**HB-52**), salicylaldehyde (**HB-53**), salicylic acid (**HB-54**), 2-methoxy-4-hydroxymethylphenol (**HB-55**), and 2-methoxy-3-nitrophenol (**HB-56**). For salicylic acid, the carboxylic OH may also form a similar six-membered hydrogen bond with the phenol O atom. However, this does not happen. Instead, the carboxylic acid forms the typical eight-membered hydrogen bonds.

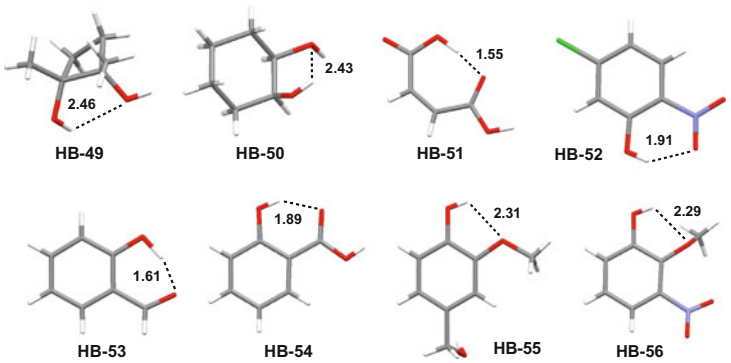

1.2.2 The N–H···X Hydrogen Bonding

The intramolecular N–H···O=C hydrogen bonding formed by aliphatic amides plays a key role in shaping the helix, β–sheet, and turn conformations of both natural and artificial peptides and proteins [51]. Extensive studies on model systems have revealed a large number of intramolecular N–H···O=C hydrogen bonding patterns. The formation of the intramolecular hydrogen bonding always faces the competition of the intermolecular ones, and natural proline, due to the rigidity of its tetrahydropyrrole ring, which has been demonstrated to favor the formation of turns by promoting the formation of the intramolecular hydrogen bonding. Many molecules have been designed to induce the formation of artificial turns [52]. For linear aliphatic diamides, ^{1}H NMR and IR measurements show that, intramolecular interaction is enthalpically favorable in the nine-membered hydrogen-bonded ring (n = 4), compared with other systems (**HB-57a**–**57f**) [53].

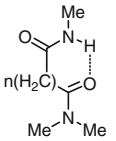

HB-57a: n = 1, **HB-57b**: n = 2
HB-57c: n = 3, **HB-57d**: n = 4
HB-57e: n = 5, **HB-57f**: n = 6

For aromatic amides, the oligomers of 2-aminobenzoic acid have been revealed to form six-membered intramolecular N–H···O=C hydrogen bonding (**HB-58**) [54]. This intramolecular hydrogen bonding is strong enough to suppress the formation of the intermolecular one. Alkoxyl group at the ortho position of the amide unit can also form stable intramolecular five- or six-membered RO···H–N hydrogen bonding (**HB-59**–**65**) [55]. For **HB-61**, probably due to the steric hindrance of the methyl group, the OH does not form five-membered hydrogen bonding with the neighboring ether O atom. The amide H atom can be engaged in two hydrogen bonds simultaneously (**HB-66**). This three-center hydrogen bonding pattern is the basis for the creation of a large number of arylamide foldamers [14, 56]. Although alkoxyl O atom is widely used, quinone and carbonyl O atoms are also strong as hydrogen bonding acceptors [14].

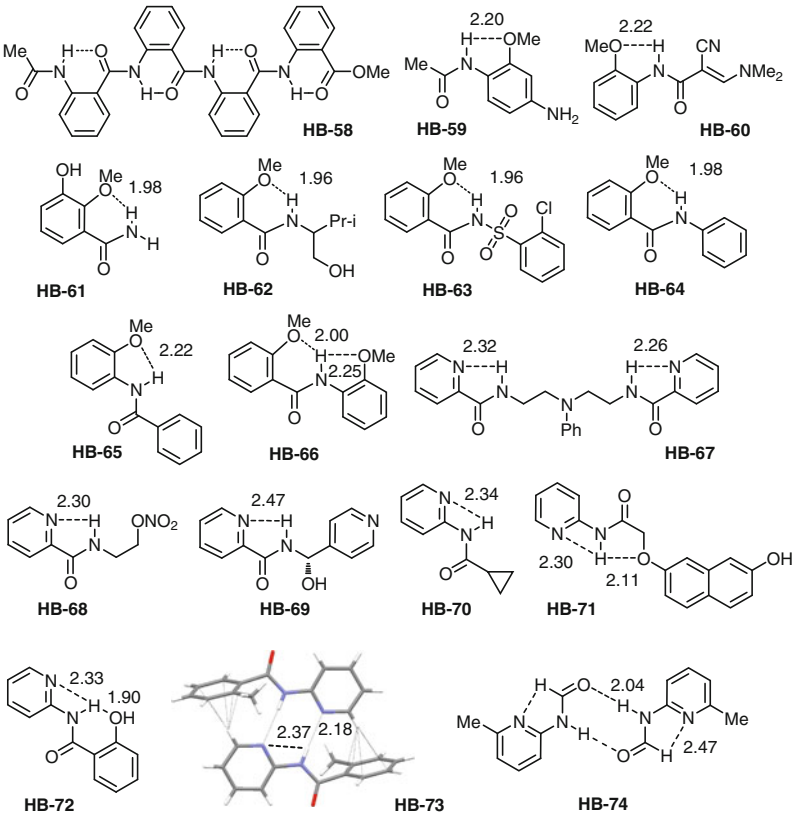

Picolinamide and *N*-(2-pyridyl)amide derivatives also form five- and four-membered N–H···N hydrogen bonding with the N atom of the heterocycle as acceptor (**HB-67–74**) [57]. Further dimerization may take place through forming six-membered N–H···N double hydrogen bonds (**HB-73**). For formamide derivatives, the intramolecular four-membered N–H···N hydrogen bonding may be broken. Instead, they favor the eight-membered N–H···O=C hydrogen bonding (**HB-74**), which may be promoted by the intramolecular five-membered O=C–H···N(py) hydrogen bonding.

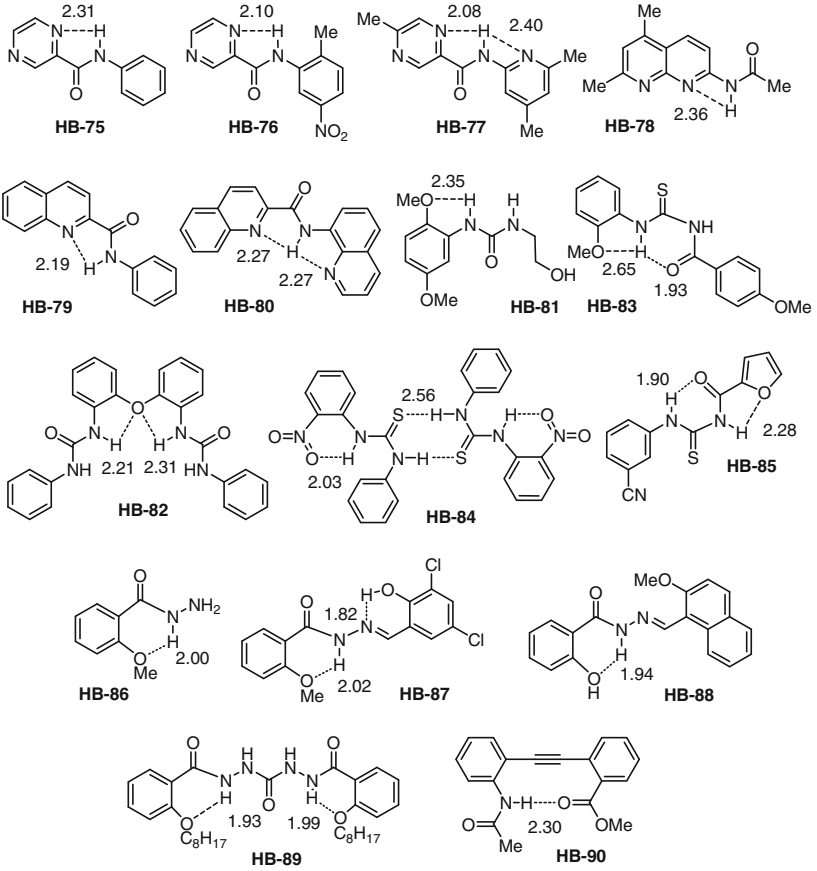

The N atom in other heterocycles, such as pyrazine (**HB-75–77**), 1,8-naphthyridine (**HB-78**), quinoline (**HB-79,80**), and pyrido[3,2-g]quinoline, can also serve as hydrogen bonding acceptor. Incorporation of these hydrogen bonding units to long linear molecules could induce the backbones to produce hollow cavity of varying size for entrapping different guests [14, 58–60]. Other amide analogues, such as urea (**HB-81**,**82**), thiourea (**HB-83–85**), and hydrazide (**HB-86–89**) derivatives, can also behave as donors to form similar hydrogen bonding [14, 61]. All the above intramolecular hydrogen bonds are four-, five- or six-membered. Phthalamide and *N*,*N*′-(1,2-phenylene)diacetamide derivatives are not able to form intramolecular seven-membered N–H···O=C hydrogen bonding due to large steric hindrance. However, for 1,2-diphenylethyne derivatives (**HB-90**), ten-membered N–H···O=C hydrogen bonding is stable in both the solid state and solution [62].

The electronegativity of halogen atoms is all obviously larger than that of the H atom. However, due to its low polarizability and tightly contracted lone pairs, the F atom is unable to compete with the O or N atom, which is the stronger H-bond

acceptor. For aliphatic compounds, only when the approach of the H atom to other better acceptor atoms is sterically hindered, hydrogen bonds with F as acceptor may be observed [63]. For *N*-phenylamides, the F atom at the 2-position of the benzene ring readily forms intramolecular N–H···F hydrogen bonding (**HB-91**–**92**). For **HB-91**, only the amide forms the intramolecular five-membered N–H···F hydrogen bonding [64]. No similar hydrogen bonding was observed for the ammonium H atoms, which are engaged in intermolecular hydrogen bonding with the carboxylate O atoms. For **HB-93**, a three-center N–H···F hydrogen bonding pattern is exhibited [28]. The crystal of *N*-(2-fluoro)phenyl 2-phenylacetamide gives rise to two conformers. In one of them, the five-membered N–H···F hydrogen bonding is formed (**HB-94**) [65]. In another one, intramolecular F···O=C contacting is observed (**HB-94′**). For both conformers, the amide unit forms strong intermolecular N–H···O=C hydrogen bond (H···O distance = 1.91 and 1.88 Å, respectively). These results show that in the presence of other strong interactions, the five-membered N–H···F hydrogen bonding may be broken.

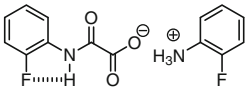

HB-91

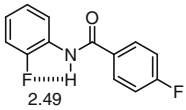

HB-92

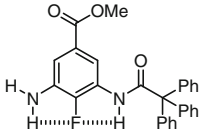

HB-93

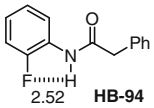

HB-94

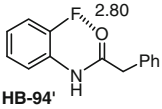

HB-94'

Crystal structures of several 2-fluorobenzamides have also been reported (**HB-95**–**99**) [28, 66]. All these compounds give rise to six-membered N–H···F hydrogen bonding. Similar to the alkoxyl analogues, three-center hydrogen bonding can also be formed for *N*-phenyl arylamides (**HB-100**–**102**). In the crystal structure of a macrocycle containing four 2-fluoroisophthalamide units, only two F atoms are engaged in the six-membered H-bonding (**HB-103**), while the other two are not, this is due to the steric tension of the macrocycle [67]. In the crystal structure of another amide bearing six F atoms (**HB-104**), six-membered N–H···F hydrogen bonding is formed, while the expected five-membered one is not [68]. Instead, this F atom and the carbonyl O atom are engaged in bifurcated hydrogen bonding with the OH unit of another molecule. Thus, three different hydrogen bonds are generated in the crystal. The result shows that the molecular conformation formed in the crystal is the outcome of the competition of different intra- and intermolecular interactions.

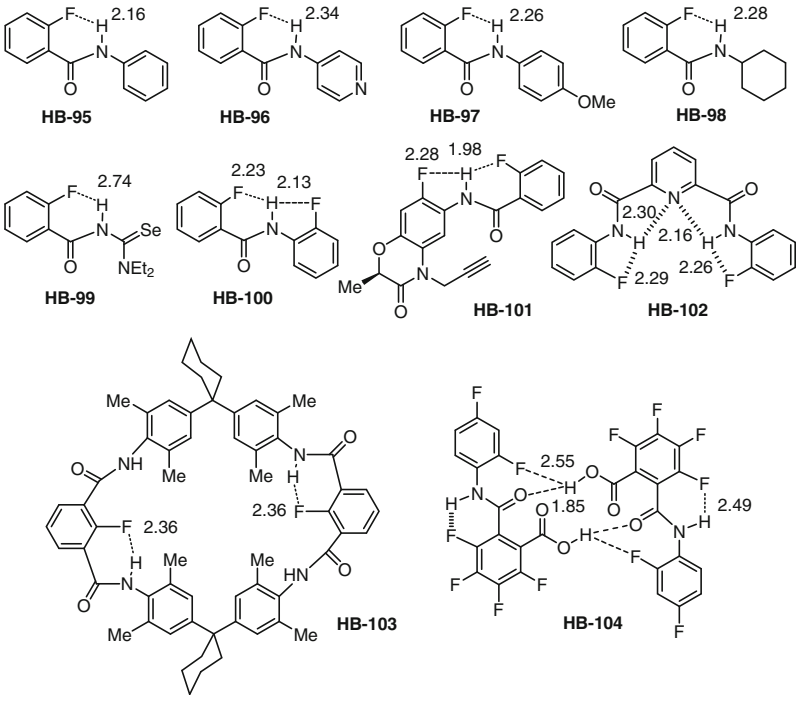

N-(2-Chloro)phenyl amides also readily form five-membered N–H···Cl hydrogen bonding (**HB-105**–**112**) [69], and the amide unit also forms intermolecular N–H···O=C hydrogen bonding. For all the compounds, the Cl or Br atoms at the α-position of the acetyl group do not involve intramolecular or intermolecular interactions.

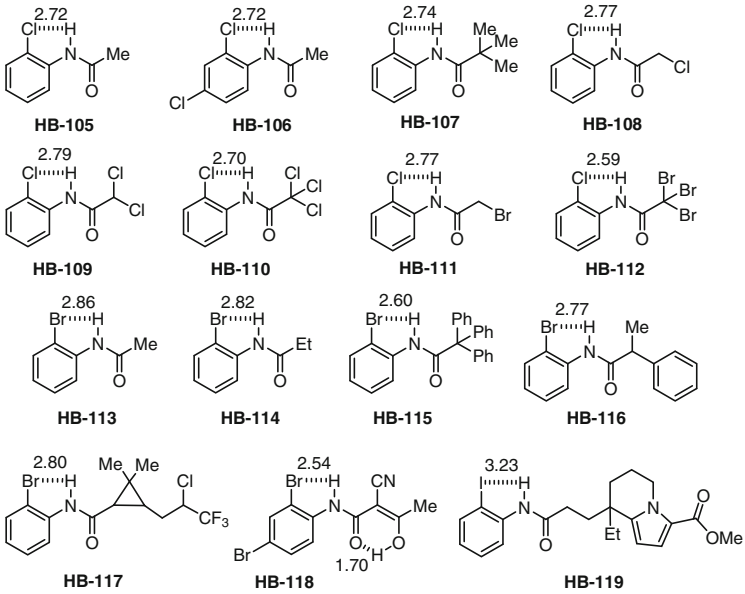

Similar five-membered N–H···X (X = Br, I) hydrogen bonding can be observed in many bromo- and iodo-substituted amides (**HB-113–126**) [70]. In most cases, the amide unit is also engaged in intermolecular N–H···O=C hydrogen bonding. These compounds bear additional cyano, ester, nitro, and hydroxyl groups that are good hydrogen bonding acceptors, but do not interfere in the formation of the five-membered intramolecular hydrogen bonding. Notably, for a trifluoroacetamide derivative (**HB-125**), one F atom is engaged in five-membered N–H···F hydrogen bonding. Crystal structures of compounds **4–7** are also available, which do not exhibit similar five-membered intramolecular hydrogen bonding with the halogen atoms serving as acceptors. Instead, the Cl atom of **4** and **5** forms weak intramolecular Cl···O halogen bonding.

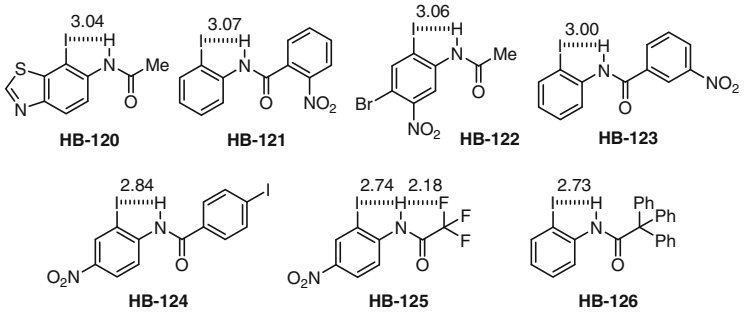

Many of 2-chloro, 2-bromo or 2-iodobenzamide derivatives do not form intramolecular six-membered N–H···X (X = Cl, Br, I) hydrogen bonding in the solid state, as demonstrated by compounds **4–18**. In the absence of other important interactions, the intermolecular N–H···O=C hydrogen bonding dominates the packing of the molecules, which causes a large torsion of the amide unit from the connected benzene ring and thus suppresses the formation of the intramolecular N–H···X (X = Cl, Br, I) hydrogen bonding. Actually, in the crystal structures of several compounds (**4**, **5**, **7**, **8**, **12–15**, **17**), weak intramolecular O···X (X = Cl, Br, I) halogen bonding is exhibited. Compound **9** bears large triphenylmethyl and admantyl groups, which, however, are not able to suppress the intermolecular the N–H···O=C hydrogen bonding [70]. The strong intramolecular N–H···O hydrogen bonding of **17** prevents it from forming intermolecular N–H···O=C hydrogen bonding, while compound **18** dimerizes through two N–H···N hydrogen bonds, which also inhibits the N–H···O=C hydrogen bonding. Even so, the intramolecular N–H···I hydrogen bonding is not formed, reflecting the weakness of the I atom in engaging in hydrogen bonding.

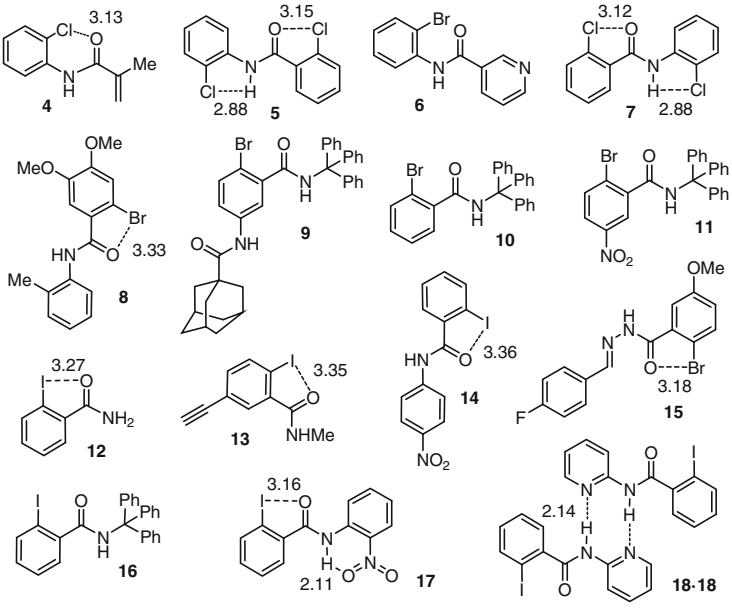

A number of 2-chloro, 2-bromo, and 2-iodobenzamides give rise to the six-membered intramolecular N–H···X (X = Cl, Br, I) hydrogen bonding in the crystal structures (**HB-127**–**140**). The carbamothio (**HB-127–129**, **HB-136**) and benzothiazo (**HB-130**) derivatives further form eight-membered N–H···S=C or N–H···N hydrogen bonding dimer, which inhibits the intermolecular N–H···O=C hydrogen bonding. The large triphenylmethyl group produces steric hindrance and thus weakens the N–H···O=C hydrogen bonding of related compounds (**HB-131**, **HB-137**–**139**) [70]. For compounds that form the three-center hydrogen bonding patterns (**HB-132**–**134**, **HB-140**), another intramolecular hydrogen bonding is stronger, which is expected to stabilize the six-membered N–H···X (X = Cl, I) hydrogen bonding by suppressing the intermolecular N–H···O=C hydrogen bonding. Compound **5** does not form the six-membered N–H···Cl hydrogen bonding, but its analogue which bears a Cl atom at the 3-position of the aniline ring does (**HB-132**), although this Cl atom does not form any intra- or intermolecular interactions, reflecting the complexity of molecular packing in the solid state. The Cl···HN distance (2.23 Å) of the six-membered N–H···Cl hydrogen bonding **HB-133** is substantially shorter than that of other similar hydrogen bondings. It is expected that the intramolecular strong O–H···O=C hydrogen bonding promotes it by increasing the co-planarity of the backbone.

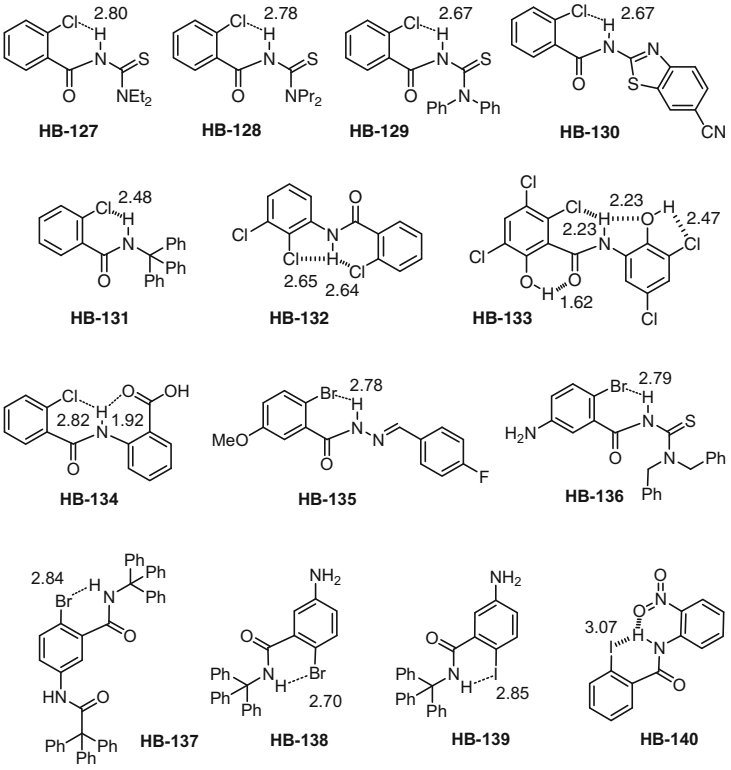

Although halogen atoms in aliphatic molecules have been demonstrated to be very weak hydrogen bonding acceptors, the crystal structures of a number of 2-fluoro and 2-chloroacetamides exhibit the formation of intramolecular five-membered N–H···X (X = F, Cl, Br) hydrogen bonding (**HB-141**–**155**). In the crystal structures of all these amide molecules, intermolecular N–H···O=C hydrogen bonding is also observed. The 2-chloro-2-difluoroacetamide derivative shows the formation of the five-membered N–H···F hydrogen bonding, reflecting the greater ability of the F atom as hydrogen bonding acceptor compared with the Cl atom. The crystal structures of several dichloroacetamides, bromoacetamide, and iodoacetamide (**19**–**25**) are also available, which do not form similar intramolecular five-membered hydrogen bonding, reflecting the weakness of these halogen atoms in forming hydrogen bonding.

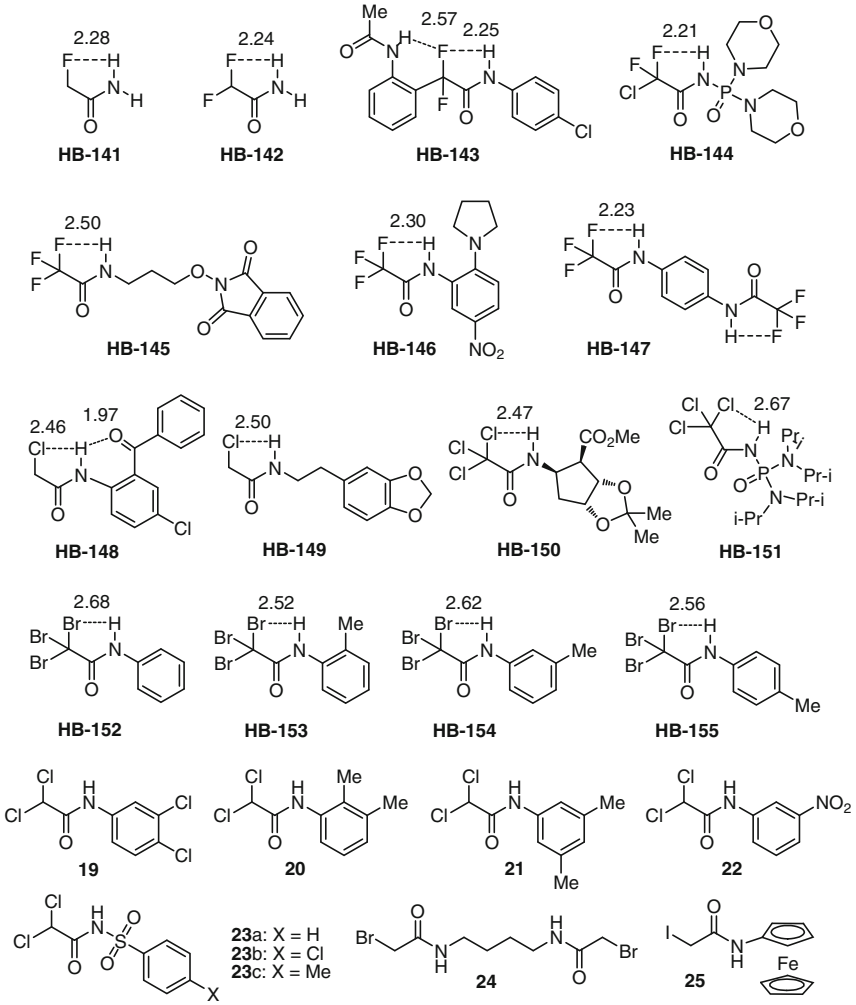

Intramolecular five- and/or six-membered N–H···SR hydrogen bonding has been observed in the crystal structures of several arylamides (**HB-156–161**) [17]. The three-center hydrogen bonding pattern of **HB-162** has been proposed to play a key role in preorganizing the conformation and thus in endowing the anti-bacterial activity of the diamide compound [71]. Although pyridine-2,6-dicarboxamide and isophthalamide derivatives produce two pairs of three-center hydrogen bonds (**HB-161**,**162**), only one methylthio group is engaged in the six-membered N–H···S hydrogen bonding (**HB-163**) [72], again reflecting the lower stability of this hydrogen bonding pattern compared with the five-membered one. The five-membered N–H···S hydrogen bonding has also been observed for thioesters (**HB-164**,**165**). Interestingly, in the crystal structure of the molecule bearing two triphenylmethyl groups, four conformers are generated [72], two of which lack the five-membered N–H···S

hydrogen bonding. Compounds **26** and **27** do not form the six- or five-membered N–H···S hydrogen bonding.

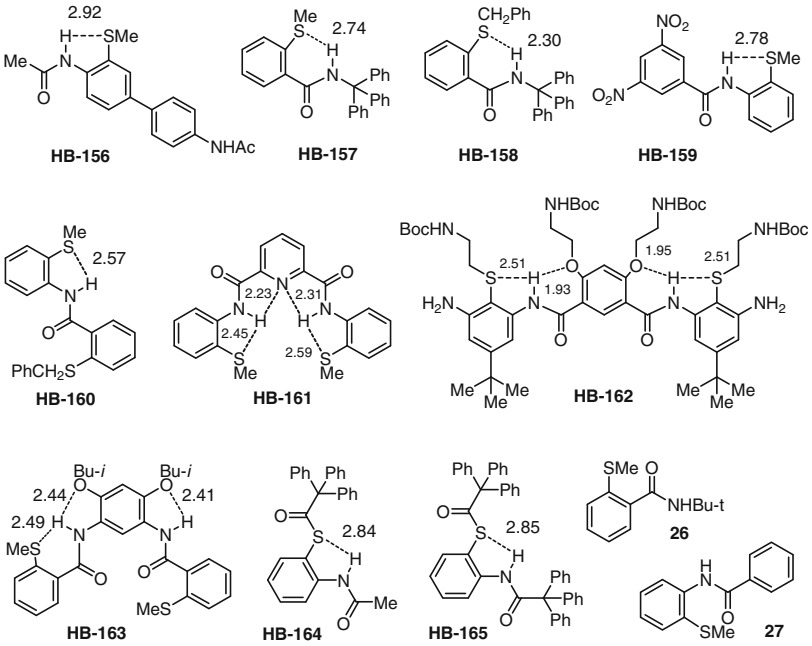

Generally, for arylamide derivatives, the five-membered N–H···X (X = Cl, Br, I) hydrogen bonding is more stable than the six-membered one, which is also evidenced by ^{1}H NMR experiments in solution [69]. Given the complexity of chemical, steric, and electronic environments of the hydrogen bonding acceptors at the two different positions, this observation does not simply suggest that the former hydrogen bonding is stronger than the latter. One straightforward reason for this difference is that the formation of a six-membered hydrogen bond requires the confinement of the rotation of three single bonds, while the formation of a five-membered one needs to confine only two.

The C^{5}–H atom of 1-phenyl or 4-phenyl 1,2,3-triazoles can also form intramolecular six-membered hydrogen bonding, which has been confirmed by the crystal structures of a number of compounds (**HB-166–173**) [29, 73]. Both alkoxyl O and F atoms can behave as the acceptor. Probably due to the structural symmetry, the molecules in the crystal of 1,2-di(2-fluorophenyl)-1,2,3-triazole are arranged alternately [73]. As a result, the N-1 and C-4 atoms appear at two identical positions with 50 % probability. In the crystal structures, the hydrogen bonding from the N-1 side is generally weak, which should be attributed to the electrostatic repulsion of the N-1 atom for the approaching acceptor at the ortho-position of the connected benzene ring. Three-center H-bonding pattern can also be generated (**HB-168** and **HB-171**). For pentafluorophenyl derivate, the six-membered hydrogen bonding is formed only

from the C-4 side [29], again reflecting the difference of the two hydrogen bonds. The pentafluorobenzene ring at N-4 is distorted remarkably from the triazole ring, which should be resulted from the electrostatic repulsion between the N-2 atom and the F atom at the 2- or 6-position [29]. The six-membered C–H···Cl hydrogen bonding can also be formed (**HB-173**) from the C-4 side [29]. ^{1}H NMR dilution experiments in $CDCl_3$ show that both Cl and Br can form similar six-membered hydrogen bonding from two sides when the intermolecular N–H···O=C hydrogen bonding is absent [29]. The crystal structure of a pyridine derivative shows two intermolecular N–H···Cl hydrogen bonds with the solvent dichloromethane (HB-174) [74]. Although the pyridine N atom is orientated on the same side, it does not form intramolecular C–H···N hydrogen bonding due to the rigidity of the backbone. Thus this orientation should be driven by the co-planarity of the aromatic backbone and the electrostatic repulsion between the pyridine N atom and the N-3 atoms of the triazole [75].

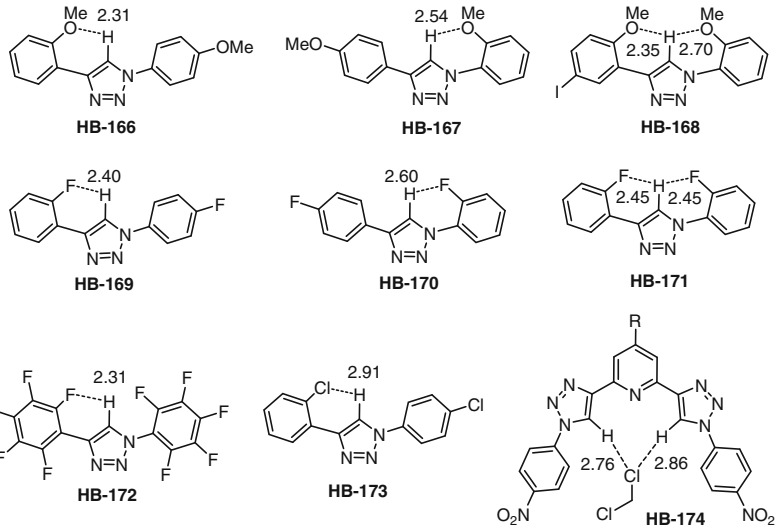

1.3 Intermolecular Hydrogen Bonding

1.3.1 Double Hydrogen Bonding

The intermolecular hydrogen bonding of the hydroxyl group is the strongest single non-covalent bonding for alcohols and phenols (**HB-12–14**). For acids (**HB-16**), amides (**HB-21–23**, **HB-25**) and thioureas (**HB-37–41**), eight-membered double hydrogen bonding is common, whereas ureas can form bifurcated double hydrogen bonding (**HB-30–35**), which is an important binding motif for the formation of supramolecular architectures. Two different groups can also form double hydrogen

bonding to afford heterodimers. The adenine-thymine base pair is the basic binding motif of double hydrogen bonding in life. In supramolecular chemistry, double hydrogen bonding motifs are usually not strong enough to drive the formation of stable architectures in solution. However, the double hydrogen bonding of two or more amides and ureas can work in a cooperative manner to drive the formation of many ordered supramolecular architectures [14, 76, 77].

1.3.2 Triple Hydrogen Bonding

Triple hydrogen bonding has received great attention in supramolecular chemistry. Nature uses purines and pyrimidines to construct DNA and RNA base pairs. Guanine and cytosine form the prototypical DDA-AAD triple hydrogen bonding motif. Inspired by Nature's use of azoheterocycles for constructing the base pairs, chemists have developed discrete heterocyclic molecules to build numerous synthetic dimeric motifs [9]. For triple hydrogen bonding, three kinds of motifs, that is, DAD-ADA, DDA-AAD, and DDD-AAA motifs, may be formed. According to the theory of secondary interactions [78], the three kinds of motifs generate four electrostatic repulsions, two electrostatic repulsions and two electrostatic attractions, and four electrostatic attractions, respectively. Thus, generally the stability of the second kind is higher than that of the first, and the stability of the third one is higher than that of the second. The association constants (K_as) of many triply hydrogen bonded heterodimers in chloroform have been determined [78]. For the first kind of motifs, the K_a values vary considerably. The K_a of **HB-175** is only 65 M^{-1}, while that of **HB-176–179** is higher by more than 10 times. Both monomers can be incorporated into one molecule. In this way, ditopic modules can be generated, which exhibit enhanced stability as revealed for **HB-180** [79].

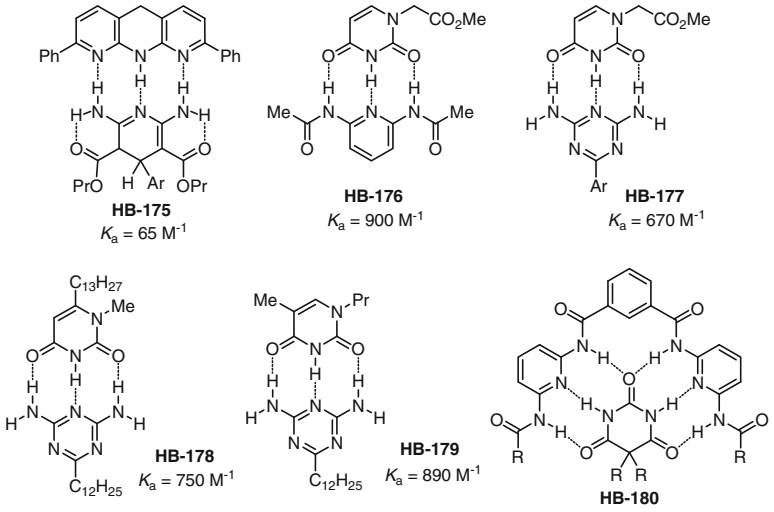

The prototypical DDA-AAD dimer (**HB-181**) has been studied extensively in chloroform [9]. Many DDA and AAD monomers have been designed. Generally, the K_a values of this kind of heterodimers, such as **HB-182** and **HB-183**, are remarkably higher than those of the DAD-ADA motifs, which reflect the important effect of the secondary interactions.

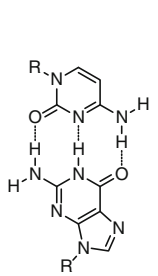

HB-181
$K_a = 10^4$-10^5 M^{-1}

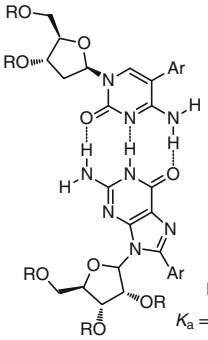

HB-182
$K_a = 1.3 \times 10^4$ M^{-1}

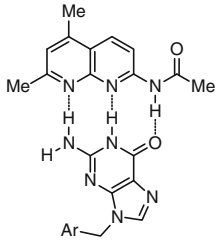

HB-183
$K_a = 10^4$ M^{-1}

Several DDD-AAA triply hydrogen bonded motifs (**HB-184**–**187**) have also been reported [80–82]. The donor monomers were designed on the basis of pyrido[2,3-b] [1, 8] naphthyridine ring, while the acceptor monomers are 1,4-dihydropyridine-2,6-diamine derivative [80, 81] or protonated 2,6-diaminopyridine [82]. The stability of these motifs is all substantially higher than that of the DDA-AAD motifs. Moreover, the stability of the dimers formed by the cationic acceptors (**HB-185** and **HB-187**) is increased remarkably compared to that of the corresponding dimers of the neutral analogues due to the increased electropositivity of the hydrogen atoms. Although secondary interactions are crucial in determining the magnitude of the hydrogen bonding, other factors may also have important effect [83, 84].

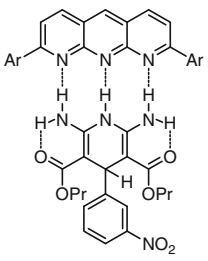

HB-184
$K_a > 10^5$ M^{-1}

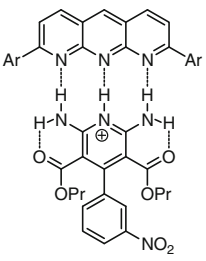

HB-185
$K_a > 5 \times 10^5$ M^{-1}

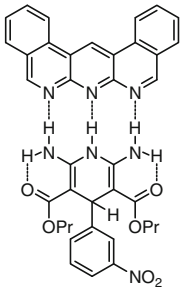

HB-186
$K_a = 2 \times 10^7$ M^{-1}
(CH_2Cl_2, 293 K)

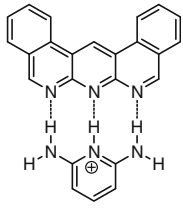

HB-187
$K_a = 3 \times 10^{10}$ M^{-1}
(CH_2Cl_2, 298 K)

1.3.3 Quadruple Hydrogen Bonding

Quadruple hydrogen bonding motifs have found extensive applications in supramolecular self-assembly. ADAD and AADD-typed monomers can form homodimers. For the same series, the stability may vary considerably. The K_a of **HB-188** and **HB-190** is 37 and 170 M^{-1}, respectively, in chloroform [85]. It is expected that the six electrostatic repulsions weaken the hydrogen bonding considerably. When an intramolecular N–H···N hydrogen bonding is introduced, the stability of motifs of the corresponding urea analogues can be increased to 2×10^4 and 2×10^5 M^{-1}, respectively. Clearly, the preorganization of the monomers remarkably enhances the hydrogen bonding. Aromatic hydrazide derivatives have also been synthesized, which can form the ADAD binding motif (**HB-191**), but quantitative study was not performed [86].

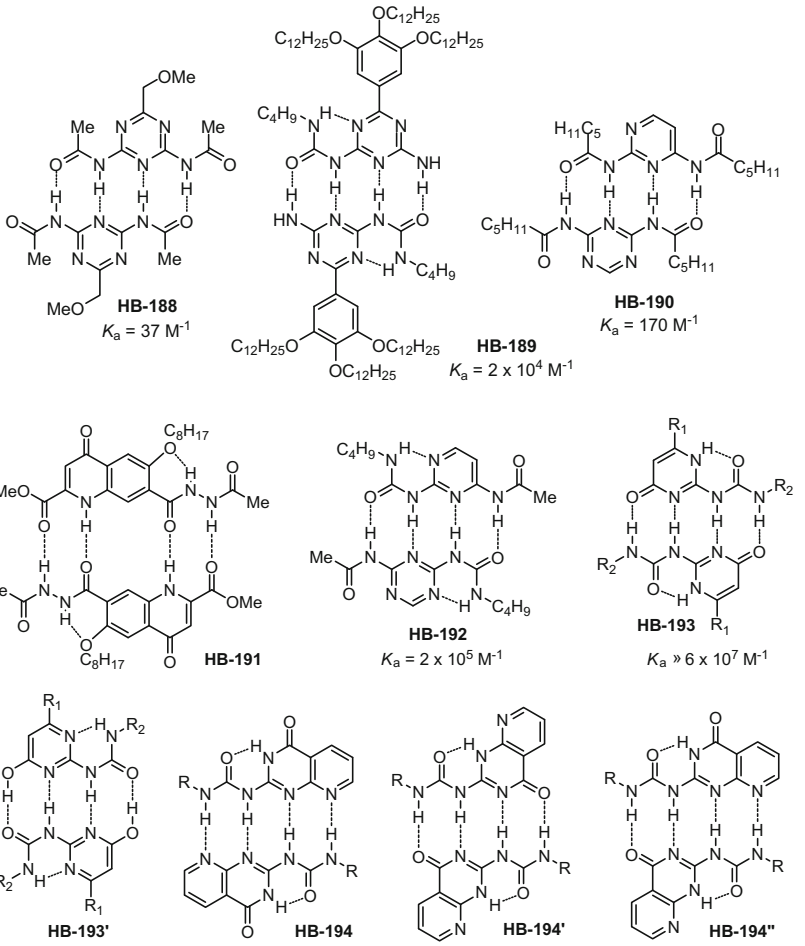

The **HB-193** motif, based on the ureidopyrimidinone backbone, is the most important self-complementary AADD quadruple hydrogen bonding motif [10]. The intramolecular N–H···O hydrogen bonding locks the conformation of the backbone to force the two ureido hydrogen atoms to point to the side of N-3. As a result, the K_a of this binding motif is as high as ca. 6×10^7 M^{-1} in chloroform. The monomers may also exist as 4-hydroxypyrimidine tautomer, the percentage of which depends on the two substituents [10]. Alkylated ureidodeazapterins also form extremely strong AADD homodimers (**HB-194**) [87]. In chloroform saturated with water, its K_a was determined to be 3.0×10^7 M^{-1}. In dried chloroform, the value was increased to be $\geq 5 \times 10^8$ M^{-1}. Again, the monomers may undergo tautomerization. Thus, **HB-194′** and **HB-194″** may also exist in solution.

2-Ureido-1,8-naphthyridine derivatives generate another kind of self-complementary AADD hydrogen bonding motifs (**HB-195**) [88]. However, the K_a is quite low, which may be attributed to the competition of the strong intramolecular hydrogen bonding (**HB-195′**).

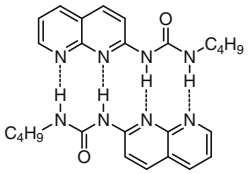

HB-195 $K_a = 105$ M^{-1}

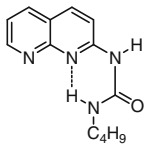

HB-195'

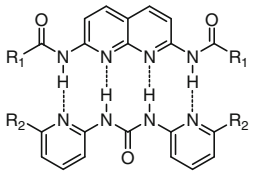

HB-196
$K_a = 2000$ M^{-1}

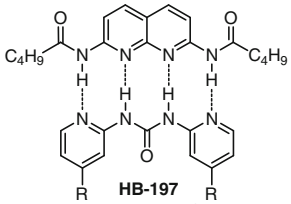

HB-197 $K_a = 1200$ M^{-1}

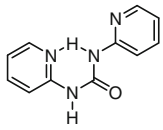

HB-198

For quadruple hydrogen bonding heterodimeric systems, in principle four different motifs, that is, DAAD-ADDA, DDDA-AAAD, DDAD-AADA, and DDDD-AAAA, may be constructed. Several DAAD-ADDA binding motifs have been developed. The stability of **HB-196** [89] and **HB-197** [88] is moderate. This is not unexpected due to the fact that the urea monomers can form a strong intramolecular hydrogen bond (**HB-198**) [88]. The stability of **HB-199** is also not high [90]. The two intramolecular hydrogen bonds should rigidify the isophthalamide monomer. However, the malonamide monomer is flexible, which does not favor the formation of the intermolecular hydrogen bonding. The **HB-200–203** motifs are much more stable [61, 91]. In particular, the extremely stable **HB-202** motif has been utilized to construct a variety of supramolecular polymers [92]. The fact that their hydrogen bonding magnitude varies very remarkably reflects the important influence of other

factors, such as steric hindrance, competition of intramolecular hydrogen bonding, backbone rigidity, and substituents. The DDDA-AAAD motifs may produce four secondary electrostatic repulsions and two secondary electrostatic attractions. However, such kind of binding motifs are not available currently.

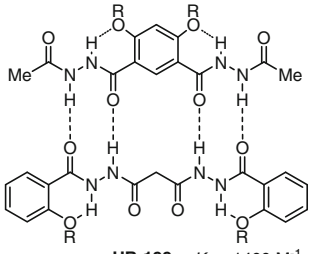

HB-199 K_a = 1400 M^{-1}

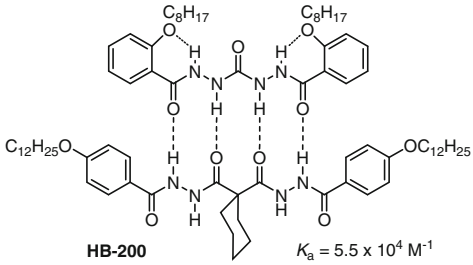

HB-200 K_a = 5.5 x 10^4 M^{-1}

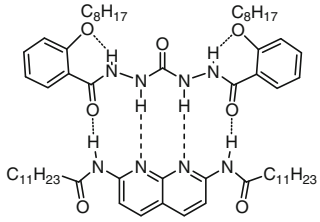

HB-201 K_a = 6.0 x 10^5 M^{-1}

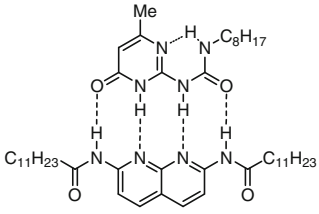

HB-202 K_a = 1.5 x 10^9 M^{-1}

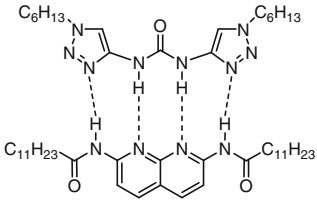

HB-203 K_a = 2.6 x 10^5 M^{-1}

Several DDAD-AADA binding motifs are also available [93, 94]. **HB-204** and **HB-205** are two examples. In this kind of binding motifs, two attractive and four repulsive secondary interactions are generated. Because the urea monomers can also from strong intramolecular hydrogen bonding (**HB-206**), these motifs have a moderate stability.

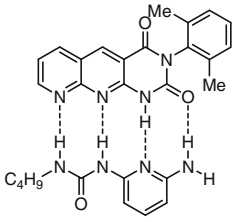

HB-204 K_a = 120 M^{-1}

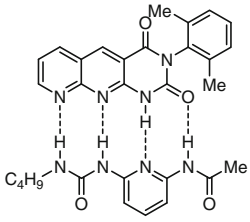

HB-205 K_a = 590 M^{-1}

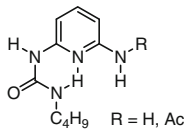

HB-206

The DDDD-AAAA hydrogen bonding motifs can produce six attractive secondary interactions. However, the **HB-207** binding motif has a surprisingly low stability [95], which may be partially attributed to the formation of the two strong intramolecular hydrogen bonds (**HB-208** and **HB-209**). When other adverse factors are absent, two rigidified monomers can form extremely stable heterodimers, as reported for **HB-210** and **HB-211** [96]. **HB-210** is stabilized with four N–H···N hydrogen bonds. Although **HB-211** is stabilized with two N–H···N and two C–H···N hydrogen bonds, its K_a is comparable to that of the self-complementary AADD quadruple hydrogen bonding motifs (**HB-193** and **HB-194**).

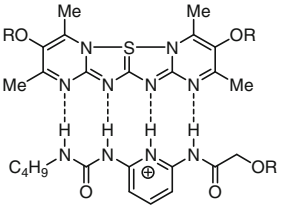

HB-207 K_a = 525 M^{-1}

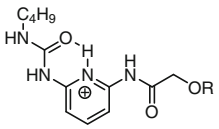

HB-208

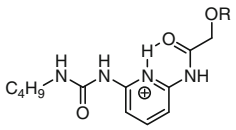

HB-209

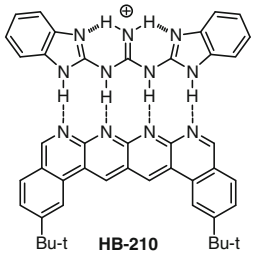

Bu-t **HB-210** Bu-t

K_a > 3 x 10^{12} M^{-1} (CH_2Cl_2)
K_a = 1.5 x 10^6 M^{-1} (MeCN)
K_a = 3.4 x 10^5 M^{-1} ($CDCl_3$/DMSO-d_6)

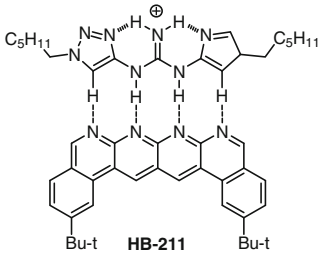

Bu-t **HB-211** Bu-t

K_a > 1 x 10^7 M^{-1} (CH_2Cl_2)
K_a = 2.6 x 10^4 M^{-1} (MeCN)

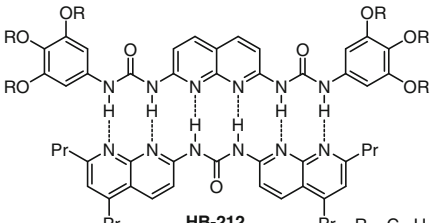

HB-212 R = $C_{12}H_{25}$
K_a = 5 x 10^5 M^{-1}

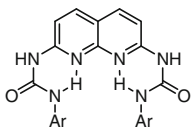

HB-213

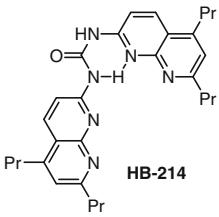

HB-214

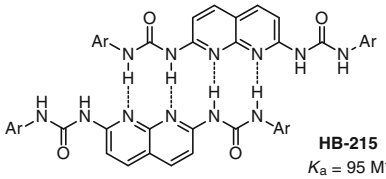

HB-215
K_a = 95 M^{-1}

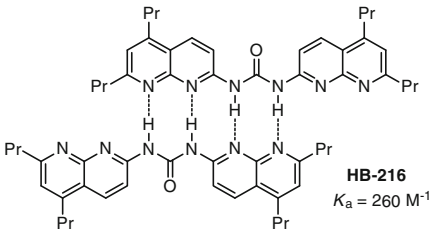

HB-216
K_a = 260 M^{-1}

In principle, increasing the number of hydrogen bonds would improve the stability of duplexes. However, introducing all binding subunits to one conjugated backbone is a challenge synthetically. In many cases, the prepared monomers have limited or poor solubility that does not allow quantitative binding studies. One efficient strategy of increasing the number of hydrogen bonds is to incorporate the binding subunits into a linear sequence [97]. For example, the AADD quadruple hydrogen bonding motif **HB-195** can be extended to the AADDAA-DDAADD sextuple hydrogen bonding heteroduplex (**HB-212**) [88]. Compared with **HB-195**, **HB-212** exhibits much increased stability. However, both monomers have been revealed to form intramolecular six-membered hydrogen bonding through folding (**HB-213** and **HB-214**) and homodimers **HB-215** and **HB-216**, which should weaken the intermolecular hydrogen bonding.

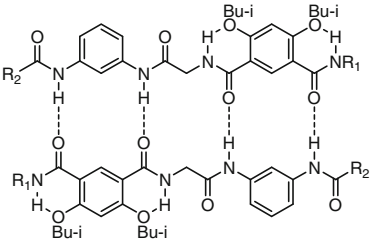

HB-217
$K_a = 6 \times 10^4\ M^{-1}$

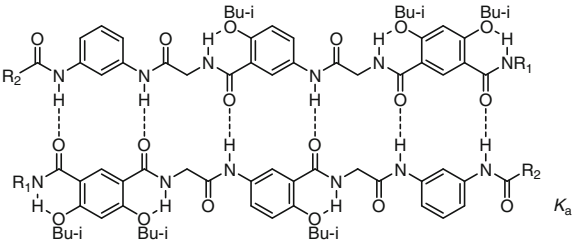

$R_1 = C_5H_{11}$
$R_2 = C_6H_{13}$

HB-218
$K_a = 6.8 \times 10^9\ M^{-1}$

The two aromatic subunits in the monomer of self-complementary AADD quadruple hydrogen bonding motif **HB-217** are connected with a flexible aliphatic chain [98]. The neighboring binding subunits are separated enough that secondary interaction should not be produced. **HB-217** is quite stable, suggesting the cooperativity of the two aromatic binding units. Longer monomers containing six binding subunits have also been prepared. They can form much more stable sextuple hydrogen bonding motifs even though the sequence is only partially rigidified. The AADADD-typed **HB-218** is one example.

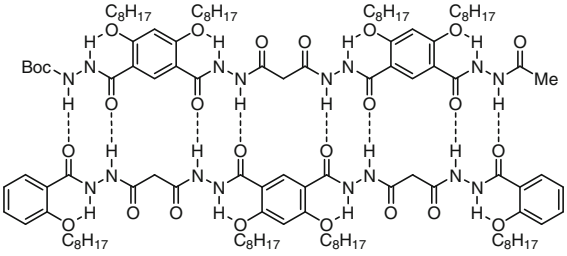

HB-219

Aromatic hydrazide derivatives connected by flexible linkers can also form similar homo- and heteroduplexes [99]. The DAADDAAD-ADDAADDA-typed **HB-219** is one of the few examples of octuple hydrogen bonding motifs formed by two different monomers [100]. The two monomers themselves form sextuple hydrogen bonding homodimers (**HB-220** and **HB-221**). Upon mixing, the octuple hydrogen bonding heterodimer is generated selectively. The stability of the three binding motifs was not investigated quantitatively. Although the backbones are not fully rigidified, the duplexes can be observed on the surface by AFM.

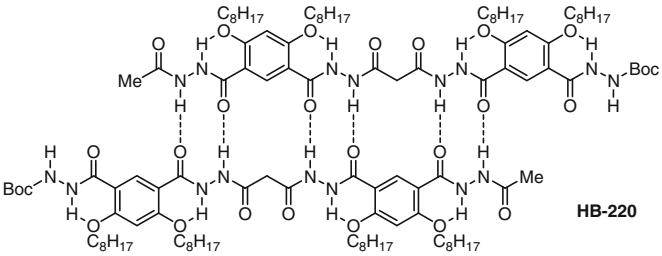

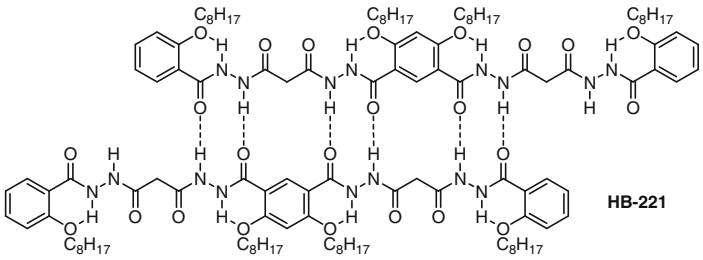

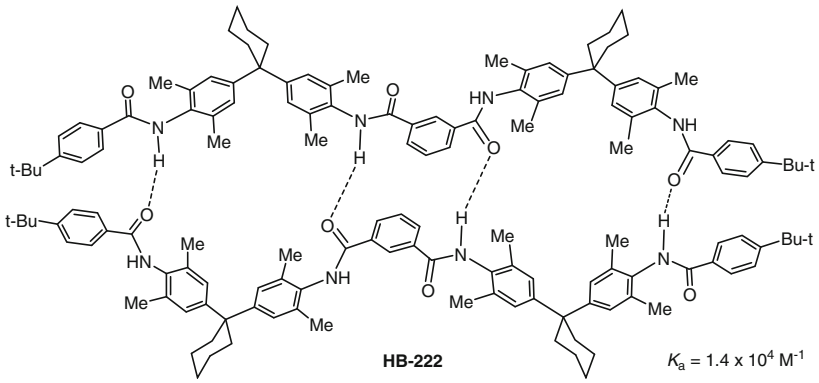

It is also reported that aromatic amide oligomers can also afford stable homodimers that are stabilized by multiple intermolecular hydrogen bonds. **HB-222** and **HB-223** are two representative examples [101, 102]. In contrast, shorter analogues only form dimers with low stability. It is also revealed that the stacking of the aromatic rings also contributes to the dimerization.

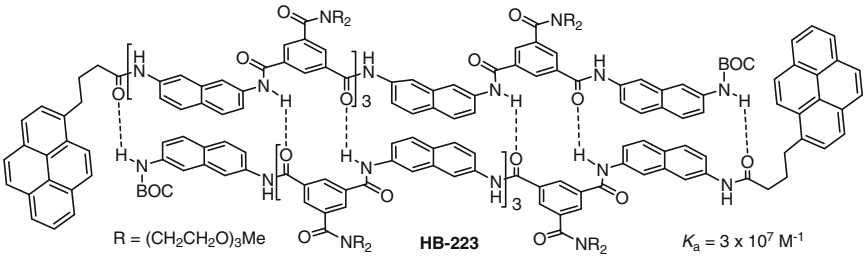

1.4 Conclusion

In this chapter, we summarize the important intramolecular and intermolecular hydrogen bonding motifs. In most cases, the motifs have been confirmed by the X-ray analysis in the solid state and by ^{1}H NMR in solution. Generally for intermolecular hydrogen bonding motifs, the stability is increased with the increase of the number of hydrogen bonds [103]. However, factors that affect binding are very complicated. Attractive and repulsive secondary interactions are crucially important in determining the stability of the dimers, and when the binding subunits are able to form stable intramolecular hydrogen bonding, their dimerization will also be weakened considerably. Thus, motifs of the same number of hydrogen bonds may exhibit very different stability. For intermolecular binding motifs, the K_a values are usually evaluated in chloroform. Because the content of impurities, in particular water and hydrochloric acid, is different, a comparison of the K_a values of different binding motifs should be careful. Although numerous hydrogen bonding motifs are available, when choosing a hydrogen bonding motif for the design of a new supramolecular system, many factors, including the stability of the binding motif, synthetic route, solubility, and modifiability of the monomers, should be considered.

Acknowledgments We thank The Ministry of Science and Technology and Ministry of Education of China, The Science and Technology Commission of Shanghai Municipality, and The National Natural Science Foundation of China for financial support.

References

1. Pauling L (1939) The nature of the chemical bond. Cornell University Press, Ithaca
2. Arunan E, Desiraju GR, Klein TA et al (2011) Definition of the hydrogen bond. Pure Appl Chem 83:1637–1641
3. Jeffrey GA, Saenger W (1991) Hydrogen bonding in biology and chemistry. Springer, Berlin
4. Jeffrey GA (1997) An introduction to hydrogen bonding. Oxford University Press, New York
5. Desiraju GR, Steiner T (1999) The weak hydrogen bond: in structural chemistry and biology. Oxford University Press, Oxford
6. Scheiner S (1997) Hydrogen bonding. A theoretical perspective. Oxford University Press, Oxford
7. Gilli G, Gilli P (2009) The nature of the hydrogen bond: outline of a comprehensive hydrogen bond theory. Oxford University Press, Oxford
8. Perrin CL, Nielson JB (1997) Ann Rev Phys Chem 48:511
9. Zimmerman SC, Corbin PS (2000) Struct Bond 96:63
10. Sijbesma RP, Meijer EW (2003) Chem Commun 5
11. Desiraju GR (2007) Angew Chem Int Ed 46:8342
12. Dalgarno SJ, Thallapally PK, Barbour LJ, Atwood JL (2007) Chem Soc Rev 36:236
13. Aakeröy CB, Champness NR, Janiak C (2010) CrystEngComm 12:22
14. Zhang DW, Zhao X, Hou JL, Li ZT (2012) Chem Rev 112:5271
15. Desiraju GR, Gautam R (2013) J Am Chem Soc 135:9952
16. Desiraju GR, Steiner T (1999) The weak hydrogen bond in structural chemistry and biology. Oxford Science Press, Chichester
17. Tew GN, Scott RW, Klein ML, DeGrado WF (2010) Acc Chem Res 43:30
18. Wang DY, Wang JL, Zhang DW, Li ZT (2012) Sci China Chem 55:2018
19. Hua Y, Flood AH (2010) Chem Soc Rev 39:1262
20. Banerjee R, Desiraju GR, Mondal R, Howard JAK (2004) Chem Eur J 10:3373
21. Steiner T, Koellner G (2001) J Mol Biol 305:535
22. Nakanaga T, Buchhold K, Ito F (2003) Chem Phys 288:69
23. Baillargeon P, Dory YL (2009) Cryst Growth Des 9:3638
24. Nishio M (2011) Phys Chem Chem Phys 13:13873
25. Fairhurst SA, Henderson RA, Hughes DL, Ibrahim SK, Pickett CJ (1995) J Chem Soc Chem Commun 1569
26. Brammer L, Charnock JM, Goggin PL, Goodfellow RJ, Orpen AG, Koetzle TF (1991) J Chem Soc Dalton Trans 1789
27. Dunitz JD (2004) ChemBioChem 5:614
28. Li C, Ren SF, Hou JL, Yi HP, Zhu SZ, Jiang XK, Li ZT (2005) Angew Chem Int Ed 44:5725
29. Lu BY, Zhu YY, Li ZM, Zhao X, Li ZT (2012) Tetrahedron 68:8857
30. Page MI, Jencks WP (1971) Proc Natl Acad Sci USA 68:1678
31. Etter MC (1991) J Phys Chem 95:4601
32. Bertolasi V, Gilli P, Ferretti V, Gilli G (2001) Acta Crystallogr B57:591
33. Liu Z, Teslja A, Pophristic V (2011) J Comput Chem 32:1846
34. Connors KA (1987) Binding constants. Wiley, New York
35. Thordarson P (2011) Chem Soc Rev 40:1305
36. Jönsson PG (1976) Acta Cryst B32:232
37. Zavodnik VE, Bel'skii VK, Zorkii PM (1987) J Struct Chem 28:793
38. Etter MC (1990) Acc Chem Res 23:120
39. Kolotuchin SV, Thiessen PA, Fenlon EE, Wilson SR, Loweth CJ, Zimmerman SC (1999) Chem Eur J 5:2537
40. Vishweshwar P, Beauchamp DA, Zaworotko MJ (2006) Cryst Growth Des 6:2429
41. Rajput L, Jana N, Biradha K (2010) Cryst Growth Des 10:4565
42. Omondi B, Fernandes MA, Layh M, Levendis DC (2008) Acta Cryst C64:o137
43. Reddy LS, Basavoju SS, Vangala VR, Nangia A (2006) Cryst Growth Des 6:161

44. Zhang Z, Schreiner PR (2009) Chem Soc Rev 38:1187
45. Gao Y, Lam Y (2006) Org Lett 8:3283
46. Schweinfurth D, Pattacini R, Strobel S, Sarkar B (2009) Dalton Trans 9291
47. Yan Y, Wang Q, Chen Y, Petersen JL, Shi X (2010) Org Lett 12:3308
48. Kilpin KJ, Gavey EL, McAdam CJ, Anderson CB, Lind SJ, Keep CC, Gordon KC, Crowley JD (2011) Inorg Chem 50:6334
49. Garg S, Shreeve JM (2011) J Mater Chem 21:4787
50. Costa MS, Boechat N, Ferreira VF (2006) Acta Crystall E 62:o1925–o1927
51. Horne WS, Gellman SH (2008) Acc Chem Res 41:1399
52. Nowick JS (2008) Acc Chem Res 41:1319
53. Gellman SH, Dado GP, Liang CB, Adams BR (1991) J Am Chem Soc 113:1164
54. Hamuro Y, Geib SJ, Hamilton AD (1996) J Am Chem Soc 118:7529
55. Parra RD, Zeng H, Zhu J, Zheng C, Zheng XC, Gong B (2001) Chem Eur J 7:4352
56. Gong B (2001) Chem Eur J 7:4337
57. Huc I (2004) Eur J Org Chem 17
58. Delnoye DAP, Sijbesma RP, Vekemans JAJM, Meijer EW (1996) J Am Chem Soc 118:8717
59. Guichard G, Huc I (2011) Chem Commun 47:5933
60. Gan Q, Ferrand Y, Bao C, Kauffmann B, Grélard A, Jiang H, Huc I (2011) Science 331:1172
61. Zhao X, Wang XZ, Jiang XK, Chen YQ, Li ZT, Chen GJ (2003) J Am Chem Soc 125:15128
62. Cary JM, Moore JS (2002) Org Lett 4:4663
63. Barbarich TJ, Rithner CD, Miller SM, Anderson OP, Strauss SH (1999) J Am Chem Soc 121:4280
64. Buyukgungor O, Odabasoglu M (2008) Acta Crystallogr E 64:o808
65. Lewis RJ, Camilleri P, Kirby AJ, Marby CA, Slawin AA, Williams DJ (1991) J Chem Soc Perkin Trans 2:1625
66. Zhu YY, Wu J, Li C, Zhu J, Hou JL, Li CZ, Jiang XK, Li ZT (2007) Cryst Growth Des 7:1490
67. Zhu SS, Nieger M, Daniels J, Felder T, Kossev I, Schmidt T, Sokolowski M, Vögtle F, Schalley CA (2009) Chem Eur J 15:5040
68. Guo D, Nichol GS, Cain JP, Yalkowsky SH (2009) Acta Crystallogr E 65:o2644
69. Zhu YY, Yi HP, Li C, Jiang XK, Li ZT (2008) Cryst Growth Des 8:1294
70. Zhu YY, Jiang L, Li ZT (2009) CrystEngComm 11:235
71. Choi S, Isaacs A, Clements D, Liu D, Kim H, Scott RW, Winkler JD, DeGrado WF (2009) Proc Natl Acad Sci USA 106:6968
72. Du P, Jiang XK, Li ZT (2009) Tetrahedron Lett 50:320
73. Zhu YY, Wang GT, Wang RX, Li ZT (2009) Cryst Growth Des 9:4778
74. Zornik D, Meudtner RM, El Malah T, Thiele CM, Hecht S (2011) Chem Eur J 17:1473
75. Hanan GS, Lehn JM, Kyritsakas N, Fischer J (1995) J Chem Soc Chem Commun 765
76. Corbin PS, Zimmerman SC (2000) J Am Chem Soc 122:3779
77. Simic V, Bouteiller L, Jalabert M (2003) J Am Chem Soc 125:13148
78. Jorgensen WL, Pranata J (1990) J Am Chem Soc 112:2008
79. Chang SK, Engen DV, Fan E (1991) J Am Chem Soc 113:7640
80. Murray TJ, Zimmerman SC, Kolotuchin SV (1995) Tetrahedron 51:635
81. Djurdjevic S, Leigh DA, McNab H, Parsons S, Teobaldi G, Zerbetto F (2007) J Am Chem Soc 129:476
82. Blight BA, Camara-Campos A, Djurdjevic S, Kaller M, Leigh DA, McMillan FM, McNab H, Slawin AM (2009) J Am Chem Soc 131:14116
83. Wang HB, Mudraboyina BP, Wisner JA (2012) Chem Eur J 18:1322
84. Lopez AH, Caramori GF, Coimbra DF, Parreira RL, da Silva ÉH (2013) ChemPhysChem 14:3994
85. Beijer FH, Kooijman H, Spek AL (1998) Angew Chem Int Ed 37:75
86. Yang Y, Yan HJ, Chen CF, Wan LJ (2007) Org Lett 9:4991
87. Corbin PS, Lawless LJ, Li Z, Ma Y, Witmer MJ, Zimmerman SC (2002) Proc Natl Acad Sci USA 99:5099

88. Corbin PS, Zimmerman SC, Thiessen PA, Hawryluk NA, Murray TJ (2001) J Am Chem Soc 123:10475
89. Lüning U, Kühl C (1998) Tetrahedron Lett 39:5735
90. Yang Y, Yang ZY, Yi YP, Xiang JF, Chen CF, Wan LJ, Shuai ZG (2007) J Org Chem 72:4936
91. Hisamatsu Y, Shirai N, Ikeda SI, Odashima K (2010) Org Lett 12:1776
92. Tom FA, De Greef MMJ, Smulders MW (209) Chem Rev 109:5687
93. Brammer S, Lüning U, Kühl C (2002) Eur J Org Chem 4054
94. Taubitz J, Lüning U (2008) Eur J Org Chem 5922
95. Taubitz J, Lüning U (2009) Aus J Chem 62:1550
96. Leigh DA, Robertson CC, Slawin AMZ, Thomson PIT (2013) J Am Chem Soc 135:9939
97. Yuan L, Zhang P, Feng W, Gong B (2011) Curr Org Chem 15:1250
98. Gong B (2012) Acc Chem Res 45:2077
99. Yang Y, Chu WJ, Liu JW, Chen CF (2011) Curr Org Chem 15:1302
100. Yang Y, Xiang JF, Xue M, Hu HY, Chen CD (2008) J Org Chem 73:6369
101. Bisson P, Carver FJ, Eggleston DS, Haltiwanger RC, Hunter CA, Livingstone DL, McCabe JF, Rotger C, Rowan AE (2000) J Am Chem Soc 122:8856
102. Xu YX, Zhan TG, Zhao X, Li ZT (2014) Org Chem Front 1:73
103. Sartorius J, Schneider HJ (1996) Chem Eur J 2:1446

Chapter 2
Understanding of Noncovalent Interactions Involving Organic Fluorine

Piyush Panini and Deepak Chopra

Abstract Due to the unpredictable nature of organic fluorine in its participation in the formation of different supramolecular motifs which concomitantly influences the physicochemical properties of the compounds of interest, the study of noncovalent interactions involving organic fluorine will always be an expanding area of research amongst the scientific community. The participation of organic fluorine in the formation of intermolecular interactions has always been questioned. In this book chapter, we provide insights into new structural features, nature, and energetics associated with intermolecular interactions, namely C–H···F–C, C–F···F–C, C–F···X (N, O, S, halogen) from researchers across the world. The studies show that interactions involving fluorine are ubiquitous and play a central role in the existence of diversified solid state properties, namely polymorphism, crystal engineering, and cocrystallization.

2.1 Introduction

Noncovalent interactions play a pivotal role in the design of a new material with specific properties [1–6]. Their role has been very well recognized in different fields related to biological, pharmacological, chemical, physical, and materials sciences [7–10]. In this regard, the strong hydrogen bonds, e.g., O/N–H···O/N with their high directional characteristics is found to be very effective in the supramolecular assembly of molecules [11]. In view of their importance in many fields of science, the debate on the nature, properties, and importance of hydrogen bonds is increasing day by day. Recently, a task group formed by IUPAC has provided a modern definition of the hydrogen bond [12, 13]. It is as follows: "The hydrogen bond is an attractive interaction between a hydrogen atom from a molecule or a

P. Panini · D. Chopra (✉)
Crystallography and Crystal Chemistry Laboratory, Department of Chemistry, Indian Institute of Science Education and Research, Bhopal 462066, Madhya Pradesh, India
e-mail: dchopra@iiserb.ac.in

Z. Li and L. Wu (eds.), *Hydrogen Bonded Supramolecular Structures*,
Lecture Notes in Chemistry 87, DOI 10.1007/978-3-662-45756-6_2

molecular fragment H–X in which X is more electronegative than H, and an atom or group of atoms in the same or a different molecule, in which there is evidence of bond formation." Keeping in mind the definition given by Pauling [14] as "Only the most electronegative atoms (such as N, O, F) should form hydrogen bonds (denoted as X–H···Y), and the strength of the bond should increase with increase in the electronegativity of the two bonded atoms," the modern definition is now more general as it extends the list of possible donors and acceptors which participate in the formation of the hydrogen bond. This includes the possibility of hydrogen bond formation when either the donor or acceptor is weak or possesses moderate electronegativity. These aspects constitute the characteristics of the "weak hydrogen bond," [15, 16]. The stabilization energy of a hydrogen bond lies approximately in the range of 170–2 kJ/mol (the higher range corresponds to ionic hydrogen bonds). Hence, the strongest hydrogen bond can provide energetic stabilization similar in magnitude to a covalent bond, while the weakest one can be close to being a van der Waals interaction. The criterion which differentiates an interaction being a hydrogen bond from a van der Waals interaction is related to the "directionality" as is emphasized by Professor Desiraju [15], and also recommended in the modern IUPAC definition of the hydrogen bond [12, 13]. The evidence of existence of weak hydrogen bonds like C–H···O, C–H···N, C–H···π(C), O/N–H···π(C) are now well established in modern supramolecular chemistry, and are being utilized in the systematic design of materials [17–20]. More ever, apart from hydrogen bonds, the π–π stacking [21], anion/*lp*···π [22–25], and halogen bonds [26–33] occupy a prominent position amongst noncovalent interactions and their importance in the area of chemistry and biology is very well recognized. The halogen bond is an attractive interaction which arises due to the anisotropy in the charge distribution over covalently bound halogen atoms. This generates a positive electrostatic potential (positive σ-holes) opposite to the C–X σ-bond and having negative electrostatic potential perpendicular to the bond, and hence the positive σ-holes site can now interact with the negative sites in an attractive manner. In addition, interactions involving halogens [O/N/C–H···X, X···X] have also received considerable attention in recent years and have been investigated in detail with inputs from crystallographic, computational, and spectroscopic studies [34–40]. Amongst these, the presence of intra- and intermolecular interactions involving fluorine has been a subject of study for over two decades [41, 42]. In spite of possessing the highest electronegativity amongst all the elements, noncovalent interactions involving fluorine have always been questioned and its existence is still a subject of debate amongst the scientific communities. Due to differences in electronegativity, the C–F bond (termed as "organic fluorine") would be highly polar and one might expect the fluorine atom to act as a good H-bond acceptor and can also participate in other related noncovalent interactions, namely C–F···F–C, C–F···π, and C–F···O, respectively. In recent years, significant inputs from crystallography, spectroscopy, and computational studies have strongly contributed toward the understanding of the nature and energetics of interactions involving organic fluorine (in particular

C–H···F and C–F···F–C respectively). In this book chapter, we wish to highlight the discovery and observation of new structural features related to interactions involving organic fluorine from researchers across the world.

2.1.1 Why Fluorine Is So Special?

Compounds containing organic fluorine have received special attention in the fields of life science and materials science as the replacement of the hydrogen atom by fluorine can alter the physical and chemical properties of the compound [41, 43–49]. Despite having similar size with hydrogen, fluorine shows greater influence on the electronic properties and stability of the compound resulting in increased resistance towards metabolic degradation [50–53]. The effect of replacement of hydrogen with fluorine was studied on enzyme reactions by Hagan and Rzepa and the results indicated that the stereoelectronic influence of fluorine can control completely, or influence partially, the stereochemical outcome of such reactions [54]. Furthermore, about 20 % of pharmaceutical products and 30 % of agrochemicals were reported to possess fluorine atoms and the number of fluorine containing drugs in the market will continue to increase [55, 56]. The effect of fluorine substitution in the design of active ingredients for modern crop protection has been reviewed [57]. Some of the important drugs containing fluorine molecules used in our daily life are listed in Fig. 2.1 [58]. Diederich et al. reviewed the fluorine substituted pharmaceuticals and observed its interactions with the protein active site through C–F···H–N, C–F···C=O, and C–F···H–C_α interactions [59]. In a recent review, the structure of top ten fluorine containing blockbuster drugs have been highlighted along with their mode of action and synthetic route [60]. All these results have inspired researchers to perform systematic studies which pertain to unravel interactions involving organic fluorine in the last decade.

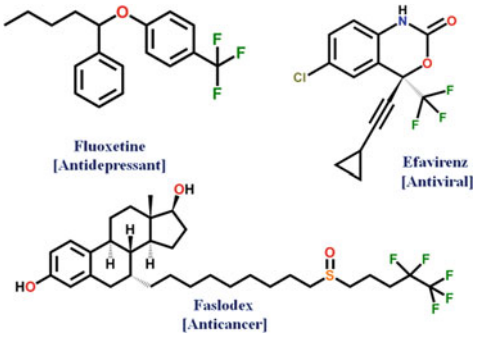

Fig. 2.1 List of important fluorinated drugs available in market

2.2 Debate on Participation of Fluorine as a Hydrogen Bond Donor: Overview of the Weak X–H···F–C; X = N, O, C Hydrogen Bond

According to Pauling, only the most electronegative atoms should form hydrogen bonds and the strength of the bond should increase with increase in the electronegativity of the two bonded atoms [14]. Hence it might be expected that fluorine being an element with the highest electronegativity [4.0, Pauling scale] in the periodic table, it can form very strong hydrogen bonds. With respect to the hydrogen bond acceptor capability of the fluoride ion (the H-bond energy of the bifluoride ion in HF_2^- is approximately 40 kcal/mol which is similar to that of a covalent bond and this makes it the strongest known Hydrogen bond) the Pauling statement seems correct. However F-atom connected with C-atom, termed as "organic fluorine," behaves as a very poor acceptor of hydrogen bond. This statement is supported by inputs from the work of Shimoni and Glusker [61]. Based on a CSD study, it was concluded that the C–F group fails to compete favorably with O and N atom as hydrogen bond acceptors when these atoms are present in the crystal structure, however in the absence of these acceptors, weak C–H···F–C interactions can be observed. Furthermore, similar conclusions have been made by Dunitz and Taylor on the study of O/N–H···F–C interactions in an article entitled "Organic Fluorine Hardly Ever Accepts Hydrogen Bonds" [62]. They stated that because of low proton affinity (low basicity, low-lying lone pair orbitals, tightness of its electron shell, i.e., low polarizability) of the covalently attached fluorine and its inability to modify this by intramolecular electron delocalization or intermolecular cooperative effects, organic fluorine possess very low capability of hydrogen bond formation except in "exceptional crystal and molecular environment." Moreover, Howard et al. performed a CSD study for the existence of C–F···H–X (where X = O, N, C) interactions in different crystal structures and concluded that C(sp^3)–F is a better hydrogen bond acceptor than C(sp^2)–F [63]. The strength of a C(sp^3)–F···H–O and C(sp^2)–F···H–O H-bond was calculated to be 2.38–1.48 kcal/mol respectively (Fig. 2.2). They also stated "the predominant C–F···H–C contacts in the Database appear to have very little significance in energy terms and are essentially van der Waals complexes."

Furthermore, Desiraju and co-workers studied the existence and nature of C–H···F–C interactions in crystalline fluorobenzenes [64]. These compounds were chosen because they have only C, H, and F and hence do not possess any other

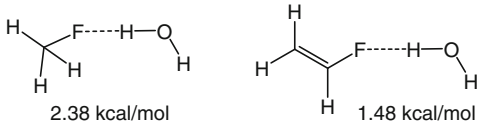

Fig. 2.2 C(sp^3)–F···H–O and C(sp^2)–F···H–O H-bond strength

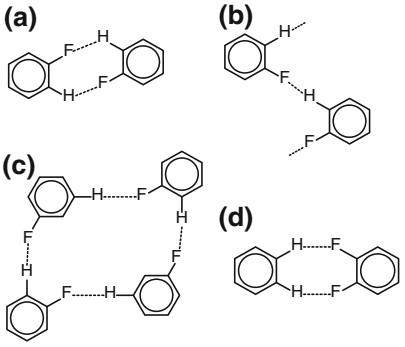

Fig. 2.3 Four types of possible supramolecular synthons for C–H···F–C interactions

elements like N or O which can compete with fluorine and are also responsible for the increase in the acidity of hydrogen atoms in its vicinity. On the basis of distance-angle (d/θ) correlation plots for the presence of C–H···F–C interactions in these crystal structures, it was observed that these interactions have the characteristics of weak hydrogen bonds. The supramolecular synthons for C–H···F (Fig. 2.3) [64] were observed to be topologically similar to well-known C–H···O and C–H···N synthons and can be used in the design of novel and functional crystals. On the comparison of these crystal structures with their chloro, bromo and iodo analogues, it was observed that fluorine prefers C–H···F interactions rather than F···F contacts, whereas the heavier halogens prefer halogen···halogen interactions. Furthermore, the significance of C–H···F–C interactions were observed in a series of crystal structures of ribonucleic acids [65] and these were claimed as "hydrogen bonds." The authors concluded that the C–H···F–C hydrogen bonds observed at distances shorter than sum of van der Waal radii of hydrogen and fluorine in their crystal structures, (for example, in the two polymorphs and a hemihydrate of 1′-deoxy-1′-(4-fluorophenyl)-β-D-ribofuranose and the nature of the C–H···F–C chain is similar in the crystal packing of these three solid forms, Fig. 2.4) are responsible to provide further stabilization in modified RNA duplex containing fluorine atoms at Watson–Crick binding site.

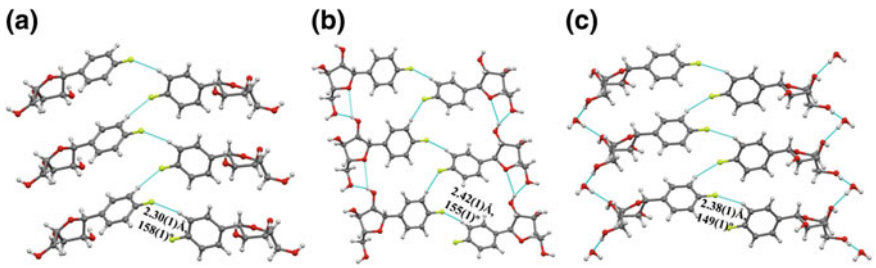

Fig. 2.4 The nature of short and directional C–H···F–C hydrogen bonds forming chains in **a** Form I, **b** Form II and **c** hemihydrate of 1′-deoxy-1′-(4-fluorophenyl)-β-D-ribofuranose are observed to be similar in the solid state [65]

A few years later, a review by Dunitz, entitled "Organic Fluorine: Odd Man Out" [66], raised further speculation about the nature of organic fluorine. Furthermore the interpretation presented by Desiraju from the crystal structure analysis of fluorobenzenes were quantified by inputs from Molecular-Pair analysis (from PIXEL [67] calculations) [68]. It was proposed that one of the hypothetical (computed) high pressure forms of benzene adopts the same tetragonal packing as fluorobenzene and hence C–H···F–C interactions behave similar to C–H···H interactions and have the same structure-directing ability. This conclusion was further supported in the crystal packing analysis of 1,2,3,4-tetrafluoronaphthalene, -anthracene, and -phenanthrene by Gavezzotti et al. [69]. It was observed that the C–H···F–C interactions does not provide any significant stabilization to the crystal packing. Following this work, immediately, Ganguly, and Desiraju [70] observed that in the hypothetical (computed) high pressure forms of benzene, the C–H···H interactions can be more accurately represented as $C–H^{\delta+}\cdots H^{\delta-}$. Further, on the basis of crystal structure analysis of 1,2,3,5-tetrafluorobenzene, by Boese and Desiraju, it was established that C–H···F–C interactions have similar structure direction ability as a hydrogen bond [71]. It was observed that the title compound which has shape and size similar to many fluorobenzenes, does not adopt the tetragonal packing in the solid. Instead it preferred to crystallize in monoclinic $P2_1/c$ space group, stabilized by the presence of C–H···F–C hydrogen bonds (Fig. 2.5).

The role of intermolecular interactions involving organic fluorine has been analyzed by many researchers in the last two decades exploiting various experimental, theoretical, and database studies. These have been excellently compiled in recent reviews [41], highlight [72] and a perspective [73]. It was initially anticipated that such weak C–H···F hydrogen bonds are only significant in the absence of any other strong intermolecular forces [74]. In the crystal structure analysis of fluorine

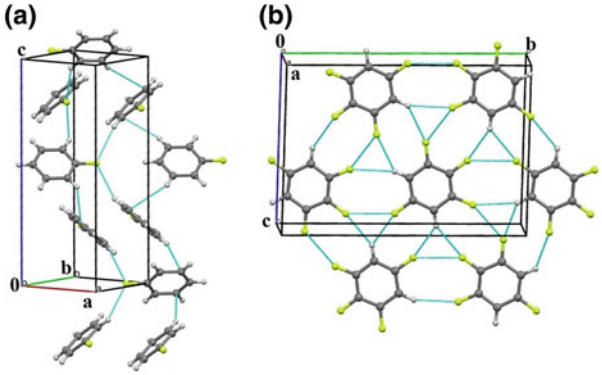

Fig. 2.5 **a** Depiction of the tetragonal packing in fluorobenzene via C–H···F–C and C–H···π interactions (ref code: FACFAQ; crystallizes in $P4_32_12$) [64]. **b** Formation of a molecular sheet down the *bc*-plane in 1,2,3,5-tetrafluorobenzene with utilization of C–H···F–C and C–F···F–C interactions (crystallizes in $P2_1/c$) [71]

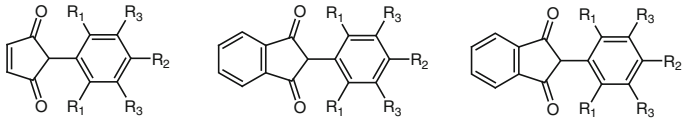

1: $R_1 = R_2 = R_3 = H$
2: $R_1 = R_3 = F$; $R_2 = H$
3: $R_1 = F$; $R_2 = R_3 = H$
4: $R_1 = R_2 = H$; $R_3 = F$
5: $R_1 = R_2 = F$; $R_3 = H$
6: $R_1 = R_2 = R_3 = F$

7: $R_1 = R_2 = R_3 = H$
8: $R_1 = R_3 = F$; $R_2 = H$
9: $R_1 = F$; $R_2 = R_3 = H$
10: $R_1 = R_2 = H$; $R_3 = F$
11: $R_1 = R_2 = F$; $R_3 = H$
12: $R_1 = R_2 = R_3 = F$

13: $R_1 = R_2 = R_3 = H$
14: $R_1 = R_3 = F$; $R_2 = H$
15: $R_1 = F$; $R_2 = R_3 = H$
16: $R_1 = R_2 = H$; $R_3 = F$
17: $R_1 = R_2 = F$; $R_3 = H$
18: $R_1 = R_2 = R_3 = F$

Fig. 2.6 Fluorine substituted phenylmaleimides and corresponding phthalimides [78]

substituted isoquinolines [75, 76], trifluoroacetophenones [77] *N*-phenylmaleimides and corresponding phthalimides [78], benzonitriles [79], pyridines [80], *N* benzylideneanilines [81], azobenzenes [82], etc., the importance of weak C–H···F–C hydrogen bonds was observed in the absence of any strong hydrogen bond donor. Crystal packing analysis of a series of fluorine substituted isoquinolines was observed to be stabilized by mainly C–H···F hydrogen bonds along with C–F···F–C and C–F···π in the absence of any other relatively stronger intermolecular forces such as hydrogen bonding, C–H···π or π···π interactions [75, 76]. The detailed analysis of eighteen crystal structures of fluorine substituted phenylmaleimides and corresponding phthalimides (Fig. 2.6) by Schwarzer and Weber revealed that although C–H···O plays the dominant role in their crystal packing, the presence of C–H···F hydrogen bonds along with other related weak interactions like C–F···F–C, C–F···π, $\pi\cdots\pi_F$ interactions provide further stabilization in the molecular assemblies [78]. The major influence of these weak interactions was observed in case of polymorphs of 12 (labeled as 12A and 12B [78]). In case of 12A, the crystal packing was stabilized by the presence of two short C–H···F hydrogen bonds (forming a chain), along with C–H···O hydrogen bond and other weak C–F···F–C and C–F···π interactions. On the other hand, short C–H···O hydrogen bonds (forming chain), along with one dimeric weak C–H···F hydrogen bond and C–F···F–C interactions were observed in the crystal packing of 12B.

Moreover, Choudhury and Guru Row noticed in the crystal packing of pentafluorophenylprop-2-ynylcarbonate that the C–H···F hydrogen bond dominated over the C–H···O hydrogen bond [83], which was considered to be highly structure directing and a preferred interaction (Fig. 2.7a). This observation promoted the debate regarding the significance of C–H···F hydrogen bond. Further, it was observed (by the same research group) that the occurrence of C–H···F hydrogen bond (utilizing acidic methylene protons in the formation of highly short and directional interaction) in the crystal packing of but-2-yne-1,4-diylbis(pentafluorophenylcarbonate) [84], stabilized the rare and unusual *cisoid* conformation of the molecule (Fig. 2.7b).

Fluorobenzonitriles [79] and fluorinated pyridines [80] were crystallized by in situ crystallization, and the significance of interactions involving "organic fluorine" was studied by Merz et al. The weak C–H···F along with C–H···N

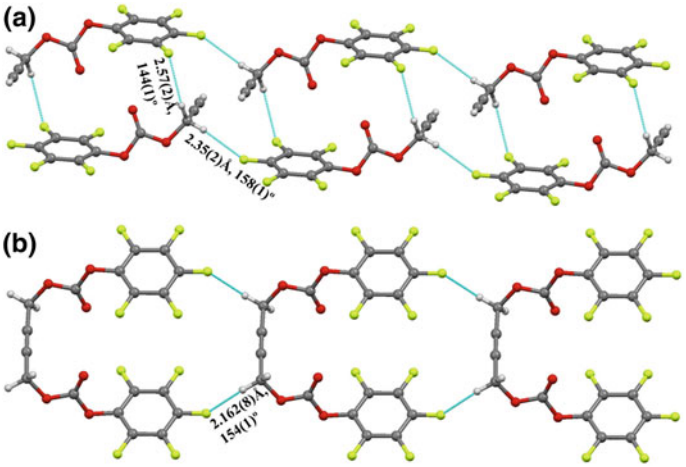

Fig. 2.7 **a** Part of crystal packing in pentafluorophenyl prop-2-ynyl carbonate, displaying short C–H···F–C hydrogen bond [83]. **b** *cisoid*-conformation of but-2-yne-1,4-diylbis(pentafluorophenylcarbonate) stabilized by the presence of short C–H···F–C hydrogen bonds in the crystal packing [84]

hydrogen bond were observed in the molecular assembly of fluoro substituted benzonitriles and subsequent increase in the melting point with the sequential change in the position of fluorine (*ortho*-, to *meta*-, to *para*-) over the phenyl ring relative to cyano group were noticed. In case of fluorine substituted pyridines with the increase in fluorine substitution, noticeable changes in their crystal packing were discovered. It was observed that the crystal packing changes stepwise from a herringbone packing in monofluorinated pyridine to parallel arrangement of the molecules in the trifluorinated pyridine and then to the edge-to-face molecular arrangement in case of perfluorinated pyridine. In crystal structure analysis of a series of 15 newly synthesized fluorine substituted (*mono*- and *di*-) isomeric *N*-benzylideneanilines [81], it was observed that C–H···F acts as a significant contributor in the construction of various supramolecular synthons in their crystal packing (Fig. 2.8a, b). Furthermore, Kaur and Choudhury, have investigated the capability of organic fluorine to participate in the formation of interactions involving fluorine in the presence of other halogens in *N*-benzylideneanilines (Figs. 2.9 and 2.10) [85]. It was observed that the replacement of noninteracting fluorine atoms by either Cl or Br does not alter the packing motifs in comparison to the corresponding difluorinated analogues while modification in the crystal packing was detected when the interacting fluorine atom was replaced (Figs. 2.9 and 2.10). Recently, Merz et al. examined changes in crystal packing behavior of toluene (α-polymorph) with systematic replacement of the H-atom with the fluorine atom on the methyl group [86]. The authors concluded that increase in fluorination due to replacement of $–CH_3$ by $–CHF_2$ and $–CF_3$ leads to the changes in molecular assembly, from corrugated layers to parallel arrangement in their crystal packing.

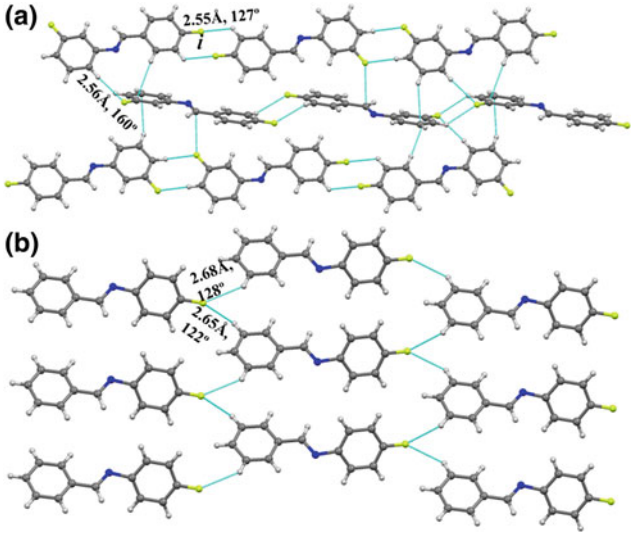

Fig. 2.8 **a** Packing of molecules in 3-fluoro-*N*-(4-fluorobenzylidene)aniline via C–H···F–C and C–H···π hydrogen bonds. **b** Formation of a molecular chain in *N*-Benzylidene-4-fluoroaniline with utilization of bifurcated C–H···F–C hydrogen bonds [81]

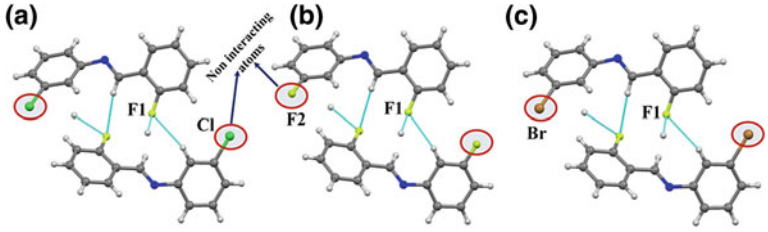

Fig. 2.9 Conservation of supramolecular motifs on replacement of noninteracting fluorine atom (F2) in case of **a** 3-chloro-*N*-(2-fluorobenzylidene)aniline **b** 3-fluoro-*N*-(2-fluorobenzylidene) aniline and **c** 3-bromo-*N*-(2-fluorobenzylidene)-aniline [85]

Further, the capability of organic fluorine as H-bond acceptor was also studied extensively in the presence of strong hydrogen bond donor [87–93]. The importance of such C–H···F interactions being weak and cooperative in nature has been realized in the crystal structure analysis of fluorinated *N*-(2-Chloropyridin-4-yl)-*N′*-phenylureas (Fig. 2.11) [87], halogenated benzanilides (fluorinated [88] and hetero halogenated with at least one side of the phenyl ring contains fluorine [88–90]), trifluoromethyl (–CF_3) substituted benzanilides [91], fluoro-*N*-(pyridyl)benzamides [92], fluorine-substituted benzimidazoles [93]. In the crystal packing of a series of fluorinated *N*-(2-Chloropyridin-4-yl)-*N′*-phenylureas (Fig. 2.11), short and highly directional C–H···F–C interactions were observed in the solid state [87]. The authors concluded that the influence in the crystal packing by fluorine substitution

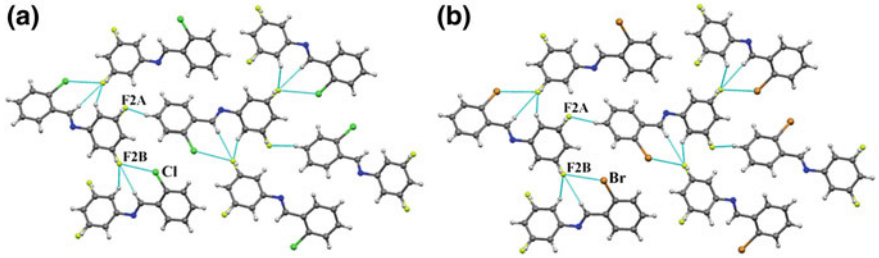

Fig. 2.10 Replacement of interacting F-atom (F1, Fig. 2.9b) with Cl or Br leads to alteration in crystal packing in case of **a** 3-fluoro-*N*-(2-chlorobenzylidene)-aniline and **b** 3-fluoro-*N*-(2-bromobenzylidene)aniline

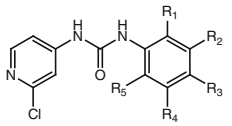

1: $R_1 = R_2 = R_3 = R_4 = R_5 = H$
2: $R_1 = F; R_2 = R_3 = R_4 = R_5 = H$
3: $R_1 = R_2 = F; R_3 = R_4 = R_5 = H$
4: $R_1 = R_2 = R_3 = F; R_4 = R_5 = H$
5: $R_1 = R_2 = R_3 = R_4 = F; R_5 = H$
6: $R_4 = F; R_1 = R_2 = R_3 = R_5 = H$
7: $R_3 = R_4 = F; R_1 = R_2 = R_5 = H$
8: $R_1 = R_5 = F; R_2 = R_3 = R_4 = H$
9: $R_1 = R_3 = R_5 = F; R_2 = R_4 = H$
10: $R_1 = R_2 = R_4 = R_5 = F; R_3 = H$

Fig. 2.11 Series of fluorinated *N*-(2-Chloropyridin-4-yl)-*N*′-phenylureas synthesized for the analysis of interactions involving "organic fluorine"

appeared mainly due to the (i) polarity of the C–F bond and the associated electrostatic changes and (ii) increase in C–H acidity neighboring to the F-atoms.

An important breakthrough on the importance and capability of organic fluorine in the formation of intermolecular interactions was realized by Desiraju and co-workers. This involved the study of the structural landscape of benzoic acid [94]. In this analysis, different structural landscapes (a total of 100 structures were predicted, corresponds to different rank) of benzoic acid was obtained using COMPASS26 and DREIDING force field using Material Studio (with restriction of space group to $P2_1/c$ and $P\text{–}1$ only, these being the most common in case of organic compounds). This study was based on crystal structure prediction (CSP) [95, 96].

This study involves the computational prediction of a series of crystal structures of a given compound having different lattice energy (called the crystal energy landscape). This may result in different hypothetical structures of the compound of interest (some of these may correspond to polymorphs as well, a fundamental application of this computational exercise). The crystal structure corresponds to the global minimum and this may be similar to the experimentally observed crystal structure. In the investigation by Prof. Desiraju and co-workers, it was observed that the experimental crystal structure of fluorinated (mono or poly) benzoic acid was similar to the "high energy" crystal structure of benzoic acid, predicted computationally (Table 2.1). In other words, it may be concluded that substitution of fluorine on benzoic acid actually stabilized its high energy form by introducing the possibilities of different intermolecular interactions like C–H···F–C and C–F···F–C (these are present in the experimental crystal structure of fluorinated benzoic acid [94]) in the crystal packing. Moreover, in the same work, this behavior was

Table 2.1 Structural landscape of benzoic acid [94]

Compound	Structure type [a]	Rank
Benzoic acid	(5-5-22)	5th and 23rd
3,4-difluorobenzoic acid		
2,3,4-trifluorobenzoic acid		
3,4,5-trifluorobenzoic acid		
2-fluorobenzoic acid	(6-4-25)	99th
3-fluorobenzoic acid		
4-fluorobenzoic acid	(4-6-26)	55th
2,3-difluorobenzoic acid		
2,4-difluorobenzoic acid		
2,5-difluorobenzoic acid	(4–14-12)	56th
3,5-difluorobenzoic acid		
2,3,5-trifluorobenzoic acid		

[a] Corresponds to nearest integer of unit cell parameters *a*, *b*, *c*; For example, for benzoic acid: a = 5.510 Å, b = 5.157 Å, c = 21.973 Å, Structure type: 5-5-22

observed to be more consistent with fluorine than with chloro or bromo substituted benzoic acid. This concept has been further extended to a two component system (cocrystal). It was observed that the experimental crystal structure of 1:1 cocrystal of fluorobenzoic acids with isonicotinamide corresponds to a high energy computed structure of 1:1 benzoic acids and the isonicotinamide cocrystal [97]. Intermolecular interactions like C–H···F–C, C–F···F–C, C–F···O were observed in the crystal packing of a different fluorinated analogue (the 1:1 cocrystal of benzoic acids and isonicotinamide) along with other related strong and weak interactions.

The detailed exhaustive investigation of nature and C–H···F–C interactions were carried out by Novoa, by a combination of CSD search and ab initio theoretical calculations [98]. It was observed that in case of the neutral molecular fragment, the C–H···F–C interaction behaves as a weak hydrogen bond with stabilization energy being ~ -0.40 kcal/mol. The interaction energy were divided into the sum of the following five components (i) the exchange-repulsion component, E_{er}, (ii) electrostatic component, E_{el}, (iii) polarization component, E_p, (iv) charge-transfer components, E_{ct} and (v) dispersion component, E_{disp} by IMPT method [99]. The results suggested that in case of C–H···F, the interaction energy is mainly dominated by the electrostatic and dispersion component with the latter being more prevalent. The relevance and nature of hydrogen bond with fluorine was further reviewed in detail in solution, gas phase, and in solid state with inputs from computational and spectroscopic studies on this interaction [100]. The free energy for C–H···F hydrogen bond in CCl_4 was computed to be 6 kJ/mol which was higher than other halogens and the value increases with the change in hybridization of C-atom connected to the fluorine atom (from sp^3 to sp^2 to sp).

Furthermore, the relevance of C–H···F–C interactions were observed in the formation of different motifs such as dimer, chain, chains of dimers, etc., in the presence of strong N–H···O=C hydrogen bond and other related weak interactions like C–H···O, C–H···π, π···π, halogen–halogen interactions in the crystal packing studies of halogenated benzanilides [88–92]. The significance of these studies was to acquire the systematic analysis of interactions involving organic fluorine when the molecular skeleton was fixed and the position of fluorine atoms were varied, thus an isomeric series was obtained. In these series of compounds, the introduction of a F-atom and its systematic variation in position over phenyl ring leads to a concomitant variation in the crystal system and space group (from centrosymmetric to noncentrosymmetric). The cooperative and robust nature (an important condition for considering an interaction as a "hydrogen bond") of C–H···F–C interactions were observed and found to contribute significantly toward the crystal packing in these series of compounds. In one such example, the molecular chain generated with the utilization of C–H···F–C H-bonds in 2-fluoro-*N*-(2-fluorophenyl)benzamide remain invariant when the fluorine not participating in this interaction is replaced by chlorine atom in case of 2-fluoro-*N*-(2-chlorophenyl)benzamide (Fig. 2.12a, b) [88, 89]. Moreover, on replacement of the Cl-atom with Br-atom in 2-fluoro-*N*-(2-bromophenyl)benzamide leads to change in the crystal packing but a similar molecular chain via C–H···F–C H-bonds were still present in the crystal packing (Fig. 2.12c) [89].

Furthermore, the focus is now shifted to analyze the changes in molecular conformation and crystal packing on replacement of a –F by a $–CF_3$ moiety at the *o*-, *m*- and *p*- positions on either or both of the phenyl rings in this class of compounds. For this purpose, 15 compounds were synthesized [10 crystal structures [91]

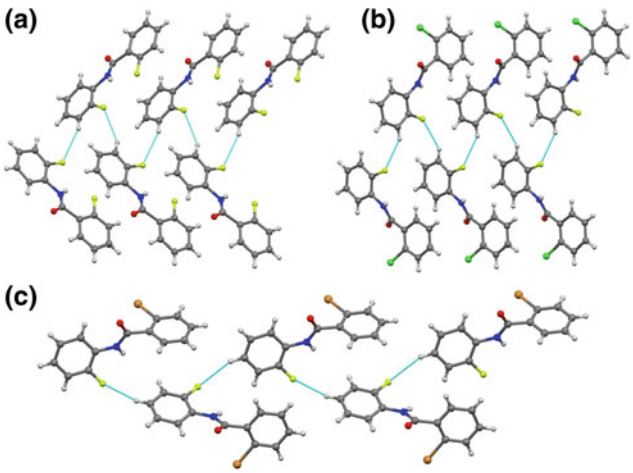

Fig. 2.12 Identical molecular chain formed via C–H···F–C H-bonds in case of **a** 2-fluoro-*N*-(2-fluorophenyl)benzamide **b** 2-fluoro-*N*-(2-chlorophenyl)benzamide. **c** Part of crystal packing in 2-fluoro-*N*-(2-bromophenyl)benzamide showing presence of C–H···F–C H-bonds [88, 89]

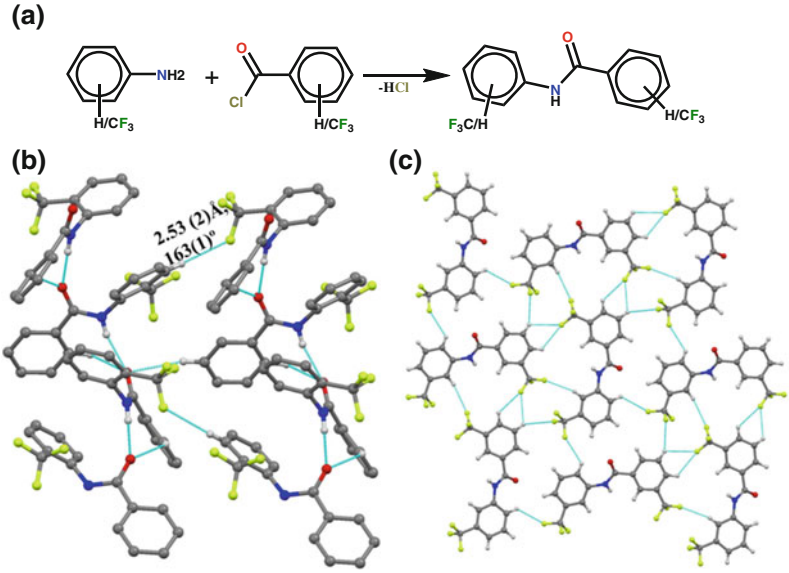

Fig. 2.13 **a** Chemical scheme for the fifteen trifluoromethyl substituted benzanilides. **b** Packing of the molecule in *N*-[2-(trifluoromethyl)phenyl]benzamide via strong N–H···O=C, weak C–H···O=C and short C(sp^2)–H···F–C(sp^3) H-bonds. **c** Formation of a herringbone arrangement in the crystal packing of 3-(Trifluoromethyl)-*N*-[3-(trifluoromethyl)phenyl]benzamide with the utilization of a network of C(sp^2)–H···F–C(sp^3) H-bonds [91]

were determined] (Fig. 2.13a). The salient purpose was to introduce the following electronic characteristics and see the changes in structure disposition: (i) The $–CF_3$ group being strongly electron-withdrawing in nature affects the behavior of hydrogen atoms present in its vicinity which participates in H-bond formation. (ii) Well documented, better H-bond acceptor abilities of C(sp^3)–F could be utilized (iii) In addition to C–H···F–C H-bonds, the possibilities of formation of other interactions like C–F···F–C and C–F···π was now increased. In this systematic and complete analysis of crystal packing of this series of compounds, the weak but directional C(sp^2)–H···F–C(sp^3) H-bonds were observed acting cooperatively to generate unique packing motifs. The acidic hydrogens (adjacent to $–CF_3$ group) appeared in the participation of the H-bonds utilizing the key symmetry elements of the corresponding space groups in which they crystallized. For examples, in case of *N*-[2-(trifluoromethyl)phenyl]benzamide (crystallizes in the rare tetragonal non-centrosymmetric space group $P4_1$), a relatively short and directional C(sp^2)–H···F–C(sp^3) H-bonds (symmetry code: $-y + 1, x, z + ¼$) were observed to connect the molecular chain formed by strong N–H···O hydrogen bond along 4_1-screw parallel to *z*-axis (Fig. 2.13b). In another example, networks of C(sp^2)–H···F–C(sp^3) H-bonds appeared to stabilize the formation of herringbone packing in case of 3-(Trifluoromethyl)-*N*-[3-(trifluoromethyl)phenyl]benzamide (Fig. 2.13c).

Furthermore, to investigate the geometrical and energetic features associated with weak C(sp^3/sp^2)–H···F–C(sp^3/sp^2) intermolecular interactions, in addition to the well-recognized N–H···O=C and C–H···O=C hydrogen bonds, a library of 12 compounds (derivatives of acetamide and benzamide, Fig. 2.14) were synthesized and their crystal structures were determined [101]. The C(sp^3/sp^2)–H···F–C(sp^3/sp^2) intermolecular interactions formed different chains (for example, Fig. 2.14a), molecular chains utilizing bifurcated C–H···F (for example, Fig. 2.14b), dimeric (two kinds, first, where two acceptors are from different molecules (for example, Fig. 2.14c) and second, where the two acceptors are from the same molecule (for example, Fig. 2.14d)) were observed in the crystal packing of these series of compounds. The interaction energies for different molecular motifs extracted from the crystal packing was determined by PIXEL calculation [102, 103]. The molecular motifs comprising C–H···F–C hydrogen bonds were observed to provide stabilization of 1.0–2.0 kcal/mol towards the crystal packing. From, the detailed investigation of all these crystal structures, it is also observed that C(sp^3/sp^2)–H···F–C (sp^3) provides more stabilization than C(sp^3/sp^2)–H···F–C(sp^2), hence supporting

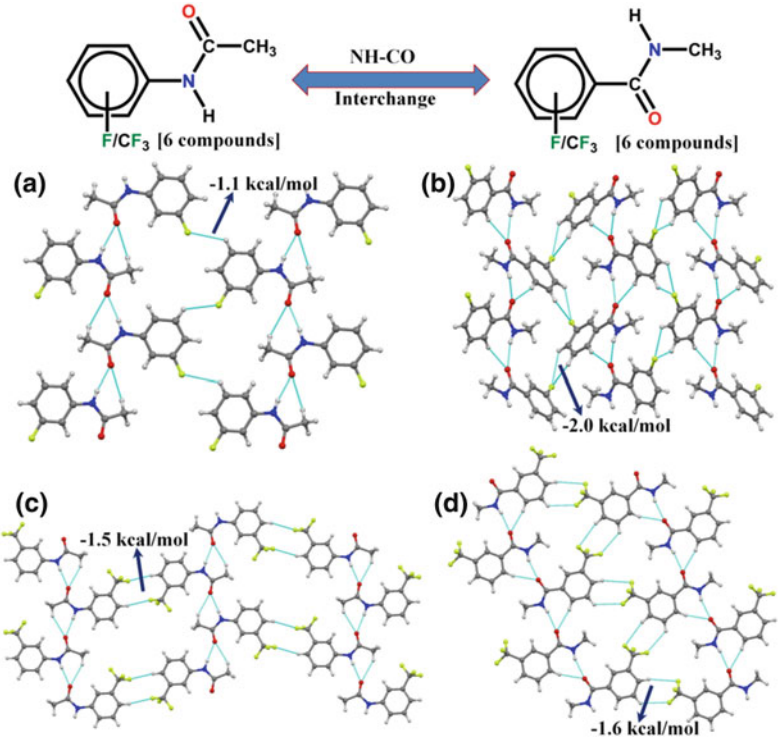

Fig. 2.14 Different molecular motifs formed via C–H···F–C hydrogen bonds in the presence of strong N–H···O=C and weak C–H···O=C hydrogen bonds in **a** *N*-(3-fluorophenyl)acetamide, **b** 3-fluoro-*N*-methylbenzamide, **c** *N*-(3-(trifluoromethyl)phenyl)acetamide, and **d** *N*-methyl-3-(trifluoromethyl)benzamide [101]

the fact that fluorine connected to sp^3 hybridized carbon has a greater propensity of forming H-bonds. In order to further extend the systematic investigation of interactions involving organic fluorine, 18 benzanilides containing –F or $–CF_3$ group on either side of the phenyl ring were synthesized and the preliminary analysis of their crystal structures revealed significant geometrical observations regarding interactions related to organic fluorine [104]. It was observed that one compound, *N*-(4-fluorophenyl)-3-(trifluoromethyl) benzamide exhibits dimorphism wherein two forms crystallize in a rare combination of noncentrosymmetric space groups (orthorhombic $Pna2_1$ and monoclinic *Cc*, respectively). In another related compound, 4-fluoro-*N*-[3-(trifluoromethyl)phenyl] benzamide (can be viewed as NH–CO interchange from the previous one) exists in a centrosymmetric form (monoclinic $P2_1/c$). The primary recognition motif consisting of N–H···O=C and π···π interaction was observed to be similar in all the three structures and the major difference appeared in the nature of the weaker interactions. In the orthorhombic form of *N*-(4-fluorophenyl)-3-(trifluoromethyl) benzamide, the crystal packing was stabilized by mainly the weak C–H···π interactions along with only one C–H···F interaction [2.61 Å/137° (neutron normalized)], the distance being less than the sum of the van der Waals radii (2.67 Å) of hydrogen and fluorine. In case of the monoclinic form, out of the 8 fluorine atoms in the asymmetric unit, six are involved in the formation of short C–H···F interactions, including the one with the H···F distance being 2.32 Å and a directionality of 162° (neutron normalized). Further, in the crystal packing of a related isomer, 4-fluoro-*N*-[3-(trifluoromethyl)phenyl] benzamide, a short and highly directional C–H···F [2.23 Å/173° (neutron normalized)] was observed. It is to be noticed that such short contacts were observed in the presence of strong N–H···O=C hydrogen bonds (involving acidic hydrogens) were observed to participate in the formation of short C–H···F–C contacts (Fig. 2.15). In the work, a molecular pair consisting of C–H···F interactions were extracted from the crystal packing and analyzed by the PIXEL method [102, 103] and Atoms in Molecule (AIM) [105, 106] theory. From the PIXEL energy calculations, it was obtained that the interaction energy of a molecular pair containing short C–H···F–C

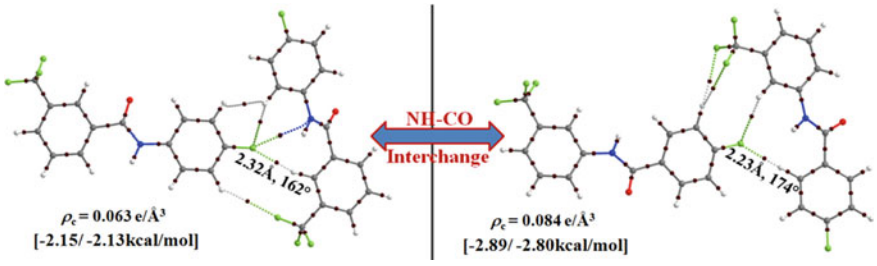

Fig. 2.15 Similar molecular motif in monoclinic form of *N*-(4-fluorophenyl)-3-(trifluoromethyl) benzamide and 4-fluoro-*N*-[3-(trifluoromethyl)phenyl] benzamide displaying short C–H···F hydrogen bonds (marked with *arrows*) with other interactions. Bond critical points are shown with *brown spheres*. Reprinted with the permission from Ref. [104]. Copyright 2014 American Chemical Society

contacts have a substantial Coulombic contribution (approx. 35 %) in comparison to the other weak interactions which are primarily of a dispersive character. The topological analysis were performed on the molecular pair consisting of C–H···F interactions, by program AIMALL and the results showed the presence of (3, −1) bond critical point (BCP) for C–H···F interactions in the molecular pairs. Topological parameters like electron density (ρ), Laplacian of the electron density ($\nabla^2\rho$), local potential (V_b), and kinetic energy density(G_b) were obtained. Local stabilization energy were obtained from equations: (i) $D.E^V(int) = -0.5V_b$ (in atomic units) [107] (ii) $D.E^G(int) = 0.429\ G_b$ (in atomic units) [108, 109]; where D.E(int) is the dissociation energy of the interaction. Interaction energy (I.E) = −D.E V_b and G_b are local potential and kinetic energy density at the bond critical points (BCP) respectively. Exponential decrease in electron density at BCP and D.E with increase in bond path distance was observed (Fig. 2.16). The magnitude of the stabilizing interaction energy were calculated to be −2.15 and −2.89 kcal/mol, for the short C–H···F interaction in the case of the monoclinic form of *N*-(4-fluorophenyl)-3-(trifluoromethyl) benzamide and 4-fluoro-*N*-[3-(trifluoromethyl)phenyl] benzamide respectively. The observed strength was found to be 30–40 % of the strength of a strong traditional H-bond in amides, N-H···O=C, whose interaction energy was calculated to be 6–8 kcal/mol. Furthermore, the value of the Laplacian of electron density was observed to be positive for all the C–H···F's which showed that these exhibit closed shell character and for the contacts below 2.7 Å, such values were observed to lie above 0.578 e/Å^5 (which is the criterion for considering an interaction as a hydrogen bond [105, 106]). Moreover, the value of |Vbl/Gb < 1 for all the ranges in R_{ij} for H···F interactions was observed, which is an important criterion for H-bond, as suggested by Espinosa [110]. Finally with respect to the criteria constituted by IUPAC it was concluded that C–H···F interactions at short distances are a true "hydrogen bond".

Recently, Azumaya et al. studied the role of fluorine substitution in the polymorphism of aromatic sulfonamides [111]. The existence of polymorphism was only observed in case of the fluorinated analogue of the sulfonamides (Fig. 2.17).

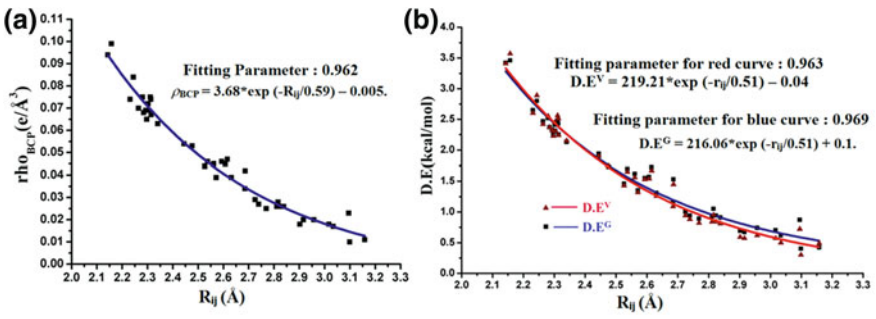

Fig. 2.16 **a** Variation of the electron density (ρ_{BCP}) at BCP versus H···F-bond path distance (Rij). **b** Variation of the dissociation energies (D.E) versus Rij. Reprinted with the permission from Ref. [104]. Copyright 2014 American Chemical Society

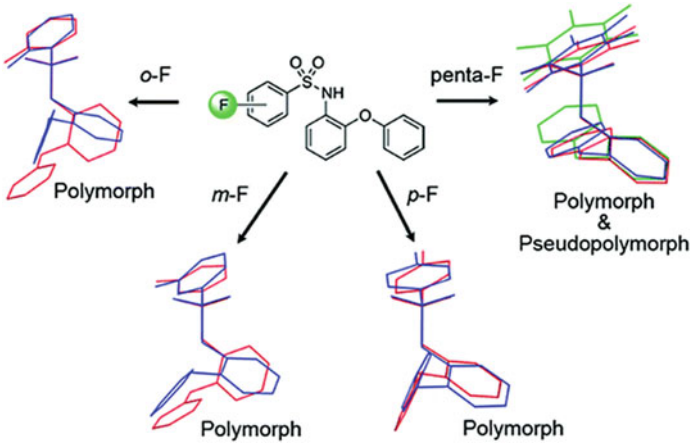

Fig. 2.17 Existence of polymorphism in fluorine-substituted *N*-(2-phenoxyphenyl)- benzene sulfonamides. Reprinted with the permission from Ref. [111]. Copyright 2012 American Chemical Society

The role of interactions involving organic fluorine like C–H···F–C, C, C–F···F–C (resulted in the formation of different molecular motifs) were observed to be crucial in the crystal packing of these polymorphs in presence of other stronger interactions like N–H···O=S, C–H···O=S, C–H···π.

2.3 Inputs from Other Interactions Involving Organic Fluorine

2.3.1 Insight into Halogen–Halogen Interactions Involving Fluorine

Halogen–halogen interactions are routinely divided into two categories: type I and type II (Fig. 2.18). Both type I and type II contacts appear frequently in the literature and CSD search wherein the heavier halogen tends to form type II more frequently while the lighter one (fluorine) appears to form mainly type I contacts. The type I contacts are often considered to arise from the consequence of dense crystal packing and "does not" or provides very low stabilization to the crystal packing. It was considered to be a van der Waal interaction and arise when two halogen atoms minimize repulsion by interfacing the neutral regions of their electrostatic potential surfaces. The type II contact involves an approach of the electrophilic region of one halogen atom with the nucleophilic region of the other halogen leading to its *L*-shaped geometry. Further, due to the very low polarizability of the fluorine atom, its participation in F···F interaction was questioned.

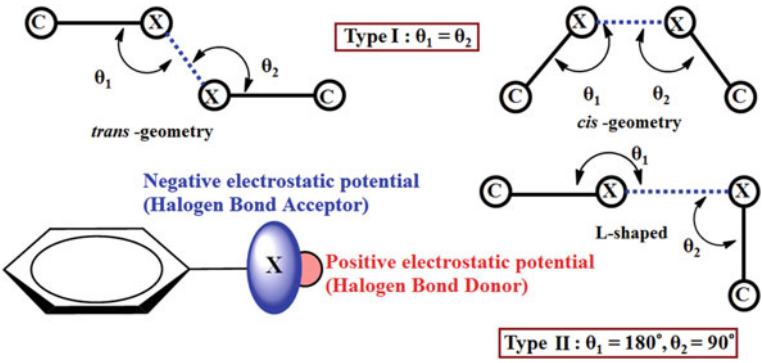

Fig. 2.18 Geometrical representation of halogen–halogen interactions

It was observed that it preferred to form weak C–H···F hydrogen bond rather than F···F interaction. However there are examples where F···F interactions have played a crucial role in the crystal packing. For example, in case of a uracil derivative, the F···F interactions were observed to be important in crystal packing [112]. In the crystal packing of (*N′*-(3-hydroxypropyl)-5-fluorouracil, a tetramer assembly of molecules held together by the presence of four type II F···F interactions was observed (Fig. 2.19a). In the crystal packing of *N′*-(4-hydroxycarbonylbutyl)-5-fluorouracil monohydrate, two molecules was observed to connect via a short (2.624 Å) type I F···F interaction in a molecular chain (Fig. 2.19b). These F···F interactions were studied by ab initio calculation using MP2/6-31+G* method. The results suggested that the tetrameric motif having four type II F···F interactions provides 4 kcal/mol stabilization to the crystal packing (hence each contributed approximately 1 kcal/mol stabilization energy). Atoms in molecule (AIM) approach for this tetrameric motif confirmed the presence of (3, −1) BCPs and the value of

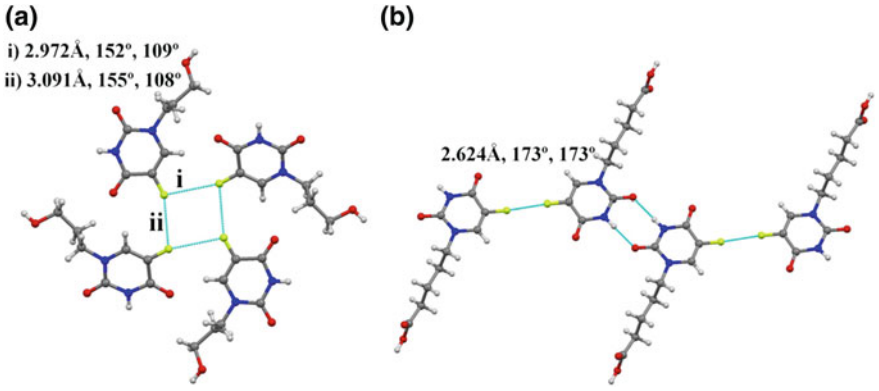

Fig. 2.19 Part of crystal packing in **a** (N^1-(3-hydroxypropyl)-5-fluorouracil and **b** N^1-(4-hydroxycarbonylbutyl)-5-fluorouracil monohydrate displaying F···F interactions [112]

the Laplacian was observed to be positive, suggesting that these were closed shell interactions. Similar results have been obtained from related experimental charge density studies [113–115]. Further, theoretical calculations at the same level for the short type I F···F interaction were performed on the parent dimer and another wherein the long alkyl chain was replaced with the methyl group on the parent dimer. The interaction energies obtained were −1.7 and −1.5 kcal/mol for the two cases respectively. From AIM analysis, the value of the electron density (ρ) at the BCP for this contact was more than that of type II F···F contacts in the previous case, Therefore, these results suggested that the type I F···F interaction can be as crucial as type II F···F in the stabilization of crystal structure.

Further detailed analysis of F···F interactions with input from ab initio calculations at MP2/aug-cc-pVDZ level, topological analysis (AIM) and SAPT calculations were performed over all nonsymmetry equivalent dimers present in CF_4, C_2F_4, and C_6F_6 crystals [116]. It was observed that all dimers are energetically stable with the stabilization energy ranging from −0.21 to −2.65 kcal/mol (Fig. 2.20). From AIM analysis the strength of a single C–F···F was obtained as −0.21 kcal/mol for F–C(sp^3), −0.25 kcal/mol for F–C(sp^2, nonaromatic) and −0.41 kcal/mol for F–C(sp^2, aromatic). The value of the Laplacian was observed to be positive for all interactions and hence these are classified as closed shell interactions. From the SAPT calculations, it was observed that the dispersion component is dominant for collinear contacts where as in many cases, particularly in most stabilized dimers, the electrostatic component was as significant as the dispersive component. Moreover, through the calculations of the stabilization energy for the C–F···F interaction (interact collinearly) in model dimers of CHF_3, CH_2F_2, and

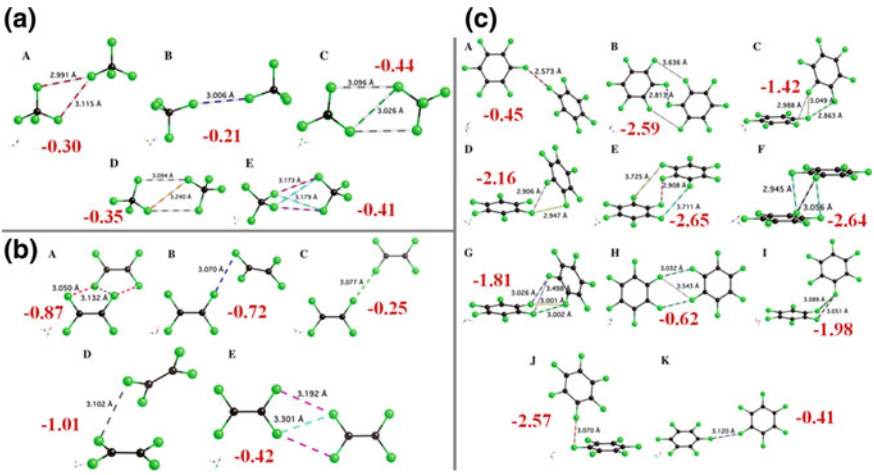

Fig. 2.20 Extracted symmetry nonequivalent dimers from the crystal packing of **a** CF_4 **b** C_2F_4 and **c** C_6F_6. Numbers in *brown colors* represent BSSE corrected interaction energy (in kcal/mol) at MP2/aug-cc-pVDZ level. Reprinted with the permission from Ref. [116]. Copyright 2010 Springer-Verlag

CH_3F, it was observed that with increase in H-atoms, the strength of C–F···F interaction is reduced.

A recent experimental (crystal structure) and theoretical study (ab initio quantum calculation and AIM theory) for fluorine–fluorine interactions was performed on compounds containing a perfluorinated chain: (**1**) $CF_3(CF_2)_5CH_2CH(CH_3)CO_2H$, (**2**) $CF_3(CF_2)_5(CH_2)_4(CF_2)_5CF_3$ and (**3**) $\{CF_3(CF_2)_5CH_2CH_2\}_3P = O$ and many short type I and type II C–F···F–C interactions along with C–H···F–C were observed in the crystal packing (Figs. 2.21 and 2.22) [117]. Selected dimers consisting of these interactions were extracted from the crystal packing and the interaction energy were calculated at DFT/B97-D using aug-cc-pV*n*Z, where *n* = D, T, or Q. basis set and stabilization energy ranging from 0.26 to 29.64 kcal/mol were

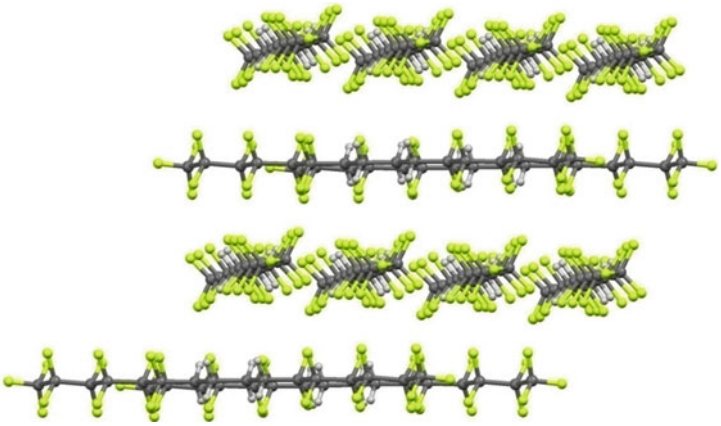

Fig. 2.21 Packing of molecules in **2**

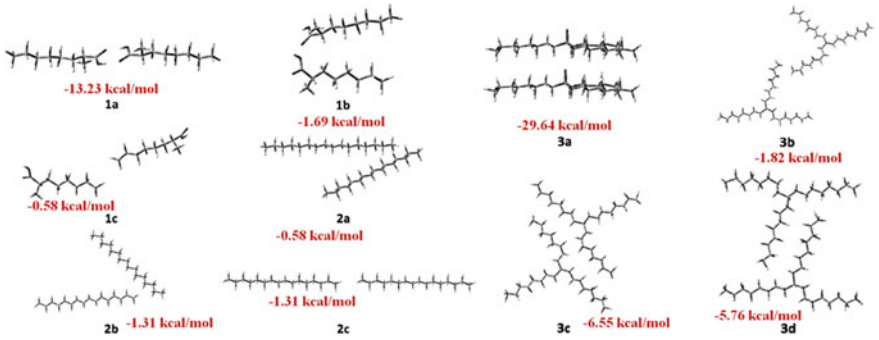

Fig. 2.22 Molecular dimers extracted from the crystal packing of **1**, **2** and **3** along with their interaction energy. Reprinted with the permission from Ref. [117]. Copyright 2012 American Chemical Society

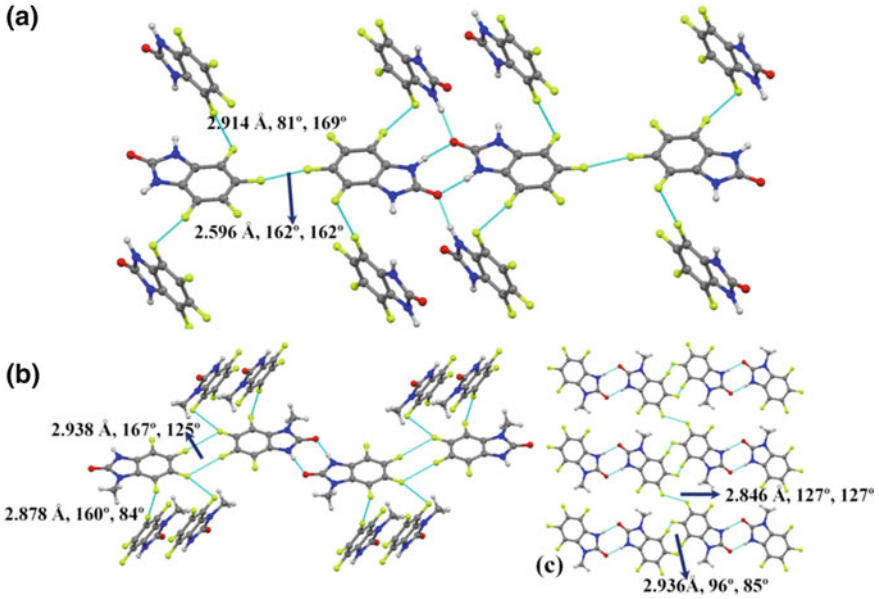

Fig. 2.23 **a** The crystal structure packing in 4,5,6,7-tetrafluoro-1*H*-benzimidazole-2(3H)-one displaying short C–F···F–C contact. Crystal packing in **b** Form I and **c** Form II of 4,5,6,7-tetrafluoro-1-methyl-1*H*-benzimidazole-2(3H)-one, displaying differences in nature of C–F···F–C interactions in these [93]

observed. The presence of these interactions in the different dimers was also confirmed by the presence of (3, −1) BCPs by Atoms in Molecule approach.

Recently, shortest F···F distances were reported (2.596(3) Å, type I, Fig. 2.23a) in the crystal packing of 4,5,6,7-tetrafluoro-1*H*-benzimidazole-2(3H)-one along with related type II F···F contacts by Pérez-Torralba et al. [93]. In the same work, it was also observed that the F···F contacts have implications in the generation of polymorphs in case of 4,5,6,7-tetrafluoro-1-methyl-1*H*-benzimidazole-2(3*H*)-one wherein the two forms have differences in molecular motifs containing F···F contacts (Fig. 2.23b, c). In case of one form, a centrosymmetric type II F···F contact along with two other short type II F···F contacts were observed to stabilize the crystal packing (Fig. 2.23b) while in the case of the second form, mainly type I F···F contacts were observed.

2.3.2 Insights into Halogen Bond Formation Involving Fluorine (C–F···X; X = Halogen, N, O, S)

After the well documented hydrogen bond, the halogen bonds constitute an important core of supramolecular chemistry [26–33]. This is an electrostatic

interaction and arises due to anisotropic distribution of the electron density over the covalently bonded halogen atom. There is presence of an electrophilic δ+ character along the axis of the σ-bonded (C–X) halogen atom, which is termed as "the positive σ-hole". Subsequently, perpendicular to the C–X bond, the halogen atoms exhibits nucleophilic δ- character. The strength of the halogen bond decreases in the order I > Br > Cl > F which is in accordance with the decrease in polarizability and increase in electronegativity. The IUPAC definition of halogen bond is given as follows: "A halogen bond occurs when there is evidence of a net attractive interaction between an electrophilic region associated with a halogen atom in a molecular entity and a nucleophilic region in another, or the same, molecular entity" [118]. In accordance with the IUPAC definition of the halogen bond, the type II halogen···halogen interactions can also be considered as halogen bond [119, 120]. The participation of fluorine as a halogen bond donor was questioned because it is the least polarizable and the most electronegative element. However, in recent years, experimental and theoretical studies support the possible role of organic fluorine as a halogen bond donor. Charge density studies on organic fluorine by Hathwar et al. [121] provides evidence for the presence of polarizability associated with a fluorine atom bonded to carbon. From recent works by Metrangolo and co-workers, it was established that fluorine can display a positive σ-hole, when connected to an electron withdrawing atom or a group [122, 123]. For example, in case of CF_3SO_2OCOF, the presence of a positive cap (can be considered as the positive σ-hole) on the fluorine attached to carbonyl group was observed on the computed electrostatic potential (0.001 au electron density molecular surface) while the $–CF_3$ group has a positive ESP on its entire surface (Fig. 2.24) [122, 123]. The computed electrostatic maxima (Vs,max, in kcal/mol) on the 0.001 au isosurface of the molecule at the B3PW91/6-31G(d,p) level was observed to be +4.2 for O=C–F and +9.6, +9.6, +10.1 for CF_3 [123]. In the crystal packing, participation of this fluorine as a halogen bond donor and oxygen atom, containing lone pair, as halogen bond acceptor was observed in the formation of a molecular chain (Fig. 2.25). The interaction energy for the $F_2C–F\cdots O=C$ contact was computed at M06-2X/6-311G (3df,2p) level to be 1.13 kcal/mol [122]. Similarly, there are many related examples where fluorine atom can act as a halogen bond donor when attached to an atom or electron withdrawing groups [122, 123].

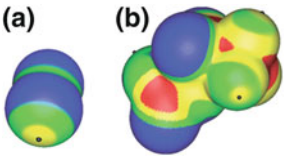

Fig. 2.24 **a** Computed electrostatic potentials (on 0.001 au molecular surfaces) of F_2 (A) and CF_3SO_2OCOF (B, the CF_3 group is at the right). *Color* ranges, in kcal/mol, are: red, greater than 20; *yellow*, between 20 and 9; *green*, between 9 and 0; *blue*, negative. *Black* hemispheres denote the positions of the most positive potentials associated with the fluorine atoms. (Reprinted with the permission from Ref. [122]. Copyright 2011 Royal Society of Chemistry

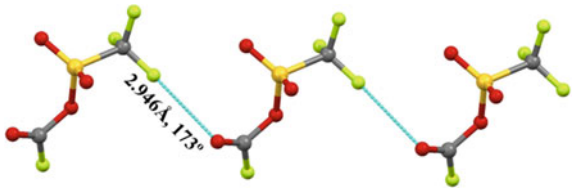

Fig. 25 Molecular chain formation via C–F···O=C halogen bond in CF_3SO_2OCOF

Recent charge density studies on 4-fluorobenzoyl chloride and 2,3-difluorobenzoyl chloride by Dikundwar and Guru Row [124] established that the fluorine atom can act as both a donor and acceptor for halogen bond formation (depicting "amphoteric" nature of fluorine, Figs. 2.26 and 2.27). Here it should be noted that the fluorine atom in the vicinity of two electron withdrawing groups (the other fluorine atom and the –C=O group) in case of 2,3-difluorobenzoyl chloride acting as halogen bond donor. The bond path (R_{ij}) for Cl···F interaction [characterized by the presence of a (3, −1) BCP's] in both the compounds was observed to be shorter than the sum of the van der Waals radii of the participating atoms (the van der Waals radii of Cl and F are 1.75 and 1.47 Å [125], respectively). In the Laplacian maps and static 3D deformation density maps, attractive nature of the Cl···F interactions was clearly visible. It was observed that the charge concentration (CC) regions were attracted towards the charge depleted (CD) regions (Fig. 2.27).

A recent charge density study on pentafluorophenyl 2,2′-bisthiazole by Pavan and Guru Row [126] has established type II C–F···F–C and C–F···S–C interactions (Fig. 2.28). The geometry of the type II C–F···F–C observed as $d_{F\cdots F}$ = 2.663 Å, $\theta_1 = 173.61°$; $\theta_2 = 88.91°$ and for C–F···S interaction as $d_{F\cdots S} = 3.286$ Å, $\theta = 162.82°$. The authors claimed it as the first experimental visualization of an σ-hole on organic fluorine. The presence of both the interactions was confirmed by the presence of (3, −1) BCP and a bond path. Laplacian maps and static 3D deformation density maps displayed the attractive nature of these interactions. The calculation of the

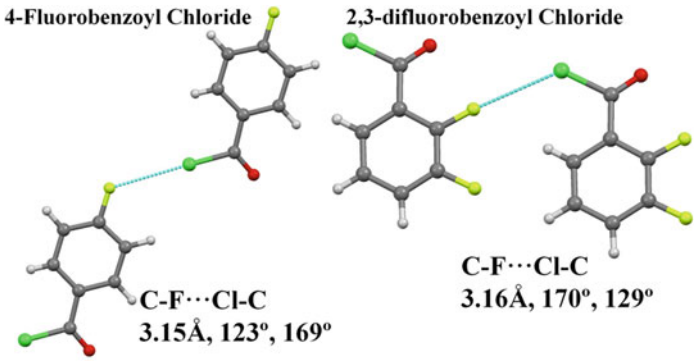

Fig. 2.26 "*Amphoteric*" nature of fluorine in halogen bonds [124]

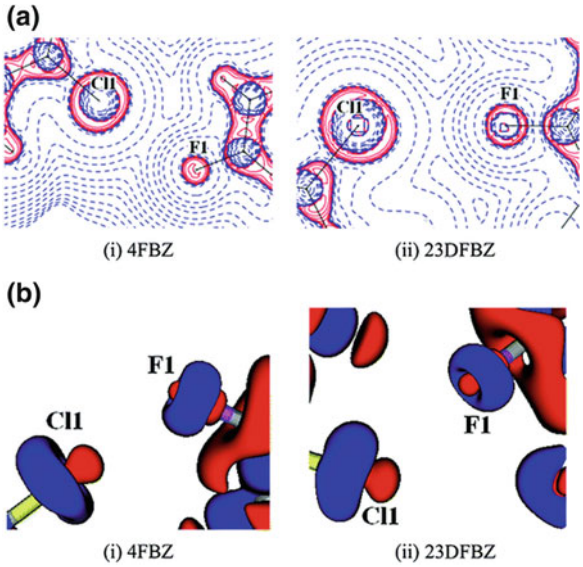

Fig. 2.27 **a** Laplacian maps and **b** 3D static deformation density maps for Cl···F intermolecular interactions in (*i*) 4-fluorobenzoyl chloride and (*ii*) 2,3-difluorobenzoyl chloride. Contours are drawn at logarithmic intervals in $\nabla^2\rho$ (r), eÅ^{-5}. *Blue lines* indicate positive contours, and *red lines* indicate negative contours. $\Delta\rho$(r) isosurfaces are drawn at ±0.1 e Å^{-3}. Reprinted with the permission from Ref. [124]. Copyright 2012 American Chemical Society

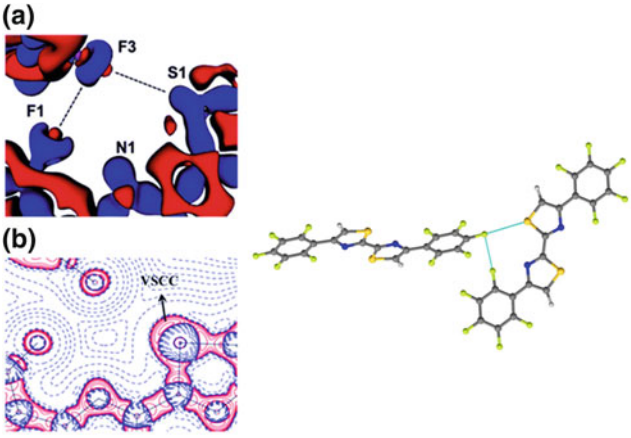

Fig. 2.28 Experimental **a** $\Delta\rho$(r) and **b** $\nabla^2\rho$(r) maps drawn on the logarithmic scale in the F···F and S···F interaction region, +ve and -ve values represented by blue and red colors. $\Delta\rho$(r) isosurfaces are drawn at ± 0.05 e Å^{-3}. Reprinted with the permission from Ref. [126]. Copyright 2014 American Chemical Society

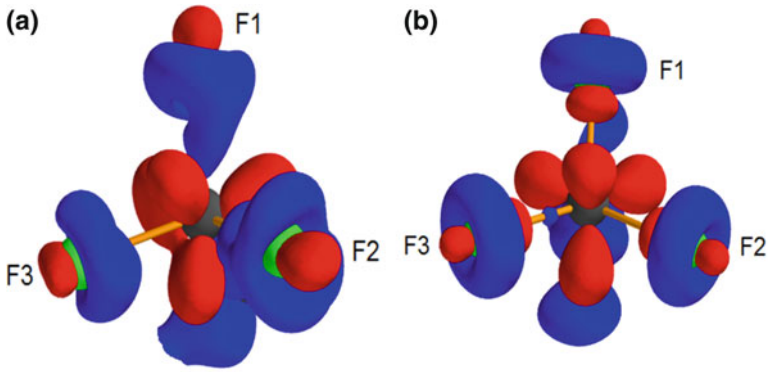

Fig. 2.29 3D-deformation density map showing the presence of CD regions (σ-holes in red) and CC regions on the fluorine atoms of the trifluoromethyl group in *N*-(2-(trifluoromethyl)phenyl) benzamide obtained from **a** experiment **b** theory. The isosurfaces are drawn at 0.15 e $Å^{-3}$. Reprinted with the permission from Ref. [128]. Copyright 2014 American Chemical Society

electrostatic interaction energies (from the multipole model) was performed by using the INTERN module in XD2006 [127] and it was observed that for the type II F···F and C–F···S interactions, the major contribution arises from the electrostatic energy rather than dispersion which suggests that both are of $\delta^{+}\cdots\delta^{-}$ type.

Furthermore, the unequivocal observation of the σ-hole on the fluorine atom of the trifluoromethyl group in the crystal has been revealed from both experimental and theoretical charge density analysis on *N*-(2-(trifluoromethyl)phenyl)benzamide (Fig. 2.29) [128]. Hence this study breaks the long accepted lore that "organic fluorine is not polarizable".

2.4 Conclusions

From the above discussions, it is of interest and significance to realize that the contribution of organic fluorine in the formation of intermolecular interactions is noteworthy and does provide stability to the crystal structure. Due to the cooperative, flexible nature associated with these soft and weak interactions, their inevitable role in crystal packing cannot be predicted, given the knowledge of the chemical structure or conformation of the molecules. The existence of disorder, problems associated with multiple molecules in the asymmetric unit, and polymorphism further complicate the prediction of the crystal structure of a given compound. In the future, we propose to investigate interactions involving organic fluorine in different electronic and steric environments (in terms of changes in the nature of the donor C–H and the acceptor C–F of varying hybridizations) in the solid state.

Acknowledgments We wish to thank IISER Bhopal for research facilities and infrastructure. DC thanks DST-Fast Track Scheme, IISER Bhopal and DRDE, Gwalior for research funding. PP thanks UGC, India for research fellowship. The authors thank Mr Abhinav Gupta for help in the compilation of the chapter.

References

1. Philip D, Stoddart JF (1996) Self-assembly in natural and unnatural systems. Angew Chem Int Ed 35:1154
2. Desiraju GR (2013) Crystal engineering: from molecule to crystal. J Am Chem Soc 135:9952
3. Hunter CA (2004) Quantifying intermolecular interactions: guidelines for the molecular recognition toolbox. Angew Chem Int Ed 43:5310
4. Schneider HJ (2009) Binding mechanisms in supramolecular complexes. Angew Chem Int Ed 48:3924
5. Dunitz JD, Gavezzotti A (2009) How molecules stick together in organic crystals. Chem Soc Rev 38:2622
6. Cerny J, Hobza P (2007) Non-covalent interactions in biomacromolecules. Phys Chem Chem Phys 9:5291
7. Glowack ED, Irimia-Vladu M, Bauer S, Sariciftci NS (2013) Hydrogen-bonds in molecular solids—from biological systems to organic electronics. J Mater Chem B 1:3742 and references therein
8. Bonin J, Costentin C, Robert M, Saveant JM, Tard C (2012) Hydrogen-bond relays in concerted proton-electron transfers. Acc Chem Res 45:372
9. Zhao GJ, Han KL (2012) Hydrogen bonding in the electronic excited state. Acc Chem Res 45:404
10. Jeffrey GA, Saenger W (1991) Hydrogen bonding in biological structures. Springer-Verlalg, New York
11. Desiraju GR (2011) A bond by any other name. Angew Chem Int Ed 50:52
12. Arunan E, Desiraju GR, Klein RA, Sadlej J, Scheiner S, Alkorta I, Clary DC, Crabtree RH, Dannenberg JJ, Hobza P, Kjaeergaard HG, Legon AC, Mennucci B, Nesbitt DJ (2011) Defining the hydrogen bond: an account (IUPAC Technical Report). Pure Appl Chem 83:1619
13. Arunan E, Desiraju GR, Klein RA, Sadlej J, Scheiner S, Alkorta I, Clary DC, Crabtree RH, Dannenberg JJ, Hobza P, Kjaeergaard HG, Legon AC, Mennucci B, Nesbitt DJ (2011) Definition of the hydrogen bond (IUPAC Recommendations 2011). Pure Appl Chem 83:1637
14. Pauling L (1939) The nature of the chemical bond. Cornell University Press, Ithaca, NY
15. Desiraju GR, Steiner T (1999) The weak hydrogen bond in structural chemistry and biology. Oxford University Press, Oxford
16. Melandri S (2011) "Union is strength": how weak hydrogen bonds become stronger. Phys Chem Chem Phys 13:13901
17. Desiraju GR (2005) C–H···O and other weak hydrogen bonds: from crystal engineering to virtual screening. Chem Comm 2995
18. Bosch E (2010) Role of sp-C–H···N hydrogen bonding in crystal engineering. Cryst Growth Des 10:3808
19. Takahashi O, Kohno Y, Nishio M (2010) Relevance of weak hydrogen bonds in the conformation of organic compounds and bioconjugates: evidence from recent experimental data and high-level *ab Initio* MO calculations. Chem Rev 110:6049
20. Nishio M (2011) The CH/π hydrogen bond in chemistry: conformation, supramolecules, optical resolution and interactions involving carbohydrates. Phys Chem Chem Phys 13:13873

21. Martinez CR, Iverson BL (2012) Rethinking the term "pi-stacking". Chem Sci 3:2191
22. Robertazzi A, Krull F, Knapp W, Gamez P (2011) Recent advances in anion–π interactions. CrystEngComm 13:3293
23. Estarellas C, Bauza A, Frontera A, Quinonero D, Deya PM (2011) On the directionality of anion–π interactions. Phys Chem Chem Phys 13:5696
24. Dawson RE, Hennig A, Weimann DP, Emery D, Ravikumar V, Montenegro J, Takeuchi T, Gabutti S, Mayor M, Mareda J, Schalley CA, Matile S (2010) Experimental evidence for the functional relevance of anion–π interactions. Nat. Chem 2:533
25. Wallnoefer HG, Fox T, Liedl KR, Tautermann CS (2010) Dispersion dominated halogen–p interactions: energies and locations of minima. Phys Chem Chem Phys 12:14941
26. Beale TM, Chudzinski MG, Sarwar MG, Taylor MS (2013) Halogen bonding in solution: thermodynamics and applications. Chem Soc Rev 42:1667
27. Erdelyi M (2012) Halogen bonding in solution. Chem Soc Rev 41:3547
28. Parisini E, Metrangolo P, Pilati T, Resnati G, Terraneo G (2011) Halogen bonding in halocarbon–protein complexes: a structural survey. Chem Soc Rev 40:2267
29. Riley KE, Hobza P (2013) The relative roles of electrostatics and dispersion in the stabilization of halogen bonds. Phys Chem Chem Phys 15:17742
30. Ibrahim MAA (2012) Molecular mechanical perspective on halogen bonding. J Mol Model 18:4625
31. Politzer P, Murray JS, Clark T (2013) Halogen bonding and other σ-hole interactions: a perspective. Phys Chem Chem Phys 15:11178
32. Zhang Y, Ma N, Wang W (2012) A new class of halogen bonds that avoids the σ-hole. Chem Phys Lett 532:27
33. Mukherjee A, Tothadi S, Desiraju GR (2014) Halogen bonds in crystal engineering: like hydrogen bonds yet different. Acc Chem Res 47:2514
34. Guzman-Percastegui E, Alvarado-Rodríguez JG, Cruz-Borbolla J, Andrade-Lopez N, Vazquez-García RA, Nava-Galindo RN, Pandiyan T (2014) Subtle C–H···Hal (Hal = Cl, Br) bonding as predominant synthon in the assembly of supramolecular architectures based on luminescent tin(IV) complexes: crystallography, hirshfeld surfaces, DFT calculations, and fluorescence. Cryst Growth Des 14:3742
35. Steiner T (2002) The hydrogen bond in the solid state. Angew Chem Int Ed 41:48
36. Thallapally PK, Nangia A (2001) A cambridge structural database analysis of the C–HCl interaction: C–H···Cl^- and C–H···Cl–M often behave as hydrogen bonds but C–H···Cl–C is generally a van der waals interaction. CrystEngComm 3:114
37. Hauchecorne D, Herrebout WA (2013) Experimental characterization of C–X···Y–C (X = Br, I; Y = F, Cl) halogen−halogen bonds. J Phys Chem A 117:11548
38. Saha BK, Nangia A, Nicoud JF (2006) Using halogen···halogen interactions to direct noncentrosymmetric crystal packing in dipolar organic molecules. Cryst Growth Des 6:1278
39. Awwadi FF, Willett RD, Peterson KA, Twamley B (2006) The nature of halogen···halogen synthons: crystallographic and theoretical studies. Chem Eur J 12:8952
40. Aubert E, Lebègue S, Marsman M, Bui TT, Jelsch C, Dahaoui S, Espinosa E, Angyán JG (2011) Periodic projector augmented wave density functional calculations on the hexachlorobenzene crystal and comparison with the experimental multipolar charge density model. J Phys Chem A 115:14484
41. Berger R, Resnati G, Metrangolo P, Weber E, Hulliger J (2011) Organic fluorine compounds: a great opportunity for enhanced materials properties. Chem Soc Rev 40:3496
42. Reichenbacher K, Suss HI, Hulliger J (2005) Fluorine in crystal engineering—"the little atom that could". Chem Soc Rev 34:22
43. Egli M (2012) The steric hypothesis for DNA replication and fluorine hydrogen bonding revisited in light of structural data. Acc Chem Res 45:1237
44. Merkel L, Budisa N (2012) Organic fluorine as a polypeptide building element: in vivo expression of fluorinated peptides, proteins and proteomes. Org Biomol Chem 10:7241
45. Vincent JM (2012) Recent advances of fluorous chemistry in material sciences. Chem Commun 48:11382

46. Zhou P, Zou J, Tian F, Shang Z (2009) Fluorine bonding—How does it work in protein-ligand interactions? J Chem Inf Model 49:2344
47. Cametti M, Crousse B, Metrangolo P, Milani R, Resnati G (2012) The fluorous effect in biomolecular applications. Chem Soc Rev 41:31
48. O'Hagan D (2008) Understanding organofluorine chemistry: an introduction to the C–F bond. Chem Soc Rev 37:308
49. Ilardi EA, Vitaku E, Njardarson JT (2014) Data-mining for sulfur and fluorine: an evaluation of pharmaceuticals to reveal opportunities for drug design and discovery. J Med Chem 57:2832
50. Smart BE (2001) Fluorine substituent effects (on bioactivity). J Fluorine Chem 109:3
51. Bohm HJ, Banner D, Bendels S, Kansy M, Kuhn B, Muller K, Obst-Sander U, Stahl M (2004) Fluorine in medicinal chemistry. ChemBioChem 5:637
52. Gouverneur V, Muller K (2012) Fluorine in pharmaceutical and medicinal chemistry. World Scientific, London ISBN: 978-1-908977-89-2
53. Ojima I (2009) Fluorine in medicinal chemistry and chemical biology. Institute of Chemical Biology and Drug Discovery, State University of New York at Stony Brook, New York ISBN: 9781444312096
54. O'Hagan D, Rzepa HS (1997) Some influences of fluorine in bioorganic chemistry. Chem Commun 645
55. Roesky H (2010) A flourish of fluorine. Nat Chem 2:240
56. Wang J, Sanchez-Rosello M, Acena JL, Pozo CD, Sorochinsky AE, Fustero S, Soloshonok VA, Liu H (2014) Fluorine in pharmaceutical industry: fluorine-containing drugs introduced to the market in the last decade (2001–2011). Chem Rev 114:2432
57. Jeschke P (2004) The unique role of fluorine in the design of active ingredients for modern crop protection. ChemBioChem 5:570
58. O'Hagan D (2010) Fluorine in health care: organofluorine containing blockbuster drugs. J Fluorine Chem 131:1071
59. Müller K, Faeh C, Diederich F (2007) Fluorine in pharmaceuticals: looking beyond intuition. Science 317:1881
60. Purser S, Moore PR, Swallow S, Gouverneur V (2008) Fluorine in medicinal chemistry. Chem Soc Rev 37:320
61. Shimoni L, Glusker JP (1994) The geometry of intermolecular interactions in some crystalline fluorine-containing organic compounds. Struc Chem 5:383
62. Dunitz JD, Taylor R (1997) Organic fluorine hardly ever accepts hydrogen bonds. Chem Eur J 3:89
63. Howard JAK, Hoy VJ, O'Hagan D, Smith GT (1996) How good is fluorine as a hydrogen bond acceptor? Tetrahedron 52:12613
64. Thalladi VR, Weiss H-C, Blaser D, Boese R, Nangia A, Desiraju GR (1998) C–H···F interactions in the crystal structures of some fluorobenzenes. J Am Chem Soc 120:8702
65. Parsch J, Engels JW (2002) C–F···H–C hydrogen bonds in ribonucleic acids. J Am Chem Soc 124:5564
66. Dunitz JD (2004) Organic fluorine: odd man out. ChemBioChem 5:614
67. Gavezzotti A (2011) Efficient computer modeling of organic materials: the atom–atom, Coulomb–London–Pauli (AACLP) model for intermolecular electrostatic-polarization, dispersion and repulsion energies. New J Chem 35:1360
68. Dunitz JD, Schweizer WB (2006) Molecular pair analysis: CH···F interactions in the crystal structure of fluorobenzene? and related matters. Chem Eur J 12:6804
69. Cozzi F, Bacchi S, Filippini G, Pilati T, Gavezzotti A (2007) Synthesis, x-ray diffraction and computational study of the crystal packing of polycyclic hydrocarbons featuring aromatic and perfluoroaromatic rings condensed in the same molecule: 1,2,3,4–tetrafluoronaphthalene, –anthracene and –phenanthrene. Chem Eur J 13:7177
70. Ganguly P, Desiraju GR (2008) Van der waals and polar intermolecular contact distances: quantifying supramolecular synthons. Chem Asian J 3:868

71. Thakur TS, Kirchner MT, Blaser D, Boese R, Desiraju GR (2010) C–H···F–C hydrogen bonding in 1,2,3,5-tetrafluorobenzene and other fluoroaromatic compounds and the crystal structure of alloxan revisited. CrystEngComm 12:2079
72. Chopra D, Guru Row TN (2011) Role of organic fluorine in crystal engineering. CrystEngComm 13:2175
73. Chopra D (2012) Is organic fluorine really "not" polarizable? Cryst Growth Des 12:541
74. Choudhury AR, Guru Row TN (2004) How Realistic Are interactions involving organic fluorine in crystal engineering? insights from packing features in substituted isoquinolines. Cryst Growth Des 4:47
75. Choudhury AR. Guru Row TN (2006) Organic fluorine as crystal engineering tool: evidence from packing features in fluorine substituted isoquinolines. CrystEngComm 8:265
76. Choudhury AR, Guru Row TN (2003) Crystal structure and molecular conformation of chloro and bromo phenyl derivatives of 1, 2-diaryl-6-methoxy-1, 2, 3, 4-tetrahydroisquinoline: a comparative study with fluoro analogues. Cryst Engg 6:43
77. Chopra D,Thiruvenkatam V, Manjunath SG, Guru Row TN (2007) Variability in halogen interactions: in situ cryocrystallization of low melting substituted trifluoroacetophenones. Cryst Growth Des 7:868
78. Schwarzer A, Weber E (2008) Influence of fluorine substitution on the crystal packing of *N*–phenylmaleimides and corresponding phthalimides. Cryst Growth Des 8:2862
79. Vasylyeva V, Merz K (2010) Fluorobenzonitriles: Influence of the substitution pattern on melting and crystallization properties. Cryst Growth Des 10:4250
80. Vasylyeva V, Shishkin OV, Maleev AV, Merz K (2012) Crystal structures of fluorinated pyridines from geometrical and energetic perspectives. Cryst Growth Des 12:1032
81. Kaur G, Panini P, Chopra D, Choudhury AR (2012) Structural investigation of weak intermolecular interactions in fluorine substituted isomeric N–benzylideneanilines. Cryst Growth Des 12:5096
82. Karanam M, Choudhury AR (2013) Study of halogen-mediated weak interactions in a series of halogen-substituted azobenzenes. Cryst Growth Des 13:4803
83. Choudhury AR, Bhat RG, Guru Row TN, Chandrasekaran S (2007) Weak C_{sp3}–H···F–C interaction overshadows the strong CC–H···O=C hydrogen bond: structure of pentafluorophenyl Prop-2-ynyl carbonate. Cryst Growth Des 7:844
84. Dikundwar AG, Venkateswarlu Ch, Piltz RO, Chandrasekaran S, Guru Row TN (2011) Crystal structures of fluorinated aryl biscarbonates and a biscarbamate: a counterpoise between weak intermolecular interactions and molecular symmetry. CrystEngComm 13:1531
85. Kaur G, Choudhury AR (2014) Understanding of the weak intermolecular interactions involving halogens in substituted N–benzylideneanilines: insights from structural and computational perspectives. Cryst Growth Des 14:1600
86. Merz K, Evers MV, Uhl F, Zubatyuk RI, Shishkin OV (2014) Role of CHF_2- and CF_3- substituents on molecular arrangement in the solid state: experimental and theoretical crystal structure analysis of CH_3/CHF_2/CF_3–substituted benzene. Cryst Growth Des 14:3124
87. Abad A, Agulló C, Cuñat AC, Vilanova C, Ramírez de Arellano MC (2006) X-ray structure of fluorinated *N*-(2-Chloropyridin-4-yl)-*Nø*-phenylureas: role of F substitution in the crystal packing. Cryst Growth Des 6:46
88. Chopra D, Guru Row TN (2008) Evaluation of the interchangeability of C–H and C–F groups: insights from crystal packing in a series of isomeric fluorinated benzanilides. CrystEngComm 10:54
89. Nayak SK, Reddy MK, Guru Row TN, Chopra D (2011) Role of hetero-halogen (F···X, X = Cl, Br, and I) or homo-halogen (X···X, X = F, Cl, Br, and I) interactions in substituted benzanilides. Cryst Growth Des 11:1578
90. Nayak SK, Reddy MK, Guru Row TN, Chopra D (2012) Evaluation of the role of disordered organic fluorine in crystal packing: insights from halogen substituted benzanilides. CrystEngComm 14:200
91. Panini P, Chopra D (2012) Role of intermolecular interactions involving organic fluorine in trifluoromethylated benzanilides. CrystEngComm 14:1972

92. Mocilac P, Donnelly K, Gallagher JF (2012) Structural systematics and conformational analyses of a 3x3 isomer grid of fluoro-N-(pyridyl)benzamides: physicochemical correlations, polymorphism and isomorphous relationships. Acta Cryst B68:189
93. Perez-Torralba M, García MA, Lopez C, Torralba MC, Torres MR, Claramunt RM, Elguer J (2014) Structural investigation of weak intermolecular interactions (hydrogen and halogen bonds) in fluorine-substituted benzimidazoles. Cryst Growth Des 14:3499
94. Dubey R, Pavan MS, Desiraju GR (2012) Structural landscape of benzoic acid: using experimental crystal structures of fluorobenzoic acids as a probe. Chem Comm 48:9020
95. Price SL (2009) Computed crystal energy landscapes for understanding and predicting organic crystal structures and polymorphism. Acc Chem Res 42:117–126
96. Kendrick J, Leusen FJJ, Neumann MA, Streek JVd (2011) Progress in crystal structure prediction. Chem Eur J 17:10736
97. Dubey R, Desiraju GR (2014) Structural landscape of the 1 : 1 benzoic acid : isonicotinamide cocrystal. Chem Comm 50:1181
98. D'Oria E, Novoa JJ (2008) On the hydrogen bond nature of the C–H/F interactions in molecular crystals: an exhaustive investigation combining a crystallographic database search and ab initio theoretical calculations. CrystEngComm 10:423
99. Hayes IC, Stone AJ (1984) An intermolecular perturbation theory for the region of moderate overlap. Mol Phys 53:83
100. Schneider HJ (2012) Hydrogen bonds with fluorine. Studies in solution, in gas phase and by computations, conflicting conclusions from crystallographic analyses. Chem Sci 3:1381
101. Panini P, Chopra D (2013) Quantitative insights into energy contributions of intermolecular interactions in fluorine and trifluoromethyl substituted isomeric *N*-phenylacetamides and *N*-methylbenzamides. CrystEngComm 15:3711
102. Maschio L, Civalleri B, Ugliengo P, Gavezzotti A (2011) Intermolecular interaction energies in molecular crystals: comparison and agreement of localized møller–plesset 2, dispersion-corrected density functional, and classical empirical two-body calculations. J Phys Chem A 115:11179
103. Dunitz JD, Gavezzotti A (2012) Supramolecular synthons: validation and ranking of intermolecular interaction energies. Cryst Growth Des 12:5873
104. Panini P, Chopra D (2014) Experimental and theoretical characterization of short H–bonds with organic fluorine in molecular crystals. Cryst Growth Des 14:3155
105. Bader RFW (1990) Atoms in molecules: a quantum theory. Oxford University Press, Oxford
106. Popelier PL (2000) Atoms in molecules: an introduction. Prentice Hall, London
107. Espinosa E, Molins E, Lecomte C (1998) Hydrogen bond strengths revealed by topological analyses of experimentally observed electron densities. Chem Phys Lett 285:170
108. Mata I, Alkorta I, Espinosa E, Molins E (2011) Relationships between interaction energy, intermolecular distance and electron density properties in hydrogen bonded complexes under external electric fields. Chem Phys Lett 507:185
109. Vener MV, Egorova AN, Churakov AV, Tsirelson VG (2012) Intermolecular hydrogen bond energies in crystals evaluated using electron density properties: DFT computations with periodic boundary conditions. J Comput Chem 33:2303
110. Mata I, Alkorta I, Molins E, Espinosa E (2010) Universal features of the electron density distribution in hydrogen-bonding regions: a comprehensive study involving H···X (X=H, C, N, O, F, S, Cl, π) interactions. Chem Eur J 16:2442
111. Terada S, Katagiri K, Masu H, Danjo H, Sei Y, Kawahata M, Tominaga M, Yamaguchi K, Azumaya I (2012) Polymorphism of aromatic sulfonamides with fluorine groups. Cryst Growth Des 12:2908
112. Barcelo-Oliver M, Estarellas C, Garcia-Raso A, Terron A, Frontera A, Quinonero D, Mata I, Molin E, Deya PM (2010) Experimental and theoretical study of uracil derivatives: the crucial role of weak fluorine–fluorine noncovalent interactions. CrystEngComm 12:3758

113. Chopra D, Cameron TS, Ferrara JD, Guru Row TN (2006) Pointers toward the Occurrence of C–F···F–C Interaction: Experimental charge density analysis of 1-(4-fluorophenyl)-3,6,6-trimethyl-2-phenyl-1,5,6,7-tetrahydro-4*H*-indol-4-one and 1-(4-Fluorophenyl)-6-methoxy-2-phenyl-1,2,3,4-tetrahydroisoquinoline. J Phys Chem A 110:10465
114. Matta CF, Castillo N, Boyd RJ (2005) Characterization of a closed-shell fluorine-fluorine bonding interaction in aromatic compounds on the basis of the electron density. J Phys Chem A 109:3669
115. Hathwar VR, Thakur TS, Dubey R, Pavan MS, Guru Row TN, Desiraju GR (2011) Extending the supramolecular synthon based fragment approach (SBFA) for transferability of multipole charge density parameters to monofluorobenzoic acids and their cocrystals with isonicotinamide: importance of C–H···O, C–H···F, and F···F intermolecular regions. J Phys Chem A 115:12852
116. Osuna RM, Hernández V, Navarrete JTL, D'Oria E, Novoa JJ (2011) Theoretical evaluation of the nature and strength of the F···F intermolecular interactions present in fluorinated hydrocarbons. Theor Chem Acc 12:541
117. Baker RJ, Colavita PE, Murphy DM, Platts JA, Wallis JD (2012) Fluorine–fluorine interactions in the solid state: an experimental and theoretical study. J Phys Chem A 116:1435
118. Desiraju GR, Ho PS, Kloo L, Legon AC, Marquardt R, Metrangolo P, Politzer P, Resnati G, Rissanen K (2013) Definition of the halogen bond (IUPAC Recommendations 2013). Pure Appl Chem 85:1711
119. Mukherjee A, Desiraju GR (2014) Halogen bonds in some dihalogenated phenols: applications to crystal engineering. IUCrJ 1:49
120. Metrangolo P, Resnati G (2014) Type II halogen···halogen contacts are halogen bonds. IUCrJ 1:5
121. Hathwar VR, Guru Row TN (2011) Charge density analysis of heterohalogen (Cl···F) and homohalogen (F···F) intermolecular interactions in molecular crystals: importance of the extent of polarizability. Cryst Growth Des 11:1338
122. Metrangolo P, Murray JS, Pilati T, Politzer P, Resnati G, Terraneo G (2011) The fluorine atom as a halogen bond donor, *viz*. a positive site. CrystEngComm 13:6593
123. Metrangolo P, Murray JS, Pilati T, Politzer P, Resnati G, Terraneo G (2011) Fluorine-centered halogen bonding: a factor in recognition phenomena and reactivity. Cryst Growth Des 11:4238
124. Dikundwar AG, Guru Row TN (2012) Evidence for the "Amphoteric" nature of fluorine in halogen bonds: an instance of Cl···F contact. Cryst Growth Des 12:1713
125. Bondi A (1964) van der waals volumes and radii. J Phys Chem 68:441
126. Pavan MS, Prasad KD, Guru Row TN (2013) Halogen bonding in fluorine: experimental charge density study on intermolecular F···F and F···S donor–acceptor contacts. Chem Commun 49:7558
127. Volkov A, Macchi P, Farrugia LJ, Gatti C, Mallinson PR, Richter T, Koritsanszky TS (2006) XD2006. University at Buffalo, State University of New York, New York
128. Hathwar VR, Chopra D, Panini P, Guru Row TN (2014) Revealing the polarizability of organic fluorine in the trifluoromethyl group: implications in supramolecular Chemistry. Cryst Growth Des 14:5366

Chapter 3
Hydrogen Bonding in Supramolecular Crystal Engineering

Lian-Cheng Wang and Qi-Yu Zheng

Abstract This chapter emphases the important role of hydrogen bonding in crystal engineering for preparing fascinating architectures and engineering desired properties. The relatively high directionality and strength of hydrogen bonds make the prediction and control of molecular orientation in organic solids practical and reliable. Especially, strong hydrogen bonds like O–H···O, O–H···N, and N–H···O interactions are more useful. The introduction of supramolecular synthons and retrosynthesis theory has helped crystal chemists a lot in understanding and designing more complex structures. A large number of crystal structures reported in Cambridge Structure Database (CSD) provided a helpful tool for searching and analyzing specific interaction modes. Up to now, with the development of basic concepts and principles and the wide applications, the subject of crystal engineering has matured. Various intriguing structures and complicated entanglements have been constructed based on hydrogen bonds, such as nanocapsules, nanotubes, and *n*-Borromean arrayed topologies. The crystal engineering strategy has lent chemists the ability to control solid state reactions regio- and stereo-specifically and improve the physicochemical properties of drugs using pharmaceutical cocrystals. In addition, it will be seen that hydrogen bonding can also be used to prepare robust porous materials for gas adsorption and separation.

3.1 Introduction

The term crystal engineering was first used by Schmidt [1] in connection with the research on solid state photodimerization reactions on the basis of topochemical principle, which correlated the solid state reactivity of monomers with their crystal

L.-C. Wang · Q.-Y. Zheng (✉)
Institute of Chemistry, Chinese Academy of Sciences, Beijing 100190, China
e-mail: zhengqy@iccas.ac.cn

Z. Li and L. Wu (eds.), *Hydrogen Bonded Supramolecular Structures*,
Lecture Notes in Chemistry 87, DOI 10.1007/978-3-662-45756-6_3

structures. Over the following years, this field developed rapidly due to its important implications in materials science. A useful modern definition was provided by Desiraju [2] in his 1989 book as "the understanding of intermolecular interactions in the context of crystal packing and the utilization of such understanding in design of new solids with desired physical and chemical properties." The main aims and pursuits of this field are to understand the nature, strength, and directionalities of interactions between molecules, to predict crystal structures from molecular structure information, and finally to customize crystals with desired properties by logically choosing suitable precursor molecules [3].

Crystal engineering is now an interdisciplinary subject and its meaning has developed to include many aspects of solid state supramolecular chemistry. Noncovalent interactions, such as hydrogen bonding, coordination interactions, halogen bonding, π···π interaction, and van der Waals (vdW) interactions, have been extensively used in crystal engineering. These noncovalent interactions are the fundamental forces for molecular recognition and assembly to form crystals. It is worthy to mention that engineering organic crystals relies largely on, but not only limited to, noncovalent interactions. Covalent-organic frameworks (COFs) [4] are a class of crystalline porous organic materials. These frameworks are constructed with reversible covalent bonds, which allow "error-checking" and "self-correcting" during the reaction to afford structure-regular and energy-minimum products [5, 6]. Although most COFs are obtained as powders, single crystals of COFs with millimeter size that can be characterized by X-ray crystallography have been constructed by taking advantage of a reversible dimerization reaction of the nitroso group (energy: 20–30 kcal/mol) very recently [7]. Afterwards, a new COF with imine linkage (energy: >100 kcal/mol) that could be determined by 3D rotation electron diffraction was also reported [8]. With no doubt, this breakthrough step will pave the way for crystal engineering to prepare more covalent organic (single) crystals with robust structures and distinguishing properties [9].

Nevertheless, hydrogen bonding has played a more important role in preparing organic crystals. Some hydrogen bonds are even stronger than the weakest covalent bonds. Due to its relatively high strength and directionality, hydrogen bonding predominates in current crystal engineering strategies, especially strong hydrogen bonds like O–H···O, O–H···N, and N–H···O interactions. Much progress has been made in predetermined assembly of organic solids with desired and well-defined connectivity using hydrogen bonding interaction. In this chapter, we will outline some recent advances that have been made from both structure and application aspects. A large number of research groups have made invaluable contribution to this field. Unfortunately, we could not list all but only a fraction of the many efforts. A missing of important contribution to this field is sincerely unintended.

3.2 Crystal Engineering Strategies

3.2.1 Supramolecular Synthons and Retrosynthesis

Crystal engineering deals with crystals, which are extended and ordered supramolecular assemblies of millions of molecules with an impressive level of precision [10]. Traditional synthetic chemistry deals with molecules based upon controlled formation and cleavage of covalent bonds. There exist analogies and connections between these two categories. Treating an organic crystal as a supermolecule, crystal engineering may be considered as a solid-state supramolecular equivalent of organic synthesis. By analogy with synthons in organic synthesis, Desiraju [11] introduced the term supramolecular synthon as "structural units within supermolecules which can be formed and/or assembled by known or conceivable synthetic operations involving intermolecular interactions." Supramolecular synthons (Scheme 3.1) are spatial arrangements of intermolecular interactions between complementary functional groups. The synthons well describe the recognition events that take place when molecules assemble into crystals. With the convenience of simplifying a crystal structure as a network [12], the analysis of a complex target

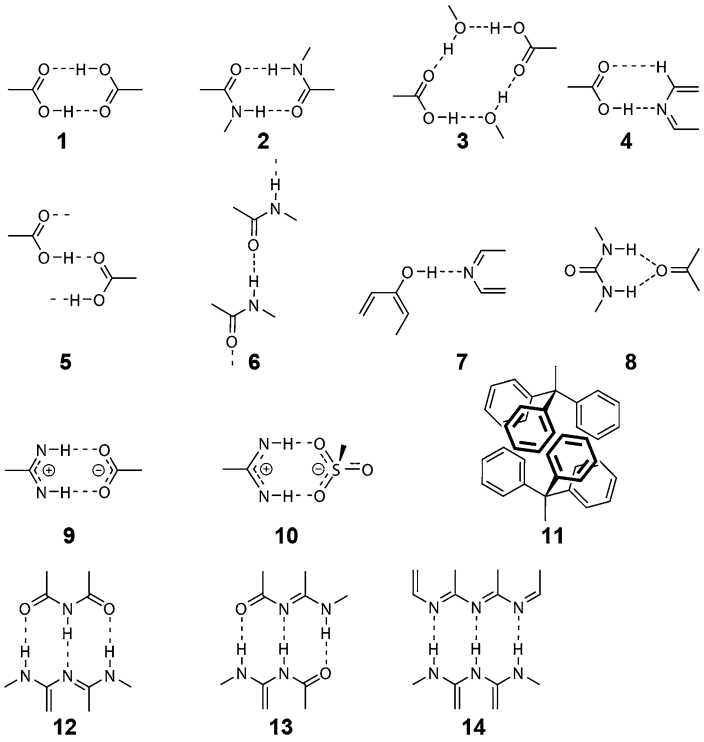

Scheme 3.1 Representative supramolecular synthons

structure to yield the nodes (molecules) and node connections (supramolecular synthons) may be termed as supramolecular retrosynthesis. Identifying structurally significant synthons is as important to crystal engineering as is an understanding of reaction mechanism to organic synthesis. Such identification facilitates the understanding of a more complex crystal packing and helps the design of new crystal structures. Given a set of particular functional groups, a robust synthon appears reliably from one network structure to another irrespective of other existing functionality. The carboxylic acid dimer synthon **1** and carboxylic acid···pyridine synthon **4** are two well-known examples. Typically, robust synthons are formed with strong and directional interactions or multipoint interactions. Interference between the robust synthons should be a minimum. Practically, the useful tool that helps better understanding of intermolecular interactions in crystal engineering is the Cambridge Structural Database (CSD) [13], which can be searched for patterns of intermolecular forces. The repetitive patterns appeared in several crystal structures can be used as a supramolecular synthon to design new materials.

The synthon theory has remained active for nearly 20 years since it was introduced to crystal engineering. It is a practical method of not only describing but also designing crystals. In spite of other methods of structure simplification and description being proposed one after another, the supramolecular synthon approach will continue to be used in the foreseen future.

3.2.2 Reticular Synthesis

The past decades have witnessed an explosive growth in the preparation of metal-organic frameworks (MOFs), which are porous crystalline materials constructed by joining metal ions or clusters with organic linkers through strong bonds. A reticular synthesis approach of directing the assembly of molecular building blocks to designed structures was developed by Yaghi and O'Keeffe [14]. It is a subclass of crystal engineering. Reticular synthesis relies on the concept of secondary building units (SBUs) (Fig. 3.1), including inorganic SBUs formed in situ under predetermined conditions and well-defined organic SBUs. SBUs with points of extension defining their shapes have intrinsic geometrical properties that facilitate network design. Unlike supramolecular synthon approach which is based on chemistry, reticular synthesis method is based on geometry and topology. The practice of reticular synthesis begins with the identification of the required SBUs for a target network. When linking these rigid SBUs by simple linkers, only a small number of known and highly symmetric structures which are called default structures will form most commonly. These important nets for reticular synthesis have been systematically enumerated into the Reticular Chemistry Structure Resource (RCSR) [15]. The use of reticular synthesis has provided opportunities to fine-tune the porosity and functionality of solid materials, which are well illustrated by the construction of isoreticular MOFs (with the same underlying topology) [16] and multivariate MOFs (multiple organic functionalities incorporated within a single

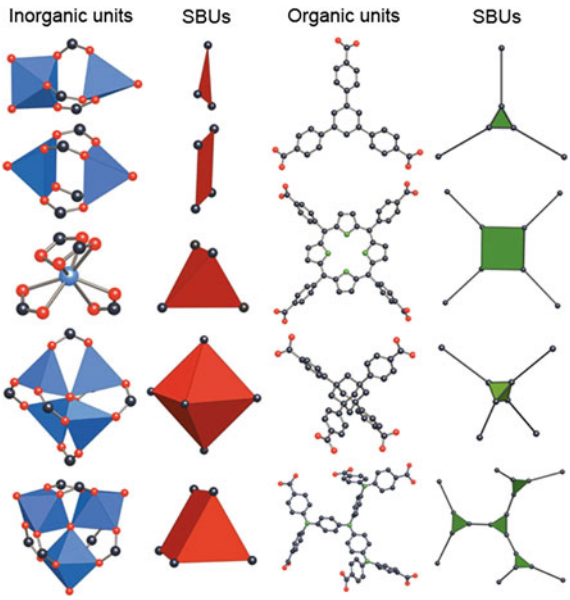

Fig. 3.1 Examples of inorganic (*left*) and organic (*right*) secondary building units (SBUs). Reprinted by permission from Macmillan Publishers Ltd: Ref. [14], copyright 2003

framework) [17]. Reticular synthesis is also quite useful in COF chemistry where powder products are often obtained and only limited powder X-ray diffraction data are available. Knowing what structures to expect can assist designed synthesis and unambiguous determination of even complex three-dimentional (3D) structures [18]. The basic concepts of reticular synthesis can also be found in the construction of hydrogen bonding frameworks. A suitable building block of selected geometry as a node, combined with proper spacer molecules with complementary hydrogen bonding interactions to join the nodes can be attempted for a specific target structure.

3.3 Hydrogen Bonding

3.3.1 Definition and Scopes

Hydrogen bonding is so important in molecular recognition and supramolecular construction that research of hydrogen bonds about what they are and what they can do is certainly of enormous significance. Besides the conventional strong hydrogen bonds, like O–H···O, O–H···N, and N–H···O, currently the weaker variants, such as C–H···O, C–H···N, O–H···π, N–H···π, and C–H···π, have been accepted as hydrogen bonds [19]. Hydrogen bonds span a wide energy range from 0.5 to 40 kcal mol^{-1}. Weak hydrogen bonds can also be used as reliable supramolecular synthons in crystal engineering (Scheme 3.2). In 2011, IUPAC recommended a new

Scheme 3.2 Some supramolecular synthons based on weak hydrogen bonds [11]

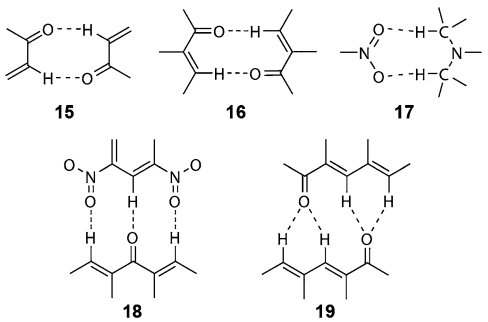

definition for hydrogen bond: "The hydrogen bond is an attractive interaction between a hydrogen atom from a molecule or a molecular fragment X–H in which X is more electronegative than H, and an atom or a group of atoms in the same or a different molecule, in which there is evidence of bond formation" [20]. Very recently, hydrogen bonding has been observed in real space with noncontact atomic force microscopy (NC-AFM) technology [21]. Hydrogen bond is mainly electrostatic in character. The finding indicates the covalent character of hydrogen bond. This should stimulate further discussion and enhance the understanding of the nature and properties of hydrogen bonds. As to crystal engineering context, no matter strong or weak hydrogen bonds, one common feature they share is that they show directional preference and influence packing modes in crystal structures. It is this directionality nature that accounts for their importance in crystal engineering, and hence deviations from close packing [22] and prediction can be achieved.

3.3.2 *Description of Hydrogen Bonding Motifs: The Graph Sets*

A method based on graph theory has been developed by Etter, Bernstein and coworkers [23, 24] for describing and comparing complex hydrogen bonding patterns within 3D structures. The benefit of graph set assignment is to bring focus onto the morphology of hydrogen bonding arrays, rather than exclusively on their geometrical characteristics. The process of assigning a graph set starts from identifying different types of hydrogen bonds of interest in the structure, and ranking the hydrogen bonds by chemical priority. Then, the highest priority hydrogen bond is selected to generate a motif. To paraphrase, a motif is a set of molecules connected with only one type of hydrogen bond. A graph set descriptor is given to the motif as $G_d^a(n)$. G is referred to the pattern of hydrogen bonding and is characterized by one of four designators, C (an infinite chain), R (a ring), D (a noncyclic dimer), or S (intramolecular). The subscript d and superscript a refer to the number of donors and acceptors used in the motif respectively, and the parameter n in bracket denotes the total number of atoms in the repeat unit (Scheme 3.3).

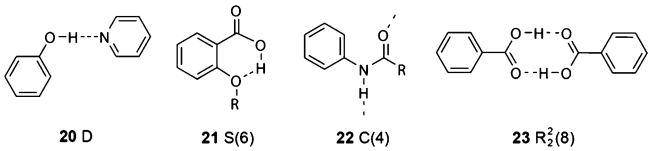

Scheme 3.3 Graph set assignments for four different patterns of hydrogen bonding (when no subscript and superscript are given, one donor and one acceptor are implied; $n = 2$ is the default degree value for a D pattern and not specified)

3.3.3 Hydrogen Bonding Rules

After an extensive survey of intermolecular contacts in CSD, Etter and coworkers [25] presented the following empirical rules for determining preferred hydrogen bonding modes in organic solids:

1. All good proton donors and acceptors are used in hydrogen bonding.
2. Six-membered-ring intramolecular hydrogen bonds form in preference to intermolecular hydrogen bonds.
3. The best proton donors and acceptors remaining after intramolecular hydrogen bond formation form intermolecular hydrogen bonds to one another.

These rules reflect energetically favored intermolecular recognition and association. Take presently abundant carboxylic acid and pyridine co-crystals as an example, pyridine nitrogen atom is a better proton acceptor than carbonyl oxygen atom, so the heteromeric synthon **4** rather than homomeric synthon **1** (Scheme 3.1) is frequently occurred as a reliable structure motif to direct the assembly. However, exceptions are common and these rules are not guaranteed. They should be taken as guidelines, not as formal rules.

3.4 Interpenetration

For those who are trying to prepare open frameworks, one frequently encountered phenomenon is interpenetration. Interpenetration, where the empty space of one net is occupied by one or more other nets is one of nature's tricks to reach a densely packed structure. It can be regarded as occurring when two or more chemically unbounded nets are spatially nonseparable without breaking bonds. Although interpenetration seems an annoyance to those seeking high porosity, a great deal of research has been focused on interpenetrating networks due to their structural complexities, topological fascination, and potential applications. Batten [26, 27] proposed to describe the different topologies of interpenetration with the formula mD(/nD) $\rightarrow$ pD parallel/inclined interpenetration, where m and n are dimensionalities of interpenetrating nets, and p is the dimensionality of the overall entanglement (m, $n \leq p$).

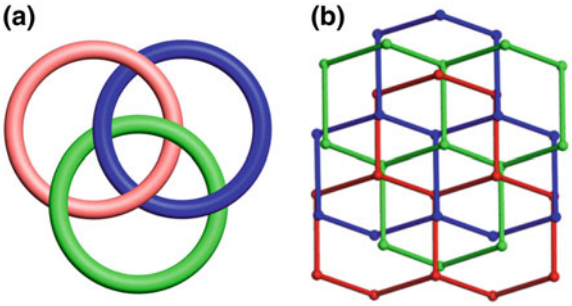

Fig. 3.2 **a** Borromean rings. **b** Borromean 2D → 2D parallel interpenetration [28, 29]

For 2D nets, there are three possibilities: 2D → 2D parallel, 2D → 3D parallel, and 2D (→3D) inclined interpenetration. Of 2D parallel interpenetration, a particularly unusual mode is Borromean interpenetration [28]. Borromean rings (Fig. 3.2a) consist of three interlocked rings in the way that no two rings are catenated but altogether they are nonseparable, such that scission of any one ring leads to the other two falling apart. Similar situations of this type can exist for parallel interpenetration of 2D nets [28, 29] (Fig. 3.2b). This complex interpenetration needs a careful examination of the structures to give the right topology, as mentioned in Ref. [28] some are not correctly recognized when first reported.

The 2D → 3D parallel interpenetration which leads to dimensional increase through polycatenation is a rarity. The first example was only reported in 1997 [30]. They are obtained based on either a very undulating motif [31] or a 'thick' motif [32], and each individual motif is catenated only with the surrounding ones but not with all the others (Fig. 3.3).

Interpenetration of a 3D net with other nets (1D, 2D or 3D) can only give rise to a 3D network. From 2004, Blatov and Proserpio et al. [33–37] have performed a systematic investigation of interpenetrating 3D metal-organic, inorganic, and organic hydrogen bonding networks with the aid of TOPOS package. Of interpenetrating 3D hydrogen bonding networks, a survey of CSD (2006/11) resulted in a comprehensive list of 122 distinct entangled architectures (based on strong hydrogen bonds) [35]. Analysis of the result reveals that the most common interpenetrating nets are the **dia** nets (31.1 %), the **cds** nets (11.5 %) and the **lvt** nets

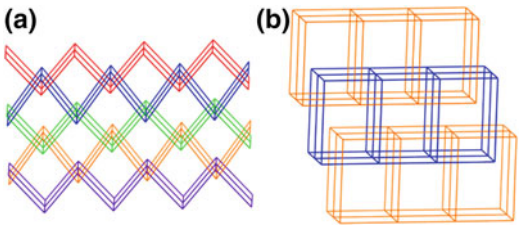

Fig. 3.3 **a** 2D → 3D parallel interpenetration of highly undulating 2D networks [31]. **b** 2D → 3D parallel interpenetration of 'thick' 2D networks [32]

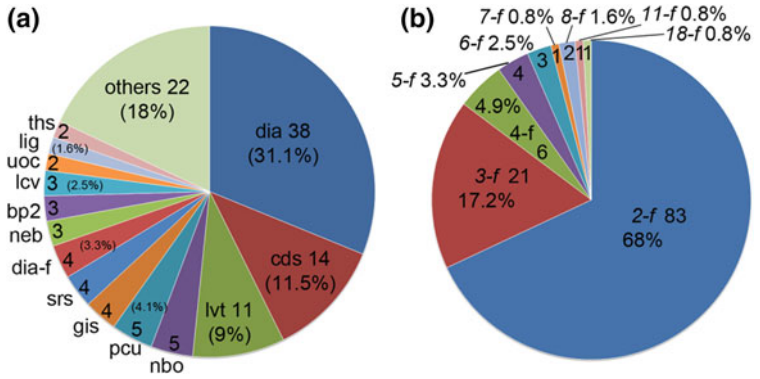

Fig. 3.4 **a** Distribution of the interpenetrating net topologies. **b** Distribution of the degree of interpenetration (within 122 structures in CSD, version 5.28 of November 2006). Reprinted with the permission from Ref. [35]. Copyright 2008 American Chemical Society

(9 %) (the three-letter designation proposed by O'Keeffe can be seen in RCSR) (Fig. 3.4a). 4-connected nets totally take a percentage of ca. 68 %. They are generally constructed from tetrahedron and square-planar nodes. An evident difference from MOFs and inorganic frameworks is that 6-connected **pcu** nets are rare. For the large majority of the nets the value of the degree of interpenetration is 2 (68 %) (Fig. 3.4b). High degrees of interpenetration are rare.

The research concerning topology of interpenetration by Blatov and Proserpio et al. has prompted crystal chemists to concentrate not only on the first molecular environment (topology of individual nets) but also on higher lever structures (like topology of interpenetration). It also has fundamental relevance in the perspective to establish useful relationships between structure and property.

3.5 Hydrogen Bonding Structures

3.5.1 Discrete Hydrogen Bonding Capsules

A virus capsid is an attracting natural supramolecular cage that protects RNA or DNA in its interior. It is constructed from many protein subunits that assemble into a well-defined polyhedron with a high degree of accuracy [38]. Mimicking nature to prepare artificial nanocapsules has been drawing a great deal of attention in recent years both for their elegant structures and wide applications [39, 40]. Hydrogen bonding has played an important role in this area because of its directional and reversible nature.

3.5.1.1 Dimeric Capsules

Rebek et al. have pioneered the use of hydrogen bonding to produce a variety of capsules. In a seminal work, Rebek and coworkers [41] presented a dimeric capsule that conformed to a molecular "tennis ball" from compound **24a** (Fig. 3.5). An important feature is that the glycoluril functions at the ends of **24a** provide curvature and a self-complementary hydrogen bonding array, which is necessary to form the dimeric capsule. From the crystal structure of $(\mathbf{24b})_2$ [42], it can be clearly seen that the two subunits are joined by eight almost linear N–H···O hydrogen bonds (167°–178°).

Afterwards, Rebek and Shimizu [43] and later Böhmer and coworkers [44] synthesized self-assembled dimeric capsules from tetraurea calix[4]arenes **25** (Fig. 3.6). The substituent groups attached to the phenolic oxygens prevent rotation and fix the cone conformation, which organizes the self-complementary urea groups in the desired position. Eight unidirectional urea groups around the equator seal two half-spheres together in common head-to-tail (HT) arrangement by way of 16 N–H···O hydrogen bonds. The capsule has a more sizable cavity of ca. 202 $Å^3$.

Resorcin[4]arene and pyrogallol[4]arene (Scheme 3.4) have the ability to easily form hydrogen bonding molecular capsules. They possess multiple hydroxyl groups at the upper rim, which can interact with each other or surrounding solvent molecules. Their bowl-shaped conformation is stabilized by four intramolecular O–H···O hydrogen bonds. Four electron-rich aromatic rings can bind cationic and neutron

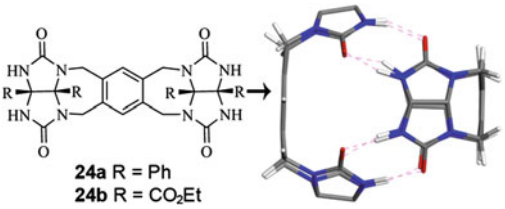

Fig. 3.5 Glycoluril based dimeric capsule. In crystal structure $(\mathbf{24b})_2$, the substituents have been omitted for clarity [42]

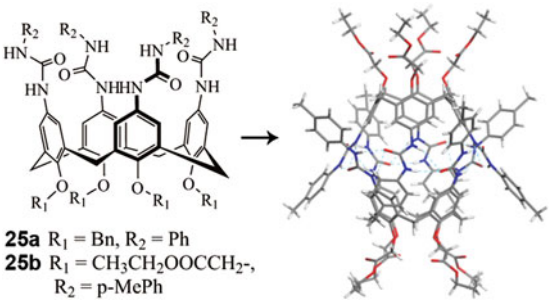

Fig. 3.6 Dimeric capsule from tetraurea calix[4]arene [44]

Scheme 3.4 Structures of resorcin[4]arene and pyrogallol[4]arene

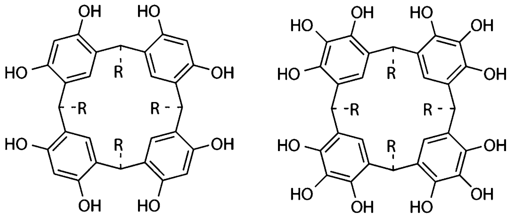

resorcin[4]arene
26a R = Me
26b R = Et
26c R = CH_2CH_2Ph

pyrogallol[4]arene
27a R = isobutyl **27b** R = C_5H_{11}
27c R = 3-pentyl **27d** R = C_6H_{13}
27e R = C_7H_{15}

guests through cation···π and C–H···π interactions. The guests can fill the cavities and in most cases serve as templates for the dimeric capsule. Another feature that facilitates their application is that they can be synthesized in only one simple step by acid catalyzed cyclolization of resorcinol or pyrogallol with aldehydes in a large scale.

When crystallized in the presence of alcoholic solvent which can act simultaneously as hydrogen bond donor and acceptor, Atwood and coworkers [45] prepared a unique dimeric capsule (**26c**)$_2$(*i*-PrOH)$_8$ (Fig. 3.7a). The two subunits are not directly but indirectly connected in a rim-to-rim fashion by eight isopropanol (*i*-PrOH) molecules via 16 intermolecular hydrogen bonds. A similar capsule TEA$^+$@(**26b**)$_2$(H_2O)$_8$ was reported by Aoki and coworkers [46] (Fig. 3.7b) at the same time. The capsule formation is driven by a tetraethylammonium ion (TEA$^+$) via cation· · ·π interactions. Using this template synthesis strategy, more solvent mediated dimeric capsules have come out in literature with different ammonium guests [47].

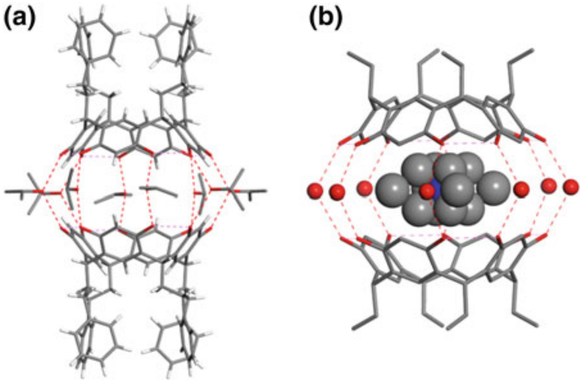

Fig. 3.7 **a** Dimeric capsule (**26c**)$_2$(*i*-PrOH)$_8$ [45]. **b** Dimeric capsule TEA$^+$@(**26b**)$_2$(H_2O)$_8$, TEA$^+$ is disordered over two positions in CPK mode, bridging water molecules are in ball-and-stick mode [46]

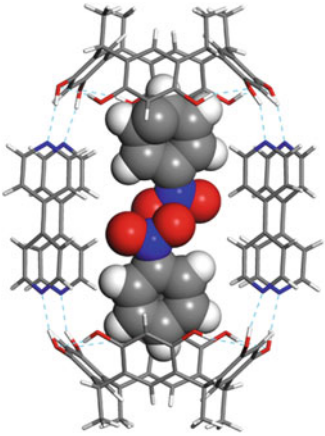

Fig. 3.8 Hetero-dimeric capsule $(\mathbf{26a})_2(BPY)_4$, inclusion nitrobenzene molecules are in CPK mode [48]

In the above examples, we discussed homo-dimeric capsules either constructed from subunits with self-complementary hydrogen bonding groups or bridged by solvent molecules. Hetero-dimeric capsules consist of components that are distinctly different. MacGillivray and coworkers [48] prepared an extended hetero-dimeric capsule by co-crystallization of *C*-methylresorcin[4]arene **26a** with 4,4′-bipyridine (BPY) (Fig. 3.8). A hydrogen bond between phenyl hydroxyl and pyridyl groups is a reliable supramolecular synthon. The two resorcinarenes are thus separated by BPY, defining a cylindrical cavity with dimensions ca. 6.0 × 14.2 Å, where two nitrobenzene molecules reside.

3.5.1.2 Hexameric Capsules

A more complex multicomponent capsule emerged in 1997, when Atwood and coworkers [49] reported the self-assembly of **26a** with water molecules into a spherical hexamer $(\mathbf{26a})_6(H_2O)_8$ (Fig. 3.9a). Six molecules of **26a** and eight molecules of water, which are held together by 60 O–H···O hydrogen bonds, form a shell-like octahedral cubic capsule. Each **26a** lies around a fourfold axis and provides two hydrogen bond donors to interact with neighboring ones (totally 12 hydrogen bonds). Each water molecule lies around a threefold axis and forms three hydrogen bonds with three different **26a** molecules (totally 24 hydrogen bonds). Additionally, each **26a** also exhibits four intramolecular hydrogen bonds (totally 24 hydrogen bonds), stabilizing its bowl-like conformation. The capsule has an internal volume of about 1,375 $Å^3$. Interestingly, the twisting of **26a** with respect to the water 'cuboid' makes the capsule chiral. A recent work by Holman and Ugono [50] shows that alcohols can also replace water molecules on the surface to complete the seam of hydrogen bonds, affording an achiral form of the hexameric capsule in the solid state (Fig. 3.9b).

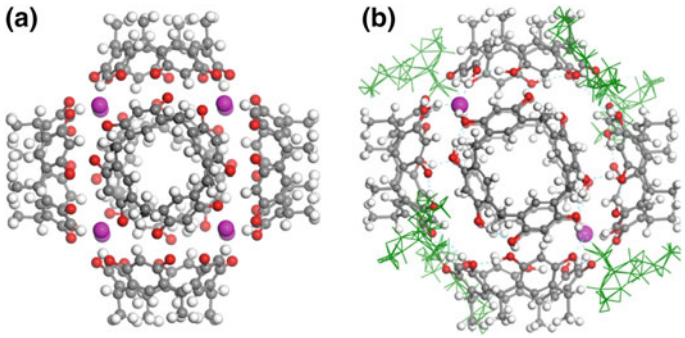

Fig. 3.9 **a** The hexameric capsule $(\mathbf{26a})_6(H_2O)_8$ [49]. **b** The achiral form with six alcohols and two water molecules, the alcohols are disordered and water molecules are in bigger balls [50]

In 1999, Mattay and coworkers [51] reported a hexameric capsule of *C*-isobutylpyrogallol[4]arene **27a** in the solid state (Fig. 3.10). The access to this capsule was quite exceptional, as they noted that pyrogallol[4]arenes typically crystallized as 2D wave-like layer structures in a face-to-face and tail-to tail fashion. Attempts to form the hexamer a second time failed. They attributed this to an inherent instability of the hexameric capsule compared with the above $[(\mathbf{26a})_6(H_2O)_8]$. In 2001, Atwood and coworkers [52] found that the extraordinary stability of the capsule even exceeded the expectation. They provided a reliable method to prepare the capsule by crystallization from diethyl ether, acetone or methanol with a few drops of nitrobenzene or *o*-dichlorobenzene upon slow evaporation. Compared with resorcin[4]arene, pyrogallol[4]arene have four more hydroxyl groups. They form the hexameric capsule by way of 72 hydrogen bonds (48 intermolecular and 24 intramolecular), without the need of water molecules. The volume within the capsule reaches nearly 1,520 $Å^3$. The pendent R groups changing from *n*-propyl to *n*-tridecyl can give rise to the expected hexamer. But a small variation of chain length can have profound influence on the crystal packing and interaction between

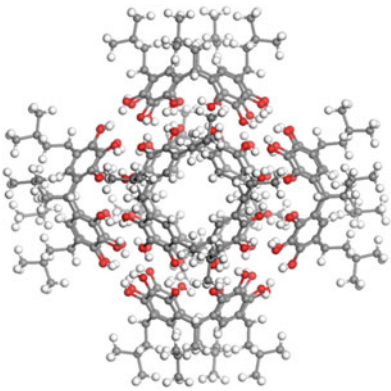

Fig. 3.10 The hexameric capsule $(\mathbf{27a})_6$ [51]

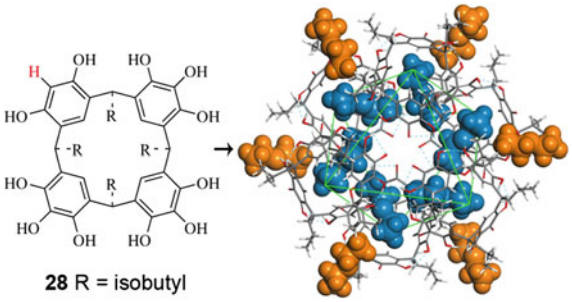

Fig. 3.11 The hexameric capsule $(\mathbf{28})_6$, hydrogen bonded diethyl ether molecules are shown in CPK mode [60]

capsules [53]. The robustness of this capsule has made it an active host for host-guest chemistry both in solution and solid state [54–58].

The intrinsic self-complementary hydrogen bonding information encoded within resorcin[4]arene and pyrogallol[4]arene results in absolute self-assembling and self-sorting into homomeric hexamers when mixed together [59]. Nevertheless, resorcinol and pyrogallol hybrid macrocycle may bind one another through complementary interactions. In 2002, Atwood and coworkers [60] synthesized a tetrameric macrocycle **28** containing one resorcinol and three pyrogallols. The mixed macrocycle **28** self-assembles to form a hexameric capsule by hydrogen bonding (Fig. 3.11). Different from the capsule $(\mathbf{27a})_6$ where exists a perfect match between hydrogen bond donors and acceptors, in the capsule $(\mathbf{28})_6$, each macrocycle **28** has 11 hydroxyl groups, providing 66 potential hydrogen bond donors in the hexamer. The capsule only uses 48 (24 intermolecular and 24 intramolecular). Of the remaining 18 hydrogen bond donors, six are oriented towards inside of the capsule and six outside, hydrogen bonding to diethyl ether molecules. The other six hydrogen bond donors are located external to the capsule, not taking part in hydrogen bonding interactions. Relative to the spherical shape of predecessors, the capsule is flatter and possesses a slightly smaller internal volume of 860 $Å^3$.

Calix[4]pyrroles are a class of tetrapyrrolic macrocycles with eight substituents at meso positions, thus preventing further oxidation to porphyrins. They are known to be effective receptors for anions. A clear conformational analogy exists between calix[4]pyrrole and calix[4]arene. As a consequence, aryl-extended calix[4]pyrrole can be an effective scaffold for constructing hydrogen bonding capsules similar to calix[4]arene. Rather than enumerating the achievements in detail, we would like to lead the readers to a recent review [61]. Here we only talk about one example in the running context. In 2007, Ballester and coworkers [62] prepared a new octahydroxyl calix[4]pyrrole **29** (Fig. 3.12), which resembles the resorcin[4]arene **26a**. When crystallized with a high excess of tetramethylammonium chloride (TMAC), a hexameric supramolecular capsule formed which can be seen as an octahedron. Three intramolecular O–H···O hydrogen bonds and the binding of one chloride anion with four NH groups impart stability to the cone conformation. Each **29** is hydrogen

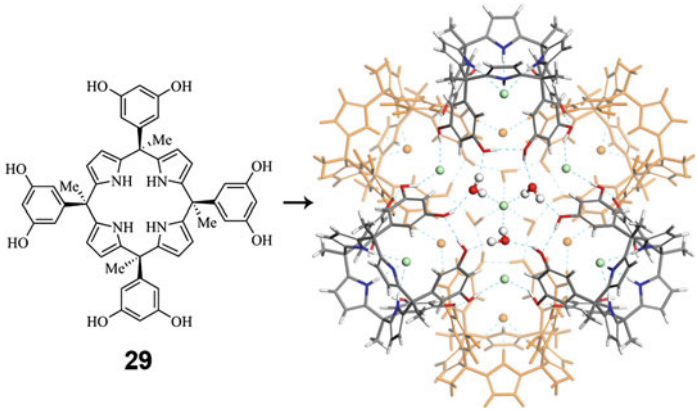

Fig. 3.12 Simplified view of the hexameric structure assembled from octahydroxyl calix[4] pyrrole **29**, hydrogen bonded water molecules and chloride anions are shown in ball-and-stick mode [62]

bonded only to two of the four neighboring calix[4]pyrrole molecules through water molecules and bridged chloride anions, forming a hemisphere. Two such hemispheres fit perfectly to yield the hexameric capsule when rotating 60° to each other, held together only through electrostatic interactions.

3.5.1.3 A Quasi-truncated Octahedron

Unlike above examples where typically are concave molecules applied as structural building units, in 2011, Ward and coworkers [63] reported a large supramolecular capsule assembled from 20 molecular components through 72 hydrogen bonds. The capsule is constructed from two kinds of planar hexagonal molecular tiles, a tris (guanidinium)nitrate cluster ($[G_3NO_3]^{2+}$, **30**) and a hexakis(4-sulfonatophenyl) benzene ($HSPB^{6-}$, **31**) (Fig. 3.13). It is because of the sulfonato groups not lying in the same plane with hexaphenylbenzene (HPB) scaffolds that makes the two planar building blocks be able to fold into a polyhedron, with quasi-truncated octahedron geometry. The quasi-truncated octahedron comprising four $HSPB^{6-}$ tiles and four $[G_3NO_3]^{2+}$ tiles is held together by 24 charged-assisted $N–H^+\cdots{}^-O–N$ hydrogen bonds within the $[G_3NO_3]^{2+}$ building blocks and 48 $N–H^+\cdots{}^-O–S$ hydrogen bonds along the edges. The capsule encloses an interior volume of ca. 2,200 $Å^3$, which is further bridged by sodium ions through (sulfonate)$O\cdots Na^+\cdots$O(sulfonate) to generate a zeolite-like 3D body-centered cubic framework. Notably, the framework can be stable up to 160 °C in the solid state, reflecting an excellent thermal robustness of this hydrogen bonding assembly. In addition, the capsules and its framework exhibit a remarkable ability to encapsulate a wide range of guest species with varying shapes, sizes, substituents, and charges. This indicates that the quasi-truncated

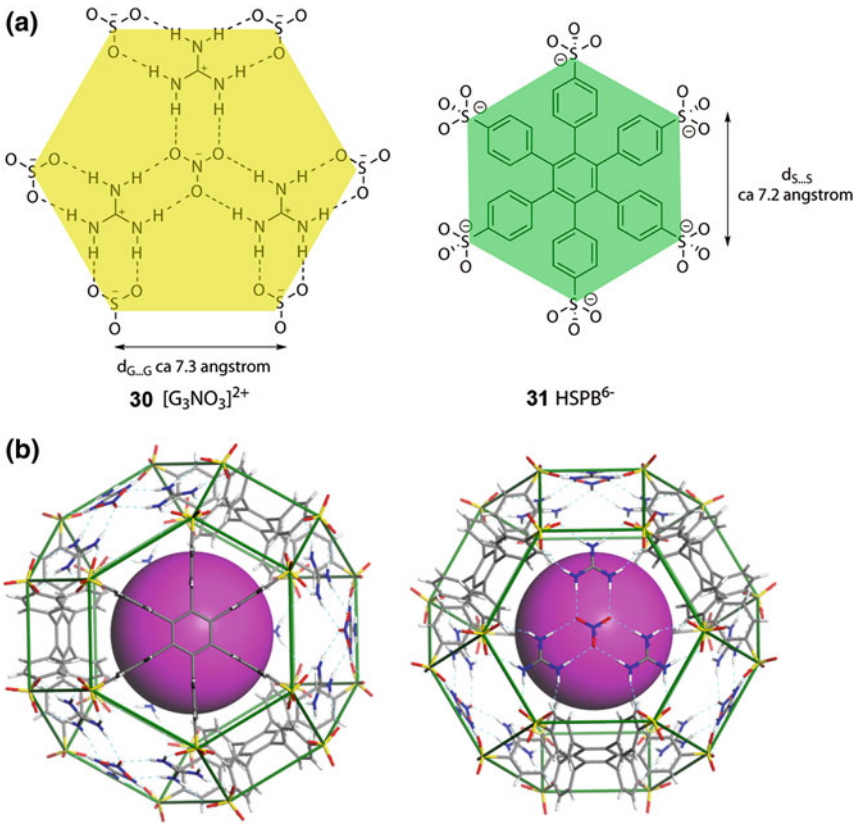

Fig. 3.13 **a** Complementary $[G_3NO_3]^{2+}$ and $HSPB^{6-}$ tiles with their corresponding edge lengths. **b** The hydrogen bonding quasi-truncated octahedron viewed perpendicular to $HSPB^{6-}$ and $[G_3NO_3]^{2+}$ tiles respectively [63]

octahedron framework is not guided by guest templating, in contrast with typical noncovalent host frameworks whose formation always needs templating by guest molecules.

3.5.2 1D Infinite Hydrogen Bonding Nanotubes

Inspired by carbon nanotubes (CNTs), the creation of tubular structures in crystal engineering has been a subject of considerable interest in recent years. Hydrogen bonding has been proved to be an effective tool in fulfilling this task. In this section, we limit ourselves to 1D-infinite independent hydrogen bonding tubes. Higher dimensional hydrogen bonding structures containing tubular channels are excluded from this discussion [64].

3.5.2.1 Tubes Constructed from Flat Macrocycles

A straightforward method for generating tubular structures is to use flat macrocycles with perpendicular interacting groups, by the way of stacking atop one another. The size and shape of the ring will determine the pore diameter of resulting tubes. Well-known macrocycles include cyclic peptides [65], cyclic oligosaccharides [66], and cyclic multiureas [67], of which cyclic bis/tetraureas are more efficient to form 1D independent tubes in solid state.

In 1999, Ranganathan and coworkers [67] prepared an amino acid-based cyclic bisurea **32** and characterized its assembly by single-crystal X-ray studies (Fig. 3.14). The crystal structure of **32** showed that the macrocycle adopts a flat disk-like conformation without any internal hydrogen bonds between the two urea groups within the same ring. All urea functionalities lie approximately perpendicular to the plane of the ring and the side chains point outward. The cyclic bisurea rings are further stacking parallel one upon another to generate an infinite tube by two strings of hydrogen bonds which are of typical urea type. The cavity has a rectangular shape. Of four walls, three are rigid, formed by the urea-type hydrogen bonding in two opposite walls and S–S stacking in the third. The fourth wall constituting of aliphatic chains is very flexible and highly disordered.

Shimizu and coworkers [68–71] prepared a series of bisurea macrocycles **33** with rigid aromatic spacers (Fig. 3.15). Similarly, these macrocycles could assemble to infinite tubes reliably through urea–urea hydrogen bonding and favorable aryl stacking interactions. Notably, the cavity size of the tubes could be systematically manipulated by tuning the length of spacers. The rigid tubes are very robust and can desorb and re-adsorb guest molecules.

Guichard and coworkers [72] applied an enantiopure cyclic tetraurea **34** to form a square-shaped nanotube (Fig. 3.16a). The four walls are all formed by 3-centered

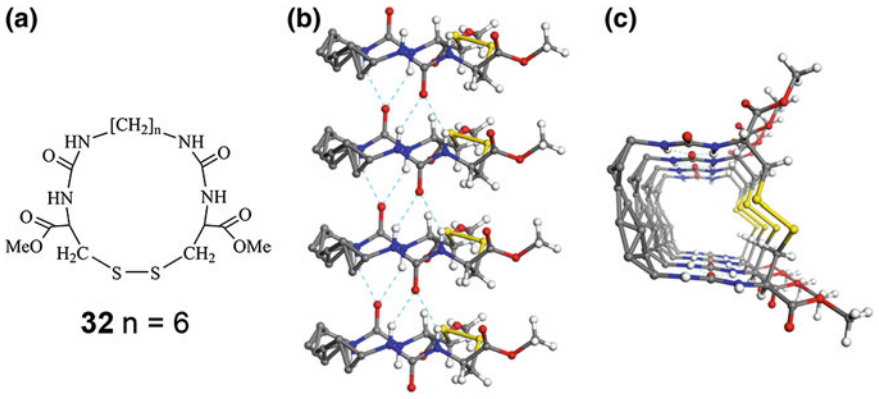

Fig. 3.14 **a** Structure of cyclic bisurea **32.** **b** The molecules are aligned in a parallel fashion to generate an infinite tubular structure, held together by typical urea-type hydrogen bonding interactions. **c** View into the cavity of the tube, the aliphatic chains are disordered [67]

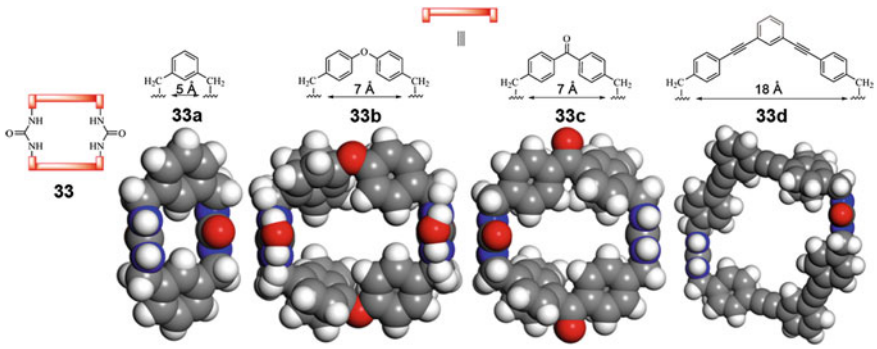

Fig. 3.15 Bisurea macrocycles **33** with rigid aromatic spacers, the cavity size of the tubes can be manipulated through tuning the length of rigid spacers [68–71]

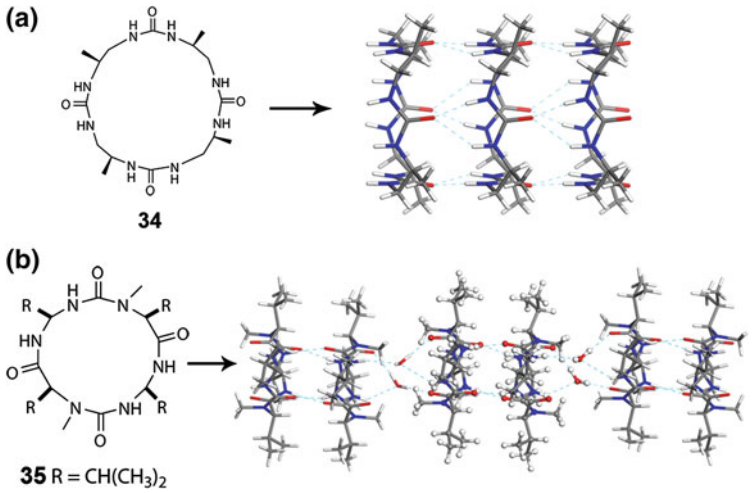

Fig. 3.16 **a** Nanotube from cyclic tetraurea **34** [72]. **b** Nanotube from a heterogeneous amide/urea macrocycle **35** [73]

urea-type hydrogen bonding chains. Different from the bisureas **32** and **33** where two carbonyl groups are aligned in parallel but in opposite directions to minimize the dipole moment, all the carbonyl and NH groups in **34** point in the same direction, forming a polar hydrogen bonding nanotube. They also utilized a backbone *N*-alkylated heterogeneous amide/urea macrocycle **35** to construct a tubular structure (Fig. 3.16b) [73]. The amide and urea groups are perpendicular to the mean plane of the ring, satisfying the essential requirement to form the tube. Their carbonyl groups point in opposite directions and form hydrogen bonded dimers by four strong hydrogen bonds between urea carbonyl and amide NH groups. The dimers are further connected by two bridging water molecules to form the tube.

3.5.2.2 Tubes Constructed from Calixarenes

In Sect. 3.5.1, we have seen that calixarenes and structural closely related resorcinarenes and pyrogallolarenes are useful building units to construct molecular capsules. On the other hand, they are also very promising in forming hydrogen bonding tubular structures under suitable conditions. The cone conformation provides the needed curvature for both capsules and tubes. However, the nondisk-like cone conformation prevents direct stacking like macrocyclic bisureas. Thus they need to arrange into a ring, and the rings are further connected to form a tube.

Kim and coworkers [74] synthesized an electrochemically active calix[4]hydroquinone **36** and investigated their assembly to tubular structures (Fig. 3.17). Lower-rim hydroxyl groups form a circular array of hydrogen bonds, stabilizing the cone conformation. Four 1D hydrogen bonding chains between upper hydroxyl groups and bridging water molecules thread along the tube axis, sealing the calixarenes in a rim-to-rim pattern.

Atwood and coworkers [75] found a suitable condition for pyrogallol[4]arene **27d** to form an organic nanotube in the presence of pyrene-functionalized molecules (Fig. 3.18a). Four **27d** units form a hydrogen bonding tetramer, and the tetramers are further linked together in a tubular fashion with each tetramer rotating ca. 45° along the axis. The tubes are interacting through a large number of vdW interactions between exterior alkyl chains and intercalating pyrene molecules. Gokel and coworkers [76] used a branched sidechained **27c** to construct a hydrogen bonding nanotube (Fig. 3.18b). Six pyrogallol[4]arenes form a flat hexameric ring with two ethanol and six water molecules, which are further linked to a nanotube. The 3-pentyl sidechains of **27c** join the nanotubes together like the cogs of gears.

Chen and coworkers [77] synthesized a novel NH-bridged azacalix[2]triptycene[2]pyridine **37** and found that it could assemble into a square-shaped nanotube (Fig. 3.19). The macrocycle **37** is in a boat-like conformation and interacts with four others through two lines of N–H···N≡C hydrogen bonds. Four such linear infinite hydrogen bonding chains are parallel to the axis of the tube, resulting in four aromatic walls that comprise of pyridine rings. The triptycene motifs that link the walls are locating in the square corners.

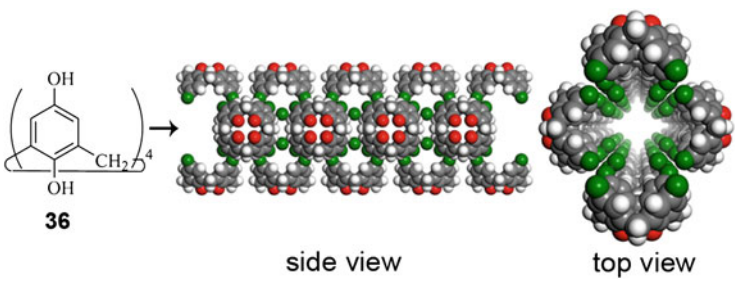

Fig. 3.17 The assembly of calix[4]hydroquinone **36** to nanotubes based on 1D infinite hydrogen bonding chains [74]

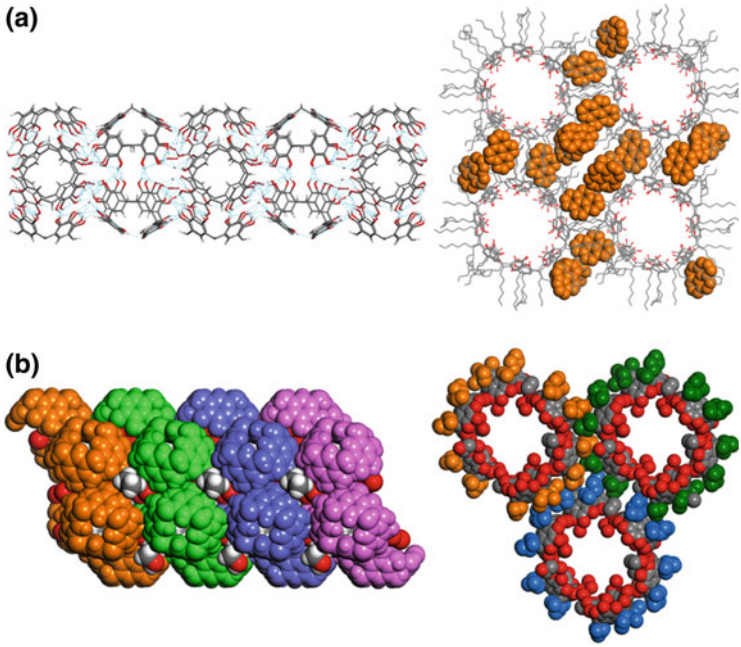

Fig. 3.18 **a** Tubular assembly of **27d** in the presence of pyrene molecules, intercalating pyrene molecules are in CPK mode [75]. **b** Tubular assembly of **27c** [76]

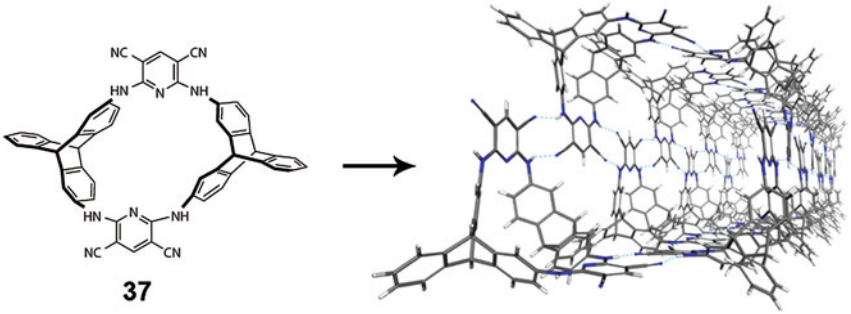

Fig. 3.19 The assembly of **37** to an organic nanotube by four infinite double N–H···N≡C hydrogen bonding chains [77]

3.5.2.3 Tubes Constructed from Acyclic Molecules

The formation of organic nanotubes from acyclic molecules is relatively rare. They are usually bent molecules that can curl up to give the required curvature. Chen and coworkers [78] reported a novel organic tubular structure from a bisdentate

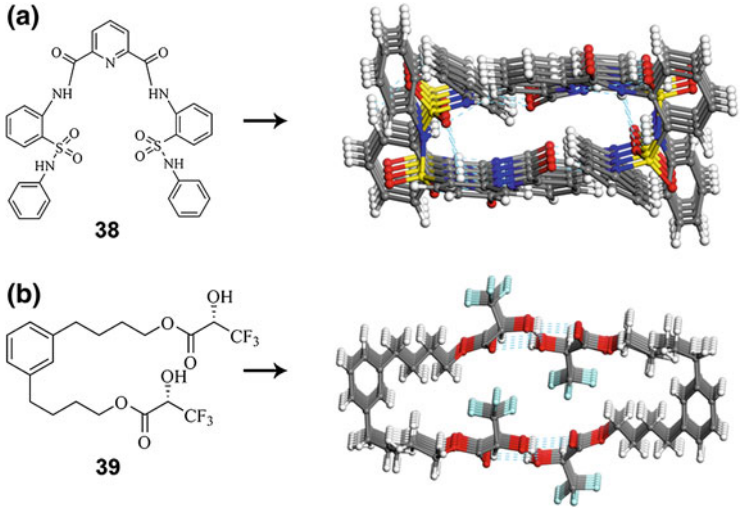

Fig. 3.20 Organic nanotubes constructed from acyclic molecules **38** and **39** [78, 79]

sulfonamide molecule **38** (Fig. 3.20a). Intramolecular hydrogen bonds made **38** in a two-dimensional sheet-like conformation. The remaining one sulfonamide NH proton is strongly hydrogen bonded to another adjacent molecule to form a flat dimer. All strong hydrogen bond donors are used up at this stage. The dimers are lined up in a tubular fashion through relatively weak C–H···O hydrogen bonds between 3-position protons of the pyridine ring and oxygen atom of the sulfonamide group. Katagiri and coworkers [79] also constructed a tubular assembly from a flexible double-headed trifluorolactate **39** based on two lines of hydrogen bonds between hydroxyl groups (Fig. 3.20b).

A beautiful tubular structure has been reported by Durka and coworkers [80] very recently from simple 1,2-phenylenediboronic acid **40** (Fig. 3.21). The diboronic moieties form an alternating hexameric ring, and the rings are further connected laterally to a tube. The tubes may host interesting water clusters, but the incorporated water molecules are interacting weakly with the boronic framework, thus are not responsible for templating the self-assembly.

Helical structures may have channels at their center, providing another way to access nanotubes. An infinite helical organic nanotube has been obtained by Sanders and coworkers [81] through self-assembly of *N*,*N*′-dimethylnaphthalenediimide **41** with pendant carboxyl groups at both ends (Fig. 3.22). They are held together by typical dimeric hydrogen bonds between carboxyl groups to a helix that units *i* and *i* + 3 are coplanar with each other. The inner diameter is ca. 12.4 Å. An important feature of the tube is the uniform supramolecular strereochemistry, which is determined by the chirality of the starting material. *R*,*R*-**41** will assemble to absolute *M*-helical nanotubes, and *S*,*S*-chirality affords *P*-helix.

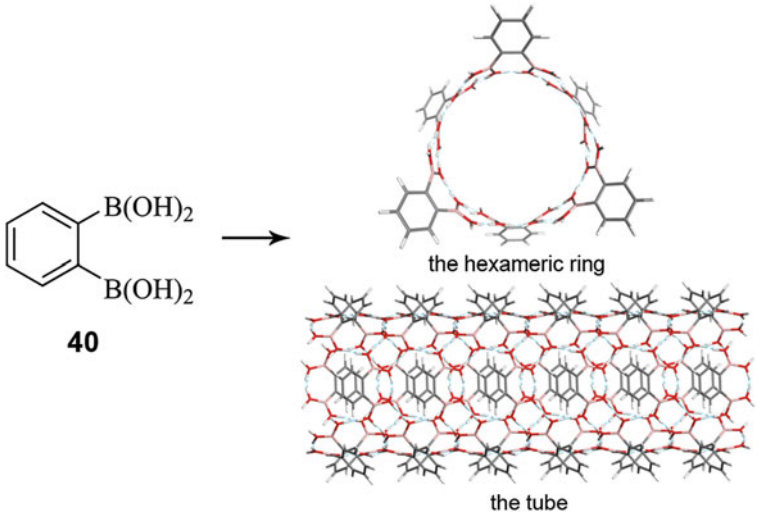

Fig. 3.21 A tubular structure from simple 1,2-phenylenediboronic acid **40** [80]

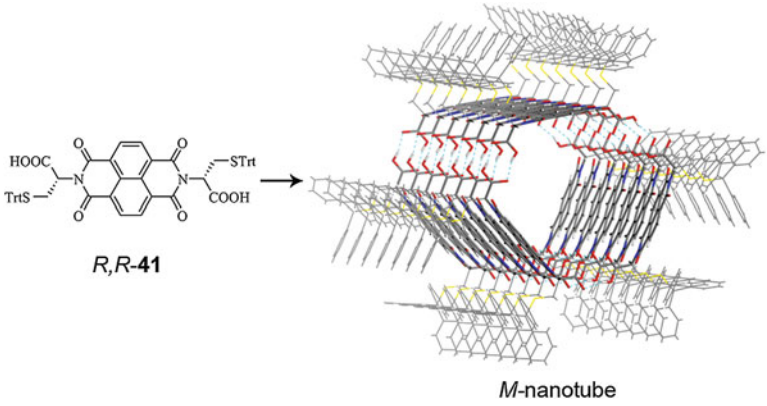

Fig. 3.22 The assembly of *R*,*R*-**41** to *M*-hydrogen bonding helical nanotube [81]

3.5.3 2D and 3D Borromean Arrayed Organic Crystals

We have devoted ourselves to constructing intriguing hydrogen bonding structures from delicate building blocks. The Borromean system (Sect. 3.4) is a very interesting pattern of crystal entanglement. We recognized that a nonplanar 6^3 honeycomb (**hcb**) net with large enough hexagonal cavities is essential to build a Borromean structure. Moreover, appropriate interactions are needed to control the

direction of interpenetration. Accordingly, we have chosen a rigid and trigonal pyramidal molecule 1,3,5-tris(4-carboxyphenyl)adamantane **42** with linear linkers **43**–**46** (Scheme 3.5) to construct a series of 2D and 3D Borromean arrayed organic crystals based on supramolecular synthons **1**, **3**, **4** and **11** (Sect. 3.2.1), rationally and modularly [82, 83].

As expected, molecule **42** assembled into 2D undulated **hcb** nets with large cavities through synthons **1** and **3** respectively, without or in the presence of methanol solvent (Fig. 3.23a). Three such nets are further interpenetrated through multiple C–H···π interactions in a Borromean way that none of them are catenated but altogether they are not separable (Fig. 3.23b). One particular feature of the structure obtained from methanol is that it contains both the two different Borromean weaves shown in Fig. 3.23b with a 2:1 ratio within the same structure.

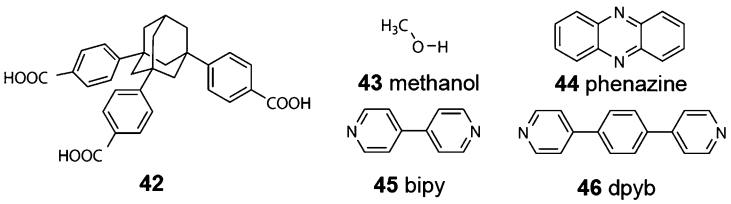

Scheme 3.5 Structures of 1,3,5-tris(4-carboxyphenyl)adamantane and linear linkers

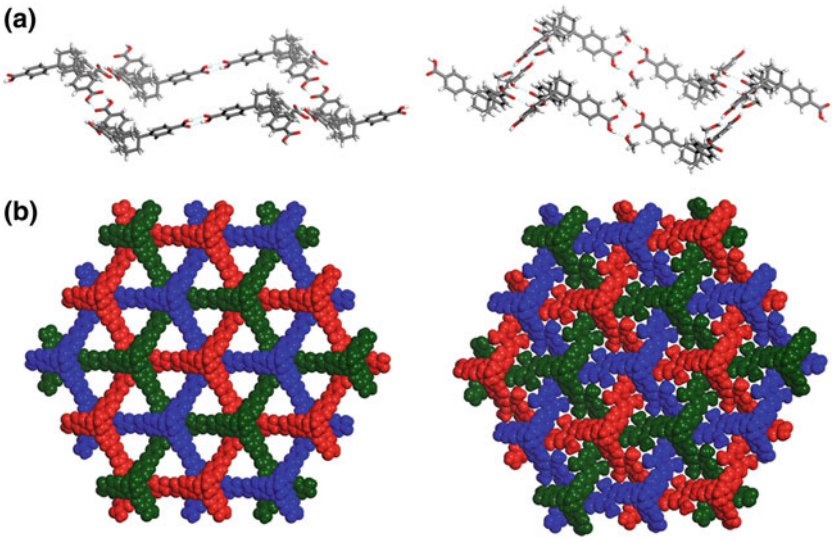

Fig. 3.23 **a** The undulated hexagonal nets assembled from **42**. **b** One Borromean weave consisting of three **hcb** nets in CPK mode [82]

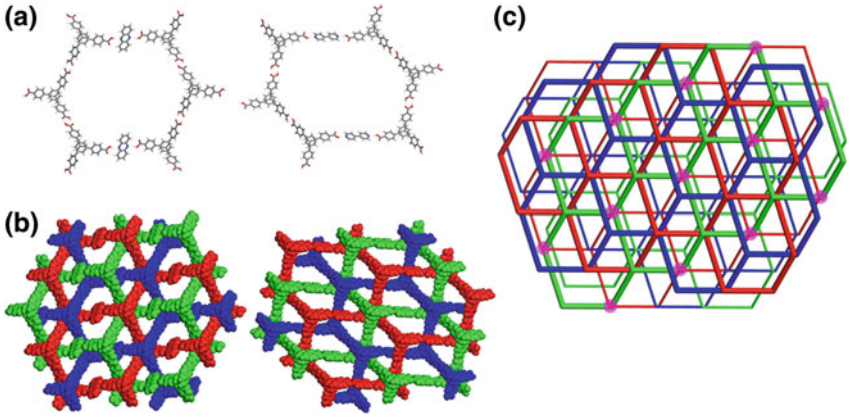

Fig. 3.24 **a** The pseudohexagonal nets of **42** with phenazine **44** and bipy **45**. **b** One Borromean weave consisting of three **hcb** nets. **c** Topological view of 2D → 3D polycatenated Borromean-linked network, the *thick* Borromean weave and the *thin* one are further interlocked by sixfold phenyl embrace interactions around the circles [82]

Motivated by the above results, we tried to enlarge the cavity for more complicated interpenetration with the reliable carboxylic acid···pyridine interaction **4**. When **44** (phenazine) and **45** (bipy) are used, the corresponding linkers are only inserted to two *para*-edges of the **hcb** nets (Fig. 3.24a). Similar Borromean weaves were also formed (Fig. 3.24b). However, due to the unequal edge lengths, half of the **42** molecules in two of the three nets do not form sixfold phenyl embrace interactions (**11**) inside this Borromean weave. Instead, they interact with other remaining molecules from either up or down weaves. In this way, all the Borromean weaves are locked together to form a 3D polycatenated *n*-Borromean structure (Fig. 3.24c).

Next, when a longer linker **46** (dpyb) was used, all the edges of the hexagonal ring are expanded by a dpyb molecule (Fig. 3.25a). The cavity size of resulting **hcb** nets expanded from the original 30 × 30 Å to ca. 51 × 51 Å with a thickness of approximately 19 Å. As in other cases, sixfold phenyl embrace interactions directed the nets to form a Borromean weave (Fig. 3.25b). But due to the large height of the corrugated **hcb** net, it is impossible for all **42** molecules to form this interaction inside the weave. Thus, a more complicated interpenetrated Borromean-linked structure has formed (Fig. 3.25c). The 2D Borromean weaves are interlocked by sixfold phenyl embrace interactions to a 3D Borromean-linked network similar to the above two cases. However, there is still big empty space left unoccupied, which allows further interpenetration. As a result, seven equivalent 3D Borromean links are then interpenetrated with π···π interactions between all **42** and dpyb edges.

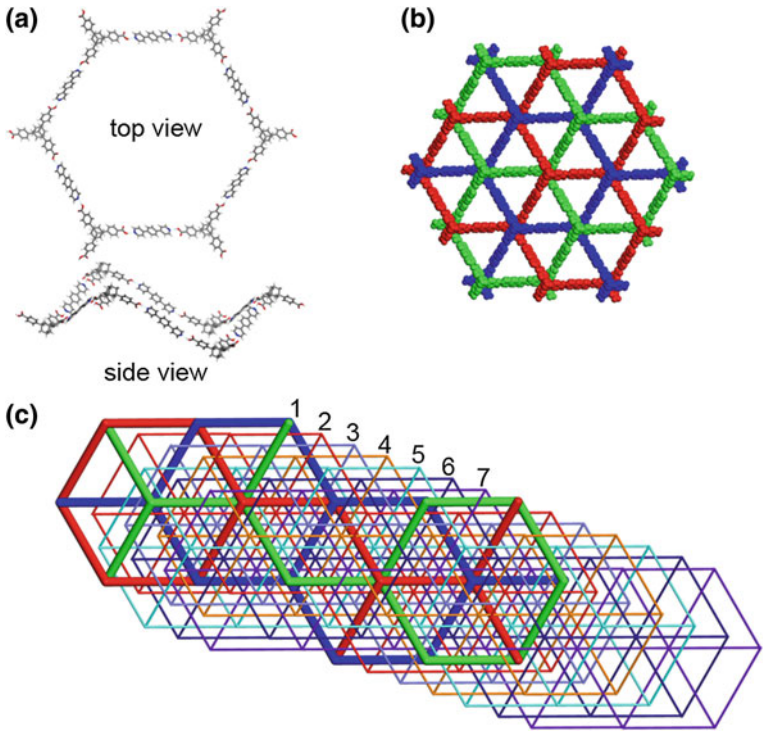

Fig. 3.25 **a** *Top and side* view of the hexagonal nets. **b** One Borromean weave. **c** Topological view of the sevenfold interpenetrated 2D → 3D Borromean-linked structure, one Borromean weave is in *thick* stick and other six in *thin* stick [83]

3.5.4 2D → 3D Parallel Polycatenated Structures

At present, predictive control of molecular positions in the out-coming crystals is still difficult, because of multicompetitions with other nondirectional weak interactions. Sometimes, the weak interactions are vital in determining the final structure and topology, even in the presence of directional and strong hydrogen bonding interactions. 1,3,5-Tris(4-carboxyphenyl)-2,4,6-tris(4-*tert*-butylphenyl)benzene (HPB-3a, **47**) has three alternating *tert*-butyl and carboxyl groups at a HPB core (Scheme 3.6a). Due to the space constraints, the typical dimeric hydrogen bonding interactions between carboxyl groups and vdW interactions between *tert*-butyl groups cannot be satisfied simultaneously. We anticipated a novel topological structure resulting from the complex interactions [84].

When **47** was crystallized from acetone, a binodal **hcb** sheet was obtained (Fig. 3.26a). Instead of forming dimeric hydrogen bonds between carboxyl groups, we observed a new trigonal planar supramolecular synthon $(H_2O)_2(COOH)_3$ **51** (Scheme 3.6b), which facilitates the vdW interactions between *tert*-butyl groups in

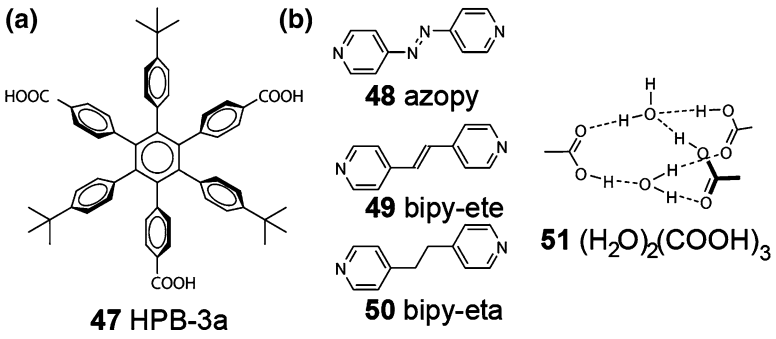

Scheme 3.6 **a** Structures of HPB-3a and bis(pyridyl) pillars. **b** The new supramolecular synthon $(H_2O)_2(COOH)_3$

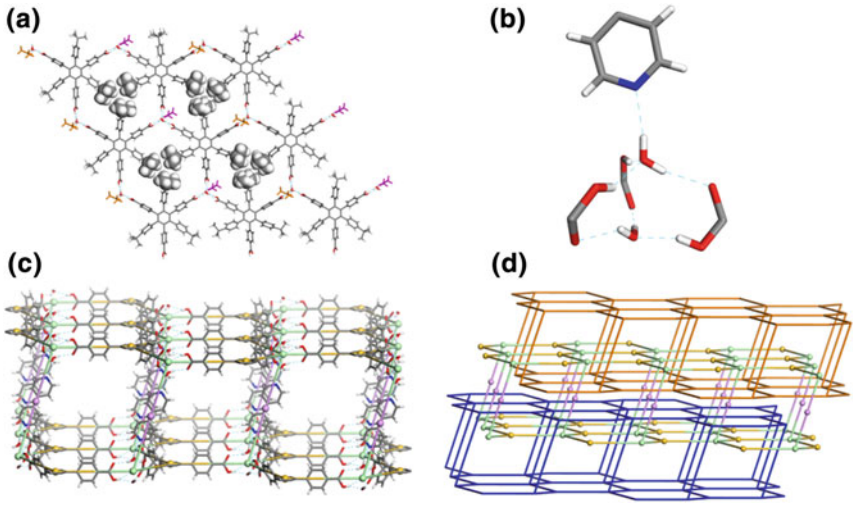

Fig. 3.26 **a** The binodal **hcb** layer, interacting *tert*-butyl groups are in CPK mode. **b** The supramolecular synthon $(H_2O)_2(COOH)_3$ with water proton hydrogen bonding to pyridine ring. **c** The chiral bilayer structure, the *tert*-butylphenyl moieties in **47** and solvent molecules are omitted for clarity. **d** Schematic view of the 2D → 3D parallel polycatenation of **hcb** bilayers [84]

the comb. One water proton is not involved in hydrogen bonding inside the synthon. It was hydrogen bonded to acetone molecules, which are pointing alternatively to both sides of the sheet and intercalated within adjacent sheets.

It is obvious that higher dimensional structures, such as 2D bilayer or 3D pillared networks, will generate if the sheets could be connected by pillared ligands at the remaining protons of **51**. Thus, linear linkers **45** and **48**–**50** were co-crystallized with **47**, resulting in four identical topological structures. As expected, the synthon **51** was persistent with the pyridyl groups and the water proton was hydrogen bonded to the ligands (Fig. 3.26b). This is in contrast to common cases where the

best proton donor (COOH) interacts with the best proton acceptor (pyridine) (Sect. 3.3.3). Two sheets are connected to form a bilayer (Fig. 3.26c). According to the rotation directions, clockwise or *anti*-clockwise, **47** has two enantiomers *P*- or *M*-. All **47** molecules in the bilayer are of the same chirality, so it is a homochiral bilayer. The large cavities and open windows promote further interpenetration in the way that each bilayer is penetrated by two others ("above" and "below") of opposite chirality to form a 3D racemic entanglement (Fig. 3.26d). It is the first example of 2D → 3D parallel interpenetration based on a bilayer motif in pure organic hydrogen bonding system (Sect. 3.4).

3.5.5 3D Interpenetrated dia and pcu Frameworks

Among a variety of 3D crystal structures, **dia** and **pcu** topologies are most popular, and they are prone to interpenetrate (Sect. 3.4). From supramolecular retrosynthesis perspective, the **dia** structure can be broken to 4-connected tetrahedron nodes and linear linkers. But it is not absolutely guaranteed. We have shown that a small change of the linkers' length and symmetry could bring about significant variation to the resulting structures, not only the interpenetration modes but also the topology from **dia** to surprising **pcu** [85, 86].

The tetrahedral methanetetrabenzoic acid (H_4MTB, **52**) (Scheme 3.7a) was co-crystallized with a linear linker phenazine (**44**). In the crystal structure, each **52** molecule is 4-connected to two other **52** molecules directly by the acid dimer synthon **1** and another two through phenazine by the heterodimer synthon **4** in a distorted tetrahedron geometry. In this way, a **dia** network with distorted adamantanoid cages is constructed (Fig. 3.27a). The large empty cages permit a normal sevenfold interpenetration (Fig. 3.27b). Then, a longer and thinner linker dipy **45** was used with the expectation for a more open framework. The result showed that all H_4MTB nodes are connected by the bipy linkers, forming a larger cage that permits more extensive interpenetration (Fig. 3.27c, d). The mode is an 18-fold interpenetration that belongs to class IIIb with $Z_t = 3 \times 3$ and $Z_n = 2$. It is the first example of 18-fold interpenetration for the **dia** net.

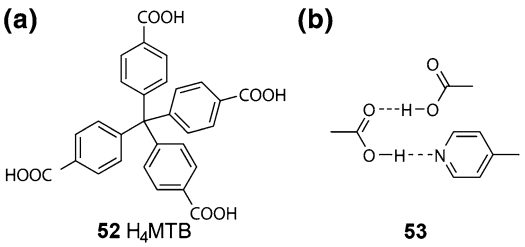

Scheme 3.7 **a** The structure of H_4MTB. **b** The bifurcated supramolecular synthon

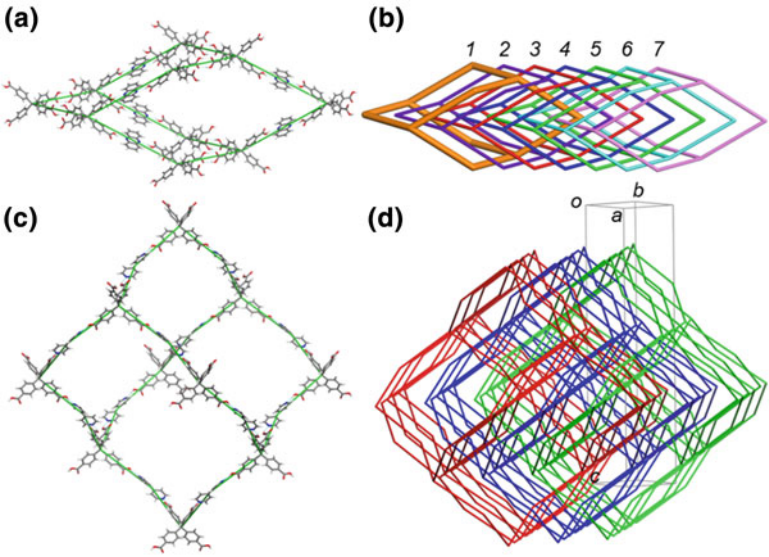

Fig. 3.27 **a** The distorted adamantanoid cage in cocrystal structure of H_4MTB with phenazine. **b** Schematic view of the sevenfold interpenetration. **c** The adamantanoid cage in cocrystal structure of H_4MTB with dipy. **d** Schematic view of the 18-fold interpenetration [85]

When two zigzag linkers azopy **48** and bipy-ete **49** were used, we obtained two same topological structures. To our surprise, they are no longer **dia** nets. A new hydrogen bonding synthon **53** played an important role in determining the structure (Scheme 3.7b). In the structure, each H_4MTB is connected to four H_4MTB molecules directly (hydrogen bond A) and two others through the linker (hydrogen bond B), acting as a 6-connected node (Fig. 3.28a). Based on the 6-connected node, a 3D **pcu** net is resulted (Fig. 3.28b), which is not common in pure organic system due to the lack of 6-connected organic building blocks. They are further interpenetrated by two other networks to form a threefold interpenetration (Fig. 3.28c).

3.5.6 Unusual Aggregation Phase of Water Molecules

The guanidium ion has an ideal C_3-symmetric geometry and three pairs of hydrogen bond donors (Scheme 3.8a). It has been a widely used building block to construct a variety of interesting rosette supramolecular structures with organic sulfonate or carbonate by strong charge-assisted $^{+}$N–H$\cdots$O^{-} hydrogen bonds [87–90]. The resulting porous frameworks provide opportunities for study of solid-state host-guest behaviors, which is an important aspect of crystal engineering. One especially attracting object is the discrete water clusters in confined pores. Highly symmetrical and esthetically beautiful aggregation morphologies of water molecules, which may

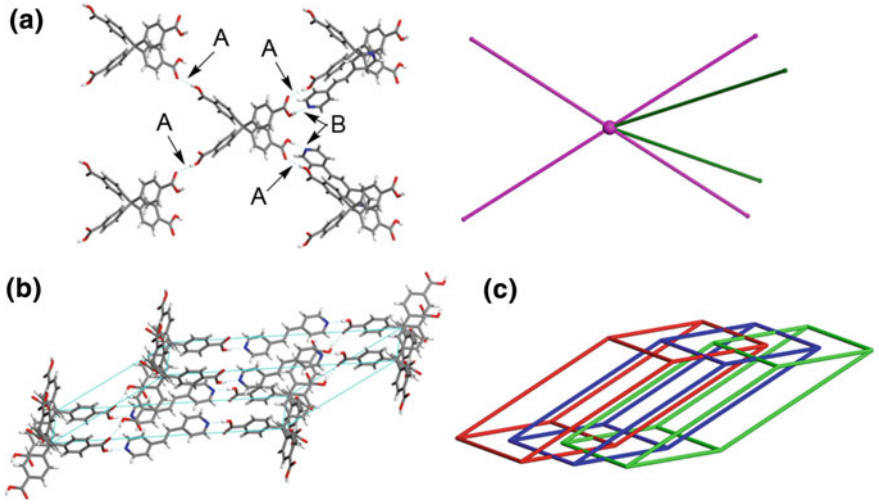

Fig. 3.28 **a** The connection of H_4MTB with two types of hydrogen bonds in cocrystal structure of H_4MTB with bipy-ete, the simplified node is a 6-connected node. **b** The distorted cubic cage. **c** Schematic view of the threefold interpenetration [86]

be not at the global energy minimum, can be obtained due to stabilization by surrounding supramolecular environment.

We have co-crystallized an aromatic unit benzenetribenzoate (BTB, **55**) with guanidium (Scheme 3.8) [91]. In the crystal structure, the BTB units and guanidium ions are linked by synthon **9** (Scheme 3.1) to form an essential **hcb** sheet with a diameter of 19.6 Å (Fig. 3.29a). The entire structure is built by parallel stacking of these sheets (Fig. 3.29b). In three adjacent layers, the BTB units are stacking one on top of the other in a staggered pattern, due to hydrogen bonding with six perpendicular guanidiums (Fig. 3.29c). Considering the three connected layers as a whole, they are packing in an ···ABAB··· pattern along the *c*-axis, generating separated hydrophobic and hydrophilic regions. The hydrophilic region has a void of ca. 913 $Å^3$, and each is occupied by a discrete $(H_2O)_{32}$ cluster (Fig. 3.29d). The cluster has an S_6 symmetry. It is constructed through HT cyclization of six six-membered

Scheme 3.8 Structures of guanidium and BTB

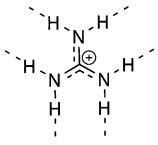

54 Guanidium

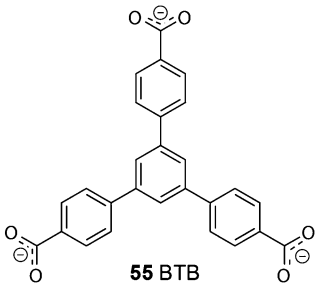

55 BTB

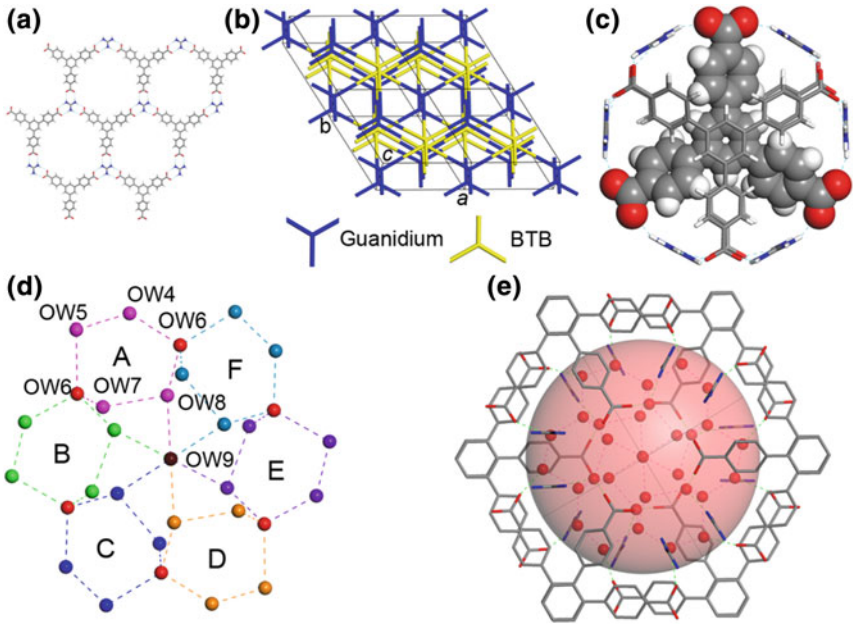

Fig. 3.29 **a** The **hcb** sheet assembled from BTB and guanidium by charge-assisted hydrogen bonds. **b** The stacking of six **hcb** sheets in one unit cell. **c** Three staggered BTBs packing along the *c* axis, the *middle* one is in CPK mode and the *top/bottom* ones and perpendicular guanidiums are in stick mode. **d** The S_6-symmetric $(H_2O)_{32}$ cluster, all are oxygen atoms. **e** *Top view* of the $(H_2O)_{32}$ cluster and surrounding organic frameworks, unrelated parts of BTBs and hydrogen atoms have been omitted for clarity [91]

rings at 1,4-positions, and six OW8 molecules are further hydrogen bonded to the central water dimer (OW9(1) and OW9(2)). The peripheral 18 water molecules (OW4, OW5 and OW7) form a puckered octadecagon conformation and are favorably hydrogen bonded with four **hcb** sheets, imparting stability to both the organic part and the water cluster (Fig. 3.29e). The number of hydrogen bonds reaches 73 (43 inner and 30 outer) in this intriguing water cluster.

In the following work, three rigid aromatic dicarboxylate 4,4′-(ethyne-1,2-diyl) dibenzoate (EYDB, **56**), (*E*)-4,4′-(ethene-1,2-diyl)dibenzoate (EEDB, **57**) and (*E*)-4,4′-(diazene-1,2-diyl)dibenzoate (ADB, **58**) (Fig. 3.30a) were co-crystallized with guanidium ions [92]. Despite the slight difference in symmetry (linear or zigzag), isostructures were obtained. The three crystal structures have almost identical unit cell parameters and molecular packing, mainly due to the strong and highly directional $^{+}N–H\cdots O^{-}$ interactions. In addition, $\pi\cdots\pi$ and cation$\cdots\pi$ interactions between aromatic planes and guanidium planes lead to alternative lamellar networks of hydrophobic aromatic regions and hydrophilic regions consisting of guanidium, carboxylate and water molecules. One-dimensional infinite water wires were observed in the channels (Fig. 3.30b). All water molecules in the wire are tetrahedrally coordinated.

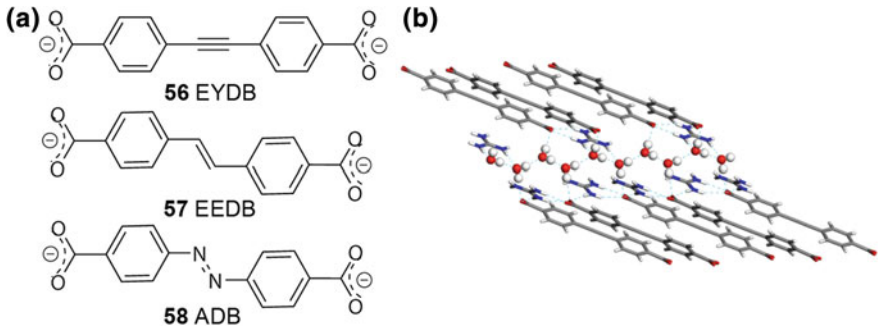

Fig. 3.30 **a** The structures of three aromatic dicarboxylates. **b** View of the water wires and surrounding EYDB and guanidiums, water molecules are in ball-and-stick mode, others in stick mode [92]

3.6 Applications

3.6.1 Crystal Engineering of Solid State Photochemical Reactions

As mentioned in the beginning part of this article, the root of crystal engineering originated from the influential work of Schmidt, who delineated geometry criteria for the [2 + 2] photodimerization to occur in organic solids [1]. Schmidt determined that the reactive double bonds should be aligned parallel and within a distance less than 4.2 Å. Up to date, this subject has been highly developed. The advances in supramolecular crystal engineering and improvements of our understanding about intermolecular interactions have enabled chemists to construct solids with predetermined physical properties for solid state reactions [93, 94]. The solid state reactions have the advantages of solvent-free conditions that related to green chemistry and stereo-specific reactions with high yields. Hydrogen bonding has become a versatile tool in this strategy. Three different approaches for preorientating olefins in organic solids have been employed: (1) self-complementary reactants, (2) auxiliary templates, and (3) confined environments of cavities.

3.6.1.1 Self-complementary Reactants

Reactants functionalized with self-complementary hydrogen bonding groups have been used to steer molecules into necessary arrangements for reaction. Feldman and Campbell [95] demonstrated that a 'J'-shaped naphthoic acid-derived cinnamic acid **59** could assemble to a dimer in the solid state through carboxylic acid synthons, where the HT alignments of two olefins conform to the topochemical criteria

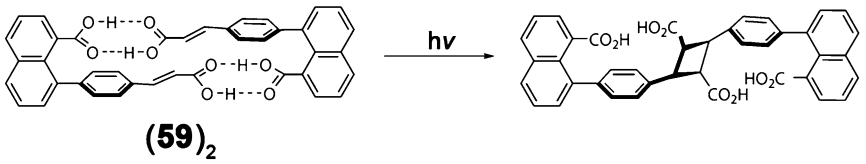

Scheme 3.9 Complementary hydrogen bonding and photodimerization of 'J'-shaped dicarboxylic acid **59**

(Scheme 3.9). Upon irradiation, the solid reacted to give the expected cyclobutane product stereo- and regio-specifically in quantitative yield.

Similarly, Wheeler and coworkers employed chiral sulfonamidecinnamic acids **60** [96–98]. No matter the use of racemic (*rac*)-**60a**, quasiracemic [(*R*)-**60a**/(*S*)-**60b**], and homochiral (*R*)-**60a** reagents, the hydrogen bonding dimer persisted and afforded the cyclobutane photoproducts in single-crystal-to-single-crystal (SCSC) transformation (Fig. 3.31a). It is worthy to note that intradimer and interdimer reaction paths are both possible according to Schmidt's criteria (Fig. 3.31b). Although the interdimer path is more favorable in distance, X-ray crystal analysis revealed that photodimerization occurred exclusively by the intradimer route. The interdimer path could be hampered in advance by increasing the size of *R* to isopropyl group, which isolated the dimers due to steric hindrance.

3.6.1.2 Auxiliary Templates

In 2000, MacGillivray and coworkers [99] presented a reliable method for preorganizing olefins in solids using auxiliary linear templates (Scheme 3.10). The external template resorcinol (res) cocrystallized with bipy-ete to form a discrete four-component assembly via four O–H···N hydrogen bonds, with two C=C bonds positioned for photodimerization. Ultraviolet (UV) irradiation of the powdered crystalline sample generated the stereocontrolled product in quantitative yield and gram scales.

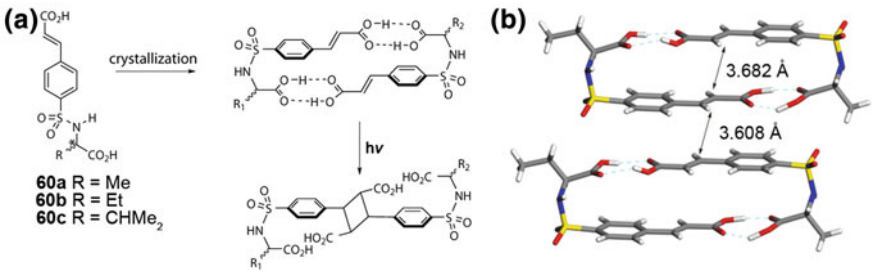

Fig. 3.31 **a** Representation of photodimerization of sulfonamidecinnamic acids. **b** Distances within and between the hydrogen bonding dimers in the quasiracemate (*R*)-**60a**/(*S*)-**60b** [96]

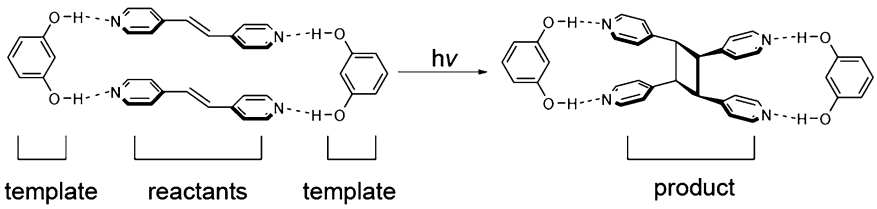

Scheme 3.10 Schematic representation of the template directed photodimerization

Resorcinol and its derivatives have been the most used linear template. Addition to this, using the concepts of supramolecular synthon, a library of hydrogen bonding templates has been engineered (Scheme 3.11), including 1,8-naphthalenedicarboxylic acid (1,8-nap) [100], 2,3-bis(4-methylenethiopyridyl)naphthalene (2,3-nap) [101], Rebek's imide (Reb-im) [102], thiourea (TU) [103], and a photoproduct *rctt*-cyclobutanetetracarboxylic acid (cbta) [104].

With the template approach, it is now facile to orient molecules in the solid state with precision and flexibility, providing access to molecules that are otherwise difficult to synthesize or nonavailable in solution, such as [2.2]paracyclophanes and [*n*]ladderanes (Scheme 3.12) [105, 106].

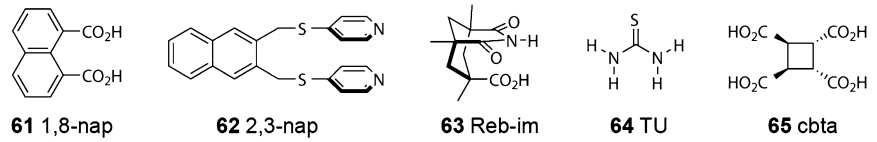

Scheme 3.11 Some representative hydrogen bonding templates

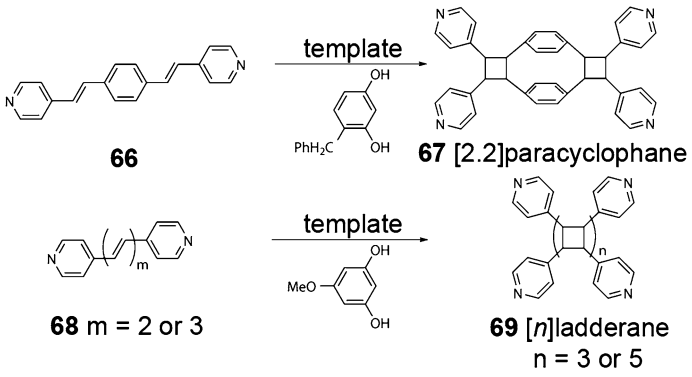

Scheme 3.12 Representation of the template directed synthesis of [2.2]paracyclophane and [*n*] ladderane in solid state

3.6.1.3 Confined Environments of Cavities

In nature, enzymes provide well-tailored microenvironments for highly substrate-specific and stereoselective reactions at ambient conditions. Nature is always the most important source of inspiration for chemists. There has long been great interest in designing artificial cavities that possess comparable efficiency and selectivity as enzymes. Often, reactions of prearranged molecules in confined environment of designed cavities can proceed at enhanced rate and with unusual regio- or stereo-selectivity.

Shimizu's self-assembled nanotube **33b**-tube was shown to promote the highly stereo-selective photodimerization of 2-cyclohexenone to *trans*-head-to-tail (HT) product, which is in stark contrast to the situation without the host (Scheme 3.13) [107]. In addition, the host could be easily recovered by extraction and reused without diminishing selectivity. It also showed size- and shape-selectivity towards different enones [108]. The host could adsorb guests of small size (**71**, **72** and **73**) but prohibited the photoreaction, while larger guests (**76**, **77** and **78**) were excluded from absorption. Only medium-sized substrates (**70**, **74** and **75**) exhibited high conversion and selectivity for the exo HT dimers. Since single crystals of the host-guest complexes suitable for X-ray diffraction could not be obtained, molecular modeling was performed to elucidate the origin of selectivity. The results indicated that the selectivity is due to the excellent match between the size and shape of these

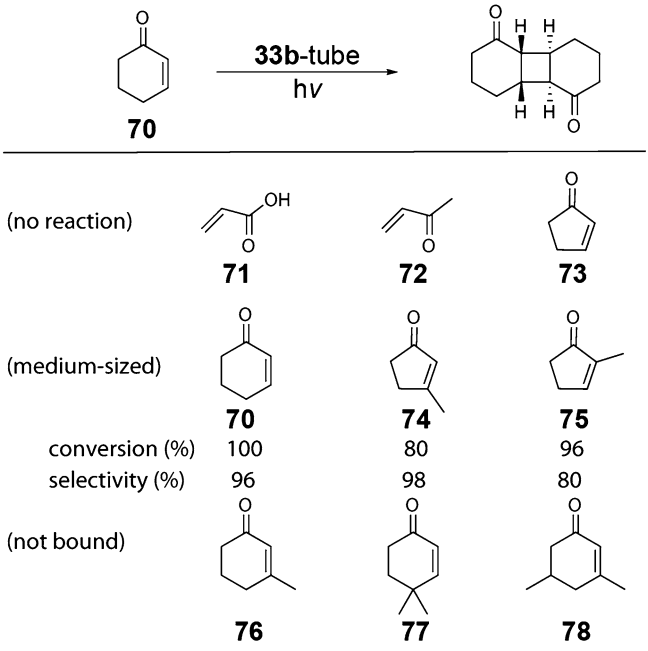

Scheme 3.13 Schematic representation of the photodimerization of enones in cavities of **33b**-tube

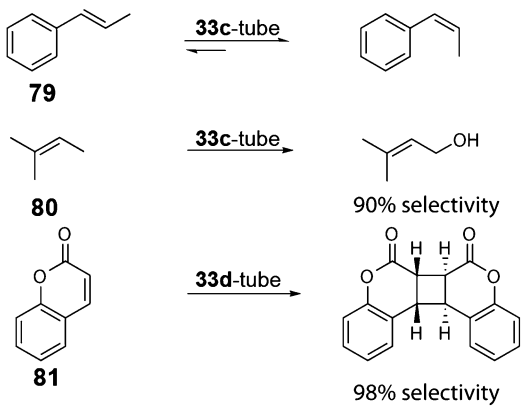

Scheme 3.14 Representation of the different reactions in different environment of bisurea nanotubes

guests and the dimension of the host channel and the preorganization of these enones into favorable reaction geometries.

Incorporation of a triplet sensitizer benzophenone into the macrocycle **33c** has little influence on the self-assembly nor the dimension of the resulting nanotube, but the reaction environment of the cavity is totally changed. Photodimerization of the above enones could not happen within **33c**-tube. Instead, the nanotube was able to act as a triplet sensitizer for the *cis-trans* photoisomerization of *trans*-β-methylstyrene and selective oxidation of 2-methyl-2-butene to a primary allylic alcohol (Scheme 3.14) [70, 109]. As well, an enlarged nanotube **33d**-tube was shown to facilitate the selective photodimerization of coumarin to the *anti*-head-to-head product [71].

3.6.2 Gas Adsorption and Separation

When talking about porous materials, people easily think of zeolites, MOFs, COFs and amorphous organic polymers. Yet, hydrogen bonded organic frameworks (HOFs) of discrete organic molecules connected by hydrogen bonds are less robust and often collapsed upon guest removal. But, in contrast to those well-established analogues, one major advantage of HOFs is solubility, which should allow easy characterization, purification, solution processability to thin films or membranes, and regeneration. In recent years, there has been a growing interest in organic molecular crystals that show permanent porosity [110, 111].

Shimizu and coworkers [112] tested their bisurea nanotube **33b**-tube by CO_2 adsorption. The CO_2 uptake was 71.5 $cm^3\ g^{-1}$ at 0.5 atm. and −78 °C and the calculated Brunauer-Emmett-Teller (BET) surface area was 341 $m^2\ g^{-1}$, comparable to those of microporous zeolites. Unlike the reliable bisurea system, the predictable assemble of molecules into solids is still very difficult. Therefore, McKeown and coworkers [113] proposed to search the existing compounds,

obviously it is a large library, for potential candidates that have not been proven permanently porous. They defined some useful criteria to perform such a search: (1) a calculated density of less than 0.9 g cm^{-3}, (2) the crystal should be composed predominantly of rigid aromatic molecules to aid stability, and (3) the apparent porosity should exist as small micropores (diameter < 10 Å) to be suitable for strong gas adsorption through multiwall interactions. Re-examination of a previously existing compound **82** (Scheme 3.15) by Chen and coworkers led to a new microporous material HOF-1 [114, 115]. HOF-1 has an apparent BET surface area of 359 m^2 g^{-1}, as well the capacity of selective adsorption of C_2H_2 over C_2H_4. Inspired by the robust hydrogen bonding interactions of 2,4-diaminotriazinyl (DAT) motifs, the same group newly synthesized a chiral building block **83** based on 1,1′-bi-2-naphthol (BINOL) scaffold [116]. The building block self-assembled into a homochiral 3D structure HOF-2 with 1D hexagonal pores. HOF-2 possesses permanent porosity with a BET surface area of 238 m^2 g^{-1}. More importantly, it exhibits an ability of enantioselective separation of secondary alcohols, especially efficient for 1-phenylethanol with 92 % enantiomeric excess (ee).

Rational construction has also been achieved. Champness, Schröder and coworkers [117] designed a rigid multifunctional and multidirectional unit **84**, which self-assembled to a 3D framework SOF-1 with pyridyl decorated channels.

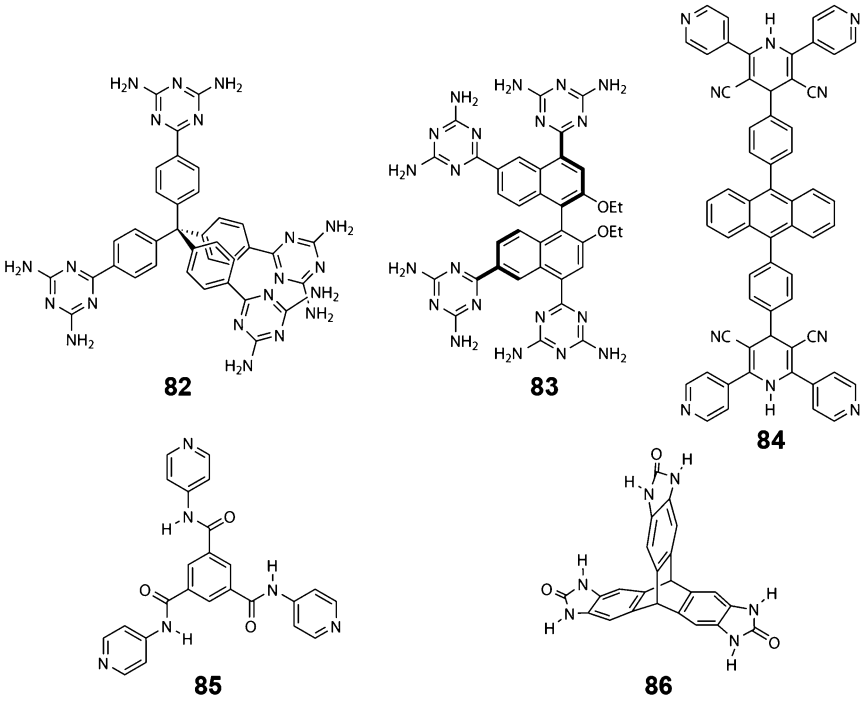

Scheme 3.15 Some representative organic building blocks for porous hydrogen bonded organic frameworks (HOFs)

SOF-1 can be thermally stable up to 420 °C. High C_2H_2 uptake (61 $cm^3\ g^{-1}$) and high selective adsorption of C_2H_2 over CO_2, CH_4, and N_2 at ambient temperature and pressure (270 K, 1 bar) have been revealed. Luo, Zhong and coworkers [118] prepared an extremely stable hydrogen bonded organic framework HOF-8 from **85**, which is not only thermally stable to 350 °C, but also chemically stable to water and common organic solvents. HOF-8 can selectively adsorb CO_2 rather than N_2 and H_2 at 298 K. Also, HOF-8 can selectively adsorb benzene over other solvents. Up to now, the state-of-the-art work was reported by Mastalerz and Oppel [119]. They constructed an extraordinarily porous solid from **86**. The BET surface area reaches 2,796 $m^2\ g^{-1}$, which is the highest among all porous materials derived from discrete molecules. The material can adsorb 80.7 $cm^3\ g^{-1}$ (15.9 wt%) CO_2 at 273 K and 1 bar, and the H_2 uptake is 243 $cm^3\ g^{-1}$ (2.2 wt%) at 77 K and 1 bar. These values can even compete with some best performing MOFs.

3.6.3 Crystal Engineering of Pharmaceutical Cocrystals

A commercial and practical application of crystal engineering is to manufacture pharmaceutical cocrystals in pharmaceutical industry. According to Zaworotko's definition [120], pharmaceutical cocrystals are formed between a molecular or ionic active pharmaceutical ingredient (API) with a cocrystal former (generally regarded as safe (GRAS) for human consumption [121]) that is a solid at ambient conditions. A pharmaceutical cocrystal is generally designed using crystal engineering principles, especially supramolecular heterosynthons. Hydrogen bonding is the prevalent interaction, for most APIs contain multiple hydrogen bond donor and acceptor functional groups, like carboxylic acid, amide, hydroxyl and aromatic azaheterorings. Given an API, a variety of coformers with complementary hydrogen bonding groups may be used. Hence, pharmaceutical cocrystals provide a convenient means to diversify the number of crystal forms of an existing API.

The methods to prepare pharmaceutical cocrystals include solvent growth, sublimation, neat solid state grinding [122], and grinding with solvent-drop addition [123]. While solvent growth can afford high-quality crystals suitable for structural characterization, solid state grinding method is regarded "green" in that it avoids the use of large quantities of solvents. In addition, it can afford nearly quantitative yields with common particle size. Solvent-drop grinding, the addition of small amount of suitable solvent to ground mixture could accelerate the crystallization process and also proved to be useful in polymorph control and selective polymorph transformation [124, 125]. High-throughput crystallization technologies have been integrated into pharmaceutical cocrystal screening, which would significantly speed up the discovery process [126].

The most useful aspect is that pharmaceutical cocrystals can be attempted to optimize the physicochemical properties of drugs such as solubility, dissolution rate, stability, tableting, and so on, without the need for covalent modification [127, 128].

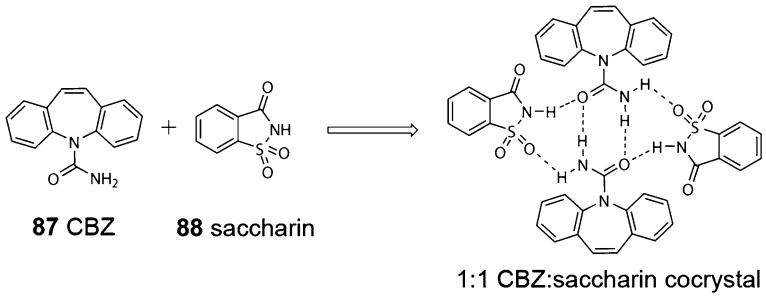

Scheme 3.16 The cocrystal formation of CBZ with saccharin

Carbamazepine (CBZ, **87**) (Scheme 3.16), is an important antiepileptic agent in use for more than 30 years but suffers from low water solubility and oral bioavailability. Hickey and coworkers [129] prepared a cocrystal with saccharin (**88**) employing the peripheral hydrogen bonding capabilities of CBZ dimer. The cocrystal was found to possess favorable dissolution properties, suspension stability and pharmacokinetics using dog models. Similarly, Zaworotko, Shytle and coworkers [130] used cocrystallization to improve solubility and oral bioavailability of quercetin.

Temozolomide (TMZ, **89**) (Scheme 3.17) is an antitumor prodrug with broad-spectrum antineoplastic activity [131], but faces a problem of stability. TMZ decomposes in aqueous medium of pH ≥ 7 but is relatively stable under acidic conditions. Coming with the instability, the white powder often turns pink and then brown upon storage. There is a need for a method to improve the stability and shelf

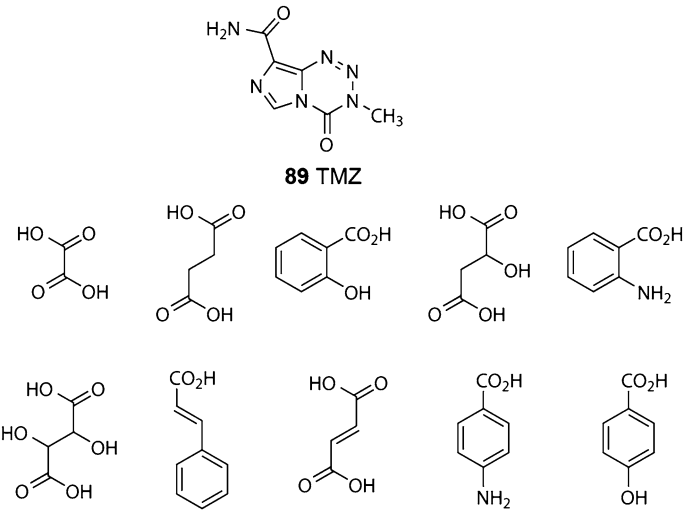

Scheme 3.17 Structures of TMZ and carboxylic acid coformers for cocrystallization

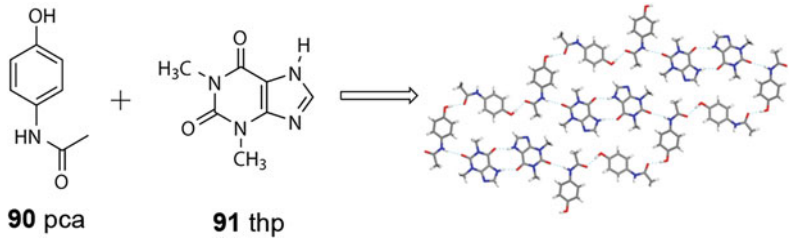

Fig. 3.32 2D hydrogen bonding layer structure of cocrystal pca:thp (1:1)

life of TMZ. Nangia and coworkers [132] adopted the cocrystallization method with organic carboxylic acid coformers in the pKa range of 1–5 as pH adjusters to inhibit the hydrolytic degradation. Many cocrystals can be crystallized for TMZ to fine-tune the physicochemical property. The cocrystal TMZ:succinic acid (1:1) can even be stable for up to 1 year under laboratory conditions with no sign of discoloration. In other cases, pharmaceutical cocrystals of caffeine [133] and nitrofurantoin [134] can also be engineered to improve the stability to moisture.

In 2009, Jones and coworkers [135] showed that the cocrystallization strategy could be used to improve the mechanical property of paracetamol (pca, **90**) (Fig. 3.32). They found the relationship between improved mechanical properties and crystallographic features that 2D layered structures exhibit enhanced ability to form tablets. The strong hydrogen bonding interactions between pca and theophylline (thp, **91**) give the best tensile strength.

References

1. Schmidt GMJ (1971) Photodimerization in the solid state. Pure Appl Chem 27:647
2. Desiraju GR (1989) Crystal engineering: the design of organic solids. Elsevier, Amsterdam
3. Desiraju GR (2013) Crystal engineering: from molecule to crystal. J Am Chem Soc 135:9952
4. Côté AP, Benin AI, Ockwig NW, O'Keeffe M, Matzger AJ, Yaghi OM (2005) Porous, crystalline, covalent organic frameworks. Science 310:1166
5. Feng X, Ding X, Jiang D (2012) Covalent organic frameworks. Chem Soc Rev 41:6010
6. Ding S, Wang W (2013) Covalent organic frameworks (COFs): from design to applications. Chem Soc Rev 42:548
7. Beaudoin D, Maris T, Wuest JD (2013) Constructing monocrystalline covalent organic networks by polymerization. Nat Chem 5:830
8. Zhang YB, Su J, Furukawa H, Yun Y, Gándara F, Duong A, Zou X, Yaghi OM (2013) Single-crystal structure of a covalent organic framework. J Am Chem Soc 135:16336
9. Mastalerz M (2013) Crystal engineering: covalent crystal growth. Nat Chem 5:810
10. Dunitz JD (1991) Phase transitions in molecular crystals from a chemical viewpoint. Pure Appl Chem 63:177
11. Desiraju GR (1995) Supramolecular synthons in crystal engineering-a new organic synthesis. Angew Chem Int Ed Engl 34:2311
12. Ermer O (1988) Five-fold diamond structure of adamantane-1,3,5,7-tetracarboxylic acid. J Am Chem Soc 110:3747

13. Allen FH, Bellard S, Brice MD, Cartwright BA, Doubleday A, Higgs H, Hummelink T, Hummelink-Peters BG, Kennard O, Motherwell WDS, Rodgers JR, Watson DG (1979) The Cambridge crystallographic data centre: computer-based search, retrieval, analysis and display of information. Acta Crystallogr B35:2331
14. Yaghi OM, O'Keeffe M, Ockwig NW, Chae HK, Eddaoudi M, Kim J (2003) Reticular synthesis and the design of new materials. Nature 423:705
15. O'Keeffe M, Peskov MA, Ramsden SJ, Yaghi OM (2008) The Reticular Chemistry Structure Resource (RCSR) database of, and symbols for, crystal nets. Acc Chem Res 41:1782. http://rcsr.anu.edu.cn
16. Eddaoudi M, Kim J, Rosi N, Vodak D, Wachter J, O'Keeffe M, Yaghi OM (2002) Systematic design of pore size and functionality in isoreticular MOFs and their application in methane storage. Science 295:469
17. Deng H, Doonan CJ, Furukawa H, Ferreira RB, Towne J, Knobler CB, Wang B, Yaghi OM (2010) Multiple functional groups of varying ratios in metal-organic frameworks. Science 327:846
18. El-Kaderi HM, Hunt JR, Mendoza-Cortés JL, Côté AP, Taylor RE, O'Keeffe M, Yaghi OM (2007) Designed synthesis of 3D covalent organic frameworks. Science 316:268
19. Desiraju GR (2002) Hydrogen bridges in crystal engineering: interactions without borders. Acc Chem Res 35:565
20. Arunan E, Desiraju GR, Klein RA, Sadlej J, Scheiner S, Alkorta I, Clary DC, Crabtree RH, Dannenberg JJ, Hobza P, Kjaergaard HG, Legon AC, Mennucci B, Nesbitt DJ (2011) Definition of the hydrogen bond (IUPAC recommendations 2011). Pure Appl Chem 83:1637
21. Zhang J, Chen P, Yuan B, Ji W, Cheng Z, Qiu X (2013) Real-space identification of intermolecular bonding with atomic force microscopy. Science 342:611
22. Kitaigorodskii AI (1973) Molecular crystals and molecules. Academic Press, New York
23. Etter MC, Macdonald JC (1990) Graph-set analysis of hydrogen-bond patterns in organic crystals. Acta Crystallogr B46:256
24. Bernstein J, Davis RE, Shimoni L, Chang N-L (1995) Patterns in hydrogen bonding: functionality and graph set analysis in crystals. Angew Chem Int Ed Engl 34:1555
25. Etter MC (1990) Encoding and decoding hydrogen-bond patterns of organic compounds. Acc Chem Res 23:120
26. Batten SR, Robson R (1998) Interpenetrating nets: ordered, periodic entanglement. Angew Chem Int Ed 37:1460
27. Batten SR (2010) Topology and interpenetration. In: MacGillivray LR (ed) Metal-organic frameworks: design and application. Wiley, New York, pp 91–130
28. Carlucci L, Ciani G, Proserpio DM (2003) Borromean links and other non-conventional links in 'polycatenated' coordination polymers: re-examination of some puzzling networks. CrystEngComm 5:269
29. Leznoff DB, Xue B-Y, Batchelor RJ, Einstein FWB, Patrick BO (2001) Gold-gold interactions as crystal engineering design elements in heterobimetallic coordination polymers. Inorg Chem 40:6026
30. Liu F-Q, Tilley TD (1997) Coordination networks based on tetrahedral silane building blocks: influence of the anion on structures adopted by Ag^{+}-Si(p-$C_6H_4CN)_4$ arrays. Inorg Chem 36:5090
31. Yang J, Ma J-F, Liu Y-Y, Batten SR (2009) Four-, and six-connected entangled frameworks based on flexible bis(imidazole) ligands and long dicarboxylate anions. CrystEngComm 11:151
32. Fu Z-Y, Wu X-T, Dai J-C, Wu L-M, Cui C-P, Hu S-M (2001) Interpenetration in [Cd(isonicotinate)$_2$(1,2-bis(4-pyridyl)ethane)$_{0.5}$(H_2O)]$_n$, a novel octahedral polymer containing an unusual two-dimensional bilayer motif generated by self-assembly of rectangle building blocks. Chem Commun 1856
33. Blatov VA, Carlucci L, Ciani G, Proserpio DM (2004) Interpenetrating metal-organic and inorganic 3D networks: a computer-aided systematic investigation. Part I. Analysis of the Cambridge structure database. CrystEngComm 6:377

34. Baburin IA, Blatov VA, Carlucci L, Ciani G, Proserpio DM (2005) Interpenetrating metal-organic and inorganic 3D networks: a computer-aided systematic investigation. Part II. Analysis of the Inorganic Crystal Structure Database (ICSD). J Solid State Chem 178:2452
35. Baburin IA, Blatov VA, Carlucci L, Ciani G, Proserpio DM (2008) Interpenetrated three-dimensional networks of hydrogen-bonded organic species: a systematic analysis of the Cambridge Structure Database. Cryst Growth Des 8:519
36. Baburin IA, Blatov VA, Carlucci L, Ciani G, Proserpio DM (2008) Interpenetrated three-dimensional hydrogen-bonded networks from metal-organic molecular and one- or two-dimensional polymeric motifs. CrystEngComm 10:1822
37. Alexandrov EV, Blatov VA, Kochetkov AV, Proserpio DM (2011) Underlying nets in three-periodic coordination polymers: topology, taxonomy and prediction from a computer-aided analysis of the Cambridge Structure Database. CrystEngComm 13:3947
38. Grimes JM, Burroughs JN, Gouet P, Diprose JM, Malby R, Ziéntara S, Mertens PPC, Stuart DI (1998) The atomic structure of the bluetongue virus core. Nature 395:470
39. Ronson TK, Zarra S, Black SP, Nitschke JR (2013) Metal-organic container molecules through subcomponent self-assembly. Chem Commun 49:2476
40. Inokuma Y, Kawano M, Fujita M (2011) Crystalline molecular flasks. Nat Chem 3:349
41. Wyler R, de Mendoza J, Rebek J Jr (1993) A synthetic cavity assembles through self-complementary hydrogen bonds. Angew Chem Int Ed Engl 32:1699
42. Valdés C, Spitz UP, Toledo LM, Kubik SW, Rebek J Jr (1995) Synthesis and self-assembly of pseudo-spherical homo- and heterodimeric capsules. J Am Chem Soc 117:12733
43. Shimizu KD, Rebek J Jr (1995) Synthesis and assembly of self-complementary calix[4]arene. Proc Natl Acad Sci USA 92:12403
44. Mogck O, Paulus EF, Böhmer V, Thondorf I, Vogt W (1996) Hydrogen-bonded dimers of tetraurea calix[4]arenes: unambiguous proof by single crystal X-ray analysis. Chem Commun 2533
45. Rose KN, Barbour LJ, Orr GW, Atwood JL (1998) Self-assembly of carcerand-like dimers of calix[4]resorcinarene facilitated by hydrogen bonded solvent bridges. Chem Commun 407
46. Murayama K, Aoki K (1998) Resorcin[4]arene dimer linked by eight water molecules and incorporating a tetraethylammonium ion: guest-driven capsule formation via cation-p interactions. Chem Commun 607
47. Beyeh NK, Rissanen K (2011) Dimeric resorcin[4]arene capsules in the solid state. Isr J Chem 51:769
48. MacGillivray LR, Diamente PR, Reid JL, Ripmeester JA (2000) Encapsulation of two aromatics by a carcerand-like capsule of nanometre-scale dimensions. Chem Commun 359
49. MacGillivray LR, Atwood JL (1997) A chiral spherical molecular assembly held together by 60 hydrogen bonds. Nature 389:469
50. Ugono O, Holman KT(2006) An achiral form of the hexameric resorcin[4]arene capsule sustained by hydrogen bonding with alcohols. Chem Commun 2144
51. Gerkensmeier T, Iwanek W, Agena C, Fröhlich R, Kotila S, Näther C, Mattay J (1999) Self-assembly of 2,8,14,20-tetraisobutyl-5,11,17,23-tetrahydroxyresorc[4]arene. Eur J Org Chem 1999:2257
52. Atwood JL, Barbour LJ, Jerga A (2001) Hydrogen-bonded molecular capsules are stable in polar media. Chem Commun 2376
53. Cave GWV, Antesberger J, Barbour LJ, McKinlay RM, Atwood JL (2004) Inner core structure responds to communication between nanocapsule walls. Angew Chem Int Ed 43:5263
54. Dalgarno SJ, Tucker SA, Bassil DB, Atwood JL (2005) Fluorescent guest molecules report ordered inner phase of host capsules in solution. Science 309:2037
55. Dalgarno SJ, Bassil DB, Tucker SA, Atwood JL (2006) Cocrystallization and encapsulation of a fluorophore with hexameric pyrogallol[4]arene nanocapsules: structural and fluorescence studies. Angew Chem Int Ed 45:7019

56. Dalgarno SJ, Szabo T, Siavosh-Haghighi A, Deakyne CA, Adams JE, Atwood JL (2009) Exploring the limits of encapsulation within hexameric pyrogallol[4]arene nano-capsules. Chem Commun 1339
57. Kvasnica M, Chapin JC, Purse BW (2011) Efficient loading and kinetic trapping of hexameric pyrogallolarene capsules in solution. Angew Chem Int Ed 50:2244
58. Palmer LC, Rebek J Jr (2005) Hydrocarbon binding inside a hexameric pyrogallol[4]arene capsule. Org Lett 7:787
59. Barrett ES, Dale TJ, Rebek J Jr (2008) Stability, dynamics, and selectivity in the assembly of hydrogen-bonded hexameric capsules. J Am Chem Soc 130:2344
60. Atwood JL, Barbour LJ, Jerga A (2002) Organization of the interior of molecular capsules by hydrogen bonding. Proc Natl Acad Sci USA 99:4837
61. Ballester P (2011) Supramolecular capsules derived from calixpyrrole scaffolds. Isr J Chem 51:710
62. Gil-Ramírez G, Benet-Buchholz J, Escudero-Adán EC, Ballester P (2007) Solid-state self-assembly of a calix[4]pyrrole-resorcinarene hybrid into a hexameric cage. J Am Chem Soc 129:3820
63. Liu Y, Hu C, Comotti A, Ward MD (2011) Supramolecular archimedean cages assembled with 72 hydrogen bonds. Science 333:436
64. Bishop R (2009) Helical tubuland diols: a synthetic and crystal engineering quest. Acc Chem Res 42:67
65. Ghadiri MR, Granja JR, Milligan RA, McRee DE, Khazanovich N (1993) Self-assembling organic nanotubes based on a cyclic peptide architecture. Nature 366:324
66. Gattuso G, Menzer S, Nepogodiev SA, Stoddart JF, Williams DJ (1997) Carbohydrate nanotubes. Angew Chem Int Ed Engl 36:1451
67. Ranganathan D, Lakshmi C, Karle IL (1999) Hydrogen-bonded self-assembled peptide nanotubes from cystine-based macrocyclic bisureas. J Am Chem Soc 121:6103
68. Shimizu LS, Smith MD, Hughes AD, Shimizu KD (2001) Self-assembly of a bis-urea macrocycle into a columnar nanotube. Chem Commun 1592
69. Shimizu LS, Hughes AD, Smith MD, Davis MJ, Zhang BP, zur Loye H-C, Shimizu KD (2003) Self-assembled nanotubes that reversibly bind acetic acid guests. J Am Chem Soc 125:14972
70. Dewal MB, Xu Y, Yang J, Mohammed F, Smith MD, Shimizu LS (2008) Manipulating the cavity of a porous material changes the photoreactivity of included guests. Chem Commun 3909
71. Dawn S, Dewal MB, Sobransingh D, Paderes MC, Wibowo AC, Smith MD, Krause JA, Pellechia PJ, Shimizu LS (2011) Self-assembled phenylethynylene bis-urea macrocycles facilitate the selective photodimerization of coumarin. J Am Chem Soc 133:7025
72. Semetey V, Didierjean C, Briand J-P, Aubry A, Guichard G (2002) Self-assembling organic nanotubes from enantiopure cyclo-N,N'-linked oligoureas: design, synthesis, and crystal structure. Angew Chem Int Ed 41:1895
73. Fischer L, Decossas M, Briand J-P, Didierjean C, Guichard G (2009) Control of duplex formation and columnar self-assembly with heterogeneous amide/urea macrocycles. Angew Chem Int Ed 48:1625
74. Hong BH, Lee JY, Lee C-W, Kim JC, Bae SC, Kim KS (2001) Self-assembled arrays of organic nanotubes with infinitely long one-dimensional H-bond chains. J Am Chem Soc 123:10748
75. Dalgarno SJ, Cave GWV, Atwood JL (2006) Toward the isolation of functional organic nanotubes. Angew Chem Int Ed 45:570
76. Kulikov OV, Daschbach MM, Yamnitz CR, Rath N, Gokel GW (2009) Self-assembled, cogged hexameric nanotubes formed from pyrogallol[4]arenes with a unique branched side chain. Chem Commun 7497
77. Xue M, Chen C-F (2011) Aromatic single-walled organic nanotubes self-assembled from NH-bridged azacalix[2]triptycene[2]pyridine. Chem Commun 47:2318

78. Hu Z-Q, Chen C-F (2005) A novel self-assembled organic tubular structure. Chem Commun 2445
79. Kataoka K, Yanagi M, Katagiri T (2011) A crystal engineering weaving of half-spiral molecules by hydrogen bonding chains into tube structures. CrystEngComm 13:6342
80. Durka K, Jarzembska KN, Kamiński R, Luliński S, Serwatowski J, Woźniak K (2013) Nanotubular hydrogen-bonded organic framework architecture of 1,2-phenylenediboronic acid hosting ice clusters. Cryst Growth Des 13:4181
81. Pantoş GD, Pengo P, Sanders JKM (2007) Hydrogen-bonded helical organic nanotubes. Angew Chem Int Ed 46:194
82. Men Y-B, Sun J, Huang Z-T, Zheng Q-Y (2009) Rational construction of 2D and 3D Borromean arrayed organic crystals by hydrogen-bond-directed self-assembly. Angew Chem Int Ed 48:2873
83. Men Y-B, Sun J, Huang Z-T, Zheng Q-Y (2010) Design and construction of an organic crystal with a novel interpenetrated n-Borromean linked topology. Chem Commun 46:6299
84. Wang L-C, Sun J, Huang Z-T, Zheng Q-Y (2013) Observation of a persistent supramolecular synthon involving carboxyl groups and H2O that guides the formation of polycatenated co-crystals of a tritopic carboxylic acid and bis(pyridyls). Cryst Growth Des 13:1
85. Men Y-B, Sun J, Huang Z-T, Zheng Q-Y (2009) Organic hydrogen-bonded interpenetrating diamondoid frameworks from modular self-assembly of methanetetrabenzoic acid with linkers. CrystEngComm 11:978
86. Men Y-B, Sun J, Huang Z-T, Zheng Q-Y (2009) Construction of 3-fold interpenetrated pcu organic frameworks from methanetetrabenzoic acid with zigzag bipyridines. CrystEngComm 11:2277
87. Holman KT, Pivovar AM, Swift JA, Ward MD (2001) Metric engineering of soft molecular host frameworks. Acc Chem Res 34:107
88. Soegiarto AC, Comotti A, Ward MD (2010) Controlled orientation of polyconjugated guest molecules in tunable host cavities. J Am Chem Soc 132:14603
89. Mak TCW, Xue F (2000) Supramolecular rosette ribbon constructed from guanidium and hydrogen carbonate ions in the crystal engineering of hydrogen-bonded networks. J Am Chem Soc 122:9860
90. Lam C-K, Xue F, Zhang J-P, Chen X-M, Mak TCW (2005) Hydrogen-bonded anionic rosette networks assembled with guanidinium and C3-symmetric oxoanion building blocks. J Am Chem Soc 127:11536
91. Xu W-Z, Sun J, Huang Z-T, Zheng Q-Y (2009) Molecular encapsulation of a discrete $(H_2O)_{32}$ cluster with S_6 symmetry in an organic crystalline supermolecule. Chem Commun 171
92. Yu Z-B, Sun J, Huang Z-T, Zheng Q-Y (2011) One dimensional infinite water wires incorporated in isostructural organic crystalline supermolecules with zwitterionic channels. CrystEngComm 13:1287
93. MacGillivray LR (2008) Organic synthesis in the solid state via hydrogen-bond-driven self-assembly. J Org Chem 73:3311
94. Biradha K, Santra R (2013) Crystal engineering of topochemical solid state reactions. Chem Soc Rev 42:950
95. Feldman KS, Campbell RF (1995) Efficient stereo- and regiocontrolled alkene photodimerization through hydrogen bond enforced preorganization in the solid state. J Org Chem 60:1924
96. Grove RC, Malehorn SH, Breen ME, Wheeler KA (2010) A photoreactive crystalline quasiracemate. Chem Commun 46:7322
97. Wheeler KA, Wiseman JD, Grove RC (2011) Enantiocontrolled solid-state photodimerizations via a chiral sulfonamidecinnamic acid. CrystEngComm 13:3134
98. Wheeler KA, Malehorn SH, Egan AE (2012) Valine sulfonamidecinnamic acid asymmetric crystal reactions. Chem Commun 48:519
99. MacGillivray LR, Reid JL, Ripmeester JA (2000) Supramolecular control of reactivity in the solid state using linear molecular templates. J Am Chem Soc 122:7817

100. Papaefstathiou GS, Kipp AJ, MacGillivray LR (2001) Exploiting modularity in template-controlled synthesis: a new linear template to direct reactivity within discrete hydrogen-bonded molecular assemblies in the solid state. Chem Commun 2462
101. Friščić T, MacGillivray LR (2005) Reversing the code of a template-directed solid-state synthesis: a bipyridine template that directs a single-crystal-to-single-crystal [2 + 2] photodimerisation of a dicarboxylic acid. Chem Commun 5748
102. Varshney DB, Gao X, Friščić T, MacGillivray LR (2006) Heteroditopic Rebek's imide directs the reactivity of homoditopic olefins within desolvated quaternary assemblies in the solid state. Angew Chem Int Ed 45:646
103. Bhogala BR, Captain B, Parthasarathy A, Ramamurthy V (2010) Thiourea as a template for photodimerization of azastilbenes. J Am Chem Soc 132:13434
104. Bhattacharya S, Stojaković J, Saha BK, MacGillivray LR (2013) A product of a templated solid-state photodimerization acts as a template: single-crystal reactivity in a single polymorph of a cocrystal. Org Lett 15:744
105. Friščić T, MacGillivray LR (2003) 'Template-switching': a supramolecular strategy for the quantitative, gram-scale construction of a molecular target in the solid state. Chem Commun 1306
106. Gao X, Friščić T, MacGillivray LR (2004) Supramolecular construction of molecular ladders in the solid state. Angew Chem Int Ed 43:232
107. Yang J, Dewal MB, Shimizu LS (2006) Self-assembling bisurea macrocycles used as an organic zeolite for a highly stereoselective photodimerization of 2-cyclohexenone. J Am Chem Soc 128:8122
108. Yang J, Dewal MB, Profeta S Jr, Smith MD, Li Y, Shimizu LS (2008) Origins of selectivity for the [2+2] cycloaddition of a,b-unsaturated ketones within a porous self-assembled organic frameworks. J Am Chem Soc 130:612
109. Geer MF, Walla MD, Solntsev KM, Strassert CA, Shimizu LS (2013) Self-assembled benzophenone bis-urea macrocycles facilitate selective oxidations by singlet oxygen. J Org Chem 78:5568
110. Tian J, Thallapally PK, McGrail BP (2012) Porous organic molecular materials. CrystEngComm 14:1909
111. Mastalerz M (2012) Permanent porous materials from discrete organic molecules-towards ultra-high surface areas. Chem Eur J 18:10082
112. Dewal MB, Lufaso MW, Hughes AD, Samuel SA, Pellechia P, Shimizu LS (2006) Absorption properties of a porous organic crystalline apohost formed by a self-assembled bis-urea macrocycle. Chem Mater 18:4855
113. Msayib KJ, Book D, Budd PM, Chaukura N, Harris KDM, Helliwell M, Tedds S, Walton A, Warren JE, Xu M, McKeown NB (2009) Nitrogen and hydrogen adsorption by an organic microporous crystal. Angew Chem Int Ed 48:3273
114. Brunet P, Simard M, Wuest JD (1997) Molecular tectonics. Porous hydrogen-bonded networks with unprecedented structural integrity. J Am Chem Soc 119:2737
115. He Y, Xiang S, Chen B (2011) A microporous hydrogen-bonded organic framework for highly selective $C2H_2/C2H_4$ separation at ambient temperature. J Am Chem Soc 133:14570
116. Li P, He Y, Guang J, Weng L, Zhao JC-G, Xiang S, Chen B (2014) A homochiral microporous hydrogen-bonded organic framework for highly enantioselective separation of secondary alcols. J Am Chem Soc 136:547
117. Yang W, Greenaway A, Lin X, Matsuda R, Blake AJ, Wilson C, Lewis W, Hubberstey P, Kitagawa S, Champness NR, Schröder M (2010) Exceptional thermal stability in a supramolecular organic frameworks: porosity and gas storage. J Am Chem Soc 132:14457
118. Luo X-Z, Jia X-J, Deng J-H, Zhong J-L, Liu H-J, Wang K-J, Zhong D-C (2013) A microporous hydrogen-bonded organic framework: exceptional stability and highly selective adsorption of gas and liquid. J Am Chem Soc 135:11684
119. Mastalerz M, Oppel IM (2012) Rational construction of an extrinsic porous molecular crystal with an extraordinary high specific surface area. Angew Chem Int Ed 51:5252

120. Almarsson Ö, Zaworotko MJ (2004) Crystal engineering of the composition of pharmaceutical phases. Do pharmaceutical co-crystals represent a new path to improved medicines? Chem Commun 1889
121. http://www.accessdata.fdagov/scripts/fcn/fcnNavigation.cfm?rpt=eafusListing
122. Pedireddi VR, Jones W, Chorlton AP, Docherty R (1996) Creation of crystalline supramolecular arrays: a comparison of co-crystal formation from solution and by solid-state grinding. Chem Commun 987
123. Shan N, Toda F, Jones W (2002) Mechanochemistry and co-crystal formation: effect of solvent on reaction kinetics. Chem Commun 2372
124. Trask AV, Motherwell WDS, Jones W (2004) Solvent-drop grinding: green polymorph control of cocrystallization. Chem Commun 890
125. Trask AV, Shan N, Motherwell WDS, Jones W, Feng S, Tan RBH, Carpenter KJ (2005) Selective polymorph transformation via solvent-drop grinding. Chem Commun 880
126. Morissette SL, Almarsson Ö, Peterson ML, Remenar JF, Read MJ, Lemmo AV, Ellis S, Cima MJ, Gardner CR (2004) High-throughput crystallization: polymorphs, salts, co-crystals and solvates of pharmaceutical solids. Adv Drug Delivery Rev 56:275
127. Babu NJ, Nangia A (2011) Solubility advantage of amorphous drugs and pharmaceutical cocrystals. Cryst Growth Des 11:2662
128. Vishweshwar P, McMahon JA, Bis JA, Zaworotko MJ (2006) Pharmaceutical co-crystals. J Pharm Sci 95:499
129. Hickey MB, Peterson ML, Scoppettuolo LA, Morrisette SL, Vetter A, Guzmán H, Remenar JF, Zhang Z, Tawa MD, Haley S, Zaworotko MJ, Almarsson Ö (2007) Performance comparison of a co-crystal of carbamazepine with marketed product. Eur J Pharm Biopharm 67:112
130. Smith AJ, Kavuru P, Wojtas L, Zaworotko MJ, Shytle RD (2011) Cocrystals of quercetin with improved solubility and oral bioavailability. Mol Pharm 8:1867
131. Darkes MJM, Plosker GL, Jarvis B (2002) Temozolomide. Am J Cancer 1:55
132. Babu NJ, Sanphui P, Nangia A (2012) Crystal engineering of stable temozolomide cocrystals. Chem Asian J 7:2274
133. Trask AV, Motherwell WDS, Jones W (2005) Pharmaceutical cocrystallization: engineering a remedy for caffeine hydration. Cryst Growth Des 5:1013
134. Cherukuvada S, Babu NJ, Nangia A (2011) Nitrofurantoin-p-aminobenzoic acid cocrystal: hydration stability and dissolution rate studies. J Pharm Sci 100:3233
135. Karki S, Friščić T, Fábián L, Laity PR, Day GM, Jones W (2009) Improving mechanical properties of crystalline solids by cocrystal formation: new compressible forms of paracetamol. Adv Mater 21:3905

Chapter 4
Hydrogen Bonding-Mediated Self-assembly of Aromatic Supramolecular Duplexes

Yong Yang and Chuan-Feng Chen

Abstract We highlight in this chapter the most recent advance in the construction of supramolecular duplexes from aromatic components mediated by hydrogen bonding. We put the emphasis on the design strategies and properties of oligoamide and oligohydrazide-based systems. Based on the analysis of the available examples, we summarize a set of general guidelines for the design of hydrogen bonding-mediated molecular duplexes.

4.1 Introduction

Hydrogen bonding is widely adopted by biological systems to assemble various kinds of complicated structures to fulfill delicate functions. For example, the double helical structure of DNA is mainly driven by hydrogen bonding in addition to π–π stacking, electrostatic interaction, and hydrophobic interaction. This structure is the basis for the storage, replication, and transcription of genetic information [1]. Another example is one of the secondary structures of proteins, β-sheet, in which two strands are tethered together by parallel and anti-parallel hydrogen bonding interactions [2]. However, biological systems are often very sophisticated and it is very difficult to deduce a general rule for controlling the self-assembly process, although this is very important to guide the design and synthesis of artificial systems to mimic the structure and function of biological systems. To simplify this circumstance, many artificial systems have been designed and synthesized by chemists.

Y. Yang
Department of Chemistry, Zhejiang Sci-Tech University, Hangzhou 310018, China
e-mail: yangyong@zstu.edu.cn

C.-F. Chen (✉)
Beijing National Laboratory for Molecular Sciences, CAS Key Laboratory of Molecular Recognition and Function, Institute of Chemistry, Chinese Academy of Sciences, Beijing 100190, China
e-mail: cchen@iccas.ac.cn

Z. Li and L. Wu (eds.), *Hydrogen Bonded Supramolecular Structures*,
Lecture Notes in Chemistry 87, DOI 10.1007/978-3-662-45756-6_4

Recently, there is great interest in the artificial construction of molecular duplexes to mimic the structure and function of the above-mentioned double helical structure of DNA and β-sheet structure of protein. Amide-derived peptidomimetics are the most widely used modules for this purpose, inspired by the chemical structures of peptides and also by the mature synthetic methods [3]. Aliphatic peptidomimetics are prone to form helical structures. Because of their relatively rigid structures, aromatic peptidomimetics are the most widely used modules in the field.

4.2 Oligoamide-Based Molecular Duplex Strands

Inspired by the hydrogen bonding pattern found in DNA system, most artificial hydrogen bonding modules are based on modified heterocyclic components [4], including Meijer's famous Ureidopyrimidinone (UPy) system [5], Zimmerman's deazapterin (DeAP) [6], and so on. But some drawbacks such as low solubility, tautomerism, secondary electrostatic effect on the stability of the complex, and difficulty of synthesis that are inherently associated with the heterocycles make the study more complicated and hinder their further applications. From 1999, Gong's group introduced a new strategy to construct nonheterocycle-based molecular duplex strands. The main idea is to link three basic building blocks: 3-aminobenzoic acid, isophthalic acid, and *m*-phenylenediamine, via amide bonds in different sequences, and to preorganize hydrogen bonding sites with intramolecular hydrogen bonding. The resulting oligoamide strands form supramolecular duplexes via hydrogen bonding between the backbone amide O and H atoms [7–11].

4.2.1 Oligoamide-Based Molecular Duplex Strands

Strands **1** and **2** (Fig. 4.1), with self-complementary hydrogen bonding sites DADA and AADD, respectively, formed quadruply hydrogen-bonded duplexes with similar dimerization constants, $K_d = 4.4 \times 10^4$ M^{-1} and $K_d = 6.5 \times 10^4$ M^{-1}, respectively, which were much higher than that for the two hydrogen-bonded complexes **3**·**3**, $K_d = 25$ M^{-1} [12]. This suggests that there exists positive cooperativity. Because the hydrogen bonding sites are not adjacent, secondary electrostatic effect does not work and the dimerization constants are sequence independent, which are determined only by the number of hydrogen bonds, given the errors of NMR binding experiments. This design strategy can be conveniently extended to the construction of six hydrogen bonds-mediated homo or heteromolecular duplexes (Fig. 4.2) [13, 14]. With the increase of hydrogen bonding sites, the dimerization constants increase geometrically: the dimerization constants for **4**·**5** and **6**·**6** are $(1.3 \pm 0.7) \times 10^9$ M^{-1} (ITC, $CHCl_3$) and $(6.8 \pm 4.1) \times 10^9$ M^{-1} (FL, $CHCl_3$),

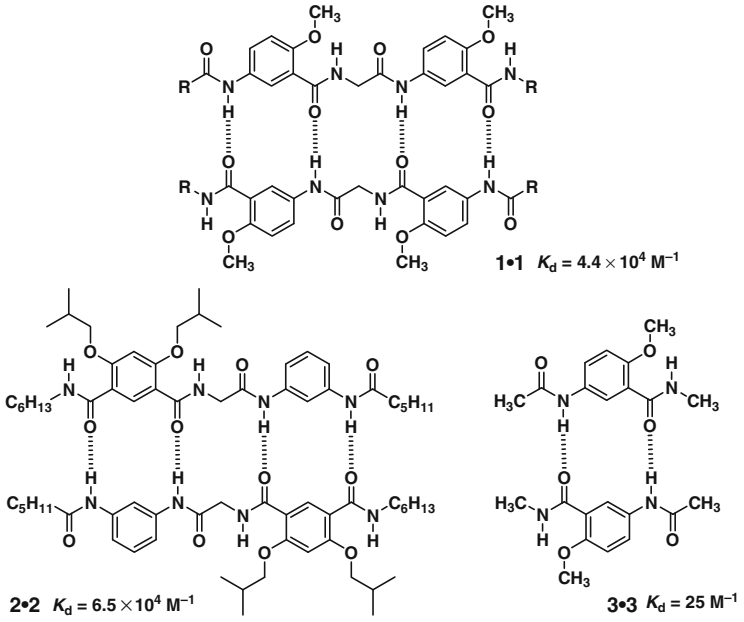

Fig. 4.1 Quadruply hydrogen-bonded molecular duplexes with self-complementary hydrogen bonding sites. Reprinted with the permission from Ref. [12]. Copyright 1999 American Chemical Society

respectively. This kind of molecular duplexes showed strict sequence specificity [15]. If unmatched hydrogen bonding sites are encoded, the stability constants for **5**.**7** and **5**.**8** (Fig. 4.3), each with one pair of unmatched hydrogen bonding sites, drop by >40-fold relative to that for **4**·**5**.

Gong's design strategy could be easily extended into the construction of oligoamides with naphthalene rings as spacers (Fig. 4.4) [16]. Though stands **9** and **10** are both with self-complementary DDAA hydrogen bonding sites, they cannot form homoduplexes because the length of spacers in each strands do not match. Upon mixing only a heteroduplex forms. If all the spacer units are naphthalenes, compound **11** forms a homo duplex. The similar idea could also be extended to six hydrogen bonds-mediated duplex **12**·**13.**

In addition to amide groups, urea and imide groups are also competent for this mission [17]. Yuan et al. integrated these two kinds of groups into one monomer, with S(6) type hydrogen bonding to control the conformation, **14** formed a tightly bonded duplex, which was exemplified by X-ray single crystal analysis. It was noteworthy that Ar–H also participated in the hydrogen bonding interaction (Fig. 4.5).

In the above examples, intramolecular hydrogen bonding was adapted to preorganize the hydrogen bonding sites for intermolecular interactions. Hunter et al. introduced steric hindrance in the following example for the hydrogen bonding sites

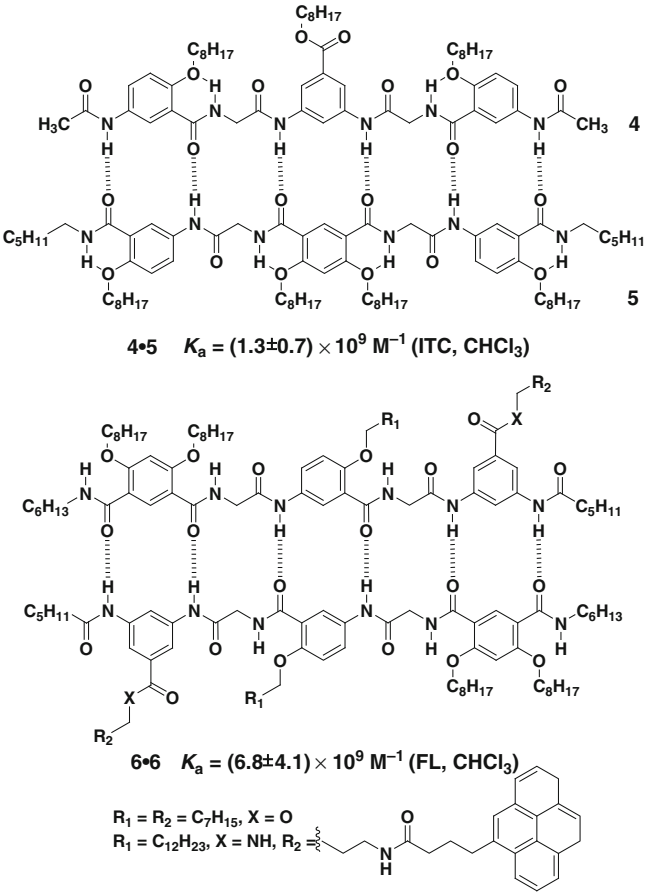

Fig. 4.2 Six hydrogen bond-mediated homo and heteromolecular duplexes. Reprinted with the permission from Ref. [13]. Copyright 2000 American Chemical Society and reproduced from Ref. [14] with permission from The Royal Society of Chemistry

to stay in register for duplex formation (Fig. 4.6) [18–21]. Bulky cyclohexyl units were attached to the oligoamide backbones. In addition to hydrogen bonding, edge-to-face π–π stacking was also an important driving force for the duplex. Hunter used it a model for quantitative determination of π–π stacking interactions.

4.2.2 Applications

The above oligoamide-based duplexes with adjustable stability found wide applications. For example, by attaching reactive olefin units into the above quadruply hydrogen-bonded duplex, Gong used it as a template for highly efficient and

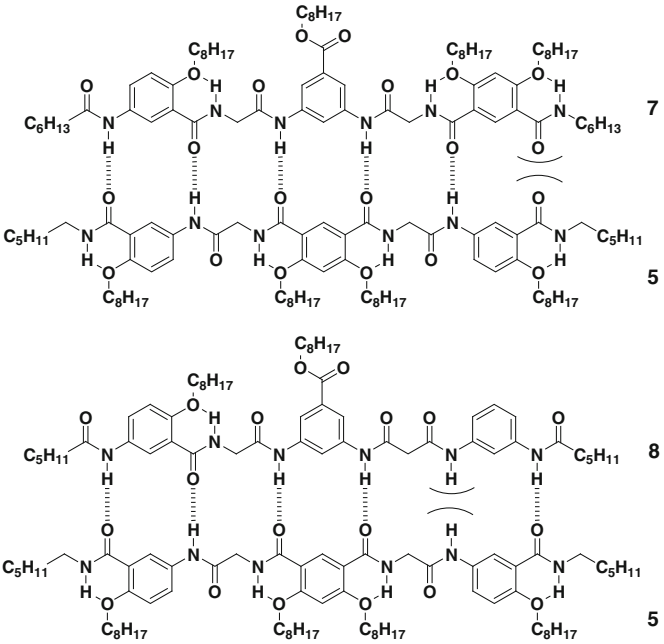

Fig. 4.3 Molecular duplexes with unmatched hydrogen bonding sites. Reprinted with the permission from Ref. [15]. Copyright 2001 American Chemical Society

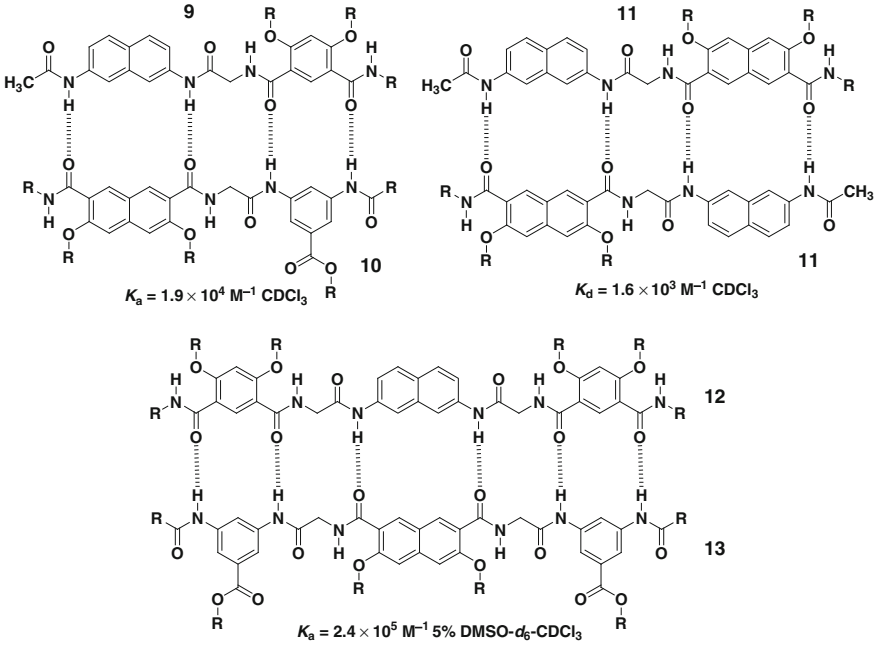

Fig. 4.4 Molecular duplexes with naphthalenes as spacers. Reprinted with the permission from Ref. [16]. Copyright 2011 American Chemical Society

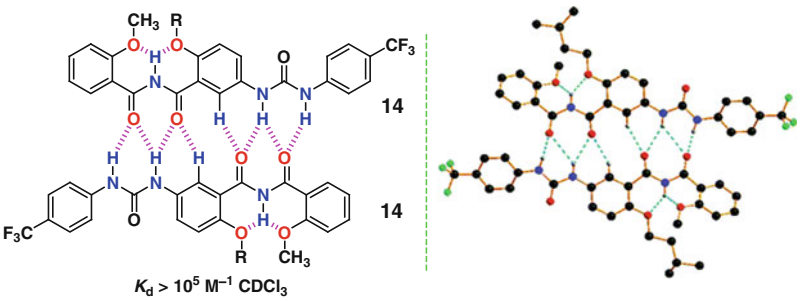

Fig. 4.5 A molecular duplex based on urea and imide hybrid and its crystal structure. Reprinted with the permission from Ref. [17]. Copyright 2011 American Chemical Society

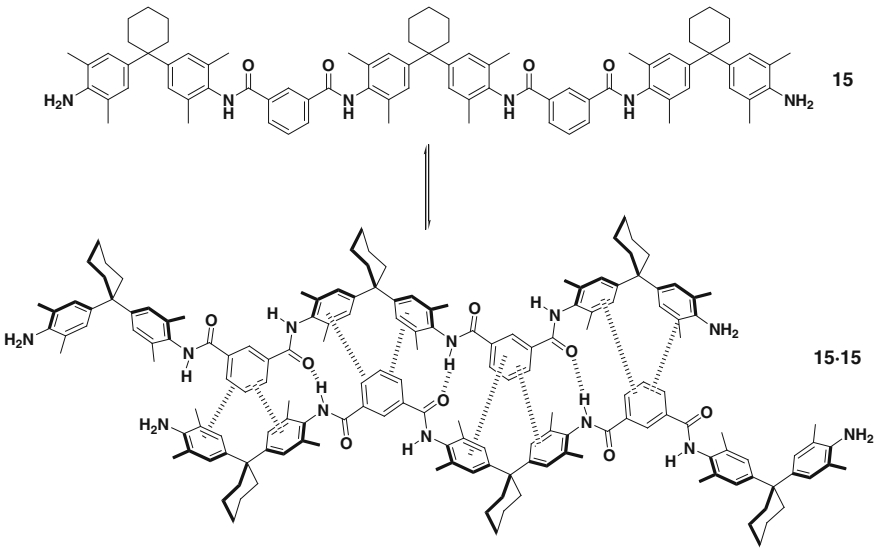

Fig. 4.6 Steric hindrance-guided molecular duplex. Reprinted with the permission from Ref. [18]. Copyright 1994 American Chemical Society

specific olefin metathesis reactions (Fig. 4.7) [22]. Formation of the duplex via quadruple hydrogen bonds brought the two olefin units into close proximity and thus lowered the $\Delta S^{\neq}$ of the reaction, which greatly facilitated the reactions. If the olefin units were present at the opposite side of the two individual strands, no cross-linked product could be isolated. A similar strategy was also adapted by Guan et al. to construct polymer materials with interesting contracting property [23].

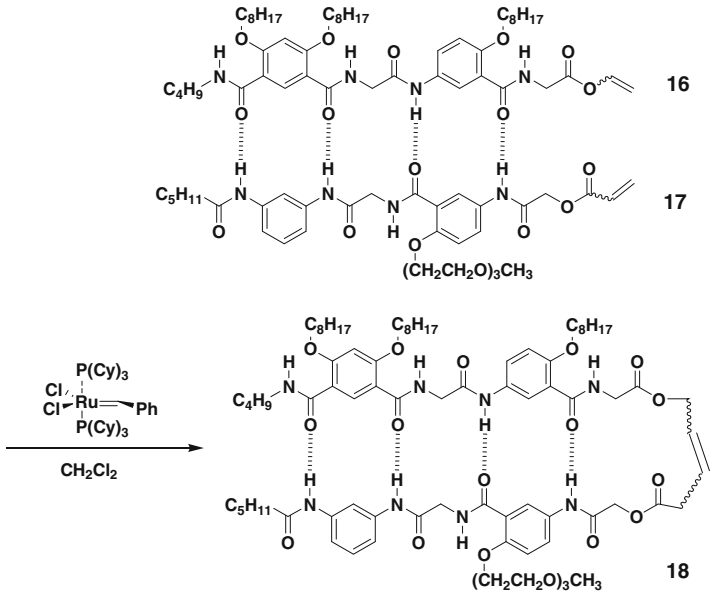

Fig. 4.7 Molecular duplexes as template for catalytic metathesis reaction. Reproduced from Ref. [22] by permission of John Wiley & Sons Ltd

In addition to catalytic metathesis reaction, dynamic disulfide bond formation reaction was also used by Gong's group to achieve hydrogen bonding in polar solvents [24]. When treated 1:1 mixed strands **19** and **20** in CH_2Cl_2, CH_3OH, and H_2O with I_2, cross-linked product **21** was detected in each case (Fig. 4.8). Mechanistic study revealed a thermodynamically controlled process [25]: two hydrogen bonds were sufficient to shift the equilibria toward the formation of the cross-linked product in aqueous solution.

The distance between the strands of Gong's duplex is about 5 Å as determined from the X-ray single crystal structure [12], which is almost the same as that for β-sheet structure of proteins. Thus, the duplexes may serve as a template for directing and nucleating the formation of β-sheet by attaching natural oligopeptide strands. The two oligopeptide chains are brought into proximity and thus forced to pair with each other to form an anti-parallel β-sheet (Fig. 4.9) [26], which in turn enhances the association strength between the two strands. Without the template only poorly defined, random aggregates form from the corresponding peptide strands.

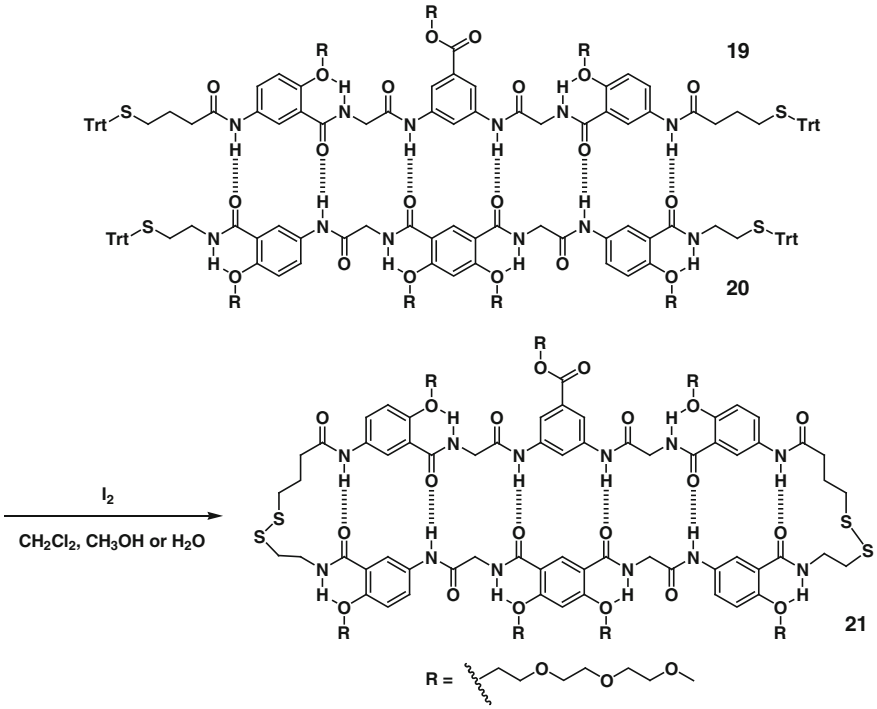

Fig. 4.8 Molecular duplexes as template for catalytic metathesis reaction. Reprinted with the permission from Ref. [24]. Copyright 2006 American Chemical Society

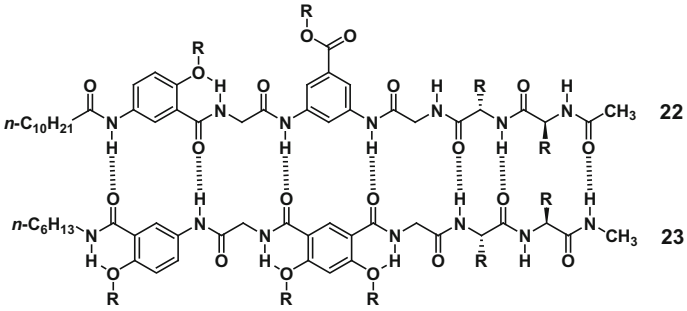

Fig. 4.9 Molecular duplex-templated β-sheet. Reprinted with the permission from Ref. [26]. Copyright 2002 American Chemical Society

4.3 Oligohydrazide-Based Molecular Duplex Strands

Following a similar design strategy by Gong's group, Chen's group also developed a new type of oligohydrazide-based hydrogen bonding-mediated aromatic molecular duplex strands [27]. Compared with amide unit, each hydrazide unit is

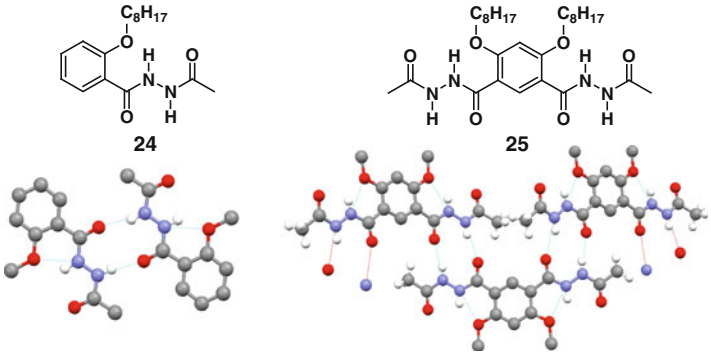

Fig. 4.10 Representation of fixation of conformation by intramolecular hydrogen bonding and a supramolecular zipper structure from ditopic hydrazide derivative. Reproduced from Ref. [28] with permission from the Centre National de la Recherche Scientifique (CNRS) and The Royal Society of Chemistry

composed of two amide groups: the number of hydrogen bonding sites doubles. Abundant hydrogen bonding sites provide many opportunities for the control of conformation via intramolecular hydrogen bonding: by placing an alkoxy group on the *ortho* position, an intramolecular hydrogen bond will fix the whole module to be planar and preorganize two hydrogen bonding sites for dimerization. The fixation or preorganization of conformation will greatly facilitate the subsequent intermolecular interactions.

4.3.1 From Supramolecular Zipper to Quadruple Hydrogen-Bonded Heterodimer

By virtue of S(6) type hydrogen bond to preorganize the conformation, X-ray single crystal analysis revealed that the monotopic **24** dimerized via two hydrogen bonds and the ditopic **25** self-assembled into a supramolecular zipper structure in solid state (Fig. 4.10) [28]. A similar strategy was also adopted by Li et al. to construct a new type of hydrazide-based quadruply hydrogen-bonded heterodimers (Fig. 4.11) [29]. Furthermore, bulky cyclohexyl group was introduced to block unwanted hydrogen bonding sites from one face. Even though, two hydrogen bonding isomers were observed in solution. Careful examination of the X-ray structure of **25** revealed that steric hindrance between two adjacent methyl groups rendered a dihedral angle of 37.0° between two adjacent aromatic rings. We envisioned that if two methyl carbons converge into one methene carbon, i.e., two hydrazide groups are connected by a malonyl group, multiple hydrogen bonds-mediated supramolecular duplex strands could be expected. Indeed quadruple hydrogen-bonded complexes as illustrated in Fig. 4.12 formed [30]. The terminal groups affected the

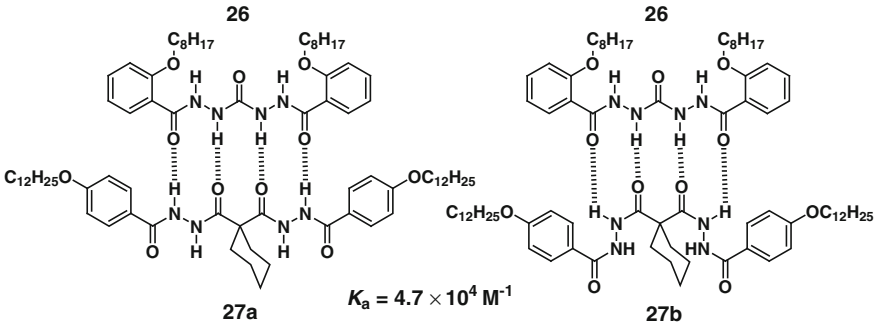

Fig. 4.11 Li's hydrazide-based quadruply hydrogen-bonded heterodimers. Reprinted with the permission from Ref. [29]. Copyright 2003 American Chemical Society

stability of the complexes substantially. For example, because of repulsive interaction between two O atoms, only weak association was observed for **28** and **29**; while by taking advantage of additional attractive interaction between urea NHs and carbonyl O atoms, an association constant of $5.8 \times 10^3\ M^{-1}$ for **33** and **28** was determined.

4.3.2 Strict Self-complementary Oligohydrazide-Based Duplexes

The successful construction of the above quadruple hydrogen-bonded systems qualified the strategy of the construction of molecular duplexes from hydrazide-based oligomers with malonyl groups and *m*-phenylene groups as geometrically complementary linkers. By iterative hydrolysis and coupling reactions, a series of hydrazide-based oligomers were synthesized. As expected, the hydrogen bonding mode observed in the quadruple hydrogen-bonded heterodimers persisted in the extended oligomers (Fig. 4.13) [30]. All these oligomers existed as duplex strands in solution. The chain length and the terminative functional groups were found to affect the stability of the duplex strands. Repulsive spectator secondary electrostatic interaction [31] inherent with the Boc groups in **35** reduced the stability. Also different dynamic behaviors were observed for oligomers with different terminative groups. For oligomers **34** with acetyl terminative groups, dimer–polymer equilibrium was found. Molecular mechanical calculations revealed that two strands wound up to form a double helical structure, which, to some extent, mimicked the structure of DNA.

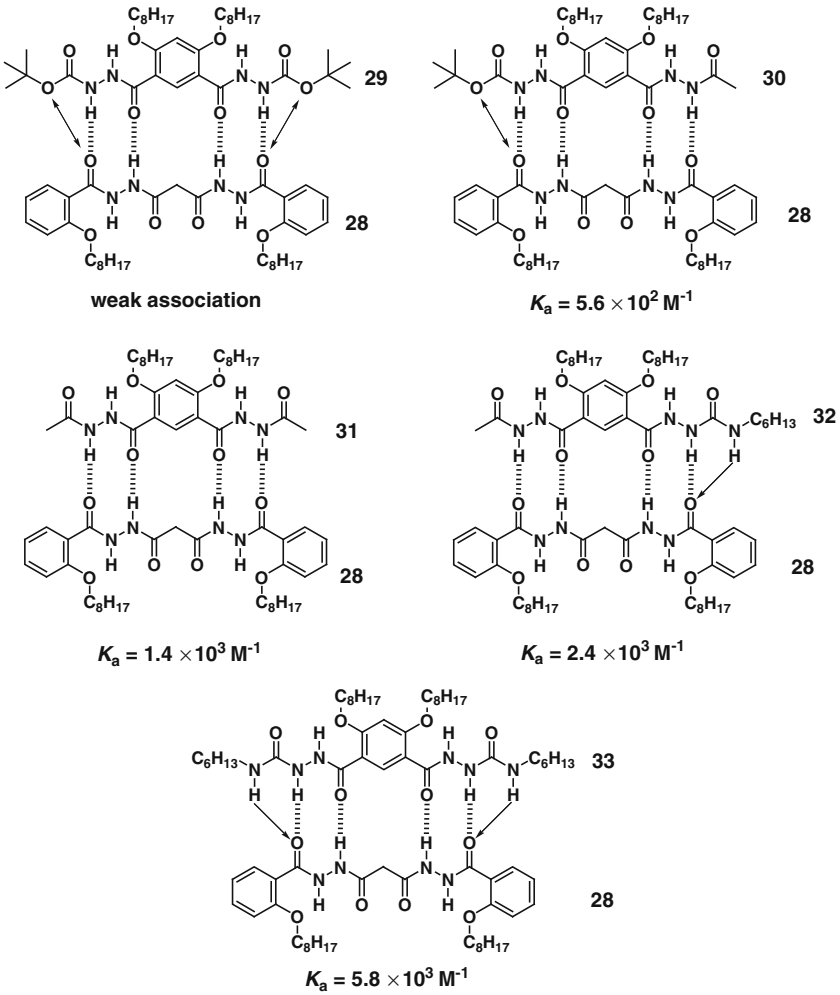

Fig. 4.12 Hydrazide-based quadruply hydrogen-bonded heterodimers using *m*-phenylene and malonyl as spacers. *Double-headed arrow* repulsive interaction; *single-handed arrow* attractive interaction. Reprinted with the permission from Ref. [30]. Copyright 2007 American Chemical Society

4.3.3 Shuttle Movement

In the above examples upon formation of duplexes, all hydrogen bonding sites were occupied and no additional hydrogen bonding sites staying in register for intermolecular interaction left. In oligomers **36a–c**, upon formation of molecular duplexes, there were still two abundant hydrogen bonding sites left for each monomer. At higher temperatures because of the quick shuttle movement as illustrated in

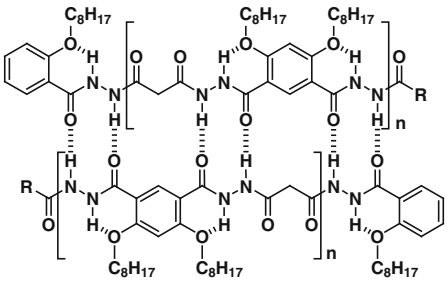

34 R= CH_3 **35** R= $OC(CH_3)_3$
a n=0; **b** n=1; **c** n=2; **d** n=3

Fig. 4.13 Representation of molecular duplex strands **34a–d** and **35a–d** with self-complementary hydrogen bonding sites. Reprinted with the permission from Ref. [30]. Copyright 2007 American Chemical Society

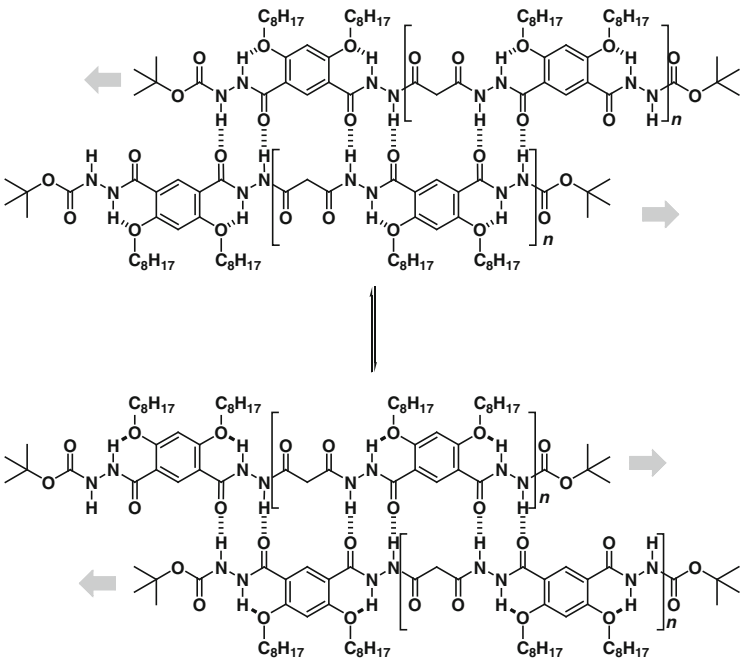

36 a n=1; **b** n=2; **c** n=3

Fig. 4.14 Representation of shuttle-like dynamic processes of **36a–c**. Reprinted with the permission from Ref. [32]. Copyright 2007 American Chemical Society

Fig. 4.14, the two terminal groups displayed only one set of broad ^{1}H NMR signals and the whole spectra corresponded to its structure with a C_2 axis; while at lower temperature, two sets of signals were observed for the hydrogen-bonded terminal

NHs and nonbonded ones and the whole spectra corresponded to centrodimeric structures with *i* symmetry due to prohibition of the shuttle movement. The lengths of the oligomers, i.e., the numbers of intermolecular hydrogen bonds in the duplexes, affected the coalesced temperatures: for **36a** with 6 hydrogen bonds, 223 K; for **36b** with 10 hydrogen bonds, 283 K; for **36c** with 14 hydrogen bonds, >318 K [32].

4.3.4 Mutual Responsive Low Molecular Mass Organic Gelators

As we can see from the above examples, the terminative functional groups affected the property of the molecular duplexes substantially. The diacetyl-terminated **37** and dinaphthyl-terminated **38** were found to form gels in $CHCl_3$ at a concentration as low as 1.0 and 0.8 % (w/w), respectively (Fig. 4.15) [33]. Careful examination of the structures of **37** and **38** revealed that in addition to forming molecular duplexes, abundant hydrogen bonding donor/acceptor sites that reside at the termini of each duplex may further interact intermolecularly to form a polymeric hydrogen-bonded structure and further entanglement of the polymeric species leads to the gel formation. Because **37** and **38** are of complementary hydrogen bonding site, 1:1 mixed **37** and **38** formed an eight hydrogen bonds-mediated heterodimer and displayed a clear solution in $CHCl_3$.

4.3.5 Supramolecular Substitution

As we can see from the above example, supramolecular substitution reaction between **37** and **38** with complementary hydrogen bonding sites led to gel–solution transformation. This is a general rule for these oligomers with complementary hydrogen bonding sites. For example (Fig. 4.16), nonsymmetric **39** with acetyl and Boc termini formed a head-to-tail homodimer in $CHCl_3$ [34]. When it was mixed with symmetric **40**, a heterodimer **39**·**40** formed. A broad signal was observed for H^e and $H^{e'}$ in the ^1H NMR spectrum at room temperature. But with lowering of temperature, it split into two separate signals. This meant that the nonsymmetric nature of **39** induced nonsymmetry of **40** upon complexation, just as one component of a molecule induced nonsymmetry of another component of the same molecule. This phenomenon was also observed in the supramolecular substitution reactions with other oligomers [35].

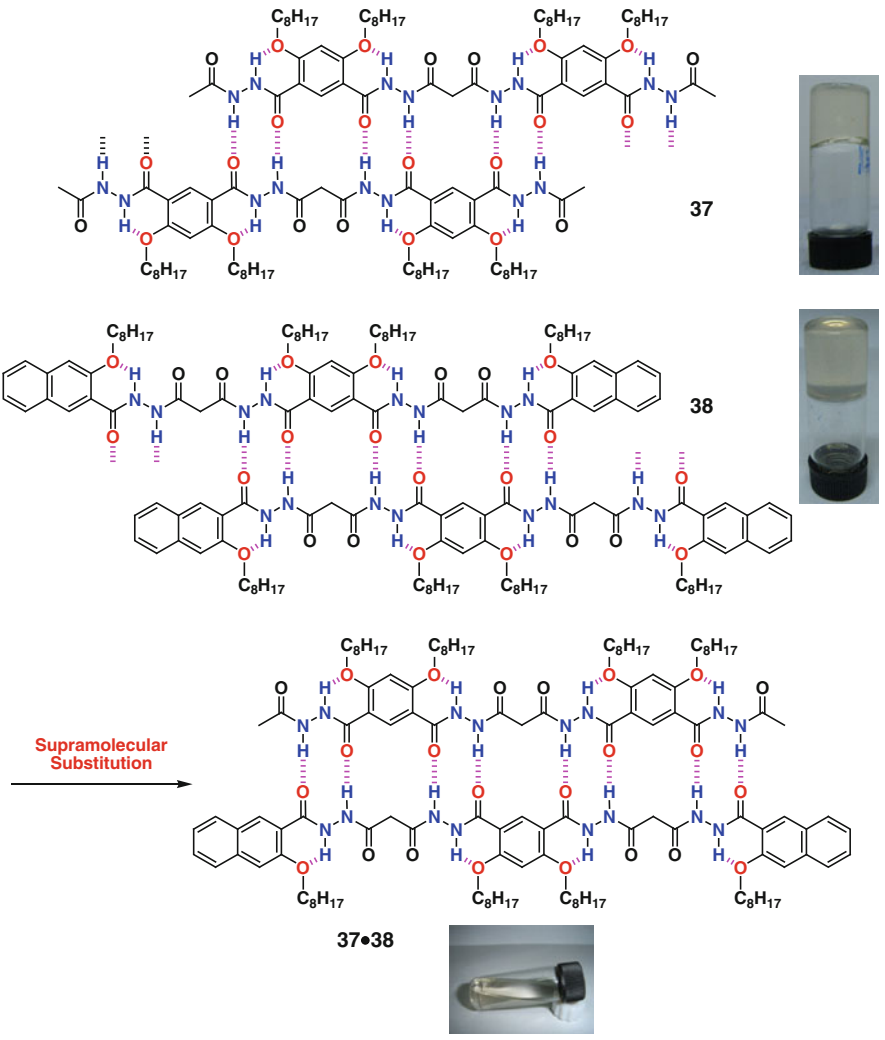

Fig. 4.15 Representation of supramolecular substitution reaction between **37** and **38**, which leads to gel-solution phase transition, with photographs of gels for **37** (2 %), **38** (0.8 %), and a solution of **37** and **38** (1:1) in $CHCl_3$, each 2 % (w/w) inserted. Reproduced from Ref. [33] by permission of John Wiley & Sons Ltd

4.3.6 Amide-Urea-Based Molecular Duplexes

An amide-urea unit can be considered as a hybrid of amide and urea groups. Compared with hydrazide unit, it has one more NH, which usually adds another hydrogen bonding interaction. For example, the dimerization constant for the

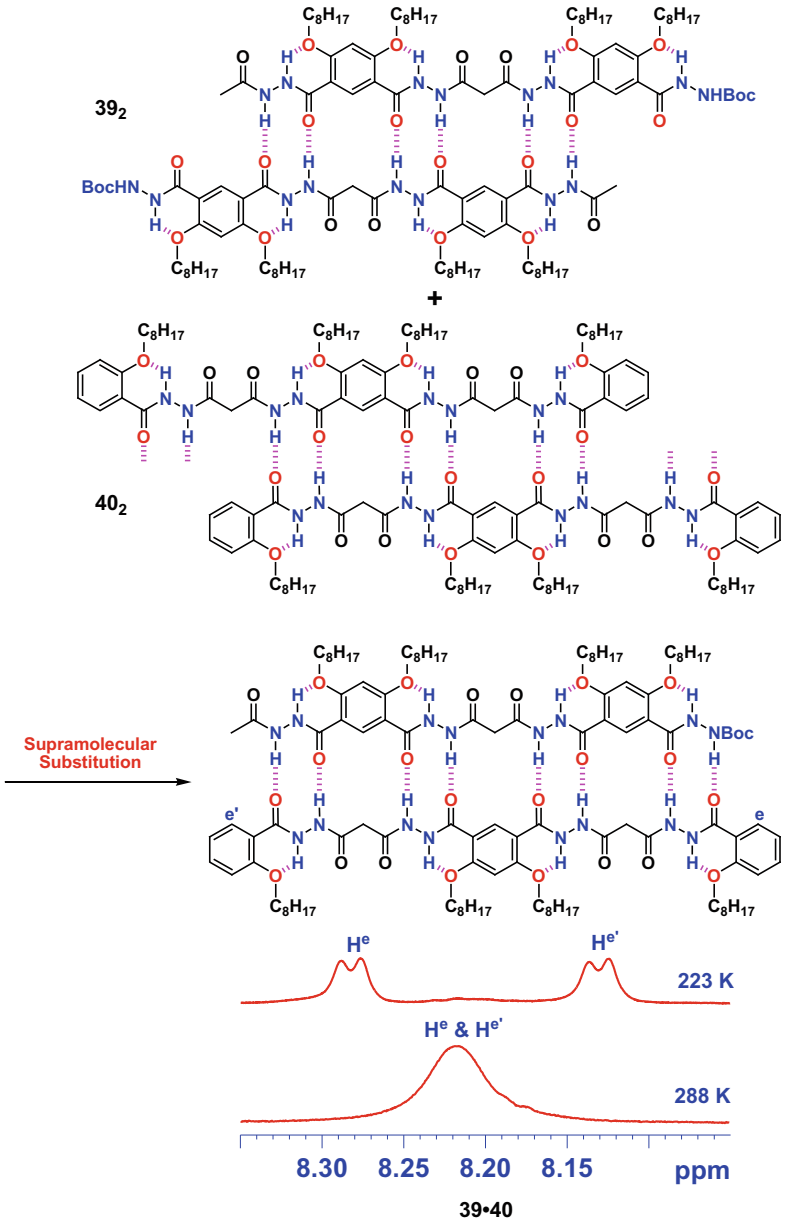

Fig. 4.16 Representation of supramolecular substitution reaction between nonsymmetric oligomer **39** and symmetric oligomer **40**. The ^{1}H NMR spectra at different temperatures indicated that the complexation induced nonsymmetry. Reprinted with the permission from Ref. [35]. Copyright 2008 American Chemical Society

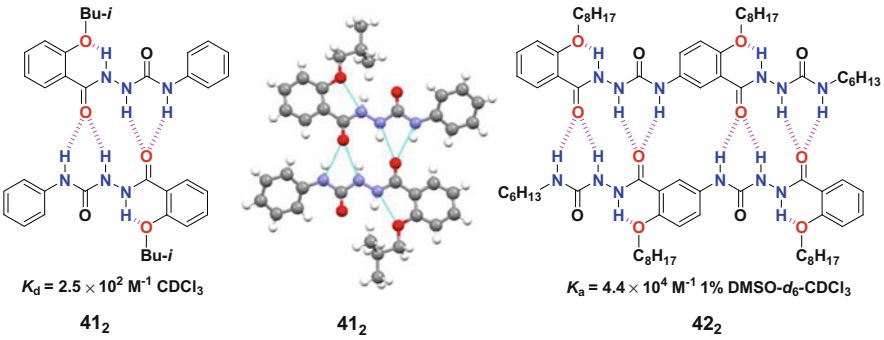

Fig. 4.17 Amide-urea-based homomolecular duplexes, with one single crystal structure showing additional hydrogen bonding interaction. Reprinted with the permission from Ref. [36]. Copyright 2010 American Chemical Society

amide-urea based dimer $\mathbf{41}_2$ is 2.5×10^2 M^{-1} (Fig. 4.17) [36], which is substantially improved compared with that for hydrazide-based dimer 42 M^{-1}. X-ray single crystal analysis confirmed the existence of additional hydrogen bonding interaction. Similar to that for hydrazide-based system, amide-urea based system can also be conveniently extended to longer oligomer. Oligomer **42**, with two amide-urea units integrated, has a dimerization constant of 4.4×10^4 M^{-1}, even in 1 % DMSO-d_6-$CDCl_3$ solution. In addition to homoduplexes, heteroduplexes are also available with this unit (Fig. 4.18) [37]. Oligomers **43** and **44** form a heteroduplex with an association constant of 1.6×10^4 M^{-1}. A duplex does not form when oligomers **43** and **45** are 1:1 mixed. Molecular modeling suggests the naphthalene ring in compound **45** is so rigid that the whole molecule is almost planar; while compound **43** has a twisted conformation. They do not complementary to each other.

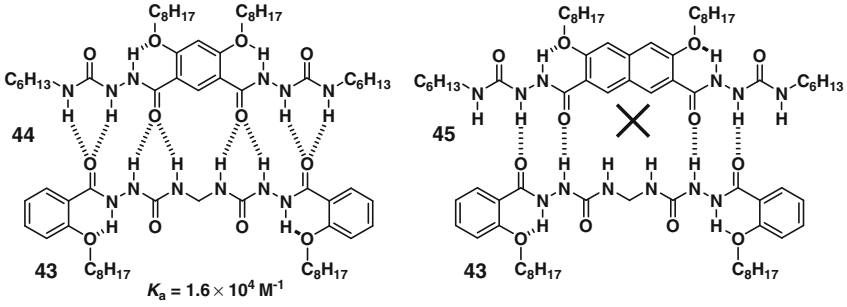

Fig. 4.18 Amide-urea-based heteromolecular duplex. Reprinted with the permission from Ref. [37]. Copyright 2012 American Chemical Society

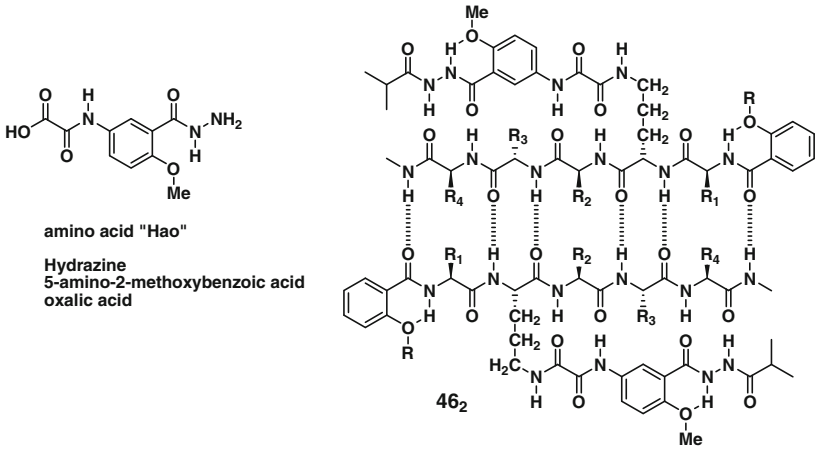

Fig. 4.19 Representation of "Hao" template molecular duplex. Reprinted with the permission from Ref. [39]. Copyright 1999 American Chemical Society

4.3.7 "Hao" Templated Molecular Duplex

Nowick et al. prepared an unnatural amino acid, "Hao" (a hydrazine, 5-amino-2-methoxybenzoic acid, and oxalic acid hybrid, Fig. 4.19), as a rigid skeleton to template natural oligopeptides via intramolecular hydrogen bonding from one face. On the one hand, hydrogen bonding sites for intermolecular hydrogen bonding were preorganized; on the other hand, unwanted sites were blocked. The left hydrogen bonding sites on the other face of the oligopeptides further dimerized to form β-sheet structures. The authors used it as a model for the investigation of sequence selectivity, enantioselectivity, and interactions among aromatic rings during the β-sheet formation process [38, 39].

4.4 "Covalent Casting" Strategy-Based Molecular Duplexes

Preorganization of conformation by intramolecular hydrogen bonding is the most widely used strategy for the above examples. Krische et al. used a "covalent casting" strategy for the construction of duplexes [40]. The main idea is to first obtain structural information from single crystal analysis of one-dimensional hydrogen bonding module and then to select appropriate spacers to integrate multiple hydrogen bonding modules into one linear molecule covalently. The iterative arrangement and cooperative action of these binding sites will lead to molecular duplexes with high stability. Obviously this strategy is inspired by the structure of DNA. They first used this strategy in the construction of melamine-based system (Fig. 4.20, up) [41–43]. For compound **48**, where X = NH, because of

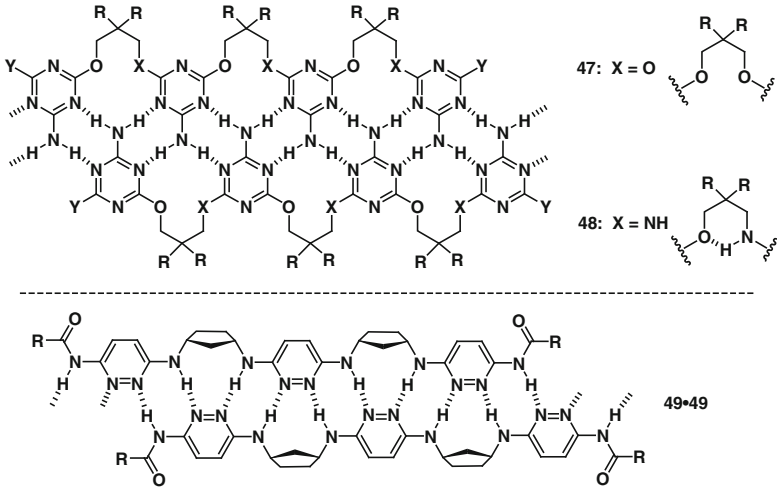

Fig. 4.20 Molecular duplexes based on covalent casting strategy. Reprinted with the permission from Ref. [41, 44]. Copyright 2001 and 2005 American Chemical Society

preorganization of conformation by intramolecular hydrogen bonding, the stability for **48**·**48** was substantially improved compared with that for **47**·**47**. Later, they successfully extended the same design strategy to the pyridazine-based system **49**·**49** (Fig. 4.20, bottom) [44].

A similar strategy was also adapted by Li et al. to construct molecular duplexes. Their idea is to put hydrogen bonding modules, such as amide, amine, urea etc. to one side of a rigid skeleton mediated by successive intramolecular hydrogen bonding (Fig. 4.21) [45, 46]. Thus the bonding sites are preorganized and iteratively arranged, which greatly improved the stabilities of the resulting molecular duplexes.

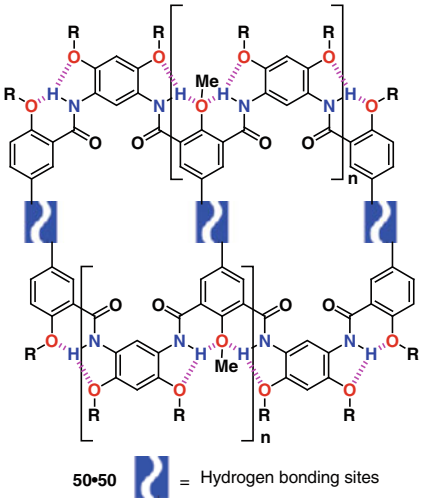

Fig. 4.21 Molecular duplexes based on covalent casting strategy. Reprinted with the permission from Ref. [45]. Copyright 2006 American Chemical Society

4.5 Other Molecular Duplex Strands

Zimmerman et al. reported a type of ureido-naphthyridine-based duplexes (Fig. 4.22) [47, 48]. Because of the intramolecular hydrogen bonding-mediated molecular folding, there existed a complicated extending-folding equilibrium for

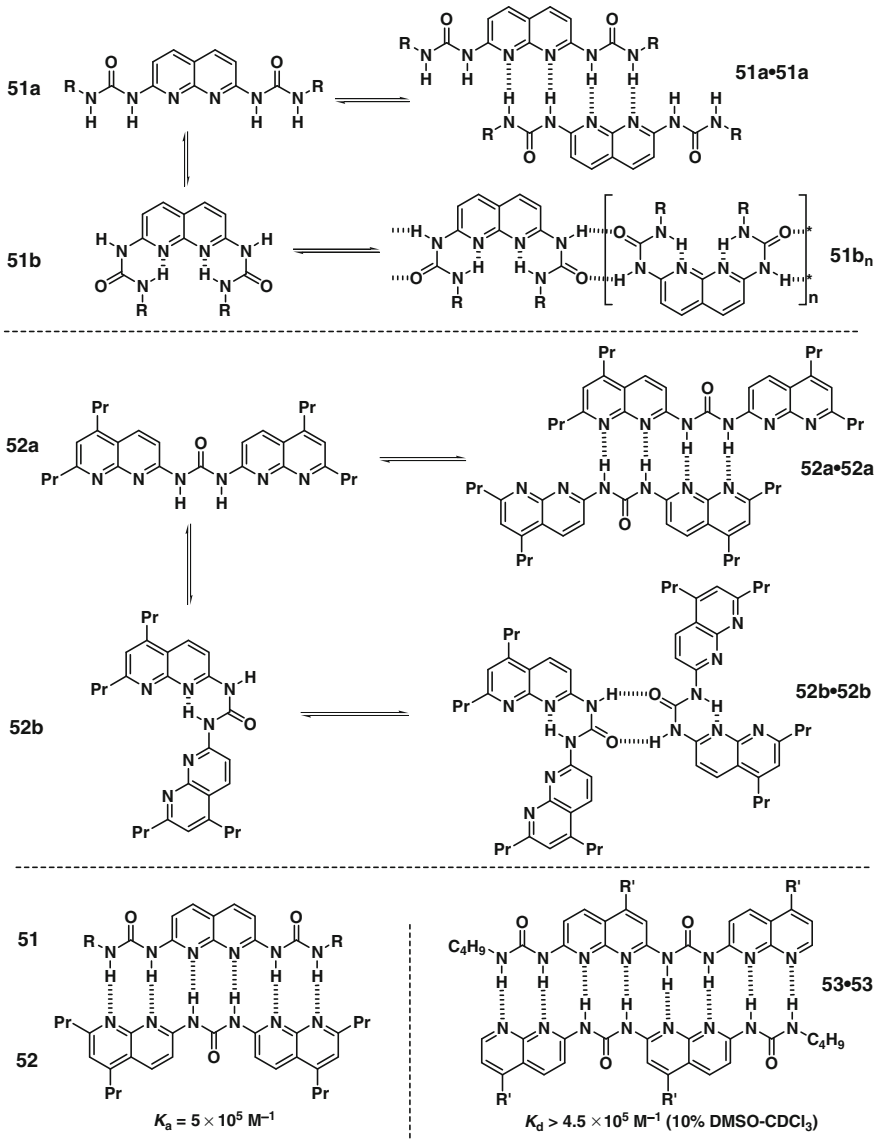

Fig. 4.22 Ureido-naphthyridine-based molecular duplexes, Reprinted with the permission from Ref. [47, 49]. Copyright 2000 and 2005 American Chemical Society

monomers **51** and **52** in solution. They have complementary hydrogen bonding sites. When they were 1:1 mixed in solution, the folded conformations were unfolded and an extended heteroduplex formed with an association constant of 5×10^5 M^{-1}. Eight hydrogen bonds-mediated homoduplex $\mathbf{53}_2$ could also be constructed with this building block [49]. The dimerization constant was larger than 4.5×10^5 M^{-1} even in a 10 % DMSO-d_6-$CDCl_3$ solution. But it dropped substantially (K_d = 40 M^{-1}) when a 20 % DMSO-d_6-$CDCl_3$ solution was applied.

An ureido-dipeptide based duplex was reported by Hirao et al. (Fig.4.23) [50]. X-ray single crystal analysis showed that two molecules formed a right-handed helical structure. The chirality center of the amino acid side chains induced this supramolecular chirality. The dimerization constant was determined to be 2.9×10^4 M^{-1} by ^{1}H NMR dilution experiments. Interestingly, variable ^{1}H NMR experiments revealed a unique shuttle movement as depicted in Fig. 4.23.

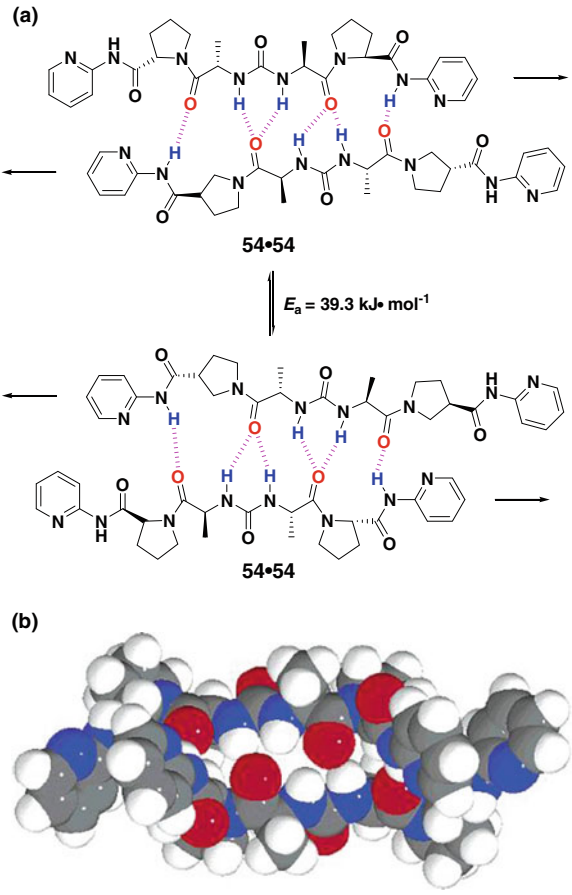

Fig. 4.23 Ureido-dipeptide-based duplex. Reprinted with the permission from Ref. [50]. Copyright 2002 American Chemical Society

4.6 Conclusions and Outlook

Great progress has been achieved in the field of hydrogen bonding-mediated aromatic molecular duplexes during the last two decades. Various building blocks have been designed and synthesized. From the above-discussed examples, some general guidelines can be summarized:

(1) One important principle is preorganizing hydrogen bonding sites that participate in hydrogen bonding interactions, while blocking unwanted hydrogen bonding sites to minimize interference.
(2) For systems with adjacent hydrogen bonding sites, secondary electrostatic effect has to be taken into account: place donors or acceptors on the same side.
(3) In order to improve the association constant, the monomers should be relatively rigid to reduce the entropy loss in the complexation process. But flexibility is necessary for conformation adjustability upon interaction.

We believe that with long-term endeavors by chemists, many new building blocks will be developed to foster this field. Maturity in fundamental research will eventually lead to wide applications of this area.

References

1. Saenger W (1984) The principles of nucleic acid structure. Springer, Berlin
2. Horton RH, Moran LA, Ochs RS, Rawn DJ, Scrimgeour GK (1992) Principles of biochemistry. Prentice Hall International Inc., Englewood Cliffs
3. Valeur E, Bradley M (2009) Chem Soc Rev 38:606
4. Yang Y, Dou DD (2014) Prog Chem 26:706
5. Sijbesma RP, Beijer FH, Brunsveld L, Folmer BJ, Hirschberg JH, Lange RF, Lowe JK, Meijer EW (1997) Science 278:1601
6. Corbin PS, Zimmerman SC (1998) J Am Chem Soc 120:9710
7. Gong B (2012) Acc Chem Res 45:2077
8. Gong B (2007) Polym Int 56:436
9. Sanford AR, Yamato K, Yang X, Yuan L, Han Y, Gong B (2004) Eur J Biochem 271:1416
10. Gong B (2001) Synlett 5:582
11. Yuan L, Zhang P, Feng W, Gong B (2011) Curr Org Chem 15:1250
12. Gong B, Yan YF, Zeng HQ, Skrzypczak-Jankunn E, Kim YW, Zhu J, Ickes H (1999) J Am Chem Soc 121:5607
13. Zeng HQ, Miller RS, Flowers RA, Gong B (2000) J Am Chem Soc 122:2635
14. Zeng H, Yang X, Brown AL, Martinovic S, Smith RD, Gong B (2003) Chem Commun 13:1556
15. Zeng H, Ickes H, Flowers RA II, Gong B (2001) J Org Chem 66:3574
16. Zhang P, Chu H, Li X, Feng W, Deng P, Yuan L, Gong B (2011) Org Lett 13:54
17. Li X, Fang Y, Deng P, Hu J, Li T, Feng W, Yuan L (2011) Org Lett 13:4628
18. Bisson AP, Carver FJ, Hunter CA, Waltho JP (1994) J Am Chem Soc 116:10292
19. Bisson AP, Hunter CA (1996) Chem Commun 15:1723
20. Bisson AP, Carver FJ, Eggleston DS, Haltiwanger RC, Hunter CA, Livingstone DL, McCabe JF, Rotger C, Rowan AE (2000) J Am Chem Soc 122:8856

21. Hunter CA, Jones PS, Tiger PMN, Tomas S (2003) Chem Commun 14:1642
22. Yang X, Gong B (2005) Angew Chem Int Ed 44:1352
23. Roland JT, Guan Z (2004) J Am Chem Soc 126:14328
24. Li M, Yamato K, Ferguson JS, Gong B (2006) J Am Chem Soc 128:12628
25. Li M, Yamato K, Ferguson JS, Singarapu KK, Szyperski T, Gong B (2008) J Am Chem Soc 130:491
26. Zeng HQ, Yang XW, Flowers RA, Gong B (2002) J Am Chem Soc 124:2903
27. Yang Y, Chu WJ, Liu JW, Chen CF (2011) Curr Org Chem 15:1302
28. Yang Y, Zhang YZ, Tang YL, Chen CF (2006) New J Chem 30:140
29. Zhao X, Wang XZ, Jiang XK, Chen YQ, Li ZT, Chen GJ (2003) J Am Chem Soc 125:15128
30. Yang Y, Yang ZY, Yi YP, Xiang JF, Chen CF, Wan LJ, Shuai ZG (2007) J Org Chem 72:4936
31. Sijbesma RP, Meijer EW (2003) Chem Commun 5
32. Yang Y, Xiang JF, Chen CF (2007) Org Lett 9:4355
33. Yang Y, Chen T, Xiang JF, Yan HJ, Chen CF, Wan LJ (2008) Chem Eur J 14:5742
34. Yang Y, Xiang JF, Xue M, Hu HY, Chen CF (2008) Org Biomol Chem 6:4198
35. Yang Y, Xiang JF, Xue M, Hu HY, Chen CF (2008) J Org Chem 73:6369
36. Chu WJ, Yang Y, Chen CF (2010) Org Lett 12:3156
37. Chu WJ, Chen J, Chen CF, Yang Y, Shuai Z (2012) J Org Chem 77:7815
38. Cheng PN, Pham JD, Nowick JS (2013) J Am Chem Soc 135:5477
39. Nowick JS (1999) Acc Chem Res 32:287
40. Archer EA, Sochia AE, Krische MJ (2001) Chem Eur J 7:2059
41. Archer EA, Goldberg NT, Lynch V, Krische MJ (2000) J Am Chem Soc 122:5006
42. Archer EA, Krische MJ (2002) J Am Chem Soc 124:5074
43. Archer EA, Cauble DF, Lynch V, Krische MJ (2002) Tetrahedron 58:721
44. Gong HG, Krische MJ (2005) J Am Chem Soc 127:1719
45. Zhu J, Lin JB, Xu YX, Shao XB, Jiang XK, Li ZT (2006) J Am Chem Soc 128:12307
46. Zhu J, Lin JB, Xu YX, Jiang XK, Li ZT (2006) Tetrahedron 62:11933
47. Corbin PS, Zimmerman SC (2000) J Am Chem Soc 122:3779
48. Corbin PS, Zimmerman SC, Thiessen PA, Hawryluk NA, Murray TJ (2001) J Am Chem Soc 123:10475
49. Mayer MF, Nakashima S, Zimmerman SC (2005) Org Lett 7:3005
50. Moriuchi T, Tamura T, Hirao T (2002) J Am Chem Soc 124:9356

Chapter 5
Hydrogen Bonding-Driven Anion Recognition

Liping Cao, Jie Zhao, Dong Yang, Xiao-Juan Yang and Biao Wu

Abstract Anion binding is a timely research field that is developing rapidly because anions play important roles in many areas. Hydrogen (H)-bonding has proven to be a highly effective tool in binding anions due to its directionality and strength. This chapter focuses on the H-bonding-driven anion recognition by neutral receptors that bear H-bond donors, such as (thio)amide, (thio)urea, pyrroles, acidic *CH*s, and hydroxyl groups. The design and synthesis of receptors based on these binding units have been explored by a number of research groups to achieve a better binding for different kinds of anions in terms of binding constant and selectivity. Recent progress in these aspects is summarized in this chapter. In particular, we emphasize the properties of XH•••anion (X = N, C, O) H-bonds in the crystal structure of anion complexes, such as the binding mode, the number of H-bonds, and the H-bond lengths and angles. Some solution studies of anion binding including the association constants are also presented. The aim is to provide an overview of this field, including the utilization of H-bonding in anion binding/coordination, the design strategies of the receptors, and their potential applications.

5.1 Introduction

The binding and recognition of anions is of great importance because anions are closely relevant to many events in the areas of biology, medicine, environment, etc. In 1968, Park and Simmons discovered that the katapinands can encapsulate a chloride ion, resulting in the first examples of anion complexes held by H-bonding [1]. Since then, in particular in the past two decades, the supramolecular chemistry of anions has developed rapidly and great progress has been achieved. It has also

L. Cao · J. Zhao · D. Yang · X.-J. Yang · B. Wu (✉)
Key Laboratory of Synthetic and Natural Functional Molecule Chemistry of the Ministry of Education, College of Chemistry and Materials Science, Northwest University, Xi'an 710069, China
e-mail: wubiao@nwu.edu.cn

Z. Li and L. Wu (eds.), *Hydrogen Bonded Supramolecular Structures*, Lecture Notes in Chemistry 87, DOI 10.1007/978-3-662-45756-6_5

been found that some anions show properties (e.g., the coordination number and geometry) that resemble the transition metal coordination chemistry, which provides very useful information for the understanding of anion binding behavior [2].

The design and synthesis of anion receptors (or ligands) is the key to anion chemistry. The interactions between anions and receptors can be a wide range of noncovalent interactions, such as van der Waals force, electrostatic (Coulomb) interaction, H-bonding, anion–π and π–π interactions, and halogen bonding. Among these interactions, H-bonding is perhaps the most important and widely applied. H-bonding is highly directional, and the strength of the H-bonding between donor groups and anions is in the range of moderate (4–15 kcal mol^{-1}) to strong (15–40 kcal mol^{-1}) [3]. Moreover, receptors with H-bonding donors are readily accessible with relative synthetic ease. Indeed, many types of H-bonding donors with appropriate acidity have been utilized in anion receptors, e.g., (thio)amide (pK_a = 12–21), amine (pK_a = 17–44), indole/pyrrole (pK_a = 20–23), (thio)urea (pK_a = 19–27), hydroxyl (pK_a = 10–31), and some activated CH donors. In this chapter, the recent progress in anion binding/coordination will be summarized, categorized by the type of H-bond donor groups. Macrocyclic and multicyclic polyammonium receptors are not included because the anion binding arises largely from electrostatic interaction. H-bonding will be emphasized, which is mainly quoted from the X-ray diffraction data and sometimes also from solution binding studies by, for example, NMR spectroscopy.

5.2 Amide-Based Anion Recognition

Amides, bearing both H-bond acceptors (C=O) and donors (NH), play an important role in Nature (e.g., α helices and β sheets of peptides and proteins, ion channels), and in technology as structural materials (e.g., Nylons) [4]. For example, the X-ray crystal structure of the sulfate-binding protein of Salmonella typhimurium shows that the sulfate is bound by seven H-bonds, five of which involve amide NH groups of polypeptides [5]. The pK_a of the amide NH is about 12–21 and becomes lower when modified with electron-deficient groups. Consequently, amide as an excellent H-bond donor to bind anionic species has attracted much attention of supramolecular, biological, and environmental chemists, especially for anion recognition, transport, and pollution remediation [6–11].

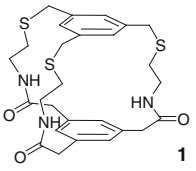

1

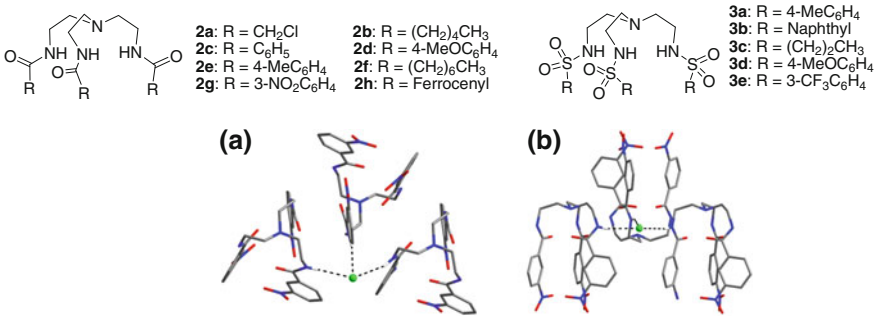

Fig. 5.1 Crystal structure of **2g**·Br^-: **a** *top* and **b** *side views*

In early 1980s, chemists started to develop amide-based receptors for selective recognition of anions. In 1986, Pascal and co-workers reported a pioneering work about the synthesis and X-ray crystal structure of an amide-based cryptand **1** [12]. Although it was not certain that fluoride was contained within its cavity, ^1H and ^{19}F NMR studies suggested that **1** could bind to fluoride through H-bonding.

Seven years later, Reinhoudt and co-workers reported tridentate amide-based anion receptors **2a–d** and **3a–b**, in which three amide or sulfonamide groups as "arm" are linked by a tris(2-aminoethyl)amine (TREN) "core" [13]. These receptors showed selective binding toward anions ($H_2PO_4^-$ > Cl^- > HSO_4^-) exclusively through H-bonding. Due to the potential C_3-symmetry that can be imposed on the binding site, tridentate amide-based anion receptors have been created by other groups. Smith and co-workers developed **2e** and **3c–e** as a potential translocases on the basis of their recognition to phosphatidylcholine through amide H-bonding [14–16]. Bowman-James and co-workers found **2f** could form a lipid-bilayer-like complex with nitrate in the solid state [17, 18]. Ghosh and co-workers examined **2g** with different anions and found that intramolecular NH•••O H-bonds could prevent the encapsulation of the anion in the cavity. In the crystal structure, one bromide ion linked three neighboring amide "arms" by three NH•••Br H-bonds at distances of 3.169, 3.285, and 3.473 Å, respectively (Fig. 5.1) [19]. Beer and co-workers developed a potential redox receptor **2h** that could selectively complex and electrochemically responded to the dihydrogen phosphate anion [20].

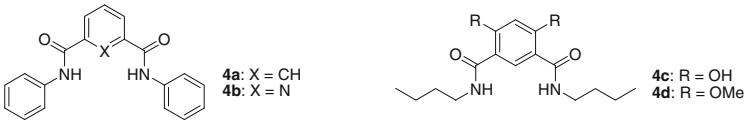

As a seminal contribution to anion recognition, in 1997, Crabtree and co-workers reported the synthesis and anion-binding properties of isophthalamide-linked bidentate amide-based receptors **4a,b** [21]. Crystal structure of **4a**·Br^- showed 1:1 complexation with Br^- (Fig. 5.2). In the structure, the bromide was held with two H-bonds by the amide NH groups at N···Br distances of 3.436 and 3.634 Å, and N–H···Br angles of 116º and 172º. The isophthalamide spacer could be replaced with a 2,6-diamidopyridine unit to give **4b**, which was selective for fluoride anion in CD_2Cl_2 ($K_a = 2.4 \times 10^4\ M^{-1}$) [22].

Davis and co-workers designed isophthalamide receptors with appended hydroxyl (**4c**) or methoxyl (**4d**) groups [23]. In the solid state, the hydroxyl groups of **4c** formed intramolecular OH···O=C H-bonds with the amide carbonyls to stabilize the *syn–syn* conformation, which complexed Cl^- ($K_a = 5{,}230\ M^{-1}$) in its cleft. On the other hand, **4d** did not bind halide anions, because the methoxy groups promoted the formation of the *anti–anti* conformation.

Gale and co-workers first reported 2,5-diamidopyrroles **5a–d** as anion receptors [24–27]. Subsequently, Jurczak and co-workers synthesized di(thio)amides **5e–h** with a pyrrole ring as spacer, and compared their anion recognition properties [28]. In the crystal structure, **5f** binds a chloride ion with the two amide NH groups at N···Cl distances of 3.333 and 3.391 Å and with the pyrrole NH group at a quite short N···Cl distance of 3.076 Å (Fig. 5.3a). Thioamides are known to be stronger acids than amides and are thus expected to exhibit stronger anion binding affinity. However, both UV-vis titration and isothermal titration calorimetry (ITC) studies revealed **5f** and **5h** had approximately the same affinity for benzoate, chloride, and

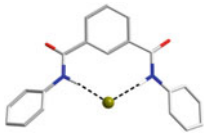

Fig. 5.2 Crystal structure of **4a**·Br^-

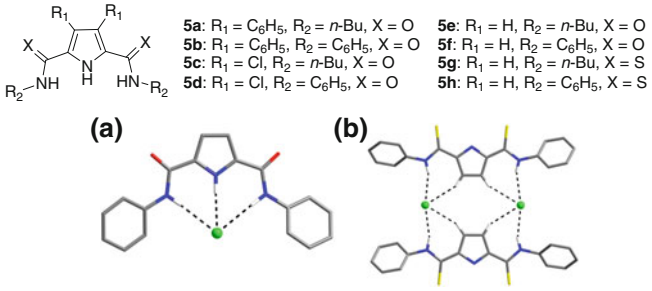

Fig. 5.3 Crystal structure of **a 5f**·Cl^- and **b 5h**·Cl^-. Reprinted with permission from Ref. [28]. Copyright 2005, Elsevier Ltd

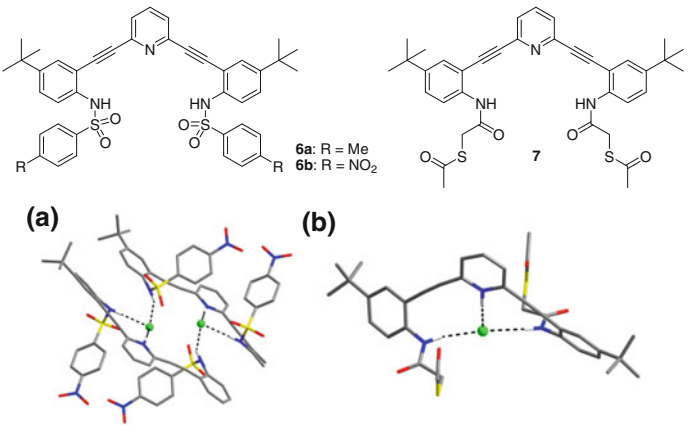

Fig. 5.4 Crystal structure of **a** $([\mathbf{H6b}]^{+}\cdot Cl^{-})_2$ and **b** $[\mathbf{H7}]^{+}\cdot Cl^{-}$. **a** Reprinted with permission from Ref. [29]. Copyright 2008, John Wiley & Sons, Ltd. **b** Reprinted with permission from Ref. [30]. Copyright 2009, American Chemical Society

dihydrogen phosphate. In the complex $\mathbf{5h}\cdot Cl^{-}$, two chloride anions and two molecules of **5b** formed a centrosymmetrical dimer in which each anion was anchored by four H-bonds involving amide N···Cl (3.256 and 3.301 Å) and weak pyrrole C···Cl (3.551 and 3.643 Å) interactions (Fig. 5.3b).

Johnson and coworkers designed more rigid diamide receptors **6–7**, which bear 2,5-diacetyleneyl pyridine as a core framework [29, 30]. Protonated ligands **6a** and **6b** could utilize two amide NHs and one pyridinium NH to bind a chloride or bromide anion, resulting in a 2+2 H-bonding dimer (Fig. 5.4a). Similarly, protonated ligand **7** could form 1:1 complex with chloride anion through three H-bonds involving one pyridinium N···Cl (3.00 Å) and two amide N···Cl (3.248 and 3.271 Å) (Fig. 5.4b).

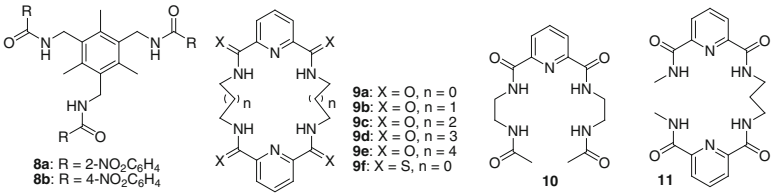

Another kind of tridentate anion receptors **8a–b** possessing trimethyl-substituted benzene ring with 1,3,5-triamide functional groups were reported by Ghosh and co-worker [31, 32]. Upon complexation with fluoride in dioxane, two **8a** molecules formed a dimeric capsule with hydrated fluoride anion $[F_2(H_2O)_6]^{2-}$ in the cavity (Fig. 5.5a). X-ray analysis of $[\mathbf{8a}]_2\cdot[F_2(H_2O)_6]^{2-}$ revealed all amide NH units of **8a** were involved in H-bonds with the oxygen atom of water or fluoride anion in the

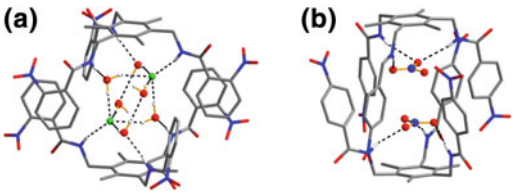

Fig. 5.5 Crystal structure of **a** $[\mathbf{8a}]_2 \cdot [F_2(H_2O)_6]^{2-}$ and **b** $[\mathbf{8b}]_2 \cdot (NO_3)_2^{2-}$. **a** Reprinted with permission from Ref. [31]. Copyright 2009, Royal Society of Chemistry. **b** Reprinted with permission from Ref. [32]. Copyright 2010, American Chemical Society

anionic cluster, with distances at N•••O (water) 5.807–5.885 Å and N•••F 5.763 Å. On the other hand, two receptor molecules of **8b** could form an intertwined capsule that included two nitrate guests by six H-bonds with N•••O distances ranging from 3.107 to 3.297 Å (Fig. 5.5b).

Jurczak and co-workers reported cyclic and acyclic amide-based receptors **9a–e**, **10** and **11** [33, 34]. The crystal structures of $\mathbf{9a} \cdot F^-$ and $\mathbf{9a} \cdot Cl^-$ indicated that the anion was coordinated by four H-bonds with N•••F distance ranging from 2.742 to 2.881 Å and N•••Cl from 3.211 to 3.520 Å, respectively (Figs. 5.6a and 5.7a). However, the fluoride ion was almost in the plane of the macrocycle (Fig. 5.6b), while the larger chloride hovered above the plane of the macrocycle (Fig. 5.7b). Solution-phase binding studies also proved that the smaller fluoride ion fit better to the macrocycle (K_a = 830 M^{-1}) than chloride (K_a = 65 M^{-1}). Base on these results, Kanbara et al. transformed amide **9a** to thioamide **9f** which was found to exhibit strong affinity toward anions [35]. Although acyclic receptors **10** and **11** have

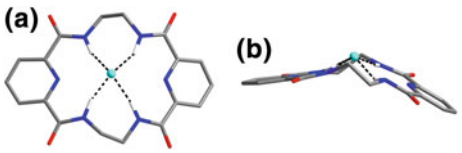

Fig. 5.6 Crystal structure of $\mathbf{9a} \cdot F^-$: **a** *top view*; **b** *side view*. Reprinted with permission from Ref. [33]. Copyright 2001, John Wiley & Sons, Ltd

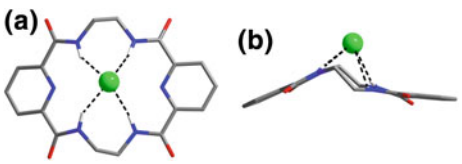

Fig. 5.7 Crystal structure of $\mathbf{9a} \cdot Cl^-$: **a** *top view* and **b** *side view*. Reprinted with permission from Ref. [33]. Copyright 2001, John Wiley & Sons, Ltd

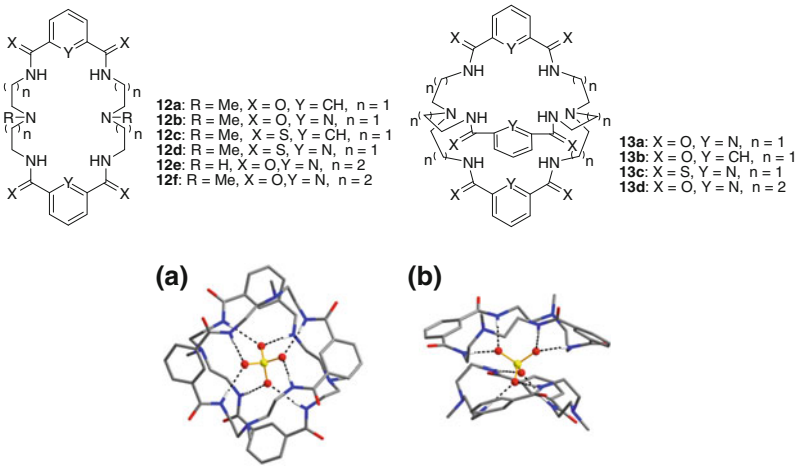

Fig. 5.8 Crystal structure of **12a**·SO_4^{2-}: **a** *top view* and **b** *side view*. Reprinted with permission from Ref. [36]. Copyright 2001, American Chemical Society

H-bonding sites similar to cyclic receptor **9a**, they interacted with anions much more weakly than the cyclic analogue due to the lack of the macrocyclic effect.

Similar macrocyclic receptors with a slightly expanded ring system containing mixed amide/amine linkers, **12a–f**, were reported by the Bowman-James group [36–39]. Interestingly, two molecules of **12a** complexed one sulfate ion (log $K = 4.50$) by eight H-bonds to form a sandwich-like structure. Each oxygen atom of sulfate was coordinated via two H-bonds to two amide NH groups with N···O distances ranging from 2.854 to 2.980 Å (Fig. 5.8) [36].

Compound **12b** prefers to fold in its complex with $Cr_2O_7^{2-}$. The two pyridine planes are almost parallel and separated by about 3.5 Å, making the four amide NH groups much closer. As shown in Fig. 5.9, the distance between the two oxygen atoms of $Cr_2O_7^{2-}$ (3.76 Å) fits well with the amide nitrogen atoms joined to opposing pyridine rings (3.66 and 3.76 Å), forming totally four H-bonds at N···O distances (2.833–2.989 Å) [37]. The corresponding thioamide macrocycles, **12c–d**,

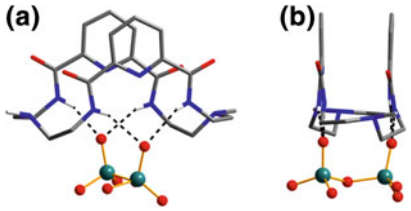

Fig. 5.9 Crystal structure of **12b**·$Cr_2O_7^{2-}$: **a** *top view* and **b** *side view*. Reprinted with permission from Ref. [37]. Copyright 2007, American Chemical Society

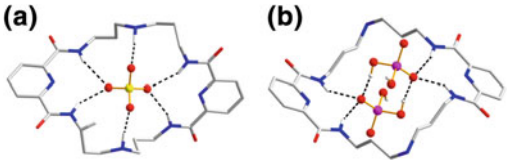

Fig. 5.10 Crystal structure of **a** $[\mathbf{12e}H_2]^{2+}\cdot SO_4^{2-}$ and **b** $\mathbf{12e}\cdot(H_2PO_4^-)_2$. Reprinted with permission from Ref. [39]. Copyright 2009, American Chemical Society

were also investigated which exhibited strong affinity for $H_2PO_4^-$ (log $K = 4.97$ and 4.63) and HSO_4^- (log $K = 3.15$ and 4.99), respectively [38].

Bowman-James and co-workers synthesized larger 28-memebered macrocyclic receptors **12e–f** [39]. Interestingly, receptor **12e** showed selective binding for SO_4^{2-} (6.4×10^4 M^{-1}) and $H_2PO_4^-$ (4.4×10^3 M^{-1}) over $CH_3CO_2^-$ (100 M^{-1}) or halides (Cl^-: 140 M^{-1}; Br^-: 15 M^{-1}) in DMSO-d_6. In the single crystal structure, sulfate was held inside the cavity of **12e** by four amide N•••O (3.050 and 3.315 Å) and two protonated amine N•••O (2.750 Å) H-bonds (Fig. 5.10a). Figure 5.10b shows that **12e** complexed two $H_2PO_4^-$ via four amide N•••O H-bonds (2.922 and 3.014 Å) and the two $H_2PO_4^-$ anions were H-bonded to each other (O•••O = 2.09 Å).

Bowman-James and co-workers also synthesized amide-based cryptands **13a–c** for anion binding [38, 40–43]. These cryptands displayed higher affinity for fluoride ($K_a = 10^4$–10^5 M^{-1}) than other anions. The crystal structures of the fluoride complexes show that the fluoride is centered in the cryptand cavity with six hydrogen bonds to all amide NH donors of receptors. The N•••F distances range from 2.821 to 2.887 Å in the fluoride complex $\mathbf{13a}\cdot F^-$, and from 2.946 to 3.113 Å in $\mathbf{13b}\cdot F^-$, respectively (Fig. 5.11a, b). They also increased the size of the amide cryptand to prepare a slightly larger analogue, **13d,** with propylene linkers between "core" N atom and amide N atoms [44]. However, this larger receptor was also selective for fluoride as observed for **13a**. In the solid state of $\mathbf{13d}\cdot 2Cl^-$, two chlorides each formed two H-bonds with amide NH groups (N•••O ranging from 3.227 to 3.560 Å), and were bridged by a water molecule. Interestingly, two water molecules as bridges also linked four amide NH groups and a sulfate ion, while the

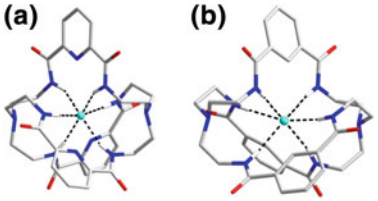

Fig. 5.11 Crystal structure of **a** $\mathbf{13a}\cdot F^-$ and **b** $\mathbf{13b}\cdot F^-$. **a** Reprinted with permission from Ref. [38]. Copyright 2003, American Chemical Society. **b** Reprinted with permission from Ref. [40]. Copyright 2004, Royal Society of Chemistry

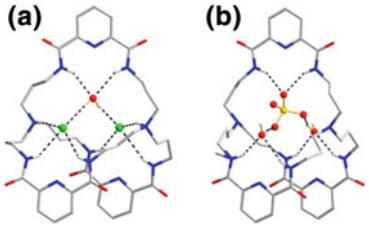

Fig. 5.12 Crystal structure of **a 13d**·$2Cl^-$ and **b 13d**·SO_4^{2-}. Reprinted with permission from Ref. [44]. Copyright 2005, American Chemical Society

remaining two amide NH groups of the receptor directly bind to the oxygen atom of sulfate (N•••O 2.915 and 2.977 Å) to form a stable complex (Fig. 5.12a, b).

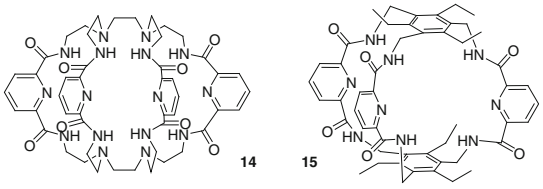

The Bowman-James group also synthesized tricyclic receptor **14** by linking two amide-based marocycles through their two secondary amine bridgeheads with an ethylene spacer [45, 46]. This multicycle bearing two tetraamido macrocycles displayed amazingly selective binding and high affinity for ditopic FHF^- anion (K_a = 5,500 in DMSO-d_6; 10^4–10^5 in $CDCl_3$). More interestingly, the crystal structure of its fluoride complex showed an encapsulated linear bifluoride anion by four N•••F H-bonds (2.724–2.754 Å) (Fig. 5.13). This is the first example of an encapsulated bifluoride in a cavity of an artificial host.

Besides the popular bridgehead TREN for cryptands, substituted benzene rings provide an alternative for bicyclic and tricyclic receptors with a 3D cavity for anion recognition. Anslyn and co-workers prepared amide-linked C_3-symmetric cryptand **15** with a cavity of 78.3 $Å^3$ [47]. X-ray crystal structure of its chloride complex showed a 1:2 stoichiometry, and each chloride formed two N•••Cl H-bonds with

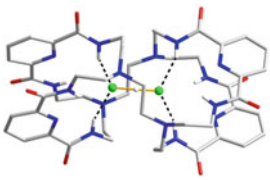

Fig. 5.13 Crystal structure of **14**·$(FHF)^-$. Reprinted with permission from Ref. [45]. Copyright 2006, John Wiley & Sons, Ltd

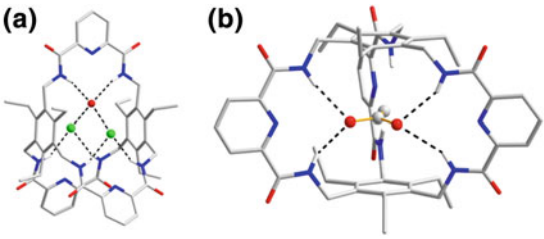

Fig. 5.14 Crystal structure of **a** **15**·2Cl and **b** **15**·$MeCO_2^-$

amide NH at distances of 3.202 Å (Fig. 5.14a). A water molecule as a bridge utilized two N···O (3.064 Å) and two O···Cl (3.240 Å) H-bonds to form a cooperative and stable network. This receptor has a selective affinity for planar anions like acetate and nitrate (10^4–10^5 M^{-1} in CD_2Cl_2) which involved H-bonding and anion–π interaction. Crystal structure of the acetate complex revealed that the planar acetate was neatly nestled between the two phenyl rings with a nearly parallel arrangement. The two oxygen atoms of acetate were bonded directly to the host, each to two of the amide NH groups, with N···O distances of 2.999, 3.196, 3.238, and 3.443 Å, respectively (Fig. 5.14b).

Due to the success on the TREN cryptands, Bowman-James, and co-workers synthesized bicyclic and tricyclic cyclophane capsules **16** and **17** which contain three or four flexible diethylamine chains and two phenyl groups as caps [48]. Although the cavity of **16** and **17** was too small to encapsulate anions, **16** displayed tight binding for F^- (K_a = 21,000 M^{-1}), while **17** showed slightly less affinity for $H_2PO_4^-$ (K_a = 21,000 M^{-1}). The single X-ray crystal structure of **16**·$[FHF]^-$ showed that there was only a single pocket for $[FHF]^-$, which was formed by two of the diethylamine chains lying in the same direction, with the third one dangling in the opposite direction. This cleft holds a $[FHF]^-$ anion by four amide N···F H-bonds with the distances of 2.831 and 3.201 Å (Fig. 5.15a). In complex **17**·$H_2PO_4^-$, each of the two clefts binds to two $H_2PO_4^-$ anions with three amide N···O (2.883, 2.951, and 3.372 Å) and two protonated N···O (2.667 and 2.917 Å) H-bonds, while the two $H_2PO_4^-$ ions were also linked by an OH···OP bond (2.597 Å) (Fig. 5.15b).

Kubik and co-workers designed amide-based cyclopeptides **18–19** from two amino acid building blocks, Boc-*L*-proline and 6-aminopicolinic acid benzyl ester [49, 50]. Cyclopeptide **18** formed sandwich-type 2:1 anion complexes with halide and sulfate anion with K_a ranging from 10^4 to 10^5 M^{-2} in 80 % D_2O/CD_3OD. Crystal structure of $\mathbf{18}_2$·I^- showed that one iodide ion was located in a cavity between two cyclopeptide molecules, which interlocked perfectly the anion with six N···I H-bonds ranging from 3.723 to 3.935 Å (Fig. 5.16). As predicted, dicyclopeptide **19** which has more amide NH sites also displayed excellent binding constants (up to 10^5 M^{-1}) to anion with 1:1 stoichiometry.

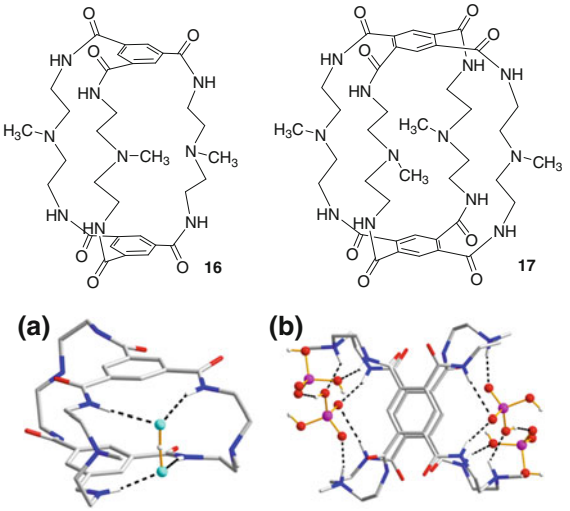

Fig. 5.15 Crystal structure of **a 16**·$[FHF]^-$ and **b 17**·$H_2PO_4^-$. Reprinted with permission from Ref. [48]. Copyright 2008, American Chemical Society

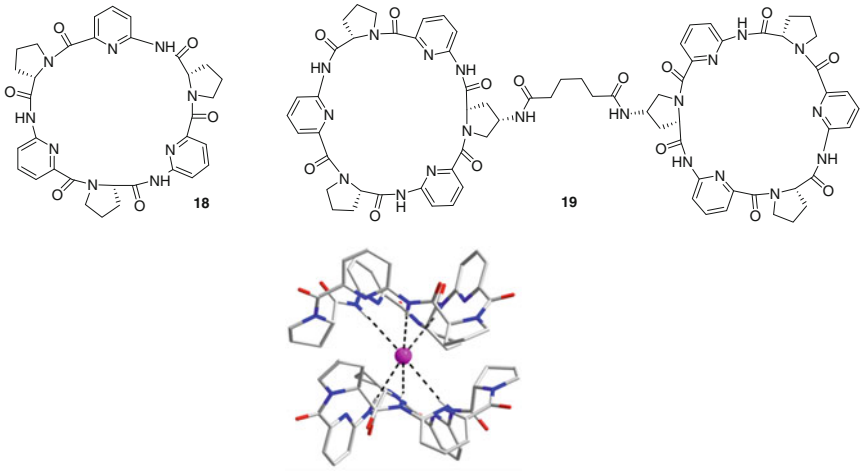

Fig. 5.16 Crystal structure of $\mathbf{18}_2$·I^-. Reprinted with permission from Ref. [49]. Copyright 2001, John Wiley & Sons, Ltd

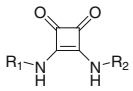

20a: $R_1 = R_2 = C_6H_5$
20b: $R_1 = R_2 = 2\text{-Py}$
20c: $R_1 = R_2 = 2\text{-}(NO_2)C_6H_4$
20d: $R_1 = R_2 = 3\text{-}(MeO)C_6H_4$
20e: $R_1 = R_2 = 3,5\text{-}(CF_3)_2C_6H_3$
20f: $R_1 = R_2 = 4\text{-}t\text{-}BuC_6H_4$
20g: $R_1 = R_2 = 4\text{-}BrC_6H_4$
20h: $R_1 = R_2 = 4\text{-}(MeO)C_6H_4$
20i: $R_1 = R_2 = 4\text{-}(NO_2)C_6H_4$
20j: $R_1 = R_2 = 4\text{-}(CF_3)C_6H_4$

21a: $R_1 = 4\text{-}BrC_6H_4$, $R_2 = C_6H_5$
21b: $R_1 = 4\text{-}BrC_6H_4$, $R_2 = 2\text{-}(MeO)C_6H_4$
21c: $R_1 = 4\text{-}BrC_6H_4$, $R_2 = 3\text{-}(MeO)C_6H_4$
21d: $R_1 = 4\text{-}BrC_6H_4$, $R_2 = 4\text{-}(MeO)C_6H_4$
21e: $R_1 = 4\text{-}(NO_2)C_6H_4$, $R_2 = 3,5\text{-}(CF_3)_2C_6H_3$
21f: $R_1 = 4\text{-}(NO_2)C_6H_4$, $R_2 = 4\text{-}t\text{-}BuC_6H_4$
21g: $R_1 = 4\text{-}(NO_2)C_6H_4$, $R_2 = 4\text{-}(MeO)C_6H_4$

Squaramides are remarkable four-membered ring systems derived from squaric acid. Although their name includes a word “amide”, squaramides could contribute two proximate and polarized NH fragments, like urea analogues [51, 52]. As a result, the ability of squaramides to act as H-bonding donors to anions was exploited by many groups. Compounds **20** and **21** are typical squaramide-based anion receptors [53–60]. Taylor and co-workers developed an efficient method for the preparation of **20a–h** and **21a–g** by Lewis acid-catalyzed condensation of various anilines and squarate esters [55]. They found **21e–g** could be used as colorimetric sensors for fluoride, acetate, and hydroxide anions in the process of deprotonation of squaramide NH groups. Fabbrizzi and co-workers reported the anion-binding properties of squaramide analogue **20i**, which showed a better affinity than urea [56]. The 1:1 complex of **20i**·Cl^- and **20i**·Br^- in the solid state were revealed by X-ray studies. In both crystal structures, one molecule of **20i** formed bifurcated H-bonding interaction with chloride or bromide anion through two squaramide NH fragments (N···Cl: 3.010 and 3.129 Å; N···Br: 3.267 and 3.308 Å) (Fig. 5.17). Based on the anion recognition of squaramides, Gale and co-workers showed that fluorinated substituents could greatly improve the transport ability of an anion receptor, and found that **20e** and **20j** were able to transport chloride out of liposomes much faster than other analogous thiourea and urea receptors [53]. This ability of **20j** to bind chloride was also confirmed by X-ray analysis. The chloride complex showed a 1:1 stoichiometry, and two convergent NH···Cl H-bonds bind to one chloride anion, illustrating the H-bonding array of squaramides is more suitable for recognizing spherical anions than other functional groups.

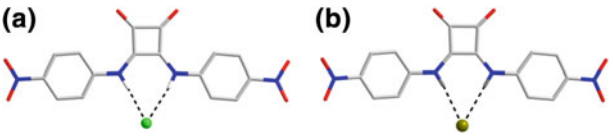

Fig. 5.17 Crystal structure of **a** **20i**·Cl^- and **b** **20i**·Br^-. Reprinted with permission from Ref. [53]. Copyright 2012, John Wiley & Sons, Ltd

5.3 Urea-Based Anion Recognition

Urea, with its two polarized NH donors, is a good anion-binding unit capable of chelating a spherical anion or donating two parallel H-bonds to two oxygen atoms of a carboxylate or an inorganic oxoanion. In 1992, Wilcox and co-workers reported that urea receptor **22** displayed good binding affinity to benzoate anion with $K_a = 2.7 \times 10^4\ M^{-1}$. Receptor **22** can also interact with sulfate, phosphonate, and carboxylate ions in weakly polar solvents such as CH_2Cl_2, forming stable 1:1 complexes by two parallel NH•••O hydrogen bonds [61].

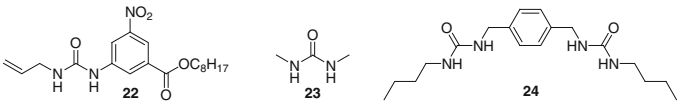

Hamilton and co-workers reported that N,N'-dimethylurea **23** could form 1:1 H-bonded complex with CH_3COO^- in DMSO-d_6 (K_a = 45 M^{-1}), while ditopic receptor **24**, in which two urea subunits are linked through a 1,4-xylyl spacer, formed a 1:1 complex with glutarate ion in DMSO-d_6 ($K_a = 6.4 \times 10^2\ M^{-1}$) [62].

Fabbrizzi and co-workers reported 1,3-bis(4-nitrophenyl)urea **25**, which interacted through H-bonding with a variety of oxoanions in MeCN to give bright yellow 1:1 complexes [63]. The stability decreased with the decreasing basicity of the anion ($CH_3COO^- > C_6H_5COO^- > H_2PO_4^- > NO_2^- > HSO_4^- > NO_3^-$). In complex **25**•$CH_3CO_2^-$ (Fig. 5.18a), the acetate ion received two NH•••O H-bonds from the two NH fragments of the urea group. The N•••O distances (2.693 and 2.770 Å) set the interaction among strong H-bonds, while the N•••O distances (2.811 and 2.790 Å) in bicarbonate complex **25**•HCO_3^- were slightly longer (Fig. 5.18b) [63].

Gale and co-workers reported the synthesis of monourea **26a** and thiourea **26b** with attached indole groups [64]. The carbonate complex of **26a** was isolated as Et_4N^+ salt with the anion surrounded by two ligands (Fig. 5.19a). The N•••O H-bond distances ranged from 2.739 to 2.938 Å. The bicarbonate analogue with thiourea **26b**

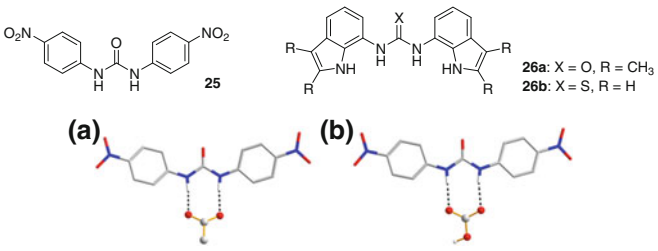

Fig. 5.18 Crystal structures of **a** **25**•$CH_3CO_2^-$ and **b** **25**•HCO_3^-

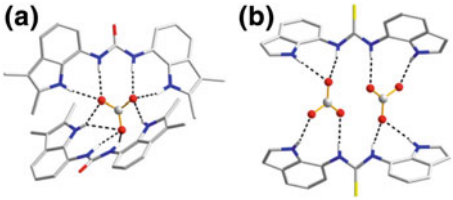

Fig. 5.19 Crystal structures of **a** $(\mathbf{26a})_2{\cdot}CO_3^{2-}$ and **b** $(\mathbf{26b})_2{\cdot}(HCO_3^{-})_2$

was isolated as Et_4N^+ salt in a 2:2 ratio (Fig. 5.19b) with shorter N•••O distances ranging from 2.798 to 2.887 Å [64].

Gunnlaugsson and co-workers reported receptors **27a–c**, which differed only in the position of their amide functionality relative to the urea moiety. This modification was shown to have a significant effect on the anion recognition ability and the binding stoichiometry [65].

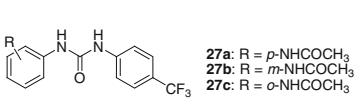

27a: R = *p*-NHCOCH$_3$
27b: R = *m*-NHCOCH$_3$
27c: R = *o*-NHCOCH$_3$

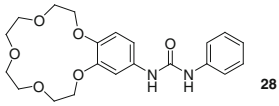

28

Barboiu and co-workers reported heteroditopic ureido crown ether receptor **28**. The coordination modes differed, depending on the anion, as illustrated by two complexes, one with NaCl and the other with $NaNO_3$. In the $NaNO_3$ complex, the crown ether portion, containing the sodium ion, lies adjacent to a neighboring urea podand chain that binds the nitrate by two long H-bonds (N•••O = 3.063 and 3.073 Å) (Fig. 5.20a). In the NaCl complex, the appended urea chains use four donor hydrogen atoms to hold the chloride ion, with N•••Cl distances ranging from 3.333 to 3.517 Å (Fig. 5.20b) [66].

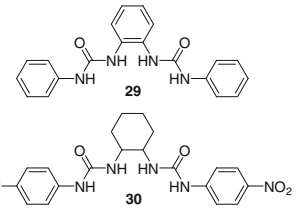

29

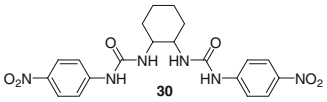

30

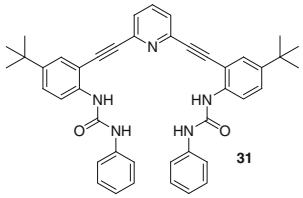

31

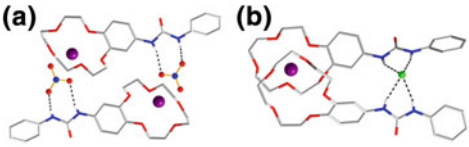

Fig. 5.20 Crystal structures of the complexes of **28** with **a** $NaNO_3$ and **b** NaCl

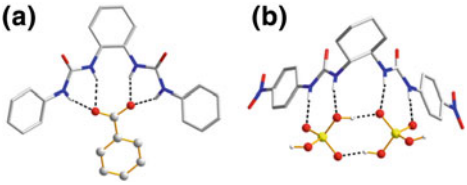

Fig. 5.21 Crystal structures of **a** **29**·$C_6H_5CO_2^-$ and **b** **30**·$(H_2PO_4^-)_2$

Efforts have also been made to enhance the anion affinity of urea-based receptors by incorporating more urea groups linked by different spacers. Gale and co-workers synthesized host **29**, with an ortho-phenylene spacer between two urea groups, which gave stable 1:1 complexes with carboxylates in a DMSO-d_6 solution containing 0.5 % water. The four H-bonds in the complex ranged from 2.740 to 2.939 Å (Fig. 5.21a) [67]. Analogous receptor **30** bears a cyclohexylene spacer between the two ureas. In its complex with two $H_2PO_4^-$ anions (Fig. 5.21b), each anion was bound by one urea subunit through two NH•••O bonds. In addition, the two anions were involved in intramolecular OH•••O H-bonding that extended throughout the crystal lattice, providing additional stability to the 1:2 complex. Binding studies in MeCN showed that CH_3COO^- ($K_a = 2.7 \times 10^3\ M^{-1}$), $C_6H_5COO^-$ ($K_a = 7.2 \times 10^2\ M^{-1}$) and $H_2PO_4^-$ ($K_a = 9.1 \times 10^2\ M^{-1}$) formed 1:1 complexes [68].

Johnson and co-workers reported that 2,6-bis(2-anilinoethynyl)pyridine-based bisurea **31** formed 1:1 complexes with halides. Protonation enhanced the binding by over one order of magnitude, altered the selectivity, and provided a colorimetric indication of anion binding. The ligand binds a chloride ion in a pentadentate manner, resulting in a five-coordinate chloride complex (Fig. 5.22). The H-bond distance to the protonated pyridinium NH group (N•••Cl = 3.030 Å) was quite short, while urea NH•••Cl distances ranged up to 3.640 Å [69].

Nabeshima and co-workers reported multi-responsive host **32**, in which two esters, two polyethers, two ureas, and two bipyridine units as ion binding sites were arranged to a calix[4]arene skeleton. Compound **32** recognized Na^+ and Ag^+ simultaneously and quantitatively and captured an anionic guest. The ability of **32** to recognize anions, including $CF_3SO_3^-$ and BF_4^-, remarkably increased in a stepwise manner using Na^+ and Ag^+ as effectors. The enhancement of the K_a eventually reached factors of 1,500 and 2,000 for NO_3^- and $CF_3SO_3^-$, respectively, in the presence of both Na^+ and Ag^+, compared to the free **32** [70].

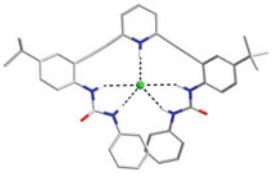

Fig. 5.22 Crystal structure of the chloride complex of the pyridinium ligand [H**31**]$^+$·Cl^-

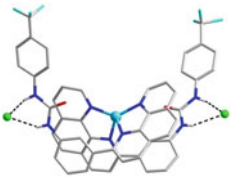

Fig. 5.23 Crystal structure of complex $[Cu^{I}(\mathbf{33})_2]^{+}\cdot Cl^{-}$

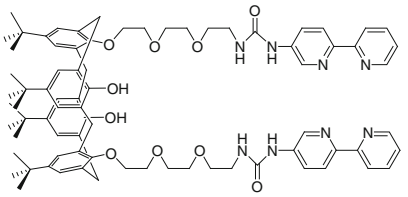

32

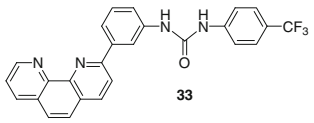

33

Besides covalent linkers, multiple urea groups can also be connected by metal coordination to yield metal-assisted receptors for anion binding. Fabbrizzi and co-workers found that receptor **33** could form solution-stable 1:2 complex through coordination of the phenanthrolinyl groups with Cu(I), $[Cu^{I}(\mathbf{33})_2]^{+}$, which behaved as anion receptor in aprotic media. The metal-assisted $[Cu^{I}(\mathbf{33})_2]^{+}$ receptor could bind halides, $H_2PO_4^{-}$ and CH_3COO^{-} ions. In the presence of anions, $[Cu^{I}(\mathbf{33})_2]^{+}$ discriminated $H_2PO_4^{-}$ over CH_3COO^{-}, inverting the basicity trend. In complex $[Cu^{I}(\mathbf{33})_2]^{+}\cdot Cl^{-}$, the N···Cl H-bond distances ranged from 3.185 to 3.368 Å (Fig. 5.23) [71].

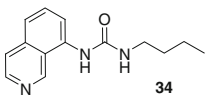

34

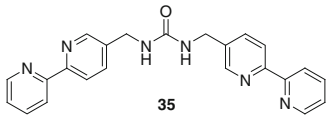

35

Loeb and co-workers reported the preparation of complex $[Pt^{II}(\mathbf{34})_4]^{2+}$ from **34**. Due to the free rotation around the Pt^{II}–N bond, the complex could assume four basic 'up and down' conformations of the butyl urea substituents. The crystal structure of $[Pt^{II}(\mathbf{34})_4]^{2+}\cdot SO_4^{2-}$ showed that the receptor was arranged in a cone conformation, with all eight N–H groups oriented toward the cavity including the sulfate anion (Fig. 5.24a), with $K_a > 10^5\ M^{-1}$. In chloride complex $[Pt^{II}(\mathbf{34})_4]^{2+}\cdot(Cl^{-})_2$, the receptor adopted a 1,2-alternate conformation (Fig. 5.24b), while the two chloride ions were located above and below the Pt^{II} center, with $K_{a1} = 1.2 \times 10^4\ M^{-1}$ and $K_{a2} = 2.2 \times 10^3\ M^{-1}$, respectively [72].

Receptor **34** was also coordinated to the $Pt(bpy)_2$ fragment to give complex $[Pt^{II}(\mathbf{34})_2(bpy)_2]^{2+}$ and form 3:2 host-guest system $[Pt^{II}(\mathbf{34})_2(bpy)_2]_3(SO_4)_2$ with

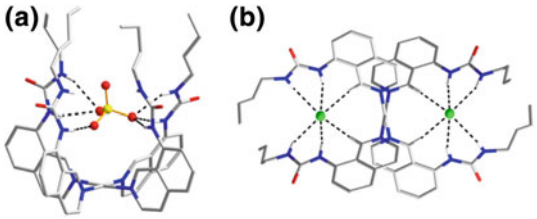

Fig. 5.24 Crystal structure of the **a** $[Pt^{II}(\mathbf{34})_4]^{2+}\cdot SO_4^{2-}$ and **b** $[Pt^{II}(\mathbf{34})_4]^{2+}\cdot(Cl^-)_2$

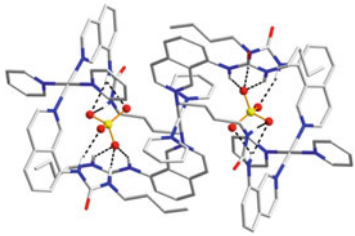

Fig. 5.25 Crystal structure of the sulfate complex of receptor **34**

sulfate (Fig. 5.25). In the crystal structure, each sulfate ion was surrounded by seven H-bonds with N•••O distances ranging from 2.771 to 3.108 Å [73].

Custelcean and co-workers synthesized symmetrical bipyridine substituted urea ligand **35** to construct a M_4L_6 cage using nickel coordination, which showed exceptionally strong sulfate binding in water, as well as shape-selective recognition for tetrahedral XO_4^{n-} anions. A sulfate ion could be included in the tetrahedral cavity by twelve H-bonds from six urea groups (Fig. 5.26). N•••O distances ranged from 2.904 to 2.942 Å, showing only a small variation for the 12 interactions [74].

Steed and co-workers synthesized pyridylurea ligand **36b** that formed coordination polymer using pyridyl groups and silver ions. Interestingly, polymer formation could be influenced by the H-bonding of the urea units with counter anions (NO_3^- or BF_4^-) [75]. Ligand **36a** has a shortened ethylene chain. Three molecules could complex two nitrates to form a Borromean weave via a total of 12 H-bonds (N•••O = 2.960–2.944 Å) (Fig. 5.27) [76].

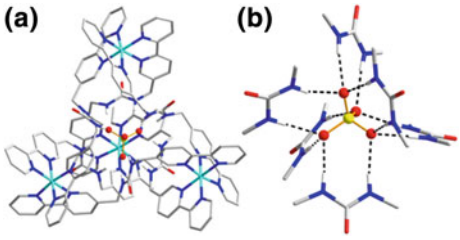

Fig. 5.26 **a** Encapsulation of sulfate inside the tetrahedral cage formed by **35** and nickel ions, and **b** hydrogen bonds from six urea groups around a sulfate ion

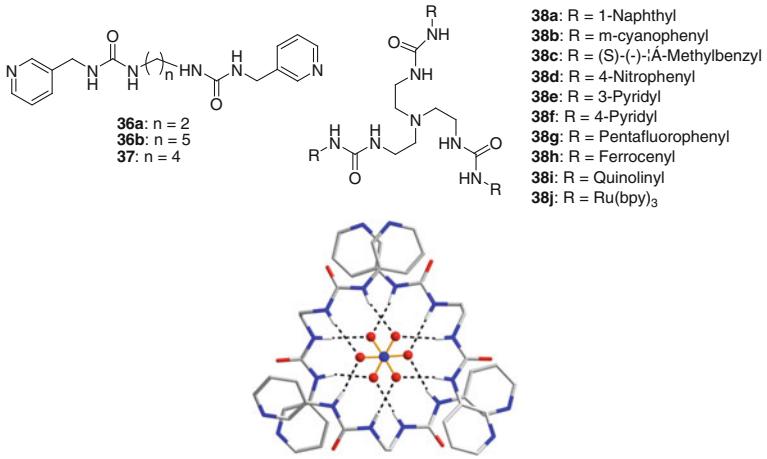

Fig. 5.27 Two nitrate anions surrounded by three bis(urea) ligands **36a** in the complex $[Ag_2(\mathbf{36a})_3](NO_3)_2$

Wu and co-workers synthesized butylene bis(3-(3-pyridyl)urea) ligand **37** which coordinated to $ZnCl_2$ in the presence of different guests to form a metallomacrocycle or a helical chain. The 0D macrocycle was obtained in the presence of toluene or xylene, which served as a template and was included in the molecule via CH•••π interactions and CH•••O H-bonds. In the absence of a guest, a 1D helical chain was favored [77].

Due to the favorable conformation for multiple H-bonds, tren-based tripodal tris (urea) receptors, including **38a–j**, have proven to be a promising scaffold for anion binding. Such receptors not only complementarily encapsulate oxoanions (sulfate, carbonate, and phosphate) but also display excellent binding ability to spherical halide ions. Several groups studied tripodal trisurea receptors with different substituents.

S.-K. Wu and co-workers also prepared tripodal naphthylurea **38a** for anion recognition (e.g., $H_2PO_4^-$ and HSO_4^-) by complexation-enhanced fluorescence in DMF solution [78].

Custelcean and co-workers reported that tripodal tren-based tris(urea) host **38b** complexed Ag_2SO_4 to form a 1D MOF structure with encapsulated sulfate ions. Interestingly, other silver salts did not result in MOFs. Therefore, the sulfate ion played a major role in the template process. Once again, the sulfate was bound by 12 H-bonds from six urea groups (Fig. 5.28) [79].

Steed and co-workers synthesized tris(urea) **38c** which gelated organic solvents. The formation of the helical gel fibers could be partially inhibited by addition of chloride, which was bound by the gelator, resulting in fully crystalline material, as characterized by X-ray crystallography [80].

Das and co-workers reported nitrophenyl-substituted tripodal tris(urea) receptor **38d** showed preferential binding for sulfate/phosphate anions. Two receptors form a neutral molecular capsule, within which a unique sulfate-$(H_2O)_3$-sulfate adduct was

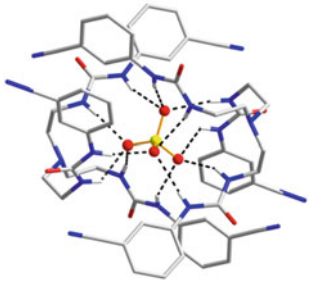

Fig. 5.28 Encapsulation of sulfate inside the crystal structure of 1D MOF formed by **38b**

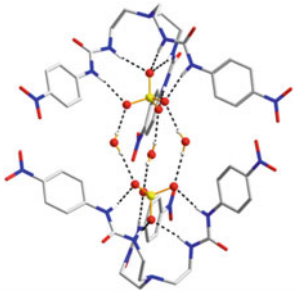

Fig. 5.29 Crystal structure of sulfate-encapsulated complex (**38d**·SO_4^{2-})$_2$

encapsulated. The urea moieties formed H-bonding with the O atoms of the sulfate anion (N•••O distances 2.870–2.901 Å). Three of the O atoms of sulfate anion that pointed toward the rim of the bowl were further H-bonded to water molecules (O•••O 2.773 Å) (Fig. 5.29) [81].

Custelcean and Wu groups independently reported tripodal tris(3-pyridylurea) receptor **38e**, which assembled with metal sulfate salts MSO_4 (M = Mn, Zn, Co, Mg, etc.) to afford supramolecular cages encapsulating SO_4^{2-} anion via multiple H-bonds in a 3D structure held by second-sphere coordination (Fig. 5.30) [82, 83].

Wu and co-workers also prepared closely related 4-pyridyl-substituted ligand **38f**, which formed complexes with oxoanions (sulfate, carbonate) or spherical

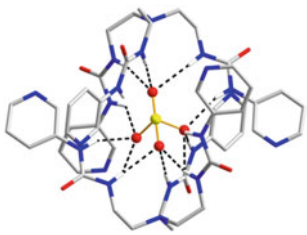

Fig. 5.30 Sulfate encapsulation by six urea groups of two receptors **38e**

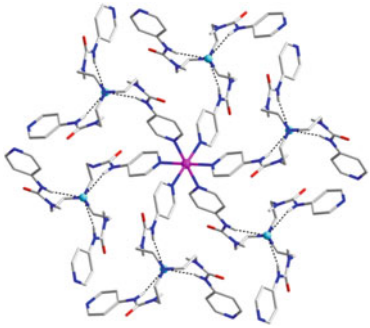

Fig. 5.31 Crystal structure of complex Co[**38f**•Cl^-]$_2$. Reprinted with permission from Ref. [84]. Copyright 2014, American Chemical Society

halide ions (MCl_n: M = Na, K, Mg, Ca, Mn, Co, n = 1 or 2). When M = Na, K, Mg, and Ca, the metal ions were not coordinated by the pyridyl groups but were involved in second-sphere coordination to form 3D structures similar to **38e**. However, in the complex of Co^{2+} (Fig. 5.31), the transition metal ions were directly coordinated by the pyridyl groups. Interestingly, the Mn^{2+} ion formed two complexes with both of the above two types of structure [84].

Ghosh and co-workers introduced electron-withdrawing C_6F_5 groups in the aromatic units of the tren-based host **38g**, which showed a high affinity for fluoride over other halides, with $K = 1.1 \times 10^4\ M^{-1}$ in DMSO-d_6. In the crystal structure of the fluoride complex, **38g** binds the fluoride ion with six H-bonds, N•••F ranging from 2.700 to 2.884 Å (Fig. 5.32a). In the sulfate complex, two symmetry-related molecules formed a capsule-like cavity that was occupied by a sulfate anion, held by 11 H-bonds to the urea NH groups with N•••O = 2.777–3.062 Å (Fig. 5.32b) [85].

Wu and co-workers further modified the tripodal tris(urea) backbone with different functional groups. Neutral tripodal tris(ferrocenylurea) receptor **38h** could electrochemically and optically recognize sulfate and phosphate anions [86], while quinolinyl and Ru(bpy)$_3$-functionalized ligands **38i** and **38j** displayed fluorescent response to anions [87–89].

Oligourea receptors bearing up to six covalently linked urea groups have been designed for anion coordination and supramolecular self-assembly. In 2010, Wu and co-workers synthesized a fully complementary tris(urea) receptor **39** by

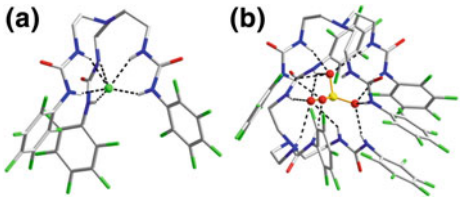

Fig. 5.32 Crystal structures for complexes of **38g** with **a** fluoride and **b** sulfate

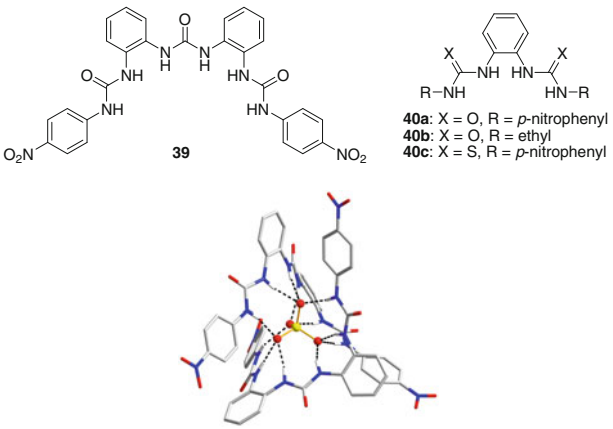

Fig. 5.33 Crystal structure of the phosphate complex $\mathbf{39}_2 \cdot PO_4^{3-}$. Reprinted with permission from Ref. [90]. Copyright 2010, Royal Society of Chemistry

mimicking the scaffold of terpyridine, which showed very high affinity and selectivity toward tetrahedral phosphate and sulfate anions. In the structure of $\mathbf{39}_2 \cdot PO_4^{3-}$, N•••O distances ranged from 2.752 to 2.901 Å (2.829 Å on average) and N–H•••O angles from 153° to 171° (164° on average) (Fig. 5.33) [90]. The same group also reported that bisureas **40a**, **b** and bisthiourea **40c** could readily form trischelates $[PO_4(L)_3]^{3-}$ with PO_4^{3-} in the solid state, in which the anion was coordinated by six urea groups through 12 H-bonds [91].

Jeong and co-workers reported that diphenylureas **41a–d** formed foldamer complexes with chloride and sulfate. Crystal structure of complex $\mathbf{41a} \cdot SO_4^{2-}$ (Fig. 5.34) showed that the sulfate ion was located in the middle of the cavity,

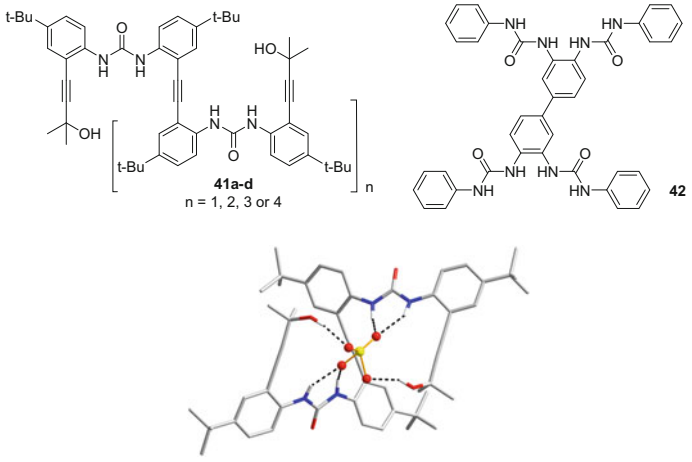

Fig. 5.34 Crystal structure of complex $\mathbf{41a} \cdot SO_4^{2-}$

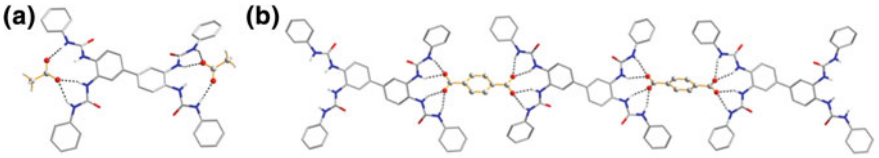

Fig. 5.35 **a** Crystal structure of acetate complex of **42** and **b** the polymeric chain obtained for **42** with ditopic terephthalate ion

forming two OH•••O and four NH•••O H-bonds. Among them, two hydroxyl groups and three urea protons formed normal H-bonds with distances of 2.67 and 2.69 Å for O•••O and 2.72–2.84 Å for N•••O, but one urea proton is a little more distant (3.05 Å) [92].

Gale and co-workers prepared expanded ditopic "compartmental" receptor **42** with a biphenyl linker. The structure of its acetate complex showed that acetate was bound in each cleft by three H-bonds (N•••O ranging 2.769–2.918 Å, Fig. 5.35a). However, by mixing the ligand with a ditopic guest, a linear polymer network was obtained, as shown for its terephthalate complex, in which each CO_2^- moiety accepted four H-bonds from two ureas (Fig. 5.35b) [93].

Burns and co-workers reported the preparation of porphyrin-based tetraurea receptor **43a**. In DMSO solution, **43a** formed a very stable 1:1 complex with chloride, two orders of magnitude more stable than $H_2PO_4^-$ and three orders of magnitude more stable than CH_3COO^-, thus inverting the order usually observed and expected in terms of anion basicity. Receptor **43b** possesses 4-chlorophenyl substituents. However, it was believed that its binding mode was the same as 4-fluorophenyl analogue **43a** [94, 95].

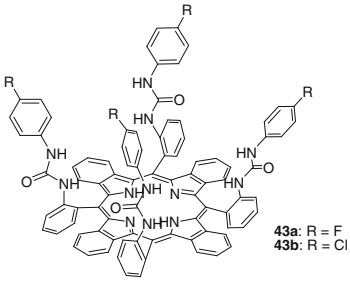

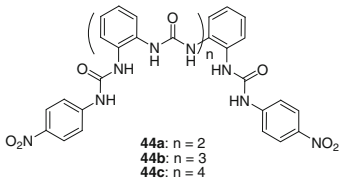

Following the research of bis- and trisureas, Wu and co-workers prepared acyclic, ortho-phenylene-bridged oligourea ligands **44a–c**. Receptors **39** and **44a–c** coordinated chloride anions in either a mononuclear pattern or a dinuclear foldamer pattern, depending on the number of the urea groups present. Crystal structure of foldamer complex **44a**•Cl^- is shown in Fig. 5.36. Each chloride anion was bound by four

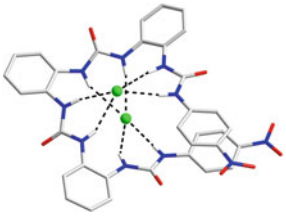

Fig. 5.36 Crystal structure of the dichloride complex of receptor **44a**

H-bonds from two alternating urea groups. The Cl•••Cl distance measured 3.613 Å, which was unusually short given that the sum of the ionic radii is 3.620 Å, indicating that electrostatic repulsion was overcome in the formation of this complex [96].

On the basis of the coordination property of bisurea with phosphate anion, Wu and co-workers designed bis-bisurea **45** and bis-trisurea **46**. In the solid state, **45** was found to form a dinuclear triple helical structure on coordination of phosphate anions, the first example of anion-coordination-based triple helicate, in which three ligands were wrapped around two PO_4^{3-} centers (Fig. 5.37a). Each phosphate ion was bound by six urea groups from three different bis-bisurea ligands through 12 H-bonds, and N•••O distances ranged from 2.735 to 2.867 Å (average 2.802 Å) and N–H•••O angles from 141° to 178° (average 163°). The interaction of **45** with PO_4^{3-} anions was also investigated in solution by ^{1}H NMR titration in DMSO-d_6–H_2O 5 %, which revealed

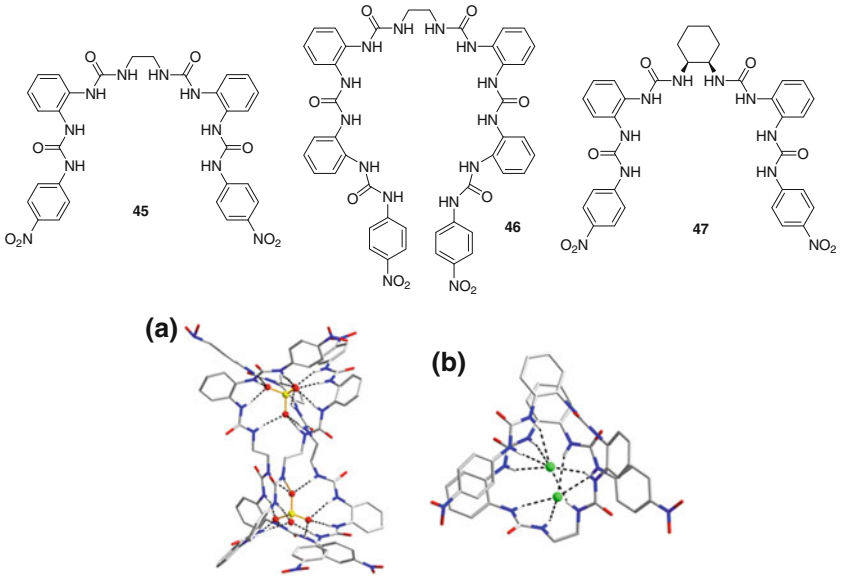

Fig. 5.37 Crystal structures of **a** triple anion helicate $[(PO_4)_2(\mathbf{45})_3]^{6-}$ and **b** complex of receptor **46** with TBACl. Reprinted with permission from Ref. [97]. Copyright 2011, John Wiley & Sons, Ltd

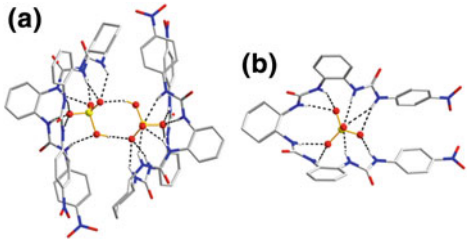

Fig. 5.38 **a** Crystal structure of $\mathbf{47}_2$·$(HPO_4^{2-})_2$ and **b** Crystal structure of $\mathbf{47}$·SO_4^{2-}. Reprinted with permission from Ref. [99]. Copyright 2012, Royal Society of Chemistry

that the major species in solution was also a 3:2 receptor-to-anion aggregate. On the other hand, hexakis-urea **46** formed a range of interesting structures in the solid state on complexation with different chloride and bromide salts. Treatment of **46** with tetraethylammonium chloride resulted in 'molecular barrel' complexes (Fig. 5.37b) [97, 98].

Ligand **47**, which bears a chiral R,R-cyclohexane-1,2-diamino spacer, was also prepared. This receptor formed an uncommon 2:2 complex with HPO_4^{2-} anion. Each anion was bound strongly by one **47** molecule via eight NH•••O H-bonds (N•••O distances range from 2.685 to 3.083 Å, average 2.880 Å; and N–H•••O angles from 132° to 174°, average 154°) with all of the four urea moieties (Fig. 5.38a). Meanwhile, **47** formed 1:1 complex with SO_4^{2-}. All of the eight NH groups pointed to the pocket and donated nine H-bonds to the sulfate ion (N•••O distances range from 2.745 to 3.260 Å, average 2.972 Å; N–H•••O angles from 120° to 178°, average 154°) (Fig. 5.38b) [99].

Another bis-bisurea ligand **48** featuring a 1,5-naphthylene-bridged spacer was also synthesized by Wu and co-workers. This rigid "bis-bidentate" ligand could act as a linker to afford 1D anion coordination polymers (ACPs) and dinuclear complexes, depending on the anions complexed [100].

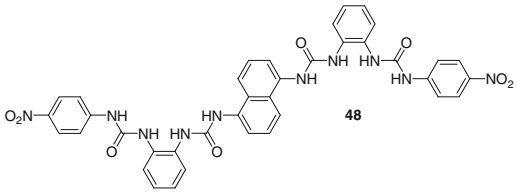

Wu and co-workers further reported the sulfate binding and extraction properties of tripodal hexaurea **49a**. In the solid state, a single sulfate anion was encapsulated by 12 H-bonds to the six urea groups (N–O distances ranging from 2.903 to 3.157 Å, average 2.992 Å; N–H•••O angles from 143° to 173°, average 161°). This was the first organic receptor reported to show saturated coordination of a sulfate anion by a

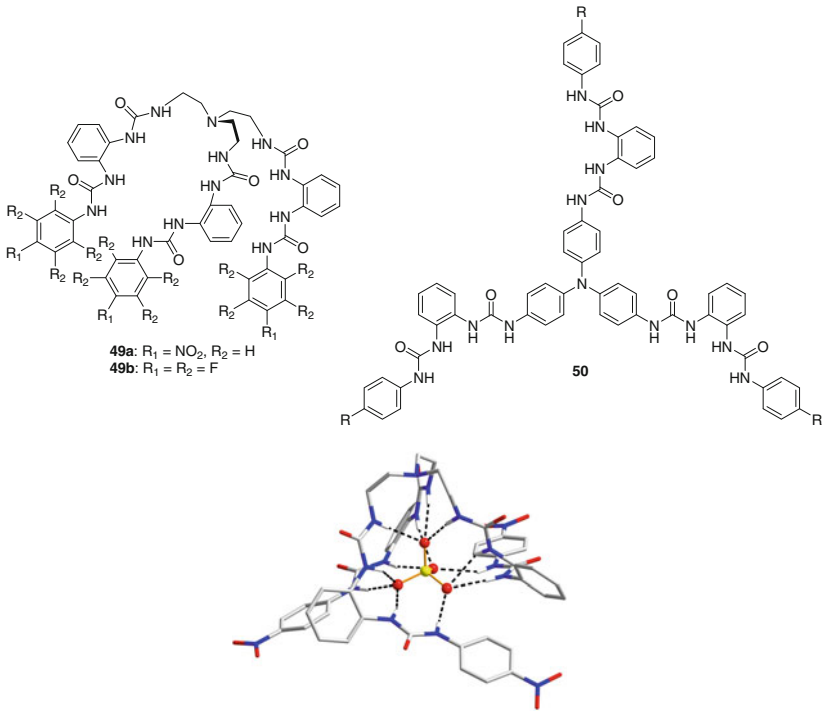

Fig. 5.39 Crystal structure of the sulfate complex of **49a**. Reprinted with permission from Ref. [101]. Copyright 2010, John Wiley & Sons, Ltd

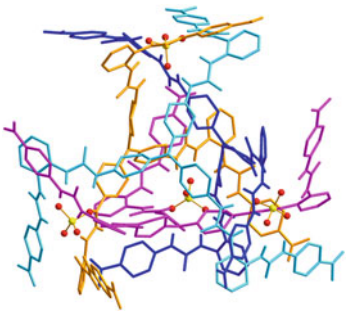

Fig. 5.40 Crystal structure of tetrahedral cage $\mathbf{50}_4 \cdot (PO_4^{3-})_4$. Reprinted with permission from Ref. [103]. Copyright 2013, John Wiley & Sons, Ltd

single host (Fig. 5.39). Moreover, this host could efficiently extract sulfate ions from aqueous $NaNO_3$–Na_2SO_4 solution into $CDCl_3$ as revealed by ^1H NMR [101]. Hossain and co-workers synthesized analogous hexaurea receptor **49b**, which absorbed atmospheric CO_2 to produce an air-stable solid carbonate complex under

normal conditions. The crystal structure of the carbonate complex showed that the carbonate was fully encapsulated within the cavity of **49b** via 12 strong NH•••O H-bonds ranging from 2.703 to 2.989 Å by six urea units [102].

The bisurea "building blocks" were also equipped to a C_3-symmetric triphenylamine platform by Wu and co-workers to form tris(bisurea) ligand **50**. This ligand readily formed a tetrahedral cage coordinated with fully deprotonated phosphate ions (PO_4^{3-}). This is the first example of the new class of anion-coordination supramolecular caged hosts. Each phosphate ion was bound to six urea groups from three different ligands through 12 strong NH•••O H-bonds (N•••O distances range from 2.811 to 2.827 Å, average 2.817 Å; N–H•••O angles range from 157° to 168°, average 163°) (Fig. 5.40) [103].

In the study of the supramolecular assembly of oligoureas, functionalization of the ligands has also been explored for potential applications. Wu and co-workers reported that tetrakis(bisurea)-decorated tetraphenylethene (TPE, a typical "aggregation induced emission (AIE)" chromophore) ligand **51**, upon coordination with phosphate ions, displayed fluorescence "turn-on" over a wide concentration range,

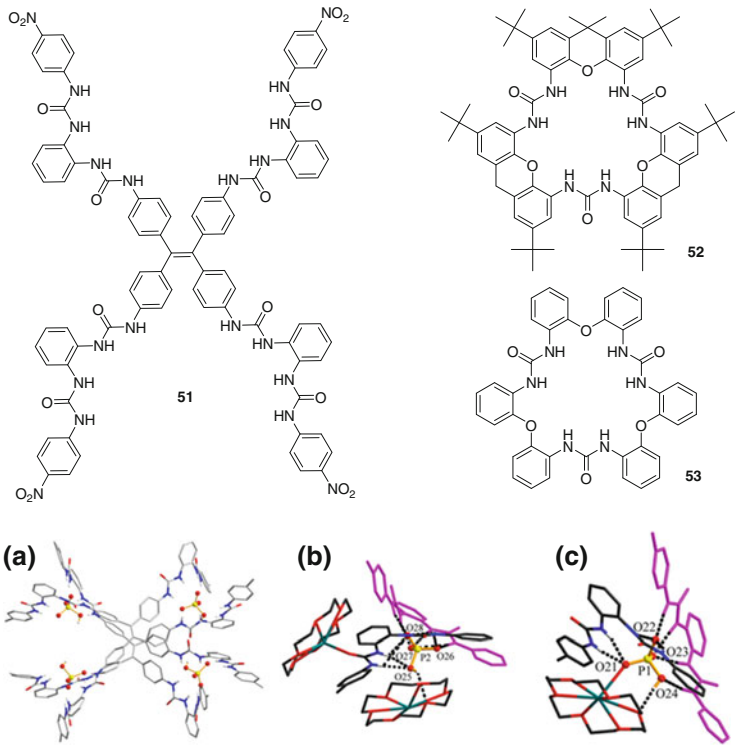

Fig. 5.41 Crystal structure of $(\mathbf{51})_2 \cdot (HPO_4^{2-})_4$: **a** The coordination of four HPO_4^{2-} ions by two ligands; **b** and **c** H-bonds (*broken lines*) around the HPO_4^{2-} ions. Reprinted with permission from Ref. [104]. Copyright 2014, John Wiley & Sons, Ltd

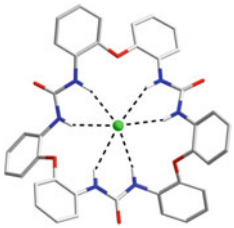

Fig. 5.42 Crystal structure of chloride complex of receptor **53**

from dilute to concentrated solutions and to the solid state. The fluorescence enhancement was attributed to the restriction of the intramolecular rotation of TPE by anion coordination. In the monohydrogen phosphate complex $(\mathbf{51})_2{\cdot}(HPO_4^{2-})_4$, two ($C_2$-related) HPO_4^{2-} ions (P2 and P2B) were each coordinated by two bisurea moieties through a total of 12 N–H•••O H-bonds, seven of which had N•••O distances less than 3.2 Å and the other five in the range 3.2–3.5 Å. The other type of HPO_4^{2-} (P1 and P1A) was also coordinated by four urea groups (through eight NH•••O H-bonds with N•••O distances in the range 2.7–3.2 Å) (Fig. 5.41) [104].

Böhmer and co-workers have synthesized a class of macrocycles in which three urea subunits were linked by xanthene (**52**) and/or diphenyl ether (**53**) spacers. Macrocycle **52** was expected to be very rigid, while macrocycle **53** should exhibit a higher degree of flexibility. The complex of **53** with tetrabutylammonium chloride showed the chloride anion was trapped in the center of the macrocycle, held by six NH•••Cl H-bonds (Fig. 5.42) [105].

Reinhoudt and co-workers reported that macrocyclic oligourea receptor **54**, which contains four urea groups, complexed tetrahedral $H_2PO_4^-$ anion. The K_a was determined to be 1.0×10^3 M^{-1} in DMSO-d_6 [106].

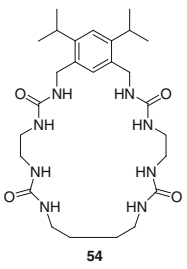

54

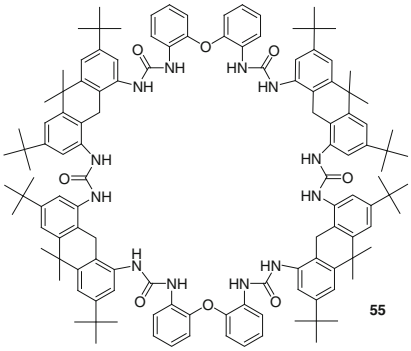

55

Böhmer and co-workers reported the synthesis of hexa-urea xanthene-derived macrocycle **55**. Hexamer **55** could form a dichloride complex when crystallized

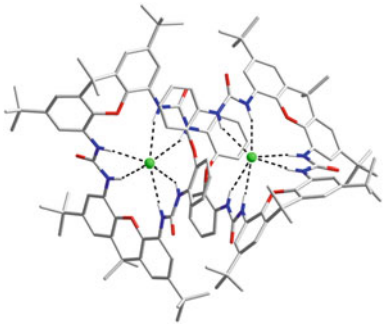

Fig. 5.43 Crystal structure of the 1:2 complex of hexamer **55** with Cl^-

from a dichloromethane/chloroform/ethanol mixture in the presence of tetrabutylammonium chloride (Fig. 5.43). The N•••Cl distances ranged from 3.18 to 3.34 Å, and the Cl•••Cl separation was 6.029 Å. In this gigantic figure-eight-like host, the presence of multiple binding sites allowed for a higher coordination number [107].

5.4 Pyrrole-Based Anion Recognition

Pyrrole contains a single NH H-bonding donor group and constitutes the basis for a wide variety of charged and neutral anion receptors. Pyrrole differs from urea discussed above as it does not contain an H-bond acceptor group.

In 1990, Sessler and co-workers developed an efficient synthesis of sapphyrin **56**, a pentapyrrolic macrocycle initially discovered by Woodward et al. [108]. X-ray structure and ^{19}F NMR analyses of its bis HPF_6 salt revealed the presence of a fluoride anion bound within the diprotonated pentapyrrclic macrocycle (Fig. 5.44) [109]. A PF_6^- counter anion was also found in the lattice but not proximate to the nearly planar sapphyrin skeleton. The fluoride anion itself was found to be within hydrogen bonding distance of all five proton-bearing nitrogen atoms.

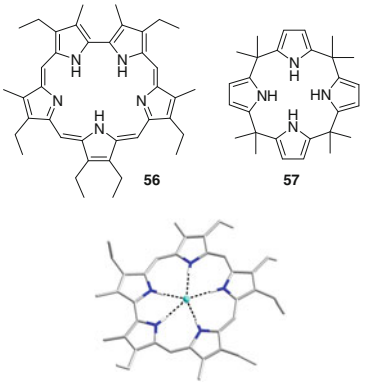

Fig. 5.44 Crystal structure of **56**•F^-

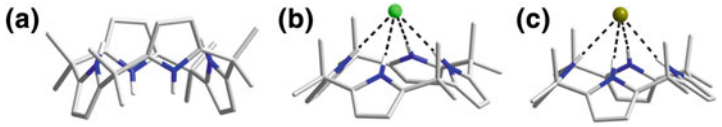

Fig. 5.45 Crystal structure of **a 57**, **b 57**·Cl^-, and **c 57**·Br^-

The simplest pyrrole-based anion receptor is mesooctamethyl calix[4]pyrrole **57** which can be synthesized in one step by the acid-catalyzed condensation of pyrrole with acetone. In 1996, Sessler and co-workers demonstrated that **57** binds fluoride anion selectively in CD_2Cl_2 solution [110]. Crystal structure of **57** (Fig. 5.45a) showed that two of the NHs point up, and the other two point down. When coordinated with anion, the four NHs all points at the anion. The selectivity of calix[4]pyrrole for anions depends on the nature of the solvent [111, 112], and fluoride selectivity could be lost under certain conditions. A detailed study by Sessler et al. with several chloride salts in solution by ITC and ^{1}H NMR titrations and in the solid state by X-ray analysis showed that the stability was highly dependent on the solvent (Fig. 5.45b) [113], with K_a ranging from 10^2 to 10^5 M^{-1}. In dichloromethane, a strong dependence on the counter cation was also observed, with K_a of the complexes with chloride varying within 10^2–10^4 M^{-1}.

Moyer et al. demonstrated that anion complexes of **57** could include large charge-diffuse cations, such as caesium and imidazolium, in the anion-induced calix[4]pyrrole cup [114]. Shielding of the imidazolium C*H* atoms in CD_2Cl_2 in the presence of an anion-binding calixpyrrole was observed and considered as evidence for ion-pair complexation in solution. Similar behavior was also observed for N-ethylpyridinium cation [115].

Gale and co-workers also reported the ability of **57** to form bromide complexes with dibromide salt in the solid state and in solution [116]. Crystallization of **57** in the presence of dibromide salts resulted in assemblies where the bromide ion was coordinated by four NH•••Br H-bonds (N•••Br distances between 3.410 and 3.503 Å) of the calixpyrrole (Fig. 5.45c). The K_a for the association of dibromide salt was determined to be 2,220 M^{-1}.

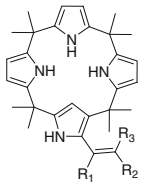

58a: $R_1 = R_3 = H$, $R_2 = C_6H_5$
58b: $R_1 = R_3 = H$, $R_2 = p$-C_6H_4-OMe
58c: $R_1 = R_3 = H$, $R_2 = p$-C_6H_4-Br
58d: $R_1 = R_3 = H$, $R_2 = p$-C_6H_4-NO_2
58e: $R_1 = R_3 = H$, $R_2 = C_6F_5$
58f: $R_1 = R_2 = R_3 = CN$

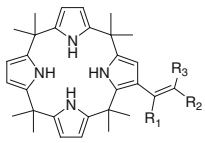

58g $R_1 = R_3 = H$, $R_2 = p$-C_6H_4-NO_2
58h $R_1 = R_2 = R_3 = CN$

Dehaen and co-workers reported the first example of substitution reaction in the free α-position of N-confused calix[4]pyrroles **58a–e** by azo-coupling with various

arenediazonium salts [117]. The stability of their anion complexes were found to be slightly higher than that of unsubstituted N-confused calix[4]pyrrole.

Anzenbacher and co-workers described the synthesis and anion binding properties of chromogenic calix[4]pyrroles **58d** and **58f–h** [118]. Compound **58f** showed significantly stronger anion-induced color changes compared to **58h**, and UV/vis titrations in DMSO indicated that they also displayed different anion binding selectivity.

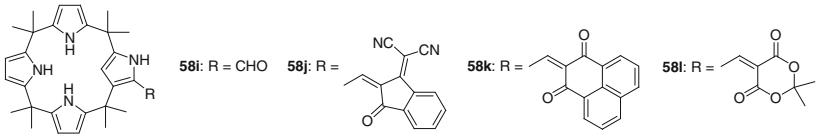

Dehaen and co-workers reported the synthesis of N-confused calix[4]pyrrole-α-carbaldehyde **58i** and its Knoevenagel reaction derivatives **58j–l**. Complexation studies on receptors **58i–l** for anions were performed with ^{1}H NMR titration in DMSO-d_6/0.5 % water. DeNamor and co-workers described the synthesis of isomeric meso-tetramethyltetrakis(3-hydroxyphenyl)calix[4]pyrroles **59a** and **59b**. They investigated their anion binding properties by ^{1}H NMR and conductometric titrations in acetonitrile and DMF [119], which revealed that **59a** showed selectivity for $H_2PO_4^{2-}$ in acetonitrile, while **59b** was selective for fluoride. Moreover, on the basis of thermodynamic, conductometric, and calorimetric data, they demonstrated that the enthalpy parameter might be a suitable reporter of the number of H-bonds formed with dihydrogen phosphate anion in acetonitrile.

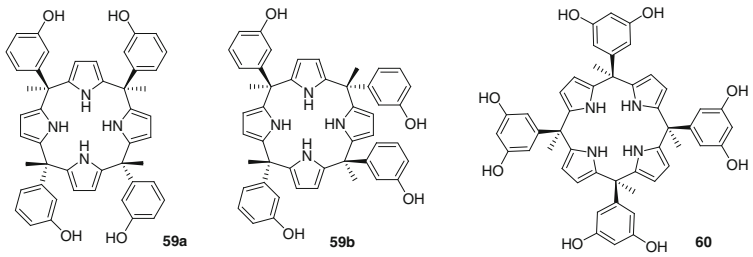

Ballester and co-workers reported the solid-state self-assembly of resorcinecalix[4]pyrrole **60** with tetramethylammonium chloride (Fig. 5.46) [120]. The solid packing was controlled by their ratio in the crystallization solutio n. A 1:1 ratio yielded a crystal structure with a columnar packing of the endo cavity complex, in which calix[4]pyrrole units were bridged together by tetramethylammonium cations.

Sessler and co-workers also studied the anion binding property of tetrathiafulvalene (TTF)-calix[4]pyrroles **61a** and **61b** using ^{1}H NMR and ITC in

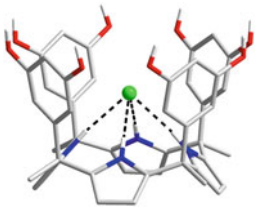

Fig. 5.46 Crystal structure of **60**·Cl^-

CD_2Cl_2, acetone-d_6 and CD_3CN [121], which revealed that the incorporation of one or more electron-rich TTF subunits improved the binding ability and changed the binding selectivity. The complexation for halides was also monitored by cyclic voltammetry in 1,2-dichloroethane, which revealed electrochemical response to Cl^- and Br^- ions.

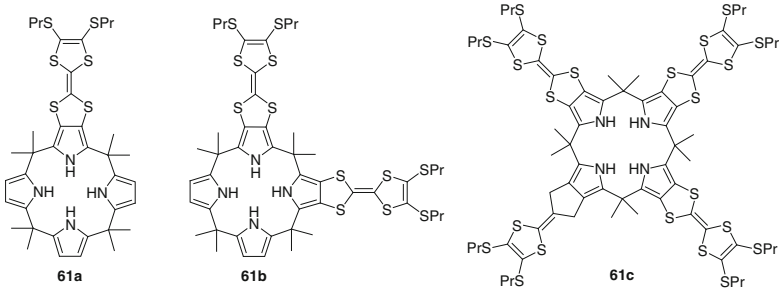

Sessler et al. further reported that calixpyrrole **61c** complexed chloride anion in dichloromethane to afford a bowl-like structure, which could encapsulate C_{60} in a 2:1 (calixpyrrole-chloride:C_{60}) ratio [122]. As observed for cation inclusion in a calixpyrrole cup, initial chloride binding served as a "trigger" for the calix[4] pyrrole to reorganize to produce a "cone" conformation, where multiple TTF units were appropriately arranged to allow for fullerene binding.

Lee and co-workers employed the anion binding ability of modified calix[4]-pyrrole **62a** to develop a selective sensor for fluoride using a fluorescent dye displacement assay [123]. When the fluorescent dye chromenolate **62d** was bound to **62a**, its fluorescence was quenched. Subsequent addition of F^- resulted in the recovery of the fluorescence. Lee et al. further reported **62b** as a selective pyrophosphate sensor by using the similar strategy [124]. The original fluorescence was shown to fully recover upon the addition of $HP_2O_7^{3-}$. This selectivity toward $HP_2O_7^{3-}$ over other anions, such as F^- and $H_2PO_4^-$, was even more pronounced in 30 % aqueous acetonitrile. The high affinity for $HP_2O_7^{3-}$ ($K_a = 2.55 \times 10^7\ M^{-1}$) was attributed to the cationic charge of **62b**, as the affinity of neutral receptor **62c** was found to be much lower ($K_a = 5.25 \times 10^5\ M^{-1}$), although H-bonding and anion···π interactions were also found to contribute to $HP_2O_7^{3-}$ binding.

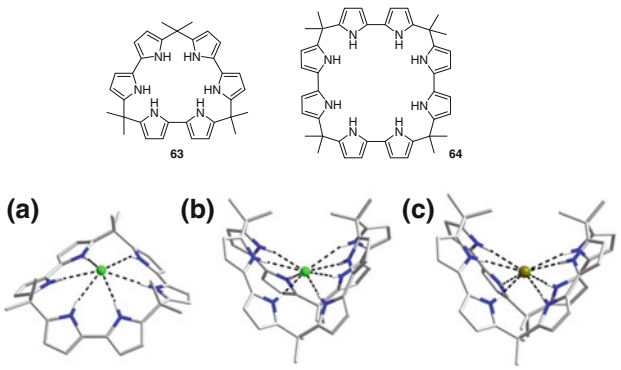

Fig. 5.47 Crystal structure of **a 63**·Cl^-; **b 64**·Cl^- and **c 64**·Br^-

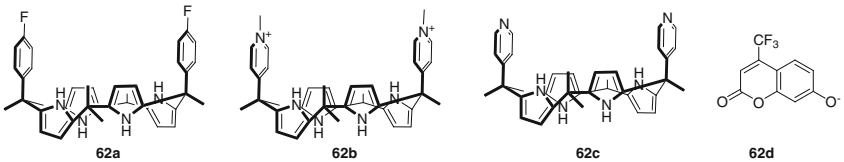

Sessler and co-workers showed that expanded macrocycle **64** had a particularly high affinity for chloride ($K_a = 2.9 \times 10^6\ M^{-1}$ in acetonitrile) [125, 126]. In the solid state, **64** adopts a V-shaped conformation (Fig. 5.47) when binding chloride by employing all eight H-bond donor NH groups, which was presumably the reason for the high affinity in solution. The smaller calix[3]bipyrrole analogue **63** has a lower affinity for chloride ($K_a = 1.1 \times 10^5\ M^{-1}$ in acetonitrile) (Fig. 5.47).

Other pyrrole-based macrocyclic anion receptors include the cyclo[*n*]pyrroles that consist solely of an array of pyrrole groups linked directly to each other via the 2- and 5-positions of the rings [127]. For example, cyclo [8] pyrrole **66a–d** can be prepared by direct coupling of bipyrroles **65a–d** in the presence of iron(III) chloride in 1 M sulfuric acid (Scheme 5.1).

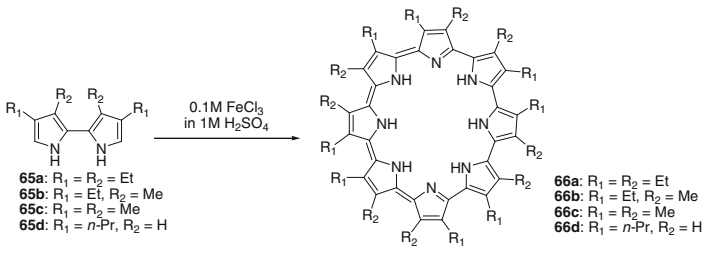

Scheme 5.1 The synthesis of **66a–d** from **65a–d**

Sessler and co-workers also reported the use of anion templates to synthesize **66a** by electrochemical oxidation of **65a** in dichloromethane in the presence of F^-, Cl^-, Br^-, NO_3^-, BF_4^-, HSO_4^- and ClO_4^- [128]. The highest yield of 68 % was achieved in the presence of HSO_4^-. They also successfully synthesized **66a** and **66e** from the simple 3,4-diethylpyrrole by the same method. The crystal structure of complex **66b**·SO_4^{2-} was obtained (Fig. 5.48).

Sessler et al. further synthesized larger oligopyrrolic macrocycles **67a–c** [129]. Macrocycle **67c** can also be obtained by ring expansion of **67a** under thermodynamic control in the presence of HSO_4^- and $H_2PO_4^-$ [130]. Macrocycle **67c** twisted to encapsulate HPO_4^{2-} anion, binding it via 12 H-bonds (Fig. 5.49). The coordination environment around the anion was similar to that found in the active site of the phosphate binding protein (PBP) in terms of bond distances and angles [131].

Sessler et al. also synthesized macrocycles **68a–c** [132], which displayed very high affinity for oxoanions with K_a being on the order of 10^7 M^{-1} in CH_3CN. Receptor **68a** can also bind large perrhenate anion (K_a = 124 000 M^{-1}), while rigid receptor **68c** showed a preference for chloride (K_a = 281 000 M^{-1}). This unusual preference for spherical halide was rationalized on the basis of DFT calculations and X-ray diffraction studies (Fig. 5.50). It was shown that in the chloride complex all the pyrrole rings and the two amide groups point into the cavity. As a consequence, the size of the cavity is relatively small and only spherical anions such as chloride or bromide can be accommodated in this fashion.

Mani and co-workers reported anion binding ability of macrocyclic **69** and open chain dipyrrolylmethane receptor **70** [133]. ^1H NMR titration experiments of **69** in acetone-d_6 revealed a strong 1:1 binding for F^- (K_a = 10^4 M^{-1}) over Cl^- (K_a = 4,763 M^{-1}) and Br^- (K_a = 317 M^{-1}). Comparable experiments with **70** in $CDCl_3$ revealed a 1:2 host/guest binding mode. However, crystallization of both receptors with two equivalents of n-Bu_4NHSO_4 resulted in the formation of 1:1 complexes [H_2**69**]$^{2+}$·SO_4^{2-} and [H_2**70**]$^{2+}$·SO_4^{2-} (Fig. 5.51), respectively. The crystal structures

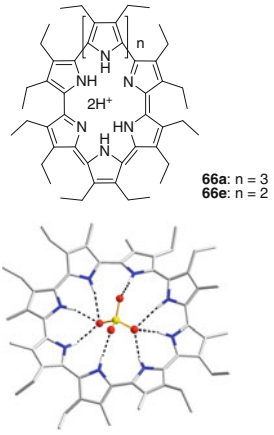

Fig. 5.48 Crystal structure of **66b**·SO_4^{2-}. Reprinted with permission from Ref. [127]. Copyright 2002, John Wiley & Sons, Ltd

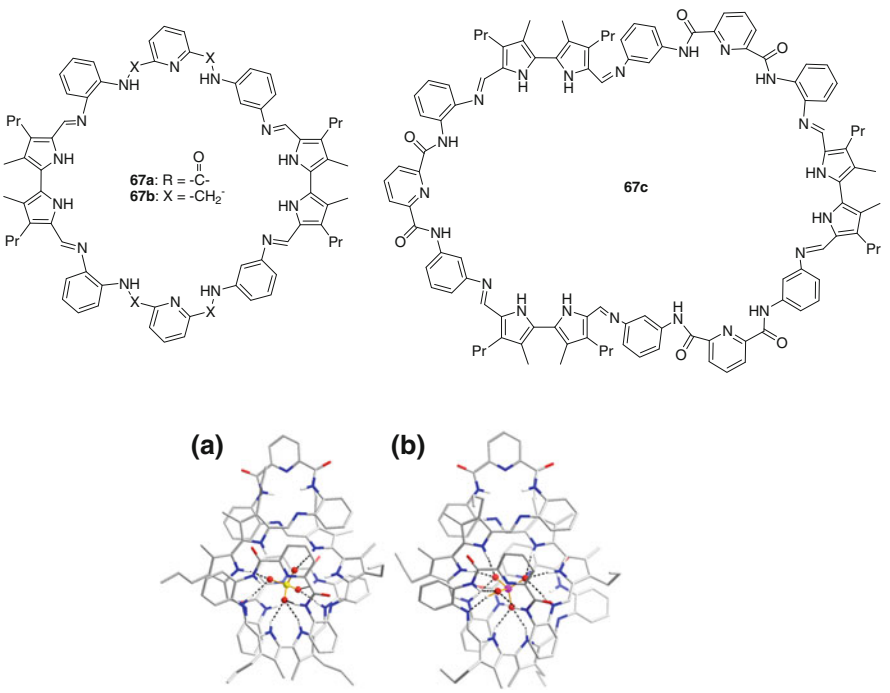

Fig. 5.49 Crystal structures of **a** **67c**·H_2SO_4 and **b** **67c**·H_3PO_4. **a** Reprinted with permission from Ref. [130]. Copyright 2005, John Wiley & Sons, Ltd. **b** Reprinted with permission from Ref. [129]. Copyright 2007, American Chemical Society

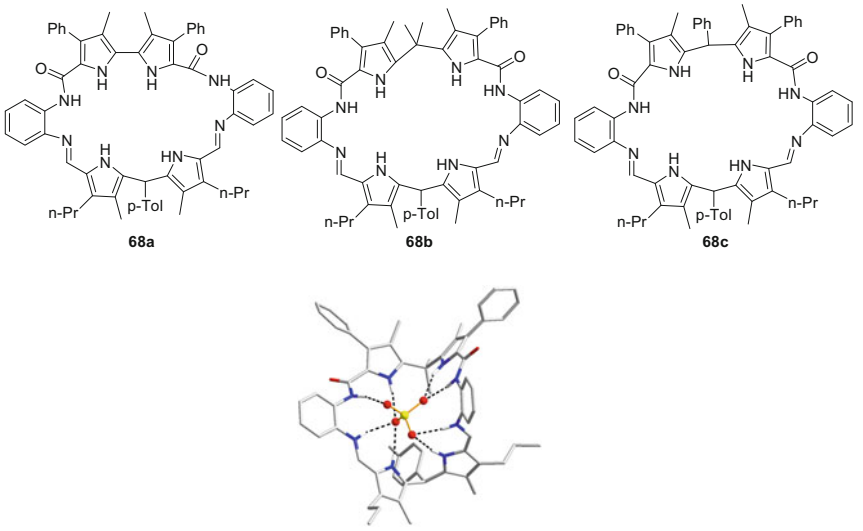

Fig. 5.50 Crystal structure of **68c**·SO_4^{2-}. Reprinted with permission from Ref. [132]. Copyright 2007, American Chemical Society

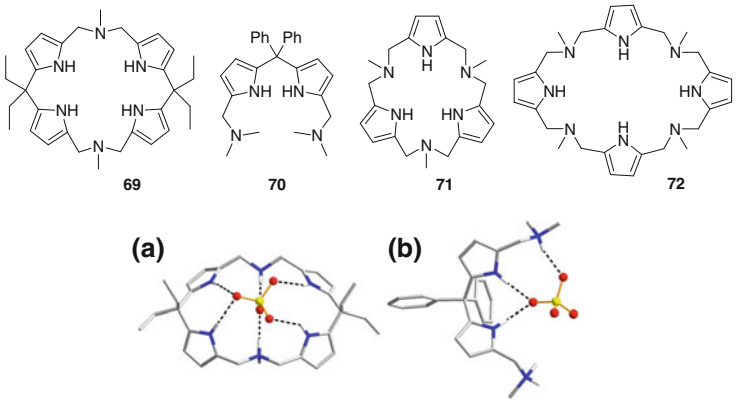

Fig. 5.51 Crystal structure of **a** $[H_2\mathbf{69}]^{2+}\cdot SO_4^{2-}$ and **b** $[H_2\mathbf{70}]^{2+}\cdot SO_4^{2-}$

revealed that both receptors were doubly protonated. The sulfate ion in $[H_2\mathbf{69}]^{2+}\cdot SO_4^{2-}$ was coordinated by NH•••O H-bonds to the pyrrole groups (N•••O distances of 2.992 and 3.076 Å) and the formed ammonium group (N•••O distances of 2.740 and 2.833 Å). In $[H_2\mathbf{70}]^{2+}\cdot SO_4^{2-}$ the anion was bound by two NH•••O H-bonds from the pyrrole groups (N•••O distances of 2.800 and 2.821 Å) and by only one of the two ammonium groups with an N•••O distance of 2.773 Å.

Mani et al. also studied the anion binding of amine-linked pyrrole-based macrocycles **71** and **72** using ^{1}H NMR titration in acetone-d_6 [134]. The smaller macrocycle **71** complexed F^- in a 1:1 binding mode with a K_a of 1,138 M^{-1}. A 1:2 stoichiometry was obtained for the binding of Cl^- and Br^- with the first K_{a1} being 3,182 and 243 M^{-1}, respectively. The larger macrocycle **72** could form more 1:1 complexes with Cl^- and Br^- (K_a = 13,586 M^{-1} for Cl^- and 1,181 M^{-1} for Br^-).

Sessler and co-workers also prepared pyrrolyl-based triazolophane **73** [135]. In the solid state, **73** binds pyrophosphate anion in a clip-like fashion via a combination of NH and CH hydrogen bonds (Fig. 5.52). UV/Vis titrations showed that the pyrophosphate anion was bound to **73** in chloroform at 300 K ($K_a = 2.3 \times 10^6$ M^{-1}) in a 1:1 stoichiometry. The receptor showed selectivity for pyrophosphate trianion, followed by HSO_4^- > $H_2PO_4^-$ Cl^- > Br^-. In the presence of 10 equiv of $TBA_3HP_2O_7$, the signals of the pyrrole NH, the triazole CH, and the endocyclic H atom of the N1-linked phenyl unit in ^{1}H NMR shifted downfield by 5.09, 1.96, and 1.22 ppm, respectively. This trend was consistent with the intrinsic strength of the H-bond donor groups, i.e., pyrrole NH > triazole CH > benzene CH, as inferred from electronic structure calculations.

Sessler and co-workers further synthesized 'strapped' calixpyrroles, including isophthalamide strapped system **74** [136, 137]. The aliphatic bridges were found to increase the binding affinity for halide anions in acetonitrile, but failed to provide size-based selectivity amongst anions (Br^-, Cl^- and I^-) due to the tilt of the strap to one side of the receptor, which allowed the formation of 2:1 (receptor:anion) complexes.

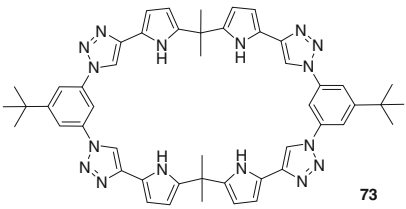

73

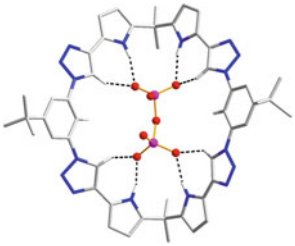

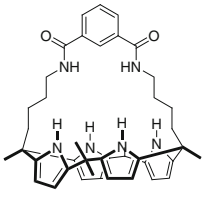

74

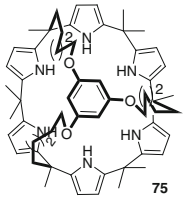

75

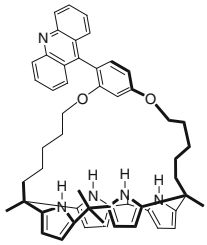

76

Fig. 5.52 Crystal structure of **73**•$P_2O_7^{4-}$. Reprinted with permission from Ref. [135]. Copyright 2010, American Chemical Society

Lee and co-workers prepared capsular calix[6]pyrrole **75** [138]. ^{1}H NMR indicated that this receptor had a high affinity for fluoride and displayed slow decomplexation/complexation kinetics, which prevented quantitative selectivity studies. However, upon addition of one equiv of fluoride, only resonances corresponding to the complex could be observed—indicative of strong complexation. For chloride, resonances corresponding to both bound and unbound pyrrole NH groups were observed upon addition of one equiv of the anion. The ratio between bound and unbound pyrrole NH resonances converged to 4:2 even in the presence of an excess of chloride (over 12 equiv). The NMR results suggested that only four of the six pyrrole groups formed H-bonds with chloride in solution.

The Lee group also synthesized acridine-bearing strapped calix[4]pyrrole **76** [139]. ITC studies in anhydrous MeCN at 30 °C showed that **76** selectively binds chloride over bromide with K_a being 2.41 × 10^7 M^{-1} and 6.81 × 10^4 M^{-1}, respectively. However, although **76** was fluorescent, no fluorescent change was detected upon anion complexation.

Sessler and co-workers compared the anion complexation property of **57** with that of **77a–c** [140, 141]. The results showed that **77b** had a 95 times-higher affinity for chloride in acetonitrile than **77c**. Crystal structure of the chloride complex

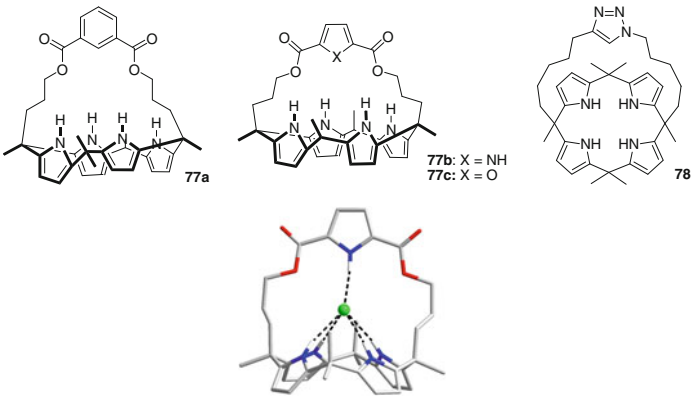

Fig. 5.53 Crystal structure of **77b**•Cl^-

revealed H-bonds from the calixpyrrole and strap pyrrole groups to the bound chloride (Fig. 5.53). Additionally, **77b** can be employed to determine the concentration of chloride in aqueous DMSO-d_6 using ^{1}H NMR due to slow exchange between the free and complexed receptor on the NMR timescale.

Gale and co-workers prepared pyrrole-triazole hybrid **78** [142]. In acetonitrile using TBACl as the chloride anion source, the enthalpy of its binding to chloride was found to be substantially more negative than that observed for unfunctionalized calix[4]pyrrole under identical conditions. This can be expected given the participation of an extra triazole CH•••chloride H-bond. It was also found that strapped calix[4]pyrrole **78** functioned as a chloride transporter in synthetic POPC and POPC–cholesterol vesicles.

A range of acyclic pyrroles and hybrid amidopyrroles have been prepared. Sessler and co-workers investigated the propensity of linear bipyrroles **79a** and **79b** and tripyrroles **79c–e** to complex and transport chloride [143]. The crystal structures of the complexes of **79a** and **79c** with Cl^- were also obtained (Fig. 5.54).

Maeda and co-workers reported the synthesis and anion binding of BF_2 complexes of β-tetraethyl-substituted pyrrolylpropanediones **80a** and **80b** [144]. They obtained the crystal structure of the complex of **80a** and chloride (Fig. 5.55) and prepared **81a–g** (Fig. 5.56) [145]. The binding constants for the 1:1 complexes of **81a–c** for various anions (Cl^-, Br^-, $CH_3CO_2^-$, $H_2PO_4^-$, and HSO_4^-) in CH_2Cl_2 were determined and found to decrease in the order **81a**, **81b**, **81c**, possibly because of differences in planarity and the number of the interacting *o*-CH units at the binding sites. Derivative **81g** afforded transparent gel in octane, which collapsed upon addition of the above anions.

Maeda et al. also studied the anion recognition of π-conjugated receptors **82a–c** [146]. X-ray diffraction and ^{1}H NMR and NOESY experiments indicated that a conformational change occurred upon anion binding with the inversion of the two pyrrole rings (Fig. 5.57). UV/Vis titration studies in CH_2Cl_2 with TBA salts of acetate and chloride gave K_a of 51,000 and 8,200 M^{-1}, respectively, for **82c**.

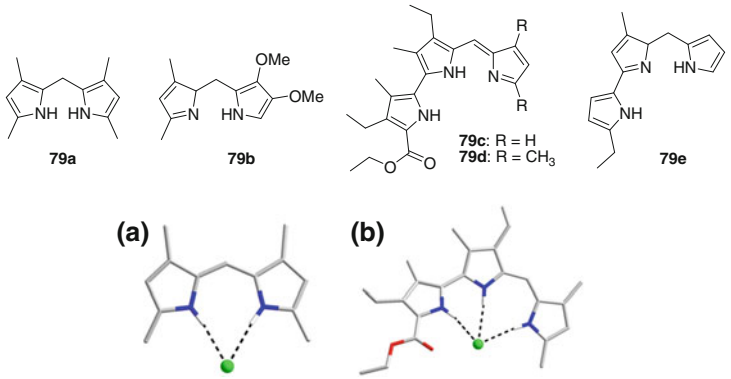

Fig. 5.54 Crystal structure of **a** **79a**·Cl^- and **b** **79c**·Cl^-. Reprinted with permission from Ref. [143]. Copyright 2005, John Wiley & Sons, Ltd

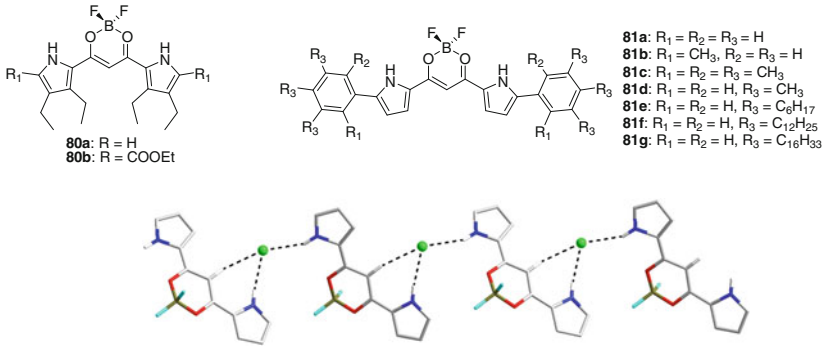

Fig. 5.55 Anion-bridged self-assembly of **80a**·Cl^-. Reprinted with permission from Ref. [144]. Copyright 2005, John Wiley & Sons, Ltd

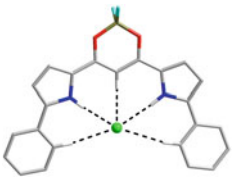

Fig. 5.56 Crystal structure of **81a**·Cl^-. Reprinted with permission from Ref. [145]. Copyright 2007, American Chemical Society

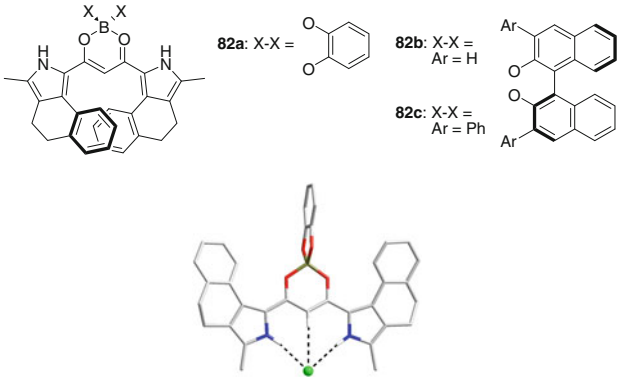

Fig. 5.57 Crystal structure of **82a**·Cl^-. Reprinted with permission from Ref. [146]. Copyright 2011, American Chemical Society

Sessler and co-workers also prepared cryptand-like calix[4]pyrrole **83** [147], which has three identical binding cavities and could bind solvents in the cavities in the solid state. Fluoride was found to be bound to six of the nine pyrrolic subunits, presumably in a 1:1 fashion, while chloride was found to interact with two **83** molecules in solution and the K_{a1} was estimated to be 3.08×10^6 M^{-1} in dichloromethane-d_2. For nitrate, a 1:2 stoichiometry was also observed, and the K_{a1} and K_{a2} values were determined to be 1,740 and 420 M^{-1}, respectively, in dichloromethane-d_2. Kohnke et al. reported cryptand **84** showed a preferred binding for F^- over Cl^-, NO_3^-, HSO_4^-, CH_3COO^-, and $H_2PO_4^-$ (as tetrabutylammonium salt) [148] and complexation was kinetically slow in CD_2Cl_2.

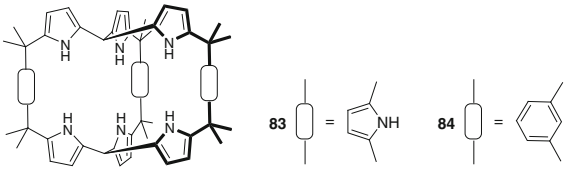

5.5 CH Donor-Based Anion Recognition

CH H-bonding has been established as a relatively weak H-bonding [149–155]. Flood and co-workers synthesized a series of shape-persistent macrocycles **85a–d** [156]. Receptor **85a** was found to bind chloride anion in 1:1 stoichiometry and the

K_a was determined to be 1.3×10^5 M^{-1} in CH_2Cl_2 at 298 K. Macrocycles **85b–d** were revealed to selectively recognize Cl^- and Br^- with high affinity ($K_a > 10^6$ M^{-1} in CH_2Cl_2), which was higher than that for F^- and I^- by 1.5 and 3 orders of magnitude, respectively. They also prepared triazolophanes **85e** and **85f** by incorporating pyridyl subunits into the backbones [157]. The presence of destabilizing N•••X^- electron pair repulsions induced them to form 2:1 sandwich complexes with halide anions. The OTg groups of **85e** were also found to favor dimerization. Both receptors exhibited a high positive cooperativity with I^- than smaller F^-, Cl^- or Br^-.

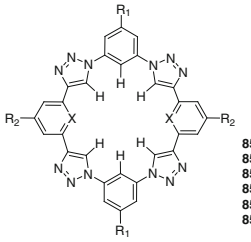

85a $R_1 = R_2 = t$-Bu; X = CH
85b $R_1 = t$-Bu; R_2= OTg; X = CH
85c R_1 = OTg; R_2= t-Bu; X = CH
85d $R_1 = R_2$ = OTg; X = CH
85e R_1 = OTg; R_2 = H; X = N
85f $R_1 = t$-Bu; R_2 = H; X = N

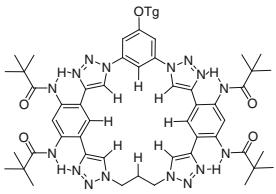

86

The Flood group further prepared macrocycle **86** for complexing bifluoride anion [158]. Anion binding was abetted by CH H-bonding provided by both the 1,2,3-triazole and phenylene subunits. This more flexible receptor allowed bifluoride anion to be bound in a non-tilted binding mode, which is different from that of the parent triazolophane.

Craig and co-workers demonstrated that oligomer **87** could fold to provide a cavity that stabilized intermolecular interactions between the electropositive CH 1,2,3-triazole sites and electron-rich guests, including anions [159]. Chloride-induced folding was confirmed via 2D NOESY experiments in acetone, as well as through molecular modeling studies.

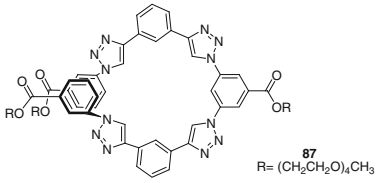

87
R= $(CH_2CH_2O)_4CH_3$

Hecht and co-workers reported another family of responsive "clickamers" **88** [160], which could undergo helix inversion when exposed to inherently achiral halide ions (KF, KCl, and KBr) in a water–acetonitrile mixture at neutral pH. The size of the halide anion was proposed to play an important role in defining the interaction with the helix.

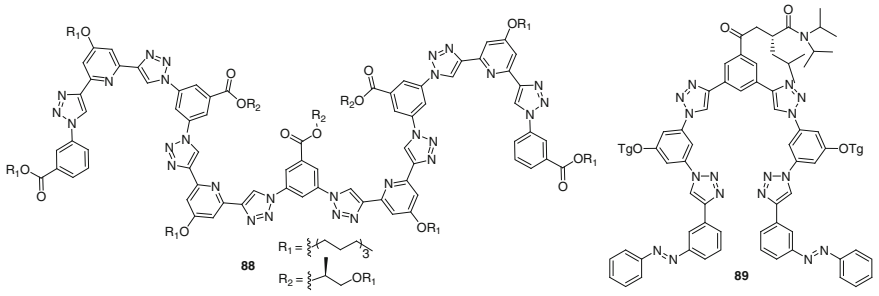

Flood and co-workers also synthesized chiral aryl-triazole foldamer **89**, which bears two azobenzene end groups [161]. In this case, light could be used as a stimulus to trigger wavelength-dependent release and re-uptake of chloride ions from its non-aqueous solution. The *trans*-dominated helical conformation became less stable upon photoisomerization to the *cis* form, with K_a being reduced by about 10-fold from 3×10^3 M^{-1} in MeCN at 298 K.

Flood and co-workers further prepared **90** [162], which was preorganized due to two intramolecular OH•••N H-bonds. This ligand can bind chloride anion with a K_a of 4.7×10^4 M^{-1} in CH_2Cl_2. The same group further prepared receptor **91** and found it also strongly complexed Cl^- in CH_2Cl_2. This strong binding was ascribed to the NH•••N H-bonding-mediated receptor preorganization and the two polarized naphthalimide CH donors that formed CH•••Cl^- H-bonding [163].

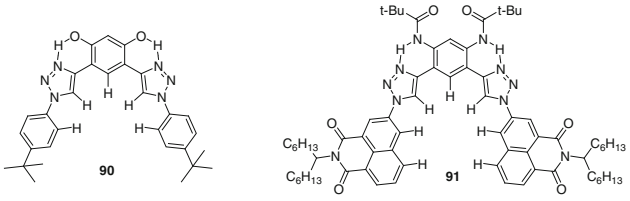

Flood and co-workers also created longer foldamer **92** [164]. It was proposed that hydrophobic interaction would stabilize its helical conformation in mixed organic–aqueous solutions. In 25 % water–acetonitrile (v/v), **92** formed a stable 2:1 complex with Cl^- through producing a double helix. Anion binding remained strong as the water content was increased to 50 %. The double helix was thought to favor a solvent-excluding microenvironment which stabilized strong CH•••Cl H-bonds.

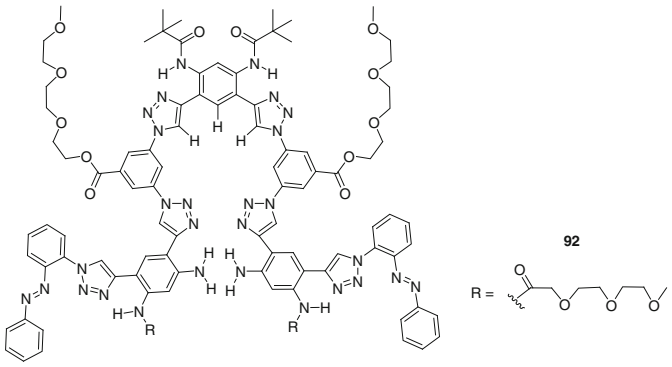

Sanchez and co-workers synthesized compounds **93** and **94** [165]. Adding bromide anion to their solution in chloroform induced the formation of an H-bonding-stabilized anion array with the receptors adopting a U-like conformation. This conformational change of the receptors was ascribed to the formation of slightly polarized aromatic CH and triazole CH H-bonds with the anion.

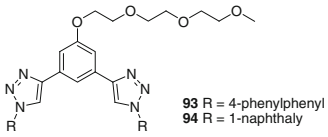

Flood and co-workers also synthesized C_5-symmetric cyanostilbene 'campestarene' macrocycle, the so-called cyanostar **95** [166]. Its electropositive central cavity could stabilize anions with CH H-bonding which was activated by electron-withdrawing cyano groups. The cyanostar formed stable 2:1 sandwich complexes with large anions BF_4^{2-}, ClO_4^{2-}, and PF_6^{2-} in solution. X-ray crystallography confirmed that two molecules of **95** coordinated around a perchlorate ion in the solid state (Fig. 5.58). A similar sandwich complex could also be formed between **96** and hexafluorophosphate ion [167].

5.6 OH-Based Anion Recognition

Hydroxyl groups of alcohol, phenol, and silanols as H-bonding donors have also been used for the construction of anion receptors. In this context, Smith et al. reported that some simple and commercially available dihydroxybenzenes, such as **97**–**99**, exhibited relatively high tunable anion selectivity [168, 169]. For example, catechol **97** displayed a strong affinity for chloride ion a K_a of 1,015 M^{-1}, while **98**

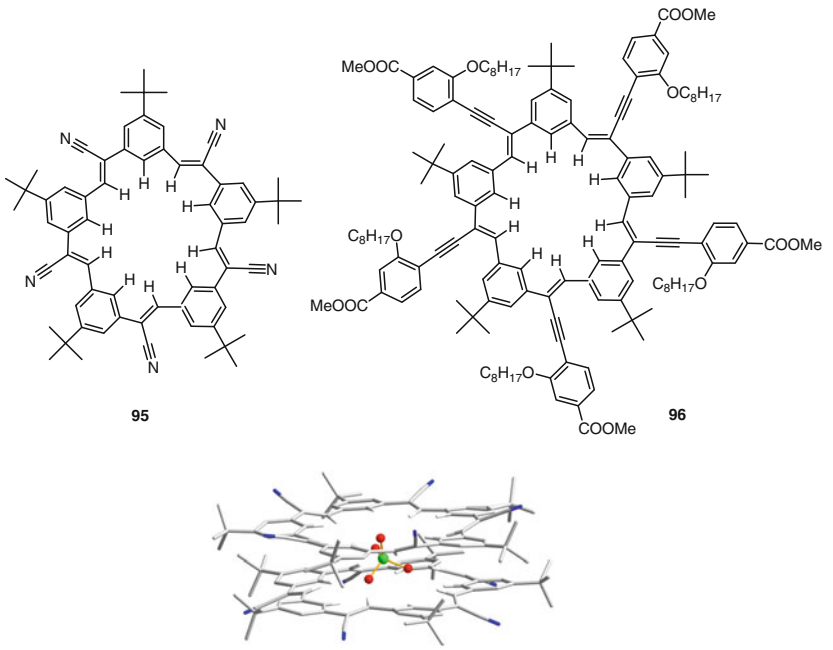

Fig. 5.58 Crystal structure of $\mathbf{95}_2 \cdot ClO_4^-$

showed less affinity for chloride ion (K_a = 145 M^{-1}). Smith and co-workers further prepared biscatechols **100–106** for anion recognition [168–170]. However, due to intramolecular H-bonding of the catechol moieties, these receptors had weak or no affinity for chloride ions.

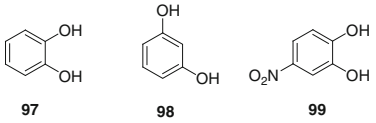

Casnati and co-workers prepared a series of difunctionalized calix[4]arenes with 2,2,2-trifluoroethanol groups at the upper rim [171]. Compounds **107a** and **107b** showed binding selectivity for RCO_2^- and $H_2PO_4^-$ over HSO_4^-, Br^-, or CN^- in chloroform, and **108** showed a fivefold increase in the binding of MeC O_2^-.

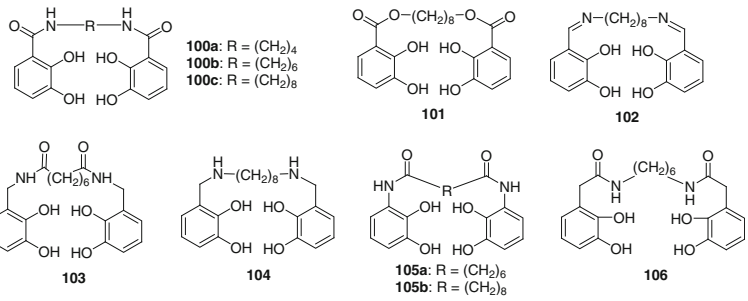

Shinmyozu and co-workers prepared photo-switchable chiral receptor *trans*-**109** by linking two chiral 2,2′-dihydroxy-1,1′-binapthyl (BINOL) groups with a stiff-stilbene core [172]. This compound could be photochemically isomerized to *cis*-**109**. The *trans*-**109** binds fluoride or chloride ions to form 1:1 complexes with K_a values being 1.0×10^3 and 4.6×10^2 M^{-1} in $CDCl_3$, respectively. However, the K_a of *cis*-**109** was only 59 M^{-1} for chloride ion.

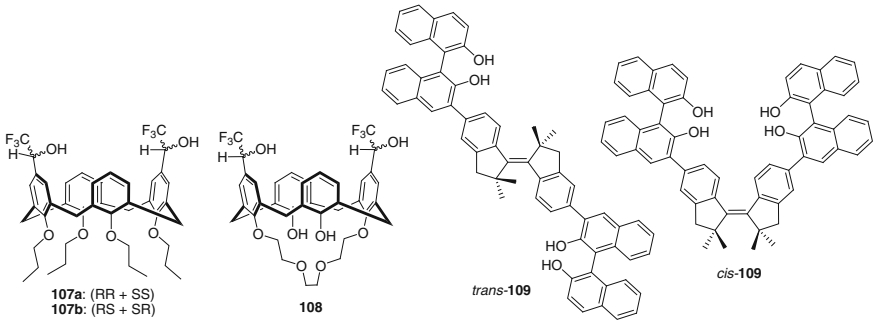

Kondo and co-workers studied the anion binding of *D*-ribose-based epimers **110** and **111** [173]. Their anion-binding abilities were in the order of $AcO^- > H_2PO_4^- > Cl^- > Br^-$, and in $CDCl_3$, the K_a of **111** (K_a = 2,450 M^{-1}) for AcO^- was two order higher than that of **110** (K_a = 72 M^{-1}). Kondo et al. also prepared silanols **112–114** [174, 175]. They found that, compared to **112** and **113**, **114a** and **114b** had a higher affinity for halides because they could utilize four OH groups to stabilize one halide ion.

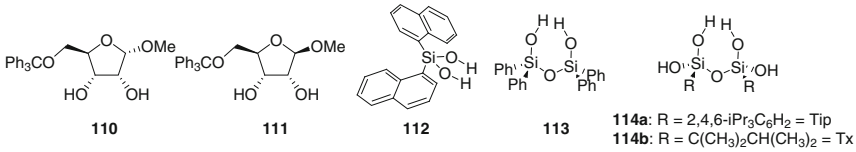

5.7 Conclusion

Hydrogen bonding has proven to be a powerful tool for anion binding. A wide variety of neutral and charged hydrogen bonding donors have been incorporated into different scaffolds to yield effective and selective anion receptors. Numerous anion complexes have been constructed by using these ligands (receptors) by forming complementary, multiple hydrogen bonds with the anions. The structures of the anion complexes have been characterized by X-ray crystal diffraction or theoretical calculations. For many systems, the binding behavior in solution has also been studied in detail using NMR, UV/vis, fluorescence, electrochemical, and thermochemical methods. These results clearly demonstrate that neutral H-bonding receptors are very promising in the field of anion coordination. Besides the fast growing interest in the receptor design and anion recognition, attention has also been devoted to the applications of anion coordination. In the future, new advance in anion-based supramolecular assembly, biological events, and materials science can be expected.

References

1. Park CH, Simmons HE (1968) J Am Chem Soc 90:2431
2. Bowman-James K, Bianchi A, García-España E (eds) (2012) Anion coordination chemistry. Wiley VCH, Weinheim
3. Jeffrey GA (ed) (1997) An introduction to hydrogen bonding. Oxford University Press, New York
4. Boonen J, Bronselaer A, Nielandt J, Veryser L, De Tre G, De Spiegeleer B (2012) J Ethnopharmacol 142:563
5. Pflugrath JW, Quiocho FA (1985) Nature 314:257
6. Gale PA, Busschaert N, Haynes CJE, Karagiannidis LE, Kirby IL (2014) Chem Soc Rev 43:205
7. Sessler JL, Gale PA, Cho WS (2006) Anion receptor chemistry. The Royal Society of Chemistry, Cambridge
8. Caltagirone C, Gale PA (2009) Chem Soc Rev 38:520
9. Gale PA (2010) Chem Soc Rev 39:3746
10. Wenzel M, Hiscock JR, Gale PA (2012) Chem Soc Rev 41:480
11. Hossain MA, Begum RA, Day VW (eds) (2012) Amide and urea-based receptors in supramolecular chemistry: from molecules to nanomaterials. Wiley, West Sussex
12. Pascal RA, Spergel J, Van Engen D (1986) Tetrahedron Lett 27:4099
13. Valiyaveettil S, engbersen JFJ, Verboom W, Reinhoudt DN (1993) Angew Chem Int Ed 32:900
14. Smith BD, Lambert TN (2003) Chem Commun 2261–2268
15. Boon JM, Smith BD (2001) J Am Chem Soc 123:6221
16. Boon JM, Lambert TN, Smith BD, Beatty AM, Ugrinova V, Brown SN (2002) J Org Chem 67:2168
17. Kavallieratos K, Danby A, Van Berkel GJ, Kelly MA, Sachleben RA, Moyer BA, Bowman-James K (2000) Anal Chem 72:5258
18. Danby A, Seib L, Bowman-James K, Alcock NW (2000) Chem Commun 973–974
19. Lakshminarayanan PS, Suresh E, Ghosh P (2006) Inorg Chem 45:4372

20. Beer PD, Chen Z, Goulden AJ, Graydon A, Stokes SE, Wear T (1993) J Chem Soc Chem Commun 1834
21. Kavallieratos K, de Gala SR, Austin DJ, Crabtree RH (1997) J Am Chem Soc 119:2325
22. Kavallieratos K, Bertao CM, Crabtree RH (1999) J Org Chem 64:1675
23. Santacroce PV, Davis JT, Light ME, Gale PA, Iglesias-Sanchez JC, Prados P, Quesada R (2007) J Am Chem Soc 129:1886
24. Camiolo S, Gale PA, Hursthouse MB, Light ME, Shi AJ (2002) Chem Commun 758
25. Lowe AJ, Pfeffer FM (2009) Org Biomol Chem 7:4233
26. Navakhun K, Gale PA, Camiolo S, Light ME, Hursthouse MB (2002) Chem Commun 2084
27. Gale PA, Camiolo S, Tizzard GJ, Chapman CP, Light ME, Coles SJ, Hursthouse MB (2001) J Org Chem 66:7849
28. Zielinski T, Jurczak J (2005) Tetrahedron 61:4081
29. Berryman OB, Johnson CA 2nd, Zakharov LN, Haley MM, Johnson DW (2008) Angew Chem Int Ed 47:117
30. Johnson CA, Berryman OB, Sther AC, Zakharov LN, Haley MM, Johnson DW (2009) Cryst Growth Des 9:4247
31. Arunachalam M, Ghosh P (2009) Chem Commun 5389
32. Arunachalam M, Ghosh P (2010) Inorg Chem 49:943
33. Agnieszka Szumna JJ (2001) Eur J Org Chem 4031
34. Chmielewski MJ, Jurczak J (2005) Chem Eur J 11:6080
35. Yoshihiko Inoue TKaTY (2003) Tetrahedron Lett 44:5167
36. Hossain MA, Llinares JM, Powell D, Bowman-James K (2001) Inorg Chem 40:2936
37. Ghosh S, Roehm B, Begum RA, Kut J, Hossain MA, Day VW, Bowman-James K (2007) Inorg Chem 46:9519
38. Hossain MA, Kang SO, Llinares JM, Powell D, Bowman-James K (2003) Inorg Chem 42:5043
39. Kang SO, Day VW, Bowman-James K (2009) Org Lett 11:3654
40. Kang SO, Hossain MA, Powell D, Bowman-James K (2005) Chem Commun 328
41. Kang SO, Llinares JM, Powell D, VanderVelde D, Bowman-James K (2003) J Am Chem Soc 125:10152
42. Kang SO, VanderVelde D, Powell D, Bowman-James K (2004) J Am Chem Soc 126:12272
43. Kang SO, Day VW, Bowman-James K (2010) J Org Chem 75:277
44. Kang SO, Powell D, Bowman-James K (2005) J Am Chem Soc 127:13478
45. Kang SO, Powell D, Day VW, Bowman-James K (2006) Angew Chem Int Ed 45:1921
46. Kang SO, Day VW, Bowman-James K (2010) Inorg Chem 49:8629
47. Bisson AP, Lynch VM, Monahan MKC, Anslyn EV (1997) Angew Chem Int Ed 36:2340
48. Kang SO, Day VW, Bowman-James K (2008) Org Lett 10:2677
49. Kubik S, Goddard R, Kirchner R, Nolting D, Seidel J (2001) Angew Chem Int Ed 40:2648
50. Kubik S, Kirchner R, Nolting D, Seidel J (2002) J Am Chem Soc 124:12752
51. Storer RI, Aciro C, Jones LH (2011) Chem Soc Rev 40:2330
52. Amendola V, Fabbrizzi L, Mosca L (2010) Chem Soc Rev 39:3889
53. Busschaert N, Kirby IL, Young S, Coles SJ, Horton PN, Light ME, Gale PA (2012) Angew Chem Int Ed 51:4426
54. Frontera A, Morey J, Oliver A, Pina MN, Quinonero D, Costa A, Ballester P, Deya PM, Anslyn EV (2006) J Org Chem 71:7185
55. Rostami A, Colin A, Li XY, Chudzinski MG, Lough AJ, Taylor MS (2010) J Org Chem 75:3983
56. Amendola V, Bergamaschi G, Boiocchi M, Fabbrizzi L, Milani M (2010) Chem Eur J 16:4368
57. Rostami A, Wei CJ, Guerin G, Taylor MS (2011) Angew Chem Int Ed 50:2059
58. Amendola V, Fabbrizzi L, Mosca L, Schmidtchen FP (2011) Chem Eur J 17:5972
59. Quinonero D, Lopez KA, Deya PM, Pina MN, Morey J (2011) Eur J Org Chem 6187
60. Ambrosi G, Formica M, Fusi V, Giorgi L, Macedi E, Micheloni M, Paoli P, Pontellini R, Rossi P (2011) Chem Eur J 17:1670

61. Smith PJ, Reddington MV, Wilcox CS (1992) Tetrahedron Lett 33:6085
62. Fan E, Van Arman SA, Kincaid S, Hamilton AD (1993) J Am Chem Soc 115:369
63. Boiocchi M, Del Boca L, Gómez DE, Fabbrizzi L, Licchelli M, Monzani E (2004) J Am Chem Soc 126:16507
64. Caltagirone C, Hiscock JR, Hursthouse MB, Light ME, Gale PA (2008) Chem Eur J 14:10236
65. dos Santos CMG, McCabe T, Watson GW, Kruger PE, Gunnlaugsson T (2008) J Org Chem 73:9235
66. Barboiu M, Vaughan G, van der Lee A (2003) Org Lett 5:3073
67. Brooks SJ, Gale PA, Light ME (2005) Chem Commun 4696
68. Amendola V, Boiocchi M, Esteban-Gomez D, Fabbrizzi L, Monzani E (2005) Org Biomol Chem 3:2632
69. Carroll CN, Berryman OB, Johnson CA, Zakharov LN, Haley MM, Johnson DW (2009) Chem Commun 2520
70. Nabeshima T, Saiki T, Iwabuchi J, Akine S (2005) J Am Chem Soc 127:5507
71. Amendola V, Boiocchi M, Colasson B, Fabbrizzi L (2006) Inorg Chem 45:6138
72. Bondy CR, Gale PA, Loeb SJ (2004) J Am Chem Soc 126:5030
73. Fisher MG, Gale PA, Light ME, Loeb SJ (2008) Chem Commun 44:5695
74. Custelcean R, Bosano J, Bonnesen PV, Kertesz V, Hay BP (2009) Angew Chem Int Ed 48:4025
75. Byrne P, Lloyd GO, Anderson KM, Clarke N, Steed JW (2008) Chem Commun 3720
76. Byrne P, Lloyd GO, Clarke N, Steed JW (2008) Angew Chem Int Ed 47:5761
77. Liang J, Wu B, Jia C, Yang XJ (2009) CrystEngComm 11:975
78. Xie H, Yi S, Yang X, Wu S (1999) New J Chem 23:1105
79. Custelcean R, Moyer BA, Hay BP (2005) Chem Commun 5971
80. Stanley CE, Clarke N, Anderson KM, Elder JA, Lenthall JT, Steed JW (2006) Chem Commun 3199
81. Jose DA, Kumar DK, Ganguly B, Das A (2007) Inorg Chem 46:5817
82. Wu B, Liang J, Yang J, Jia C, Yang XJ, Zhang H, Tang N, Janiak C (2008) Chem Commun 1762
83. Custelcean R, Remy P, Bonnesen PV, Jiang DE, Moyer BA (2008) Angew Chem Int Ed 47:1866
84. Zhang R, Zhao Y, Wang J, Ji L, Yang XJ, Wu B (2014) Cryst Growth Des 14:544
85. Ravikumar I, Lakshminarayanan PS, Arunachalam M, Suresh E, Ghosh P (2009) Dalton Trans 4160
86. Li M, Wu B, Jia C, Huang X, Zhao Q, Shao S, Yang XJ (2011) Chem Eur J 17:2272
87. Hao Y, Jia C, Li S, Huang X, Yang XJ, Janiak C, Wu B (2012) Supramol Chem 24:88
88. Li M, Hao Y, Wu B, Jia C, Huang X, Yang XJ (2011) Org Biomol Chem 9:5637
89. Hao Y, Yang P, Li S, Huang X, Yang XJ, Wu B (2012) Dalton Trans 41:7689
90. Jia C, Wu B, Li S, Yang Z, Zhao Q, Liang J, Li QS, Yang XJ (2010) Chem Commun 46:5376
91. Li R, Zhao Y, Li S, Yang P, Huang X, Yang XJ, Wu B (2013) Inorg Chem 52:5851
92. Kim MJ, Lee HW, Moon D, Jeong KS (2012) Org Lett 14:5042
93. Brooks SJ, Gale PA, Light ME (2005) Cryst Eng Comm 7:586
94. Jagessar RC, Shang M, Scheidt WR, Burns DH (1998) J Am Chem Soc 120:11684
95. Burns DH, Calderon-Kawasaki K, Kularatne S (2005) J Org Chem 70:2803
96. Wu B, Jia C, Wang X, Li S, Huang X, Yang XJ (2012) Org Lett 14:684
97. Li S, Jia C, Wu B, Luo Q, Huang X, Yang Z, Li QS, Yang XJ (2011) Angew Chem Int Ed 50:5720
98. Li S, Wei M, Huang X, Yang XJ, Wu B (2012) Chem Commun 48:3097
99. Wei M, Wu B, Zhao L, Zhang H, Li S, Zhao Y, Yang XJ (2012) Org Biomol Chem 10:8758
100. Meshcheryakov D, Bohmer V, Bolte M, Hubscher-Bruder V, Arnaud-Neu F (2009) Chem Eur J 15:4811
101. Jia C, Wu B, Li S, Huang X, Zhao Q, Li QS, Yang XJ (2011) Angew Chem Int Ed 50:486

102. Pramanik A, Emami Khansari M, Powell DR, Fronczek FR, Hossain MA (2014) Org Lett 16:366
103. Wu B, Cui F, Lei Y, Li S, Amadeu NdS, Janiak C, Lin YJ, Weng LH, Wang YY, Yang XJ (2013) Angew Chem Int Ed 52:5096
104. Zhao J, Yang D, Zhao Y, Yang XJ, Wang YY, Wu B (2014) Angew Chem Int Ed 53:6632
105. Meshcheryakov D, Arnaud-Neu F, Bohmer V, Bolte M, Hubscher-Bruder V, Jobin E, Thondorf I, Werner S (2008) Org Biomol Chem 6:1004
106. Snellink-Ruël BHM, Antonisse MMG, Engbersen JFJ, Timmerman P, Reinhoudt DN (2000) Eur J Org Chem 2000:165
107. Meshcheryakov D, Bohmer V, Bolte M, Hubscher-Bruder V, Arnaud-Neu F, Herschbach H, Van Dorsselaer A, Thondorf I, Mogelin W (2006) Angew Chem Int Ed 45:1648
108. Bauer VJ, Clive DLJ, Dolphin D, Paine JB, Harris FL, King MM, Loder J, Wang SWC, Woodward RB (1983) J Am Chem Soc 105:6429
109. Sessler JL, Cyr MJ, Lynch V, McGhee E, Ibers JA (1990) J Am Chem Soc 112:2810
110. Gale PA, Sessler JL, Kral V, Lynch V (1996) J Am Chem Soc 118:5140
111. Camiolo S, Gale PA (2000) Chem Commun 1129
112. Schmidtchen FP (2002) Org Lett 4:431
113. Sessler JL, Gross DE, Cho WS, Lynch VM, Schmidtchen FP, Bates GW, Light ME, Gale PA (2006) J Am Chem Soc 128:12281
114. Custelcean R, Delmau LH, Moyer BA, Sessler JL, Cho WS, Gross D, Bates GW, Brooks SJ, Light ME, Gale PA (2005) Angew Chem Int Ed 44:2537
115. Bates GW, Gale PA, Light ME (2006) Cryst Eng Comm 8:300
116. Caltagirone C, Bill NL, Gross DE, Light ME, Sessler JL, Gale PA (2010) Org Biomol Chem 8:96
117. Gu R, Depraetere S, Kotek J, Budka J, Wagner-Wysiecka E, Biernat JF, Dehaen W (2005) Org Biomol Chem 3:2921
118. Nishiyabu R, Palacios MA, Dehaen W, Anzenbacher P Jr (2006) J Am Chem Soc 128:11496
119. Danil de Namor AF, Shehab M, Abbas I, Withams MV, Zvietcovich-Guerra J (2006) J Phys Chem B 110:12653
120. Gil-Ramírez G, Benet-Buchholz J, Escudero-Adán EC, Ballester P (2007) J Am Chem Soc 129:3820
121. Nielsen KA, Cho WS, Lyskawa J, Levillain E, Lynch VM, Sessler JL, Jeppesen JO (2006) J Am Chem Soc 128:2444
122. Nielsen KA, Cho WS, Sarova GH, Petersen BM, Bond AD, Becher J, Jensen F, Guldi DM, Sessler JL, Jeppesen JO (2006) Angew Chem Int Ed 45:6848
123. Sokkalingam P, Yoo J, Hwang H, Lee PH, Jung YM, Lee CH (2011) Eur J Org Chem 2911
124. Sokkalingam P, Kim DS, Hwang H, Sessler JL, Lee CH (2012) Chem Sci 3:1819
125. Sessler JL, An D, Cho WS, Lynch V, Marquez M (2005) Chem Commun 28:540
126. Sessler JL, An D, Cho WS, Lynch V (2003) Angew Chem Int Ed 42:2278
127. Seidel D, Lynch V, Sessler JL (2002) Angew Chem Int Ed 41:1422
128. Buda M, Iordache A, Bucher C, Moutet JC, Royal G, Saint-Aman E, Sessler JL (2010) Chem Eur J 16:6810
129. Katayev EA, Sessler JL, Khrustalev VN, Ustynyuk YA (2007) J Org Chem 72:7244
130. Katayev EA, Pantos GD, Reshetova MD, Khrustalev VN, Lynch VM, Ustynyuk YA, Sessler JL (2005) Angew Chem Int Ed 44:7386
131. Luecke H, Quiocho FA (1990) Nature 347:402
132. Katayev EA, Boev NV, Khrustalev VN, Ustynyuk YA, Tananaev IG, Sessler JL (2007) J Org Chem 72:2886
133. Mani G, Guchhait T, Kumar R, Kumar S (2010) Org Lett 12:3910
134. Mani G, Jana D, Kumar R, Ghorai D (2010) Org Lett 12:3212
135. Sessler JL, Cai J, Gong HY, Yang X, Arambula JF, Hay BP (2010) J Am Chem Soc 132:14058
136. Lee CH, Lee JS, Na HK, Yoon DW, Miyaji H, Cho WS, Sessler JL (2005) J Org Chem 70:2067

137. Miyaji H, Kim HK, Sim EK, Lee CK, Cho WS, Sessler JL, Lee CH (2005) J Am Chem Soc 127:12510
138. Yoon DW, Jeong SD, Song MY, Lee CH (2007) Supramol Chem 19:265
139. Jeong SD, Yoo J, Na HK, Chi DY, Lee CH (2007) Supramol Chem 19:271
140. Yoon DW, Gross DE, Lynch VM, Sessler JL, Hay BP, Lee CH (2008) Angew Chem Int Ed 47:5038
141. Yoon DW, Gross DE, Lynch VM, Lee CH, Bennett PC, Sessler JL (2009) Chem Commun 1109
142. Fisher MG, Gale PA, Hiscock JR, Hursthouse MB, Light ME, Schmidtchen FP, Tong CC (2009) Chem Commun 3017
143. Sessler JL, Eller LR, Cho WS, Nicolaou S, Aguilar A, Lee JT, Lynch VM, Magda DJ (2005) Angew Chem Int Ed 44:5989
144. Maeda H, Kusunose Y (2005) Chem Eur J 11:5661
145. Maeda H, Haketa Y, Nakanishi T (2007) J Am Chem Soc 129:13661
146. Maeda H, Bando Y, Shimomura K, Yamada I, Naito M, Nobusawa K, Tsumatori H, Kawai T (2011) J Am Chem Soc 133:9266
147. Bucher C, Zimmerman RS, Lynch V, Sessler JL (2001) J Am Chem Soc 123:9716
148. Cafeo G, Colquhoun HM, Cuzzola A, Gattuso M, Kohnke FH, Valenti L, White AJP (2010) J Org Chem 75:6263
149. Pauling L (1935) J Am Chem Soc 57:2680
150. Kumler WD (1935) J Am Chem Soc 57:600
151. Zhu SS, Staats H, Brandhorst K, Grunenberg J, Gruppi F, Dalcanale E, Lützen A, Rissanen K, Schalley CA (2008) Angew Chem Int Ed 47:788
152. Bedford RB, Betham M, Butts CP, Coles SJ, Hursthouse MB, Scully PN, Tucker JHR, Wilkie J, Willener Y (2008) Chem Commun 21:2429
153. Pedzisa L, Hay BP (2009) J Org Chem 74:2554
154. Farnham WB, Roe DC, Dixon DA, Calabrese JC, Harlow RL (1990) J Am Chem Soc 112:7707
155. Ilioudis CA, Tocher DA, Steed JW (2004) J Am Chem Soc 126:12395
156. Li Y, Flood AH (2008) Angew Chem Int Ed 47:2649
157. Li Y, Pink M, Karty JA, Flood AH (2008) J Am Chem Soc 130:17293
158. Ramabhadran RO, Liu Y, Hua Y, Ciardi M, Flood AH, Raghavachari K (2014) J Am Chem Soc 136:5078
159. Juwarker H, Lenhardt JM, Pham DM, Craig SL (2008) Angew Chem Int Ed 47:3740
160. Meudtner RM, Hecht S (2008) Angew Chem Int Ed 47:4926
161. Hua Y, Flood AH (2010) J Am Chem Soc 132:12838
162. Lee S, Hua Y, Park H, Flood AH (2010) Org Lett 12:2100
163. McDonald KP, Ramabhadran RO, Lee S, Raghavachari K, Flood AH (2011) Org Lett 13:6260
164. Hua Y, Liu Y, Chen CH, Flood AH (2013) J Am Chem Soc 135:14401
165. Garcia F, Torres MR, Matesanz E, Sanchez L (2011) Chem Commun 47:5016
166. Lee S, Chen CH, Flood AH (2013) Nat Chem 5:704
167. Hirsch BE, Lee S, Qiao B, Chen CH, McDonald KP, Tait SL, Flood AH (2014) Chem Commun 50:9827
168. Smith DK (2003) Org Biomol Chem 1:3874
169. Winstanley KJ, Sayer AM, Smith DK (2006) Org Biomol Chem 4:1760
170. Winstanley KJ, Smith DK (2007) J Org Chem 72:2803
171. Casnati A, Sartori A, Pirondini L, Bonetti F, Pelizzi N, Sansone F, Ugozzoli F, Ungaro R (2006) Supramol Chem 18:199
172. Shimasaki T, Kato Si, Ideta K, Goto K, Shinmyozu T (2007) J Org Chem 72:1073
173. Kondo SI, Kobayashi Y, Unno M (2010) Tetrahedron Lett 51:2512
174. Kondo SI, Harada T, Tanaka R, Unno M (2006) Org Lett 8:4621
175. Kondo SI, Okada N, Tanaka R, Yamamura M, Unno M (2009) Tetrahedron Lett 50:2754

Chapter 6
Formation of Hydrogen-Bonded Self-assembled Structures in Polar Solvents

Supratim Banerjee and Carsten Schmuck

Abstract In this chapter a few recent examples of H-bond driven supramolecular assemblies in aqueous and polar organic media are discussed. H-bonding has been extensively utilized in the past for the generation of various nanostructures but those studies were mainly restricted to non-polar organic media. In recent years, however, the attention has shifted to obtain similar assemblies also in aqueous and polar media. The main principles that have been employed for this purpose are shielding of H-bonds from competing solvent molecules by hydrophobic residues or strengthening them by additional interactions such as electrostatic interactions or π–π stacking. The examples discussed here highlight the key structural features of the building blocks used and present an overview of the different types of nanostructures obtained with an emphasis on the functional properties of the resulting materials.

6.1 Introduction

In recent years self-assembly [1] has become an important strategy for the generation of a wide variety of materials with exciting functionalities. The forces that drive the self-assembly of the corresponding building blocks are based on a variety of non-covalent interactions. Although such interactions are comparatively weaker than covalent bonds, by working in unison they provide sufficient stability to the self-assembled structures. Hence, self-assembly is also the strategy of choice in biological systems to generate intricate superstructures which are essential to our living systems [2]. Functional materials generated by self-assembly are adaptable [3] and respond to external stimuli. On the contrary, the materials obtained through

S. Banerjee · C. Schmuck (✉)
Institute of Organic Chemistry, University of Duisburg-Essen, Universitaetsstrasse 7, 45141 Essen, Germany
e-mail: carsten.schmuck@uni-due.de

Z. Li and L. Wu (eds.), *Hydrogen Bonded Supramolecular Structures*,
Lecture Notes in Chemistry 87, DOI 10.1007/978-3-662-45756-6_6

conventional covalent synthesis are comparatively more robust but also more difficult to process and recycle.

Among the different kinds of non-covalent interactions, H-bonding is one of the most frequently utilized interactions in nature. This stems from the strength, specificity, and directionality of H-bonds compared to other non-covalent interactions (at least under some specific conditions). But the use of H-bonds for the generation of synthetic nanostructures has mainly been restricted to organic non--polar solvents [4–7]. In aqueous and polar media, the hydrogen bonding donor and acceptor fragments are well solvated and hence, the strength of the H-bonds is reduced considerably. But for real-life applications, self-assembly has to occur also in aqueous media. Hence, a significant effort has been directed in recent years toward the design of assemblies in polar or aqueous media utilizing H-bonding. In biological systems, H-bonds are shielded from the competing water molecules within hydrophobic microenvironments (e.g., within a protein). Implementing a similar principle in synthetic systems, the H-bonds are generally strengthened by coupling with hydrophobic (solvophobic) interactions, π-stacking, or charge interactions.

In this chapter, we specifically focus on supramolecular nano-assemblies that have been designed for aqueous and polar organic media utilizing H-bonding as one of the driving forces. We concentrate on some illustrative selected examples from the last 5–6 years, mainly examples in which small molecular building blocks have been employed to generate nano-assemblies. Examples from peptide amphiphiles and other peptide-based molecules, block copolymers and other polymeric systems, etc. have not been included. For convenience, we have divided this chapter based on the type of nanostructures/nanomaterials obtained through self-assembly.

6.2 Nucleobase Pairing and Nanostructure Formation in Water

The DNA duplex structure is stabilized by H-bonding and π-stacking between the complementary base pairs. In enzyme pockets, even short oligonucleotides can form base pairs as the H-bonds are shielded from the water molecules by the hydrophobic microenvironment within the protein surrounding. The situation, however, is dramatically different for small molecules in aqueous media. For example, the three hydrogen bonds in a single Watson-Crick G·C nucleobase pair are not strong enough to drive their association and H-bonds between individual nucleotides or nucleobases are not observed in aqueous media until higher order oligomers are employed (ca. $n \geq 4$) [8]. To obtain stable self-assembly even for single nucleobases, the hydrophobic shielding of an enzyme pocket has to be mimicked. We herein discuss two such examples; in one case H-bonding between individual mononucleotides has been achieved in a hydrophobic cavity in aqueous

media and in the other case multiple nucleobase derivatives self-assemble to form a stacked aggregate stabilized by an organized array of H-bonds.

Fujita and coworkers cleverly utilized the artificial hydrophobic cavity of self-assembled coordination cages of pyrazine pillars to encapsulate nucleobases (Fig. 6.1) and demonstrated that it is possible to form anti-Hoogsteen base pairs between 5′-adenosine (A) and 5′-uridine (U) monophosphates in aqueous media [9]. The cages possess interplanary distance of 6.6 Å suitable for the accommodation of planar aromatic molecules. The encapsulation of the guests is driven by hydrophobic interactions, π–π stacking, and electrostatic interaction between the anionic guests and the cationic host. Once encapsulated, the complementary nucleotides form H-bonds within the hydrophobic cavity. The **5**·**6** pair was thus found to bind more strongly than either the $\mathbf{5}_2$ or $\mathbf{6}_2$ pairs due to this additional H-bonding.

The host-guest complexation and base-pair formation were investigated using ^{1}H NMR spectroscopy. Aqueous solutions of 5′-adenosine monophosphate (**5**, 2.0 μmol) and 5′-uridine monophosphate (**6**, 2.0 μmol) were stirred in the presence of cage **1** (2.0 μmol). The nucleobase protons of 5 and 6 exhibited noticeable upfield shifts (−0.68 and −1.81 ppm for adenine H8 and H2 of **5**; −0.19 and −0.85 ppm for uracil H6 and H5 of **6**). Among the ribose protons, H1′ of **5** and **6** were shifted (−1.08 and −1.01 ppm, respectively) (Fig. 6.2b, c), but only negligible shifts were observed for the protons H2′ to H5′ of both **5** and **6**. These observations clearly suggested that the nucleobases were encapsulated inside the cavity but the ribose moiety still remained exposed to the outside environment.

Furthermore, the formation of anti-Hoogsteen type of base pairing between **5** and **6** was ambiguously proved by X-ray single crystallography. Due to higher crystallinity, an analogous Pt (II) cage **2** containing (S, S)-1,2-diaminocyclohexane as an ancillary ligand was used. The crystal structure of 2 ⊃ (**5**·**6**) clearly showed that **5** and **6** formed anti-Hoogsteen base pairs within the cage (Fig. 6.3). The N7 (A)···N3(U) distance is 2.92 Å and the NH2(A)···O(U) distance is 2.88 Å. The

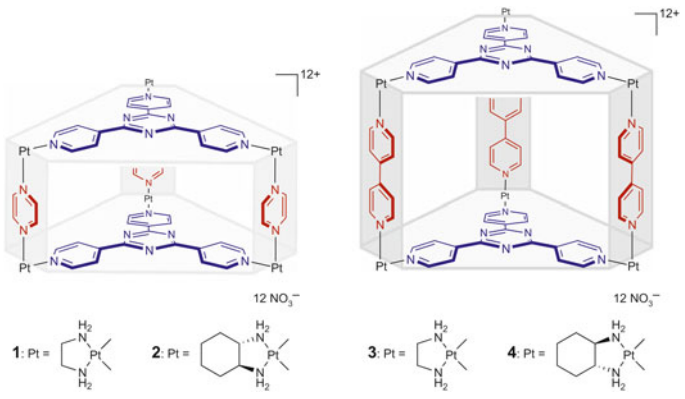

Fig. 6.1 Structures of the organic pillared coordination cages **1**–**4**. Reprinted by permission from Macmillan Publishers Ltd: Ref. [9], copyright 2009

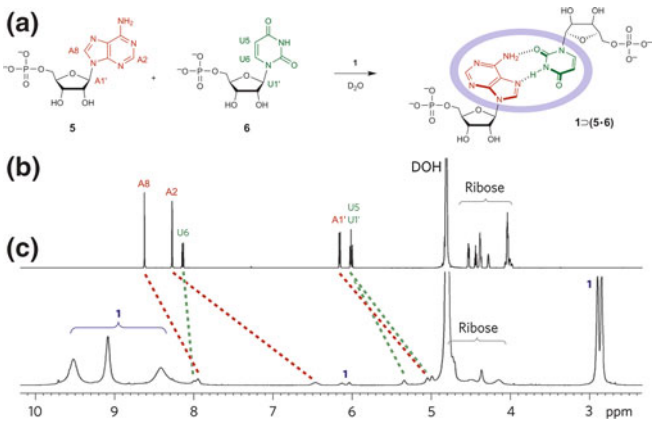

Fig. 6.2 ^{1}H-NMR spectroscopic observations for the formation of the **5**·**6** nucleotide base pair. **a** Schematic representation of nucleotide base-pair formation. **b** ^{1}H-NMR spectrum of a 1:1 mixture of **5** and **6** in D_2O solution at room temperature. No interactions between **5** and **6** are observed. **c** ^{1}H-NMR spectrum of **1** ⊃ (**5**·**6**) in D_2O solution at room temperature. Reprinted by permission from Macmillan Publishers Ltd: Ref. [9], copyright 2009

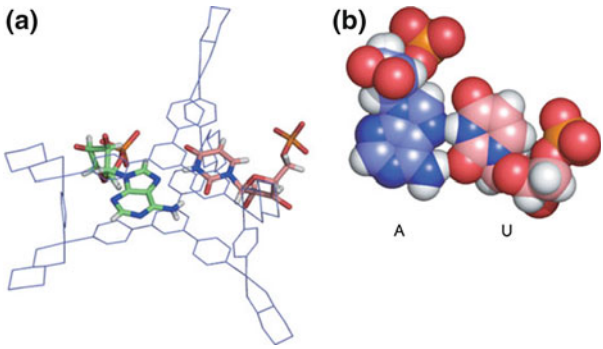

Fig. 6.3 **a** Wire-and-stick representations of **2** and the **5**·**6** base pair. **b** Space-filling representation of the **5**·**6** base pair only. For clarity, counter-ions and solvents are omitted from these diagrams. Reprinted by permission from Macmillan Publishers Ltd: Ref. [9], copyright 2009

planar AU base pair was situated comfortably within the cavity stabilized by π–π interactions (approximately 3.3 Å) with the cage's triazine panels. The crystal structure also showed that although the base-pair was encapsulated within the cavity, the ribose monophosphate tails remained outside as also determined by NMR spectroscopy. The same group later reported the encapsulation of a single Watson-Crick G·C base pair in aqueous solution inside the cavity of cage **1** and studied the specific interactions of anions and water molecules with this isolated base pairs through X-ray crystallography [10].

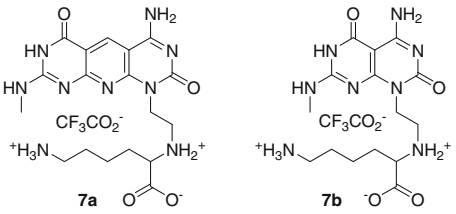

Fig. 6.4 Hybrid G^C motifs **7a** and **7b**

Fenniri and coworkers reported water-soluble J-Type rosette nanotubes with high molar ellipticity using a G^C motif [11], a hydrophobic base unit containing the Watson-Crick donor-donor-acceptor (DDA) H-bond array of guanine and acceptor-acceptor-donor (AAD) of cytosine [12]. This motif undergoes a hierarchical self-assembly process in water forming a six-membered super-macrocycle held together by 18 H-bonds. The more hydrophobic rosettes further assemble to form a linear stack named as rosette nanotube (RNT) [13–15]. Hence, the formation of RNT is driven by a combination of H-bonding and hydrophobic interactions. Here, the authors have utilized a tricyclic variant which possesses the same H-bonding arrays, but separated by an internally fused pyridine ring (Fig. 6.4). The idea was to have a RNT with a higher diameter and a larger π system that can allow electronic transport along the RNT's main axis.

Characterization of **7a** by SEM (Fig. 6.6) revealed that this tricyclic compound rapidly self-assembled into RNTs (Fig. 6.5) when dissolved in water at room temperature (pH = 2.8). TM-AFM and TEM images (Fig. 6.6) showed that the RNT's outer diameter is 4.2 ± 0.2 nm and 4.4 ± 0.2, respectively. These values are in excellent agreement with the theoretical value of 4.3 nm.

The self-assembly process was monitored by time-dependent CD and UV-Vis spectroscopy. The CD spectra of **7a** (2.1×10^{-5} M) contain two bands at 264 and 388 nm (Fig. 6.7). The intensity of the CD signal increased dramatically (40 fold) when kept for 7 days reaching a giant molar ellipticity of 4×10^6 deg M^{-1} m^{-1} unprecedented so far for a chiral helical stack [16–18]. Heating the solution to 100 °C or addition of acid resulted in a complete disappearance of the CD signal thus suggesting that the induced CD originated from the supramolecular chirality of RNT's. UV-Vis spectra of **7a** and **7b** showed that there was a pronounced red shift in the former case. Additionally, **7a** showed a unique, sharp, and lower energy band at 388 nm. As the intensity of this narrow and red-shifted band decreased with increasing temperature, dilution, and addition of acid, the authors proposed that **7a** probably assumed a J-type arrangement within the RNTs. This was further supported by the fact that the newly formed red-shifted J band coincided with the extremely strong CD band. This indicates a strong coupling of the electric dipole transitions between the adjacent molecules in the RNT's resulting from a higher polarizability, a larger π electron surface and more precise arrangement of the dipole moments of **7a** relative to the parent module **7b**.

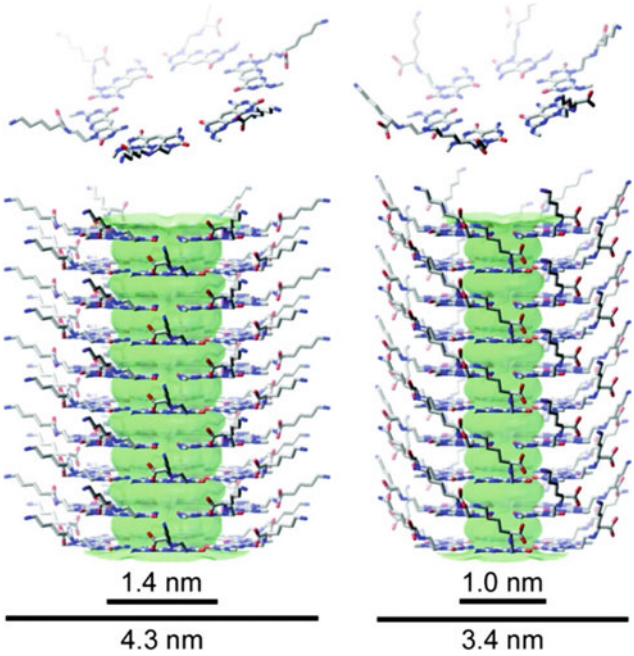

Fig. 6.5 Hexameric rosettes (*top*) and RNTs (*below*) from **7a** and **7b**. Reprinted with the permission from Ref. [11]. Copyright 2010 American Chemical Society

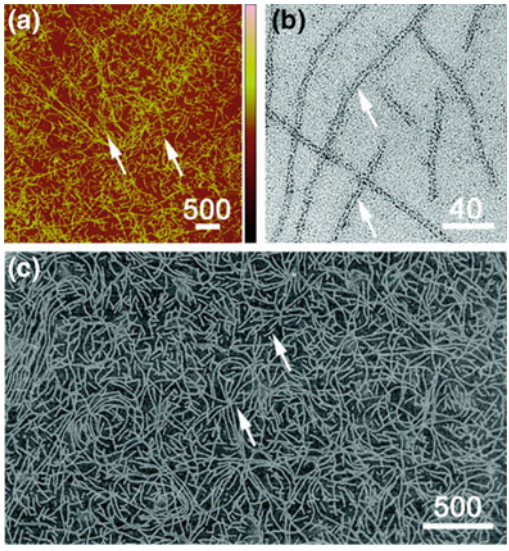

Fig. 6.6 Imaging of **7a** RNTs (0.1 mg/mL in water) by **a** TM-AFM (5 μm scan, height scale) 0–10 nm), **b** TEM, and **c** SEM. *White arrows* point to individual RNTs; *scale bars* in nm. Reprinted with the permission from Ref. [11]. Copyright 2010 American Chemical Society

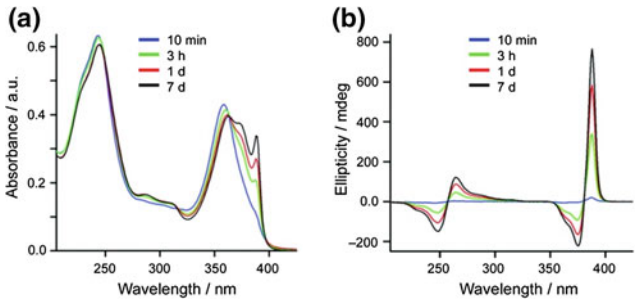

Fig. 6.7 **a** UV-vis, **b** circular dichroism spectra of **7a**-RNTs (ca. 2×10^{-5} M in water). Reprinted with the permission from Ref. [11]. Copyright 2010 American Chemical Society

6.3 Self-sorting/Orthogonal Self-assembly

One fascinating aspect of biological systems is that different parallel processes occur in a controlled way at the same time without affecting each other. Sugars, amino acids, and fatty acids assemble to form large aggregates which self-sort through a series of very efficient but complex processes to ultimately build a cell, the essential unit of life. In a cell, multiple levels of compartmentalization arising from the self-sorting of their molecular components allow the coexistence of different functional architectures acting independently [19, 20]. This idea has been implemented to design mimics of the natural systems. In this section, we will discuss a few examples in which self-sorting and orthogonal self-assembly was achieved utilizing H-bonding in combination with other non-covalent interactions.

One recent example of self-sorting in an artificial system in aqueous media mediated by H-bonding is reported by Sijbesma et al. [21]. They described the formation of multiple hydrophobic compartments from mixtures of urea bolaamphiphiles (UnU, Fig. 6.8) which form rod-like micelles stabilized within the membranes by H-bonds between the urea moieties. The self-sorting behavior of these

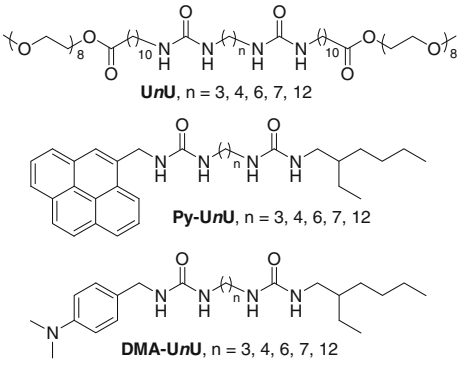

Fig. 6.8 Urea bolaamphiphiles used for self-sorting of rod-like micelles

micelles was investigated by employing two fluorescent probes, Py-UnU and DMA-UnU, which display exciplex emission when they are in close proximity to each other. When these probes were added to micelles made from the different bolaamphiphiles, the dynamically co-existing micelles specifically bind only to their corresponding guest counterparts. The observed specificity in the inclusion of the guests is governed by the efficient H-bonding between the bis-urea segments in the hydrophobic compartment of the micelles. The oligoethyleneglycol-bisurea bolaamphiphiles U3U, U4U, U6U, U7U formed stable micelles upon dissolution in water (up to ~3 % w/v). When two separately prepared micellar solutions of U4U (4 mM) containing 0.01 equiv of Py-U4U and 0.15 equiv of DMA-U4U, respectively were mixed, an exciplex band at 520 nm was observed which grew over time following a first-order kinetics. Interestingly, when the same experiment was performed with the DMA-U4U probe incorporated in the U6U micelles, the rate constant of exciplex formation was found to be the same, but the final emission intensity was twice as high suggesting that the probes are confined to half the micellar space. On the other hand, when non-matching micelles U4U (containing 0.01 equiv of Py-U4U) and U6U (containing 0.15 equiv of DMA-U6U) were mixed, no indication of exciplex formation could be observed. These observations clearly suggest that U4U and U6U bolaamphiphiles form separate rod-like micelles and that the probes were selectively confined to their matching micelles (Scheme 6.1).

The same group later on extended the aforementioned concept to demonstrate self-sorting based on chiral recognition in the trans-1,2-bisureido cyclohexane moiety [22]. For this purpose, bolaamphiphiles USU and fluorescent probes Py-USU, DMA-USU, Naph-USU, and their corresponding R-stereoisomers were designed (Fig. 6.9). USU and URU formed stable rod-like micelles in water with CMC values around 7×10^{-6} M. The pyrene and dimethylaniline probes were used to investigate the self-sorting behavior of the micelles. It was observed that when DMA-USU (final concentration 15 mol% with respect to the total amphiphile) was titrated into a binary solution of USU and URU (2 mM each) containing Py-USU

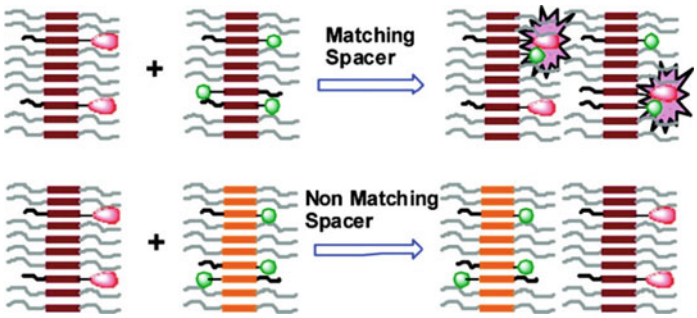

Scheme 6.1 Cartoon of the use of exciplex fluorescence to probe the self-sorting in the bisurea rod-like micelles. Reprinted with the permission from Ref. [21]. Copyright 2010 American Chemical Society

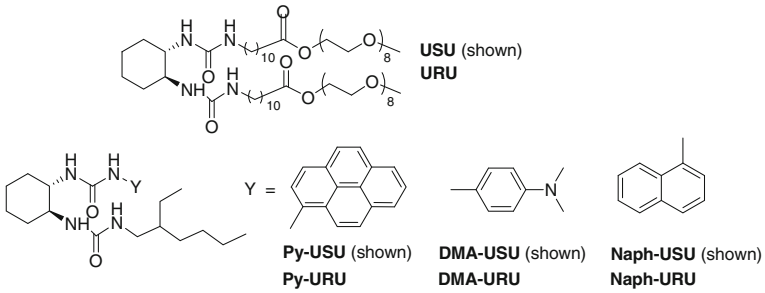

Fig. 6.9 Chiral bolaamphiphiles and the fluorescent probes

(0.5 mol%), formation of an exciplex band was observed whereas the addition of DMA-URU did not show any exciplex formation. This clearly suggested that in the solution, there are coexisting micelles which recognize their matching amphiphiles. Furthermore, when matching micelles of USU (containing 0.5 mol% Py-USU or 15 mol% of DMA-USU) were mixed, exciplex formation was observed. However, mixing non-matching micelles of USU (containing 0.5 % of Py-USU) and URU (containing 15 mol% of DMA-URU) did not result in the exciplex band. These observations again pointed out the fact that USU and URU form separate rodlike micelles.

Along with the complementary intermolecular interactions, compartmentalization in natural systems also results from the incompatibility of the components leading to micro phase separation as observed in the case of protein folding and biological membrane. van Esch and coworkers [23] demonstrated that an orthogonal self-assembly approach can be employed to generate a system in which different structures co-exist resulting from multiple components. In this particular case interpenetrating networks along with vesicular structures were shown to exist in the fibrous network of a hydrogel. Low-molecular weight hydrogelators derived from a modular 1,3,5-cyclohexyltricarboxamide moiety were chosen [24, 25]. As can be seen from Scheme 6.2, the main structural feature of the gelators includes a hydrophobic core surrounded by successive hydrophilic and hydrophobic segments. Their self-assembly is thus driven by hydrogen bonding and hydrophobic interactions. The properties of the resultant hydrogels can be varied by choosing different peripheral functionalities (solvophilic and pH responsive groups).

The authors first investigated whether the hydrogels resulting from **8a–d** (Scheme 6.2) were compatible with various surfactants. To test this, the gelators were dissolved in surfactant solutions above their critical gel-sol transition temperatures (T_{gel}). The surfactants which were chosen included CTAB or SDS (both of them form spherical micelles) or CTAT (known to form both spherical and elongated/entangled micelles depending on its concentrations) and three zwitterionic lipids (DOPC, DPPC, and DMPC). Other than the combination of **8a** and SDS which formed a precipitate, all other combinations resulted in the formation of transparent hydrogels.

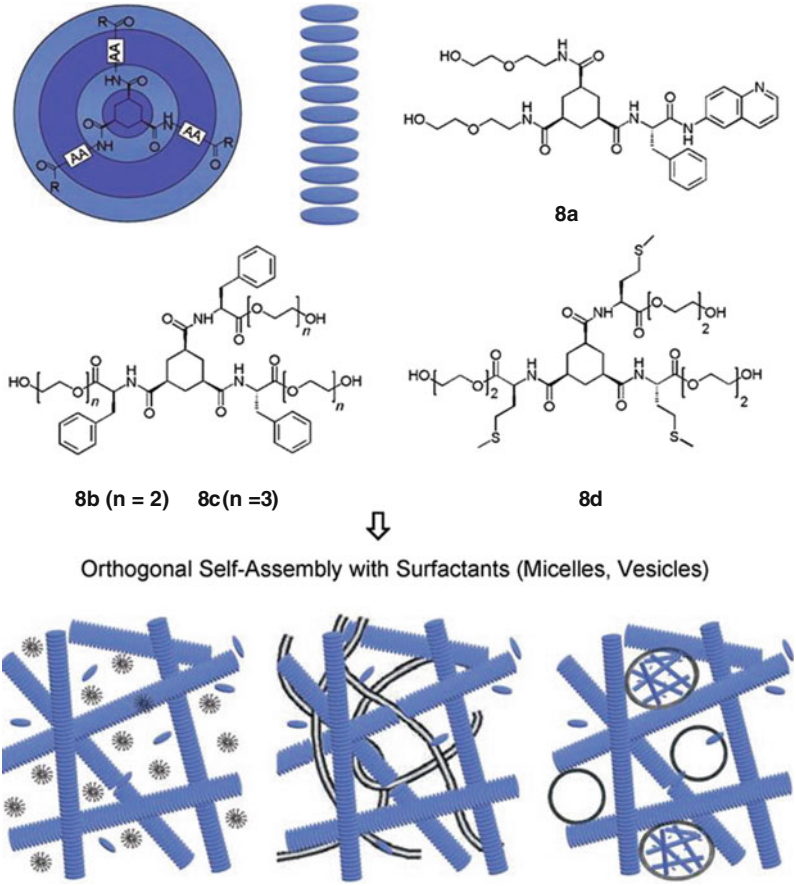

Scheme 6.2 Schematic representation of hydrogelators, which self assemble preferentially in one dimension. *Lighter* regions correspond to hydrophilic groups and *darker* areas to hydrophobic entities (*AA* amino acids). Chemical structures of hydrogelators **8a–d** are based on 1,3,5-cyclohexyltricarboxamide. Reproduced with permission from Ref. [23], copyright 2008 WILEY-VCH Verlag GmbH & Co. KGaA, Weinheim

Hence, it was evident that the hydrogel formation was unperturbed at the macroscopic level in the presence of surfactants. But it was also important to know whether the aggregation property of one component was influenced by the other at the supramolecular level. Interestingly it was found that the CMC of C_{14}TAB or SDS did not change in the hydrogels of **8a** and **8b**, as revealed by the conductivity measurements. DSC also revealed that for the lipid DPPC in the hydrogel of **8a,** there was no noticeable change in its phase transition temperature. In contrary, the presence of the surfactants in the hydrogels reduced the thermal stability (decrease in the T_{gel} values) of the gels. The extent of destabilization was found to be dependent on the morphology of the surfactant aggregates. For example, the

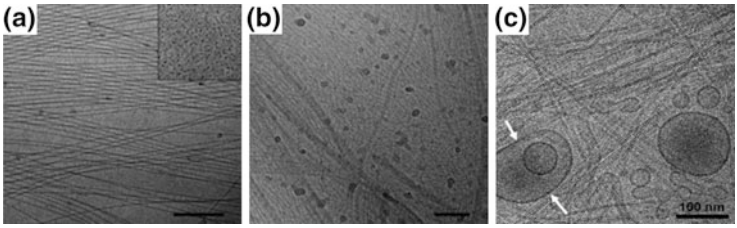

Fig. 6.10 Cryo-TEM images of fibrous networks of **a 8a** (4 mM) coexisting with spherical micelles of C_{14}TAB at 20 mm; **b 8b** (4 mM) in the presence of CTAT at 100 mm (cylindrical micelles) and **c** unilamellar DOPC vesicles coexisting with a network of well-defined fibers of **8a** with a high aspect ratio. *Scale bar* is 100 nm. Reproduced with permission from Ref. [23], copyright 2008 WILEY-VCH Verlag GmbH & Co. KGaA, Weinheim

incorporation of lipid bilayers led to a higher destabilization compared to that of micelles. The co-existence of different morphologies through orthogonal self-assembly was clearly observed from the cryo-TEM images (Fig. 6.10).

Although block copolymers have been used quite frequently to generate systems where multiple compartments exist together, the examples of such systems derived from small molecule amphiphiles are rather rare. Boekhoven et al. reported an example of such a system in which a gelator segment is connected to a surfactant segment (Scheme 6.3) through a hydrophilic linker [26]. This "multi-segment amphiphile" **9c** is capable of undergoing microphase separation phenomenon at the molecular length scales and behaves as a small molecule "block copolymer". The amphiphile was designed from a previously reported gelator **9a** belonging to the aforementioned 1,3,5-cyclohexyltrisamide based gelators (Scheme 6.3). Upon cooling the hot solution of **9c** to room temperature, a viscous transparent solution was obtained below 0.25 mM whereas a turbid gel formed above 5 mM. The critical gelation concentration (CGC) of **9c** was found to be comparable (7 mM) to the parent hydrogelators **9a**. FT-IR showed that the N–H and C=O vibrations in the xerogel appeared at wavenumbers characteristic for the hydrogen-bonded systems.

To find out what the effect of the C8 tail on the stability of the gel is, the thermal stability of the gels of **9a** and **9c** was compared. Below concentrations of 15 mM, the T_{gel} values for **9c** were higher than that of **9a**. The higher stability might result from the additional hydrophobic interactions between the C8 tails. A detailed morphological investigation of the gelator **9a** and the amphiphile **9c** was carried out using cryo TEM. The TEM images of the gels of **9a** revealed the presence of fibers and extended sheets in the concentration range 0.25–1.0 mM. These observations were also supported by the turbidity and viscosity studies. The fibers and sheets exhibited quite high dispersity ranging from 50 to 500 nm.

The multisegment amphiphile **9c**, on the other hand, showed mainly monodisperse, elongated fibers of 9 nm at a concentration of 0.25 mM along with some thinner fibrils of 3 nm. But increasing the concentration above 0.25 mM resulted in the formation of polydisperse, twisted tapes of diameters ranging from 50 to 200 nm. At high magnifications it could be seen that the tapes have a periodic fine

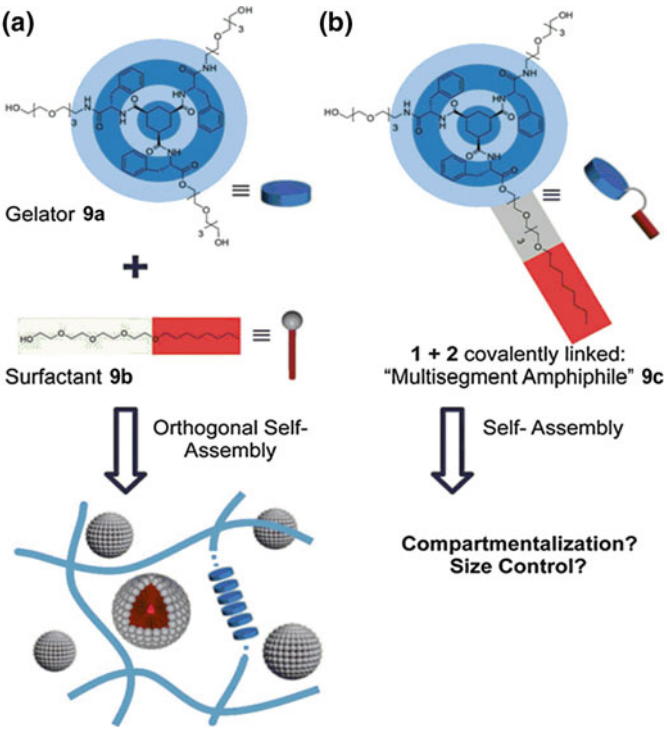

Scheme 6.3 **a** Schematic representation of hydrogelator **9a** and micelle forming surfactant **9b**, which undergo orthogonal self-assembly into their individual architectures. **b** Multisegment amphiphile **9c** is expected to give assemblies with structural features and compartments inherited from the parent compounds **9a** and **9b**. Light areas represent hydrophilic domains whereas dark areas represent hydrophobic domains. Reproduced from Ref. [26] by permission of The Royal Society of Chemistry

structure of parallel stripes with respect to the long fiber axis with a spacing ~3 nm (comparable to the diameter of the thinner fibrils observed in samples with a concentration below 0.25 mM). The 3 nm fibrils correspond quite well to the diameter of a discotic molecule of the gelator and most likely result from the single stacks of the molecules of **9c** hydrogen bonded in the z-direction. These thinner fibrils subsequently associate into parallel bundles resulting in 9 nm fibers stabilized by hydrophobic interaction between the aliphatic chains (a schematic representation of the self-assembly is shown in Fig. 6.11).

In an extension of the above work the same group later demonstrated that by using suitable small molecular chaperone analogues it is possible to switch off the self-assembly of one of these segments in the multisegment amphiphile **9c** in a selective fashion which results in structures characteristic of the other segment [27]. The authors postulated that by using a surfactant or a co-solvent, the hydrophobic interactions can be weakened whereas urea or hexafluoroisopropyl alcohol (HFIP)

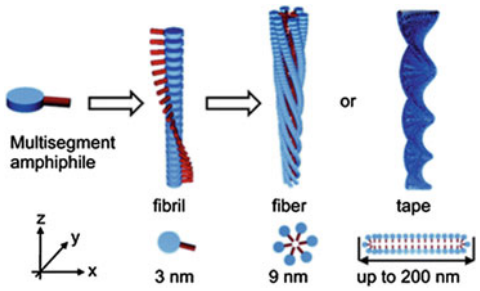

Fig. 6.11 Schematic representation of the self-assembly of **9c** into fibrils hydrogen bonded in the z-direction. Additionally, due to hydrophobic interactions between the surfactant segments, 5–7 fibrils assemble into 9 nm fibers or up to 200 nm tapes depending on the concentration. Reproduced from Ref. [26] by permission of The Royal Society of Chemistry

can break the hydrogen-bonding network. It was noted that when the surfactants were added in excess of their critical micellar concentration (CMC values), the critical concentration required to form a gel (CGC) was reduced. Interestingly, the transparency of the gels improved noticeably in the presence of surfactants above their CGCs. The parent gelator **9a** on the other hand showed only marginal changes in the properties of its gels in the presence of much higher amount of surfactants (100 mM CTAB or surfactant **9b**). To ensure that the morphology changes in the gels did not result from the aggregation resulting from the added surfactants themselves, EtOH was added as the chaperone analogue. As observed with the surfactants, the addition of EtOH also reduced the turbidity of the gels drastically. These observations indicate that in the presence of the chaperone analogues, the surfactant segment does not participate in the aggregation process although the hydrogen-bonding interactions between the gelator segments remain intact as evidenced from the C=O vibrations (FTIR study). In the presence of CTAB and **9b**; this vibration appeared at wavenumbers characteristic for hydrogen-bonded amides.

The co-aggregation process between the amphiphile and the surfactant was further investigated by recording the TEM images of the gels at different surfactant concentrations (Fig. 6.12). For example, with increasing concentrations of CTAB the tapes slowly disappeared with the appearance of monodisperse fibers of 6.6 ± 1 nm diameters. The dissociation of the twisted tapes into smaller fibrils increased the number of the fibrils per unit volume which probably led to the observed decrease in the CGC. But upon addition of further CTAB, the length of these fibers decreased which explains the observation of a higher CGC at higher CTAB concentrations. Similar observations were also noted from the studies with the surfactant **9b**.

Similar morphological transitions could also be effected by the addition of HFIP at room temperature and at a time scale faster than that observed for the addition of surfactants. In this case (a similar observation was noted when urea was added), the gel transformed into a transparent solution. FTIR studies showed that the C=O vibrations now appear at wavenumbers characteristic for amide groups hydrogen

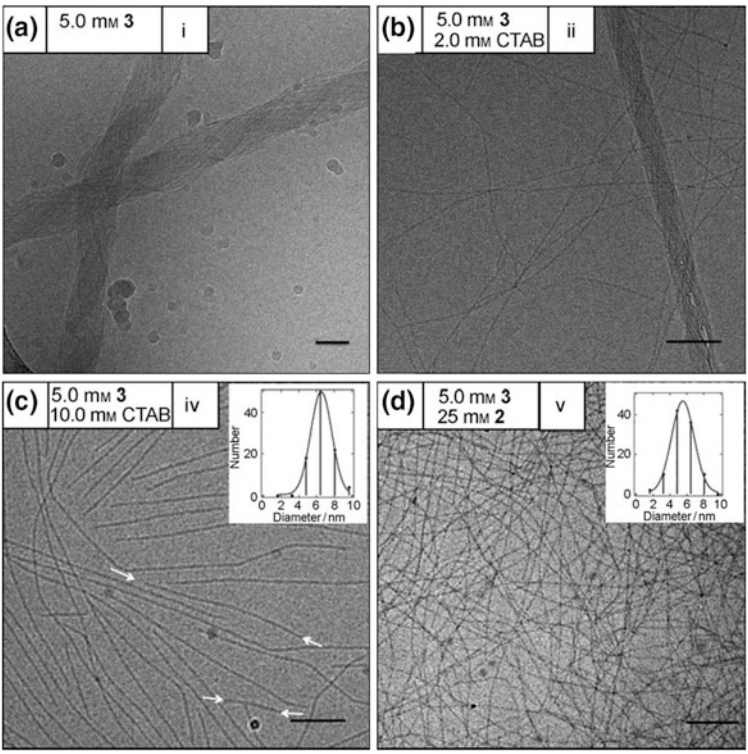

Fig. 6.12 Cryo-TEM images of: **a** gel of **9c** at 5.0 mM showing twisted tapes with diameters up to 100 nm; **b** gel of 5.0 mM **9c** and 2.0 mM CTAB showing both bundles of fibers and smaller 6.6 ± 1 nm fibers; **c** gel of 5.0 mM **9c** and 10.0 mM CTAB showing only 6.6 ± 1 nm fibers, increasing the CTAB concentration leads to the formation of shorter fibers (*white arrows*); **d** gel fibers of 5.0 mm 3 and 25 mm 2 showing 5.5 ± 1 nm fibers (v). The *insets* in Fig. 6.12c, d show the statistical distribution of fiber diameters and the Gaussian fit. All *scale bars* are 100 nm. Reproduced with permission from Ref. [27], copyright 2011 WILEY-VCH Verlag GmbH & Co. KGaA, Weinheim

bonded to HFIP. Cryo-TEM images of the samples containing urea or HFIP revealed the presence of micelles. These clearly pointed out the fact that by using small molecule-based chaperone analogues it was possible to switch off the self-assembly of one of the two segments. The morphological transition from twisted tapes to thinner fibrils in the presence of the surfactants is similar to what is obtained only from the gelator fragment of the amphiphile. In other words, the addition of the surfactants did not affect the hydrogen-bonding interactions between the gelator fragments as the surfactant molecules do not inhibit or compete with the hydrophobic interactions that are responsible for the formation of twisted tapes from the thinner fibrils. On the contrary, the addition of HFIP or urea switched off the H-bond induced self-assembly of the gelator fragment and hence, the samples only showed the presence of micelles as expected from the self-assembly of the

surfactant fragment. Interestingly, the typical dynamics of self-assembly process of each segment were also retained, for example, slow morphological transition for the gelator segment and fast dynamics for the surfactant segment.

6.4 Supramolecular Polymers

Supramolecular polymers in which the building blocks (monomers) are connected to each other through a variety of non-covalent interactions have gained a significant interest in the recent years. Owing to the dynamic and reversible interactions that hold the polymer backbone together, these polymers possess several advantageous properties compared to their traditional covalent analogues. These include responsiveness to external stimuli, recyclability, and self-healing properties [28]. But controlling the polymer size and stability has remained a challenging task especially in aqueous and polar media. In the following sections, a few recent examples of supramolecular polymers in which H bonds play a crucial role will be discussed.

Meijer and co-workers demonstrated that by tuning the ionic character of C_3-symmetrical discotic amphiphiles, the shape, size, and stability of their helical columnar aggregates can be controlled in aqueous media [29]. The molecular structure of the building blocks was based on the well-known benzene-1,3,5-tricarboxamide (BTA) core that has been previously shown to self-assemble into triple hydrogen-bonded helices [30]. The authors attached a fluorinated L phenylalanine and aminobenzoate spacer to the core to introduce additional H-bonding, π–π stacking, and solvophobic interactions so as to enhance the stability of the resultant assemblies (Fig. 6.13) [29]. More importantly, this modification allowed the creation of a hydrophobic pocket to shield the hydrogen bonds increasing their strength. Among the three discotics that were synthesized, compound **10** was based on the M(III)-DOTA (1,4,7,10-tetraazacyclododecane-N,N′,N″,N‴-tetraacetic acid) monoamide chelate which is a neutral complex. Compounds **11** and **12** are both DTPA (diethylenetriaminepentaacetic acid) derivatives and contain three and six negative charges overall, respectively. Three paramagnetic discotics **10a**, **11**, and

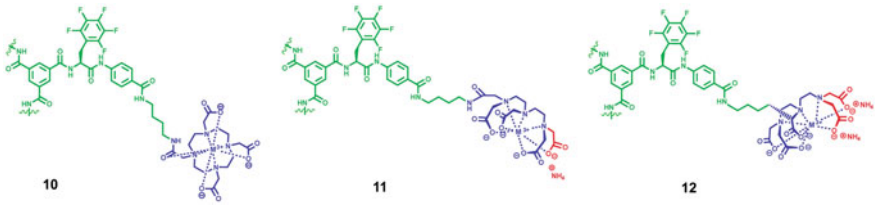

Fig. 6.13 Structures of the fluorinated discotic amphiphiles. Reproduced with permission from Ref. [29], copyright 2010 National Academy of Sciences, USA

12a from Gd(III) and two diamagnetic discotics **10b** and **12b** were prepared from Y(III) (Fig. 6.13).

The idea of increasing the ionic character of the peripheral M(III) complexes is to control the one-dimensional growth of the stacks through electrostatic repulsions. The shape and size of the supramolecular aggregates were determined by SAXS studies. Discotic **10a** was found to form rod-like objects. The rod radii were approximately 3.1 nm which compared quite well with the radii of the flattened monomeric building blocks (R $\sim$ 2.9 nm). The lengths of the rods were larger than 75 nm at 1 mM and around 25 nm at lower concentrations. On the other hand, for the discotic **12a**, the data could be fitted using a homogenous monodisperse spherical form suggesting the presence of aggregates with an aspect ratio close to 1. Cryo-TEM micrographs (Fig. 6.14) [29] further supported the data obtained from the SAXS measurements. The building block **10a** showed the presence of rod-like supramolecular polymers whereas discotic **12a** produced spherical objects. The helical nature of the aggregates from all the discotics was proved from the bisignate cotton effects observed in their CD spectra.

In an extension of the above work, the same group later varied the hydrophobic core and studied the effect of these structural variations on aggregate formation [31]. The discotics **13**–**15** (Fig. 6.15) were based on the highly charged peripheral M(III)–DTPA (diethylene tri-amine pentaacetic acid) which restricted the one-dimensional growth of the objects as already pointed out in the previous example. To see the effect of hydrophobic shielding of the hydrogen bonding motif, small, medium, and large Gd(III)- and Y(III)-DTPA discotics were synthesized. The aggregation behavior of the paramagnetic Gd(III) complexes was investigated by CD and UV-Vis spectroscopy, cryo TEM, and by longitudinal relaxation time (T_1) measurements. For the diamagnetic Y(III) discotic **15b**, ^{1}H NMR DOSY spectroscopy was also employed.

For the small discotic **13a**, the CD spectra did not show any cotton effect and also no aggregates could be observed from the cryo-TEM images. T_1 measurement performed for **13a** with varying Gd(III) concentrations between 0 and 18 mM also confirmed that the complex was in a molecularly dissolved state in the whole

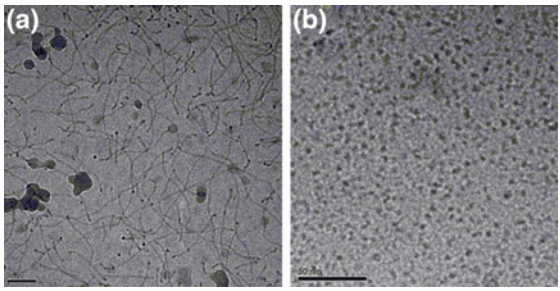

Fig. 6.14 Cryo-TEM images of **a 10a** (0.66 mM) and **b 12a** (1 mM). Both samples were vitrified at 288 K in citrate buffer (100 mM, pH 6). Reproduced with permission from Ref. [29], copyright 2010 National Academy of Sciences, USA

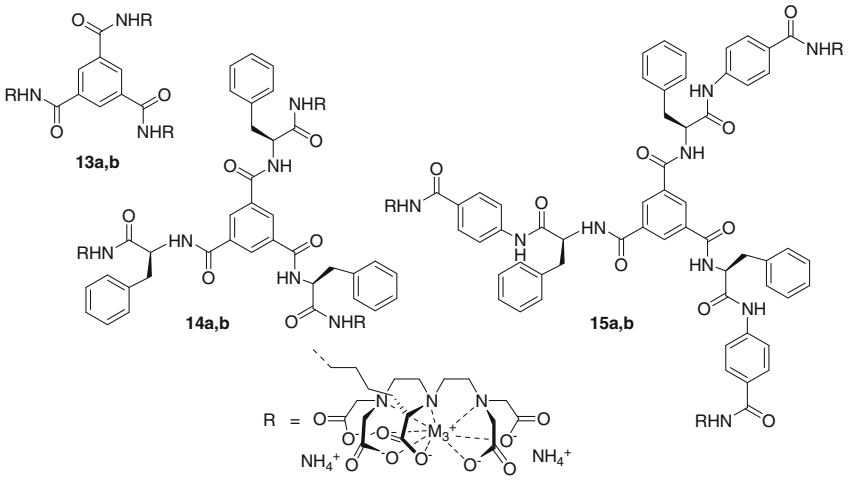

Fig. 6.15 Structures of the amphiphilic M(III)–DTPA discotics **13**–**15** (**13a**–**15a**): M(III) = Gd (III), **13b**–**15b**: M(III) = Y(III). Reproduced with permission from Ref. [29], copyright 2010 National Academy of Sciences, USA

concentration range. In case of the medium Gd(III) discotic **14a**, only aggregates of undefined size and shape could be visualized from the TEM images. CD spectra recorded at two different temperatures (293 and 363 K) for **14a** showed that in both cases the solutions were CD active but no concentration or temperature-dependence was observed. This suggests that probably the observed Cotton effect was inherent of the chiral discotics, rather than induced by the formation of aggregates. T_1 measurements performed between 0 and 13 mM of Gd(III) showed that around 0.27 mM the disks started aggregating.

The CD spectra of the large Gd(III) discotic **15a**, showed a bisignate cotton effect pointing out the presence of helical stacks. Small-angle X-ray scattering (SAXS) studies performed for the discotics **15a** or **15b** suggested the presence of homogeneous monodisperse spherical objects with radii of 2.9 nm in 100 mM citrate buffer at pH 6.0 or 2.5 nm in D_2O. ^{1}H-DOSY NMR and cryo-TEM measurements were also carried out for the diamagnetic Y(III) analogue **15b**. ^{1}H-DOSY NMR measurements in D_2O revealed that in a 2.8 mM solution of disk **15b**, the stacks are about 3.6 nm long (approximately eleven discotics were stacked on top of each other). Similar hydrodynamic diameters were reproduced from ^{1}H DOSY NMR experiments in buffered conditions. This is in good agreement with the diameter of about 5 nm of the spherical objects found from the cryo-TEM images. The noticeable difference in the aggregation behavior of the small, medium, and large discotics clearly suggests the importance of solvophobic effects and hydrophobic shielding in these supramolecular polymerizations.

Schmuck and co-workers reported the formation of supramolecular polymer from a small heteroditopic monomer **16** in DMSO and aqueous media which can be

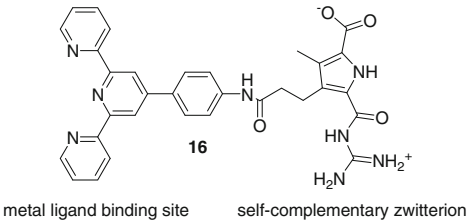

Fig. 6.16 Structure of the heteroditopic monomer **16**

switched between the monomer and polymer by applying two different external stimuli: pH and metal ions [32]. The monomer **16** (Fig. 6.16) contains a terpyridine ligand which is connected to a self-complementary guanidiniocarbonyl pyrrole carboxylate zwitterion. The zwitterion forms strong hydrogen-bond-assisted ion-paired dimers in polar solvents such as DMSO, with high stability ($K_{dim} > 10^{10}$ M^{-1}) and even in water, with reasonably high-dimerization constant ($K_a > 10^2$ M^{-1}) [33, 34]. In the presence of Fe(II), the ion-paired dimers are further converted into linear polymers.

Monomer **16** was transformed in a reversible manner from monomer **A** (the protonated chloride salt **16**·HCl) to the 2:1 metal complex **B** or to the ion-paired dimer **C** depending on the presence of Fe(II) ions or the pH value (Scheme 6.4). In the presence of both chemical stimuli, larger aggregates **D** were formed. As the zwitterion is only present in a narrow pH range of 5–7 (pK_a of the carboxylic acid and the guanidinium cation are 4–5 and 6–7, respectively), the dimer formation can be controlled in a reversible fashion by protonation/deprotonation. The metal ion can be removed in the presence of a competing ligand such as HEEDTA.

The formation of supramolecular polymers was evidenced from viscosity studies. When Fe(II) was added in a stepwise manner to a solution of the ion-paired dimer **C**, an increase in the viscosity was observed till 0.5 equivalents of Fe(II) were added. This suggests that in the presence of Fe(II), the initially present ion-paired dimer **C** was converted into the polymer **D** through the formation of a 1:2 Fe(II)-terpyridine complex. The relative viscosity of **D** was found to be significantly higher (η_{rel} = 1.22 at c = 8.5 mM), than either for the monomer **A** (c = 8.5 mM, η_{rel} = 1.02) or for the 2:1 metal complex **B** (c = 8.5 mM, η_{rel} = 1.04).

A concentration dependent viscosity study of polymer **D** was carried out to investigate the mechanism of the supramolecular polymer formation. A double-logarithmic plot of the specific viscosity ($\eta_{specific}$) against the concentration (Fig. 6.17) was made which showed two lines with distinct slopes of 0.56 and 1.17. Their intersection point gave a critical polymerization concentration (CPC) of $c \approx 0.35$ mM. The appearance of a CPC strongly suggested that the mechanism involved was a ring-chain polymerization mechanism [35, 36]. At lower concentrations (below CPC), cyclic oligomers predominate resulting in only small changes in viscosity in this regime. Above the CPC, the elongation of the chain length occurred at the expense of the cyclic structures and the formation of linear polymers

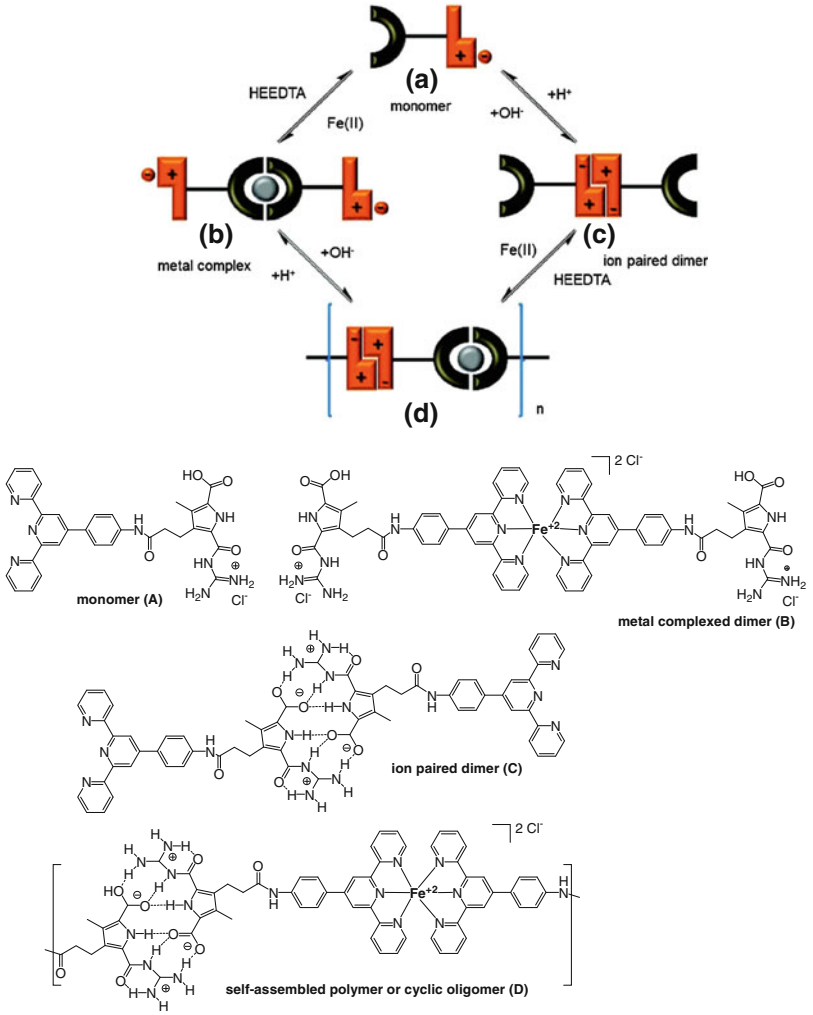

Scheme 6.4 Self-assembly of the heteroditopic monomer **16** based on two orthogonal binding interactions, metal-ligand binding, and ion-pair formation. Reprinted with the permission from Ref. [32]. Copyright 2011 American Chemical Society

leads to a steeper slope in the specific viscosity plot. The ring-chain model was supported from the TEM images recorded at different concentrations. For examples, the images recorded below CPC (0.1 mM) clearly showed the presence of small cyclic structures with diameters of 2–4 nm whereas above CPC (1 mM), linear polymer strands of around 1 nm thickness and lengths of more than 20 nm could be observed (Fig. 6.17). The existence of cyclic structures and linear polymers were also confirmed by DLS studies.

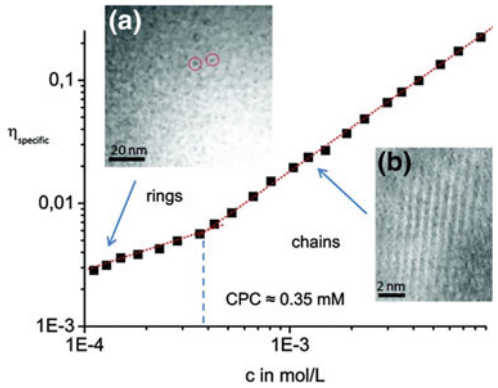

Fig. 6.17 Double-logarithmic plot of the specific viscosity ($\eta_{specific}$) versus the concentration of **D**, suggesting a ring-chain polymerization mechanism. The *insets* show TEM images recorded below (0.1 mM, a) and above (1 mM, b) the CPC, also confirming the predominant formation of cyclic and linear structures under these conditions. Reprinted with the permission from Ref. [32]. Copyright 2011 American Chemical Society

As the self-assembly of the monomer **16** is critically dependent on the presence of metal ions as well as the correct pH range, it could be reversibly switched by the addition of acid/base or by adding/removing the metal ion. Such changes could easily be monitored through UV-Vis spectroscopy in DMSO. The blue–violet color of the self-assembled cyclic oligomers **D** (c = 0.06 mM in DMSO) was completely decolorized by adding an excess of a competing ligand HEEDTA (10 equiv, N-(2-hydroxyethyl)ethylenediaminetriacetic acid), having a higher affinity for Fe (II) than terpyridine. As a result, the polymers **D** were transformed into the ion-paired dimer **C**. However, by adding an excess of Fe(II), the blue–violet color arising from the MLCT-band reappeared (reformation of the aggregates **D**). Similarly, the effect of protonation/deprotonation on the self-assembled aggregates was observed. The relative viscosity of η = 1.16 of the polymer **D** (6.8 mM in DMSO), decreased significantly to η = 1.04 when aq. HCl (100 μL, 1 M) (Fig. 6.18) was added as metal-complex dimer **B** was formed. After neutralizing by NaOH (100 μL, 1 M), the viscosity increased again. This occurred because now **B** was converted to the self-complementary zwitterion again, which subsequently dimerized and thus, the polymer **D** was reformed. This switching between **D** and **B** was completely reversible as further additions of acid or base resulted in the same changes in the viscosity.

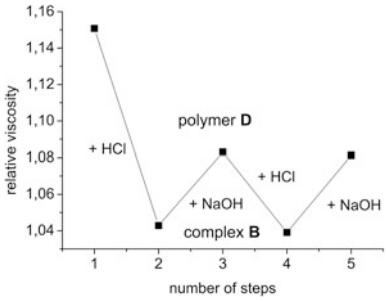

Fig. 6.18 Relative viscosity of a solution of polymer **D** ([**16**] = 6 mM in DMSO) upon stepwise addition of equal amounts of acid or base. Reprinted with the permission from Ref. [32]. Copyright 2011 American Chemical Society

6.5 Supramolecular Gels in Aqueous and Polar Organic Media

Supramolecular gels are a class of soft solid-like materials in which a liquid is entrapped by a 3D fibrous network formed by the self-assembly of low-molecular weight organic compounds. The reversible nature of the non-covalent interactions involved allows tuning of the functional properties of these gels. As a result, they have found applications in the design of hybrid materials, biomaterials, and sensors, for drug delivery and tissue engineering [37–41]. In this section, we will discuss two examples of responsive supramolecular gels in aqueous and polar media along with one example in which the kinetics of the formation of the fibers of a hydrogel could be controlled by using a catalyst.

Schmuck and co-workers reported a multi-responsive gel based on a quadruple zwitterionic molecule **17** in DMSO (Scheme 6.5) [42]. As mentioned previously, the zwitterionic moiety undergoes strong dimerization through H-bond assisted ion-pair formation in DMSO and the ion-pair formation is critically dependent on the pH of the medium. Utilizing this property, it was demonstrated that the gels showed dual pH responsiveness. The gels were transformed to sols by either adding acid or base and the original gels were restored back by neutralizing the excess acid or base. The four zwitterionic moieties were connected to a tetrahedral pentaerythritol core. As the arms are reasonably flexible, the molecule was present as two intramolecular ion pairs even at low concentrations ($\sim$0.5 mM). DOSY measurements at different concentrations clearly indicated a strong self-aggregation of the molecule. For example, at 1 mM, the diffusion coefficient (D) was found to be $D = 8.6 \times 10^{-11}$ m^2 s^{-1} which corresponds to a hydrodynamic diameter of 2.6 nm, comparable to the extended length of a single molecule of **17**. By increasing the concentration to 25 mM, a diffusion coefficient of 1.9×10^{-12} m^2 s^{-1} was obtained which is significantly lower ($\sim$45 fold) than that obtained at 1 mM. Such a drastic

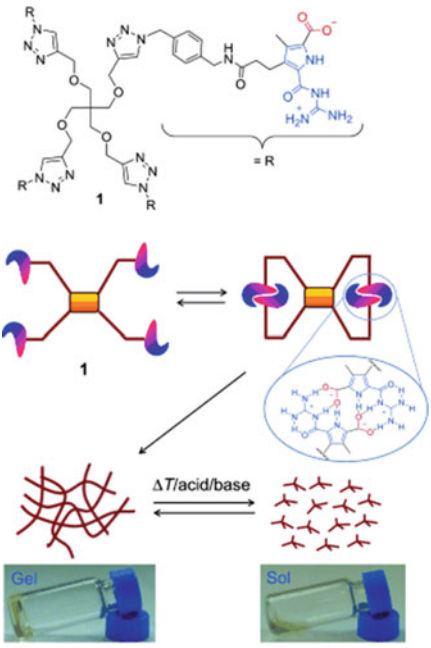

Scheme 6.5 Self-assembly of quadruple zwitterion **17** leads to a multiresponsive supramolecular gel in DMSO. The self-assembly and hence, the gel formation can be switched not only by temperature but also by the addition of either acid or base. Reproduced with permission from Ref. [42], copyright 2013 WILEY-VCH Verlag GmbH & Co. KGaA, Weinheim

decrease in the diffusion coefficient indicates that the molecule forms extended polymeric species at higher concentrations.

In agreement with this, the viscosity of the DMSO solutions of the quadruple zwitterion was found to be strongly concentration dependent. In the concentration range 1–15 mM, the viscosity change is gradual, but above 15 mM it increased rather sharply. The viscosity subsequently increased so much that in the concentration range 20–40 mM, it could no longer be measured. Gel formation was observed above 40 mM. The gels were visually transparent and exhibited excellent thermoreversibility: for example a 50 mM gel melted to sol by heating to 100 °C, but transformed into the gel again by cooling to room temperature. The strong pH dependence of the ion-paired dimer formation was utilized to impart multiresponsive behavior on the gels. For example, upon the addition of TFA or Et_3N (10 eqv), the gels were converted to sols. But these sols could be restored back to gels in a completely reversible manner by neutralizing the acid or base (Fig. 6.19).

Schmuck and coworkers [43] recently reported that by attaching the self-complementary guanidiniocarbonyl pyrrole carboxylate zwitterionic moieties to the amino groups of polyethyleneimine (PEI), the polymer can be converted to a pH switchable hydrogel. After functionalization (**18**, Scheme 6.6), PEI was transformed from a viscous liquid to a solid. Using the characteristic UV absorption of the GCP group, the approximate loading of the zwitterionic units onto the polymer was calculated to be 40 %. This was further confirmed by GPC analysis of the molecular mass of the functionalized polymer. The functionalized PEI polymer **18** was readily soluble in water but produced more viscous samples than that observed with PEI.

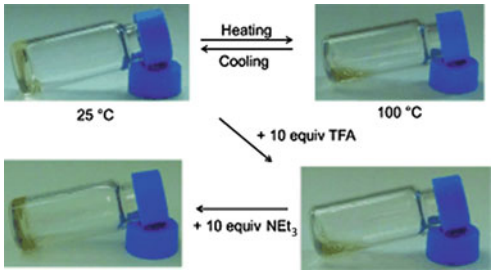

Fig. 6.19 Reversible gel–sol transitions of a gel of **17** in DMSO upon heating/cooling and by the addition of acid and base ([**17**] = 50 mM). Reproduced with permission from Ref. [42], copyright 2013 WILEY-VCH Verlag GmbH & Co. KGaA, Weinheim

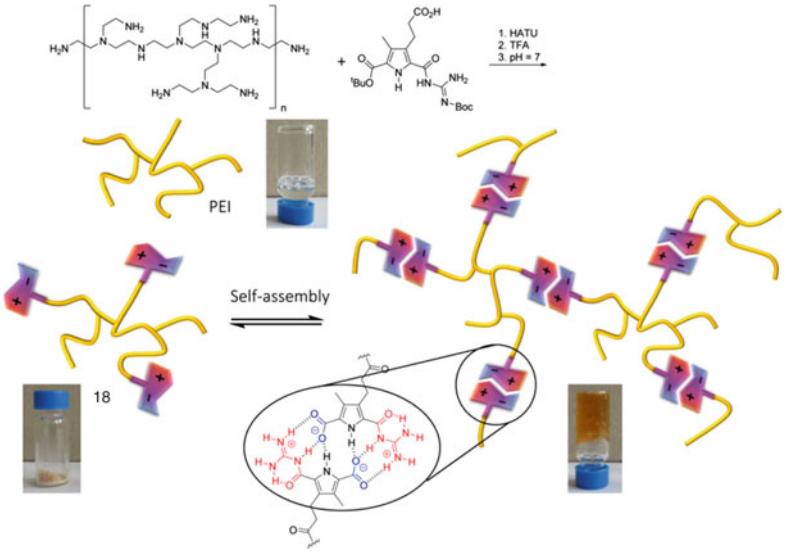

Scheme 6.6 The primary amino groups of polyethylenimine (PEI) can be functionalized with a self-complementary zwitterion by coupling with the protected precursor **18′**. The resulting hybrid material **18** forms a stable hydrogel in solution, because the zwitterions function as sticky ends, introducing additional supramolecular crosslinks into the material. Reproduced from Ref. [43] by permission of The Royal Society of Chemistry

The viscous solutions observed at lower concentrations were turned into transparent hydrogels at concentrations >160 mg/mL. This clearly suggested that the zwitterionic moieties in the main backbone of the polymer dimerize to produce supramolecular crosslinks between the polymer chains which immobilize the solvent.

AFM images of the functionalized and nonfunctionalized PEI, obtained by spin coating the solutions on mica surface were recorded in noncontact tapping mode. In case of PEI, only spherical aggregates of varying size on the surface (Fig. 6.20a) were

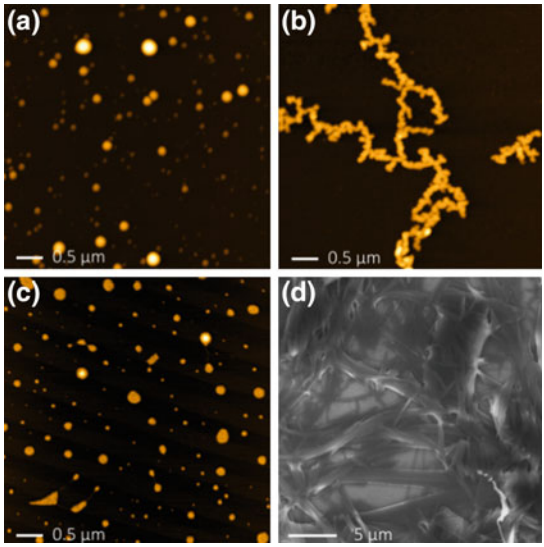

Fig. 6.20 AFM height images of PEI (**a**), **18** at pH = 7 (**b**) and pH = 3 (**c**) ([**18**] = 2 mg/mL) and FESEM image of **18** (**d**) ([**18**] = 1.7 mg/mL). Reproduced from Ref. [43] by permission of The Royal Society of Chemistry

seen. On the other hand, polymer **18** showed the presence of long compact polymer strands (Fig. 6.20b). FESEM images (Fig. 6.20d) of the dried xerogel samples of the hydrogel showed an entangled network of fibers characteristic for such kind of gels. Dynamic light scattering (DLS) of aqueous solutions of PEI showed the presence of particles with a hydrodynamic radius of ca. 1.3 nm whereas **18** at pH 7 formed significantly larger aggregates of ca. 17.4 nm radius at the same concentration.

As the self-complementary zwitterion is only present in the pH range of 5–8, the supramolecular crosslinks in the hydrogel can be turned-off either by protonation or deprotonation. Hence **18** was found to show a hydrodynamic radius of 1.7 nm at pH 3 (from DLS) which is only slightly larger than the size of the nonfunctionalized PEI. Furthermore, AFM images of the functionalized polymer **18** at pH 3 did not show any network structure but the similar kind of spherical aggregates as seen for PEI itself (Fig. 6.20c). A similar kind of observations was noted upon deprotonation at pH = 10. Visibly, the hydrogel was turned into a liquid both by the addition of acid or base (Fig. 6.21). The gel-sol transition was also induced by heating. These changes were fully reversible and the hydrogel was restored upon cooling or readjustment of the pH to 7.

In a recent work van Esch and co-workers demonstrated that by generating gelator molecules in situ through catalytic action, the formation of supramolecular hydrogels can be accelerated which drastically improves the mechanical property of the resulting soft materials [44]. They utilized a cyclohexane-based gelator in which the normally employed amide linkages were replaced by hydrazones, also possessing a good hydrogen-bond donor-acceptor property to design gelator **19c**. The hydrazone groups are linked to hydrophobic phenyl substituents, tagged with oligoethylene glycol tails to enhance the solubility of the building blocks (**19b**) and prevent crystallization of the gelator (Fig. 6.22). The gelator can be formed in situ

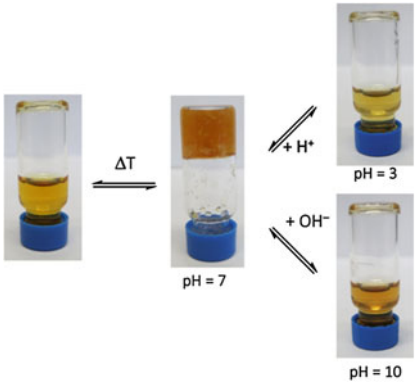

Fig. 6.21 The formation of the hydrogel is pH dependant as only the zwitterion can dimerize. Both protonation and deprotonation switch the supramolecular crosslinks off, turning the gel into a sol ([**18**] = 170 mg/mL). Reproduced from Ref. [43] by permission of The Royal Society of Chemistry

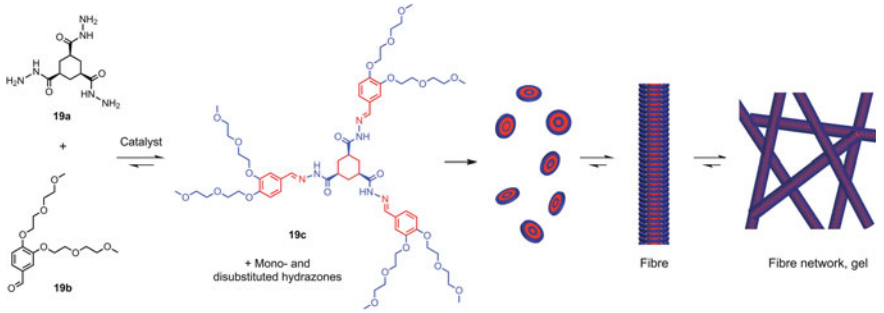

Fig. 6.22 Catalytic formation of trishydrazone hydrogelator **19c** from soluble building blocks **19a** and **19b** leads to supersaturation followed by fiber formation, which eventually crosslink to form a network that traps the surrounding solvent, leading to gelation. *lighter part* = hydrophilic, *darker part* = hydrophobic functional groups. Reprinted by permission from Macmillan Publishers Ltd: Ref. [44], copyright 2013

efficiently by the reaction of the cyclohexane trishydrazide building block **19a** and three molecules of aldehyde **19b**. The hydrazone bond, a reversible covalent bond, has been extensively applied in dynamic combinatorial chemistry as its rate of formation can be controlled by acid and nucleophilic aniline catalysis action [45–47]. When clear aqueous solutions of trishydrazide **19a** and aldehyde **19b** were mixed in a 1:6 molar ratio at pH 7.0 (1:2 ratio of hydrazide to aldehyde functional groups, [**19a**] = 8 mM, 0.1 M phosphate buffer) at room temperature, only turbid solutions were formed. However, when they are mixed at pH 5.0, formation of stable opalescent gels could be observed with a CGC of 4.5 ± 0.5 mM. Similarly, a stable turbid gel could be formed from the same mixture at pH 7.0 in the presence

of 10 mM aniline (CGC of 3.8 ± 0.5 mM). Although increasing the concentration of **19a** to 20 mM at pH 7.0 without catalyst did eventually result in the formation of weak crystalline gels, the determined CGC was significantly higher than that observed in the presence of the catalyst. Gel formation could be reversed by adding strong acid (pH < 1, gel to sol) but could be reinstated using base (pH > 4, sol to gel). Indeed, both confocal laser scanning fluorescence microscopy and scanning electron microscopy (Fig. 6.23) showed the formation of dense homogeneous networks that consisted of heavily branched interconnecting fibers in case of both catalyzed samples, whereas the uncatalyzed system mainly consisted of poorly connected unbranched bundles of fibers and networks of thick fiber bundles. The kinetics of gel formation was significantly affected by the presence of the catalysts. The gelation time could be reduced either by decreasing the pH from 7 to 5 or in the presence of aniline. However, the most noticeable change occurred in terms of the material properties of the gels. There was an increase of almost one order of magnitude in the storage modulus of the gels formed under acid catalysis ([**19a**] = 20 mM, pH 5). The observation that the stronger gels, obtained under catalytic conditions, contain a dense, heavily branched fiber network whereas the weaker uncatalyzed mixtures are made up of unbranched fiber bundles signifies that the rate of gelator formation can critically influence the structure of the assembled materials (Fig. 6.23).

Nandi et al. reported hydrogel formation using H-bonding as the main driving force between two complementary partners: gallic acid (G) and melamine (M) [48]. As both of the components contain multiple hydrogen bonding sites, complexes having different stoichiometry of the components are possible (Fig. 6.24). The authors thus investigated the aggregation behavior of three complexes (1:1, 3:1 and 1:3, termed as GM11, GM31, and GM13, respectively). When the complexes were dissolved by heating in water (∼2 % w/v) and subsequently cooled to room temperature, all of them produced gels. H-bonding interactions between the >C=O group of G and the NH- groups of M was supported by FTIR studies carried out on the xerogels. Furthermore, a comparison of the ^{1}H NMR spectra of G, the GM11 gel, and the GM11 sol in D_2O clearly showed the aromatic C–H protons of G at

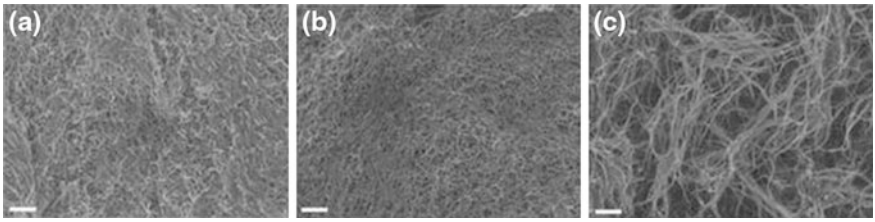

Fig. 6.23 Scanning electron micrographs show differences in network morphology and fiber thickness that depend on catalyst loading at pH 5.0 (**a**) and pH 7.0 with 10 mM aniline (**b**), and uncatalyzed at pH 7.0 (**c**). All samples were prepared by mixing solutions of **19a** and **19b** ([**19a**] = 4 mM, **19a**: **19b** = 1:6, 0.1 M phosphate buffer) at room temperature. *Scale bar* 500 nm. Reprinted by permission from Macmillan Publishers Ltd: Ref. [44], copyright 2013

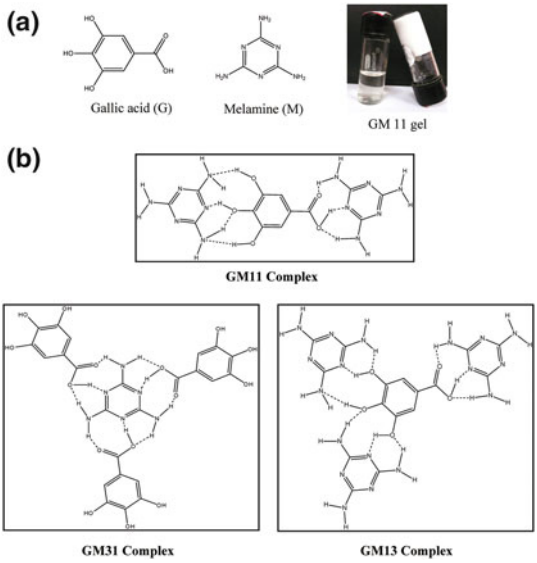

Fig. 6.24 **a** Chemical structure of gallic acid and melamine and visual image of a 2 % (w/v) hydrogel of the GM11 complex. **b** Schematic illustration of possible modes of H-bonding in GM complexes having different molar proportions of the components. Reprinted with the permission from Ref. [48]. Copyright 2009 American Chemical Society

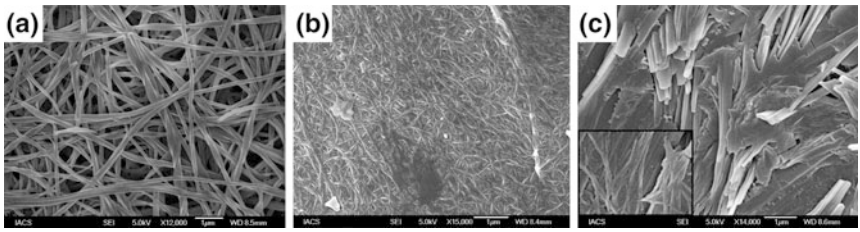

Fig. 6.25 FESEM images of 2 % (w/v) xerogels of **a** GM11, **b** GM13, and **c** GM31 (*inset* containing threefold enlarged picture of rods) hydrogels. Reprinted with the permission from Ref. [48]. Copyright 2009 American Chemical Society

6.95 ppm were shifted to 6.92 ppm in the GM11 gel but remained almost unchanged at 6.96 ppm for GM11 sol. Probably, initially formed H-bonded complexes undergo π stacking in the gel state causing a shielding of the aromatic protons. So, the driving force for the self-assembly process is the H-bonding coupled with the π-stacking between the aromatic moieties. Interestingly, the morphology of the dried xerogels obtained from the different compositions of the two components was found to be different. For both GM11 and GM13 gels, fibrous entangled networks were seen from the SEM images whereas more rod-like structures were found from GM31 gels (Fig. 6.25).

6.6 Vesicles, Bilayers, Micelles Through H-Bonding

Molecular recognition events at the lipid membrane-water interface are governed by multivalency and preorganization [49]. In biomembranes such recognition events play pivotal role in the intracellular signaling pathways [50, 51]. Intramembrane H-bonding between native lipids has been reported to be a crucial factor for lipid bioactivity and different functions of membrane [52]. It is hypothesized that the H-bonding at the lipid-water interface can partially overcome the competition from solvent molecules and such lipid-mediated H-bonding interactions have been reported for bilayer, micellar and vesicular systems [53–55]. In this section we will discuss about a few recent examples from the literature in which H-bonding has been utilized to induce vesicle fusion and vesicle-vesicle recognition.

Li and coworkers reported the self-assembly of foldamers which formed vesicles in a polar solvent like MeOH [56]. They previously reported foldamers which adopted planar crescent conformation stabilized by three center hydrogen bonding [57–59]. Based on these findings, they modified the structures of the foldamers by introducing aromatic moieties. These newly designed foldamers (**20**, **21a–b**, Fig. 6.26) thus possess aromatic groups capable of additional intermolecular π-stacking interactions other than the hydrogen bonding between the amide groups and van der Waals interaction resulting from long peripheral alkyl chains. When hot solutions in MeOH were deposited on a mica surface, the SEM images showed the presence of vesicles with diameters mainly ranging from 1 to 5 μm (Fig. 6.27a–c). It was also observed that some of the vesicles fused to form even larger vesicles. Their hollow nature was further confirmed by fluorescence microscopy images (Fig. 6.27d–f). The noticeable difference of the emission intensity from the outer rings relative to that of the inner areas of the spots clearly showed that they were indeed centrally hollow structures filled with non-fluorescent solvent molecules.

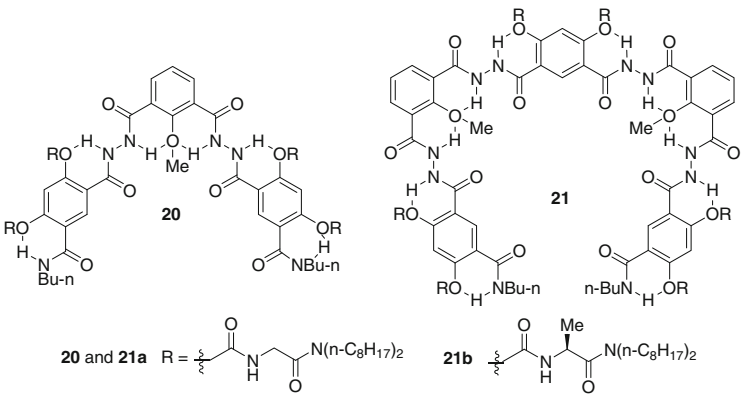

Fig. 6.26 Structures of foldamers **20**, **21a–b**

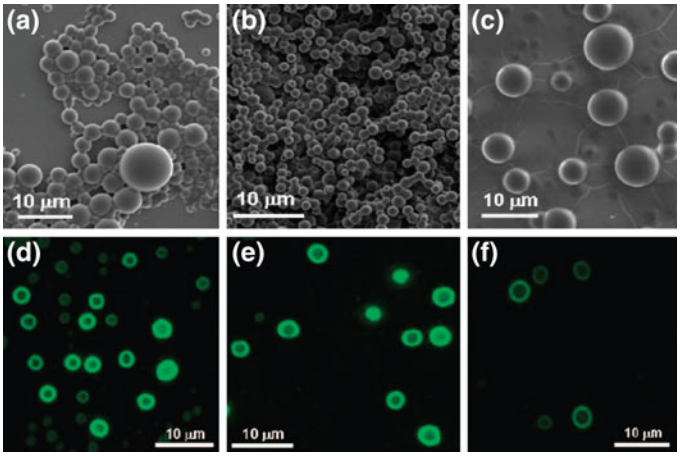

Fig. 6.27 SEM images of the sample of **a 20**, **b 21a**, and **c 21b** in methanol (4 mM) on mica surface after the solvent was evaporated and fluorescence microscopy images of **d 20**, **e 21a**, and **f 21b** formed in methanol (1 mg/mL). Reprinted with the permission from Ref. [56]. Copyright 2008 American Chemical Society

Analysis of the TEM images showed that the wall thickness of the vesicles from all the three foldamers was ca. 3 nm. The diameter of **21** as obtained from space-filling models revealed that is around 1.8 nm in the folded state, whereas the peripheral chains are approximately 1.6 nm in length in their extended state. This indicates that the vesicles had monolayer morphology and were formed by the two-dimensional packing of cylindrical aggregates of the folded skeleton (Scheme 6.7). The polar aryl amide groups are probably exposed to MeOH, while the alkyl chains are entangled with each other along the cylinders. Interestingly, compounds **20** and

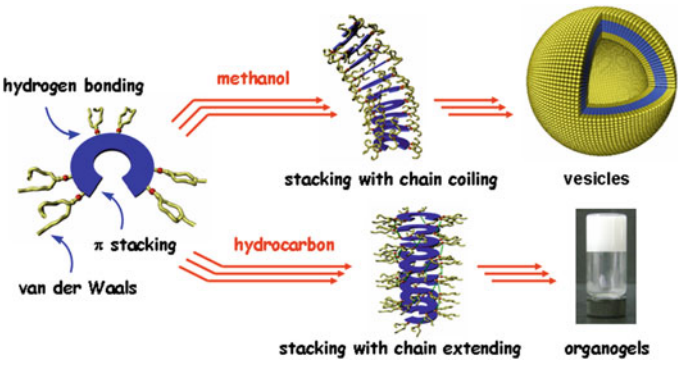

Scheme 6.7 Tentative model for the self-assembly of nonamphiphilic foldamers to vesicles and organogels. Reprinted with the permission from Ref. [56]. Copyright 2008 American Chemical Society

21b were also found to gelate nonpolar aliphatic hydrocarbons including *n*-hexane, cyclohexane, *n*-heptane, *n*-octane, and *n*-decane.

In a subsequent work, the same group investigated vesicle formation from structurally more flexible amphiphilic aromatic oligoamides (**22a–c**, Fig. 6.28) [60]. The oligoamides have two important structural features: (a) one to three hydrophilic glycol moieties were attached to the benzene units to introduce amphiphilicity, (b) large naphthalene rings are incorporated in the structure to induce stronger intermolecular stacking, and (c) the ends are capped with bulky (*tert*-butoxycarbonylamino) groups to inhibit head to tail stacking. All three compounds formed vesicles in MeOH as evidenced by AFM, SEM, TEM, and fluorescence microscopy. AFM images showed the presence of flattened spherical aggregates. SEM images revealed that among the three molecules, **22c** produced vesicles with 2–5 μm diameters whereas those formed from **22a** and **22b** were noticeably smaller (Fig. 6.29).

Ravoo, Schmuck, and co-workers reported the aggregation and adhesion of vesicles by combining host-guest interaction and dimerization of a self-complementary zwitterion [61]. Amphiphilic cyclodextrin vesicles were found to undergo fusion in the presence of a zwitterionic guest molecule. The guest molecule **23a** (Fig. 6.30) combines an adamantyl group, which is widely used to form inclusion complexes with β-cyclodextrin ($K_a > 10^4\ M^{-1}$) and the self-complementary guanidiniocarbonylpyrrole carboxylate zwitterion already mentioned before. The interaction between the guest **23a** and the vesicles of cyclodextrin **23b** was investigated by optical density measurements at λ = 400 nm. The addition of guest **23a** (0.14 mM) to an aqueous solution of vesicles of **23b** (0.3 mM) at pH 7.10 led to

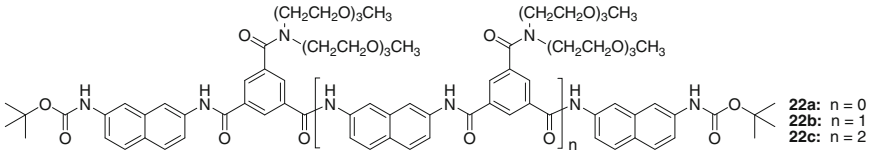

Fig. 6.28 Structures of the amphiphilic aromatic oligoamides **22a–c**

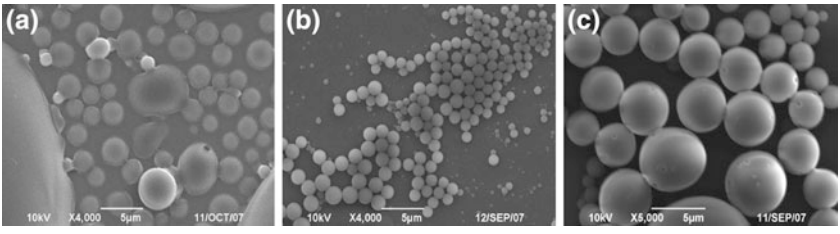

Fig. 6.29 SEM images of the samples (4 mg/mL) from MeOH: **a 22a**, **b 22b**, **c 22c**. Reprinted with the permission from Ref. [60]. Copyright 2009 American Chemical Society

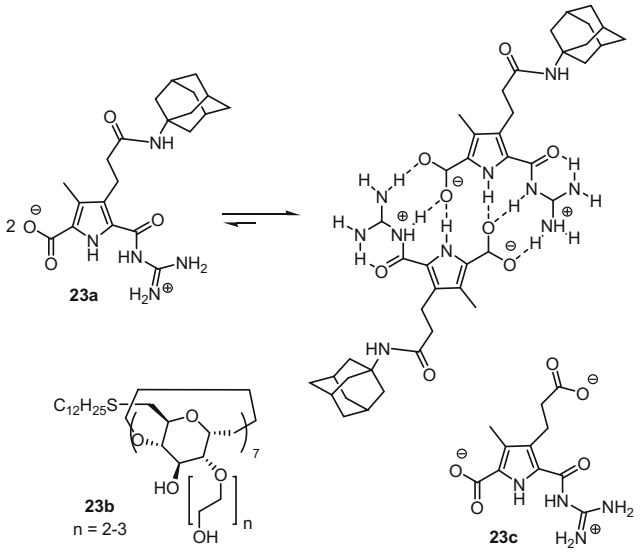

Fig. 6.30 *Top* Molecular structure and dimerization of adamantyl-substituted zwitterionic guanidiniocarbonylpyrrole carboxylate **23a** through hydrogen-bonding and electrostatic interactions in polar media. *Bottom* Molecular structures of amphiphilic β-cyclodextrin **23b** and guanidiniocarbonylpyrrole dicarboxylate **23c**. The molecular structures of **23a** and **23c** indicate the protonation state at neutral pH

a noticeable increase in turbidity (i.e., optical density at λ = 400 nm) with time. In contrast, only a minor change in optical density was observed at pH 4.75, or at pH 9.14. The aggregation of vesicles and the concomitant increase in the size of the vesicles could directly be observed from DLS measurements. The vesicles without the guest molecule **23a** typically had sizes around 160 nm. But upon addition of the guest (pH = 7.1), a significant increase to 400 nm in the size was observed. But no increase was observed at pH 4.75 or at pH 9.14.

The combination of optical density measurement and DLS clearly indicated the aggregation of vesicles at a particular pH and this can be controlled by changing the pH. The control molecule **23c** on the other hand could not induce vesicle aggregation. Hence, the aggregation of vesicles of **23b** upon addition of **23a** needs (a) the formation of cyclodextrin-adamantane inclusion complex at the surface of the vesicles and (b) subsequently the adhesion of these vesicles due to the formation of multiple H-bond assisted ion-paired dimers of **23a** at the surface of two vesicles. AFM measurements of the spin-coated samples of vesicles of **23b** (without the guest **23a**) on mica showed the presence of flattened structures with diameter around 200 nm (Fig. 6.31) in accordance with the size obtained from the DLS measurements. On the other hand, the vesicles of **23b** in the presence of **23a** (pH 7.10) formed flattened aggregates with higher average height of 70–80 nm and a higher diameter of 300–500 nm.

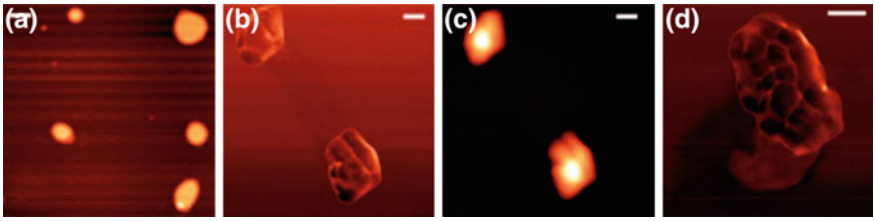

Fig. 6.31 AFM (A–E, *scale bars* = 200 nm) images. **a** Height image of vesicles of **23b**, z-scale 14 nm; **b** and **d** phase-contrast images of aggregated vesicles of **23b** in the presence of guest **23a**; **c** height image of aggregated vesicles of **23b** in the presence of guest **23a**, z-scale 60 and 70 nm Concentrations: [**23a**] = 0.5 mM, [**23b**] = 1.0 mM in phosphate buffer (pH 7.10). Reproduced with permission from Ref. [61], copyright 2010 WILEY-VCH Verlag GmbH & Co. KGaA, Weinheim

Bong and co-workers reported vesicle apposition, fusion, and adhesion utilizing H-bonding between melamine and cyanuric acid [62]. Cyanuric acid and melamine have been previously reported to produce different kinds of nanostructures like rosette, tapes in solution and in solid state driven by H-bonding [63]. They synthesized cyanuric acid (CA) and melamine (M)-derivatized phospholipids CA-PE and M-PE (Fig. 6.32) which when dispersed in buffer solutions produced vesicles individually. The interaction between the pure vesicles of **CA-PE** or **M-PE** was investigated using a pyrene functionalized lipid (Pyr-PC). The excimer/monomer (E/M) ratio of this lipid gives an indication of lipid mobility [64]. It was found that vesicles composed of only the pure components or 2-oleoyl-phosphatidyl-choline (POPC, a fluid phase lipid at room temperature) exhibited similar E/M ratios and a linear temperature dependence as expected for monophasic fluid membranes. On the contrary, membranes obtained from 1:1 ratio of the **CA-PE** and **M-PE** showed more rigid gel phase behavior with a shallow phase transition around 22 °C and a much stronger transition at 65 °C (Fig. 6.33). Further evidence was obtained from differential scanning calorimetry (DSC) studies (Fig. 6.33) which revealed exothermic and endothermic peaks on the upscan at 20 and 75 °C, respectively; whereas these transitions shifted on the downscan to 65 °C (exothermic) and 22 °C (endothermic). The intermembrane binding between **CA-PE** LUV and **M-PE** LUV

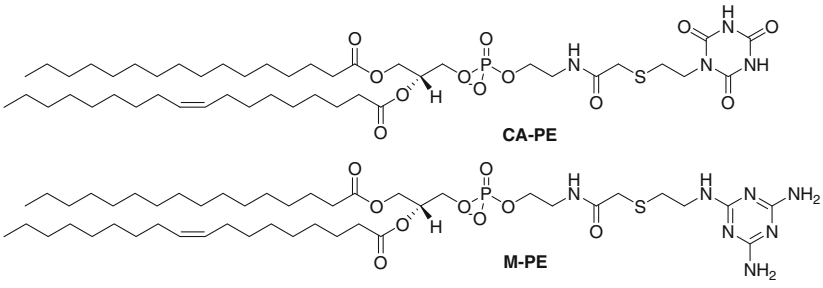

Fig. 6.32 Structures of the cyanuric acid and melamine derivatized phospholipids

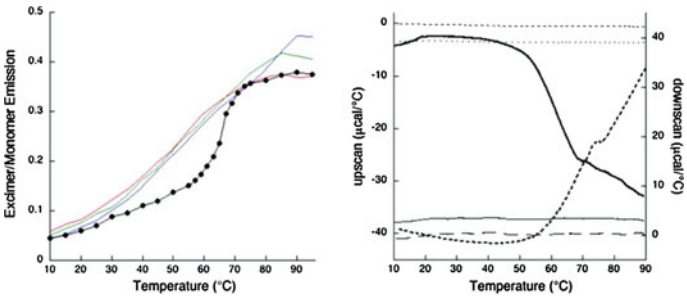

Fig. 6.33 Intramembrane lipid recognition. *Left* Temperature dependence of pyrene PC excimer/monomer emission intensity in suspensions of **CA-PE** (*dark gray*), **M-PE** (*light gray*), POPC (*black*), and a 1:1 mixture of **CA-PE** and **M-PE** (*black*). *Right* DSC upscan (–) and downscan (—) traces of a suspension of a 1:1 mixture of **CA-PE** and **M-PE**; **CA-PE** and **M-PE** upscans (–, ⋯) and downscans (-, —) are all flat traces. Reprinted with the permission from Ref. [62]. Copyright 2008 American Chemical Society

was also evident from the DLS studies which showed that upon mixing these two vesicles there was a rapid increase in the particles size. Selective intermembrane binding between lipids **CA-PE** and **M-PE** was also evident by DLS; mixing **CA-PE** LUVs with **M-PE** LUVs resulted in a rapid and irreversible increase in particle size. It was interesting to note that both the individual vesicles had similar zeta potential of −11 mV in PBS buffer and still bind to each other overcoming this electrostatic repulsion. Cryo-TEM images (Fig. 6.34) revealed that the vesicles of **CA-PE** and **M-PE** appear morphologically similar and are predominantly

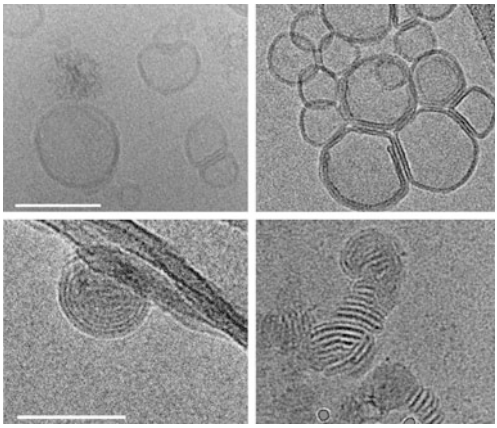

Fig. 6.34 *Top left* Cryo-EM of **CA-PE** LUVs. *top right* **M-PE** LUVs. *lower left* **CA-PE** + **M-PE** premixed 1:1. *lower right* product of **CA-PE** LUVs reacted with **M-PE** LUVs; round objects are gold beads. *Scale bars* (100 nm) in *left panels* apply to each row. All samples were prepared at room temperature. Reprinted with the permission from Ref. [62]. Copyright 2008 American Chemical Society

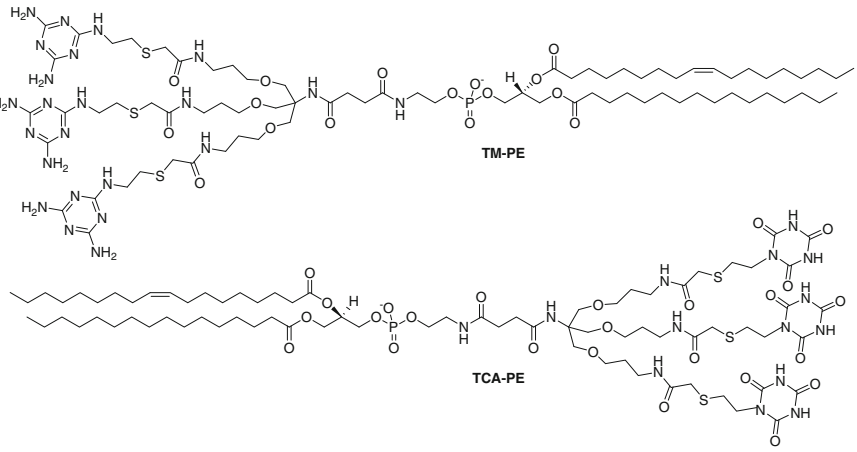

Fig. 6.35 Structure of the trivalent lipids **TCA-PE** and **TM-PE**

unilamellar, with a few aggregated vesicles, consistent with the DLS measurements. However, the structures derived from a 1:1 mixture of the two lipids, as well as the fusion product, exhibited the presence of hexagonal phase. The strong lipid-lipid binding at the lipid-water interface resulting from the H-bonding between the headgroups leads to the desolvation of the surface and this eventually creates a hexagonal phase as observed in the TEM images.

In an extension of the above work, the authors designed lipids where three cyanuric acid or melamine head-groups were connected covalently to a single lipid headgroup (**TCA-PE** and **TM-PE**, respectively, Fig. 6.35) so as to obtain a small lipid recognition cluster [65]. When these trivalent lipids were incorporated in small amounts (0.1–5 %) in fluid phospholipid membranes, both vesicle-vesicle binding and vesicle fusion were observed. The CA or M groups in this case are forced into proximity as they are covalently connected to the single lipid head. Lipid films were prepared containing **TCA-PE** (0.1–5 mol%) in egg phosphatidylcholine (ePC) or **TM-PE** at the same concentration in ePC (containing 20 % phosphatidylglycerol lipid (POPG) in order to inhibit the self-aggregation of tendency of TM-PE). The vesicles were obtained by film hydration method and by passing the vesicle solutions through 100 nm membrane. Monodisperse vesicles were obtained which are in non-aggregated state as revealed by DLS studies. Although the pure **TM-PE** and **TCA-PE** had repulsive potentials of −13 and −23 mV, mixing them in 1:1 ratio resulted in the formation of vesicles of double size induced by the hydrogen bond mediated recognition between the vesicles (Scheme 6.8).

SPR (surface plasmon resonance) was used to probe the interactions between the vesicles. When one of the LUVs was bound to the surface of an SPR substrate, the addition of complementary LUVs produced noticeable concentration dependent signals whereas no signals were observed in the case of the control LUVs. Cryo-TEM was used to check whether mixing of 5 % TM-PE and 5 % TCA-PE LUVs

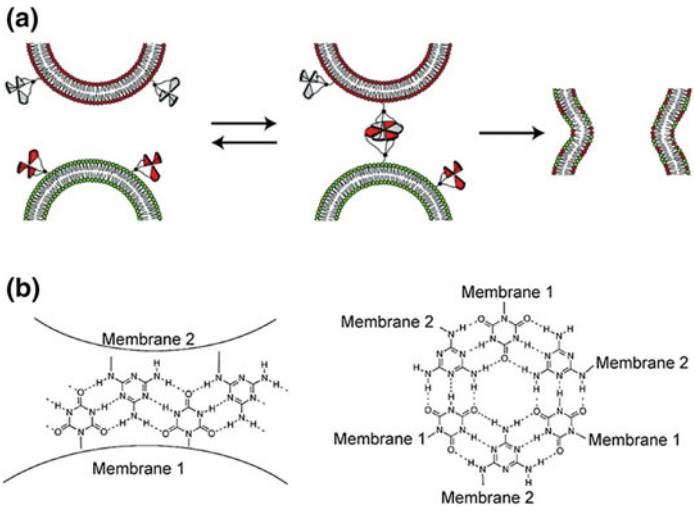

Scheme 6.8 **a** Schematic illustration of how membrane anchored lipids trifunctionalized with CA or M (symbolized as *dark* and *gray* wedges) might direct lipid membrane apposition and fusion. **b** Possible modes of intermembrane hydrogen bonding, based on known CA/M assembly topologies: tape (*left*) and rosette (*right*). Reprinted with the permission from Ref. [65]. Copyright 2009 American Chemical Society

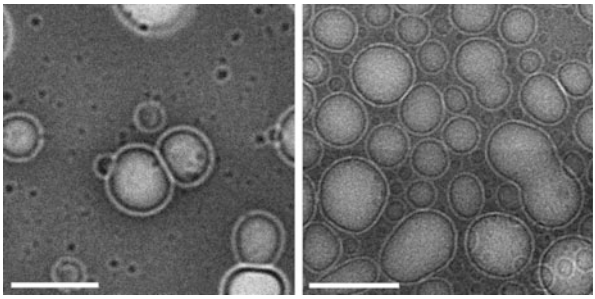

Fig. 6.36 Cryo-TEM of 5 % TM-PE/ePC LUVs reacted with 5 % TCAPE/ePC LUVs; *left* adherent vesicles, *right* adherent and possibly fused vesicles. *Scale bar* 100 nm. Reprinted with the permission from Ref. [65]. Copyright 2009 American Chemical Society

leads to the formation of hexagonal phase and vesicular adhesion (Fig. 6.36). The LUV mixture indicated the presence of lamellar phase LUVs along with the presence of vesicular aggregates as well as other structures that probably formed immediately after fusion.

Ghosh et al. have described the formation of vesicles from naphthalene diimide (NDI) based bolaamphiphiles using synergistic H-bonding and π-stacking in aqueous media [66]. The key strategy involved in this work was to connect hydrazide moieties to NDI (**NDI-1**, Scheme 6.9) in such a way that they can form

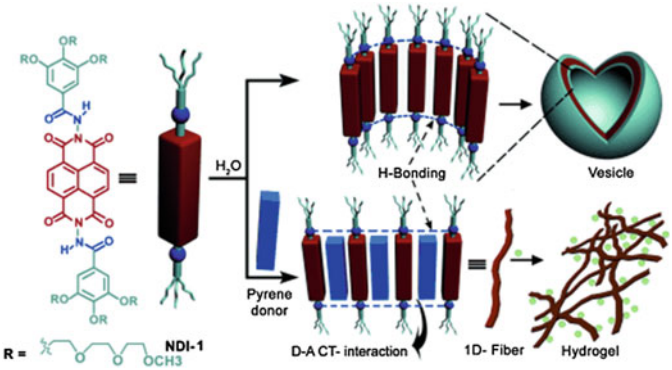

Scheme 6.9 *Top* Structure and vesicular assembly of **NDI-1**. *Bottom* CT-interaction-mediated morphological transition (2D-to-1D vesicle-to-fiber) and gelation by pyrene intercalation. Reproduced with permission from Ref. [66], copyright 2012 WILEY-VCH Verlag GmbH & Co. KGaA, Weinheim

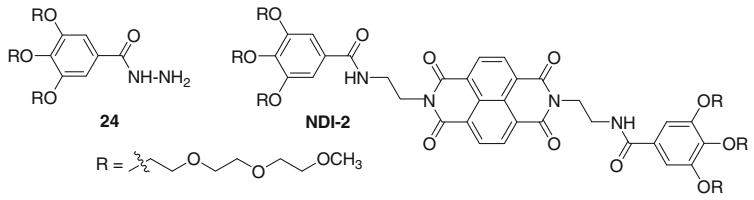

Fig. 6.37 Structures of the control molecules **24** and **NDI-2**

intermolecular H-bonds which are shielded from the bulk water molecules. When the FTIR spectra of **NDI-1** recorded in THF and water were compared, it was found that the carbonyl group of the hydrazide moiety shifted from 1,696 cm^{-1} in THF to 1,655 cm^{-1} in water, suggesting hydrogen bonding between the hydrazide groups. In order to ascertain the fact that the aforementioned shift resulted from the H-bonding only between the hydrazide groups and not with the solvent water molecules, FTIR spectra for two other control compounds were recorded: compound **24** which contains a bare hydrazide group and **NDI-2** which is structurally similar to **NDI-1**, but the amide functionality is linked to the NDI core by a relatively flexible ethylene linker (Fig. 6.37). From the FTIR spectra it was clearly observed that in case of **24**, the hydrazide carbonyl group appeared almost at the same position in THF and water (1,647 and 1,643 cm^{-1}). A similar observation was noted for **NDI-2**. These observations clearly suggest that (a) in **NDI-1**, the shift in the hydrazide carbonyl group indeed resulted from the intermolecular H-bonding between them and (b) a rigid placement of the hydrazide groups close to the NDI chromophore is required for the desired hydrogen-bonding-driven self-assembly.

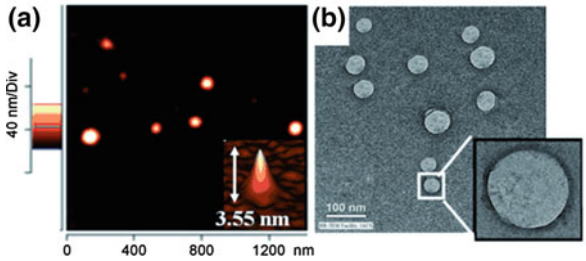

Fig. 6.38 **a** AFM height image (*inset* shows 3D view of one vesicle) and **b** TEM image of **NDI-1** vesicles. Reproduced with permission from Ref. [66], copyright 2012 WILEY-VCH Verlag GmbH & Co. KGaA, Weinheim [66]

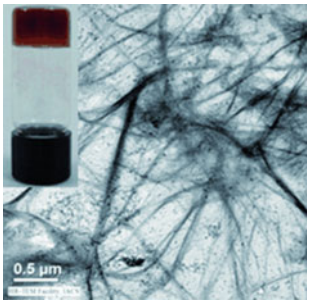

Fig. 6.39 TEM images of the NDI-1 + pyrene (1:1) gel; *inset* Photograph of the hydrogel (10 mm). Reproduced with permission from Ref. [66], copyright 2012 WILEY-VCH Verlag GmbH & Co. KGaA, Weinheim

AFM images of **NDI-1** solutions in water (Fig. 6.38a) revealed the presence of spherical objects with heights and widths of (3.5 ± 0.2) nm and 50–70 nm, respectively. TEM images (Fig. 6.38b) similarly showed the presence of spherical structures (diameter 50–80 nm) with hollow interiors. These microscopic observations thus clearly indicated the presence of vesicular structures resulting from **NDI-1**.

Interestingly, the electron deficient NDI chromophores could accommodate electron rich, water insoluble pyrene in the vesicular membrane through intercalation in a stoichiometric ratio. The CT interactions (as evident from the red coloration of the solution) thus provided an additional stabilization but did not disrupt the hydrogen-bonding framework between the hydrazide moieties as found from the FTIR studies. Moreover, pyrene intercalation resulted in a 2D-to-1D vesicle-to-fiber transition and upon prolonged standing (2–3 days), the red solution turned to be more viscous and above a threshold concentration (5 mM of each component), a transparent red gel (Fig. 6.39) was obtained. TEM images (Fig. 6.39) recorded for the gel revealed the presence of micrometer-sized fibers, in clear contrast to the spherical vesicles observed for **NDI-1**.

References

1. Lehn JM (2002) Science 295:2400
2. Ball P (2008) Chem Rev 108:74
3. Rybtchinski B (2011) ACS Nano 5:6791
4. Sijbesma RP, Beijer FH, Brunsveld L, Folmer BJB, Hirschberg JHK, Lange RFM, Lowe JKL, Meijer EW (1997) Science 278:1601
5. Li Y, Park T, Quansah JK, Zimmerman SC (2011) J Am Chem Soc 133:17118
6. Zeng H, Miller R, Flowers R, Gong B (2000) J Am Chem Soc 122:2635
7. Blight BA, Camara-Campos A, Djurdjevic S, Kaller M, Leigh DA, McMillan FM, McNab H, Slawin AMZ (2009) J Am Chem Soc 131:14116
8. Philp D, Stoddart JF (1996) Angew Chem Int Ed Engl 35:1154
9. Sawada T, Yoshizawa M, Sato S, Fujita M (2009) Nat Chem 1:53
10. Sawada T, Fujita M (2010) J Am Chem Soc 132:7194
11. Borzsonyi G, Beingessner RL, Yamazaki T, Cho JY, Myles AJ, Malac M, Egerton R, Kawasaki M, Ishizuka K, Kovalenko A, Fenniri H (2010) J Am Chem Soc 132:15136
12. Fenniri H, Mathivanan P, Vidale KL, Sherman DM, Hallenga K, Wood KV, Stowell JG (2001) J Am Chem Soc 123:3854
13. Moralez JG, Raez J, Yamazaki T, Motkuri RK, Kovalenko A, Fenniri H (2005) J Am Chem Soc 127:8307
14. Johnson RS, Yamazaki T, Kovalenko A, Fenniri (2007) J Am Chem Soc 129:5735
15. Moralez JG, Raez J, Fenniri H (2004) J Am Chem Soc 126:16298
16. Kim OK, Je J, Jernigan G, Buckley L, Whitten D (2006) J Am Chem Soc 128:510
17. Nuckolls C, Katz TJ, Castellanos L (1996) J Am Chem Soc 118:3767
18. von Berlepsch H, Kirstein S, Böttcher C (2003) J Phys Chem B 107:9646
19. Jaeger KE, Eggert T (2004) Curr Opin Biotechnol 15:305
20. Hough DW, Danson MJ (1999) Curr Opin Chem Biol 3:39
21. Pal A, Karthikeyan S, Sijbesma RP (2010) J Am Chem Soc 132:7842
22. Pal A, Besenius P, Sijbesma RP (2011) J Am Chem Soc 133:12987
23. Brizard A, Stuart MA, van Bommel K, Friggeri A, de Jong M, van Esch J (2008) Angew Chem Int Ed 47:2063
24. Hanabusa K, Kawakami A, Kimura M, Shirai H (1997) Chem Lett 26:191
25. van Bommel KJC, van der Pol K, Muizebelt I, Friggeri A, Herees A, Meetsma A, Feringa BL, van Esch JH (2004) Angew Chem Int Ed 43:1663
26. Boekhoven J, van Rijn P, Brizard AM, Stuart MCA, van Esch JH (2010) Chem Commun 46:3490
27. Boekhoven J, Brizard AM, van Rijn P, Stuart MCA, Eelkema R, van Esch JH (2011) Angew Chem Int Ed 50:12285
28. Aida T, Meijer EW, Stupp SI (2012) Science 335:813
29. Besenius P, Portale G, Bomans PHH, Janssen HM, Palmans ARA, Meijer EW (2010) PNAS 107:17888
30. van den Hout KP, Martin-Rapún R, Vekemans JA, Meijer EW (2007) Chem Eur J 13:8111
31. Besenius P, van den Hout KP, Albers HMHG, de Greef TFA, Olijve LLC, Hermans TM, de Waal BFM, Bomans PHH, Sommerdijk NAJM, Portale G, Palmans ARA, van Genderen MHP, Vekemans JAJM, Meijer EW (2011) Chem Eur J 17:5193
32. Gröger G, Meyer-Zaika W, Böttcher C, Gröhn F, Ruthard C, Schmuck C (2011) J Am Chem Soc 133:8961
33. Schmuck C (1999) Eur J Org Chem 2397
34. Schmuck C, Wienand W (2003) J Am Chem Soc 125:452
35. Hagy MC, Chen CC, Dormidontova EE (2007) Macromolecules 40:3408
36. Ercolani G, Mandolini L, Mencarelli P, Roelens S (1993) J Am Chem Soc 115:3901
37. Hirst AR, Escuder B, Miravet JF, Smith DK (2008) Angew Chem Int Ed 47:8002
38. Banerjee S, Das RK, Maitra U (2009) J Mater Chem 19:6649

39. Zelzer M, Ulijn RV (2010) Chem Soc Rev 39:3351
40. Steed JW (2011) Chem Commun 47:1379
41. Dawn A, Shiraki T, Haraguchi S, Tamaru S, Shinkai S (2011) Chem Asian J 6:266
42. Hisamatsu Y, Banerjee S, Avinash MB, Govindaraju T, Schmuck C (2013) Angew Chem Int Ed 52:12550
43. Fleischer M, Schmuck C (2014) Chem Commun 50:10464
44. Boekhoven J, Poolman JM, Maity C, Li F, van der Mee L, Minkenberg CB, Mendes E, van Esch JH, Eelkema R (2013) Nat Chem 5:433
45. Corbett PT (2006) Chem Rev 106:3652
46. Lehn JM (1999) Chem Eur J 5:2455
47. Dirksen A, Dirksen S, Hackeng TM, Dawson PE (2006) J Am Chem Soc 128:15602
48. Saha A, Roy B, Garai A, Nandi AK (2009) Langmuir 25:8457
49. Binder WH, Barragan V, Menger FM (2003) Angew Chem Int Ed 42:5802
50. Anderson RGW, Jacobson K (2002) Science 296:1821
51. Grakoui A, Bromley SK, Sumen C, Davis MM, Shaw AS, Allen PM, Dustin ML (1999) Science 285:221
52. Boggs JM (1987) Biochim Biophys Acta 906:353
53. Kawasaki T, Tokuhiro M, Kimizuka N, Kunitake T (2001) J Am Chem Soc 123:6792
54. Nowick JS, Cao T, Noronha G (1994) J Am Chem Soc 116:3285
55. Menger FM, Zhang H (2006) J Am Chem Soc 128:1414
56. Cai W, Wang GT, Xu YX, Jiang XK, Li ZT (2008) J Am Chem Soc 130:6936
57. Gong B (2001) Chem Eur J 7:4337
58. Huc I (2004) Eur J Org Chem 1:17
59. Li ZT, Hou JL, Li C, Yi HP (2006) Chem Asian J 1:766
60. Xu YX, Wang G, Zhao X, Jiang XK, Li ZT (2009) Langmuir 25:2684
61. Voskuhl J, Fenske T, Stuart MCA, Wibbeling B, Schmuck C, Ravoo BJ (2010) Chem Eur J 16:8300
62. Ma M, Paredes A, Bong D (2008) J Am Chem Soc 130:14456
63. Fyfe MCT, Stoddart JF (1997) Acc Chem Res 30:393
64. Galla HJ, Hartmann W (1980) Chem Phys Lipids 27:199
65. Ma M, Gong Y, Bong D (2009) J Am Chem Soc 131:16919
66. Molla MR, Ghosh S (2012) Chem Eur J 18:9860

Chapter 7
Hydrogen Bonded Capsules: Chemistry in Small Spaces

Li Juan Liu and Julius Rebek Jr

Abstract This chapter reports the behavior of molecules confined to spaces barely large enough to accommodate them—encapsulation complexes. The molecules respond to the limited spaces with adapted shapes, prolonged contacts, and intensified interactions including accelerated reactions. Emphasis is placed on reversible encapsulation and the differences between molecules in free solution and those in hydrogen-bonded capsules.

7.1 Why Study Encapsulated Molecules?

This chapter describes the world of molecular encapsulation, the behavior of molecules temporarily isolated in space and time. The capsules are synthetic, made in the laboratory and engineered to control their sizes, shapes, and chemical surfaces. The capsules consist of assemblies of other molecules that fit together to make hollow, roughly spherical cages with dimensions on the nanoscale (10^{-9} m) and volumes about 10^{-24} L. This scale is hard to imagine, but try this: the space of the capsule is roughly twice the size of the molecule(s) inside. In more manageable numbers, the capacity of the capsules we emphasize here is about 400 $Å^3$, which can be compared to the familiar benzene molecule of about 75 $Å^3$. The capsules are small, but they provide spaces large enough to surround two or more molecules and hold them for a while. For two molecules in the same capsule, the time of the encounter ranges from milliseconds to hours and is typically on the order of 1 s. If you compare these times with those of encounters between molecules in typical liquids you will see what is so special about these capsules: in liquids, two molecules diffuse into contact for less a nanosecond

L.J. Liu · J. Rebek Jr
Department of Chemistry, Fudan University, 220 Handan Road, Shanghai 200433, China

J. Rebek Jr (✉)
The Skaggs Institute for Chemical Biology and Department of Chemistry,
The Scripps Research Institute, 10550 North Torrey Pines Road, La Jolla, CA 92037, USA
e-mail: jrebek@scripps.edu

Z. Li and L. Wu (eds.), *Hydrogen Bonded Supramolecular Structures*,
Lecture Notes in Chemistry 87, DOI 10.1007/978-3-662-45756-6_7

before they drift apart to find other partners. The result is a frenzied exchange of partners in solution, but inside a capsule the pairwise encounters can last for minutes. This protracted encounter is one of the capsule's unique properties, it allows interactions and arrangements of molecules that cannot be seen by other methods.

Because the space in the capsules is small, every molecule inside enjoys high (molar) concentrations. This is another one of the capsule's special features: the amplified concentrations of encapsulated molecules accelerate their rates of reaction. The capsules come together spontaneously and reversibly—they self-assemble—they form and dissipate constantly under mild conditions in organic solvents. The encapsulation complexes exist when and only when the spaces inside the capsules are appropriately filled. This requirement that they are never empty is the third special property. It can be used to select different, one-on-one combinations of molecules to be encapsulated because they fill the space properly. The fourth property arises from the very isolation of the inside of the capsule from the bulk solvent. Without competition from the solvent, the interactions of the encapsulated molecules are intensified and amplified. The fifth property has to do with the shape of the space inside; like other forms of architecture, the structure is about the space it encloses and we will see that encapsulated molecules conform, even contort to fill the space. One consequence is that reactions inside can be channeled down one path that is compatible with the space while the corresponding reactions in bulk solvent can take many paths. The reader will recognize that many of the features listed above are shared by the spaces at enzyme active sites and receptors. But the studies described below were not intended as models for biology. Instead, they grew out of physical organic chemistry from studies in molecular recognition, and we will maintain that perspective with questions such as: What's it like inside a capsule? What's inside and how do molecules get in and out? How many molecules can be there at the same time? Can asymmetric (chiral) spaces be made? Answers to these questions will be provided but, as is often the case in the studies of basic science, even more questions will arise.

7.2 The Capsules and Their Contents

7.2.1 The Tennis Ball

Our initial capsule, a collaborative effort with Javier de Mendoza in Madrid, was a spherical structure, a notional tennis ball or baseball (Fig. 7.1). The synthesis was rather simple and can now be performed in undergraduate chemistry laboratories using inexpensive and commercially available materials. The capsule consists of two identical concave structures that fit together, with a "seam" resembling that of a baseball but the stitches are not thread. Rather, the seam is made up of eight hydrogen bonds to hold the capsule together [1, 2].

Hydrogen bonds are attractive forces involving the partial positive charge on the hydrogens of one molecule interacting with the electrons of atoms (in this case,

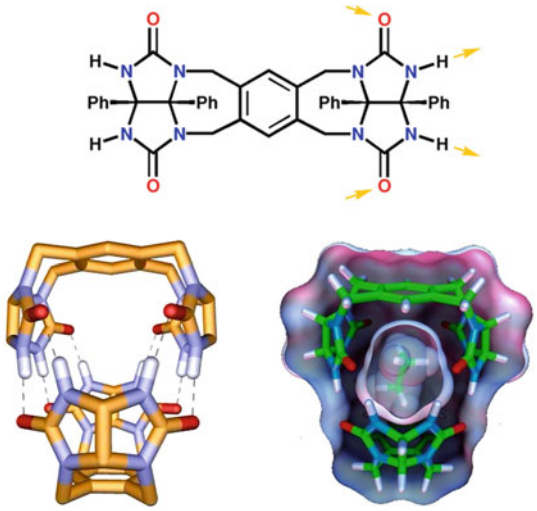

Fig. 7.1 *Top* the structure of a self-complementary module capable of forming a capsule through hydrogen bonding. Hydrogen bond donors and acceptors are indicated. *Bottom* The empty capsule and an encapsulated ethane molecule. The rendering of capsule's solvent accessible surfaces shows the available space inside. Reprinted with permission from Ref. [2] Copyright 2005 John Wiley and Sons

oxygen) of another molecule. The forces are weak; individual hydrogen bonds form and break very rapidly but the eight hydrogen bonds of the capsule act in concert, so the two halves of the tennis ball are held together for about 1 s in organic solvents like chloroform. This is plenty of time to take snapshots of the intact assemblies with instruments like NMR spectrometers. The NMR spectra report the magnetic environment experienced by encapsulated molecules, from which their arrangements in the space can be deduced. For example, molecules that are surrounded with aromatic surfaces (such as those of the capsules) give unmistakable and easily identified, upfield-shifted signals in their NMR spectra [3]. In the case of the tennis ball, the spectrum in Fig. 7.2 shows both encapsulated ethane (−0.4 ppm) and encapsulated methane (−0.9 ppm) and their signals are due to the sandwiching of the gases between the benzene panels above and below.

The signals for the bound gases are sharp and widely separated from those of free ethane and methane at +0.85 and +0.2 ppm, respectively. These features indicate the presence of a sizable (15–20 kcal/mol) energy barrier for motion between inside and outside; in other words, the in/out exchange is slow on the NMR timescale. It is fast on the human timescale as equilibrium is established in the few minutes elapsed between mixing the agents and recording the spectrum.

The dynamic nature of hydrogen bonds allows the capsule to form and dissociate and allow the uptake and release of smaller molecules. The cavity size accommodates only one much smaller molecule such as methane (the major component of natural gas). While there is little interest in sequestering methane, one molecule at a

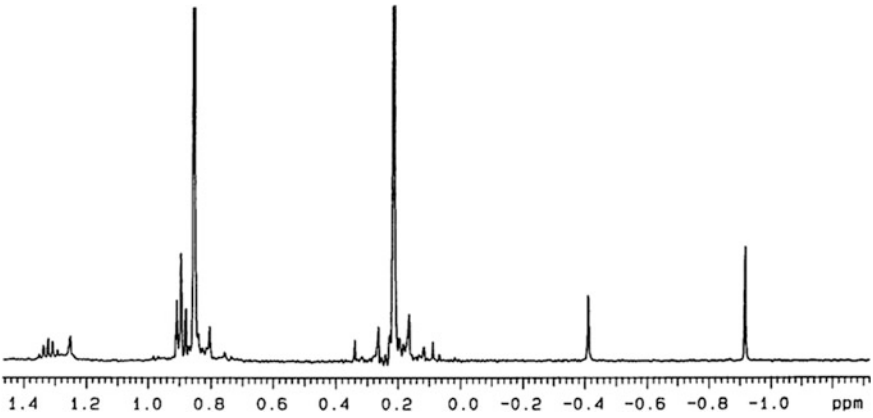

Fig. 7.2 NMR Spectrum of the tennis ball in $CDCl_3$ saturated with commercial methane gas. The signals at −0.4 and −0.9 represent encapsulated CH_3–CH_3 and CH_4, respectively

time for, say, mining the huge reserves of ice/methane clathrates in the oceans, the encapsulation encouraged us to build larger cages for bigger targets.

7.2.2 The Softball

We used a similar array of hydrogen bonds to hold together the larger semispherical structure as shown in Fig. 7.3 [4]. Here the synthesis was much more difficult and involved some 19 steps. On the scale of the tennis ball capsule, this assembly is

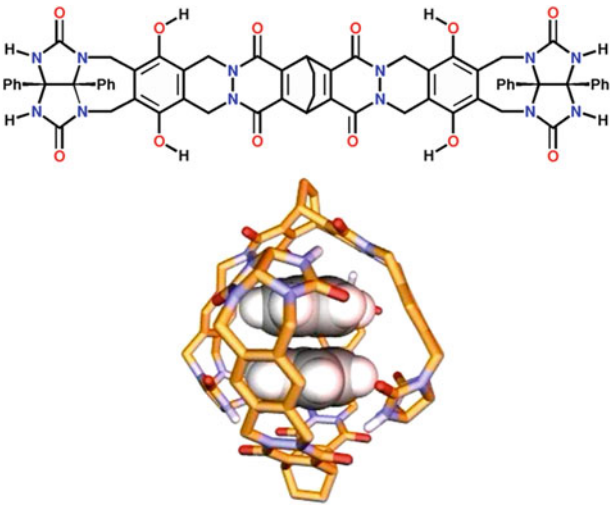

Fig. 7.3 *Top* the structure of a module for a large (400 $Å^3$) capsule. *Bottom* The molecule assembles as a spherical dimer and coencapsulates two solvent molecules in benzene

about the size of a softball. The larger semispherical cavity can contain two sizable molecules such as the common solvent benzene, or a single large molecule, adamantane, which is a tiniest part of the diamond structure. The detection of two molecules inside was the first indication of coencapsulation and hinted at the possible use of capsules as reaction chambers.

7.2.3 A Cylindrical Capsule

It was not until we had in hand a nonspherical (or more specifically, a cylindrical) capsule that additional rules governing coencapsulated molecules emerged. On the table with the tennis ball and softball, this capsule would resemble a can for three tennis balls and it has been used to demonstrate many features of molecules at close range. The synthesis and various renderings of this capsule's structure are shown in Fig. 7.4, and our initial experiments in filling its space showed *the preferential encapsulation of two different molecules* [5].

An extreme example, involving a large and small combination, is shown with anthracene and methane in Fig. 7.5. Neither molecule alone is encapsulated but when both are present, the capsule takes up exactly one of each.

7.2.4 The Volleyball

The largest of the reversibly formed capsules are, ironically, the easiest to make. This accounts for their active pursuit in laboratories worldwide [6–15]. In relation to the other capsules, they are of the size of volleyballs [16] and show the symmetry

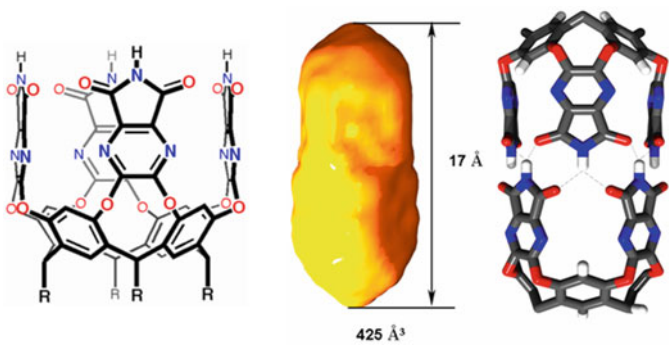

Fig. 7.4 *Left* Structure of a cylindrical capsule. The peripheral alkyl groups, R = $C_{11}H_{23}$, are not shown but impart solubility in organic solvents. *Center* The space available inside the capsule is a tapered cavity with a volume of 425 $Å^3$. *Right* A belt of eight bifurcated hydrogen bonds holds the capsule together

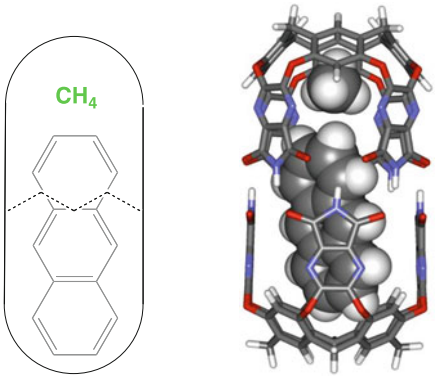

Fig. 7.5 *Left* A cartoon depiction of coencapsulated methane and anthracene. *Right* The complex with the guests rendered as space filling models

of an inflated cube (Fig. 7.6). They result from the self-assembly of resorcinarenes and the closely related pyrogallolarenes and both of these are made in one step in the laboratory; some are even commercially available. For example, in wet benzene, six resorcinarenes make up the sides of the cube and one water molecule is at each corner. The capsule is then composed of 14 molecules that create a huge cavity ($\sim$1,300) that accommodates 6–8 chloroforms, as shown in the left figure. The pyrogallolarene's extra hydroxyl provides the hydrogen bonding at the cube's corners and a similar structure is formed in the presence of simple alkanes such as octane shown in the right figure.

7.3 What's It Like Inside the Capsules?

Most of the atoms that make up the capsule units, the carbon, nitrogen, or oxygen atoms are bonded to each other through strong π bonds. These bonds make for rigid molecular skeletons and they bear electrons on the outer and inner surface of the capsules that are loosely held. These surfaces may be thought of as showing a thin layer of negative charge and they naturally attract molecules that feature positive charge on their surfaces. Many organic molecules such as hydrocarbons are coated with hydrogens that provide the positive charge on their surfaces and these are encapsulated through this complementarity of surfaces between capsule and guest. The capsule's units are held together by hydrogen bonds and these "seams" offer specific areas of partially positive charge on the capsule surface. Molecule guests bearing atoms with a slight negative charge, e.g., the nonbonded electrons of bases are attracted to this seam. For example, the cylindrical capsule offers a gradient of environments along its length: the four aromatics at the tapered ends offer a shallow and electron-coated surface that is rigidly fixed; the four pyrazines nearer the center offer a similar surface but are capable of slight breathing motions; the seam of

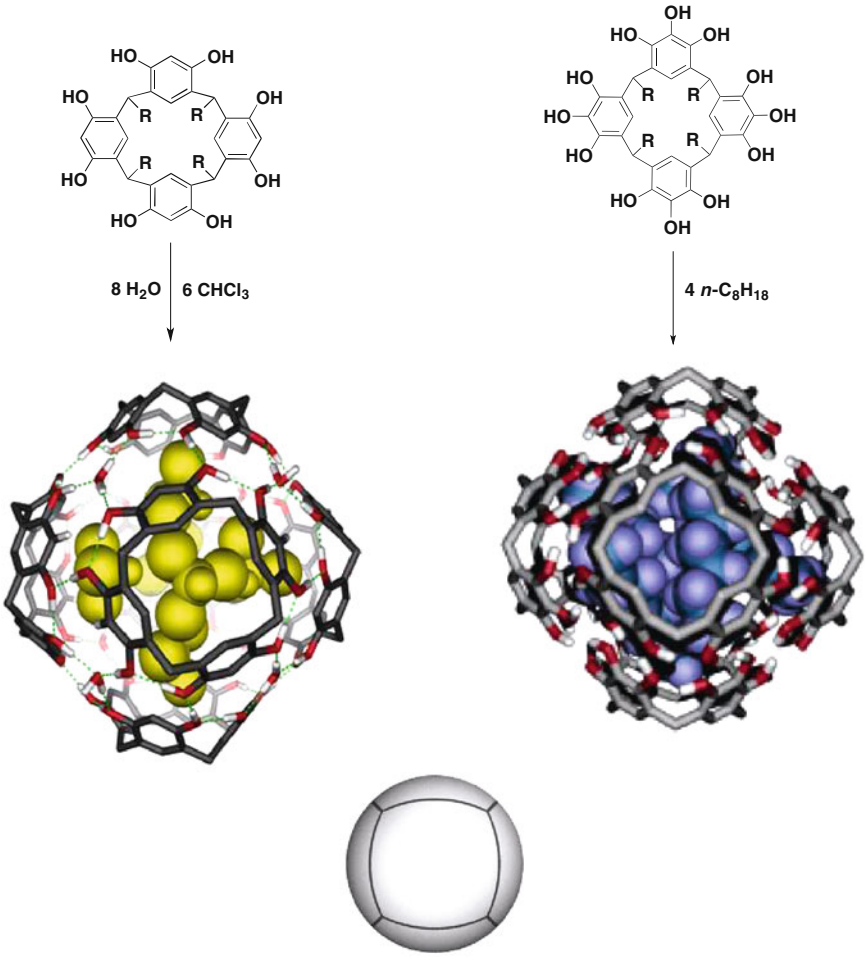

Fig. 7.6 *Top* Line drawings of resorcinarene and pyrogallolarene subunits. *Center* The coencapsulation of six $CHCl_3$ molecules in the resorcinarene and four octanes in the pyrogallolarene are modeled. *Bottom* The hexameric assemblies resemble an inflated cube with one subunit at each face. Reprinted with permission from Ref. [16] Copyright 2011 The Royal Society of Chemistry

hydrogen bond donors and acceptors—partially positive and negative sites and is the most mobile. The entry and exit occur through motions here, and this region attracts highly polar groups of encapsulated molecules while the tapered ends attract the less polar hydrocarbon surfaces. These preferences help the selection and orientation of guests in the capsules' space that give rise to the characteristic interactions seen inside [17, 18].

7.4 How Do Molecules Get In and Out of the Capsules?

In the simplest answer to this question—the guest exchange mechanism—it is easy to imagine the pulling apart of a capsule and letting the guest(s) drift out as new guests or solvent drift in. Then they reassemble as the new capsule. But this sequence must be energetically the most costly: all of the hydrogen bonds are ruptured and all of the attractive forces between host and guest must be overcome. We consider the softball, where extensive kinetic studies were possible because of convenient exchange rates, but the conclusions are true for all our capsules. By opening two adjacent "flaps" of the softball, the resident guest is exposed to the solvent and an S_N2—like sequence can occur. This is depicted in Fig. 7.7, where six hydrogen bonds remain intact throughout the process. The incoming guest **B** simply displaces the resident **A**. This was found to be the case at low incoming guest concentrations: the rate of the reaction was proportional to the incoming guest's concentration. That is, the flaps open and close many times before guest substitution occurs. However, the reaction rate remains constant at high concentrations of incoming guest: the opening of the flaps is the rate-determining step very much like an S_N1 process.

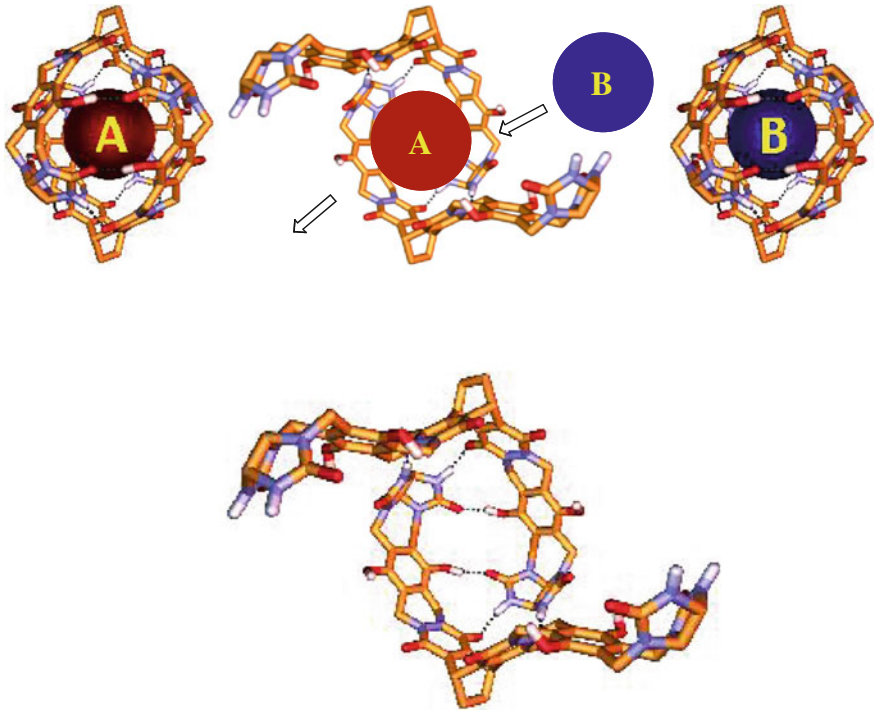

Fig. 7.7 *Top* Supramolecular substitution of guest *A* by *B* in the softball. *Bottom* Two adjacent "flaps" open leaving six hydrogen bonds while the exchange reaction occurs

7.5 Amplified Intermolecular Forces

As mentioned in the introduction, a molecule inside a capsule—typically for one second or so—appears isolated in time and in space. Its interactions with the capsule and other coencapsulated molecules are extended and, compared to the random and rapid collisions (10^9 per second) and exchange of partners that occur in bulk solution outside the capsule, they are intensified or amplified. The capsule provides a synthesized solvent cage that lasts a long time.

In the cylindrical capsule especially, it is possible to align the two molecules inside so that only certain areas of their surfaces come into contact. To our knowledge this cannot be achieved by other methods. Coencapsulation provides a means by which weak, intermolecular forces can be evaluated at the level of a prolonged, one-on-one molecular encounter. We applied this to the subtle interactions known as halogen bonds.

$$\text{R-X} + \text{B} \rightleftharpoons \text{R-X - - - - - B} \tag{7.1}$$

Halogen bonds are feeble attractive forces between polarized halide donors and Lewis base acceptors (Eq. 7.1) [19, 20]. Typical donors are perfluorohalocarbons such as **CF_3Br** and **CF_3I** which feature sigma "holes" (Fig. 7.8), while acceptors include nitrogen-containing heterocycles such as pyridine. Like the much stronger hydrogen bonds, the interaction is moderately directional and an arrangement of anchor (R), donor (X), and acceptor (B) atoms of 180° is preferred. The halogen bonding interactions between perfluorohalides and acceptors in solution are readily monitored by ^{19}F NMR (Fig. 7.9). For example, the perfluoropropyl iodide and

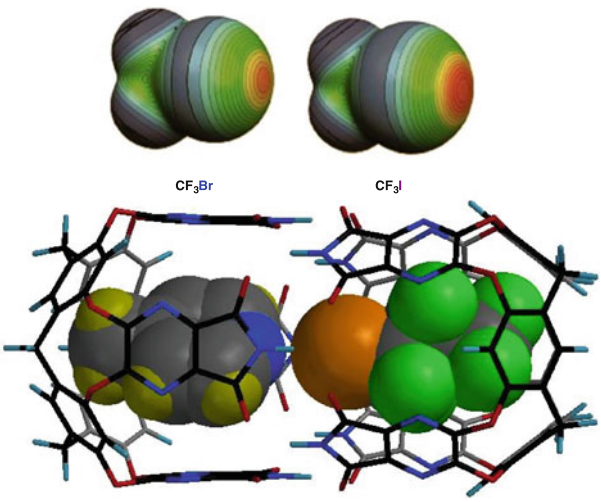

Fig. 7.8 *Top* Energy surfaces of electron deficient halides showing the sigma hole. *Bottom* Modeled halogen bonding between γ-picoline and perfluoropropyl iodide in the capsule

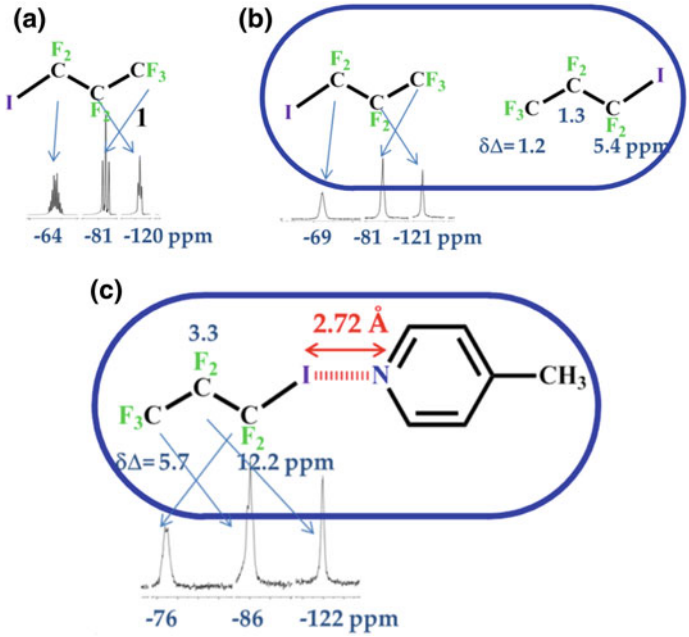

Fig. 7.9 The effects of halogen bonding on ^{19}F NMR shifts: **a** Bonding of perfluoropropyl iodide to the solvent mestylene–d_{12}. **b** Bonding of the iodide to the resorcinarene of the capsule causes modest upfield shifts. **c** Bonding to γ-picoline inside the capsule causes large upfield shifts

4-picoline interact weakly in aromatic solvents as evidenced by a small (<2 ppm) upfield shift of the signals for the nearest CF_2 group. When the capsule is added, however, a coencapsulation complex is formed and the signal makes a dramatic upfield shift of >12 ppm [21]. In a related experiment, both the prefluoroiodide and the picoline form 2:1 complexes with the capsule. When these are mixed, disproportionation occurs (Fig. 7.8) driven by the halogen bonding inside. The shape of the space enforces this result: neither 2- nor 3-picoline coencapsulates with the iodide since these bases cannot achieve the alignment of donor and acceptor required for halogen bonding while inside the capsule.

This happy circumstance allowed us to look at molecules that we have otherwise not been able to encapsulate. These studies also led to the (not surprising) conclusion that gases need more space: for typical liquids, filling about 55 % of the space is optimal [22], but gases have need for more space, as little as 30 % is possible. It is a good question to ask: what does a single molecule experience as a phase inside these capsules? Its collisions with the walls are hardly elastic, particularly as attractive forces exist between the π lining of the capsule and the C–H bonds of small hydrocarbon gases [23]. These are not billiard balls knocking around on a 3-dimensional table. The notion of pressure is, accordingly, hard to define under these conditions.

We were able to use rigid organic molecules to act as rulers to measure the interior of these cavities. Specifically, the cylindrical capsule would accept a benzanilide and three additional carbons but no more—addition of the fourth carbon no longer allows the capsule to form. But what about flexible molecules? We prepared a series of amino acid derivatives with ever increasing length of the carboxylic esters. We measured the association constants and found that the longer esters were poorer guests even though they filled the appropriate amount of space. Molecular modeling, however, showed that the longer guest must begin to fold in order to be accommodated by the capsule. Now, normal alkane groups adopt as their lowest energy conformations extended structures and any bending, such as a gauche interaction raises the energy little more than 0.5 kcal/mol (in the liquid state) [24]. Accordingly, a typical alkane at room temperature would have a population of shapes: the greatest number of molecules would be extended at any given time, and these would be in rapid equilibrium with a smaller population of those whose shapes have one bend (a *gauche* conformation) and those would be in rapid equilibrium with an even smaller population having two bends, and so on.

We studied the series of such alkanes in the cylindrical capsule and found normal decane (10 carbons long) and its homologs C_{11}, C_{12}, C_{13}, and C_{14} all went in the capsule, but C_{15} did not at all. NMR allowed us to look at the conformations and showed us a real surprise. C_{11} featured the NOEs for a perfectly extended structure. In contrast, C_{14} shows NOEs that can only be interpreted in terms of a coiled or helical structure in Fig. 7.10. This structure has never before been seen for normal alkanes but represents a compromise of filling space, making attractive CH-π contacts and the avoidance of vacuums. The price paid for the contortion is reflected in the reduced affinity of C_{14} for the capsule: direct competition experiments that C_{13} is some 120 times a better guest than C_{14} [25].

Finally, to what extent do the encapsulated molecules respond to events outside? Of course, for these systems that are at equilibrium with the outside, their very existence represents a response to the situation in bulk solution. But there is evidence that more subtle influences also exist. Specifically, a chiral environment *outside* an achiral capsule can affect the spectrum of a molecule *inside*. Accordingly, the steric effects and magnetic effects can be separated by encapsulation. It appears that the capsule is best regarded as a window rather than a wall [26].

7.6 Arrangements in Encapsulation Space: New Stereochemistry

7.6.1 Social Isomers

The limitations on the translational motions of molecules inside capsules are easily appreciated as the structure of the capsule itself provides mechanical boundaries. But there are also restricted motions of tumbling and, as we encountered above, spinning.

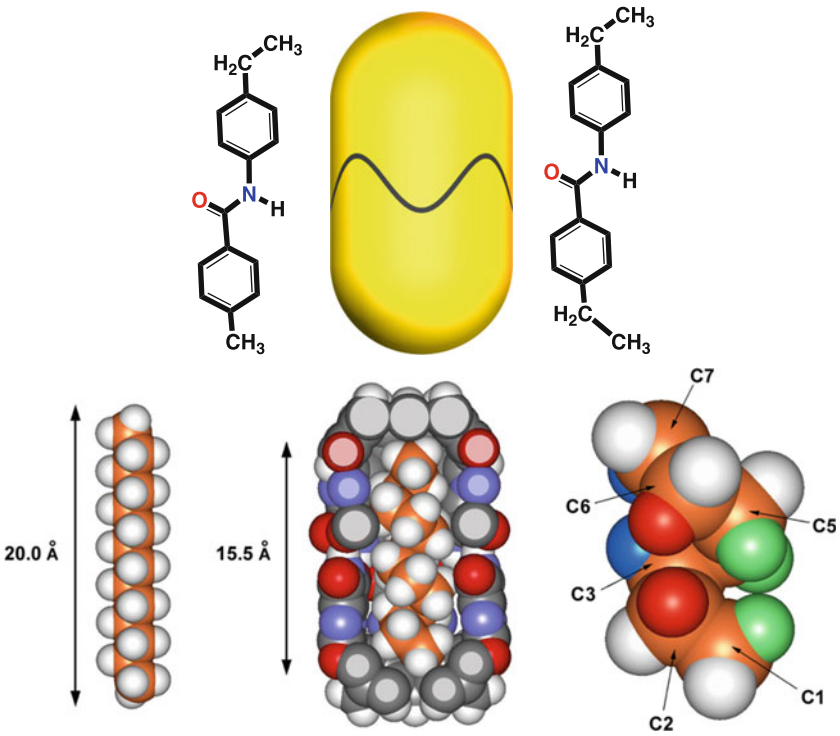

Fig. 7.10 *Top* Cartoon of the cylindrical capsule and two rigid "rulers"; the shorter compound is encapsulated but the longer is not. *Bottom Left*: Length of fully extended $C_{14}H_{30}$. *Center* Model of coiled $C_{14}H_{30}$ in the capsule showing CH-π interactions between guest and host. *Right* Helically coiled alkanes place hydrogens on C_i near hydrogens on C_{i+4}. These interactions are observed in 2D NMR spectra

When coencapsulation occurs with one molecule of chloroform and one molecule of *N*-methyl-*p*-toluidine in the cylinder, two different arrangements—*social isomers*—are observed by NMR spectroscopy (Fig. 7.11). The arrangements could, in principle, interconvert through the tumbling of the aromatic molecule while still inside the cylindrical capsule. This process is quite slow on the NMR timescale at ambient temperatures (the shorter *p*-xylene does begin to tumble inside on heating) [27]. The other means by which the two isomers could interconvert requires that one molecule slides past the other *within the capsule*. We have evidence of this only for narrow molecules such as short, normal alkanes; these "linear" molecules can snake past others of their kind inside, but any branching creates high steric barriers to the process.

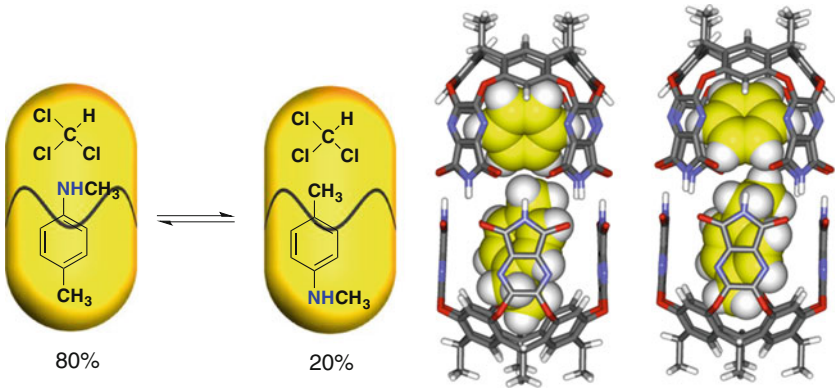

Fig. 7.11 Single molecule interactions of solvents and solutes. *Left* The coencapsulation of chloroform and *N*-methyl-*p*-toluidine shows two "social isomers," in which the interaction of the chloroform with the *N*-methyl group is favored. *Right* coencapsulated benzene with *p*-ethyl-toluene. These social isomers do not interconvert within the capsule, as the *p*-disubstituted aromatics are too long to tumble inside

7.6.2 Single Molecule Solvation

The social isomerism is a consequence of the dimensions of the cylindrical capsule and those of the molecules inside. We have used social isomerism to assess interactions between specific functional groups of the coencapsulated molecules. The limitations on motion constrain intermolecular contact between the guests to two areas. Again, the concentrations are amplified—the volume of the capsule (~4 x 10^{-25} L) translates into molar concentrations of each coencapsulated molecule. In another view, we can observe the interaction of a solute with a single molecule of solvent, in equilibrium at ambient temperatures. We tested three related molecules: toluenes with *p*-ethyl; *p*-*N*-methyl and *p*-*O*-methyl substituents—against a panel of 12 coencapsulated, common solvents [28]. The preferences of the solvents for one end or the other of the toluenes were determined directly by NMR integration. The interaction of benzene with the ethyl group of *p*-ethyl-toluene (Fig. 7.11) inside the capsule is favored by 1 kcal/mol. The NMR spectra offer snapshots of short-lived relationships between molecules isolated from bulk solution. We know of no other method that is capable of this determination.

7.6.3 Isotope Effects

One of the subtlest cases of social isomerism was encountered with the isotopic substitution of one of the ends of an encapsulated molecule. Equilibrium isotope effects are somewhat of a rarity in molecular recognition but are not insignificant [29, 30]. Deuterium substitution of C–H bonds in molecules tends to make behave as

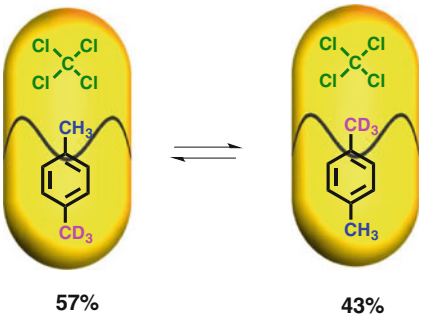

Fig. 7.12 Equilibrium isotope effects through coencapsulation: the CD_3 is more attracted than the CH_3 to the resorcinarene at the end of the capsule

they are slightly more polar. We found perdeuterated *p*-xylene was preferred for encapsulation with carbon tetrachloride over *p*-xylene. The isotope effect in the competition experiments was about 1.3 in favor of the deuterated material [31]. We were then able to locate the regions of the structure that were susceptible these subtle changes. Most of the isotope effect was located at the methyl groups of the *p*-xylene, as isotope substitutions on the aromatic ring had marginal effects. Ultimately, we prepared a sample in which one methyl group was deuterated and one was not. This showed the preferential binding of the deuterated methyl to the tapered end of the cavity, away from the coencapsulated carbon tetrachloride (Fig. 7.12). The experimental results were also reproduced by high-level computational analyses [32].

7.6.4 Constellations

The cylindrical capsule detains three molecules each of $CHCl_3$, 1,2-dichloroethane or isopropyl chloride, and two NMR signals are seen for each in a 2:1 ratio. These represent molecules at the ends of the capsule and those near its center, respectively. Again, the coencapsulated molecules do not exchange positions while inside. Any three molecules (73–75 $Å^3$ each) optimally fill the capsule as they occupy about 52–54 % of the space (420 $Å^3$). When two different guests are encapsulated, the spectra show up to four additional species—two sets of constellational isomers (Fig. 7.13). The isomers represent molecules held in different arrangements in the space of the capsule, in different *constellations* [33]. In every pairwise combination of the solvents, all isomers could be identified. The equilibrium distributions of isomers depended on the concentrations of the solvents in the bulk solution. The relative stability of the constellational isomers is a function of the polarity of the guest molecule and its ability to interact with the capsule's components. All combinations of two guests appear to be energetically acceptable and provide a good fit. The different arrangements represent information and some possibilities exist for their use in data storage.

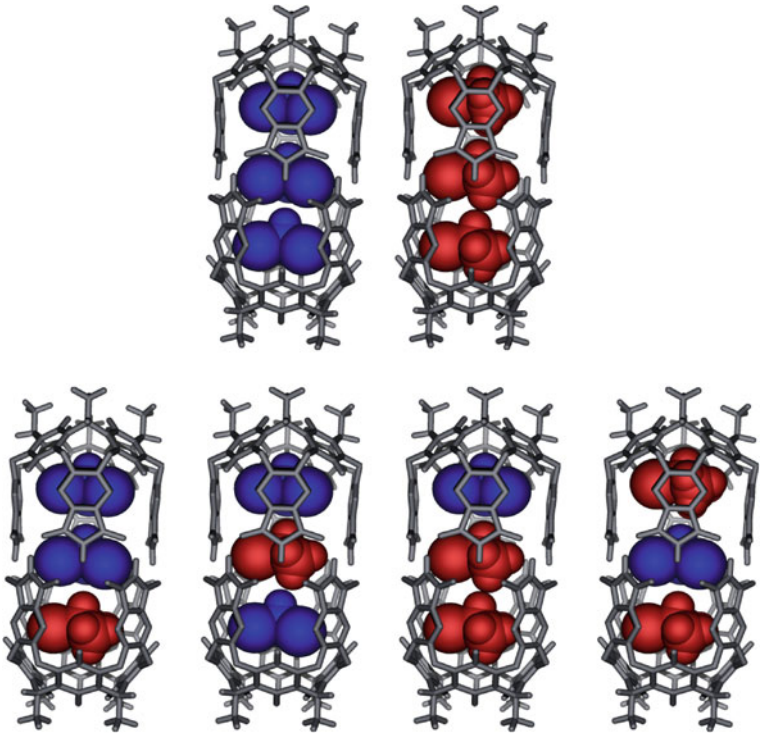

Fig. 7.13 *Top* the capsule accommodates either three molecules of chloroform or three molecules of isopropyl chloride. *Bottom* New diastereomeric arrangements (isomeric constellations) can be observed in the space when both solvents are present

The use of only two isomeric constellations is binary in nature, and the symmetry of the capsule limits the number of possibilities to six [34]. Three different guests offer 18 possibilities including a constellational triplets with one of each guest inside. It is unlikely that NMR will be able to resolve all 18 combinations of these solvents inside and alternative spectroscopic techniques must be brought to bear. Such an assembly exists but involves the encapsulation of anions (Fig. 7.14) [35]. Unexpectedly, a number of anions are driven into the capsule when dissolved in $CHCl_3$ as their tetrabutylammonium salts. A cavitand of readily accessible size can completely surround an ion pair [36], but we chose the large cation to avoid this. The driving force is believed to be the ion's ability to interact with the polar groups at the capsule's center and the relatively weak interactions of the ions with solvent. With the coencapsulated PF_6^- ion, we found it could be sandwiched between chloroform and isopropyl chloride and were able to show the formation of other combinations of three different molecules inside [37].

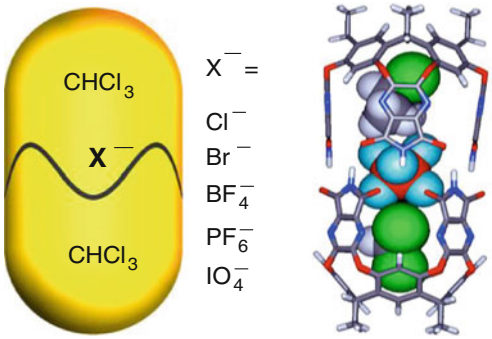

Fig. 7.14 Three species. *Left* Coencapsulation of anions with solvent chloroform. The anions occupy the center of the capsule and interact with its seam of hydrogen bonds. *Right* Three different species—PF_6^- anion, chloroform, and isopropyl chloride—are present in the capsule

7.6.5 Diastereomers

We have also observed that three small chiral molecules, e.g., three propylene sulfides, can be accommodated inside the cylindrical capsule. The odd number of molecules inside has the ineluctable consequence that each capsule is chiral: the constellational isomerism shown here involves diastereomers (Fig. 7.15) [38]. The assignments could be made using an optically pure propylene sulfide and the gradual addition of racemic material and at 60 % ee each isomer could be assigned. Put another way, it is possible to use encapsulation to determine enantiomeric excesses of small molecules inside, but there are many other ways to do this.

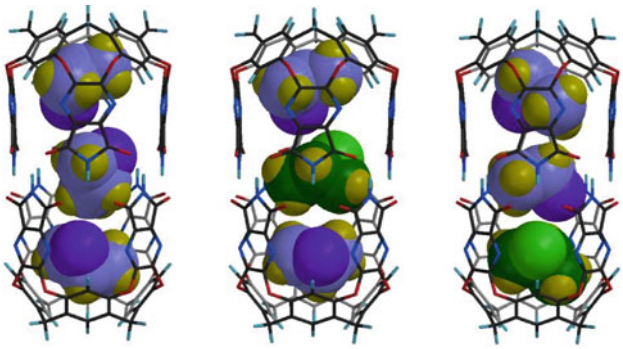

Fig. 7.15 Diastereomeric constellations. Six possible arrangements are possible for a small chiral molecule, propylene sulfide, in the cylindrical capsule. Four of the assemblies contain both enantiomers and were identified by NMR spectroscopy. All assemblies are chiral as an odd number of molecules are in each capsule. The (*R*)-propylene is in purple; the (*S*)-propylene is in *green*

7.7 Chiral Spaces

The synthesis of capsules with asymmetric spaces can be accomplished with assemblies held together with covalent bonds [39–41], or, through the principles of self-assembly, with hydrogen bonds [42–46] and metal/ligand interactions [47–50]. Enantioselection within these systems has been disappointing and the syntheses are lengthy and problematic. An alternative involves the placement of a chiral molecule in an achiral capsule, *because the remaining space is also chiral*! But can that space distinguish between enantiomers of the second molecule? Coencapsulation is ideally, perhaps uniquely, suited to this situation where two different chiral molecules are in an achiral cavity. Diastereomeric complexes can be formed, in a process similar to classical resolution methods. The longer lifetimes and limited inner space of capsules are likely to amplify recognition phenomena. Consider the alternative, a stereochemical encounter in bulk solution. In every encounter of a molecule with, say, mandelic acid asymmetry is involved, but contacts are made at random and many of these place the asymmetric centers at a distance. Only the average is experienced and recorded. Inside the capsule the asymmetric carbon of mandelic acid and its constituents are presented *toward* the remaining space in the cavity (Fig. 7.16). This cluster of functions—as a single enantiomer—is presented to the coencapsulated molecule, for a lifetime on the order of one second. The frenzied exchange of partners that occurs in bulk solution contrasts with the strict pairing, and with the fixed orientations of the two coencapsulated molecules. We observed the effects of the asymmetric environment on molecules, such as isopropyl chloride where the two methyls become diastereotopic. That is, they experience the steric asymmetry presented by the three different groups of the nearby mandelic acid—hydrogen, hydroxyl, and carboxyl. The chiral molecule imparts a magnetic asymmetry as well, affecting the remaining space [51]. The phenyl group is at the end of the capsule, "behind" the asymmetric center and acts as an excellent anchor. The positioning is optimal but we can hardly claim control of the process. Rather, each system has its characteristics and the experimenter contrives to make things happen within those constraints by manipulating sizes, shapes, and functional groups. With molecules such as racemic 2-butanol, which can offer attractive contacts to mandelic acid, some diastereoselectivity results in the coencapsulation complex. While the levels of diastereoselectivity are, at best, 60–70 % and are low by the standards of modern catalytic asymmetric synthesis, they are quite high for systems held together by only hydrogen bonding [52].

Even when two related molecules are coencapsulated, unexpected results can emerge. We encountered these initially as "complexes within complexes" as shown in Fig. 7.17. The benzoic acid and pyridone dimers are isolated in the capsule, protected from exchange of partners from the bulk solution, and are held in contact by hydrogen bonding. The *trans* cyclohexane diols, when given the choice, are in a more stable arrangement when one molecule and its mirror image occupy the capsule, rather than two identical molecules.

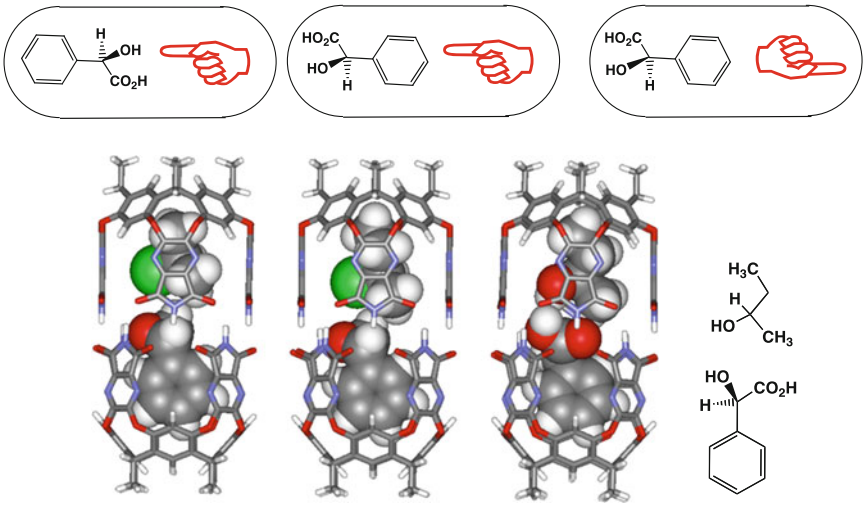

Fig. 7.16 *Top* A chiral molecule in the achiral capsule creates a chiral space around it. *Left* Styrene oxide is coencapsulated with isopropyl chloride, and the two methyl groups of the latter show different signals in the NMR spectrum. *Center* Coencapsulated styrene oxide and 2-chlorobutane; two diastereomers are observed in the NMR spectrum of this material. *Right* Mandelic acid is coencapsulated with 2-butanol and the two asymmetric centers interact with each other near the center of the capsule

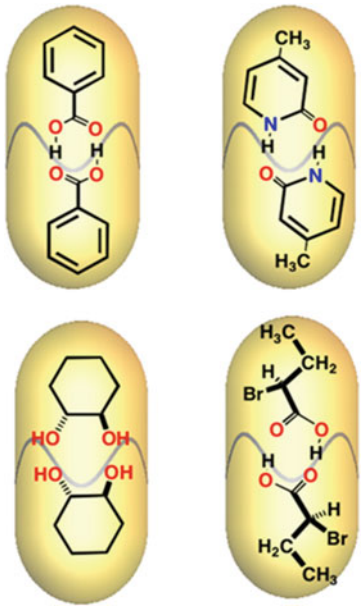

Fig. 7.17 Complexes within complexes. *Top* Two molecules of benzoic acid or pyridone are encapsulated as their hydrogen-bonded dimers. *Bottom* When *trans* cyclohexane diol is encapsulated, one molecule and its mirror image are preferred; but 2-bromo-butyric acid prefers the complex with two identical molecules inside

7.8 Reactivity

Coencapsulation creates an environment in which two molecules might be induced to react, or, if their arrangement is wrong, would be prevented from reaction. We arranged an encapsulated bimolecular reaction using *p*-benzoquinone and cyclohexadiene (Fig. 7.18). These are known to undergo Diels–Alder reactions, but at millimolar concentrations in deuterated *p*-xylene solution the reaction in bulk solution has a half-life of more than 1 year. When exposed to the capsule at these concentrations the product could be seen inside the capsule after only 1 day [53].

The cycloaddition of phenylacetylene and phenylazide is also very slow at NMR concentrations and gives roughly equal amounts of two regioisomeric triazoles. The rate at ambient temperature and molar concentrations in mesitylene is very slow; at millimolar concentrations, the rate is negligible on the human timescale. However, the encapsulated product can be detected within three days in the presence of the cylindrical capsule under these conditions. Moreover, the encapsulated product is exclusively the 1,4-isomer. The NMR spectra gave an unexpected bonus in this system. When both azide and acetylene are present, *the favored species is the capsule containing one molecule of each reactant* [54]. This result is a consequence of the similarity of the two guests and it allowed the direct observation of the fully loaded "Michaelis' complex" (Fig. 7.19). The concentrations inside are ~4 M each and viewed this way, there is no acceleration: the capsule merely concentrates the reactants, temporarily and apparently in an orientation appropriate for reaction. Compared with the reaction rate outside the capsule (at 25 mM each reactant) the acceleration is ~30,000-fold inside. Product inhibition is the norm in reactions where the products resemble transition states, and this case was no exception, but overcoming the general problem remains a challenge.

What is the source of the enhanced rate? One way of understanding the acceleration is through calculation of the capsule's volume (~400 A^3). Each molecule in that space enjoys a concentration of about 4 molar. We prefer to use these real

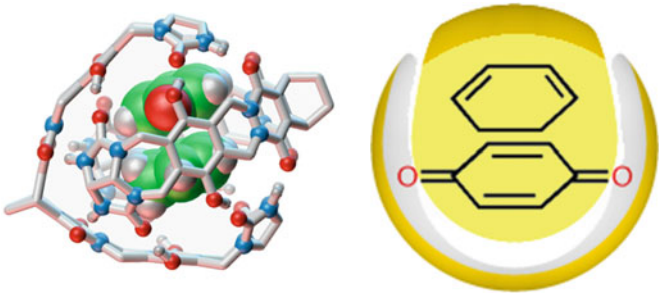

Fig. 7.18 An encapsulated cycloaddition reaction. Coencapsulation of *p*-benzoquinone and cyclohexadiene leads to a concentration of ~4 Molar in the semispherical space. The acceleration in reaction rate is nearly 200-fold in the capsule, but product inhibition prevents turnover and true catalysis

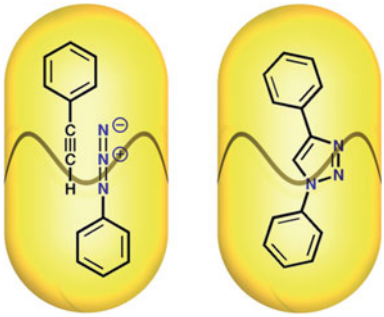

Fig. 7.19 Phenyl azide and phenyl acetylene are coencapsulated to give a "Michaelis' complex" with high molarity and effective molarity. The cycloaddition (click) reaction takes place without copper catalysis

concentrations: molecules in a given volume, but alternatively, this system has been calculated to exhibit one of the highest effective molarities on record [55]. Another view involves timing: the coencapsulation complex has a lifetime on the order of 1 s, while in bulk solution a diffusion complex of the two reactants lives less than a nanosecond. A third consideration involves solvation: *the walls of the capsule are the solvent molecules*, fixed during the capsule's synthesis. Changes in structure undergone by the coencapsulated reactants, from ground state to transition state and products, are not mirrored by changes in solvation. No organization or reorganization of the walls can take place; the arrangement was determined by the synthesis. We submit that the combination of well-defined volume, extended timing and fixed solvation of the encounter in a coencapsulation complex is a departure from earlier systems. Whatever the source or sources of the effect, the potential of coencapsulation complexes to influence chemical reactivity was established with these capsules and has been borne out with many other encapsulation complexes [56–60].

7.9 Conclusion

Hydrogen-bonded capsules are at the same time expressions of molecular self-assembly and the prefix "nano" could be appropriately applied to them. We entered through the side door of physical organic chemistry. It is a door that is still wide open.

Acknowledgments I am grateful to the Skaggs Institute for Research, Fudan University, and the National Institutes of Health (GM 50174) for financial support. The many coworkers, whose names appear on the primary publications, have made this research far more than work.

References

1. Wyler R, de Mendoza J, Rebek J Jr (1993) Angew Chem Int Ed 32:1699
2. Rebek J Jr (2005) Angew Chem Int Ed 44:2068
3. Branda N, Wyler R, Rebek J Jr (1994) Science 263:1267
4. Meissner R, Rebek J Jr, de Mendoza J (1995) Science 270:1485
5. Heinz T, Rudkevich DM, Rebek J Jr (1998) Nature 394:764
6. Gerkensmeier T, Iwanek W, Agena C, Fröhlich R, Kotila S, Näther C, Mattay J (1999) Eur J Org Chem 2257
7. Atwood JL, Barbour LJ, Jerga A (2001) Chem Commun 22:2376
8. Atwood JL, Barbour LJ, Jerga A (2002) Proc Natl Acad Sci USA 99:4837
9. Cave GWV, Antesberger J, Barbour LJ, McKinlay RM, Atwood JL (2004) Angew Chem Int Ed 43:5263
10. Avram L, Cohen Y (2002) J Am Chem Soc 124:15148
11. Avram L, Cohen Y (2002) Org Lett 4:4365
12. Avram L, Cohen Y (2004) J Am Chem Soc 126:11556
13. Yamanaka M, Shivanyuk A, Rebek J Jr (2004) J Am Chem Soc 126:2939
14. Shivanyuk A, Rebek J Jr (2001) Proc Natl Acad Sci USA 98:7662
15. Palmer LC, Rebek J Jr (2005) Org Lett 7:787
16. Avram L, Cohen Y, Rebek J Jr (2011) Chem Commun 47:5368
17. Heinz T, Rudkevich DM, Rebek J Jr (1999) Angew Chem Int Ed 38:1136
18. Ebbing MHK, Villa MJ, Valpuesta JM, Prados P, de Mendoza J (2002) Proc Natl Acad Sci 99:4962
19. Metrangolo P, Resnati G (2008) Structure and bonding mingos DMP (ed). Springer, Berlin
20. Cavallo G, Metrangolo P, Pilati T, Resnati G, Sansotera M, Terraneo G (2010) Chem Soc Rev 39:3772
21. Sarwar MG, Ajami D, Theodorakopoulos G, Petsalakis ID, Rebek J Jr (2013) J Am Chem Soc 135:13672
22. Mecozzi S, Rebek J Jr (1998) Chem Eur J 4:1016
23. Nishio M, Umezawa Y, Hirota M, Takeuchi Y (1995) Tetrahedron 51:8665
24. Eliel E, Wilen SH (1994) Conformation of acyclic molecules, Chap 10. In: Stereochemistry of organic compounds. Wiley, New York, pp 597–664
25. Jiang W, Ajami D, Rebek J Jr (2012) J Am Chem Soc 134:8070
26. Spence MM, Rubin SM, Dimitrov IE, Ruiz EJ, Wemmer DE, Pines A, Yao SQ, Tian F, Schultz PG (2004) Proc Natl Acad Sci USA 98:10654
27. Craig SL, Lin S, Chen J, Rebek J Jr (2002) J Am Chem Soc 124:8780
28. Scarso A, Shivanyuk A, Rebek J Jr (2003) J Am Chem Soc 125:13981
29. Wade D (1999) Chem Biol Interact 117:191
30. Turowski M, Yamakawa N, Meller J, Kimata K, Ikegami T, Hosoya K, Tanaka N, Thornton ER (2003) J Am Chem Soc 125:13836
31. Rechavi D, Scarso A, Rebek J Jr (2004) J Am Chem Soc 126:7738
32. Zhao YL, Houk KN, Rechavi D, Scarso A, Rebek J Jr (2004) J Am Chem Soc 126:11428
33. Shivanyuk A, Rebek J Jr (2003) Angew Chem Int Ed 42:684
34. Yamanaka M, Shivanyuk A, Rebek J Jr (2004) Proc Natl Acad Sci USA 101:2669
35. Hayashida O, Shivanyuk A, Rebek J Jr (2002) Angew Chem Int Ed 41:3423
36. Atwood JL, Szumna A (2002) J Am Chem Soc 124:10646
37. Amaya T, Rebek J Jr (2004) Chem Commun 16:1802
38. Yamanaka M, Rebek J Jr (2004) Chem Commun 15:1690
39. Canceill J, Lacombe L, Collet A (1985) J Am Chem Soc 107:6993
40. Yoon J, Cram DJ (1997) J Am Chem Soc 119:11796
41. Judice JK, Cram DJ (1991) J Am Chem Soc 113:2790
42. Rivera JM, Martín T, Rebek J Jr (2001) J Am Chem Soc 123:5213
43. Tokunaga J, Rebek J Jr (1998) J Am Chem Soc 120:66

44. Castellano RK, Nuckolls C, Rebek J Jr (1999) J Am Chem Soc 121:11156
45. Castellano RK, Kim BH, Rebek J Jr (1997) J Am Chem Soc 119:12671
46. Nuckolls C, Hof F, Martín T, Rebek J Jr (1999) J Am Chem Soc 121:10281
47. Fujita M, Umemoto K, Yoshizawa M, Fujita N, Kusukawa T, Biradha K (2001) Chem Commun 6:509
48. Hiraoka S, Fujita M (1999) J Am Chem Soc 121:10239
49. Kusukawa T, Fujita M (2002) J Am Chem Soc 124:13576
50. Caulder DL, Raymond KN (1999) Acc Chem Res 32:875
51. Scarso A, Shivanyuk A, Hayashida O, Rebek J Jr (2003) J Am Chem Soc 125:6239
52. MacGillivray LR, Atwood JL (1997) Nature 389:469
53. Kang J, Rebek J Jr (1997) Nature 385:50
54. Chen J, Rebek J Jr (2002) Org Lett 4:327
55. Cacciapaglia R, Di Stefano S, Mandolini L (2004) Acc Chem Res 37:113
56. Kaanumalle LS, Gibb CLD, Gibb BC, Ramamurthy V (2004) J Am Chem Soc 126:14366
57. Leung DH, Fielder D, Bergman RG, Raymond KN (2004) Angew Chem Int Ed 43:963
58. Yoshizawa M, Takeyama Y, Okano T, Fujita M (2003) J Am Chem Soc 125:3243
59. Ziegler M, Brumaghim JL, Raymond KN (2000) Angew Chem Int Ed 39:4119
60. Yoshizawa M, Kusukawa T, Fujita M, Yamaguchi K (2000) J Am Chem Soc 122:6311

Chapter 8
Hydrogen Bonded Organic Nanotubes

Jun-Li Hou

Abstract This chapter summarizes the application of hydrogen bonding in the construction of organic nano-tubes. Different tubular systems, including unimolecular nanotubes formed from helical and cavity-possessing molecules, and supramolecular nanotubes assembled from the bundles of rod-like molecules, the stacking of macrocyclic molecules, and the aggregation of wedge-like molecules through hydrogen bonding, are discussed by introducing typical examples.

8.1 Introduction

In biological systems, many proteins possess hollow tubular structures which are well suited for the presentation of functionality. For example, protein-degradation enzymes possess a cylindrical internal surface that provides a close reaction environment and functional group complementarities for substrates and proteins, and thus enhance the activity of the enzymes [1]. Furthermore, the functionalized tubular inner space provides a chemical environment which allows selectivity on the basis of substrate size and binding strength. Transmembrane ion channels formed by membrane proteins also provide striking demonstrations, as they can transport specific ions through their central pores that are able to discriminate against all other solutes [2].

Inspired by the remarkable functions of tubular structures in biology, chemists have shown enormous interest in the development of nano-sized tubular structures [3]. Among these structures, nanotubes composed of hydrogen bonded organic molecules are particularly interesting due to their potential applications in ion sensing, molecular inclusion and separation, catalysis, molecular devices, chemotherapy, transmembrane transport, as well as drug delivery [4].

J.-L. Hou (✉)
Department of Chemistry, Fudan University, 220 Handan Road, Shanghai 200433, China
e-mail: houjl@fudan.edu.cn

Z. Li and L. Wu (eds.), *Hydrogen Bonded Supramolecular Structures*,
Lecture Notes in Chemistry 87, DOI 10.1007/978-3-662-45756-6_8

Although noncovalent interactions are typically much weaker than covalent bonds, nanotubes self-assembled by utilizing noncovalent interactions have exhibited some significant advantages over covalently bonded analogues. For example, such supramolecular nanotubes can be assembled very efficiently from simple molecular blocks, which remarkably simplify chemical synthesis of the target molecules. The assembly process may be error-correcting and self-adaptive, and thus thermodynamically controlled supramolecular structures can be formed against other energetically less-favored structures. Hydrogen bond, owing to its relatively higher bonding energy, as compared with other noncovalent forces, such as π-π stacking and van der Waals interaction, and its highly directional nature, has been widely utilized for inducing the formation of organic nanotubes. This chapter will discuss the advance in this area. This chapter as a whole should be read as an introduction to the vast and still rapidly developing field of organic nanotubes. Only original and representative references have been selected, which necessarily cover a very small part of the reported works.

8.2 Strategies for the Construction of Hydrogen Bonding-Driven Organic Nanotubes

Conceptually, there have been several strategies developed for the formation of hydrogen bonded organic nanotubes. Generally, organic nanotubes can be unimolecular and supramolecular, i.e., multimolecular. For the unimolecular systems, the structures could be built from helical oligomers (Fig. 8.1a) or single tubular molecules (Fig. 8.1b). The synthesis of these kinds of molecules is usually time-consuming, and careful design of the molecules is needed to ensure that the intramolecular hydrogen bonds can occur to induce the designed conformation or shape. The construction of self-assembled nanotubes requires relatively simple molecular blocks. The retrosynthetic analysis for the formation of such kind of

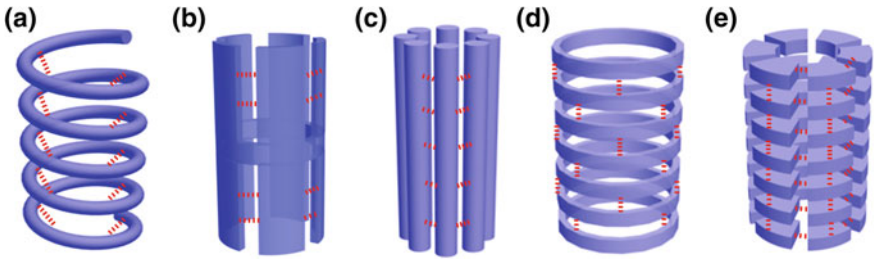

Fig. 8.1 Schematic presentation of strategies for the construction of hydrogen bonded organic nanotubes. Nanotubes from unimolecular, **a** helical, **b** tubular molecules, supramolecular, **c** bundles of rod-like molecules, **d** the stacking of macrocyclic molecules, and **e** aggregation of wedge-like molecules. The dotted red lines represent hydrogen bonding

nanotubes could be considered as the cutting of unimolecular nanotubes into simple subunits which can self-assemble into the designed structures driven by intermolecular hydrogen bonds. Thus, vertical cutting gives rod-like units (Fig. 8.1c), and horizontal cutting gives cyclic units (Fig. 8.1d), while both vertical and horizontal cutting gives wedge-like units (Fig. 8.1e).

8.3 Nanotubes from Hydrogen Bonding-Induced Helical Structures

In biological systems, the protein backbones may be induced by intramolecular hydrogen bonding and hydrophobicity to fold into helical structures which generate porous spaces to accommodate physiologically active solutes. Examples of this motif include β-helices in which the backbone folds into a helical conformation stabilized by parallel β-sheet-type hydrogen bonding [5]. In all such structures, amino acid side chains radiate outward of the helical backbone to allow the backbone to generate a central pore. The radius of the pore depends on the number of residues per turn. Indeed, computational studies have indicated that single-stranded β-helices with 4.8, 6.3, and 8.2 residues per turn may possess pore diameters of 2.3, 3.3, and 4.7 Å, respectively [6]. β-Helical conformations are common in linear peptides composed of alternating D- and L-amino acids due to the conformational requirements for β-sheet hydrogen bonding. One typical example is gramicidin A (gA) which is a linear pentadecapeptide composed of alternating D- and L-amino acids. In a lipid environment, two gA monomers associate in a head-to-head manner via six interpeptide hydrogen bonds (H-bonds) to form a water-filled ion channel that is selective to monovalent cations [7].

Inspired by the simple principle for the formation of the gA dimer, chemists have devoted a great deal of efforts to constructing artificial molecules for mimicking this important biological structure. In 1975, DeSantis and co-workers reported the first example of preparation of β-helix-forming oligopeptides with general sequence of X(L-Ala-D-Val)$_m$Y [8]. In trifluoroethanol (TFE), the circular dichroism (CD) spectra of the peptide suggested that it formed a β-helical conformation. In addition, ^{1}H NMR spectra of hexa- and octapeptides (X = benzyloxycarbonyl (Cbz), Y = OMe) in DMSO-d$_6$ were well dispersed and showed $^3J_{NH,\alpha H}$ values of nearly 8.5 Hz, which strongly supported β-type $\varnothing$ torsion angles. Other oligomers with saturated carbon chains separating amide or urea groups, such as β- [9], γ- [10] and δ-peptides [11], oligoureas [12], azapeptides [13], pyrrolinones [14], α-aminoxy-peptides [15] and sugar-based peptides [16] have also been prepared, all of which were revealed to be capable of forming helical nanotubes driven by intramolecular H-bonding (Fig. 8.2).

Another family of organic molecules that spontaneously form helical nanotubes are the long hydrogen bonding-driven aryl-based foldamers [17–19]. The main considerations for the structural design of helical foldamers are the size of the monomers and the substitution pattern of the aromatic rings used. Indeed, once

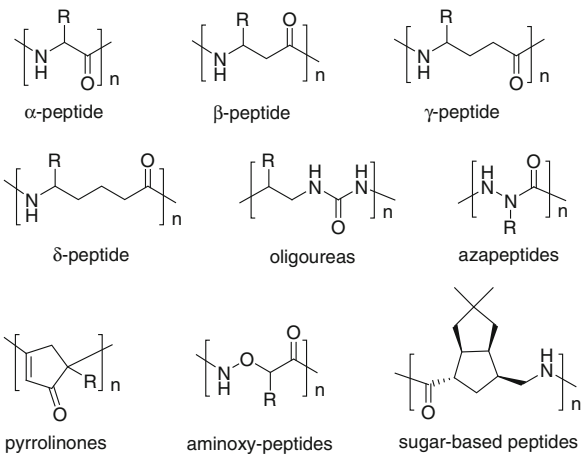

Fig. 8.2 Hydrogen bonded helical nanotubes from discrete aliphatic oligomers

these two factors are established, the cavity of a designed nanotube can be predicted quite reliably using computer simulation. Like the development of well-defined secondary structures of peptides of aliphatic amino acids, the construction of the aromatic foldamers also requires the consideration of localized noncovalent interactions. In addition to solvophobicity, hydrogen bonding has been widely employed for the construction of aromatic foldamers. Since the first report in 1994 by Hamilton and co-workers [20], a variety of hydrogen bonding patterns have been designed for the formation of linear helical structures [19]. Hydrogen bonding may stabilize the secondary structure from the interior or the exterior, or the both sides of the backbone. For the formation of a nanotube, the backbone should at least have two helical turns.

The most typical examples of these systems are aromatic oligoamides derived from 2,6-diaminopyridine and 2,6-pyridine dicarboxylic acid units (Fig. 8.3a) [21]. There are several characteristics that differentiate this type of helical structures from helices of α and β peptides: (1) the conjugation of π orbitals along the entire oligomer backbone reduces the conformational freedom, and thus provides favorable contacts between overlapping aromatic rings and amide bonds; (2) hydrogen bonds occur between consecutive units in a non-cooperative way; (3) hydrogen bonds lay perpendicular to the helix axis in or outside the helix hollow and are thus, for long backbones, shielded from solvent due to the stacking of the aromatic units; and (4) the helix can shrink and extend like a spring with minor distortions of the H-bonds. For pyridine-1,6-diamine and pyridine-1,6-dicarboxylic acid-derived sequences, one unique feature is that they can encapsulate solvent or other guest molecules in the cavity, while the acidification and de-acidification of the diaminopyridine units make the formation of the helical conformation a tunable process [22]. After the addition of a strong acid such as trifluoromethanesulfonic acid, the diaminopyridine rings can be preferentially protonated, which leads to the loss of the helical structure (Fig. 8.3). Adding a base like triethylamine neutralizes the acid, which causes the helical conformation to recover.

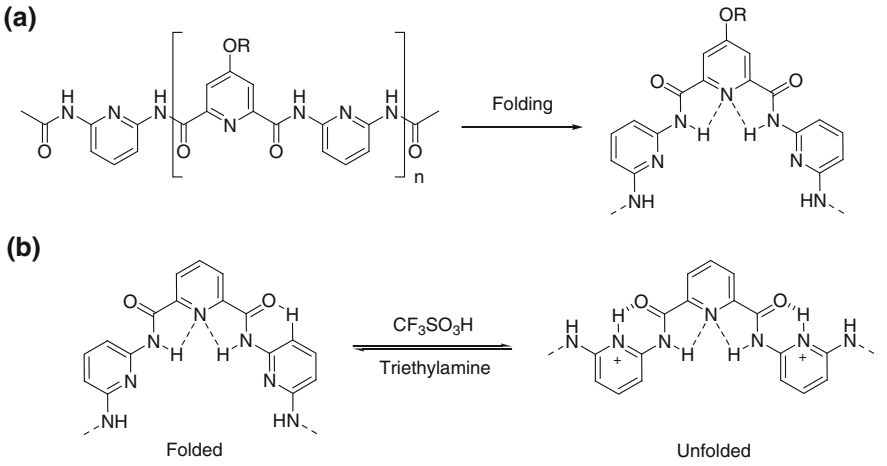

Fig. 8.3 Hydrogen bonded nanotube from aromatic oligoamides. **a** The structure of an aromatic oligoamide derived from 2,6-diaminopyridine and 2,6-pyridine dicarboxylic acids and the hydrogen bonding pattern in the formation of the helical structure. **b** Hydrogen bonding patterns that cause the oligoamide backbone to switch between the folded and unfolded conformations

By introducing hydrogen bonding from the interior and the exterior of the backbone, Li and co-workers prepared a helical foldamer from a tridecameric aromatic hydrazide (Fig. 8.4a) [23]. The presence of the three-centered hydrogen bonding helps to stabilize the helical conformation which forms a tubular structure composed of two turns (Fig. 8.4b, c). In this helical structure, half of the carbonyl

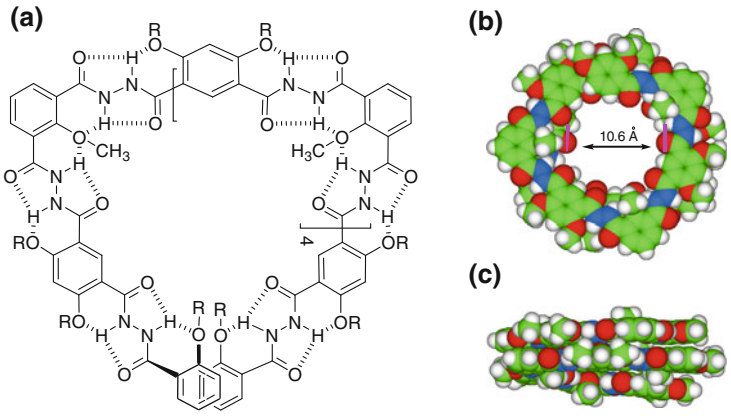

Fig. 8.4 Hydrogen bonded nanotube from tridecameric aromatic hydrazide. **a** The structure of the hydrazide tridecamer and the hydrogen bonding pattern for inducing the formation of the helical structure. **b** *Top view* and **c** *side view* of the nanotube molecular model. Reprinted with permission from Ref. [23]. Copyright 2004, American Chemical Society

groups are oriented toward the inner cavity. Thus, it can bind saccharides and aliphatic ammoniums through forming intermolecular C=O···H–O or C=O···H–N hydrogen bonding.

8.4 Nanotubes from Tubular Molecules

The synthesis of tubular molecules with discrete length in the range of 1–10 nm has been a challenge [24]. Harada and co-workers reported an elegant strategy on the design and synthesis of nanotubes based on cyclodextrins (CDs) [25]. This strategy involves the use of a rod-like molecular structure as template through which CDs are threaded driven by hydrophobicity in water, followed by the covalent linking of the hydroxyl groups of the neighboring CD molecules. After removing the linear template, macromolecular nanotubes with a very high kinetic stability can be produced. Ogoshi and co-workers proposed to construct other kind of molecular nanotubes by employing a cylindrical macrocycle as template and extending its depth. However, this has not been successful until in 2008 they succeeded in the synthesis of pillar-shaped molecules called pillar[n]arenes [26].

Typical pillararenes bear two hydroxyl groups for one benzene units. The hydroxyl groups point toward to the both ends of the rigid tubular backbones. Hou and co-workers extended the depth of the rigid backbones by introducing aliphatic chains of varying length [27]. The first generation of nanotubes of such kind were prepared by treating pillar [5] arene with ethyl bromoacetate to produce decaester-derived pillar [5] arene (Fig. 8.5a). In the solid, the molecule presents a beautiful tubular structure (Fig. 8.5b). However, in solution, the side chains are flexible, which makes the tubular conformation unstable. Subsequently, they succeeded in connecting hydrazide chains to the pillar [5] arene backbone (Fig. 8.5c) [28]. The hydrazide units in the side chains form pentameric cylinders through intramolecular hydrogen bonding, which induce the whole molecules to produce a tubular structure with a length of 5.1 nm. The length of this second generation of unimolecular nanotubes matches well with that of the lipid bilayer and thus they shows excellent activity for the transport of water and OH^- ions by a single-molecular transport mechanism. More importantly, the introduction of polyhydrazide-appended side chains results in the formation of alternative hydrophobic/hydrophilic regions on the two ends of the nanotube, which disrupts the formation of a water wire across the tube, as demonstrated by the X-ray crystal structure analysis of a model compound (Fig. 8.5d), and thus blocks the proton transmembrane transport.

The same group further revised the nanotubes by attaching peptides to the pillararene backbones (Fig. 8.5e) [29]. For molecules that bear the D-Phe-L-Phe-D-Phe-COOH sequence, ^{1}H NMR, IR, and molecular modeling studies revealed that the pillar[n]arene derivatives adopted a tubular conformation in both solution and lipid bilayer membranes due to the induction of the intramolecular hydrogen bonding formed from the amide groups of the peptide chains (Fig. 8.5f). Compared with other tubular systems, this kind of unimolecular nanotubes have several unique

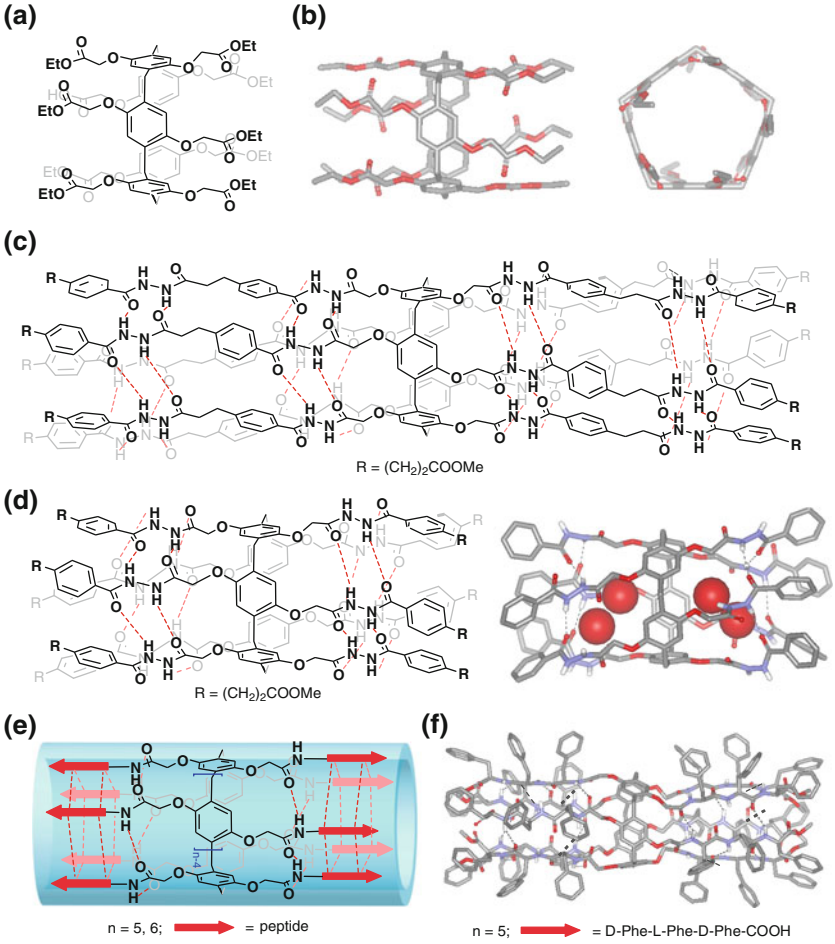

Fig. 8.5 Nanotubes from pillar[n]arene (n = 5, 6) derivatives. **a** The structure of decaester-derived pillar [5] arene and **b** its crystal structure. **c** The structure of hydrazide-incorporated-pillar [5] arenes and **d** the crystal structure of the model compound. Reprinted with permission from Ref. [28]. Copyright 2012, American Chemical Society. **e** The structure of peptide-attached pillar [n]arenes (n = 5, 6) and **f** the modeling structure of the model compound. Reprinted with permission from Ref. [29]. Copyright 2013, American Chemical Society

features: (1) the cavity radius could be modulated by the size of pillar[n]arene backbones; (2) the stability of the tubular conformation could be adjusted by varying the amino acids; (3) the length of the nanotubes could be changed by varying the length of the peptides; (4) the hydrophilicity of the nanotube surface could be modified by changing the amino acid units and their sequence; (5) the tubular cavity is chiral, which could be tuned by incorporating different chiral

amino acid residues. By making use of these features, the group has constructed quite a number of tubular systems that exhibited different functions. For example, size- and chirality-selective transmembrane transport of amino acids has been realized by attaching D-Phe-L-Phe-D-Phe tripeptides to the pillar[n]arene (n = 5, 6) backbones [29], while tubular systems that bear positively charged D-Phe-L-Phe-D-Arg tripeptide can be utilized for voltage-gated transmembrane transport of K^+ [30].

8.5 Nanotubes from Hydrogen Bonded Rod-like Molecular Units

Hollow structures can also be prepared by the self-assembly of rod-like molecules into bundle-shaped frameworks. This is also an efficient strategy for the formation of transmembrane channels by rod-like proteins of β-sheets or α-helices of amphipathic character in biological systems. The central cavity of the hollow structures is hydrophilic, while their outside area is lipophilic, which match with the lipophilic layer of the lipid membrane. A natural example of this type of proteins is α-hemolysin [31], a bacterium toxin self-assembled from seven identical subunits in cell membranes. This assembly gives rise to a mushroom-shaped structure, whose trunk is formed by a β-barrel that is inserted into the cell membrane. The resulting channel has a diameter of 13 Å at its narrowest point and can transport ions and other solutes.

This natural model has inspired chemists to develop artificial β-barrels to mimic their tubular assembling character. However, the synthetic access to artificial β-barrels is of a great challenge, because the molecular subunits may easily misfold into insoluble supramolecular polymers, rather than assemble into soluble, well-defined β-barrels. However, Matile and co-workers have developed a strategy for the formation of such kind of artificial barrel nanotubes from polybisphenols (Fig. 8.6) [32]. For all the monomers, short peptide strands with 3-5 amino acid residues are attached to each phenyl ring of their *p*-oligophenyl stave. It was proposed that these monomers might self-assemble into ordered structures through interdigitation of peptides of adjacent staves. This process should afford antiparallel hydrogen bonded β-sheets. Assisted by facial amphiphilicity of the β-sheets, the rigid-rod turns then should force the planar β-sheets to roll into cylindrical β-barrels, in which the peptide side chains point toward both sides of the oligophenyl rod in an alternate fashion. In such a way, the inner and outer properties of the channel can be tuned. In the nanotubes, the amino acid residues i +1, i + 3, i + 5 side chains are oriented toward the outer surface, while i + 2, i + 4 are oriented toward the lumen of the cavity. In this way, the hydrophilic amino acids in the outer cavity and the hydrophobic ones in the inner part allow the formation of nanotubes that are soluble in water with a hydrophobic inner cavity. Nanotubes that are soluble in organic solvents have also been prepared by using this strategy. They can form transmembrane channels in lipid bilayer [33]. These results also revealed strong

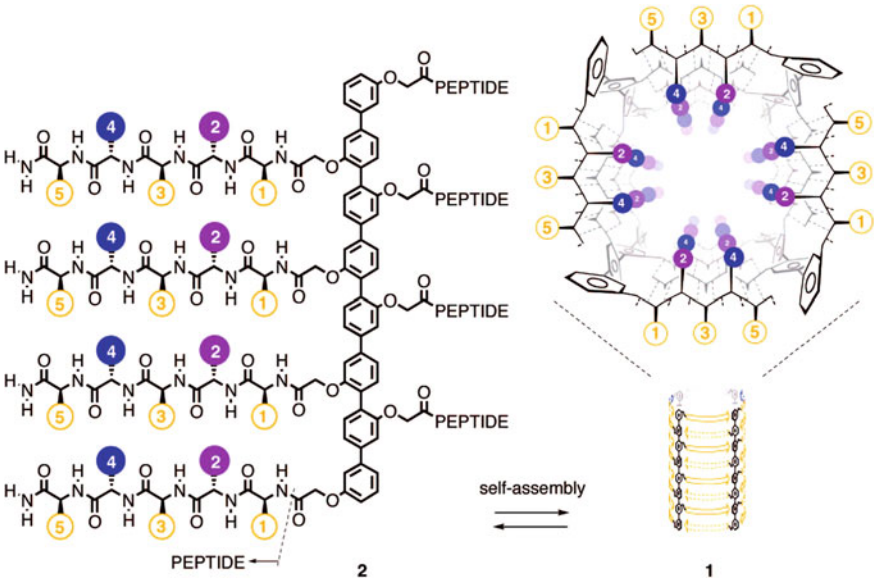

Fig. 8.6 β-Barrel nanotubes from hydrogen bonding-induced self-assembly of rigid-rod peptide-attached oligobisphenol. Reprinted with permission from Ref. [32]. Copyright 2008, American Chemical Society

preference for matched rod length over matched charges, which demonstrated that topological matching is an important driving force in the formation of nanotubes with interdigitating rigid-rod scaffolds of different lengths.

The length of β-barrel nanotubes is controlled by the number of the bisphenol units. This class of self-assembled nanotubes has been revealed to exhibit discrete functions. For example, they can serve as lipocaline mimics to host carotenoids in water [34]. The tubes can also open (ligand gating) and close (blockage) in response to a chemical stimulation [35]. Several nanotubes have been illustrated as ion channels that opens in response to charge-transfer complex formation [36], while several others have been developed as artificial tongues for multicomponent sensing in complex matrices [37].

α-Helical structures are also stable in the context of intact proteins and can also be used to construct nanotubes. Lee and co-workers reported an excellent α-helix-coated β-barrel nanotube formed by a macrocyclic peptide that contains an α-helix-forming segment and a β-sheet segment which are connected by two oligoethylene glycol chains (Fig. 8.7) [38]. The α-helix segment and the β-sheet segment stabilized each other, and the β-sheet segments of eight macrocycles self-assembled into a bundle-shaped nanotube that was stabilized by hydrogen bonding. The cyclic structure partially stabilized the helical structure by decreasing the conformational entropy of the unfolded state. The bundle-shaped nanotube was further stabilized by the self-assembly-induced coil-to-rod transition in the β-sheet segment.

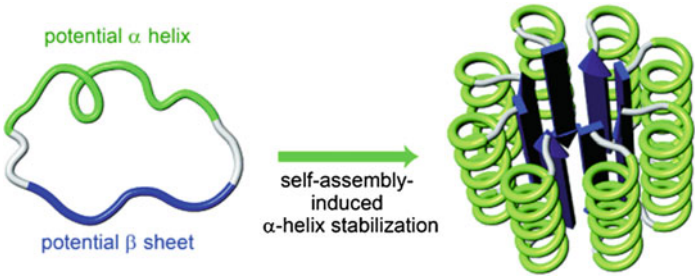

Fig. 8.7 β-Barrel nanotube derived from a macrocyclic peptide containing α-helix and β-sheet segments. Reprinted with permission from Ref. [38]. Copyright 2009, Wiley-VCH Verlag Gmbh and Co. KGaA, Weinheim

8.6 Nanotubes from Hydrogen Bonded Cyclic Molecules

Another common method which has been used to build nanotubes is based on macrocyclic molecules that are capable of stacking with each other to form the tubular structure. The main advantage of this method is the precise control of the nanotube diameter, which depends only on the size of the macrocycle used in the self-assembly.

8.6.1 Nanotubes from Hydrogen Bonded Cyclic Peptides

Self-assembled peptide nanotubes are formed by the stacking of cyclic peptides driven by the intermolecular hydrogen bonding formed from the peptide bonds of the cyclic backbone. Suitable peptides are those whose ring backbones can adopt a flat conformation in which all of the amino acid side chains have outward-pointing orientation and the carbonyl and amino groups of the peptide bonds are oriented perpendicular to the ring. In addition to the controlled macrocycle size, this kind of nanotube can also be readily modified from the outside by varying the side chains of the amino acid residues.

In 1974, on the basis of a theoretical analysis, De Santis predicted that peptides composed of an even number of alternating D- and L-amino acid residues would stack in a one-dimensional space through hydrogen bonding between the adjacent peptide backbones [39]. In 1993, the first peptide-based artificial nanotube was prepared from the octapeptide cyclo-[(L-Gln-D-Ala-L-Glu-D-Ala-)$_2$] by Ghadiri and co-workers (Fig. 8.8a) [40, 41]. The formation of the nanotube can be modulated by changing pH and thus regulating the ionization of the side chain of the glutamic acid residues, and acidification of the basic solution of the peptide led to crystalline aggregates that showed ordered hollow tubes formed by the stacking of cyclic peptides through anti-parallel β-sheet-type hydrogen bonding. Since then, the

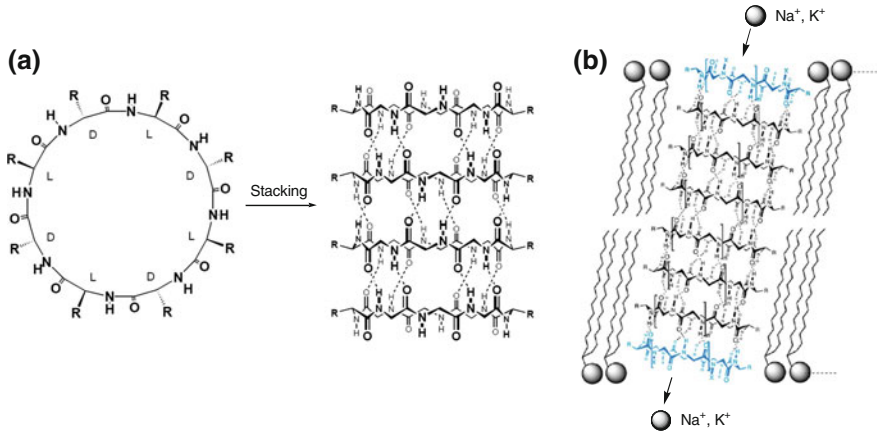

Fig. 8.8 **a** Nanotube from hydrogen bonding induced self-assembly of cyclic D, L-α-peptides. **b** Model of the transmembrane channels in the lipid bilayer. Reprinted with permission from Ref. [41]. Copyright 2013, American Chemical Society

same group have prepared a number of solid nanotubes using various uncharged cyclic octapeptides and also explored the effect of inter-tubular hydrophobic packing interactions on crystal formation [41]. The unit cell parameters of the crystals obtained from the cryoelectron microscopy and electron diffraction analyses are also fully in accordance with the expected tubular structures. The observed inter-subunit distance of 4.8 Å strongly evinced the anticipated β-sheet structures.

Ghadiri et al. also proposed that cyclic D, L-peptides bearing appropriate hydrophobic side chains would partition into nonpolar lipid bilayers and undergo self-assembly. On the basis of this hypothesis, they had prepared cyclo-[L-Gln-(D-Leu-L-Trp)$_3$-D-Leu-] and found that the cyclic peptides could self-assemble into ion channels in lipid membrane (Fig. 8.8b) [42]. The grazing-angle reflection/absorption, polarized attenuated total reflectance, and transmission Fourier transform infrared spectroscopic analysis of the complexes formed from multiple lipid bilayers and peptides have shown that the nanotubes orient themselves nearly parallel to the lipid acyl chains [43]. Such orientation also supports their proposed model of the peptide nanotubes as the active channel species. The same group have also prepared several other cyclic octapeptides and examined their transport properties by fluorescence proton-transport assays and single-channel conductance measurements. These self-assembling ion channels display transport activities for K^+ and Na^+ greater than 10^7 ions s^{-1}, which is comparable to that of natural channel gramicidin A [42].

Cyclic peptides composed of β, δ, and ε-amino acids can also form tubular assemblies. Seebach and co-workers prepared three cyclic tetrapeptides that consist of β^3-amino acid residues of different chirality (Fig. 8.9a) [44]. These cyclic β-peptides were revealed to stack to form nanotubes in the same way as cyclic

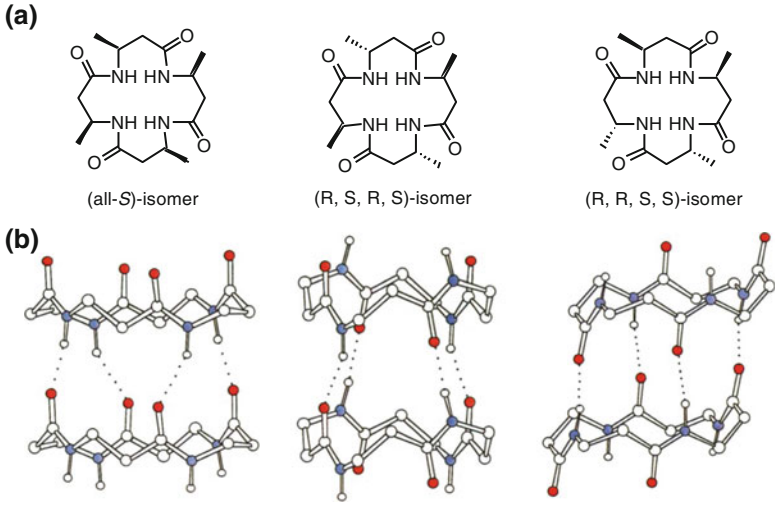

Fig. 8.9 Nanotubes formed from hydrogen bonding-induced self-assembly of cyclic β-peptides. **a** Structure of cyclic peptide containing β^3-amino acids with different chirality. **b** The corresponding stacking model of the three isomers in the solid state (Me substituents and H atoms on the backbones are omitted for clarity). Reprinted with permission from Ref. [44]. Copyright 1997, Wiley-VCH Verlag Gmbh and Co. KGaA, Weinheim

peptides formed from α-amino acids. Two stacked cyclic peptides are held together by four nonlinear C=O···H–N hydrogen bonds (Fig. 8.9b). However, because of their different chirality, the hydrogen bonding patterns are different. In the (all-S)-isomer, all four 14-membered rings were built from two seven-atom components HNCCCNH and OCNCCCO. Different from the nanotubes from cyclic peptides that contain D,L-α-amino acids, the nanotubes formed from this isomer were based on parallel-type hydrogen bonding interactions in which all of the carbonyl groups were oriented in the same direction due to the even number of atoms between the carbonyl and amino groups of each residue. This type of arrangement of hydrogen bonds led to a large dipole moment for the nanotubes. In the (R, S, R, S)-isomer, four 14-membered-ring hydrogen bonds were formed between six-atom OCCCNH and eight-atom OCNCCCNH components. While in the stacking of the (R, R, S, S)-isomer, two (7 + 7) and two (8 + 6) hydrogen bond rings were observed.

Dory and co-workers synthesized a tripeptide composed of α,β-unsaturated δ-amino acids (Fig. 8.10a) [45]. The *trans* geometry of the vinyl group was used to induce the peptide to adopt a flat conformation required for the self-assembling process. In a similar way to the nanotubes from β-peptides, the peptide backbone has an even number of atoms between the carbonyl and amino groups of each residue. As a result, all the hydrogen bonds were parallel in the nanotube (Fig. 8.10b). The same group further extended this pattern to di-, tri-, and tetrapeptides of δ-amino acids with a *trans* β,δ-double bond (Fig. 8.10c). All of these cyclic peptides were found to self-assemble into hydrogen bonded nanotubes [46].

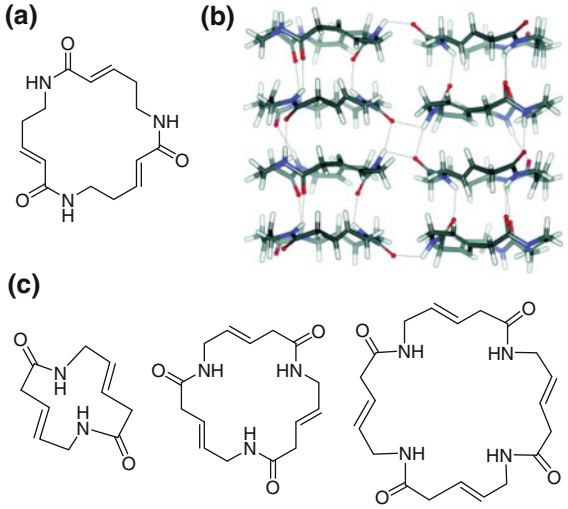

Fig. 8.10 **a** The structure of a tripeptide containing α, β-unsaturated δ-amino acids and **b** its stacking pattern in the crystal structure. **c** The structure of di-, tri-, and terapeptide containing β,δ-unsaturated δ-amino acids. Reprinted with permission from Ref. [45]. Copyright 2004, Wiley-VCH Verlag Gmbh and Co. KGaA, Weinheim

8.6.2 Nanotubes from Hydrogen Bonded Cyclic Ureas

Cyclic ureas have also been used to build nanotubes in which the urea units act as hydrogen bonding donor and acceptor to drive the self-assembly of the backbones. In this context, Shimizu and co-workers utilized the urea-urea interaction to induce a variety of macrocycles to self-assemble into infinite nanotubes that have guest-accessible channels [47]. The first generation of this family of macrocycles contained two urea groups separated by two rigid aromatic units. These cycloureas all assembled with high fidelity into the desired nanotubes even when the sizes and angles of the rigid spacer units were varied from *m*-xylene [48], 4,4'-dimethyldiphenylether [49] to 4,4'-dimethylbenzophenone (Fig. 8.11a) [50, 51]. In the crystal structures, the individual macrocycles were held together by three-centered urea hydrogen bonds that displayed H···O distances from 1.98 to 2.21 Å. The two ureas were oriented oppositely to minimize dipole interactions and were tilted slightly to bring the phenyl groups closer within the optimal distance 3.3 Å for the slip-stacked aryl interactions (Fig. 8.11b).

In addition to rigid bisurea macrocycles, more flexible bisurea-derived macrocycles can also form tubular assemblies in the solid state. For example, Ranganathan and co-workers reported that macrocyclic bisureas prepared from L-cystine was able to form nanotubes of uniform shape and internal diameter [52]. The two adjacent rings were bound together by two hydrogen bonds from bisamides and four hydrogen bonds from bisureas. The tubular structure was further stabilized by

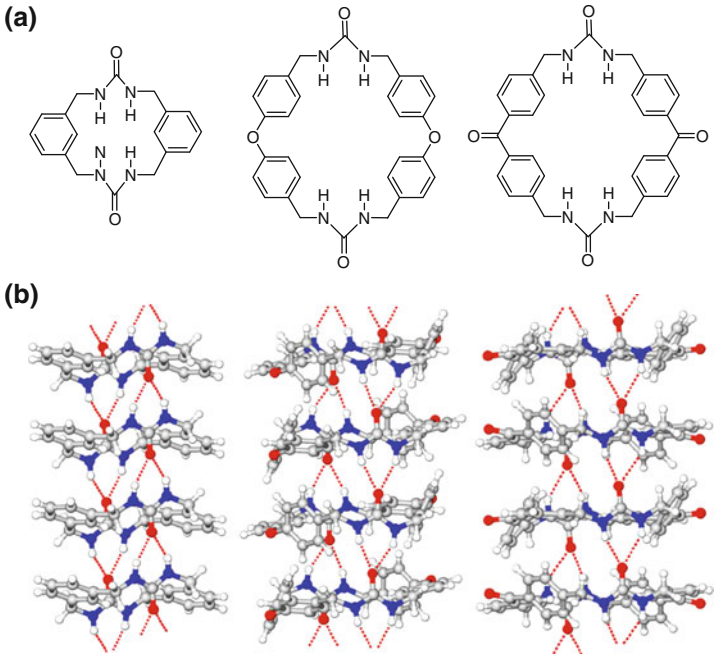

Fig. 8.11 Hydrogen bonded nanotubes from the stacking of cyclic ureas. **a** The structure of bisurea macrocycles and **b** their crystal structures. Reprinted with permission from Ref. [47]. Copyright 2014, American Chemical Society

the hydrophobic collapse of the alkyl bridge. Shimizu and co-workers reported their second-generation nanotubes from the self-assembly of bisurea macrocycles formed by more flexible building blocks [53]. They introduced heteroatoms to the backbone of the macrocycles to provide additional recognition sites for guest encapsulation. The stacking fidelity of these macrocycles was reduced and in some cases the intermolecular urea-urea hydrogen bonds were disrupted by the formation of intramolecular hydrogen bonds. However, new offset assembly motifs that maintained the urea-urea interaction were observed, which suggested that the stacking of the aromatic units in their first-generation systems was important in guiding the formation of nanotubes.

8.7 Nanotubes from Hydrogen Bonded Wedge- or Sector-like Molecules

Another approach to nanotubes relies on the hydrogen bonding-induced self-assembly of wedge- or sector-shaped building blocks. The building blocks could first form disk-like assemblies which further stack to form nanotubes or helical

assemblies of tubular structures. This is a more complex approach, because it demands higher-order self-assembly of numerous molecules and accurate control of the self-assembly process.

Whitesides and co-workers first explored this disk-assembly approach for the construction of molecular "rosettes" from melamine and cyanuric acid [54]. In a similar way, Fenniri and co-workers constructed rosette-styled nanotubes through the self-assembly of a synthetic DNA-base analogue, the G-C motif (Fig. 8.12a) [55]. Intermolecular hydrogen bonding mediated the self-assembly of six G-C motifs in water to form a supermacrocycle (rosette) which was maintained by 18 H-bonds (Fig. 8.12b). The resulting and substantially more hydrophobic rosettes then self-organized to produce a nanotube with tunable dimensions and properties (Fig. 8.12c). The side chain was oriented toward the outer surface, thus allowing the introduction of a variety of groups such as crown ethers. These rosette-styled nanotubes represent a new class of biocompatible materials since they were built under physiological conditions.

Bouteiller and co-workers reported that in nonpolar solvents a low molecular weight bisurea were able to self-assemble into two distinct, extremely long nanotubes by hydrogen bonding in a cooperative process (Fig. 8.13) [56]. Nanotube formation took place only when the solvent molecules were small enough to be accommodated within the tubes, thereby contributing to their stabilization. The group further constructed chiral dynamic nanotubes from chiral bisurea monomers or from racemic monomers induced by chiral solvent [57]. Competition experiments revealed the relative strength of the helical bias induced by the chiral monomer or by the chiral solvent. It was found that the nanotube handedness was imposed by the monomer chirality in chiral solvent. However, the chirality of the solvent has a significant effect on the degree of chiral induction.

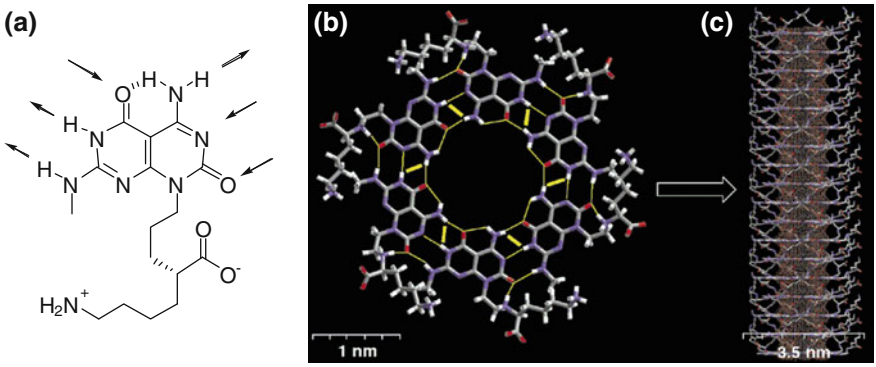

Fig. 8.12 Hydrogen bonded nanotube formed from the G-C motif. **a** The structure of the G-C motif. **b** Molecular model of the resulted rosette-styled structure. **c** Molecular model of the proposed nanotube. Reprinted with permission from Ref. [55]. Copyright 2001, American Chemical Society

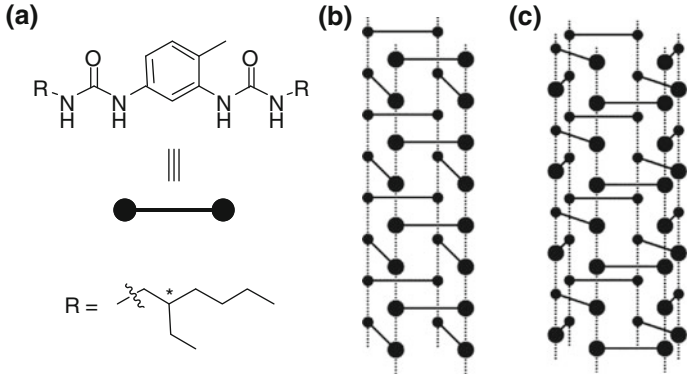

Fig. 8.13 Hydrogen bonded nanotube formed from the bisurea sector. **a** The structure of the bisurea. **b** and **c** Proposed models for the formation of nanotube induced by hydrogen bonding of urea units. Reprinted with permission from Ref. [56]. Copyright 2005, American Chemical Society

Sanders and co-workers reported that amino acid-derived naphthalene diimides could also self-assemble into hydrogen bonded helical nanotubes with a diameter of 12.4 Å (Fig. 8.14) [58]. The monomers were held together by hydrogen-bonded dimerization of the CO_2H unit between the *i* and *i* + 1 monomers and also by non-classical C–H···O hydrogen bonds between the *i* and *i* + 3 monomers. This kind of nanotubes have been characterized by circular dichroism and X-ray diffraction analysis and were found to act as receptors for fullerenes [59], condensed aromatic systems [60], and quaternary ammonium ions [61]. The self-assembly of the nanotubes was revealed to occur through a cooperative process. This unexpected behavior was considered as a manifestation of entropy-enthalpy compensation. Fundamental insights into the thermodynamics governing this self-assembly were

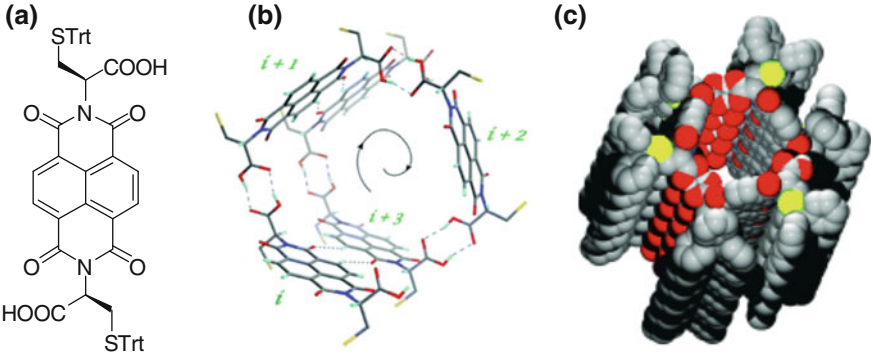

Fig. 8.14 Hydrogen bonded nanotube formed from a naphthalene diimide derivative. **a** The structure of the naphthalene diimide. **b** Hydrogen bonding pattern for the formation of the helical nanotube. **c** Crystal structure of the nanotube. Reprinted with permission from Ref. [58]. Copyright 2007, Wiley-VCH Verlag Gmbh and Co. KGaA, Weinheim

further obtained through the fitting of the isodesmic model to ^{1}H NMR spectrometry and circular dichroism spectroscopy measurements. Furthermore, they have extended the application of this mathematical model to quantitatively estimate the effect of guests, solvents, and side chains on the stability of the nanotube [62]. It was demonstrated that C_{60} could act as a template to stabilize the nanotube assembly and thereby substantially increase the degree of polymerization.

8.8 Conclusions and Outlooks

Organic nanotubes are one type of important structures for their potential application in nanotechnology and the development of new organic soft materials. In the last two decades, chemists have developed several efficient approaches to the formation of such kind of hollow structures. Hydrogen bonding-driven self-assembly strategy is important because of its high efficiency and error-correction feature. Currently, a variety of unimolecular and self-assembled nanotubes have been created, and some of them exhibit unique functions, in particular as ion channels and for molecular recognition. It is expected that in the future new construction strategies will be developed, which will allow for the generation of new kinds of advanced structures. In this context, macromolecular tubes should be attractive targets because of their potential to encapsulate polymeric guests, like polypeptides or nucleic acids, and to exhibit new chirality behavior. Molecular and supramolecular nanotubes with controllable nano-scaled length are also interesting not only for their structural uniqueness, but also for their potential application as microreactors or transmembrane transporters.

References

1. Voges D, Zwickl P, Baumeister W (1999) Annu Rev Biochem 68:1015
2. Hille B (2001) Ionic channels of excitable membranes, 3rd edn. Sinauer, Sunderland
3. Garcia-Fandino R, Amorin M, Granja JR (2012) In: Steed JW, Gale PA (eds) Supramolecular chemistry: from molecules to nanomaterials. Wiley, Hoboken, p 2149
4. Terrones M, Hsu WK, Kroto HW, Walton DRM (1999) Top Curr Chem 199:189
5. Urry DW (1971) Proc Natl Acad Sci USA 3:672
6. DeSantis P, Morosetti S, Rizzo R (1974) Macromolecules 7:52
7. Andersen OS, Koeppe RE, Roux B (2007) In: Chung SH, Andersen OS, Krishnamurthy V (eds) Biological membrane ion channels. Springer, New York
8. Ascoli F, DeAngelis G, DelBianco F, DeSantis P (1975) Biopolymers 14:1109
9. Cheng RP, Gellman SH, DeGrado WF (2001) Chem Rev 101:3219
10. Seebach D, Hook DF, Glattli A (2006) Biopolymers 84:23
11. Trabocchi A, Guarna F, Guarna A (2005) Curr Org Chem 9:1127
12. Violette A, Averlant-Petit MC, Semetey V, Hemmerlin C, Casimir R, Graff R, Marraud M, Briand JP, Rognan D, Guichard G (2005) J Am Chem Soc 127:2156
13. Zega A (2005) Curr Med Chem 12:589

14. Smith AB III, Knight SD, Sprengeler PA, Hirschmann R (1996) Bioorg Med Chem 4:1021
15. Li X, Wu YD, Yang D (2008) Acc Chem Res 41:1428
16. Claridge TDW, Long DD, Baker CM, Odell B, Grant GH, Edwards AA, Tranter GE, Fleet GWJ, Smith MD (2005) J Org Chem 70:2082
17. Huc I (2004) Eur J Org Chem 5:17
18. Gong B (2008) Acc Chem Res 41:1376
19. Zhang DW, Zhao X, Hou JL, Li ZT (2012) Chem Rev 112:5271
20. Hamuro Y, Geib SJ, Hamilton AD (1994) Angew Chem Int Ed Engl 33:446
21. Huc I, Maurizot V, Gornitzka H, Léger J-M (2002) Chem Commun 578
22. Kolomiets E, Berl V, Lehn J-M (2007) Chem Eur J 13:5466
23. Hou JL, Shao XB, Chen GJ, Zhou YX, Jiang XK, Li ZT (2004) J Am Chem Soc 126:12386
24. Shimizu T, Masuda M, Minamikawa H (2005) Chem Rev 105:1401
25. Harada A, Li J, Kamachi M (1993) Nature 364:516
26. Ogoshi T, Kanai S, Fujinami S, Yamagishi TA, Nakamoto Y (2008) J A Chem Soc 130:5022
27. Si W, Chen L, Hu XB, Tang G, Chen Z, Hou JL, Li ZT (2011) Angew Chem Int Ed 50:12564
28. Hu XB, Chen Z, Tang G, Hou JL, Li ZT (2012) J Am Chem Soc 134:8384
29. Chen L, Si W, Zhang L, Tang G, Li ZT, Hou JL (2013) J Am Chem Soc 135:2152
30. Si W, Li ZT, Hou JL (2014) Angew Chem Int Ed 53:4578
31. Song L, Hobaugh MR, Shustak C, Cheley S, Bayley H, Gouaux JE (1996) Science 274:1859
32. Sakai N, Mareda J, Matile S (2008) Acc Chem Res 41:1354
33. Das G, Matile S (2001) Chirality 13:170
34. Baumeister B, Matile S (2000) Chem Eur J 6:1739
35. Gorteau V, Perret F, Bollot G, Mareda J, Lazar AN, Coleman AW, Tran DH, Sakai N, Matile S (2004) J Am Chem Soc 126:13592
36. Bhosale S, Sisson AL, Talukdar P, Fürstenberg A, Banerji N, Vauthey E, Bollot G, Mareda J, Röger C, Würthner F, Sakai N, Matile S (2006) Science 313:84
37. Litvinchuk S, Tanaka H, Miyatake T, Pasini D, Tanaka T, Bollot G, Mareda J, Matile S (2007) Nat Mater 6:576
38. Lim YB, Moon KS, Lee M (2009) Angew Chem Int Ed 48:1601
39. De Santis P, Morosetti S, Rizzo R (1974) Macromolecules 7:52
40. Ghadiri MR, Granja JR, Milligan RA, McRee DE, Khazanovich N (1993) Nature 366:324
41. Montenegro J, Ghadiri MR, Granja JR (2013) Acc Chem Res 46:2955
42. Ghadiri MR, Granja JR, Buehler LK (1994) Nature 369:301
43. Kim HS, Hartgerink JD, Ghadiri MR (1998) J Am Chem Soc 120:4417
44. Seebach D, Matthews JL, Meden A, Wessels T, Baerlocher C, McCusker LB (1997) Helv Chim Acta 80:173
45. Leclair S, Baillargeon P, Skouta R, David Gauthier, Zhao Y, Dory YL (2004) Angew Chem Int Ed 43:349
46. Bélanger D, Tong X, Soumaré S, Dory YL, Zhao Y (2007) Chem Eur J 13:9223
47. Shimizu LS, Salpage SR, Korous AA (2014) Acc Chem Res 47:2116
48. Shimizu LS, Smith MD, Hughes AD, Shimizu KD (2001) Chem Commun 1592
49. Shimizu LS, Hughes AD, Smith MD, Davis MJ, Zhang P, zur Loye HC, Shimizu KD (2003) J Am Chem Soc 125:14972–15000
50. Yang J, Dewal MB, Profeta S, Smith MD, Li YY, Shimizu LS (2008) J Am Chem Soc 130:612
51. Dewal MB, Xu Y, Yang J, Mohammed F, Smith MD, Shimizu LS (2008) Chem Commun 3909
52. Ranganathan D, Samant MP, Karle IL (2001) J Am Chem Soc 123:5619
53. Yang J, Dewal MB, Sobransingh D, Smith MD, Xu Y, Shimizu LS (2009) J Org Chem 74:102
54. Mathias JP, Simanek EE, Zerkowski JA, Seto CT, Whitesides GM (1994) J Am Chem Soc 116:4316
55. Fenniri H, Mathivanan P, Vidale KL, Sherman DM, Hallenga K, Wood KV, Stowell JG (2001) J Am Chem Soc 123:3854
56. Bouteiller L, Colombani O, Lortie F, Terech P (2005) J Am Chem Soc 127:8893

57. Isare B, Linares M, Zargarian L, Fermandjian S, Miura M, Motohashi S, Vanthuyne N, Lazzaroni R, Bouteiller L (2010) Chem Eur J 16:173
58. Pantos GD, Pengo P, Sanders JKM (2007) Angew Chem Int Ed 46:194
59. Wietor JL, Pantos GD, Sanders JKM (2008) Angew Chem Int Ed 47:2689
60. Tamanini E, Ponnuswamy N, Pantos GD, Sanders JKM (2010) Faraday Discuss 145:205
61. Tamanini E, Pantos GD, Sanders JKM (2010) Chem Eur J 16:81
62. Ponnuswamy N, Pantos GD, Smulders MMJ, Sanders JKM (2012) J Am Chem Soc 134:566

Chapter 9
H-Bonding-Assisted One-Pot Macrocyclization for Rapid Construction of H-Bonded Macrocyclic Aromatic Foldamers

Huaqiang Zeng

Abstract The study of macrocycles has crossed many disciplines such as chemistry, physics, biology, medicine, and engineering with many research areas concentrating on specific and selective molecular recognition, self-organization and its already demonstrated, and other promising applications. Compared to traditional strategies to synthesize macrocycles with widely ranging structures using such as templated cyclization or dynamic covalent bond formation, the use of multiple-center intramolecular H-bonds for the efficient one-pot H-bonding-assisted construction of macrocycles of varying structures and functions is among the newest and the most noteworthy additions to the toolbox for macrocycle synthesis. This strategy has allowed the creation of sizable interior cavities of as small as 1.4 Å and as large as 15 Å in radius in these H-bonded macrocycles with a number of them expressing tailor-made functions. This chapter summarizes the recent works on such "greener" syntheses of H-bonded macrocycles which help to create a whole new dimension of scientific research, markedly expanding both the structural and functional repertoires of shape-persistent macrocycles that offer a new bottom-up strategy for constructing functional architectures and materials.

9.1 Introduction

Since the seminal works on macrocyclic ligands by Pedersen [1, 2], Lehn [3, 4], and Cram [5, 6] macrocyclic chemistry has prospered over the past four decades to become one of the most dynamic and promising frontiers of chemical research, offering specific and selective molecular recognition, self-organization, and specific

H. Zeng (✉)
Institute of Bioengineering and Nanotechnology, 31 Biopolis Way, The Nanos, Singapore 138669, Singapore
e-mail: hqzeng@ibn.a-star.edu.sg

Z. Li and L. Wu (eds.), *Hydrogen Bonded Supramolecular Structures*,
Lecture Notes in Chemistry 87, DOI 10.1007/978-3-662-45756-6_9

functions that cut across many traditional scientific boundaries among chemistry, physics, biology, medicine, and engineering. Simultaneous with these innovative progresses are their enormous applications primarily involving host–guest interactions as a focal point. These apparently limitless applications can be illustrated by their uses in catalysis, sensors, ion selective electrodes, separation technology, molecular electronics/photonics, enzyme mimicry, channel replacement therapy, medical diagnostics, tumor/antivirus therapy, etc. Accordingly, researching and identifying new macrocyclic molecules with novel properties have therefore continuously attracted multidisciplinary interests.

One salient feature of macrocyclic hosts is a degree of substantial rigidity offered by the preorganized backbone, physically conferring a particular shape onto the host–guest structure and directly contributing to the enhanced binding with the guest over their acyclic analogs. Traditionally, this effect has been termed as "macrocyclic effect" [7]. Efficient construction of macrocyclic backbones to derive "macrocyclic effect," however, has been a constant challenge as forming preorganized macrocyclic structures is entropically disfavored with the cost typically paid from the reaction enthalpy. Such entropic penalty complicates the reactions and largely accounts for the low yield formation of the desired macrocycles along with an observation of many by-products, including linear/cyclic oligomers of various lengths [8]. To diminish this entropic cost and also to promote the effective macrocyclization, various strategies have been developed that include one-step cyclization [8, 9], templated cyclization [8, 9], intramolecular ring closure, intermolecular coupling [8], and dynamic covalent bond formation [10]. Despite these advances, most of the cyclization reactions are still carried out under conditions of high dilution [8, 11], and critical challenges still remain in the efficient construction of macrocycles with precise control over the ring sizes and the regiospecific functionalization around the periphery.

Within the context of establishing alternative protocols for improved macrocyclization efficiency, conformation-directed macrocyclization [12] was conceived that operates in a way akin to templated cyclization. Typically, the templated reaction relies on the auxiliary templates to bring the reactive sites into close proximity (pre-organization) such that they readily undergo efficient "intramolecular" cyclization. The newly disclosed conformation-directed macrocyclization, however, utilizes the biased backbone to purposely predispose the two reactive termini into a predictable geometry, inducing a "template effect" that accelerates the intramolecular macrocyclization reaction while minimizing the "overshooting" by-products. In the majority of reported conformation-assisted macrocyclization reactions, conformational bias is an intrinsic feature of the overall molecular backbone or functional groups such as urea [13], amide [14–16], or sulphonamide [17, 18], which results from an interplay of multiple forces including covalent bonds, hydrogen bonding (H-bonding), steric, and electronic factors [19].

Elegant examples recently appeared in the literature, describing another type of conformation-assisted one-pot multi-molecular macrocyclization reactions for folding molecules of varying structural diversities. In these cases, the conformational preorganization is induced and stabilized by intramolecular H-bonding forces [20–22]

to facilitate one-pot multi-component macrocyclization reactions. Every monomer to be incorporated into the macrocyclic backbone is characterized by its unique H-bond-enforced conformational bias that determines and parameterizes the H-bonded backbone curvature. The more monomers incorporated, the more curved the resulting backbone until it reaches a point where the terminal reactive sites are placed within reacting distances, leading to an efficient intramolecular macrocyclization reaction that prevents the chain from overgrowth. Undoubtedly, this strategy is among the newest, arguably the most efficient addition to the macrocyclization toolbox as it requires simple starting material and high yields can be possibly obtained with minimized by-products. This attractive approach capitalizes on all the beneficial features (pros) associated with (i) one-step cyclization (pros: simplicity of the method, simple starting materials; cons: low yield, many by-products), (ii) templated cyclization (pros: high yields, minimized by-products; cons: need auxiliary template, synthesis of the precursor can be very labor-intensive, difficult to scale up), and (iii) intramolecular ring closure (pros: high yields, minimal by-products; cons: synthesis of the precursor can be very labor-intensive, difficult to scale up) while circumventing the disadvantages (cons) accompanying the respective methods.

This chapter was rewritten based on the recent two review articles [23, 24], and will summarize the very recent synthetic works, investigating the use of intramolecular H-bonds to assist one-pot macrocyclization that has allowed for the "greener" synthesis of cavity-containing H-bonded macrocycles with different sizes and structures. Special attention is therefore given to the one-pot reactions that are multi-molecular in nature, involve readily available monomers, rely on the intramolecular H-bonds for backbone rigidification and produce macrocycles consisting of more than two repeating units.

9.2 Concept Formulation

The pioneering study on H-bond-assisted macrocyclization was performed by Hunter and co-workers in 1991 [20]. In their study, the preferred *cis*-NH arrangement of 2,6-pyridyl (**1a**) or the preferred *trans*-NH of *iso*-phthaloyl (**1b**) diamide derivatives were used to facilitate and direct the formation of various macrocycles (Fig. 9.1). By reacting different diamines (**3**) with different diacid chlorides (**2**), various cyclic dimers, tetramers or higher oligomers could be obtained in high yields of 80–90 %. The proposed non-covalent intramolecular H-bonding forces orient and preorganize the uncyclized intermediates such that the reactive sites at the two ends of the reacting partners are brought into close proximity, forming the macrocycles. It was further demonstrated that higher yields of macrocycles were obtained with the stronger H-bonding network. On the other hand, higher yield of catenanes can be obtained when the H-bonding interactions are weaker and this was usually observed in cases when the unfavorable *cis*-NH of *iso*-phthaloyl was stabilized through complexation.

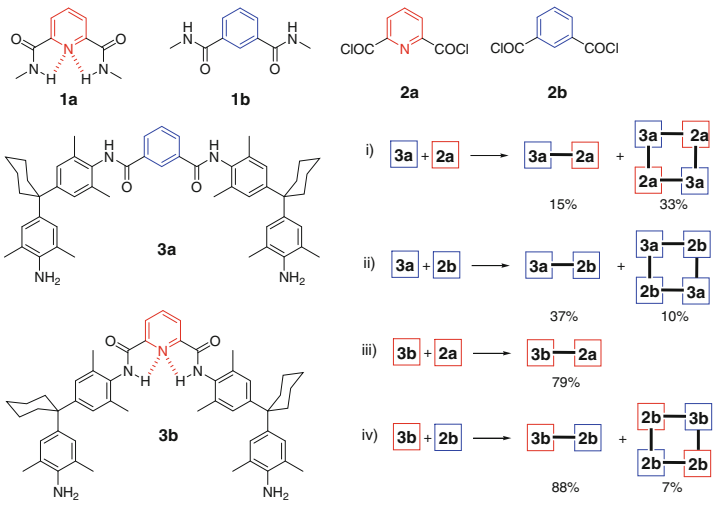

Fig. 9.1 Structures of 2,6-pyridyl and *iso*-phthaloyl diamide derivatives **1**, showing the preferred *cis*-NH (H-bonds in *red broken lines*) and *trans*-NH H-bonds conformations. Illustrated also are the formation reactions between diacid chlorides **2** and diamines **3** that produce cyclic dimers and tetramers in various yields

Although Hunter et al. attempted to use H-bond-directed self-organization as one way for an efficient preparation of macrocycles, it has not led to good synthetic utilities as a result of limited availability in H-bonding motifs able to form intramolecular H-bonds. Another more recent pioneering work exploring the important concept of using a multiple-center H-bonding system to direct the intramolecular folding was carried out by Hamilton et al. in 1994 [25], focusing on the construction of sheet-like or helical structures such as **4** (Fig. 9.2a) [26, 27]. Despite that the intramolecular H-bonds of both five and six-membered types found in the 2,6-pyridinedicarboxamide motif could be weak, the formation of such H-bonding

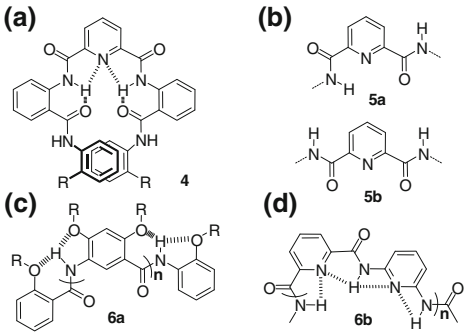

Fig. 9.2 **a** Helically folded pyridine-based oligomer **4**, **b** alternative conformations **5a** and **5b** versus **4**, **c** helically folded methoxybenzene-based foldamers **6a** and **d** pyridine-based foldamers **6b** that assemble into a double stranded structure

system is favored due to (1) the electrostatic repulsion between pyridine N-atom and amide O-atom existing in the nearly planar alternative conformations such as **5a** and **5b** in Fig. 9.2b involving a 180° rotation of amide bond in **4** and (2) a possible existence of a positive cooperativity in forming the three-center H-bonding system, e.g., formation of one intramolecular H-bond energetically increases the bond strength of the other nearby H-bond, and vice versa [28]. In 2000, Gong and co-workers [29, 30] and Lehn and co-workers [31] extended the concept to include the H-bonded oligomeric carboxyamides respectively derived from aromatic methoxybenzene (**6a** in Fig. 9.2c) and pyridine motifs (**6b** in Fig. 9.2d).

Building on their previous works on the H-bond-rigidified oligomers such as **6a** (Fig. 9.2c), an inspiring work came from the group of Gong in 2004 [21], a year of the renaissance for re-examining the pivotal role of H-bonds in macrocycle synthesis. By using a localized three-center intramolecular H-bonding system (Fig. 9.3a) to preorganize the in situ generated intermediate acyclic oligomers into a

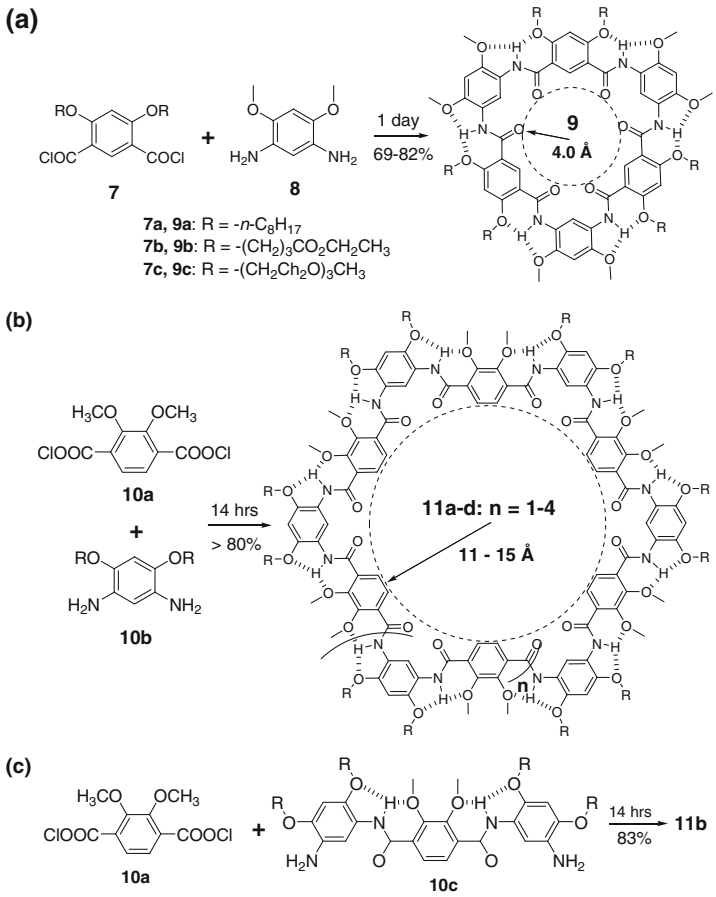

Fig. 9.3 Synthesis of AB-type macrocycles composed of **a** 3 and **b** 7–10 AB units using various diacid chlorides and diamines via one-pot macrocyclization

defined crescent-shaped conformation, Gong and co-workers succeeded in producing AB-type hexameric aryl amide macrocycles containing an internal cavity of ~8 Å and bearing different exterior side chains (**9**) in high isolated yields of 69–82 % by coupling different diacid chlorides (**7**) with 4,6-dimethoxy-1,3-phenylenediamine (**8**) via one-pot H-bonding-directed macrocyclization reactions in about 1 day under very mild conditions [21]. In the absence of the three-center intramolecular H-bonding network, the yield obtained for the respective cyclic hexamers was found to be extremely low even when the reaction was carried out in the presence of a template or in high dilution conditions due to the backbone flexibility of the conformationally ill-defined intermediate oligomers [32].

9.3 Aryl Amide Macrocycles

9.3.1 Non-fivefold Symmetric Aryl Amide Macrocycles

Apparently, the preorganized backbone of the acyclic hexamer precursors generated in situ via intramolecular H-bonds explains the highly efficient formation of symmetric AB-type macrocycle **9**. A lack of significant strain in the transition state of these acyclic hexamers accounts for the fact that six-residue macrocycles were formed as the predominant products with macrocycles of other sizes remaining scarcely present in solution. This type of acyclic oligomers with H-bond-rigidified backbones has been shown crystallographically to require ~6.5 building blocks in order to form a helical turn [30]. This suggests that acyclic oligomers shorter than hexamer could not cyclize easily due to the rigidity of their backbones while the intramolecular cyclization of other helically folded oligomers with longer backbones cannot proceed readily, either, as a result of substantial amount of ring strains. Only in the case of the acyclic hexamer precursor can a folded backbone of suitable length bring the amino and acid chloride end groups into close proximity, resulting in a rapid intramolecular cyclization with minimized strains.

A detailed mechanistic investigation of the above one-pot macrocyclization reaction was then attempted by the same group who carried out a step-by-step synthesis approach where a series of oligoamides of varying lengths and sets of carefully designed bimolecular reactions were tested. It was found that the reaction is bimolecular in nature and largely kinetically controlled, and that it is the remote steric effect that discourages the formation of oligomers longer than six residues [33]. The suggested mechanism was further supported by the efficient synthesis of 16-residue macrocycle with a cavity of 2.5 nm across (**11b** with $n = 2$, Fig. 9.3b) in 81 % yield using monomeric -diacid chloride **10a** and *meta*-diamines **10b** with concurrent productions of 14- and 18-residue macrocycles that enclose a respective lumen size of 2.2 and 2.9 nm.

The above result is also in line with further computational analyses, revealing 16-residue macrocycle to be the most stable. By alternatively performing the condensation reaction using not only monomeric reactants such as **10a** but also

oligomers of suitable lengths such as trimer **10c** as exemplified by 16-residue macrocycle **11b** in Fig. 9.3c, selective formation of 16- and 18-residue macrocycles was demonstrated to proceed respectively in yields of 83 and 85 %. The same strategy was applied to make "unfavored" 8-residue macrocycle, structurally similar to **9** (Fig. 9.3a) but having one more AB unit, by the condensation involving a pentameric diamine and a trimeric diacid chloride in yield of 75 % [34]. Further extension of the strategy using a pentameric diamine as one substrate and variable diacid chlorides from monomer up to pentamer as the other leads to the synthesis of highly strained macrocycles composed of up to 10 residues [35].

Additional tuning in reaction conditions showed that the condensation reactions using only monomeric building blocks as the starting materials are, as expected, temperature-dependant with the yield for the thermodynamically more stable six-residue macrocycle **9** (Fig. 9.3a) decreasing from 65–80 % at −20 °C to 40 % at 20 °C and that of less stable macrocyclic octamer increasing from trace amount at −20 °C to 23 % at 20 °C [34].

Li et al. later assessed the abilities of H-bonding motifs of F•••H–N, MeO•••H–N and N•••H–N to direct one one-pot macrocyclization reactions using the corresponding diamines and diacid chlorides (Fig. 9.4a) [36]. Depending on the types of monomer units used, macrocycles of different structures containing inwardly located F-, O-, and N-atoms that lead to intramolecular H-bonding networks for backbone rigidification can be prepared in good to modest yields of up to 45 % in just 1 h under mild conditions. Interestingly, by using monomers of different types such as **12a** and **12e**, 2-, 4-, and 6-residue macrocycles containing 1:1 ratio of units **12a** and **12e** can be prepared with 4-residue macrocycle produced in the highest yield of 40 % (Fig. 9.4b).

The reports discussing one-pot macrocyclization reactions by Gong and Li invariably used symmetric bifunctional monomers (e.g., diacid chloride or diamine) to form macrocycles. Asymmetric bifunctional monomers are also suitable candidates for investigating the macrocyclization that however could be more difficult due to the presence of both acid and amine groups, possibly needing chemistry beyond the classical conditions for acid chloride generation. By treating asymmetric monomeric 8-amino-2-quinolinecarboxylic acid (**14a**) with triphenylphosphite ($P(OPh)_3$) in polar solvent and at high temperature, a cyclic trimer (**15a**) and a highly strained cyclic tetramer (**15b**) could be obtained with about 20 % yield each (Fig. 9.5) [37]. In this case, the H-bonding network similarly preorganizes the acyclic trimer intermediate for the cyclization reaction, and its formation thus can be anticipated. The formation of the highly strained cyclic tetramer in 20 % is somewhat unusual as the helically folded acyclic tetramer intermediate would have extended by about 1.5 turns, making the two reactive ends of the oligomer too far apart for cyclization and in mean time introducing ring strain. Hence, the yield of cyclic tetramer is, as expected, much lower than the cyclic trimer. The X-ray crystal structure of the tetramer indeed confirms a strong deviation of its macrocyclic backbone from planarity, leading to a saddle shape (Fig. 9.5a). This saddle shape

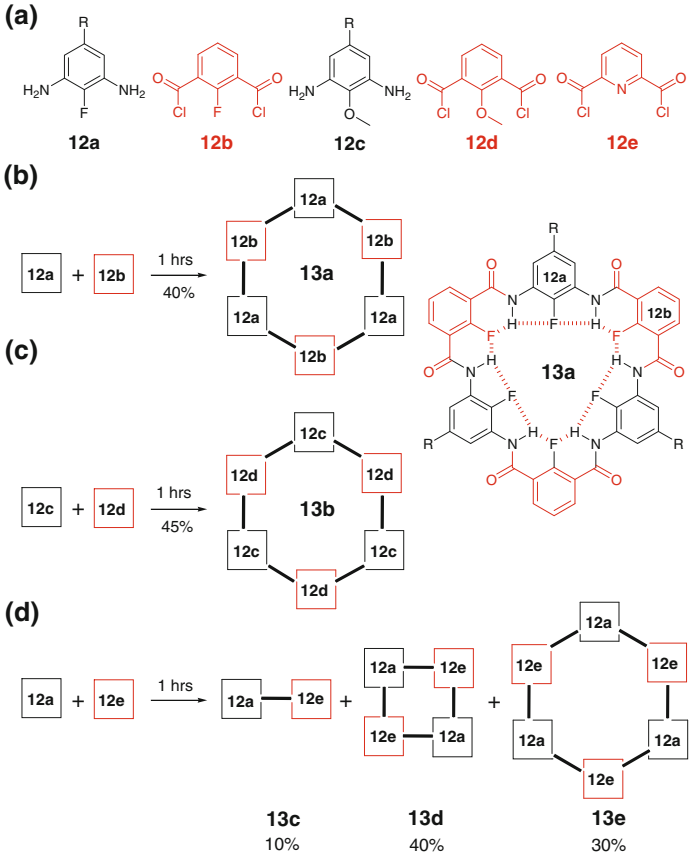

Fig. 9.4 Construction of AB-type macrocycles composed of 1–3 repeating AB units using various diacid chlorides and diamines via one-pot macrocyclization. The H-bonds are located in the interior as opposed to those in macrocycles in Fig. 9.3

results in a loss of two intramolecular H-bonds in the inner rim, and breaks two pairs of conjugations between the aryl and their adjacent amide groups as the dihedral angle between them were found to be near 90°. The loss of the H-bonds and conjugation would lead to some strain in the cyclic tetramer. It was proposed that the use of polar solvent, high temperature, and the coordination of Li^+ ions help the formation of the unusual cyclic tetramer as only trace amount of it was observed when a milder reaction condition was used. For comparison, 50 % of cyclic trimer was isolated under the same conditions. By using a slightly different 2-quinoline derived monomer **14b**, Jiang and co-workers reported one-pot reaction mediated by dichlorotriphenylphosphorane (PPh_3Cl_2) to form another new class of cyclic tetramers (**15c** and **15d**, Fig. 9.5b) [38].

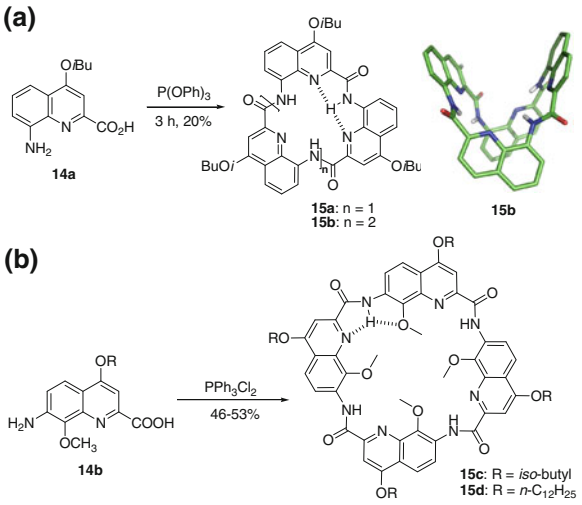

Fig. 9.5 **a** $P(OPh)_3$- and **b** PPh_3Cl_2-mediated one-pot macrocyclization with the use of asymmetric bifunctional monomers by Huc and Jiang, yielding cyclic trimer **15a** and highly strained tetramer **15b**. Also shown in (**a**) is the *side view* of the crystal structure of highly strained tetramer **15b**

9.3.2 Fivefold Symmetric Aryl Amide Macrocycles

9.3.2.1 Evolution of Fivefold Symmetric Macrocycles

The H-bonded macrocycles studied by Zeng and his co-workers since 2008 [39] carry an intrinsic peculiarity, requiring five identical repeating units to form a macrocycle, which is quite unusual and bears no precedents among synthetic foldamers [24]. Except for the Schiff-base macrocycles reported by MacLachlan in 2011 [40], all the other known H-bonded macrocycles contain no fivefold symmetry. This aesthetically pleasing fivefold symmetry further appears to have been scarcely studied in the hitherto reported shape-persistent macrocycles of varying types including porphyrin derivatives or analogues [41, 42], arylene ethynylene macrocycles [8] and macrocyclic Schiff bases [43, 48]. In addition to their unique symmetry, this class of modularly tunable, H-bonded, and shape-persistent macrocycles we have developed contain a high degree of precisely tunable interior properties, including effective cavity size, steric crowding, cavity hydrophobicity and cation-binding capacity. A few of these macrocyclic receptors have been demonstrated to be able to selectively recognize specific alkali metal cations with high binding affinities [44, 45].

Our design of fivefold symmetric macrocycles was largely inspired by our careful analysis of the crystal structures reported by the group of Gong [29, 30] suggested a likelihood for the amide linkages to display a breathing-type behavior in bond angles, resulting in the amide-linked backbone being curved more toward the H-bonded side. This plasticity in bond angles allows the helices (e.g., **6a** in Fig. 9.2c and its other analogues such as **6c** in Fig. 9.6a) with the H-bonds decorating the exterior of their helical backbones to have ~6.5 residues (Fig. 9.6a), rather than six residues, per helical turn [30]. This plasticity involving the amide bond can be further substantiated by the ab initio calculation at the high level of

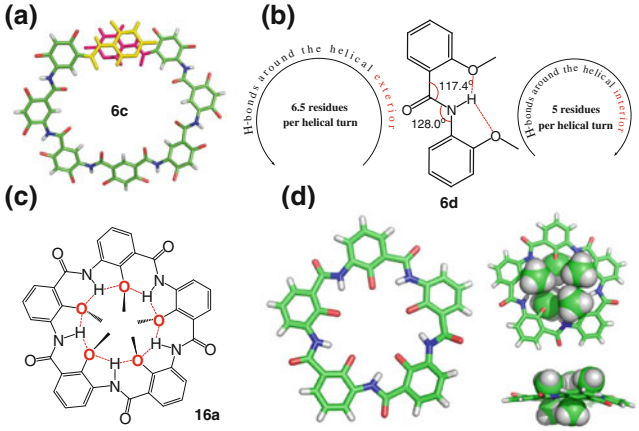

Fig. 9.6 **a** *Top view* of the crystal structure of a helically folded symmetric nonamer molecule **6c** consisting of one central symmetrical unit and two flanking tetramers that possess ~6.5 residues per helical turn. **b** The bond angles of 117.4° and 128.0° in **6d** were determined by the ab initio calculation at the B3LYP/6-311+G(2d,p) level. Experimentally, these two angles fall within a range of 116.2–117.7° and 126.6–128.7° respectively. These deviations from 120° make the helical backbone curve more toward the H-bonded side. **c** Chemical structure of designed pentamer **16a**. **d** *Top and side views* of **16a** in the solid state with the methyl groups in CPK representations. The hydrophobic caps made up of methyl groups apparently block the cavity and prevent **16a** from binding to metal cations. All the exterior side chains in **6c** were removed

B3LYP/6-311+G(2d,p), which has consistently enabled us to accurately predict the 3D topography of oligomers of varying types that were later experimentally verified by crystal structures [37–39]. The two highlighted bond angles in dimer **6d** computationally deviate from 120° by 2.6° and 8.0° (Fig. 9.6b), suggesting that the helices derived from this type of building blocks and having the H-bonds around their helical interiors likely require a smaller number of repeating units per helical turn. As expected, on the basis of these two bond angles, a rough mathematical calculation shows that only five repeating units are needed to form a helical turn if H-bonds are to be located inside the helices. On these grounds, we reasoned that an oligomeric backbone incorporating an inward-pointing, continuous H-bonding network would require about five repeating units per helical turn [46]. Consequently, the end-to-end cyclization of a rigidified, crescent acyclic pentamer into a circular form as sketched in circular pentamer **16a** (Fig. 9.6c) might not impose too much angle strain on the molecular backbone and so a planar conformation with a smaller cavity may result. Following this speculation, **16a** was computationally optimized at the B3LYP/6-31G(d) level [39], revealing **16a** to adopt an almost flat disk geometry with an appreciable cavity size of 2.85 Å. Using the established amide coupling methods, **16a** was prepared in a stepwise manner [47, 48] and its crystal structure pleasantly demonstrates a geometrical shape of a nearly planar pentagon involving five repeating units that are nearly ideally disposed around a rotational axis of C_5 symmetry with internal angles of close to 108° (Fig. 9.6d) [39].

In the crystal structure of **16a**, all the five methoxy oxygen atoms and amide protons point inward and contribute to the formation of a continuous intramolecularly H-bonded network (NH•••OMe = 2.2–2.4 and 1.9–2.0 Å for S(5) and S(6) intramolecular H-bonds, respectively) [39]. The rigidified circular backbone encloses a cavity of 2.85 Å in radius (or 1.45 Å after deducting a covalent radius of 1.4 Å for an oxygen atom) measured from the cavity center to the nucleus of the methoxy O-atoms. This structure also features five methoxy groups spatially arranged in an up-down-up-down-up fashion (Fig. 9.5b, c). This sequential arrangement turns out to be the most stable and more stable than other alternative arrangements involving five interior methyl groups by 2.5–7.5 kcal/mol at the B3LYP/6-31G(d) level. These alternating methyl groups further form two hydrophobic caps made up of three and two methyl groups, respectively, covering either side of the pentamer plane and completely blocking the cavity. It is also worth pointing out that the X-ray determined structure of **16a** is remarkably similar to its ab initio calculated structure at the level of B3LYP/6-31G*. This highlights a high applicability and reliability of ab initio calculations at the B3LYP/6-31G(d) level to accurately derive the structures of intramolecularly H-bonded aromatic backbones in the absence of crystal structures.

9.3.2.2 Fivefold Symmetric Macrocyclic Alkoxybenzene Pentamers

The reported stepwise construction of the macrocycles such as **16a** nevertheless gives a very low overall yield of ~5 % after months' efforts [39]. Therefore, it would be of high interest to see whether these H-bonded organic pentagons can be made more efficiently by one-pot macrocyclization in shorter times (Fig. 9.7) [50].

Compared to one-pot macrocyclization systems involving symmetric monomers [21, 33, 34], our system is further complicated by (i) the presence of both acid and amine groups on the same unsymmetrical bifunctional monomers, forcing us to look beyond the classical conditions for acid chloride generation, (ii) the H-bonding enforced, more curved backbone that either lowers down the reactivity of both acid and amine or introduces the steric hindrance in backbone, rendering the typical amide coupling agents (DCC, EDC, HATU, etc.; Table 9.1) totally ineffective, and

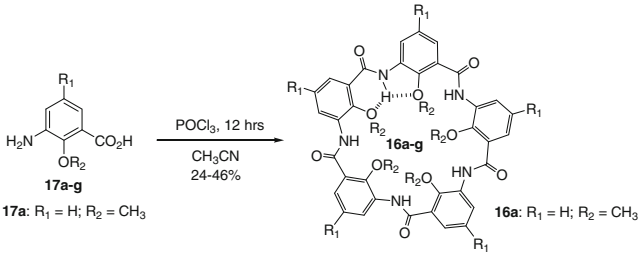

Fig. 9.7 $POCl_3$-mediated one-pot macrocyclization of **17a–g** that affords aromatic pentamers **16a–g**

Table 9.1 Searching for suitable conditions[a] for one-pot preparation of circular pentamer **16a** from monomer **17a**

Entry	Coupling reagent	Base	Solvent	Yield[b] (%)
1	DCC or EDC	–[c]	CH_2Cl_2	–[d]
2	HATU or BOP	DIEA	DMF/CH_2Cl_2 (1:1)	–[d]
3	HATU/HOBt	DIEA	DMF/CH_2Cl_2 (1:1)	Trace
4	TSTU or CDI	DIEA	DMF/CH_2Cl_2 (1:1)	Trace
5	$P(OPh)_3$	Pyridine	NMP	–[d]
6	Ph_3PCl_2	–[c]	$CHCl_3$ or THF	–[d]
7	$POCl_3$	–[c]	THF	–[d]
8	$POCl_3$	–[c]	Toluene	5
9	$POCl_3$	–[c]	CH_2Cl_2	6
10	$POCl_3$	DIEA	CH_2Cl_2	10
11	$POCl_3$	DIEA	CH_3CN	36
12	**$POCl_3$**	**TEA**	**CH_2Cl_2**	**25**
13	**$POCl_3$**	**TEA**	**CH_3CN**	**46**
14	$POCl_3$	Pyridine	CH_2Cl_2 or CH_3CN	Trace
15	$POCl_3$	NMM	CH_2Cl_2 or CH_3CN	Trace
16	$POCl_3$	DMAP	CH_2Cl_2	6
17	$POCl_3$	DMAP	CH_3CN	Trace

NMP *N*-methylpyrrolidone; *NMM* *N*-methylmorpholine; *DMAP* 4-dimethylaminopyridine

[a] Reaction conditions: **17a** (0.2 mmol), coupling reagents (0.4 mmol), base (0.6 mmol), solvent (2.0 ml), room temperature, 12 h

[b] Isolated yield by flash column chromatography

[c] No base is used

[d] No product can be detected

(iii) the additional steric hindrance originating from five sticking-out interior methyl groups [39], increasing the energetic barrier for macrocyclization and possibly impeding its efficient cyclization, especially when combined with the remote steric hindrance between the end residues. This likelihood can be manifested by the considerable difficulty encountered during the last step end-to-end amide coupling reaction that transforms acyclic pentamer precursor into circular pentamer **16a** by intramolecular cyclization [39].

Peptide coupling reagents were tested first because of the simplicity in procedure and mild conditions under which amide bonds form from carboxylic acids and amines. The well-known coupling reagents of varying types were tested that, in some cases (entries 1, 2, Table 9.1), failed to produce detectable amounts of circular pentamer **16a**, and in other cases (entries 3, 4) yielded **16a** in a trace amount. The initial screening of phosphorus-based reagents, allowing the in situ generation of acid chloride, turned out to be unsuccessful (entries 5–7). The subsequent screening of $POCl_3$ in either toluene (entry 8) or dichloromethane (entry 9) gave rise to a very encouraging yield of 5 and 6 %, respectively. Addition of three equivalent organic bases such as diisopropylethylamine (entry 10) increased the chemical yield to 10 % in CH_2Cl_2. Replacement of CH_2Cl_2 with CH_3CN further increased the chemical

yield of **16a** to 36 % (entry 11). A further screening of various bases (entries 12–17) in both CH_2Cl_2 and CH_3CN led to the discovery of triethylamine as the powerful organic base that allowed the efficient production of **16a** under high concentration of 100 mM in good and excellent yields of 25 and 46 %, respectively. A chemical yield of 46 % is considered excellent with respect to the stepwise construction of **16a** that gives an overall yield of ~5 % after dedicated months' efforts [39].

The one-pot macrocyclization reaction is influenced significantly by the amount of coupling reagent ($POCl_3$) and base (TEA) used (Table 9.2). While 1:2:3 ratio of **17a**:$POCl_3$:TEA (entry 2) produced **16a** with 25 and 46 % yields in dichloromethane and acetonitrile, respectively, only a trace amount or a low yield of 5 % for **16a** can be obtained in the same solvents when the amount of $POCl_3$ was reduced from two to one equivalents (entry 1). The use of either more of $POCl_3$ (entry 3) or less of TEA (entry 4) lowered down the chemical yields significantly when compared to entry 2. Other solvents permitting one-pot preparation of **16a** include acetone (12 %), THF (14 %), $CHCl_3$ (20 %) and toluene (17 %). No cyclization product **16a** can be generated when DMSO is used as the solvent possibly due to its strong H-bonding ability that disrupts the crescent conformation in the intermediate oligomers, a prerequisite for the efficient backbone cyclization.

The general utility of one-pot macrocyclization conditions was demonstrated by the satisfactory preparation of other circularly folded aromatic pentamers **16b–g**, sharing the same aromatic backbone but differing by interior (R_1) and exterior (R_2) side chains (Table 9.3). Pentamer **16e** with a poor solubility of <0.04 mM in CH_3CN was produced in a comparably much lower yield of 24 %. Bulky groups such as isopropyl groups and ethyl groups decreased the production yields of **16d** and **16f** considerably to 31 and 32 %, respectively. In addition to bulky ethyl groups in its interior, the poor yield of **16g** via one-pot condensation possibly can be accounted for by its poor solubility (<0.25 mM) in CH_3CN. The evidences that (i) no circular tetramers or heptamers were observed during the synthesis of **16** and (ii) 6 % of hexamer was only obtained during the preparation of **16a** but not **16b–g** suggesting that the pentameric macrocycle consisting of five identical repeating units is energetically more favored over other four-, six- and seven-residue macrocycles. Consistent with this experimental observation, theoretical treatments of circularly folded macrocycles containing from 4 to 7 residues at the B3LYP/6-

Table 9.2 Effects of coupling reagent ($POCl_3$) and base (TEA)[a] on one-pot preparation of circular pentamer **16a** from monomer **17a**

Entry	$POCl_3$ (equiv.)	TEA (equiv.)	Yield (%)[b]	
			CH_2Cl_2	CH_3CN
1	1.1	3.0	Trace	5
2	**2.0**	**3.0**	**25**	**46**
3	3.0	3.0	21	35
4	2.0	2.0	18	28

[a] Reaction conditions: **17a** (0.2 mmol = 1 equiv.), $POCl_3$, TEA, CH_3CN (2.0 ml), room temperature, 12 h

[b] Isolated yield by flash column chromatography

Table 9.3 One-pot preparation[a] of circular aromatic pentamers **16** from their respective monomers **17**, and the half-lives (h) of H–D exchange[b] of amide protons in **16**

Aromatic pentamer	R_1	R_2	Yield[c] (%)	Half-life (h)[b]	
				2.0 mM	0.2 mM
16a	H	Me	46 (6)[d]	6.3	1.49
16b	O*n*–C_8H_{17}	Me	42	8.7	4.28
16c	OMe	Me	45	–[e]	5.74
16d	O*iso*-Pr	Me	31	31.6	7.50
16e	Me	Me	24	–[e]	2.40
16f	H	Et	32	5.2	0.22
16g	OMe	Et	26	∞[f]	12.4

[a] Reaction conditions: **17** (0.2 mmol), $POCl_3$ (0.4 mmol), TEA (0.6 mmol), CH_3CN (2.0 ml), room temperature, 12 h

[b] Half-lives of H–D exchange data were measured at 2.0 or 0.2 mM in 5 % D_2O/47.5 % DMSO-d_6/47.5 % $CDCl_3$ (v:v) at room temperature

[c] Isolated yield by flash column chromatography

[d] Yield of the hexamer **18b** (Fig. 9.8)

[e] Not soluble at 2.0 mM

[f] No H–D exchange was observed over 3 days

31G* level show that the relative stability per repeating unit increases in the order of highly strained tetramer < highly strained heptamer < strained hexamer < pentamer with or without explicit solvents (Fig. 9.8a–d) [50].

The strength of intramolecular H-bonds in **16** was quantitatively measured by amide proton-deuterium (H–D) exchange experiments carried out at 2.0 mM (Table 9.3) [46]. Since the intermolecular aggregation in **16** is an unlikely event [39], the half-lives of H–D exchange should enable the direct correlation between the H–D half-life and H-bond strength. From entry 6, it is evidenced that the steric crowdingness involving bulkier ethoxy groups in **16f** does not impede the efficient H–D exchange, and amide protons can be accessed well by D_2O molecules. The determined half-life values show that the H-bond strength among **16** highly likely increases in the order of **16f** < **16a** < **16e** < **16b** < **16c** < **15d** < **16g**.

A further examination of these H–D exchange values shows that the exteriorly located electron-donating alkoxy side chains (i) cause a large variation in H-bond strength and (ii) make intramolecular H-bonds in pentamers **16b–d** and **16g** stronger than those found in pentamers **16a** and **16f** that carry no side chains. These findings agree well with the similar trends seen on other H-bonding stabilized crescent-shaped oligomers [46]. Comparison of H–D exchange data for amide protons in **16a** ($t_{1/2}$ = 1.49 h) and **16f** ($t_{1/2}$ = 0.22 h) suggests much weakened intramolecular H-bonds in **16f** relative to those in **16a**. Largely, this may be due to the bulkier interior ethyl groups in **16f** that cause a larger backbone distortion and so weaken the H-bonds in **16f** more than those in **16a**. Computationally, the aromatic backbone in **16f** is more distorted than that in **16a**.

In short, by using $POCl_3$ as the "coupling" reagent, monomer building blocks (**17**) such as methoxy and other alkoxy based aromatic amino acid can react to form

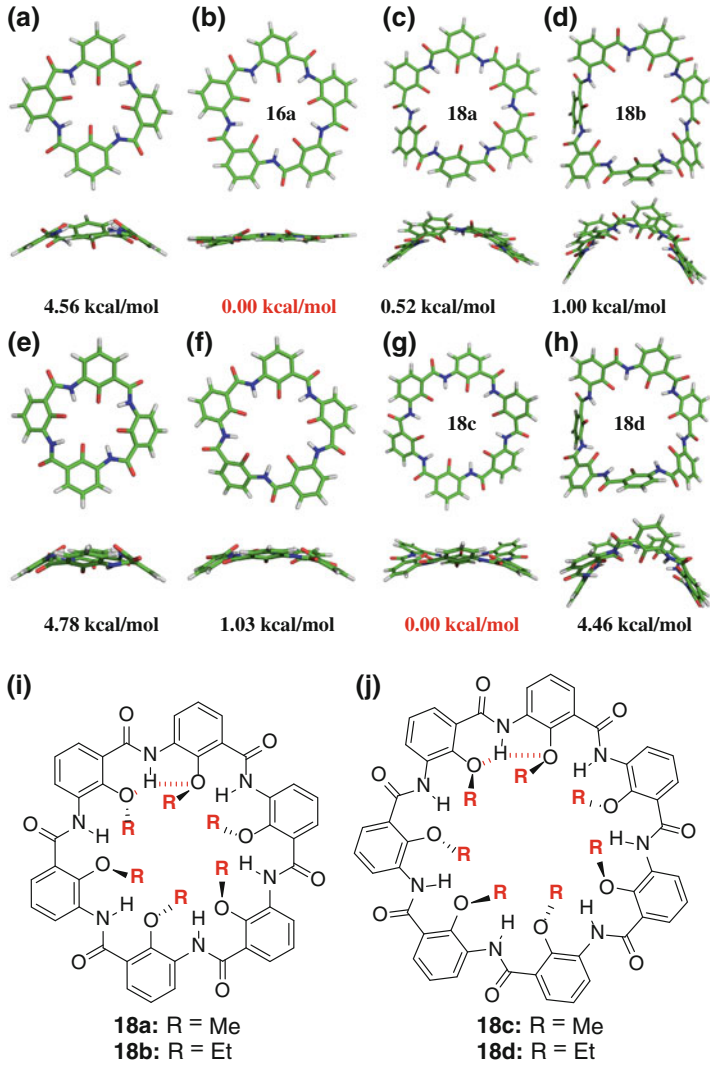

Fig. 9.8 *Top and side views* of ab initio-optimized structures of methoxy-containing circularly folded **a** tetramer, **b** pentamer **16a**, **c** hexamer **18a** and **d** heptamer **18b** as well as ethoxy-containing circularly folded **e** tetramer, **f** pentamer, **g** hexamer **18c** and **h** heptamer **18d** in acetonitrile at the B3LYP/6-31G(d) level. **i** and **j** show the structures of macrocycles **18**. The computationally derived relative energy per repeating unit among these circular foldamers is normalized based on the most stable pentamer **16a** or hexamer **18c**. For clarity of the view, all the interior methyl or ethyl groups were removed

the nearly planar cyclic pentamers as the predominant product (**16**) with a yield of up to 46 % (Table 9.3) at a concentration of 100 mM at room temperature in "ordinary" HPLC grade acetonitrile containing ≤0.01 % water.

By re-investigating the $POCl_3$-mediated one-pot reactions as rigorously as possible by using CaH_2 to remove trace amounts of water from reaction solvent CH_3CN, an overall yield inclusive of 5-, 6-, and 7-residue macrocycles was boosted from 52 % (46 % pentamer **16a** + 6 % hexamer **18a**) in "ordinary" CH_3CN to 78 % in "dry" CH_3CN (40 % pentamer **16a** + 24 % hexamer **18a** + 14 % heptamer **18c**) at room temperature [50], suggesting that even trace amounts of water present in the reaction significantly impede the one-pot macrocyclization reaction possibly by inactivating the acid chloride of intermediate oligomers. Due to the bulkier nature of ethyl group relative to methyl group, it is anticipated that macrocyclization reactions be impeded to a larger extent by interior ethoxy ethyl groups present in **18b** and **18d** than by interior methoxy methyl groups found in **18a** and **18c**. This expectation is completely in accord with the experimental findings, demonstrating consistently obtained lower yields for **18b** and **18d** than for **18a** and **18c** under identical conditions. For instance, at room temperature in "dry" CH_3CN, yields of 34 % for pentamer **16f**, 16 % for hexamer **18c** and 9 % for heptamer **18d** were obtained. Some general trends persists for macrocycles **18**: (1) higher reaction temperatures facilitate the macrocyclization reactions, (2) best overall macrocyclization efficiency is produced at 40 °C, and (3) a lower reagent concentration from 100 to 10 mM led to a lower yield.

9.3.2.3 Fivefold Symmetric Macrocyclic Pyridone Pentamers

Very recently, we described an entirely new class of pentameric macrocycles made up of five alkylated 4(1*H*)-pyridone motifs meta-linked by secondary amide groups (Fig. 9.9a) [45]. Similar to other foldamer systems reported by us that base on the use of building blocks of methoxybenzene [46, 51], pyridine [52, 53] and fluorobenzene [54], the foldable pentamers **20** are also rigidified by internally placed high-strength intramolecular H-bonds formed among the interior carbonyl O-atoms and the amide protons, restricting the conformational freedom of the amide bonds and biasing the aromatic backbone into a crescent shape [45]. Geometrically, the circularly folded pyridone pentamers contain a rarely observed *C*5-symmetry intrinsic to the molecules [40, 55, 56] and perfect planarity in the pentameric backbone (Fig. 9.9b). Functionally, the convergently aligned, properly spaced O-atoms enclose a cooperative cation-binding cavity of 2.85 Å, near-identical to the average coordination bond distance between K^+ ions and covalently bound O-atoms (Fig. 9.9c). Accordingly, pentameric molecules such as **2** display high binding affinities of $\sim 10^8$ M^{-1} toward alkali metal cations. Aided further by their planar geometry, these pentamer molecules self- assemble into 1D columnar aggregates that associate to form unusual cation-containing or scarcely reported ion pair-induced fibers of varying morphologies controllable by alkali metal ions or halide salts [45].

However, these pentameric macrocycles are typically obtained after 15–16 steps with an overall yield of 1–2 % [45], greatly limiting their potential uses in targeting biological pentamers [39], searching such as novel 1D molecular magnets, or as

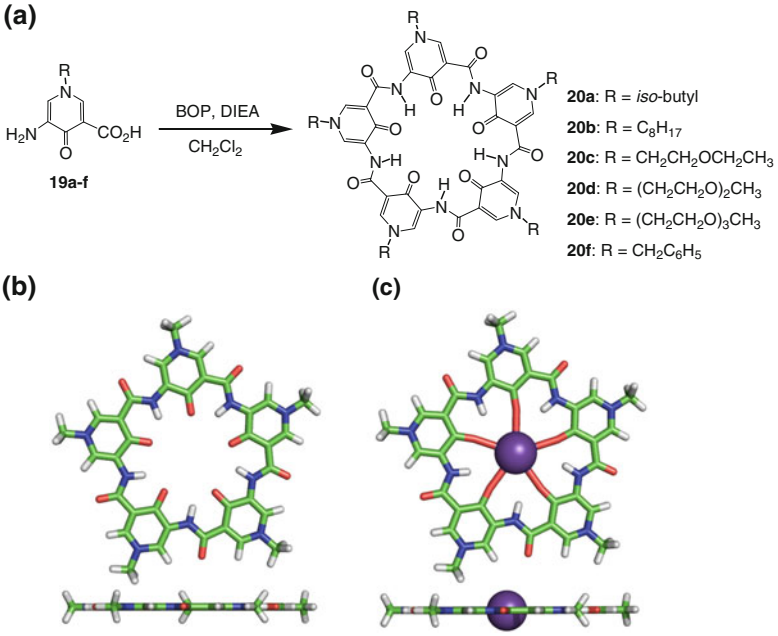

Fig. 9.9 **a** Schematic illustration of one-pot synthesis of macrocyclic pyridone pentamers **20** from their respective monomer precursors **19a–f**. Computationally optimized structure of pyridone pentamer **b** without or **c** with a K^+ in its interior at the level of B3LYP/6-31G*. A cavity of 2.85 Å in radius and macrocyclic planarity in both free and complexed forms clearly exists in these pyridone pentamers

effective sequestrators of heavy metals, imaging reagents, etc., [57, 58]. To overcome this low-yielding synthetic bottleneck and prompted by the above successful precedents and our own recent works [49, 59, 60] on the use of one-pot, H-bonding-assisted macrocyclization to efficiently generate varying macrocycles, we have investigated whether or not the H-bonded pyridone pentamers **20** can be selectively produced via one-pot macrocyclization of their respective monomer building blocks **19** (Fig. 9.9a) [61].

Due to its poor solubility in almost all organic solvents, pentamer **20a** easily precipitates out of solution and can be purified to high purity with ease by simply washing the precipitated **20a** with excessive solvents (CH_2Cl_2, MeOH, etc.), **20a** was therefore chosen as an ideal substrate for the initial screening of varying reagents that can selectively promote one-pot synthesis of circular pentamer (Table 9.4).

As a recently discovered powerful macrocyclization reagent for promoting one-pot synthesis of related pentamers consisting of five methoxybenzene repeating units from its monomer units [49, 59], $POCl_3$ (entry 1, Table 9.4) was first attempted. Surprisingly, even though with a complete consumption of starting monomer **19a**, no trace amount of **20a** can be detected from the reaction product composed of unknown compounds of varying types. The subsequent screening of

Table 9.4 Searching for suitable conditions[a] for one-pot preparation of circular pentamer **20a** from monomer **19a**

Entry	Coupling reagent	Base	Solvent	Yield[b] (%)
1	$POCl_3$	DIEA	CH_2Cl_2 or CH_3CN	–[d]
2	$P(OPh)_3$	DIEA	CH_2Cl_2 or THF	–[d]
3	Ph_3PCl_2	DIEA	$CHCl_3$ or THF	–[d]
4	CDI	DIEA	CH_2Cl_2	–[d]
5	EDC	–[c]	CH_2Cl_2	–[d]
6	DCC	–[c]	DMF/CH_2Cl_2 (1:1)	–[d]
7	TSTU	DIEA	DMF/CH_2Cl_2 (1:1)	–[d]
8	HATU	DIEA	DMF/CH_2Cl_2 (1:1)	–[d]
9	HATU + HOBt	DIEA	DMF/CH_2Cl_2 (1:1)	–[d]
10	HBTU+HOBt	DIEA	DMF/CH_2Cl_2 (1:1)	–[d]
11	PyBOP	DIEA	CH_2Cl_2	–[d]
12	**BOP**	**DIEA**	**CH_2Cl_2**	**25**
13	BOP	TEA	CH_2Cl_2	2
14	BOP	Pyridine	CH_2Cl_2	–[d]
15	BOP	NMM	CH_2Cl_2	–[d]
16	BOP	DMAP	CH_2Cl_2	–[d]
17	BOP	DIEA	$CHCl_3$	19
18	BOP	DIEA	CH_3CN	17
19	BOP	DIEA	THF	17
20	BOP	DIEA	DMSO	6
21	BOP	DIEA	DMF	8
22	BOP	DIEA	DMF/CH_2Cl_2 (1:1)	11
23	BOP[e]	DIEA	CH_2Cl_2	18
24	BOP[f]	DIEA	CH_2Cl_2	26

BOP Benzotriazole-1-yl-oxy-tris-(dimethylamino)-phosphonium hexafluorophosphate

[a] Reaction conditions: **19a** (0.2 mmol), coupling reagent (0.4 mmol), base (0.8 mmol), solvent (3.0 ml), room temperature, 30 h

[b] Isolated yield by washing with CH_2Cl_2 and MeOH

[c] No base is used

[d] No product can be detected

[e] 1.1 equivalents of BOP is used

[f] 3 equivalents of BOP is used

other phosphorus-based reagents (entries 2, 3, Table 9.4) was not encouraging either. Although we have shown previously that peptide coupling reagents including BOP that are advantaged by the simplicity in procedure and mild conditions are totally ineffective in promoting one-pot macrocyclization of methoxybenzene units [50], we still decided to carry out a further investigation on these reagents. Among a number of peptide coupling reagents tested, BOP was the only coupling reagent that allows for the preparation of **20a** under a high concentration of >60 mM via one-pot macrocyclization in dichloromethane with a very decent chemical yield of 25 % in about a day (entry 12, Table 9.10) [62] that compares

very favorably with an overall yield of 1–2 % by the stepwise construction of **20a** after dedicated months' efforts [45]. It would be interesting to note that PyBOP, structurally very similar to BOP, does not give rise to circular product **20a**.

A further screening of other bases in CH_2Cl_2 does not improve the macrocyclization efficiencies (entries 13–16, Table 9.4) and neither does the screening of varying solvents (entries 17–22). Possibly as a result of their strong H-bonding abilities that disrupt the crescent conformation in the intermediate oligomers that is a prerequisite for the efficient backbone cyclization, the use of dimethylformamide (DMF) or dimethyl sulfoxide (DMSO) seems to significantly impede the macrocyclization reaction, resulting in low yields of 6–11 % (entries 20–22). By additionally varying the amounts of BOP used, it was found that two equivalents of BOP gives a satisfactory result (entry 12) better than or comparable to the use of less (entry 23) or more of it (entry 24).

The general utility of one-pot macrocyclization conditions was demonstrated by the satisfactory preparation of other circularly folded aromatic pentamers **20b–e**, sharing the same aromatic backbone but differing by exterior side chains (Table 9.5). Because the solubility of monomers **19c–e** is not as good as **19a** and **19b** containing alkyl side chains, more CH_2Cl_2 (6 ml in Table 9.11 vs. 3 ml in Table 9.4) is needed to dissolve **19c–e**. With the use of more solvent, yield for **20a** decreases from 25 % (entry 12, Table 9.4) to 23 % (entry 1, Table 9.5) and **20b–e** all can be produced satisfactorily with a respective yield of 18, 12, 10, and 16 %.

However, one-pot synthesis of pentamer **20f** turned out to be quite troublesome (Table 9.6). Under identical conditions using CH_2Cl_2 as the solvent where monomer **19f** can hardly dissolve, no product can be obtained (entry 1, Table 9.6). In DMF, a low but encouraging yield of 2 % for **20f** was obtained. As discussed above, the BOP-mediated one-pot reaction proceeds well in CH_2Cl_2 but not in DMF. We reasoned that a solvent pair involving both CH_2Cl_2 and DMF may better dissolve **19f** and thus may allow the reaction to proceed to better extents. Hence, the subsequent screening was carried out by fine-tuning the solvent compositions (entries 3–6) with ~10 % yield obtained from CH_2Cl_2:DMF (6:1, v:v). But the use of other solvents such as CH_3CN decrease yields to 3–5 %.

BOP, a commonly used peptide coupling reagent, has often been employed in making cyclic peptides via intramolecular cyclizations [63]. Its use in inducing

Table 9.5 One-pot preparation[a] of circular pentamers **20a–e** from their respective monomers **19a–e**

Pyridone pentamer	R	Yield (%)[b]
20a	*iso*-butyl	23
20b	*n*-C_8H_{17}	18
20c	$CH_2CH_2OCH_2CH_3$	12
20d	$(CH_2CH_2O)_2CH_3$	10
20e	$(CH_2CH_2O)_3CH_3$	16

[a] Reaction conditions: **19a–e** (0.2 mmol), BOP (0.4 mmol), DIEA (0.8 mmol), CH_2Cl_2 (6.0 ml), room temperature, 30 h

[b] Isolated yield by washing with CH_2Cl_2 and MeOH (**20a** and **20c**) or recrystallization from MeOH (**20b**, **20d** and **20e**)

Table 9.6 One-pot preparation[a] of pentamer **20f** from monomer **19f**

Entry	Solvent	Volume (mL)	Yield (%)[b]
1	CH_2Cl_2	3	0
2	DMF	3	2
3	CH_2Cl_2 + DMF	3 + 1	3
4	CH_2Cl_2 + DMF	6 + 1	10
5	CH_3CN + DMF	3 + 1	3
6	CH_2Cl_2 + CH_3CN	3 + 3	5

[a] Reaction conditions: **19f** (0.2 mmol), BOP (0.4 mmol), DIEA (0.8 mmol), solvent, room temperature, 30 h
[b] Isolated yield by washing with CH_2Cl_2 and MeOH

one-pot H-bonding-assisted macrocyclizations, selectively leading to five-residue macrocycles **20** from their monomeric building blocks **19a–f**, bears no literature precedents. At the present time, we are still totally puzzled by the fact that $POCl_3$ and BOP only allows the circular pentamers to be prepared from their monomeric methoxybenzene [39, 49] and pyridine [45, 61] building blocks, respectively, and that all the amide coupling conditions outlined in Table 9.4 including $POCl_3$ and BOP do not yield any circular pyridine tetramer or fluoropentamer respectively built from monomeric pyridine [52, 53] or fluorobenzene [54] motifs. The inference is such that every type of monomer building block destined to form the most stable circular pentamer or tetramer requires their own unique "cognate" macrocyclization regents that seem to be "orthogonal" to each other and function well only against their own specific set of "cognate" monomer units. As of now, we have not been able to identify any "cognate" macrocyclization regent for pyridine and fluorobenzene motifs. Nevertheless, the BOP-mediated one-pot macrocyclization protocol decently produces its "cognate" pyridone pentamers **20** at yields of 10–25 % in about a day, a greener process that is far more cost-effective and time-saving than the step-by-step lengthy synthesis, producing pentamers **20b** and **20f** in 1–2 % yields after months' effort [45]. This one-pot macrocyclization protocol now enables a facile access to cation-binding pentamers with tunable exterior side chains that may promise some interesting applications in chemistry and biology.

9.3.3 Highly Selective Production of Strained Aromatic Hexamers

As discussed in Sects. 9.3.2.2 and 9.3.2.3 and further summarized in Fig. 9.10, it is now possible to produce H-bonded pentamers **16** and **20** by "greener" one-pot syntheses from monomeric methoxybenzene and pyridone motifs with yields of as high as 46 % in about a day. One perplexing observation during our investigations is that $POCl_3$ and BOP only allow the circular pentamers **16** and **20** to be formed from their own "cognate" building blocks, and do not yield any circular fluoropentamer (Fig. 9.10c) or pyridine-based pentamer from their corresponding

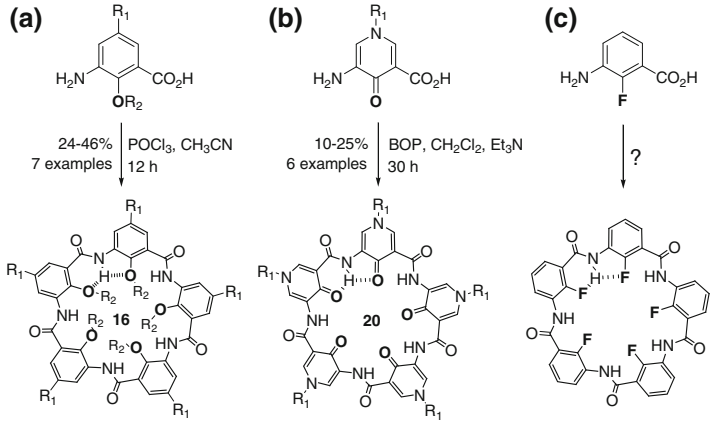

Fig. 9.10 **a** and **b** describe one-pot synthesis of macrocyclic pentamers **16** and **20** from their respective monomers by using macrocyclization reagents $POCl_3$ and BOP under mild conditions. **c** shows that no macrocyclization reagent thus far has been identified for the synthesis of fluoropentamer. Except for R_2 = ethyl group, our computational results suggest the pentameric backbones are more stable than their corresponding tetramers or hexamers

monomeric fluorobenzene [54, 64] or pyridine [65–67] amino acids. This suggests that every type of monomer building block destined to form the most stable circular structure possibly may require its own unique "cognate" macrocyclization reagents that appear to be "orthogonal" to each other and function well only against its own specific set of "cognate" monomer units. It is therefore of outstanding interest to us to continue searching for suitable one-pot macrocyclization reagents capable of selectively producing other types of pentamers such as a fluoropentamer.

Encouraged by the reports using strong alkali or other metal salts (NaH, BuLi, $AlMe_3$, etc.) to directly convert unactivated esters into amides via ester aminolysis [16, 68–72], we decided to explore the possibility of using these metal salts to effect one-pot macrocyclization reactions for a possible production of circularly folded aromatic pentamers of various types (Fig. 9.10) [73]. In a typical reaction setup, amino ester such as **21a** (0.5 mmol, Fig. 9.11) was dissolved in anhydrous THF (5.0 mL), to which metal salt (1.5 mmol) was added in one pot under nitrogen. The reaction vessel was then tightly sealed and heated at 70 °C under constant stirring for 12 h. Under these conditions and with the use of various metal salts (entries 1–6, Table 9.7), hexamer **18a** (Fig. 9.11) was produced from **21a** in 24 % yield along with trace amounts of pentamer **16a** by using aluminum salts (entries 5 and 6, Table 9.7). Under the same conditions, no pyridone- or fluorobenzene-based circular pentamers or the hexameric versions were generated from the corresponding monomeric amino esters.

Selective generation of hexamer **18a** versus pentamer **16a** is surprising in view of the computational results at the level of B3LYP/6-31G* (Fig. 9.8b, c), pointing to a highly distorted structure for **18a** that is energetically less stable than the nearly planar **16a** by 0.69 and 7.96 kcal/mol per repeating unit in THF and the gas phase,

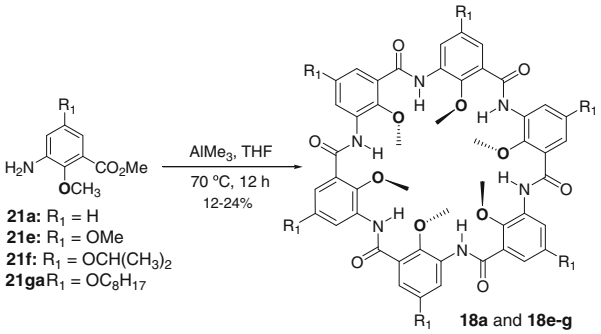

Fig. 9.11 One-pot synthesis of macrocyclic hexamers **18a** and **18e–g** by using macrocyclization reagent $AlMe_3$ under mild conditions

Table 9.7 Searching for suitable reagents[a] for one-pot preparation of hexamer **18a** from monomer **21a**

Entry	Coupling reagent	Anhydrous solvent	Yield (%)[b]	
			16a	**18a**
1	MH (M = Li, Na, or K)	THF	–[c]	
2	CaH_2	THF	–[c]	
3	$ZnEt_2$	THF	–[c]	
4	LiHMDS	THF	–[c]	
5	$AlEt_3$	THF	1	11
6	**$AlMe_3$**	**THF**	**3**	**24**
7	$AlMe_3$	Toluene	6	17
8	$AlMe_3$	Dioxane	6	15
9	$AlMe_3$	CH_2Cl_2	4	15
10	$AlMe_3$	$CHCl_3$	–[c]	–[c]

[a] Reaction conditions: **21a** (0.5 mmol, 100 mM), coupling reagents (1.5 mmol), solvent (5.0 mL), 70 °C, 12 h

[b] Isolated yield by flash column chromatography

[c] No circular products **16a** and **18a** were detected

respectively. This high level ab initio calculation has consistently allowed us to predict diverse structures of a series of H-bond-rigidified foldamer molecules including **16a** that subsequently were verified by their crystal structures [40, 45, 46, 52, 53, 64]. The inherent instability and high structural distortion in **18a** may suggest more stable and more planar **16a** to be produced predominantly in the macrocyclization reactions. In fact, our earlier investigations do show that macrocyclization regent $POCl_3$ invariably produces **16a** as the major product of up to 46 % in yield and **18a** as the minor product of up to 33 % in yield from monomer **17a** in acetonitrile [49, 50, 59, 60]. By using **21a** as the starting material and $AlMe_3$ as the macrocyclization regent, an opposite trend is found, i.e., less stable and more distorted **18a** was unexpectedly produced as major product (entry 6, Table 9.7).

This trend persists in solvents (e.g., toluene, dioxane, and dichloromethane) where macrocyclization can take place, albeit with lower yields of **18a** and higher yields of **16a** (entries 7–9). This $AlMe_3$–mediated cyclohexamerization reaction likely proceeds via an intermediate aluminum amide formed by reaction of $AlMe_3$ with RNH_2 with loss of methane, followed by coordination of the Al center to the carbonyl to activate the ester and deliver the amide nucleophile to form amide bonds. In light of this mechanism, such reactions are expected to be prone to inhibition by Lewis basic solvents and additives. The use of Lewis basic solvents such as DMF, DMSO, CH_3CN, acetone, and ethyl acetate indeed completely halts the macrocyclization reaction, resulting in no generation of **16a** and **18a**. Similarly, in the presence of Lewis basic additives such as HMPA, TMEDA, and PMDTA, circular products **16a** and **18a** remain undetectable either.

With respect to entry 1 in Table 9.8, either a deviation from the optimum reagent concentration of 100 mM as seen in entries 2–4 or addition of the same amount of $AlMe_3$ in three portions as seen in entry 5 decreases the yield of **18a** from 24 to 14–22 %. A prolonged reaction time of up to 48 h marginally helps increase the yield of **18a** by up to 2 % (entry 3 vs. entries 6 and 8). The substrate scope was then examined by applying the optimized macrocyclization conditions to monomeric **21b–d** (Fig. 9.11). Except for **21b** for which no macrocyclization product **18b** was observed, **18c** and **18d** both were produced satisfactorily from **21c** and **21d** with respective yields of 17 and 12 %.

Substantiated by the crystallographically proven helically folded structures adopted by hexamers of related structures [46, 51], hexamer **P6** is computationally determined to also take a helically folded structure that is rigidified by strong H-bonds (see structure in Table 9.9). As a result, the two reacting end groups in **P6** are rigidly placed far away from each other and the intramolecular ring closing reaction thus does not occur readily to produce **18a**. Consistent with this structural constraint and going from 25 to 70 °C, **18a** is produced increasingly with increasing

Table 9.8 Effects of solvent volume, reaction time, and addition sequence involving $AlMe_3$ on one-pot preparation of hexamer **18a** from monomer **21a** in THF at 70 °C

Entry	Solvent volume (mL)	Reaction time (h)	Yield (%)[a, b]	
			16a	**18a**
1	**5.0**	**12**	**3**	**24**
2	2.5	12	2	22
3	10.0	12	2	18
4	15.0	12	2	15
5	10.0[c]	12	2	14
6	10.0	24	2	19
7	10.0[c]	36	2	19
8	10.0	48	2	20

[a] Reaction conditions: **21a** (0.5 mmol), $AlMe_3$ (1.5 mmol), THF, 70 °C, 12 h
[b] Isolated yield by flash column chromatography
[c] $AlMe_3$ was added in three portions at intervals of 4 and 12 h for entries 4 and 7, respectively

Table 9.9 Temperature-dependent distributions of intermediate and circular oligomers from one-pot cyclohexamerization of **21a** in THF

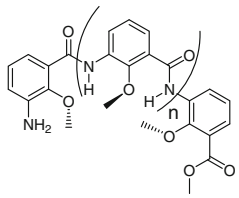

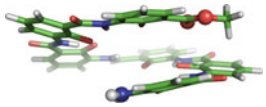

H, N, and O atoms at the two helical ends are in gray, blue and red balls, respectively

Helically folded P6

Temp (°C)	Yield (%)[a, b]					
	Intermediate oligomers				Circular oligomers	
	P2	**P3**	**P4**	**P5**	**16a**	**18a**
25	20	15	12	7	1	4
40	14	7	11	6	1	11
60	6	4	7	4	2	19
70	3	2	3	3	3	24

[a] Reaction conditions: **21a** (0.5 mmol), $AlMe_3$ (1.5 mmol), THF (5 mL), 12

[b] Isolated yield by flash column chromatography

consumptions of **P2–P4** possibly via bimolecular reactions. In regard with the yields of pentamer **16a**, the presence of equal or more amounts of **P5** at various temperatures suggests an energetically less favored process for conversion of **P5** into **16a** during the $AlMe_3$-mediated cyclo oligomerization reaction. Similar unfavorability is expected for conversions of **P5** into **P6** and of **P6** into **18a**.

To summarize, although we thus far have not been able to find any "cognate" macrocyclization reagent for monomeric fluorobenzene **5** [54, 64] and pyridine [65–67] motifs, our continued investigations do help to identify trimethyl aluminum as a very surprising macrocyclization reagent, selectively producing energetically less favored strained macrocyclic hexamers such as **18a** via one-pot cyclohexamerization of **21a**. However, the possible structural origins accounting for this unusual selectivity still remain unclear.

9.3.4 Chemo- and Regio-Selective Demethylations

Very recently, tetrabutylammonium chloride or bromide salts (TBACl/Br) were serendipitously found to be capable of achieving efficient folding-promoted chemo- and regio-selective demethylations, eliminating up to two out of five methyl groups situated in similar macrocyclic chemical microenvironments as in **16a** [74, 75]. By combining with the one-pot synthesis of **16a** in 46 % yield, macrocyclic anionic pentamers can now be prepared in just two steps with an overall yield of ~45 % within a day rather than ~5–10 % yields after months' efforts. Efficient

construction of circularly folded anionic pentamers is important given their recently proven abilities to differentiate between Na^+/K^+ and Rb^+/Cs^+ ions in a highly selective and tight fashion [45].

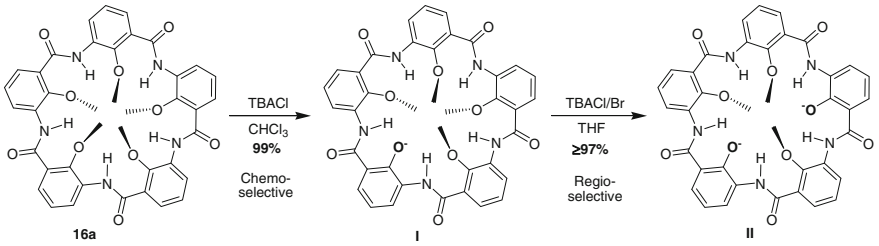

From the ^{1}H NMR-based analyses, some conclusions can be confidently drawn: (1) TBACl-mediated mono-demethylation allows for producing essentially pure forms of **I** in its anionic state, (2) the mono-demethylation is chemo-selective, removing one of the two *ortho* methyl groups that are immediately adjacent to each other and that point to the same hydrophobic side containing three methyl groups, and (3) the demethylation mechanism proceed by allowing Cl^- anion to attack the methoxy carbon atom and removes the methyl group to produce a phenolate anion in **I**. The observed chemo-selectivity can be explained on the basis of the ring strain resulting from electrostatic repulsions among the five interior methyl groups. The repulsive CH_3•••CH_3 interactions engaging two immediately adjacent methyl groups on the same side, measuring at 1.57 kca/mol is stronger than those involving two methyl groups at meta positions (0.27 kcal/mol) at the level of B3LYP/6-31G* with the single point energy calculation carried out at the B3LYP/6-311+G(d,p) level. Transforming **16a**–**I** by the first mono-demethylation reaction therefore results in a release of molecular strain of $\sim$1.84 kcal/mol by removing two CH_3•••CH_3 interactions. Comparatively, producing **II** from **I** by the 2nd mono-demethylation step allows releasing a much smaller molecular strain worth about 0.27 kcal/mol, and undesirably however introduces four repulsive interactions among two negatively charged phenolate O-atoms and two adjacent methoxy O-atoms, making the 2nd mono-demethylation a rate-determining step in TBACl-mediated di-demethylation reaction in THF.

9.4 Macrocycles Containing Non-amide Linkages

Beside the above aryl amide macrocycles, one-pot intramolecular H-bond-directed macrocyclization reactions have also been demonstrated to work with macrocycles containing formamidine [13], urea [13, 76, 77], hydrazide [78], and Schiff-base [40, 79] linkages. Using naphthyridine-based building blocks (**22a**), Cuccia and co-workers synthesized macrocycles containing formamidine- (**22b**) and urea-linkages

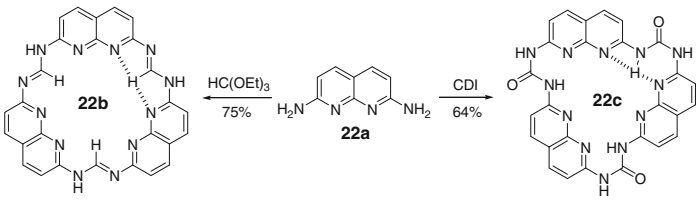

Fig. 9.12 One-pot macrocyclization of naphthyridine diamine, forming macrocycles that contain urea (**22b**) and formamidine (**22c**) linkages

(**22c**) in yields of 64 and 75 % by the condensation of building block **22a** respectively with triethyl orthoformate and 1,1-carbonyldiimadazole (Fig. 9.12) [13]. The presence of the H-bonding network and good planarity of the synthesized macrocycle **22b** was supported by the crystal structure.

Gong et al. further studied the likelihood of producing macrocycles containing linkages other than amide bonds by employing the same one-pot macrocyclization approach. While diaryl urea **23a** affords macrocyclic tetramers **24** by a bimolecular reaction, the corresponding urea **23b** has thus far not been demonstrated to produce **24** possibly due to the highly deactivated nature of the corresponding monomeric diamines that bear two electron-withdrawing ester groups (Fig. 9.13a) [76].

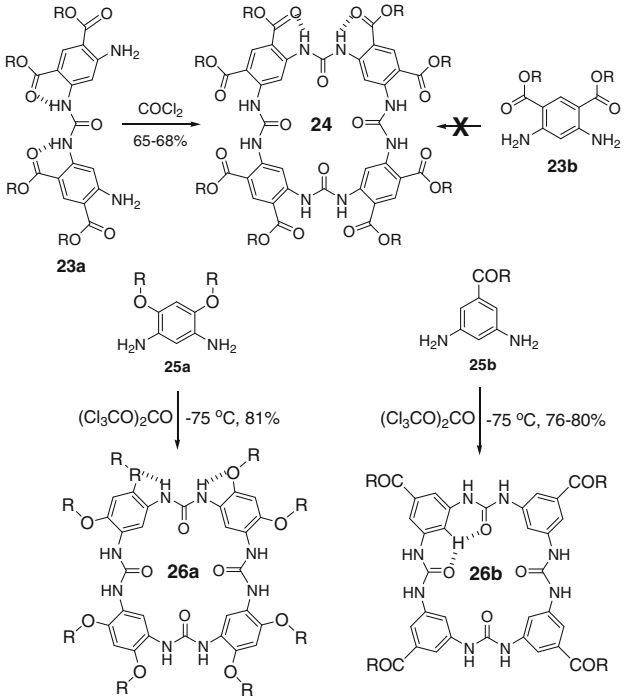

Fig. 9.13 One-pot macrocyclization that produces macrocycles containing urea or hydrazine linkages by Gong and co-workers

By replacing the electron-withdrawing ester groups with electron-donating alkoxy groups, monoaryl urea **25a** pleasantly allows for the production of tetramer **26a** in high yield of 81 % by using triphosgene at very low temperature of −75 °C (Fig. 9.13b) [77]. At higher temperatures, complex mixture was produced, a fact pointing to possible instability of diamine **25a** or other in situ generated intermediates at elevated temperature. Surprisingly, four macrocycles of type **26b**, which lack intramolecular H-bonds, can also be prepared in high yields of 76–80 % via one-pot macrocyclization of **25b** (Fig. 9.13b). The hybrid tetramer consisting of 1:1 ratio of **25a**:**25b** can be similarly prepared in high yields of 77–79 %. The successful preparation of **26b** and the hybrid tetramers indicates that strong intramolecular H-bonds are not necessarily required for preorganizing the oligourea precursors for cyclization. Sufficient preorganization of the macrocyclic tetraurea backbone can be provided by (1) partial rigidification and curvature introduced by the steric bulkiness of substituents at *meta* position, (2) trans-trans conformational preference adopted by the urea linkage and (3) weak H-bonds formed among aromatic protons and urea O-atoms (Fig. 9.13b). On the basis of this understanding, a wider design is anticipated that relies on the use of an interplay of multiple weak forces in producing macrocycles of varying structures and cavities.

An ease of controlling the size of the macrocyclic cavities is demonstrated by the same group [78]. In the study, hydrazine linkages were introduced into the macrocycles by using hydrazide derivative **27a** to react with pyridine-based diacid chloride **27b**, giving rise to a cyclic AB-type hexamer **28a** containing an interior cavity of ∼1 nm in diameter (Fig. 9.14a). By simply changing the pyridine-based building block **27b** having two acyl chloride reacting groups at *meta* position into the -position as shown in 2, 3-dimethoxyterephthalic acid chloride **27c**, a cyclic AB-type decamer having a lumen size of >2 nm across was obtained in high yields (Fig. 9.14b). Computational analyses show that both macrocycles **28a** and **28b** adopt a planar geometry.

The Schiff-base macrocycles such as [2 + 2], [3 + 3] and [4 + 4] macrocycles were traditionally synthesized by the condensation of symmetric dialdehydes with diamines mostly in the presence of a template [79]. Introducing the hydroxyl group that participates in forming a strong intramolecular H-bonding network with the imine groups preorganizes the oligomeric intermediates into a crescent conformation and controls the size of the macrocycles [80]. This strategy allows for the synthesis of very large Schiff-base macrocycles (**30** and **32**) by condensing symmetric aldehydes **29a** and **31a** respectively with diamines **29b** and **31b** (Fig. 9.15) without the use of a template [79]. A direct condensation using monomers **29a** and **31b** produces macrocycle **30** in 2 % yield. Replacement of **31b** with trimer **29b** make one-pot macrocyclization work better and boost the yield to 25 % with a range of other undesired open-chain oligomers and, to a lesser extent, closed cycles. Mysteriously, coupling of **31a** with either **31b** or **29b** works very well and leads to **32** in 78 % yield. Both macrocycles **30** and **32** seem to be very distorted, and metallation of them likely planarizes the macrocyclic backbones.

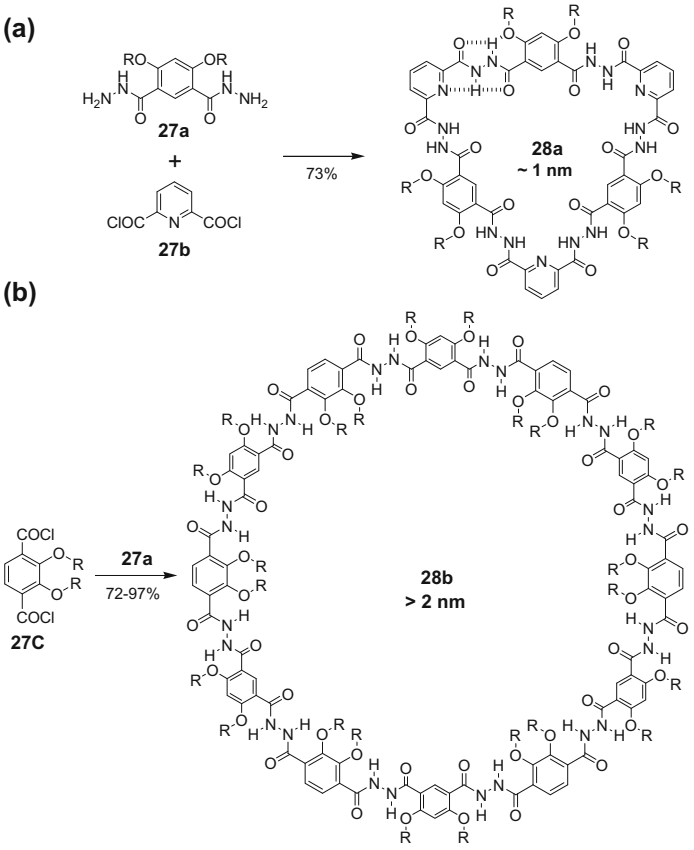

Fig. 9.14 Efficient synthesis of macrocycles with easily tunable interior cavities

The use of one single asymmetric precursor containing both the formyl and amino groups for the preparation of Schiff-base macrocycles has been studied previously, a few problems still remain: (1) low yield, (2) a mixture of products were obtained, and (3) if a template was used, metal ions became difficult to remove. MacLachlan and co-workers overcame these problems by introducing a hydroxyl group into the asymmetric bifunctional precursor (**34a** and **34b**, Fig. 9.15c) [40]. Using sodium dithionite, which does not reduce imines or aldehyde, as the reducing agent and starting from **34a**, five-fold symmetric macrocyclic pentamers with good planarity were obtained in high yields of 70–99 %. An alternative route using a cyclic aminal to protect formyl groups and Pd/C for reduction of nitro group produces the same macrocycles in near quantitative yields.

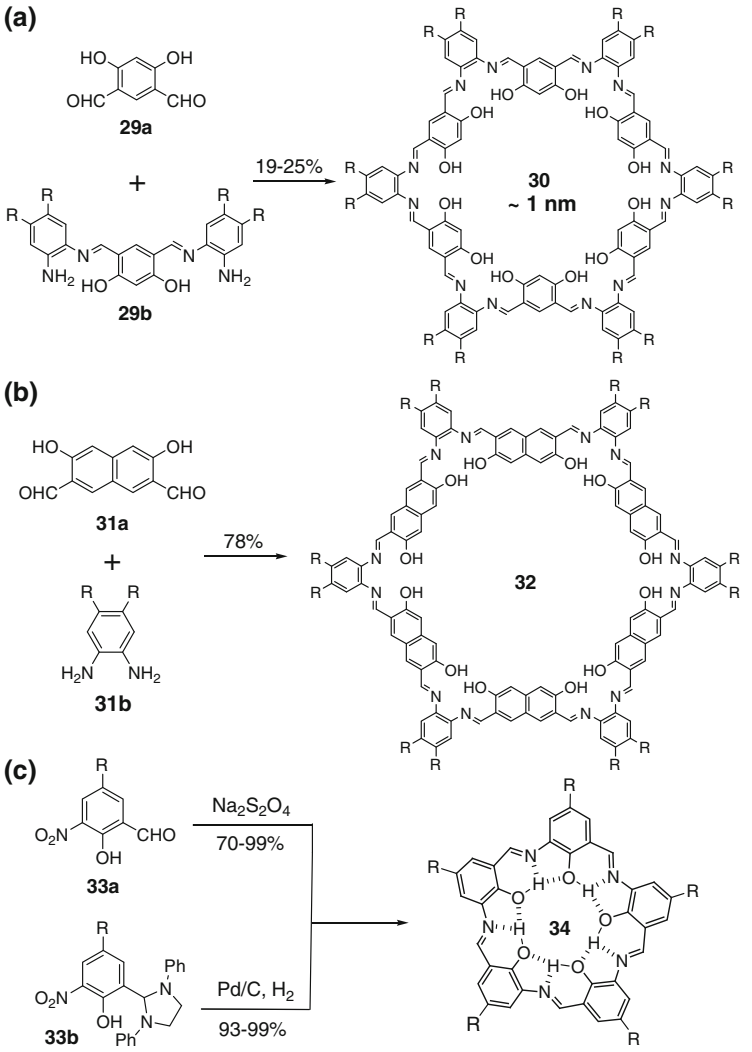

Fig. 9.15 Synthesis of Schiff base macrocycles **a 30**, **b 32**, and **c 34** using one-pot macrocyclization reactions aided by hydroxyl groups that form the H-bonds with imine N-atoms and direct the macrocyclization reactions

9.5 Mechanism of One-Pot Macrocyclization

One-pot macrocyclization can start from either symmetric or unsymmetrical bifunctional monomers. As discussed in Sect. 9.3.1 and for symmetric bifunctional building blocks, it was demonstrated by Gong and his co-workers that longer oligomers such as a trimeric diamine and a trimeric diacid chloride preferentially

react with each other to undergo one-pot 3 + 3 bimolecular cyclization reactions, producing a H-bonded macrocyclic hexamer **9**. This finding suggests that one-pot macrocyclization from the respective monomers to produce hexamers does not occur via a chain-growth mechanism, and is bimolecular in nature that is largely kinetically controlled, and that it is the remote steric effect that discourages the formation of oligomers longer than six residues long [33]. The suggested mechanism was further supported by the efficient synthesis of 16-residue macrocycle **11b** (Fig. 9.3b) in 81 % yield, which is in line with further computational analyses, revealing 16-residue macrocycle to be the most stable. We were intrigued to find out whether this privileged cross-reactivity seen in higher oligomers is equally applicable to our *unsymmetrical* bifunctional building blocks or not. In other words, what is the mechanism that underlies the preferred formation of aromatic pentamers **16** (Fig. 9.7) and **20** (Fig. 9.9) as well as strained hexamers **18a–b** (Figs. 9.8 and 9.11) and highly strained heptamers **18c–d** (Fig. 9.8)?

9.5.1 Variable Functionalizations Around the Pentameric Periphery

Among the initial attempts to identify the likely reaction mechanism, macrocyclization yields of circular pentamer **16a** were examined using various pairs of reacting partners (Table 9.10) [59]. Although it cannot be completely ruled out, the insignificant difference in yields among entries 1–5 does not favor the formation of **16a** by a mechanism involving a $n + m$ (both n and $m \geq 2$) bimolecular reaction between longer oligomers such as dimer **17h** and trimer **17i** (entry 5). The high yield production of **16a** by acyclic pentamer **17k** (76 %; entry 6) suggests the existence of low-yielding steps among entries 1–5. It is obvious that the bimolecular reaction of 2 + 3 type between dimer **17h** and trimer **17i** (entry 5) constitutes one of those low-yielding steps with an estimated chemical yield of $\sim$50 % that leads to acyclic pentamer **17k**, which subsequently undergoes an intramolecular cyclization with a 76 % yield to afford **16a** in an overall yield of 39 %. The 2 + 2 or 3 + 3 bimolecular reaction types involving dimer **17h** (entry 7) or trimer **17i** (entry 8), respectively, are not favored, either, as evidenced from no or low yield production of their respective cyclized tetramer or hexamer. In fact, the crescent-shaped acyclic tetramer cannot even undergo an intramolecular ring cyclization to produce the circularly folded tetramer (entry 9). The production of hexamer from **17i** (entry 8) was also completely suppressed in the presence of competing monomer **17a** (entry 3), suggesting that the reaction between **17a** and **17i** or between **17h** (generated in situ from **17a**) and **17i** was faster than that between trimer **17i** itself. A low yield production of hexamer from entry 1 further suggests that the reaction rate involving an acyclic pentamer and a monomer to produce the hexamer is slower than that dictating the intramolecular cyclization of an acyclic pentamer into a circular one. Possibly, this may be due to the remote steric effect between the two end residues that discourage the formation of oligomers longer

Table 9.10 Chemical yields for one-pot preparation[a] of circular pentamer **16a** from the corresponding oligomers **17a–17k**

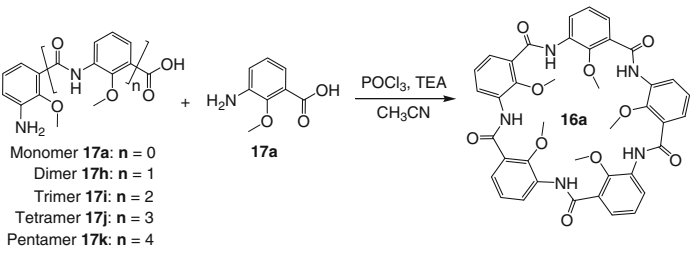

Monomer **17a**: **n** = 0
Dimer **17h**: **n** = 1
Trimer **17i**: **n** = 2
Tetramer **17j**: **n** = 3
Pentamer **17k**: **n** = 4

Entry	Reacting partners	Molar ratio	Yield (%)[b]
1	**17a**	N.A.	46 (6[c])
2	**17h:17a**	1:3	49
3	**17i:17a**	1:2	38
4	**17j:17a**	1:1	40
5	**17h:17i**	1:1	39
6	**17k**	N.A.	76
7	**17h**	N.A.	–[d]
8	**17i**	N.A.	29[c]
9	**17j**	N.A.	–[d]

[a] Reaction conditions: reactants **17a–17k** (total = 0.2 mmol), $POCl_3$ (0.4 mmol), TEA (0.6 mmol), CH_3CN (2.0 mL), room temperature, 12 h
[b] Isolated yield by flash column chromatography
[c] Yield of the hexamer
[d] No tetramer was formed

than pentamer [33]. Therefore, in addition to a chain-extension process that is highly likely, whether or not and to what extent a bimolecular reaction between in situ generated dimer **17h** and trimer **17i** does take place in entries 1–3, however, remain unclear.

To clarify the reaction mechanism, a few competition experiments were designed and carried out. Although the macrocyclization yields of **16a** (46 %, entry 1 of Table 9.10) and **16b** (42 %) from their respective monomers **17a** and **17b** are comparable, to ensure a fair comparison, the cross-reactivity between **17a** and **17b** within the same experimental setting at a constant total concentration of 100 mM involving both reactants **17a** and **17b** was assessed first. Combinatorially, up to eight pentamers (Fig. 9.16) containing **17a** and **17b** in varying ratios in the backbone can be produced. After reacting **17a** and **17b** in molar ratios of 4:1, 1:1, and 1:4 under the optimized one-pot cyclization conditions, the produced reaction mixtures containing circular aromatic pentamers of different types were analyzed using Thin Layer Chromatography (TLC) and results are presented in Fig. 9.16.

Mixing **17a** and **17b** in a 4:1 ratio produced two major spots, corresponding to pentamers **16a** and **16m**, containing five and four **17a** units (Lane 3, Fig. 9.16), respectively. Similarly, mixing **17a** and **17b** in 1:4 ratio produced another two

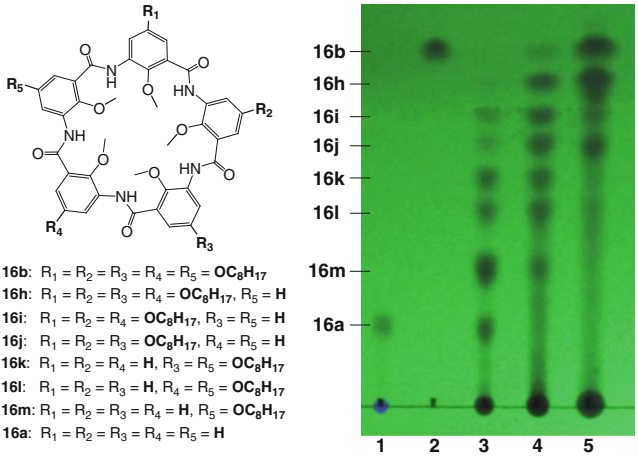

Fig. 9.16 Structures of pentamers **16a**, **16b** and **16h–16m** containing monomeric units of **17a** and **17b** in varying ratios. Using ethyl acetate:hexane: dichloromethane (5:18:5, v:v) as the eluent, all the eight pentamers **16a**, **16b** and **16h–16m** can be well separated in TLC plate. Lanes 3–5 = macrocyclization reaction products generated by reacting **17a** and **17b** in molar ratios of 4:1, 1:1, and 1:4, respectively. From Lanes 3–5, it can be seen that **17a** and **17b** indiscriminately cross-reacted with each other. Please note that the *dark spots* at the *origin line* actually derive from very tiny amount of unknown compounds from the reaction. Reprinted with the permission from [59]. Copyright 2011 American Chemical Society

major spots, corresponding to pentamers **16b** and **16h**, containing five and four **17b** units (Lane 5, Fig. 9.16), respectively. The isolated chemical yields for **16m** from Lane 3 and **16h** from Lane 5 were 20 and 21 %, respectively, illustrating an excellent compatibility between **17a** and **17b** in participating one-pot cyclization reaction. On the other hand, from the reaction involving **17a** and **17b** in equivalent amounts, the six pentamers **16h–16m** statistically should be produced in equal amounts that are five times as much as either **16a** or **16b** that also should be produced in equal amounts. This statistical distribution pattern matches quite well the experimental distribution pattern seen by TLC (Lane 4 in Fig. 9.16), providing further a convincing illustration on excellent cross reactivity between **17a** and **17b**, and among oligomers containing **17a** and **17b** in varying ratios.

On the basis of the above demonstrated excellent cross reactivity between **17a** and **17b** as well as the in situ generated oligomeric intermediates, competition experiments involving monomer **17b** and oligomers **17h–17j** in various ratios were performed (Table 9.11). Reaction involving a 1:3 molar ratio of **17h:17b** produced pentamer **16j** with undetectable occurence of pentamer **16b** (entry 1), suggesting that the formation of **16j** proceeds largely by a chain-growth mechanism, rather than by 2 + 2 or 2 + 3 bimolecular condensation reactions between higher oligomers, e.g. between dimer **17h** and the in situ generated octyloxy-containing dimer or trimer. If the latter is the predominate mechanism to produce pentamer **16j**, the in situ generated octyloxy-containing dimer and trimer should be present in

Table 9.11 Variable functionalization of pentamers **16j**, **16l** and **16m** by one-pot co-macrocyclization[a] of oligomers **17h–17j** with **17b**

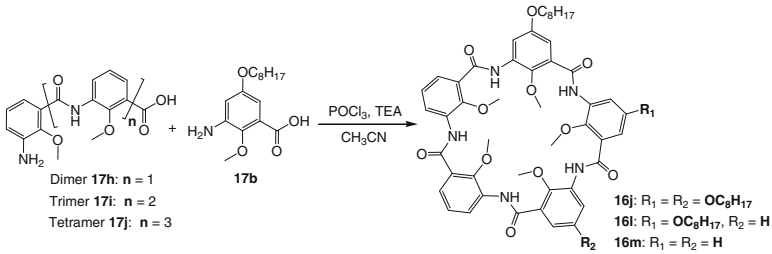

Entry	Reacting partners	Molar ratio	Yield (%)[b]
1	**17h:17b**	1:3	**16j** (38)
2	**17i:17b**	1:2	**16l** (42)
3	**17j:17b**	1:1	**16m** (39)

[a] Reaction conditions: reactants **17b** and **17h–17j** (total = 0.2 mmol), $POCl_3$ (0.4 mmol), TEA (0.6 mmol), MeCN (2.0 mL), room temperature, 12 h
[b] Isolated yield by flash column chromatography

substantial amounts that should further couple to each other to form **16b** directly by a 2 + 3 reaction, or indirectly by a 2 + 2 reaction, followed by a 4 + 1 reaction with a chemical yield comparable to **16j**. This, however, is in contradictory with the negligible presence of pentamer **16b** from the reaction. In addition, the 1 + 1 bimolecular reaction involving monomer **17b** should be comparably slower than $n + 1$ ($n \geq 2$) reaction involving oligomers **17h–17j** and monomer **17b**. Otherwise, the in situ generated octyloxy-containing dimer by the 1 + 1 reaction involving monomer **17b** may lead to an appreciable amount of pentamer **16b** by 2 + 3 or 2 + 2 reactions.

The above conclusions are also consistent with and can be inferred from entries 2 and 3 in Table 9.11 whereby **16l** and **16m** were produced as major products with **16b** remaining insignificant. Similar to **16j**, the formation of pentamers **16l** and **16m** as well as **16a** (Table 9.10) should also proceed by a continuous chain-growth mechanism. Examination of similar chemical yields among entries 1–4 from Table 9.10 and entries 1–3 from Table 9.11 led to the inference that except for 4 + 1 type reaction that could be a low yielding step, all the other chain growth steps of $n + 1$ type reactions likely give high yields of the corresponding oligomers. Reasonably assuming all $n + 1$ (n = 1–3) type reactions give a quantitative yield, then based on the respective 40 % (entry 4, Table 9.10), 39 % (entry 3, Table 9.11) and 76 % (entry 6, Table 9.10) yields, the chemical yield of 4 + 1 reaction to produce acyclic pentamers can be estimated to be ~50 %. The predominant formation of hybrid pentamers **16j**, **16l** and **16m** made up of different building blocks is a direct demonstration of a variable functionalization around the periphery achievable by reacting monomers with higher oligomers that differ by exterior side chains.

In conclusion, it was established here that the $POCl_3$-mediated one-pot macrocyclization proceeds predominantly by a chain-growth mechanism whereby the

addition of monomer into the growing backbones is faster than other competing bimolecular reactions between two monomers or between two higher oligomers. This one-pot macrocyclization protocol now allows an efficient preparation of aromatic pentamers carrying side chains of varying types in both its interior as previously reported [60] and exterior as demonstrated in the present work. These H-bonded pentagon-shaped molecules with a modifiable interior and exterior may promise some good applications in chemistry, materials sciences, and biology.

9.5.2 *A Chain-Growth Mechanism Underlying the Formation of Aromatic Pentamers*

As summarized in Sect. 9.5.1, a continuing exploration reveals that the $POCl_3$-mediated one-pot macrocyclization also leads to the variable functionalizations around the pentameric periphery (Fig. 9.17). More specifically, hybrid macrocycles **16h–m** can be conveniently prepared as the major product via one-pot co-macrocyclization of two different monomers that differ by their exterior side chains. We postulated that the $POCl_3$-mediated one-pot macrocyclization proceeds predominantly by a chain-growth mechanism whereby the addition of monomer into the growing backbones (n + 1 type reaction between monomer and the oligomer containing n repeating units) is faster than other competing bimolecular reactions between two monomers or between two higher oligomers. In other words, the inequality (Eq. 9.1) should hold qualitatively:

$$K_{1+1}, K_{2+2} \text{ or } K_{3+2} < K_{n+1} (n = 2-4) \tag{9.1}$$

As illustrated in Fig. 9.18, this section [60] will provide convincing evidences and detailed analysis that support a stepwise chain-growth mechanism underlying the preferred formation of five-residue aromatic pentamers by one pot macrocyclization

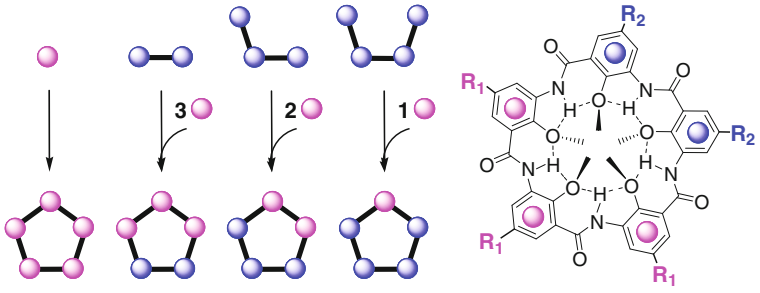

Fig. 9.17 $POCl_3$-mediated regiospecific functionalization around the pentameric periphery can be achieved by reacting monomers (*purple circles*) with higher oligomers (*blue circles*) that bear different exterior side chains. The produced cyclic planar pentamers can have *purple* and *blue* repeating units in varying ratios within the same pentamer molecule

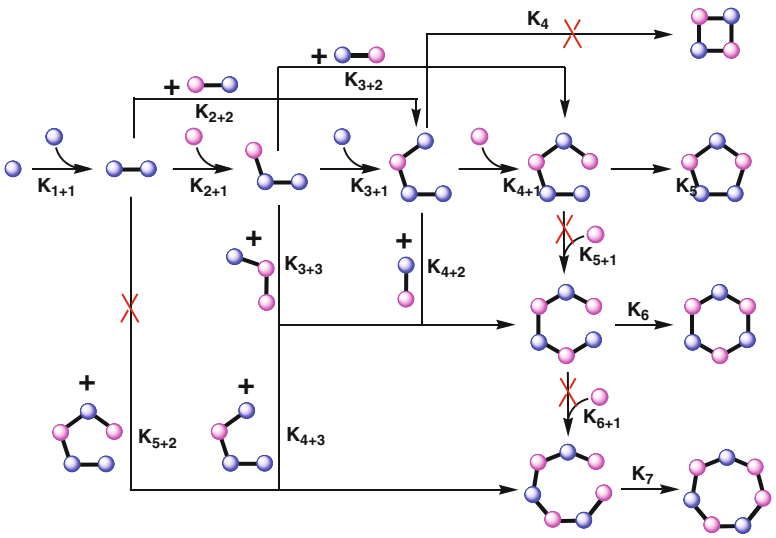

Fig. 9.18 Possible reaction pathways accounting for the preferred formation of acyclic oligomeric intermediates and circular aromatic oligomers. The circular tetramers (under-shooting products) are not formed while hexamers and pentamers (over-shooting products) may be possibly formed via different pathways from the reaction. Due to the steric hindrance and a possible difference in the thermodynamic stability of various oligomers, some reactions are faster than the others, which determine the mechanistic pathways underlying the one-pot macrocyclization. The balls in *blue* or *purple* represent the repeating aromatic units. *K* is reaction rate constant and $K_{n+m} = K_{m+n}$. Reactions of K_4, K_{5+1}, K_{5+2} and K_{6+1} types are expected to be much slower than other types of reactions shown in the scheme

with an in-depth understanding of reaction mechanism going beyond that contained within inequality (9.1). This was achieved by carrying out tailored competition experiments and performing kinetic simulations using experimental yields. Additionally, a low to undetectable experimental occurrence of four-, six-, and seven-residue macrocycles can be explained computationally on the basis of the relative energy per repeating unit that becomes increasingly more stable in the order of tetramer < heptamer < hexamer < pentamer (Fig. 9.8a–d).

The efficient $POCl_3$-mediated one-pot macrocyclization stems from the persistent folding of backbone into a crescent-shaped conformation induced by internally located continuous H-bonding forces. At the start of macrocyclization reaction, intermolecular reactions dominate that result in the formation of intermediate oligomers with a H-bonding enforced curved backbone. As sketched in Fig. 9.18, the oligomers of suitable lengths such as a dimer and a trimer may undergo bimolecular 2 + 3 type cyclization reactions to produce aromatic pentamers. The over-shooting products such as a hexamer are minimized due to the remote steric hindrance. This mechanism was demonstrated to be operational during the highly efficient preparation of macrocycles containing even number of *symmetrical* bifunctional monomers via one-pot multi-molecular macrocyclization [33]. Is this

mechanism equally applicable to the presently studied aromatic pentamers consisting of *unsymmetrial* bifunctional building blocks?

Alternatively, the incorporation of additional blocks into short intermediate oligomers by a chain-growth mechanism (Fig. 9.18) eventually should lead to an acyclic pentamer precursor whose increasingly curved backbone brings two reactive sites at its two ends into a close proximity to facilitate an intramolecular cyclization, producing aromatic pentamers. This simplified scenario leaves us a few outstanding questions: (i) how the acyclic pentamer precursor is produced? (ii) what are their relative reaction rates? (iii) is there any rate-determining step during the chain-extension process? (iv) how under- or over-shooting macrocycles and other acyclic oligomers are minimized, giving rise to the preferred formation of pentagon-shaped five-residue macrocycles? Since the formation of circular hexamer is very minimal and no circular tetramer has been experimentally observed [49], the mechanistic investigation therefore will need to be focused only on the desired pathways that lead to the formation of circular pentamer.

Competition experiments for mechanistic elucidation. The data presented in Sect. 5.1 only provide very preliminary insights into chain growth mechanism underlying one-pot macrocyclization. To further confirm this hypothetical mechanism, a new set of competition experiment has to be and was designed that involves monomer **17b**, dimer **17h**, and trimer **17i** in various ratios, affording reaction mixtures containing up to five circular pentamers **16a**, **16b**, **16j**, **16l** and **16m** with their isolated chemical yields tabulated in Table 9.12 and TLC-mediated separation illustrated in Fig. 9.19.

A few useful conclusions can be drawn from the presently designed competition experiment involving **17h**, **17i** and **17b**. (i) Given $K_{4+1} > K_{2+3}$ from inequality (9.1), it can be concluded from entry 1 of Table 9.12 that K_{2+2} is much slower than K_{3+2}. Otherwise, with respect to **16a**, pentamer **16m** should be produced in >24 % yield, a yield much higher than 14 % (entry 1), by combining a two-step process (e.g., by a K_{2+2} reaction involving dimer **17h**, producing a tetramer that subsequently reacts with **17b** by a K_{4+1} reaction) with the K_{2+3} reaction involving dimer **17h** and in situ generated trimer. (ii) As discussed above, K_{1+1} may be slower than K_{n+1} ($n > 1$), nevertheless, its value shall be quite similar to K_{n+1} as inferred from entry 3 of Table 9.12 where pentamer **16b** was produced with K_{1+1} reaction as the first step and with a 12 % yield that compares very favorably with a 14 % yield for **16j**. While the differential rate constants between K_{1+1} and K_{2+3} cannot be confidently deduced from these competition experiments, the discussion from the succeeding section on kinetic simulations does suggest that K_{1+1} reaction be faster than K_{3+2} reaction. (iii) Although K_{4+1} possibly can be a low-yielding step ($\sim$50 % from the above discussion), its reaction rate, however, shall be quite similar to K_5 and other K_{n+1} ($n = 2$ and 3) reactions. The support for this comes from the fact that the production of pentamer **16j** by a four-step coupling process is about 50–80 % of that of **16l** by a shorter three-step coupling process (entries 1–5).

If one of the above coupling reactions involving K_5 and K_{n+1} (n = 2–4) is significantly much slower than all the others, a comparable yield for producing **16j** and **16l** is expected. Indeed, in the absence of other closely related competing

Table 9.12 Chemical yields[8a] for one-pot preparation[a, b] of circular pentamers **16** from the corresponding oligomers **17h**, **17i**, and **17b**

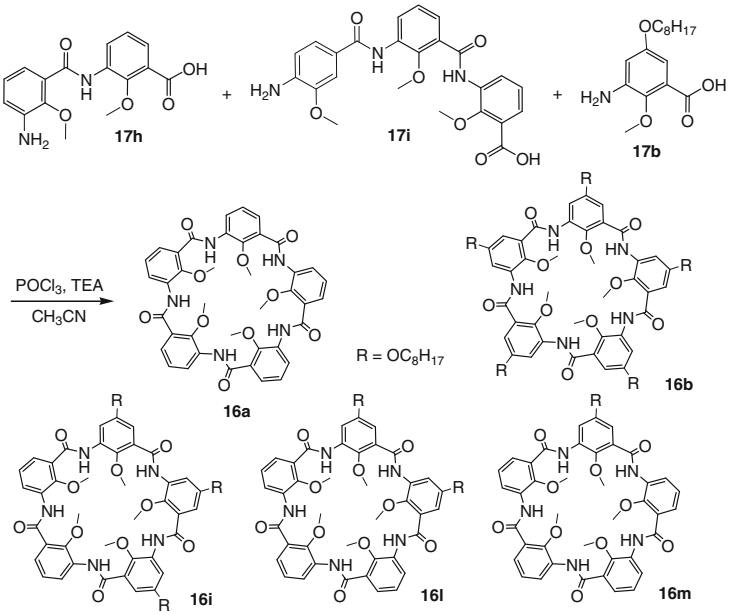

Entry	Reacting partners (**17h**:**17i**:**17b**)	Product distribution patterns and yields (%)[a]				
		16a	**16b**	**16j**	**16l**	**16m**
1	**1:1:1**	41 ± 2	Trace	8 ± 1	18 ± 1	14 ± 2
2	**1:1:2**	26 ± 3	6 ± 2	12 ± 1	25 ± 2	13 ± 2
3	**1:1:3**	18 ± 3	12 ± 2	14 ± 2	24 ± 3	12 ± 1
4	**1:1:4**	12 ± 4	10 ± 2	21 ± 2	32 ± 2	10 ± 1
5	**1:1:5**	6 ± 1	11 ± 1	25 ± 2	31 ± 1	4 ± 1

[a] Isolated yield by preparative TLC plates and averaged over a triplicate run
[b] Reaction conditions: reactants **17h**, **17i**, and **17b** (total = 0.2 mmol), $POCl_3$ (0.4 mmol), TEA (0.6 mmol), CH_3CN (2.0 ml), room temperature, 12 h

parties, pentamers **16a**, **16j**, **16l**, and **16m** are produced in similar yields of 46 % [49], 38 % [59], 42 % [59] and 39 % [59] respectively. Additionally, both dimer and tetramer shall be present in good amounts during the 1 + 2 + 3 type reaction where monomer, dimer, and trimer couples with each other to produce different pentamers (entries 1–5 from Table 9.12), which however does not give rise to hexamer. This suggests that K_{4+2} reaction be slower than either K_{3+2}, K_{n+1} (n = 1–4) or K_5. On these basis, inequality (Eq. 9.2) can be derived:

$$K_{2+2} \text{ or } K_{4+2} < K_{3+2} < K_{1+1} < K_{n+1} \approx K_5 (n = 2-4) \tag{9.2}$$

Similar to **16a**, we believe that **16m** was also formed by the K_{2+3} reaction involving **17h** and in situ produced trimer that was produced by the K_{2+1} reaction

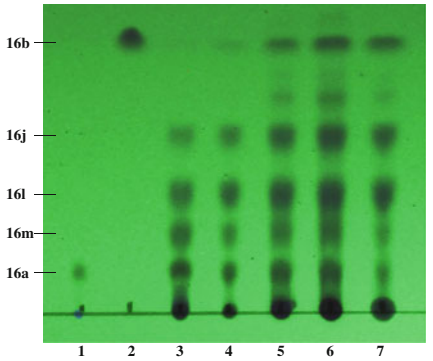

Fig. 9.19 Product distributions illustrated by TLC that involve **16** produced from the reactions specified in Table 9.12. Lane 1 = **16a** containing no exterior side chains, Lane 2 = **16b** containing five exterior octyoxy side chains, Lanes 3–7 = macrocyclization reaction products **16j**, **16l**, and **16m** generated by reacting **17h**, **17i** and **17b** in molar ratios of 1:1:1, 1:1:2, 1:1:3, 1:1:4, and 1:1:5, respectively. Eluent: ethyl acetate:hexane = 1:3 (v:v). Note that the *dark spots* at the *origin line* actually derive from very tiny amount of unknown compounds from the reaction. Reproduced from [60] by permission of John Wiley and Sons Ltd

between **17h** and **17b**. With increasing amounts of **17b** (entries 3–5), both the trimer intermediate and **17h** were rapidly converted into tetramer and trimer by the respective faster K_{3+1} and K_{2+1} reactions, diminishing K_{3+2} reaction to an negligible extent. The reasoning that **16m** is produced firstly by a K_{2+2} reaction involving **17h**, producing a tetramer intermediate that subsequently reacts with **17b** by a K_{4+1} reaction is not supported by the inequality (Eq. 9.2).

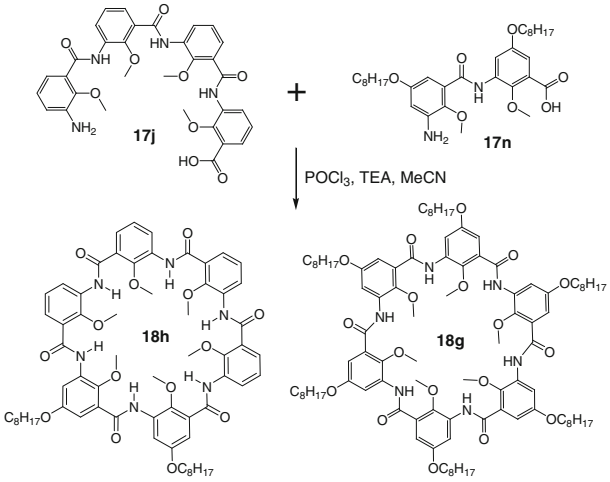

To additionally differentiate the reaction rates between K_{2+2} and K_{4+2}, another competition experiment was undertaken, involving 1:1 mixture of **17j** containing no exterior side chains and **17n** containing two exterior octyloxy side chains. Experimentally, only a single type of **18h** containing two octyloxy-containing repeating units was formed in 25 % yield, implying that K_{2+2} is significantly much slower than K_{4+2}. If K_{2+2} is comparable to or faster than K_{4+2}, a tetramer containing four octyloxy-containing units in situ generated by a K_{2+2} reaction would be produced that competes with **17j** in the reaction with **17n** to produce a second type of hexamer **18g** having six octyloxy-containing repeating units in it.

$$K_{2+2} < K_{4+2} < K_{3+2} < K_{1+1} < K_{n+1} \approx K_5 (n = 2\text{–}4) \tag{9.3}$$

K_{1+1} for A1 + A1 → A2
K_{1+2} for A1 + A2 → A3
K_{1+3} for A1 + A3 → A4
K_{2+2} for A2 + A2 → A4
K_{1+4} for A1 + A4 → A5a
K_{2+3} for A2 + A3 → A5a
K_5 for A5a → **A5b** = **16b**

} A1 = **17b** Production of pentamer **16b**

K_{1+2} for A1 + B2 → B3
K_{1+3} for A1 + B3 → B4
K_{2+2} for A2 + B2 → B4
K_{1+4} for A1 + B4 → B5a
K_{2+3} for A2 + B3 → B5a
K_{2+3} for A3 + B2 → B5a
K_5 for B5a → **B5b** = **16j**

} B2 = **17h** Production of pentamer **16j**

K_{1+3} for A1 + C3 → C4
K_{1+4} for A1 + C4 → C5a
K_{2+3} for A2 + C3 → C5a
K_5 for C5a → **C5b** = **16l**

} C3 = **17i** Production of pentamer **16l**

K_{2+2} for B2 + B2 → D4
K_{1+4} for A1 + D4 → D5a
K_{2+3} for A2 + B3 → D5a
K_5 for D5a → **D5b** = **16m**

} Production of pentamer **16m**

K_{2+3} for B2 + C3 → E5a
K_5 for E5a → **E5b** = **16a**

} Production of pentamer **16a**

Kinetic simulation of reaction rates. The dependability of certain components in inequality (Eq. 9.3) dictating the preferred formation of pentamers of varying types can be verified by applying kinetic simulations onto entries 1–5 in Table 9.12 by assuming a best-case scenario in which (i) the same type of K_{n+m} reaction has the

same rate constant regardless of the identity of monomers and oligomers and (ii) oligomers higher than pentamers are not formed from the reaction, which is true experimentally, in order to reduce the complexity of simulations. Some assumptions made include (i) Acyclic pentamers **A5a**–**E5a** are quantitatively converted into corresponding circular pentamers **A5b**–**E5b**, which are largely true experimentally, (ii) the same type of K_{n+m} reaction has the same rate constant regardless of the identity of monomers and oligomers and (iii) oligomers higher than pentamers are not formed from the reaction, which is true experimentally, in order to reduce the complexity of simulations. In the simulation, no assumption on chain-growth process for forming various pentamers was made. Instead, monomers and oligomeric intermediates are allowed to grow not beyond pentamers by any bimolecular reaction. By subjecting to a mechanism-based kinetics simulator freely available online [81], the following 24 equations were used in kinetic simulations where **An** = **Bn** = **Cn** = **Dn** = **En** = oligomers containing n repeating units, **A1** = acyclic monomer **17b**, **A2** = acyclic dimer, **B2** = acyclic dimer **17h**, **A3** = **B3** = **C3** = acyclic trimer where **C3** = acyclic trimer **17i**, **A4** = **B4** = **C4** = acyclic tetramer, **A5a** = **B5a** = **C5a** = **D5a** = **E5a** = acyclic pentamer, and **A5b** = **B5b** = **C5b** = **D5b** = **E5b** = cyclic pentamers where **A5b** = **16b**, **B5b** = **16j**, **C5b** = **16l**, **D5b** = **16m** and **E5b** = **16a**.

Based on the respective chemical yields (entries 1–5, Table 9.12), a total of 24 reactions using seven variable reaction rates of K_{n+m} ($2 \le n+m \le 5$) and K_5 types were performed. Simulations evolved over 3,600 s with a step length of 1 s. The longer sampling time ensured that all the simulated yields obtained on circular pentamers are the maximum yields possible under the stipulated set of kinetic rates with >99.9 % formation of the respective pentamers that should have be produced. The convergent criteria were chosen in such a way that the simulated chemical yields shall fall within the experimental ranges. For instance, from entry 2 of Table 9.12, **16b** was produced in 6 ± 2 % over a triplicate run, it would be considered as ideal if the simulated chemical yield of **16b** falls within 4–8 %, preferably equal to the average value of 6 %. In addition, the rate constants obtained based on one entry ideally shall be applicable to other entries to cross-test the reliability of obtained values.

After going through iterations of numerous rounds using kinetic simulators [81], the close to best-fit kinetic rate constants and the simulated chemical yields were obtained, compiled, and compared to experimental ones as shown in Tables 9.13 and 9.14. It was found that a slight change in value for K_{2+2} relative to K_{3+2} significantly influenced the simulated yields of both **16a** and **16m** for entries 1 and 2 of Table 9.14, leading to larger deviations from experimental ranges. For instance, with respect to (i) K_{2+2} = 0.002 and (ii) all the other rate constants remained unchanged, the simulated yields of **16a** and **16m** for $K_{2+2} = 0$ increased from 39 and 15 % to 46 and 17 %, respectively. For $K_{2+2} = K_{3+2} = 0.008$, the simulated yields for **16a** and **16m** decreased from 39 and 15 % to 29 and 11 %, respectively. With $K_{2+2} = 5 \times K_{3+2} = 0.04$, the simulated yields for **16a** and **16m** further decreased to respective 14 and 8 %. These comparisons are consistent with experimental observations and our expectation that K_{2+2} shall be less than K_{3+2} so that, in the

Table 9.13 Simulated rate constants for the bimolecular reactions used to model the cyclopentamerization for circular pentamers **16** made from oligomers **17h**, **17i** and **17b** as shown in Table 9.12

Entry	Reacting partners **(17h:17i:17b)**	Simulated kinetic rate constants (s^{-1})[a]						
		K_{1+1}	K_{2+1}	K_{3+1}	K_{4+1}	K_{2+2}	K_{3+2}	K_5
1	**1:1:1**	0.036	0.060	0.045	0.040	0.002	0.008	>0
2	**1:1:2**	0.036	0.060	0.045	0.040	0.002	0.008	>0
3	**1:1:3**	0.025	0.065	0.035	0.030	0.002	0.008	>0
4	**1:1:4**	0.011	0.065	0.035	0.030	0.002	0.008	>0
5	**1:1:5**	0.011	0.065	0.035	0.030	0.002	0.008	>0

[a] Simulation over 3,600 s that allows the respective yields to reach >99.9 % of the maximally allowed chemical yields

Table 9.14 Simulated chemical yields[a] for circular pentamers **16** made from oligomers **17h**, **17i**, and **17b** as shown in Table 9.12

Entry	Reacting partners **(17h:17i:17b)**	Product distribution patterns and yields (%)[a]				
		16a	**16b**	**16j**	**16l**	**16m**
1	**1:1:1**	39 (0)	2 (−2)	5 (−2)	11 (−6)	15 (0)
2	**1:1:2**	27 (0)	8 (0)	14 (1)	22 (−1)	15 (0)
3	**1:1:3**	17 (0)	12 (0)	20 (4)	25 (0)	12 (0)
4	**1:1:4**	7 (−1)	11 (0)	23 (0)	30 (2)	7 (−2)
5	**1:1:5**	5 (0)	15 (3)	27 (0)	34 (2)	5 (0)

negative values deviations from the lower boundary, *positive values* deviations from the upper boundary, 0 % no derivations from the experimental ranges

[a] The values in bracket are the deviations of simulated yields from experimental ranges shown in Table 9.12

presence of lesser amount of **17b** (entry 1, Table 9.13), K_{2+2} will not substantially compete with K_{3+2} to significantly decrease the yields of **16a** and **16m**. Similarly, for entries 3–5 of Table 9.13, a slight difference in values of K_{n+1} (n = 2–4) leads to larger deviations of the simulated chemical yields from experimental ones. Except for K_{1+1}, all the simulated K_{n+m} (n, $m \geq 1$) values do not vary significantly among entries 1–5, which allow the consistent reproduction of experimental trends in chemical yields shown in Table 9.12, though to a lesser degree for entry 1 where the simulated yield derivatives quite substantially for **16l**. From these simulated rate constants, the real rate constants highly likely increase in the order of $K_{2+2} < K_{3+2} < K_{1+1} < K_{3+1} \approx K_{4+1} < K_{2+1}$. This order nicely matches the qualitatively derived reactivity order shown in inequality (Eq. 9.3).

Since K_5 corresponds to the intramolecular reaction that converts an acyclic pentamer into a circular one (Fig. 9.18) and acyclic pentamers does not readily react

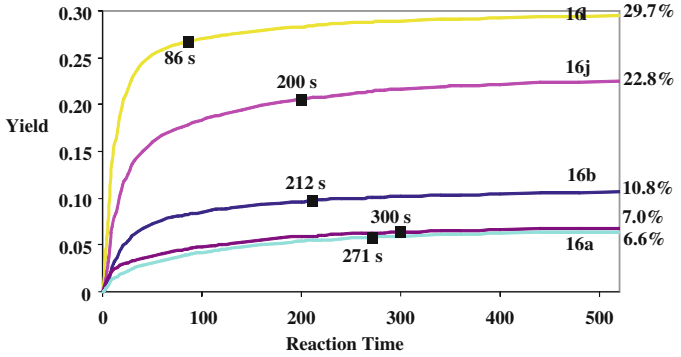

Fig. 9.20 Kinetic simulation based on entry 4 of Table 9.12 on the formation and accumulation of circular pentamer **16** by one-pot macrocyclization starting from bifunctional oligomers **17h**, **17i**, and **17b**. The filled *black rectangles* refer to the time point at which 90 % of the respective pentamers was produced from the cyclization reaction

with a monomer to form circular hexamers, reaction of K_5 type is essentially a non-competing reaction that does not compete with other reactions for reactants or intermediates of different types. With a sufficiently long enough reaction time, any positive value of K_5 in terms of reaction rate constant eventually transforms all the available acyclic pentamers into circular ones. As a result, its value can not be confidently deduced on the basis of experimental yields (Table 9.13).

As exemplified by the obtained kinetic data for entry 4 of Table 9.13, Fig. 9.20 illustrates simulated reaction progresses with the accumulated chemical yields for pentamers **16a–3** plotted against the reaction time. The plateaus were reached at t = 271, 212, 200, 86, and 300 s for **16a**, **16b**, **16j**, **16l**, and **16m**, respectively, which correspond to the 90 % formation of these respective pentamers with their maximally allowable yields approaching 7.0, 10.8, 22.8, 29.7, and 6.6 %. Within 1,000–1,100 s, all the pentamers reached 99.9 % of their maximally allowable yields. In addition, all the starting oligomers **17h**, **17i**, and **17b** reached 90 % consumption in about 50–60 s, and 99.9 % consumption in about 800 s.

To assess the applicability of the above elucidated chain-growth mechanism onto the BOP-mediated macrocyclization, **19g** was reacted with three equivalents of **19e** in CH_2Cl_2. Statistically, pentamer **20e** could be a possible product along with another two hybrids **20g** and **20h** consisting of mixed units of **19g** and **19e** with a ratio of 1:3 and 2:1, respectively. A predominant production of **20g** would be consistent with a chain-growth mechanism. Analyses by HRMS, ^{1}H NMR and TLC of the reaction mixture indeed confirm **20g** as the major product with **20e**, **20g** and **20h** produced in a molar ratio of 2:8:5, suggesting that BOP-mediated one-pot macrocyclization largely proceeds by a chain-growth mechanism.

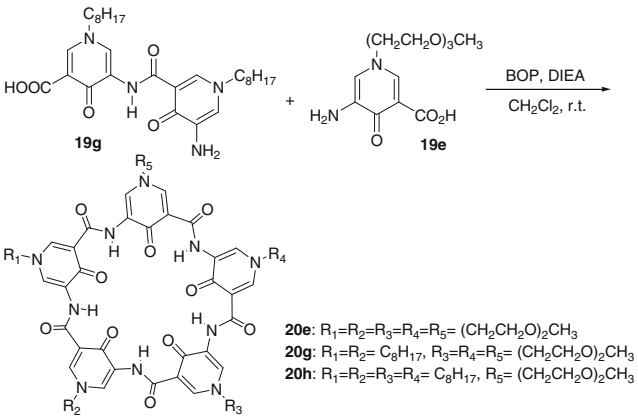

9.5.3 *A Non-chain Growth Mechanism Underlying the Formation of Strained Aromatic Hexamers and Heptamers*

For strained hexamers **18a–b** (Figs. 9.8 and 9.11) and highly strained heptamers **18c–d** (Fig. 9.8), it turned out that a chain-growth mechanism is not applicable. It has been shown that the use of $POCl_3$ in CH_3CN allows pentamer **16a** to be produced as the predominant macrocycle in 46 % yield along with hexamer **18a** in 6 % yield (Table 9.3) [49]. In carrying out these one-pot reactions, the "ordinary" HPLC grade CH_3CN after a simple distillation was used. This is because we thought that a water content of ≤0.01 % in HPLC grade CH_3CN corresponds to a water concentration of 5 mM, which is relatively insignificant when compared to the reagent concentration of $POCl_3$ at 200 mM and should not affect the reaction to a noticeable extent.

Prompted by the computational results (Fig. 9.8e–h) which suggest a possibility to produce hexamer **18b** as the major product among macrocycles **16f**, **18b** and **18d**, we decided to re-investigate the one-pot reactions under varying conditions as rigorously as possibly by using CaH_2 to remove trace amounts of water from reaction solvent CH_3CN as much as possible (Table 9.14). This stringent treatment increases the overall yield inclusive of 5-, 6-, and 7-residue macrocycles from 52 % (46 % pentamer **16a** + 6 % hexamer **18a**) in "ordinary" CH_3CN to 78 % in "dry" CH_3CN (40 % pentamer **16a** + 24 % hexamer **18a** + 14 % heptamer **18c**) at room temperature [50], suggesting that even trace amounts of water present in the reaction significantly impede the one-pot macrocyclization reaction possibly by inactivating the acid chloride of intermediate oligomers. A screening of temperature effect shows that one-pot macrocyclization efficiency initially increases from 71 % at 0 °C to 91 % at 40 °C (entry 2, Table 9.14) but gradually levels off to 86 % at 80 °C. This led us to believe that the reactivities of either acid chloride or amine groups are intrinsically low and can be much augmented at higher reaction

temperatures. Indeed, reactions proceed to the largest extent at 40 °C, and also to a much better extent at temperatures above 40 °C with regard to those at room or lower temperatures. Notably, strained hexamer **18a** can be produced as much as 33 % at 40 °C, a yield that is very close to that of pentamer **16a**. And highly strained heptamer **18c** is produced increasingly more with increasing reaction temperatures of up to 80 °C, around which a 22 % yield of heptamer can be obtained. Undesirably, a 15-fold scale up of the reaction at the same concentration of 100 mM dramatically decreases the overall yield from 78 to 23 %. Nevertheless, increasing the concentration of monomer **17a** from 100 to 1,000 mM actually helps improve the macrocyclization efficiency by 10 % while lowering the reagent concentration down to 10 mM diminishes the macrocyclization yield to 50 %.

Similar investigations were then carried out on macrocycles **16f**, **18b** and **18d** formed from their bifunctional monomeric amino acid **17f** (Table 9.15). Due to the bulkier nature of ethyl group relative to methyl group, it is anticipated that macrocyclization reactions be impeded to a larger extent by interior ethoxy ethyl groups present in **18b** and **18d** than by interior methoxy methyl groups found in **18a** and **18c**. This expectation is completely in accord with the experimental findings, demonstrating consistently obtained lower yields for **18b** and **18d** than for **18a** and **18c** under identical conditions. For instance, at room temperature in "dry" CH_3CN, yields of 34 % for pentamer **16f**, 16 % for hexamer **18c** and 9 % for heptamer **18d** were obtained. Some general trends persist for macrocycles **18**: (1) higher reaction

Table 9.15 Production of pentamers, hexamers, and heptamers via $POCl_3$-mediated one-pot macrocyclization of **17a** and **17g** at 25 and 40 °C[a]

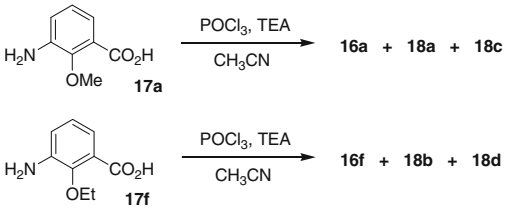

Entry	Conc of 17a (mM)	Reaction temp (°C)	Yield (%)[b]			Total yield (**16a + 18b + 18c**)
			16a	**18a**	**18c**	
1	100	25	40 ± 2	24 ± 3	14 ± 2	78
2		40	42 ± 2	33 ± 2	16 ± 2	91
Entry	Conc of 17f (mM)	Reaction temp (°C)	Yield (%)[b]			Total yield (**16a + 18b + 18c**)
			16f	**18b**	**18d**	
3	100	25	34 ± 2	16 ± 4	9 ± 3	59
4		40	30 ± 2	20 ± 2	14 ± 4	64

[a] Reaction conditions: **17a** or **17g** (100 mM), $POCl_3$ (2 equiv.), Triethylamine (3 equiv.), anhydrous CH_3CN (2 ml), 12 h

[b] Isolated yields by preparative thin layer chromatography and refer to the percentage of monomer **17a** and **17f** being converted into the respective macrocycles; the yields are the averaged values over three runs

temperatures facilitate the macrocyclization reactions, (2) best overall macrocyclization efficiency is produced at 40 °C, and (3) a lower reagent concentration from 100 to 10 mM led to a lower yield. However, unlike methoxybenzene macrocycles **16a**, **18a**, and **18s**, a tenfold increase in reaction concentration does not improve the macrocyclization efficiency. Rather, it lowers down the yield from 59 to 36 %.

Kinetic simulation of reaction rates (see Sect. 9.5.2 for a more detail). Based on the respective chemical yields (entries 1–4 from Table 9.16), a total of 15 reactions using 15 variable reaction rates of K_{n+m} ($2 \leq n + m \leq 7$) were performed. Simulations evolved over 4,000 s with a step length of 1 s. The longer sampling time ensured that all the simulated yields obtained on circular oligomers are the maximum yields possible under the stipulated set of kinetic rates with >99.9 % formation of the respective circular oligomers that should have been produced. The following 15 equations were used in kinetic simulations where **An** = acyclic oligomers containing *n* repeating units of types **17a** or **17g** and **Bn** = cyclic oligomers containing *n* repeating units types **17a** or **17g**.

$$\left.\begin{array}{l} K_{1+1} \text{ for A1} + \text{A1} \rightarrow \text{A2} \\ K_{2+1} \text{ for A2} + \text{A1} \rightarrow \text{A3} \\ K_{3+1} \text{ for A3} + \text{A1} \rightarrow \text{A4} \\ K_{4+1} \text{ for A4} + \text{A1} \rightarrow \text{A5} \\ \text{K}_{2+2} \text{ for A2} + \text{A2} \rightarrow \text{A4} \\ \text{K}_{3+2} \text{ for } \textit{A3} + \text{A2} \rightarrow \text{A5} \\ K_5 \quad \text{for} \quad \text{A5} \rightarrow \textbf{B5} \end{array}\right\} \begin{array}{l} \text{A1} = \textbf{17a} \text{ or } \textbf{17f} \\ \text{Pentamers} \\ \textbf{B5} = \textbf{16a} \text{ or } \textbf{16f} \end{array}$$

$$\left.\begin{array}{l} K_{4+2} \text{ for A4} + \text{A2} \rightarrow \text{A6} \\ K_{3+3} \text{ for A3} + \text{A3} \rightarrow \text{A6} \\ K_{5+1} \text{ for A5} + \text{A1} \rightarrow \text{A6} \\ K_6 \quad \text{for} \quad \text{A6} \rightarrow \textbf{B6} \end{array}\right\} \begin{array}{l} \text{Hexamers} \\ \textbf{B6} = \textbf{18a} \text{ or } \textbf{18c} \end{array}$$

$$\left.\begin{array}{l} K_{4+3} \text{ for A4} + \text{A3} \rightarrow \text{A7} \\ K_{6+1} \text{ for A6} + \text{A1} \rightarrow \text{A7} \\ K_{5+2} \text{ for A5} + \text{A2} \rightarrow \text{A7} \\ K_7 \quad \text{for} \quad \text{A7} \rightarrow \textbf{B7} \end{array}\right\} \begin{array}{l} \text{Heptamers} \\ \textbf{B7} = \textbf{18b} \text{ or } \textbf{18d} \end{array}$$

Consistent with findings outlined in Sect. 9.5.2, it was also found here that addition of monomer unit onto either another monomer or the growing oligomeric backbone is faster than other types of bimolecular condensations involving oligomers longer than monomer, suggesting the one-pot reaction involving monomers containing either methoxy or ethoxy groups in its interior proceeds by a chain-growth mechanism to produce circularly folded pentamers. However, circularly folded hexamers and heptamers appear to be made largely by bimolecular reactions of K_{3+3}, K_{4+2}, and K_{4+3} types while both K_{5+1}, K_{6+1} and K_{5+2} types make insignificant contributions as suggested by (Eq. 9.1) the much smaller rate constants of K_{n+1} types with respect to others (Table 9.15) and (Eq. 9.2) fast consumption of monomer **17a** that reaches 90 % consumption in about 60 s, and 99.9 %

Table 9.16 Simulated kinetic rate constants for the bimolecular reactions used to model cyclooligomerization and the corresponding simulated chemical yields for circular oligomers made from their respective monomers **17a** and **17g** as shown in Table 9.14

	Simulated kinetic rate constants (s^{-1})[a]										
	K_{1+1}	K_{2+1}	K_{3+1}	K_{4+1}	K_{2+2}	K_{3+2}	K_{4+2}	K_{3+3}	K_{4+3}	K_{5+1} or K_{6+1} or K_{5+2}	K_5 or K_6 or K_7
Entry 1 (Table 9.14)	0.01	0.023	0.035	0.021	0.007	0.005	0.0038	0.004	0.002	0.0003	>0
Entry 2 (Table 9.14)					0.0025	0.006	0.0048	0.005	0.0045		
Entry 3 (Table 9.14)	0.007			0.01	0.006	0.0035	0.0016	0.002	0.0005		
Entry 4 (Table 9.14)	0.0073				0.005	0.0023	0.002		0.0008		

[a] Simulation over 4,000 s that allows the respective yields to reach >99.9 % of the maximally allowed chemical yields

[b] All the simulated chemical yields fall within the experimental ranges and are deviated from experimental averaged values shown in Table 9.15 by ≤1 %. Addition of a monomer to either pentamer or hexamer, or a dimer into a pentamer is kinetically very slow as evidenced by their small values in their rate constants(K_{1+5}, K_{1+6}, and K_{2+5}) with respect to others

consumption in about 130 s. This provides a sound explanation to the discrepancy between the computational results, suggesting hexamer **18b** being more stable than pentamer **16f** to be produced as the major product, and our careful experimental securitizations that do not support this theoretical perception (Table 9.14). That is to say, although the hexameric macrocycle **18b** is thermodynamically more stable, pentameric macrocycle **16f** is kinetically more accessible and thus is generated substantially more than **18b**. On the other hand, since K_n (n = 5–7) corresponds to the intramolecular reaction that converts an acyclic oligomer into a circular one (Fig. 9.18), it is essentially a non-competing reaction that does not compete with other reactions for reactants or other various intermediates. With a sufficiently long enough reaction time, any positive value of K_n in terms of reaction rate constant eventually allows transforming all the available acyclic oligomeric precursors into circular ones. As a result, K_n values can not be confidently deduced (Table 9.15).

It would be interesting to note that performing one-pot macrocyclization at 40 °C not only increases the reaction yields, but also allows more of the strained 6- and 7-residue macrocycles to be produced when compared to the reactions at room temperature (Table 9.14). For methoxy-containing macrocycles **18a** and **18c**, this is achieved mainly by slowing down bimolecular reaction of K_{2+2} type while accelerating K_{3+2}, K_{4+2}, K_{3+3} and K_{4+3} reactions. For ethoxy-containing macrocycles **18b** and **18d**, the changes are effected largely by slowing down bimolecular reaction of K_{2+2} and K_{3+2} types while accelerating K_{4+2} and K_{4+3} reactions with K_{3+3} reaction rate remaining unaltered.

To summarize, $POCl_3$-mediated H-bonding-assisted one-pot macrocyclization protocols in dry acetonitrile enable the generation of foldamer-based macrocycles containing from 5 to 7 repeating units with built-in H-bonding abilities. Except for circular pentamer **16a** that is roughly planar and pentagon-shaped as verified by both its crystal structure and computationally optimized structure, all the other circularly folded pentamers, hexamers, and heptamers take up a distorted geometry due to ring strains originating from either the intrinsic requirement of five residues per macrocycle or the steric hindrance imposed by the interior ethyl groups. The low reactivities of acid chloride and amine groups from these H-bond-enforced aromatic backbones can be partially alleviated by increasing reaction temperature. Interestingly, bimolecular reactions involving only oligomers higher than monomers appear to be facilitated by high temperature at certain ranges more than the chain-growth reactions involving the addition of a monomer into another monomer or the growing oligomeric backbones. As a result, the strained hexamers and heptamers are produced not only in higher yields at 40 °C than that at room temperature but also proportionally more in regard with pentamers, a finding that can be corroborated by kinetic simulations. Aided further by kinetic simulations, a discrepancy between computational prediction and experimental observations concerning both thermodynamic stability and kinetic production of pentamer **16f** versus hexamer **18b** led us to believe that acyclic pentamers are not the ideal precursors for producing acyclic hexamers or heptamers via K_{5+1}, K_{5+2} and K_{6+1} reactions. Highly likely, these strained acyclic oligomers are generated predominantly from bimolecular reactions of K_{4+2}, K_{3+3} and K_{4+3} types.

Similarly, a bimolecular reaction mechanism via K_{4+2} or K_{3+3} types, rather than a chain-growth mechanism, seems to be in operation as well for $AlMe_3$-mediated one-pot cyclohexamerization of **17a** that affords 1**8a** (Fig. 9.11 and Table 9.9).

9.6 Conclusion

The use of intramolecular H-bonds to facilitate the one-pot macrocyclization reaction for the efficient preparation of various macrocycles from folded oligomeric intermediates and precursors have proven to be a very attractive and general approach due to its simplicity, requiring only simple starting materials, and a possibility to obtain high yields at the gram scale with minimized by-products. Since a careful structural design is critical that determines the structures and functions of the macrocycles to be obtained, this field is largely driven by chemists' intuition and imagination. In less than 10 years since the fabulous report by Gong in 2004 [21], many noteworthy examples illustrating rapid constructions of diverse macrocyclic structures have appeared. The developed one-pot methodologies targeting varying substrates have allowed for their noncollapsible internal cavity to be tuned from ~0.3 to 3 nm with systematically modifiable interior and exterior surfaces. And in some cases, the exterior surface modifications can be carried out in a regiospecific fashion by one-pot macrocyclization [59]. These unique features coupled with their now ready availability should greatly facilitate the subsequent functional studies and applications. In fact, a number of functions recently have arisen from these H-bonded macrocycles which include tight associations with neutral molecules such as fullerenes/coronene [36] and *p*-toluenesulfonic acid [37], selective binding of inorganic [44, 45] and organic [82] cations in high affinity, stabilization of G-quadruplex structures [83], formation of highly conducting transmembrane pores [84], and catalyzing the direct arylations of unactivated arenes [85]. In particular, the pentameric systems represented by aromatic pentamers **16**, **20** and others (Fig. 9.10) are characterized by a small cavity size of ~2.8 Å in radius suitable for cation recognition, and further by their macrocyclic backbones that are modularly tunable by using building blocks of different types in different ratios and at different positions. These notable traits enable a combinatorial production of an enriched family of modularly engineerable cavity-forming macrocyclic pentamers. Their shape-consistent skeletons effectively preorganize electronic (e.g., oxygens and fluorines) and steric/hydrophobic (e.g., methyl groups and hydrogens) features into a convergent alignment that may eventually allow the circular pentamers to tightly, yet selectively bind metal cations. Accordingly, diverse and influential functions crossing traditional boundaries and extending into chemistry, biology, materials sciences, and medicine are likely to arise from the existing and quickly emerging macrocycles of varied designs and structures.

References

1. Pedersen CJ (1967) Cyclic polyethers and their complexes with metal salts. J Am Chem Soc 89(10):2495–2496
2. Pedersen CJ (1967) Cyclic polyethers and their complexes with metal salts. J Am Chem Soc 89(26):7017–7036
3. Dietrich B, Lehn JM, Sauvage JP (1969) Les cryptates. Tetrahedron Lett 10(34):2889–2892
4. Dietrich B, Lehn JM, Sauvage JP (1969) Diaza-polyoxa-macrocycles et macrobicycles. Tetrahedron Lett 10(34):2885–2888
5. Kyba EP, Siegel MG, Sousa LR, Sogah GDY, Cram DJ (1973) Chiral, hinged, and functionalized multiheteromacrocycles. J Am Chem Soc 95(8):2691–2692
6. Helgeson RC, Koga K, Timko JM, Cram DJ (1973) Complete optical resolution by differential complexation in solution between a chiral cyclic polyether and an .alpha.-amino acid. J Am Chem Soc 95(9):3021–3023
7. Cabbiness DK, Margerum DW (1969) Macrocyclic effect on the stability of copper(II) tetramine complexes. J Am Chem Soc 91(23):6540–6541
8. Zhang W, Moore JS (2006) Shape-persistent macrocycles: structures and synthetic approaches from arylene and ethynylene building blocks. Angew Chem Int Ed 45(27):4416–4439
9. Borisova NE, Reshetova MD, Ustynyuk YA (2007) Metal-free methods in the synthesis of macrocyclic Schiff bases. Chem Rev 107(1):46–79
10. Hoger S (2005) Shape-persistent phenylene-acetylene macrocycles: large rings-low yield? Angew Chem Int Ed 44(25):3806–3808
11. Höger S (2004) Shape-persistent macrocycles: from molecules to materials. Chem Eur J 10 (6):1320–1329
12. Blankenstein J, Zhu JP (2005) Conformation-directed macrocyclization reactions. Eur J Org Chem 2005(10):1949–1964
13. Xing LY, Ziener U, Sutherland TC, Cuccia LA (2005) Hydrogen bond directed synthesis of pyridazine and naphthyridine containing macrocycles. Chem Commun: 5751–5753
14. Holub JM, Jang HJ, Kirshenbaum K (2007) Fit to be tied: conformation-directed macrocyclization of peptoid foldamers. Org Lett 9(17):3275–3278
15. Campbell F, Plante J, Carruthers C, Hardie MJ, Prior TJ, Wilson AJ (2007) Macrocyclic scaffolds derived from p-aminobenzoic acid. Chem Commun: 2240–2242
16. Yokoyama A, Maruyama T, Tagami K, Masu H, Katagiri K, Azumaya I, Yokozawa T (2008) One-pot synthesis of cyclic triamides with a triangular cavity from trans-stilbene and Diphenylacetylene monomers. Org Lett 10(15):3207–3210
17. He L, An Y, Yuan LH, Feng W, Li MF, Zhang DC, Yamato K, Zheng C, Zeng XC, Gong B (2006) Shape-persistent macrocyclic aromatic tetrasulfonamides: Molecules with nanosized cavities and their nanotubular assemblies in solid state. Proc Natl Acad Sci USA 103 (29):10850–10855
18. Geng M, Zhang D, Wu X, He L, Gong B (2009) One-pot formation and characterization of macrocyclic aromatic tetrasulfonates. Org Lett 11(4):923–926
19. Morokuma K (1977) Why do molecules interact? The origin of electron donor-acceptor complexes, hydrogen bonding and proton affinity. Acc Chem Res 10(8):294–300
20. Carver FJ, Hunter CA, Shannon RJ (1994) Directed macrocyclization reactions. Chem Commun: 1277–1280
21. Yuan L, Feng W, Yamato K, Sanford AR, Xu D, Guo H, Gong B (2004) Highly efficient, one-step macrocyclizations assisted by the folding and preorganization of precursor oligomers. J Am Chem Soc 126(36):11120–11121
22. Li ZT, Hou JL, Li C, Yi HP (2006) Shape-persistent aromatic amide oligomers: new tools for supramolecular chemistry. Chem Asian J 1(6):766–778
23. Ong WQ, Zeng HQ (2013) Rapid construction of shape-persistent H-bonded macrocycles via one-pot H-bonding-assisted macrocyclization. J Incl Phenom Macrocycl Chem 76:1–11

24. Fu HL, Liu Y, Zeng HQ (2013) Shape-persistent H-bonded macrocyclic aromatic pentamers. Chem Commun 49:4127–4144
25. Hamuro Y, Geib SJ, Hamilton AD (1994) Novel molecular scaffolds: formation of helical secondary structure in a family of oligoanthranilamides. Angew Chem Int Ed 33(4):446–448
26. Hamuro Y, Geib SJ, Hamilton AD (1997) Novel folding patterns in a family of oligoanthranilamides: non-peptide oligomers that form extended helical secondary structures. J Am Chem Soc 119(44):10587–10593
27. Hamuro Y, Geib SJ, Hamilton AD (1996) Oligoanthranilamides. Non-peptide subunits that show formation of specific secondary structure. J Am Chem Soc 118(32):7529–7541
28. Parra RD, Zeng HQ, Zhu J, Zheng C, Zeng XC, Gong B (2001) Stable three-center hydrogen bonding in a partially rigidified structure. Chem Eur J 7(20):4352–4357
29. Zhu J, Parra RD, Zeng HQ, Skrzypczak-Jankun E, Zeng XC, Gong B (2000) A new class of folding oligomers: crescent oligoamides. J Am Chem Soc 122(17):4219–4220
30. Gong B, Zeng HQ, Zhu J, Yuan LH, Han YH, Cheng SZ, Furukawa M, Parra RD, Kovalevsky AY, Mills JL, Skrzypczak-Jankun E, Martinovic S, Smith RD, Zheng C, Szyperski T, Zeng XC (2002) Creating nanocavities of tunable sizes: hollow helices. Proc Natl Acad Sci USA 99 (18):11583–11588
31. Berl V, Huc I, Khoury RG, Krische MJ, Lehn JM (2000) Interconversion of single and double helices formed from synthetic molecular strands. Nature 407(6805):720–723
32. Kim YH, Calabrese J, McEwen C (1996) $CaCl_3^-$ or Ca_2Cl_4 Complexing cyclic aromatic amide. Template effect on cyclization. J Am Chem Soc 118(6):1545–1546
33. Feng W, Yamato K, Yang L, Ferguson JS, Zhong L, Zou S, Yuan L, Zeng XC, Gong B (2009) Efficient kinetic macrocyclization. J Am Chem Soc 131(7):2629–2637
34. Zou SL, He YZ, Yang YA, Zhao Y, Yuan LH, Feng W, Yamato K, Gong B (2009) Improving the efficiency of forming 'Unfavorable' products: eight-residue macrocycles from folded aromatic oligoamide precursors. Synlett (9):1437–1440
35. Yang LQ, Zhong LJ, Yamato K, Zhang XH, Feng W, Deng PC, Yuan LH, Zeng XC, Gong B (2009) Aromatic oligoamide macrocycles from the bimolecular coupling of folded oligomeric precursors. New J Chem 33(4):729–733
36. Zhu YY, Li C, Li GY, Jiang XK, Li ZT (2008) Hydrogen-bonded aryl amide macrocycles: synthesis, single-crystal structures, and stacking interactions with fullerenes and coronene. J Org Chem 73(5):1745–1751
37. Jiang H, Léger J-M, Guionneau P, Huc I (2004) Strained aromatic oligoamide macrocycles as new molecular clips. Org Lett 6(17):2985–2988
38. Li F, Gan Q, Xue L, Wang Z-m, Jiang H (2009) H-bonding directed one-step synthesis of novel macrocyclic peptides from ε-aminoquinolinecarboxylic acid. Tetrahedron Lett 50 (20):2367–2369
39. Qin B, Chen XY, Fang X, Shu YY, Yip YK, Yan Y, Pan SY, Ong WQ, Ren CL, Su HB, Zeng HQ (2008) Crystallographic evidence of an unusual, pentagon-shaped folding pattern in a circular aromatic pentamer. Org Lett 10(22):5127–5130
40. Guieu S, Crane AK, MacLachlan MJ (2011) Campestarenes: novel shape-persistent Schiff base macrocycles with 5-fold symmetry. Chem Commun 47:1169–1171
41. Sessler JL, Seidel D (2003) Synthetic expanded porphyrin chemistry. Angew Chem Int Ed 42 (42):5134–5175
42. Misra R, Chandrashekar TK (2008) Structural diversity in expanded porphyrins. Acc Chem Res 41(2):265–279
43. Brooker S (2001) Complexes of thiophenolate-containing Schiff-base macrocycles and their amine analogues. Coord Chem Rev 222(1):33–56
44. Qin B, Ren CL, Ye RJ, Sun C, Chiad K, Chen XY, Li Z, Xue F, Su HB, Chass GA, Zeng HQ (2010) Persistently folded circular aromatic amide pentamers containing modularly tunable cation-binding cavities with high ion selectivity. J Am Chem Soc 132(28):9564–9566
45. Ren CL, Maurizot V, Zhao HQ, Shen J, Zhou F, Ong WQ, Du ZY, Zhang K, Su HB, Zeng HQ (2011) Fivefold-symmetric macrocyclic aromatic pentamers: high affinity cation recognition, ion-pair induced columnar stacking and nanofibrillation. J Am Chem Soc 133(35):13930–13933

46. Yan Y, Qin B, Ren CL, Chen XY, Yip YK, Ye RJ, Zhang DW, Su HB, Zeng HQ (2010) Synthesis, structural investigations, hydrogen−deuterium exchange studies, and molecular modeling of conformationally stablilized aromatic oligoamides. J Am Chem Soc 132 (16):5869–5879
47. Yi HP, Li C, Hou JL, Jiang XK, Li ZT (2005) Hydrogen-bonding-induced oligoanthranilamide foldamers. Synthesis, characterization, and complexation for aliphatic ammonium ions. Tetrahedron 61(33):7974–7980
48. Hou J-L, Yi H-P, Sha X-B, Li C, Wu Z-Q, Jian X-K, Wu L-Z, Tung C-H, Li Z-T (2006) Helicity induction in hydrogen-bonding-driven zinc porphyrin foldamers by chiral C_{60}-incorporating histidines. Angew Chem Int Ed 45(5):796–800
49. Qin B, Ong WQ, Ye RJ, Du ZY, Chen XY, Yan Y, Zhang K, Su HB, Zeng HQ (2011) Highly selective one-pot synthesis of H-bonded pentagon-shaped circular aromatic pentamers. Chem Commun 47:5419–5421
50. Liu Y, Qin B, Zeng HQ (2012) $POCl_3$-mediated H-bonding-directed one-pot synthesis of macrocyclic pentamers, strained hexamers and highly strained heptamers. Sci China Chem 55 (1):55–63
51. Yan Y, Qin B, Shu YY, Chen XY, Yip YK, Zhang DW, Su HB, Zeng HQ (2009) Helical organization in foldable aromatic oligoamides by a continuous hydrogen-bonding network. Org Lett 11(6):1201–1204
52. Ong WQ, Zhao HQ, Du ZY, Yeh JZY, Ren CL, Tan LZW, Zhang K, Zeng HQ (2011) Computational prediction and experimental verification of pyridine-based helical oligoamides containing four repeating units per turn. Chem Commun 47:6416–6418
53. Ong WQ, Zhao HQ, Fang X, Woen S, Zhou F, Yap WL, Su HB, Li SFY, Zeng HQ (2011) Encapsulation of conventional and unconventional water dimers by water-binding foldamers. Org Lett 13(12):3194–3197
54. Ren CL, Xu SY, Xu J, Chen HY, Zeng HQ (2011) Planar macrocyclic fluoropentamers as supramolecular organogelators. Org Lett 13(15):3840–3843
55. Zhang Z, Xia B, Han C, Yu Y, Huang F (2010) Syntheses of copillar[5]arenes by co-oligomerization of different monomers. Org Lett 12(15):3285–3287
56. Zhang Z, Luo Y, Xia B, Han C, Yu Y, Chen X, Huang F (2011) Four constitutional isomers of BMpillar[5]arene: synthesis, crystal structures and complexation with n-octyltrimethyl ammonium hexafluorophosphatew. Chem Commun 47:2417–2419
57. Young SW, Qing F, Harriman A, Sessler JL, Dow WC, Mody TD, Hemmi GW, Hao Y, Miller RA (1996) Gadolinium(III) texaphyrin: a tumor selective radiation sensitizer that is detectable by MRI. Proc Natl Acad Sci USA 93(13):6610–6615
58. Sessler JL, Tomat E, Lynch VM (2006) Coordination of oxovanadium(V) in an expanded porphyrin macrocycle. Chem Commun 42:4486–4488
59. Qin B, Sun C, Liu Y, Shen J, Ye RJ, Zhu J, Duan X-F, Zeng HQ (2011) One-pot synthesis of hybrid macrocyclic pentamers with variable functionalizations around the periphery. Org Lett 13(9):2270–2273
60. Qin B, Shen S, Sun C, Du ZY, Zhang K, Zeng HQ (2011) One-pot multi-molecular macrocyclization for the expedient synthesis of macrocyclic aromatic pentamers by a chain growth mechanism. Chem Asian J 6(12):3298–3305
61. Du ZY, Ren CL, Ye RJ, Shen J, Lu YJ, Wang J, Zeng HQ (2011) BOP-mediated one-pot synthesis of C5-symmetric macrocyclic pyridone pentamers. Chem Commun 47:12488–12490
62. The remaining 75 % of starting monomeric building block forms a conjuated product with BOP that does not react further. The monomer may also get transformed into oligomeric intermedates that form conjugated products with BOP that do not participate in further reactions to make circular pentamer **1**, either
63. Davies JS (2003) The cyclization of peptides and depsipeptides. J Peptide Sci 9:471–501
64. Ren CL, Zhou F, Qin B, Ye RJ, Shen S, Su HB, Zeng HQ (2011) Crystallographic realization of the mathematically predicted densest "All Pentamer" packing lattice by C5-symmetric "sticky" fluoropentamers. Angew Chem Int Ed 50(45):10612–10615

65. Sun C, Ren CL, Wei YC, Qin B, Zeng HQ (2013) Patterned recognition of amines and ammonium ions by a stimuli-responsive foldamer-based hexameric oligophenol host. Chem Commun 49:5307–5309
66. Zhao HQ, Ong WQ, Zhou F, Fang X, Chen XY, Li SFY, Su HB, Cho N-J, Zeng HQ (2012) Chiral crystallization of aromatic helical foldamers via complementarities in shape and end functionalities. Chem Sci 3:2042–2046
67. Ong WQ, Zhao HQ, Sun C, Wu JE, Wong ZC, Li SFY, Hong YH, Zeng HQ (2012) Patterned recognitions of amines and ammonium ions by a pyridine-based helical oligoamide host. Chem Commun 48:6343–6345
68. Bassett HL, Thomas CR (1954) The bodroux reaction. J Chem Soc: 1188–1190
69. Yong KW, Cannon JG, Rose JG (1970) N-butyllithium in aminolysis and ammonolysis of esters. Tetrahedron Lett 11(21):1791–1794
70. Huebner CF, Lucas R, McPhullamy HB, Troxell HA (1955) Rauwolfia alkaloids. XIV. Derivatives of Yohimbé Alkaloids. J Am Chem Soc 77(2):469–472
71. Basha A, Lipton M, Weinreb SM (1977) A mild, general method for conversion of esters to amides. Tetrahedron Lett 18(48):4171–4174
72. Novak A, Humphreys LD, Walker MD, Woodward S (2006) Amide bond formation using an air-stable source of $AlMe_3$. Tetrahedron Lett 47:5767–5769
73. Fu HL, Chang H, Shen J, Lu Y-J, Qin B, Zhang K, Zeng HQ (2014) An unusual macrocyclization reagent for highly selective one-pot synthesis of strained macrocyclic aromatic hexamers. Chem Commun 50:3582–3584
74. Qin B, Jiang LY, Shen S, Sun C, Yuan WX, Li SFY, Zeng HQ (2011) Folding-promoted TBACl-mediated chemo- and regio-selective demethylations of metoxybenzene-based macrocyclic pentamers. Org Lett 13(23):6212–6215
75. Du ZY, Qin B, Sun C, Liu Y, Zheng X, Zhang K, Conney AH, Zeng HQ (2012) Folding-promoted TBAX-mediated selective demethylation of methoxybenzene-based macrocyclic aromatic pentamers. Org Biomol Chem 10(21):4164–4171
76. Zhang AM, Han YH, Yamato K, Zeng XC, Gong B (2006) Aromatic oligoureas: enforced folding and assisted cyclization. Org Lett 8(5):803–806
77. Wu ZH, Hu T, He L, Gong B (2012) One-pot formation of aromatic tetraurea macrocycles. Org Lett 14(10):2504–2507
78. Ferguson JS, Yamato K, Liu R, He L, Zeng XC, Gong B (2009) One-pot formation of large macrocycles with modifiable peripheries and internal cavities. Angew Chem Int Ed 48 (17):3150–3154
79. Hui JKH, MacLachlan MJ (2006) [6+6] Schiff-base macrocycles with 12 imines: giant analogues of cyclohexane. Chem Commun 42:2480–2482
80. Filarowski A, Koll A, Sobczyk L (2009) Intramolecular hydrogen bonding in o-hydroxy aryl Schiff bases. Curr Org Chem 13(2):172–193
81. The kinetic simulations were carried out by using a mechanism-based kinetics simulator from http://www.stolafedu/depts/chemistry/courses/toolkits/126/js/kinetics/
82. Sanford AR, Yuan LH, Feng W, Flowersb KY, Gong B (2005) Cyclic aromatic oligoamides as highly selective receptors for the guanidinium ion. Chem Commun 42:4720–4722
83. Shirude PS, Gillies ER, Ladame S, Godde F, Shin-Ya K, Huc I, Balasubramanian S (2007) Macrocyclic and helical oligoamides as a new class of g-quadruplex ligands. J Am Chem Soc 129(39):11890–11891
84. Helsel AJ, Brown AL, Yamato K, Feng W, Yuan LH, Clements AJ, Harding SV, Szabo G, Shao ZF, Gong B (2008) Highly conducting transmembrane pores formed by aromatic oligoamide macrocycles. J Am Chem Soc 130(47):15784-15785
85. Zhao HQ, Shen J, Guo JJ, Ye RJ, Zeng HQ (2013) A macrocyclic aromatic pyridone pentamer as a highly efficient organocatalyst for the direct arylations of unactivated arenes. Chem Commun 49:2323–2325

Chapter 10
Hydrogen-Bonded Supramolecular Polymers

Chen Lin, Tangxin Xiao and Leyong Wang

Abstract Supramolecular polymers constructed by different kinds of low-molecular-weight monomers or high-molecular-weight conventional polymeric species based on hydrogen bonding interactions have attracted more and more attention due to their fascinating and unconventional chemical and physical properties. A series of multiple hydrogen-bonding building blocks are described herein, which make the expansion of the research field of hydrogen-bonded supramolecular polymers and allow the fabrication of more new and functional supramolecular polymers. This chapter focuses on linear hydrogen-bonded supramolecular polymers and networks which are described in three parts. The first part is the main-chain supramolecular polymers, in which the polymeric backbone is constructed by noncovalently bonded low-molecular-weight monomers. The second part is the conventional polymer-based supramolecular polymers, in which the main polymeric backbone part is constructed by covalently bonded conventional polymer, but functionalized by hydrogen-bonding motifs. The last part is supramolecular polymers constructed by orthogonal hydrogen bonding-driven self-assembly and other noncovalent interactions.

10.1 Introduction

In view of the reversible and dynamic nature of noncovalent interactions, supramolecular polymers have attracted much attention in recent years as they not only possess conventional polymeric properties, but also show new distinct material properties, which ensure their potential application in a broad range of fields [1–5]. The secondary interactions involved in the construction of the supramolecular structures include hydrogen bonding, metal–ligand coordination, π–π stacking, ionic interaction, and host–guest interaction etc. Each of these noncovalent interactions

C. Lin · T. Xiao · L. Wang (✉)
School of Chemistry and Chemical Engineering, Nanjing University,
Nanjing 210093, Jiangsu Province, China
e-mail: lywang@nju.edu.cn

Z. Li and L. Wu (eds.), *Hydrogen Bonded Supramolecular Structures*,
Lecture Notes in Chemistry 87, DOI 10.1007/978-3-662-45756-6_10

has unique bond strength and advantages. Among these noncovalent interactions, multiple hydrogen-bonding interactions are strong and directional, and have high-fidelity that has unsurpassed potential for specificity [6, 7]. People cannot begin a study on hydrogen bonding without fully understanding the significance of this noncovalent electrostatic interaction in biological systems. Biology provides lots of excellent examples of hydrogen-bonded polymers, including double-helical DNA, as well as protein β-sheets [8, 9]. Motivated by these biological systems, chemists have been trying to fabricate artificial supramolecular architectures based on multiple hydrogen-bonding interactions. The supramolecular architectures should be intricate and complex, yet as simple and efficient in function, as those found in nature.

Hydrogen bonds are relatively strong, directional, as well as reversible, which ensures that hydrogen-bonded polymers can be produced with lengths and properties that are highly dependent upon temperature, pH, concentration, and competitive additives. It should be noted that individual hydrogen bond, although weak, may sum in multivalent contacts to provide high stability. Stadler and coworkers first recognized that hydrogen bonds could be employed to bring polymers together [10]. Inspired by linear arrays found in nucleic acids, such as double hydrogen bonds in adenine and thymine, triple hydrogen bonds in guanine and cytosine, scientists have developed several different types of hydrogen bond arrays whose length increases with the increasing number of binding sites. A hydrogen bonding site is either a donor (D), or an acceptor (A), and heterocyclic molecules with equidistant acceptor- and donor-binding sites can be extended by adding rings or other functional groups, such as amide and urea group. In 1990, Lehn and coworkers synthesized the first main-chain triple hydrogen-bonding-based supramolecular polymer (Scheme 10.1) [5]. This opened the door of hydrogen-bonding-based supramolecular polymer chemistry, generating materials with reversible interactions, and thereby introducing the opportunity of producing materials with properties that otherwise would have been impossible or difficult to obtain in the conventional way.

Although hydrogen-bonded dendrimers, ribbons, and helices are relatively common structural motifs found in solution or in the solid state, which may be classified as supramolecular polymers, a detailed introduction of these architectures is not described herein. Therefore, this chapter will primarily focus on linear hydrogen-bonded supramolecular polymers and networks. Generally, supramolecular polymers can be divided into two classes: (1) one is the main-chain supramolecular polymers in which the polymeric backbone (linear types or networks) is constructed by noncovalently bonded low-molecular-weight monomers; (2) the other is the conventional polymer-based supramolecular polymers in which the main polymeric backbone part is constructed by covalently bonded conventional polymer, but it is functionalized by hydrogen bonding motifs in two different ways: **a** hydrogen-bonded telechelic polymers in which hydrogen-bonding motifs are linked on the two ends of the linear conventional polymers, and **b** side-chain supramolecular polymers in which the hydrogen-bonding motifs served as pendant groups on the conventional polymer chain. This chapter will describe these two

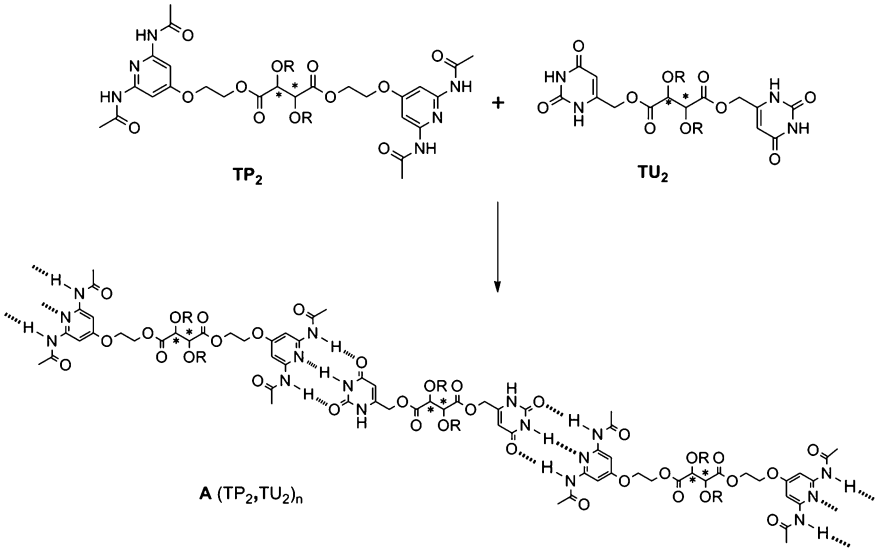

Scheme 10.1 The formation of a hydrogen bonding-based supramolecular polymer reported by Lehn et al. Reproduced from Ref. [5] by permission of John Wiley and Sons Ltd

kinds of hydrogen-based supramolecular polymers in two main parts. Moreover, hydrogen bonding-based supramolecular polymers constructed by orthogonal self-assembly have particularly become a popular research topic in recent years, where "orthogonal" was defined as different types of noncovalent interactions that do not interfere with each other [11–13]. In general, the multiple noncovalent interactions involved in one supramolecular polymer system should be orthogonal to each other. Thus we also describe hydrogen bonding-based supramolecular polymers constructed by multiple hydrogen bonds orthogonally combined with other noncovalent interactions in the last part of this chapter.

10.2 Hydrogen-Bonding Building Blocks

Prior to the review of the hydrogen-bonding building blocks, it is important to address several issues that influence the stability of hydrogen-bonded supramolecular polymers. The association constant of the multiple hydrogen-bonding motif is influenced by several factors, such as temperature, the nature of donor and acceptor, polarity of solvents etc. In general, the strength of a single hydrogen bond depends on the nature of the hydrogen bond acceptor (A) and donor (D). For a specific hydrogen-bonded array, it is worthy to propose that secondary electrostatic interactions between adjacent sites in the building block are critical to the binding constant. According to Jorgensen's concept of secondary interactions, the secondary electrostatic interactions are repulsive between the sites possessing the same

electrical property, while disparate sites attract each other (Fig. 10.1) [14]. For example, there are three different types of triple hydrogen bonds arrays, such as ADA-DAD, DAA-ADD, and AAA-DDD. Although the ADA-DAD and AAA-DDD arrays exhibit an equal number of hydrogen bonds, the binding constants of these two motifs are totally different. The binding constant of ADA-DAD is about 10^2 M^{-1} due to two repulsive secondary bonds, while AAA-DDD's association constant is more than 10^5 M^{-1} on accounts of two additional attractive secondary bonds. This theory was confirmed by Zimmerman and coworkers by measuring the binding constants experimentally [15].

Similar to double and triple hydrogen-bonding arrays, quadruple hydrogen-bonded dimers include six different types of binding modes, two of which are self-complementary arrays [$(DDAA)_2$ and $(DADA)_2$]. The estimated value of the binding constant of DDAA-type hydrogen bonding is 3.6×10^6 M^{-1} in $CHCl_3$. Meijer and coworkers first enclosed a DDAA-type hydrogen bonding motif, ureidopyrimidinone (UPy), and achieved an experimental value of more than 10^7 M^{-1} in $CHCl_3$ for its association constant [16, 17].

During the last two decades, there have been several reports of hydrogen-bonding motifs capable of forming exceptionally robust dimers to achieve hydrogen-bonded supramolecular polymers. Inspired by DNA base pairs, almost all of the artificial, multiple hydrogen-bonding motifs are developed from heterocycles.

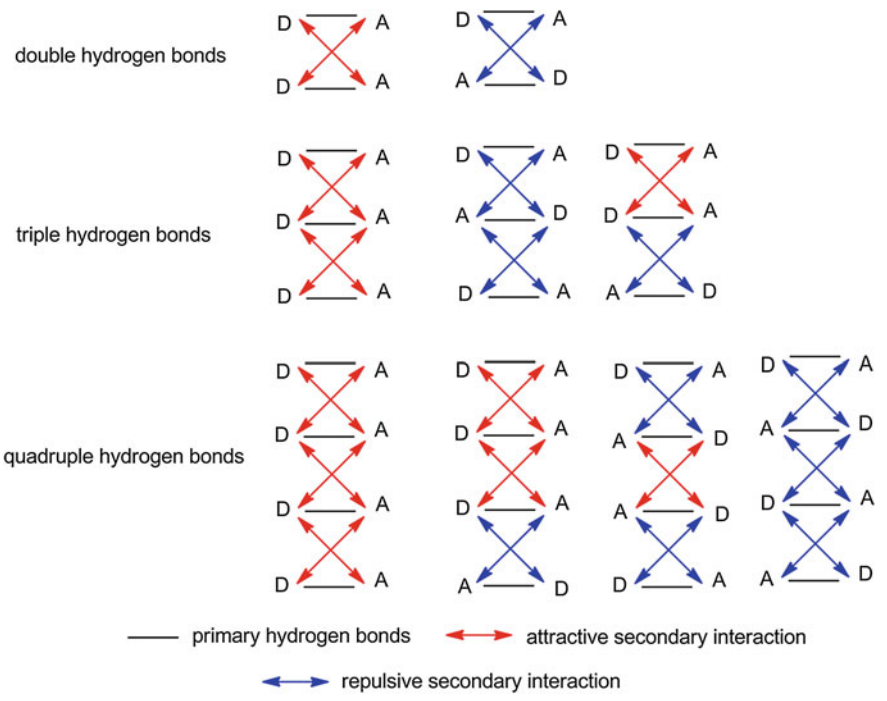

Fig. 10.1 Dimers formed by linear arrays of different types of hydrogen-bonding sites

In this part, we will initially introduce several typical multiple hydrogen-bonding motifs which have been studied most often in the construction of hydrogen-bonded supramolecular polymers.

In the design of artificial hydrogen-bonded host molecules, the incorporation of several inwardly facing hydrogen-bonding sites of guest molecules into a cavity of defined structure of host molecules should lead to strong and selective binding with complementary H-bonding characteristics. In 1988, Hamilton and coworkers reported the recognition and strong binding of barbiturate derivatives by a macrocyclic host molecule containing six inwardly facing hydrogen bonds (Scheme 10.2a) [18]. The complexation behavior of host molecule **1** and barbital **2** was investigated by ^{1}H NMR. Addition of 1 equiv of barbital **2** into a $CDCl_3$ solution of **1** caused large downfield shifts of the amide (1.65 and 1.63 ppm) of host molecule **1** and the imide (4.38 ppm) of barbital **2**, indicating the formation of the sextuple hydrogen-bonding complex. They also studied the complex in CPK (Corey-Pauling-Koltun) molecular modeling, which suggests that in the resulting complex the isophthaloyl-2 proton is forced to lie in the deshielding region of the carbonyl group of barbital **2**, and, indeed, this resonance is shifted downfield by 0.4 ppm. The large association constant of 1.37×10^6 M^{-1} for the host–barbiturate complex was determined by ^{1}H NMR titration data. The host molecule was then developed to the open fashion and called Hamilton receptor, which can also bind with cyanuric acid derivatives.

Compared to triple hydrogen bonds, the increased binding ability of hydrogen-bonded building blocks was observed in preorganized ureidotriazine **3** which

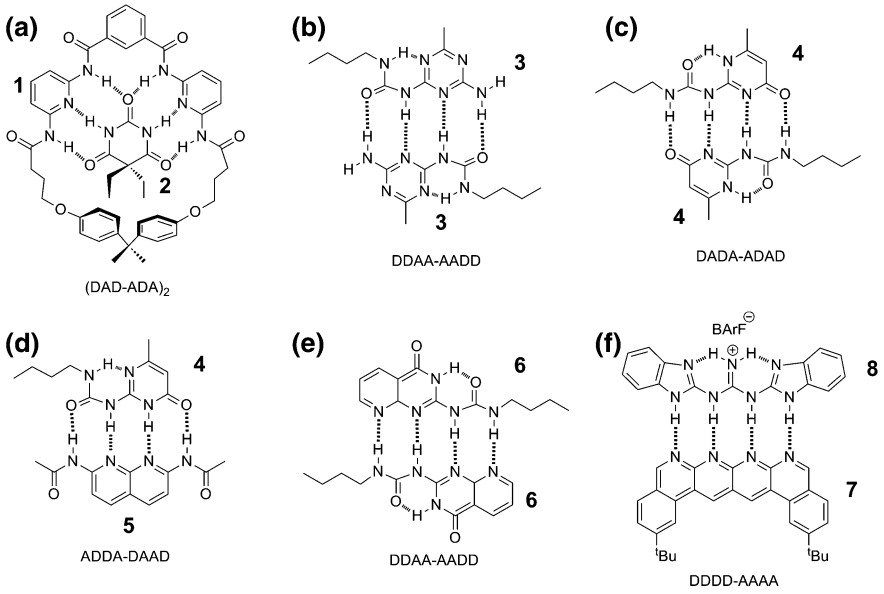

Scheme 10.2 Examples of multiply hydrogen-bonded complexes

adopted a DADA quadruple hydrogen bonds binding mode (Scheme 10.2b) [19]. There is an intramolecular hydrogen bond in **3** that preorganizes the shape of the motif, and then **3** can self-assemble into dimer through four intermolecular hydrogen bonds in a self-complementary way. Meijer and coworkers studied the crystal structure of such a dimer and investigated its association constant. They reported a dimerization constant of $2 \times 10^4\ M^{-1}$ for this preorganized ureidotriazine **3**. The ease of synthesis of diaminotriazines, and the large dimerization constant of the mono-ureido derivative encouraged them to employ this building block for the self-assembly of highly organized supramolecular structures in the last two decades.

The binding constant of the most stable DADA dimers could probably reach a value of $2 \times 10^5\ M^{-1}$, and the preparation of monomer requires chromatographic separation and a relatively expensive starting material. According to Jorgensen's concept of secondary interactions, DADA-type self-complementary quadruple hydrogen-bonding building block is less stable than DDAA type. In 1997, Meijer and coworkers found an excellent DDAA-type self-complementary quadruple hydrogen-bonding building block **4**, ureidopyrimidinone (UPy), which can be easily synthesized in two steps from an isocytosine molecule (Scheme 10.2c) [17]. Compound **4** is also preorganized by an intramolecular hydrogen bonding. The K_{dim} values of **4** were determined to be approximately $2 \times 10^7\ M^{-1}$ in chloroform and $10^8\ M^{-1}$ in toluene. Meijer and coworkers have demonstrated that ditopic monomers containing **4** motif are wonderful for constructing hydrogen-bonded supramolecular polymers with interesting properties. Although the UPy motif exhibits a high association constant, the binding mode of dimer of **4** during self-assembly is highly dependent on the substituent on its 6-position of the pyrimidinone ring, since different tautomeric forms can be present [16]. With various substituents in **4**, its tautomeric equilibrium might shift to the pyrimidine-4-ol tautomer, which is self-complementary as a DADA hydrogen-bonding form. However, the pyrimidinone tautomer which follows DDAA form predominates in most cases. Li and coworkers found that in $CDCl_3$, homodimer UPy could dissociate and bind with NaPy **5** to selectively afford heterodimer UPy-NaPy **4–5** (ADDA-DAAD), as indicated by the ^1H NMR spectroscopy [20]. Therefore, the combination of **4** and **5** could be applied for the preparation of AB-type monomer containing both UPy and Napy quadruple hydrogen-bonding moieties, which solves the problems of stoichiometric imbalance in the construction of AA + BB-type supramolecular polymer.

Zimmerman and coworkers studied the dimer formed from ureido pyridopyrimidine **6** and its tautomer (Scheme 10.2d) [21]. They pointed out that prototropy can be detrimental to hydrogen-bonded complex formation. Therefore, heterocycle **6** was designed to contain only one self-complementary hydrogen-bonding array (DDAA) eliminating others. They measured the self-association constant by employing ^1H NMR dilution studies in chloroform, which was estimated to be more than $10^7\ M^{-1}$.

As mentioned above, the secondary electrostatic interactions between adjacent hydrogen bonds in the hydrogen-bonded building blocks can have a significant effect on the stability of a hydrogen-bonded complex. In theory, the binding strength could be maximized if all the hydrogen bond donors (D) are in one

component and all the hydrogen bond acceptors (A) are in the other. In 2011, Leigh and coworkers reported such a quadruple hydrogen bonding array (DDDD-AAAA, **7** and **8**) that exhibits exceptionally strong binding with a binding constant even up to 3×10^{12} M^{-1} in CH_2Cl_2 as a small-molecule hydrogen-bonded complex (Scheme 10.2e) [22]. Although the photostability of **7** may be a concern for applications with strong light, the extremely strong strength of binding of the DDDD-AAAA quadruple hydrogen-bond motif makes it a promising candidate for incorporation into supramolecular polymers and other functional materials. The synthesis of each partner seems easy, but compared with UPy, it is still a little tedious.

The multiple hydrogen-bonding building blocks described above are just a few examples of various ones. However, they have been widely used or have strong potential to be useful in the construction of hydrogen-bonded supramolecular polymers. In this chapter, we will focus on hydrogen-bonded supramolecular polymers constructed by these hydrogen-bonding building blocks. With these hydrogen-bonding building blocks, it will be reviewed in the following three sections: (1) hydrogen-bonded "main-chain" supramolecular polymers constructed by low-molecular-weight monomers; (2) hydrogen-bonded supramolecular polymers constructed by high-molecular-weight conventional polymers that are functionalized by hydrogen-bonding motifs, which contain (a) telechelic supramolecular polymers and (b) "side-chain" supramolecular polymer networks; and (3) supramolecular polymers constructed by orthogonal hydrogen bonding-driven self-assembly and other noncovalent interactions.

10.3 Hydrogen-Bonded Main-Chain Supramolecular Polymers Constructed by Low-Molecular-Weight Monomers

In conventional polymers, the monomeric units are linked by covalent bonds. As mentioned above, Lehn and coworkers pioneered a new area within the field of polymer chemistry in 1990 by creating a "new" polymer in which the monomers were brought together by triple hydrogen bonding, resulting in a liquid crystalline supramolecular polymer [5]. In 1997, Meijer and coworkers introduced supramolecular polymers based on the ureido pyrimidinone (UPy) motif, which can form self-complementary quadruple hydrogen bonding, leading to a high degree of polymerization even in semi-dilute solution [17]. This event was a milestone in the area of supramolecular chemistry. Since then, a large number of supramolecular polymers and dynamic materials constructed from quadruple hydrogen bonding have been reported. In 2001, Meijer and coworkers defined supramolecular polymers as "…polymeric arrays of monomeric units that are brought together by reversible and highly directional secondary interactions, resulting in polymeric properties in dilute and concentrated solutions, as well as in the bulk [4]. The monomeric units of the supramolecular polymers themselves do not possess a

repetition of chemical fragments. The directionality and strength of the supramolecular bonding are important features of these systems, that can be regarded as polymers and behave according to well-established theories of polymer physics." It should be noted that herein in this section, the monomeric units refer to low-molecular-weight monomers and the backbone of the supramolecular polymer is constructed from these low-molecular-weight monomers through hydrogen bonds, which we call main-chain supramolecular polymers. If only two hydrogen-bonding moieties are located in one molecule of monomer, linear main-chain supramolecular polymers can be obtained. If three or more hydrogen-bonding moieties are located in one molecule of monomer, it can also generate main-chain supramolecular polymer networks. In a word, no matter how the supramolecular polymers are linear shaped or networks reviewed in this section, the building units should be low-molecular-weight monomers (usually the molecular weight is less than 5,000 Da.). Nowadays, a number of supramolecular materials are fabricated from those types of main-chain supramolecular polymers.

To obtain a high degree of polymerization (DP) in "dilute" solution, the association constant of dimerization of the monomers should be large. In 1997, Meijer and coworkers reported one example of hydrogen-bonded polymers with significant lengths in solution, which was ascribed to the high association constant of the UPy monomer that forms very stable dimers via quadruple hydrogen bonding [17]. The K_{dim} value of the UPy was determined to be approximately 2×10^7 M^{-1} in chloroform. These linear supramolecular polymers with different length of alkyl chains self-assembled from the ditopic unit **9** (Scheme 10.3), which contains the quadruple hydrogen bonding unit **4** (Scheme 10.2c). The examined viscosities of solutions of **9** in chloroform were high and exhibited a concentration dependence, which could

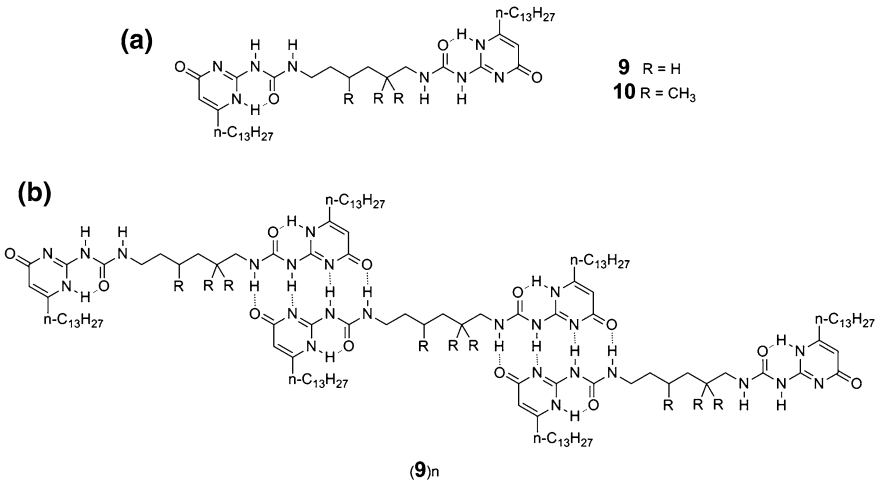

Scheme 10.3 **a** Ditopic ureidopyrimidine monomers **9** and **10**; **b** The supramolecular polymer formed from **9**

be attributed to length difference of resulting polymer as well as varying monomer concentration. The viscosity of a **9** solution could be lowered upon addition of **4**, as the result of **4** acting as a "stopper" to decrease the average DP, which was consistent with the reversible nature of hydrogen-bonded polymers in chloroform solution. The average DP of **9** was estimated to be 700 at a concentration of 40 mM, which is also in line with the large dimerization constant measured for **4**.

In addition to supramolecular polymers constructed from **9**, bifunctional monomer **10** (Scheme 10.3), incorporating a less-flexible trimethylhexyl linker, exists in an equilibrium between cyclic and linear aggregates in solution as evidenced by viscosity studies and diffusion-ordered NMR spectroscopy (DOSY). These results are in line with the proposal of equilibrium between linear polymeric and oligomeric cyclic structures (i.e., ring-chain equilibrium). Because of its restricted conformational freedom, **10** is more prone to the formation of rings than **9**.

Although bifunctional UPy derivatives are self-complementary ditopic monomers, supramolecular polymers can be prepared by employing heterocomplementary Hamilton receptor-cyanuric acid within ditopic monomers AA and BB. Lehn and coworkers reported the synthesis and study of ditopic monomers **11** and **12**, which, respectively, incorporated complementary cyanuric acid $(ADA)_2$ and diamidopyridine $(DAD)_2$ subunits (Scheme 10.4) to produce linear polymers based on hydrogen bondings between **11** and **12**, as verified by ^{1}H NMR, solution viscometry, and electron microscopy [23]. Fiber formation was observed in a micrograph of a sample prepared from a 1:1 mixture of **11** and **12** in tetrachloroethylene. These results further contribute to the development of supramolecular polymers with good reversibility through recognition-controlled noncovalent connections between the monomers. These materials are dynamic and show adaptive characteristics in view of their ability of responding to environmental stimuli.

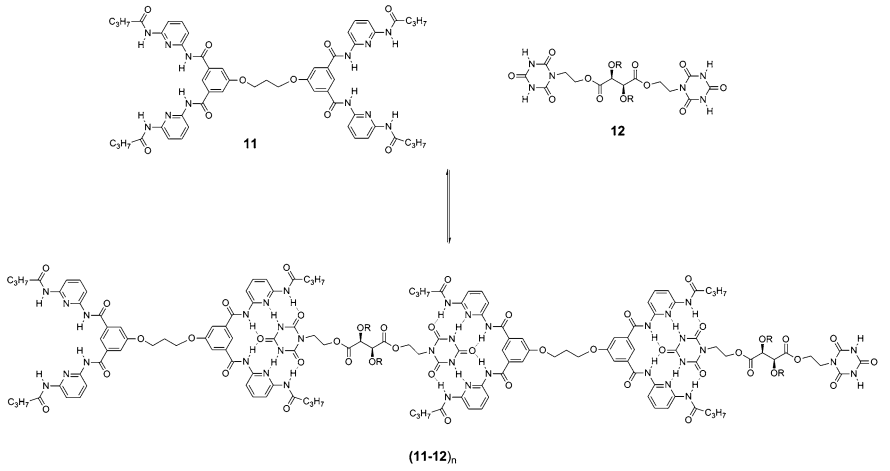

Scheme 10.4 Supramolecular polymerization of hetero complementary monomers **11** and **12**. Reproduced from Ref. [23] by permission of John Wiley & Sons Ltd

Generally, it is widely believed that hydrogen-bonded supramolecular polymers cannot be formed in water on account of the competitive hydrogen bonding of water. However, hydrophobic compartmentalization is widely found in nature and can shield hydrogen bonds from the aqueous environment. Meijer and coworkers reported a bifunctional ureidotriazine **13** linked with penta (ethyleneoxide) side chains which were able to self-assemble in water, leading to helical columns via cooperative stacking of the hydrogen-bonded pairs (DADA array), while monofunctional ureidotriazine did not form such helical architectures [24]. The presence of a linker, covalently connecting the two ureidotriazine units, is essential as it generates a high local concentration of aromatic units, favorable for stacking interactions. This hierarchical process results in the formation of a helical self-assembled polymer in water at concentrations above 0.1 mM. Chiral side chains attached to the ureidotriazine units bias the helicity of these columns as evidenced from the CD spectroscopy and "Sergeants and Soldiers" experiments. The findings presented in this work provide valuable design rules for the formation of highly ordered aggregates in water by using a combination of noncovalent interactions.

During the procedure of design and synthesis of supramolecular polymers, scientists gradually recognize that the supramolecular polymerization mechanism is of great importance to direct the growth of monomers and affect the properties of the resulting supramolecular polymers. Among the supramolecular polymerization mechanisms, the most important one is the ring-chain equilibrium mechanism, which is usually employed to describe a wide range of supramolecular polymers. The theory of ring-chain mechanism is characterized by the fact that linear oligomers and polymers are in equilibrium with their cyclic counterpart in solution. Of particular interest is the existence of a critical polymerization concentration (CPC), below which the cyclic assemblies are predominant species and above which the concentration of cyclic species remains constant and excess monomers mainly produce linear species. In the production of covalent polymers, the ring formation is usually considered as a byproduct that should be prevented as much as possible. However, optimization of a high yield of one specific aggregate with well-defined size and structure in self-assembled systems is one of the goals of synthetic research in supramolecular chemistry [25]. In this context, an increasing number of well-defined cyclic oligomers based on bifunctional UPy monomers have been developed for various applications due to their unusual three-dimensional structures and properties. No matter how chemists would like to optimize the yield of a well-defined cyclic structure or reduce the CPC to prevent the cyclic structure in the construction of supramolecular polymers, understanding the parameters related to the ring-chain equilibrium is useful and imperative for controlling the product distribution.

In 2012, Wang and coworkers first reported a highly stable cyclic monomer formed from a bifunctional UPy derivatives directed by ring-chain equilibrium theory (Fig. 10.2) [26]. They provided a detailed study to demonstrate the relationship of the π–π stacking interaction and the ring-chain equilibrium of DNP-bridged bifunctional UPy derivatives in supramolecular system. It was recognized that the strength of the π–π stacking interaction in the cyclic monomers was

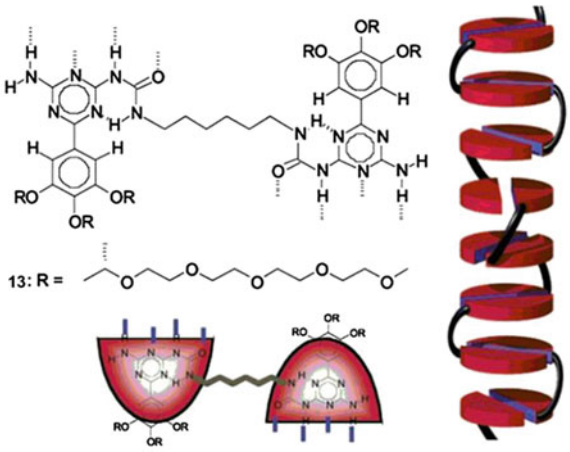

Fig. 10.2 Helical supramolecular ureidotriazine polymer in which the hydrogen-bonding motif is shielded from the solvent by hydrophobic interactions, creating aggregates in water. Reproduced with permission from ref [24] Copyright (2002) National Academy of Sciences, U.S.A

inversely proportional to the distance between DNP plane and intramolecularly dimerized UPy plane which was directly determined by the length of oligo(ethylene oxide) chain as spacers in the derivatives. They designed, respectively, **L1a** with shorter spacer (n = 1) that would possess stronger π–π stacking interaction in its cyclic form and **L3** with longer spacer (n = 3) that would have weaker π–π stacking interaction (Fig. 10.3). The stronger π–π stacking interaction involved in the cyclic monomer is, the more stable architecture it has. Thus, they suppose that, compared to **L2**, **L1a** would possess a larger CPC value while **L3** would have a relatively smaller CPC value during supramolecular polymerization process, which was verified by the final experimental results. Surprisingly, they found that **L1a** possessed a very huge CPC value larger than 500 mM, leading to a highly stable cyclic monomer over this concentration range in solution. The stability and morphology of the assemblies of **L1a**, **L2**, and **L3** were found to be greatly influenced by their subtle structural variation of spacers and different polarity of solvents used. Moreover, in an attempt to gain further insight into cyclic monomer formation, the crystal structure of the methyl-substituted UPy analogue **L1b** (n = 1) was obtained (Fig. 10.4), which strongly supported the "ring" of ring-chain equilibrium theory.

Organic photochromic materials have attracted considerable interest due to their potential applications in photo-memory and photo-switching devices. In particular, diarylethene, as an excellent photochromic compound, has proved to be the most promising switchable unit due to its excellent fatigue resistance and thermal stability. Wang and coworkers designed and synthesized a bifunctional UPy derivative **14** with a dithienylethene bridging unit and two flexible alkyl C_3 chains (Fig. 10.5) [27]. First, they used the photochemical reactivity of the diarylethene building block, along with ^{1}H and DOSY NMR spectroscopy and viscometry to investigate the ring-chain equilibrium in the supramolecular polymerization process in solution.

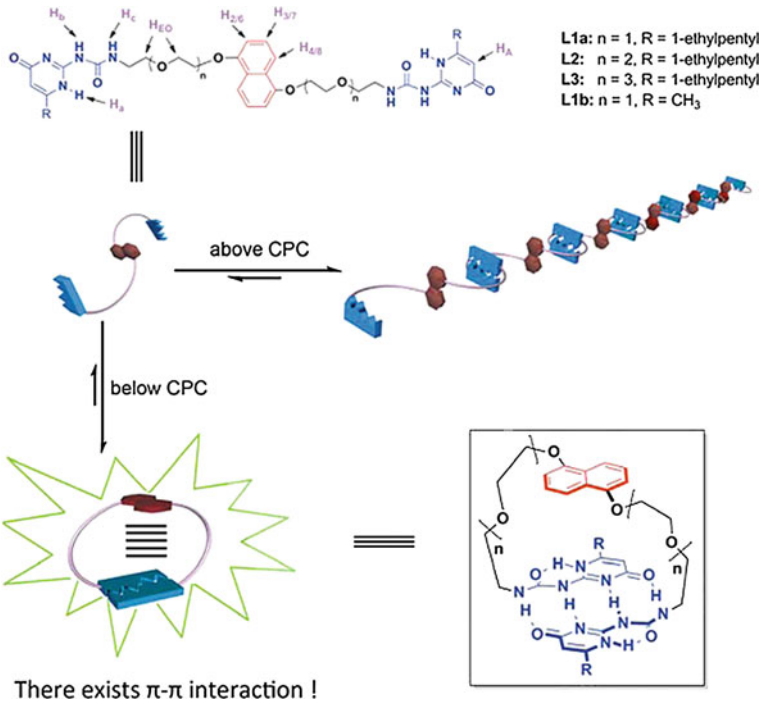

Fig. 10.3 Representations of the ring-chain equilibrium of DNP-bridged bifunctional UPy derivatives

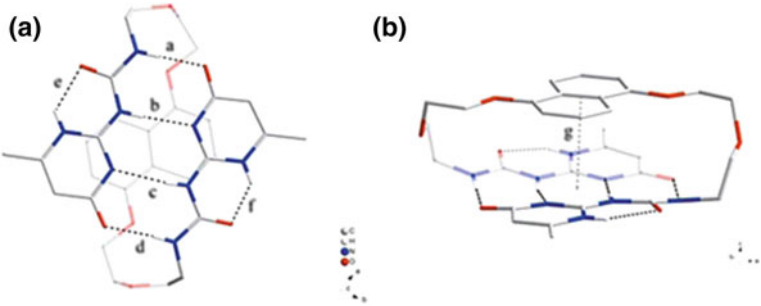

Fig. 10.4 *Top view* **a** and *side view* **b** of the crystal structure of **L1b** showing the intramolecular quadruple hydrogen-bonded array

Then they made a mixed polymer film with a fluorescent dye noncovalently end capping the photochromic linear polymers through quadruple hydrogen bonding. The fluorescence of the resulting film could be switched by UV/Vis light, which thus represents a fluorescent switch with nondestructive readout ability for data storage and high-resolution imaging technology.

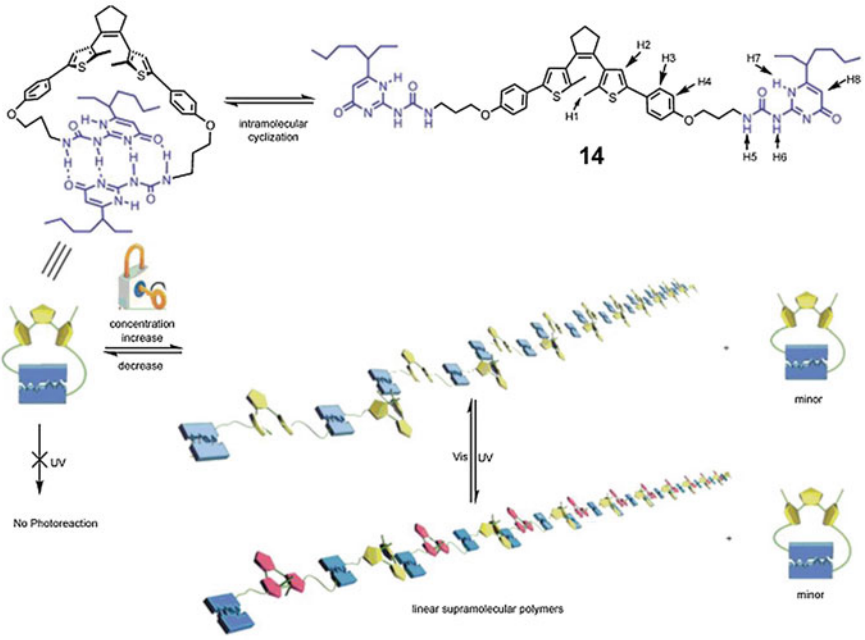

Fig. 10.5 Proposed ring-opening polymerization of **1** and its photoreaction under UV or visible irradiation

Supramolecular polymers are arrays of low-molecular-weight building blocks held together by hydrogen bonding or other reversible noncovalent interactions. Stiff stilbene (1, 1-biindane, Fig. 10.6) moiety, which exists as structurally distinct *E* and *Z* isomers, offers considerable advantages over azobenzene as a chromophore

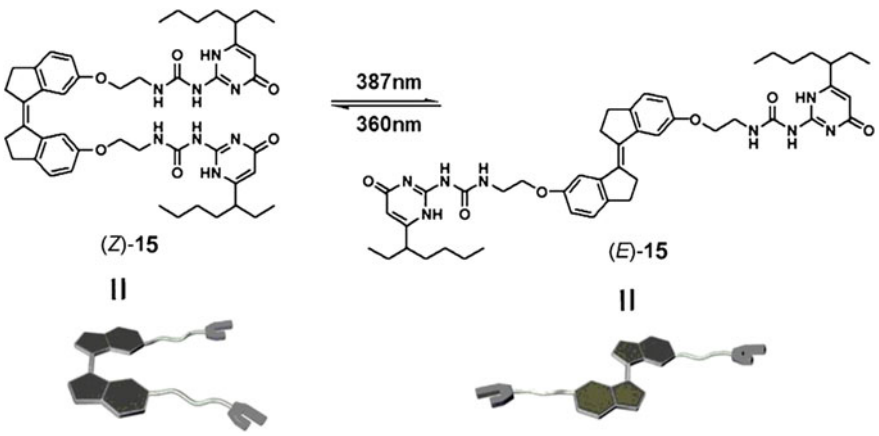

Fig. 10.6 Photoisomerization of the UPy-linked stiff stilbene derivates (Z)-1 and (E)-1. Reproduced from Ref. [28] by permission of John Wiley & Sons Ltd

for photoresponsive supramolecular polymers. Recently, Yang, Wu and coworkers have reported a stiff stilbene-bridged bifunctional UPy derivative **15**, which exhibits excellent photochromic properties. Their study showed that the polymerization mechanism and photochromic properties strongly depended on the isomeric state of the chromophore [28]. Electrospinning the polymer formed from the *Z* isomer produced fluorescent nanofibers, while the *E* analogue could form a multiresponsive gel. Moreover, the *Z* isomer follows a ring-chain supramolecular polymerization and the *E* analogue forms a supramolecular polymer by an isodesmic growth mechanism. This work suggests that the stiff stilbene chromophore would prove to be at least as good as, and maybe more useful than, azobenzene for the fabrication of various photoresponsive supramolecular polymers and smart materials with controllable properties.

10.4 Hydrogen-Bonded Supramolecular Polymers Constructed by High-Molecular-Weight Conventional Polymers that Are Functionalized by Hydrogen-Bonded Motifs

Materials with good mechanical properties at room temperature and a low melt viscosity are interesting for many applications. The mechanical properties and low melt viscosity of supramolecular polymers can be improved significantly by the combination of noncovalent functional groups and a piece of conventional polymer. It should be noted that herein the backbone of the hydrogen-bonded supramolecular polymer reviewed in this section is high-molecular-weight conventional polymers, and hydrogen-bonding motifs are linked to both ends of one piece of conventional polymer chain to obtain telechelic supramolecular polymers or linked to the backbone of conventional polymers as side groups to obtain side-chain supramolecular polymer networks.

10.4.1 Telechelic Supramolecular Polymers

A relatively high binding constant of the monomer unit is a prerequisite for obtaining chains of a high degree of polymerization. Meijer and coworkers functionalized telechelic poly(ethylene-butylene) oligomers with the ureidopyrimidinone (UPy) motif (Fig. 10.7) [29]. Functionalization of hydroxy telechelic poly (ethylene-butylene) with UPy resulted in a dramatic change in materials properties. The obtained supramolecular polymer displays a remarkable improvement in macroscopic properties, creating a supramolecular thermoplastic elastomer (Fig. 10.8). Although the UPy exhibits an extremely high dimerization constant, it was not expected to lead to a thermoplastic elastomer upon isodesmic supramolecular polymerization of this molecule, since both poly(ethylene-butylene)

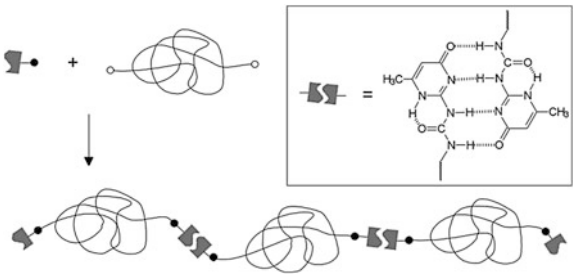

Fig. 10.7 Schematic drawing of functionalization of telechelic polymers with quadruple hydrogen-bonded ureidopyrimidinone units. Reproduced from Ref. [29] by permission of John Wiley & Sons Ltd

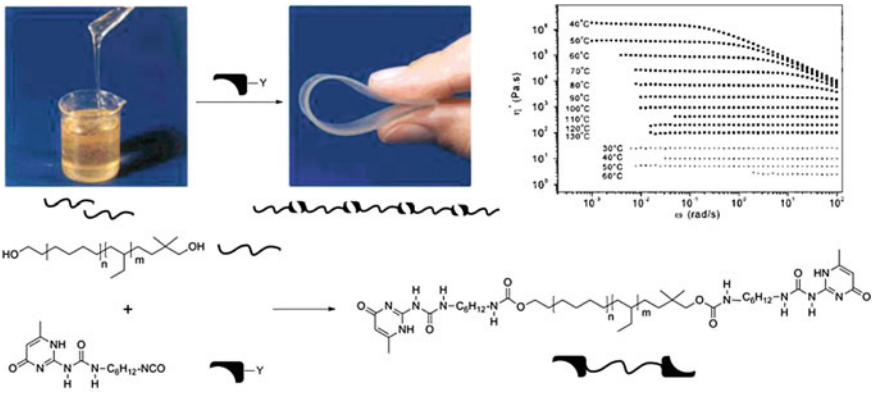

Fig. 10.8 Poly(ethylene/butylene) with OH end groups (*left*), poly(ethylene/butylene) functionalized with UPy units (*right*). Reproduced from Ref. [29] by permission of John Wiley & Sons Ltd

oligomer and its high-molecular-weight counterpart are amorphous with a glass transition temperature well below room temperature. The point of this work is to close the gap between polymers and oligomers, and the straight forward synthetic methodology for functionalizing the telechelic polymers and the easy work-up procedure makes this strategy applicable for general use on an industrial scale.

The technique of tissue engineering has become very important in producing new tissue employing polymeric scaffolds and cells. Generally, the covalent attachment of bioactive components to polymer backbones exhibits great promise. However, the synthetic versatility of this method still remains limited and the obtained polymers require high processing temperatures. In 2005, Meijer and coworkers reported a kind of novel supramolecular polymers based on quadruple hydrogen-bonding UPy moieties, which are extremely suitable for fabricating such bioactive materials owing to their favorable degradation, biocompatible behavior, and low-temperature processability [30]. Bioactive materials are achieved by easily mixing UPy-modified biomolecules with UPy-functionalized polymers that are

hydrogen-bonded supramolecular polymers constructed from bis-UPy-oligocaprolactones (Fig. 10.9). The UPy-modified biomolecules are UPy-Gly-Arg-Gly-Asp-Ser (**UPy-GRGDS**) and the synergistic UPy-Pro-His-Ser-Arg-Asn (**UPy-PHSRN**) peptide sequences, which are attached to UPy-functionalized polymers via quadruple hydrogen bonding, establishing the possibility to obtain a dynamic biomaterial that is similar to the extracellular matrix due to its noncovalent property. The incorporation of UPy-functionalized cell adhesion peptides into the supramolecular biomaterial increases cell adhesion and spreading compared to the bare construction, revealing the applicability of this method. Due to the reversible nature of the hydrogen bonds, the biomaterial could be fabricated by different techniques into different scaffolds varying from fibers and films to grids and meshes (Fig. 10.10). For example, it is possible to electrospin fibrous membranes with diameters less than 1 mm.

The ability of biological systems to spontaneously self-heal and to restore their functions upon the infliction of environmentally-induced damage is enormously amazing. Inspired by this, scientists have been trying their best to design and impart intriguing self-healing properties to well-defined materials, thereby extending the lifetime of the materials, lowering production costs, and improving product safety. Progress toward generally applicable and mechanically robust self-healing polymers have been hampered by a basic dilemma: the mechanical strength and rapid

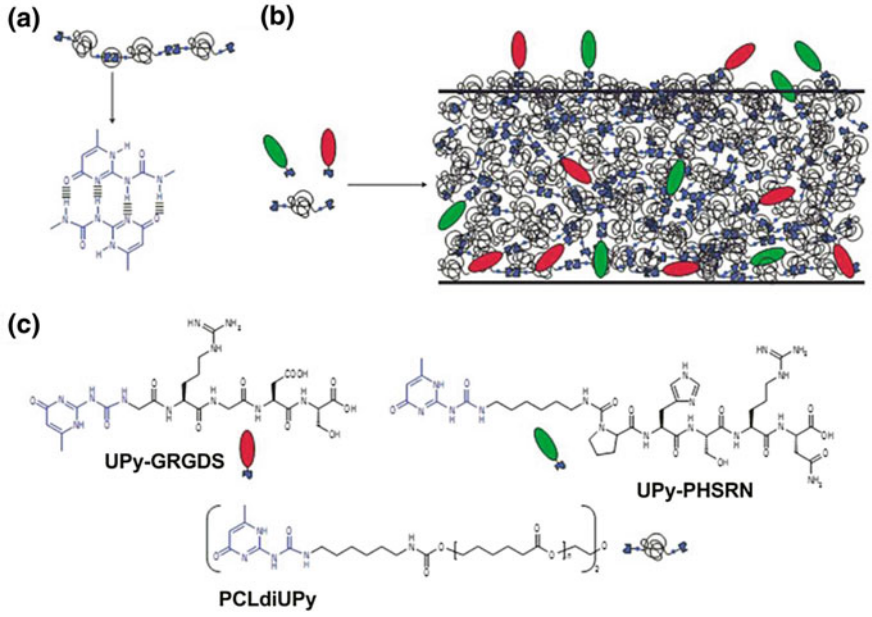

Fig. 10.9 Modular approach to supramolecular biomaterials using the noncovalent interactions for the anchoring of bioactive molecules. Reprinted by permission from Macmillan Publishers Ltd: Ref. [30], copyright 2005

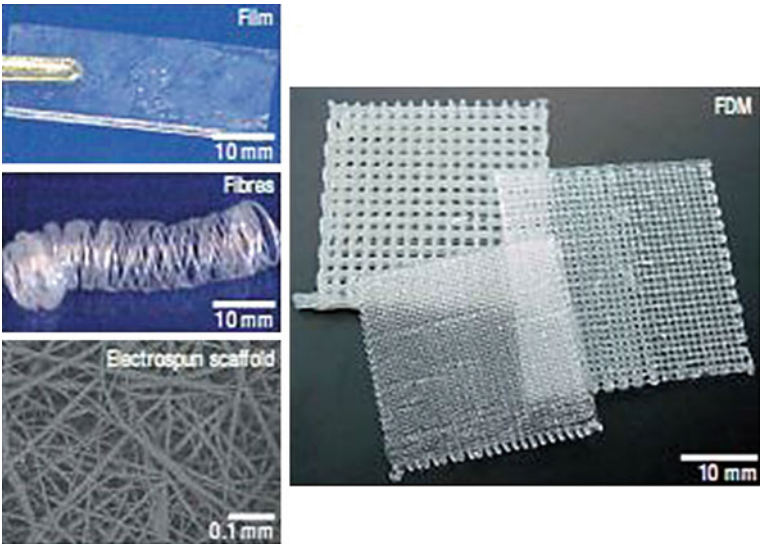

Fig. 10.10 Processability of the supramolecular UPy-materials. The PCLdiUPy polymer was processed into several scaffolds; films, fibers, meshes (SEM pictures), and grids by FDM. Reprinted by permission from Macmillan Publishers Ltd: Ref. [30], copyright 2005

macromolecular dynamics usually have an inverse dependent relationship. To address this dilemma, Guan and coworkers has been exploring a multiphase design of polymers that combine high modulus and toughness with spontaneous healing capability (Fig. 10.11) [31]. They reasoned that the supramolecular block copolymer should retain the hard/soft two-phase morphology found in conventional covalent block copolymer architectures, affording advantageous mechanical properties. At the same time, the healing motifs located within the soft phase should remain dynamic and reversible, realizing self-healing capability. As a result, the mechanical fracture of covalent polymers results in irreversible covalent bond rupture and permanent loss of properties. However, by replacing the covalent linkage in the center of the poly(*n*-butyl acrylate) (PBA) soft block with a dynamic quadruple hydrogen-bonding UPy junction, the supramolecular block copolymer should be able to self-heal after mechanical damage. Efficient recovery of extensibility and mechanical strength is observed with mild thermal treatment.

10.4.2 "Side-Chain" Supramolecular Polymer Networks

Generally, self-healing mechanisms of materials are either based on the release of repair agents upon damage or the inclusion of potential molecular functional groups of polymers to trigger repair. As an intriguing and unique subject of self-assembled supramolecular materials, supramolecular polymer gels have attracted intense

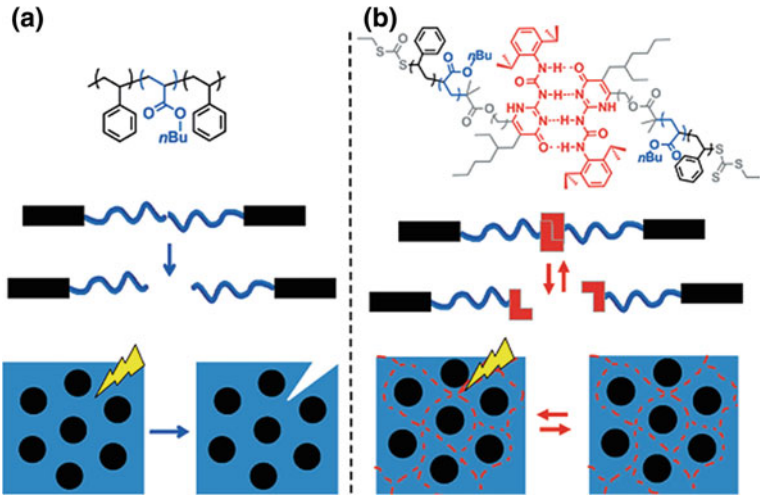

Fig. 10.11 The concept of self-healing supramolecular block copolymer design. **a** Conventional PS-b-PBA-b-PS triblock copolymers form a microphase-separated thermoplastic elastomer. **b** Supramolecular triblock copolymers combine the advantageous thermoplastic elastomeric properties of microphase-separated block copolymer systems with the reversible H-bonding interactions at the junction of the soft PBA block to afford dynamic, self-healing properties. Reproduced from Ref. [31] by permission of John Wiley & Sons Ltd

attention on account of the stimuli-responsiveness and processability inherent to the noncovalent units and the mechanical properties gained. In 2012, Campo and coworkers exploited the associated multivalent hydrogen bonds of the UPy unit to form stable, cross-linked hydrogel networks by copolymerization of a UPy-functionalized building block with different water-soluble monomers [32]. The obtained materials could form self-healing hydrogels by dimerization of the UPy motifs without the help of covalent bonds. The chemical structures of two different side-chain components of the copolymer are shown in Fig. 10.12: 2-(dimethyl-amino)-ethyl methacrylate (DMAEMA) and 2-(3-(6-methyl–4-oxo-1,4-dihydro-pyrimidin-2-yl)ureido)ethyl methacrylate (SCMHBMA). DMAEMA is the main side-chain component of the copolymer which provides water solubility for the material, while SCMHBMA of the side-chain component of copolymer containing UPy units could form dimmers of copolymers via quadruple hydrogen bonding. The self-healing properties could be combined to the thermal response of the polymer matrix to produce hydrogels with thermoregulated self-healing behavior. This strategy can be further extended to other commercially available monomers, and it is a versatile approach toward self-healing hydrogels with different functions.

Low-density natural materials such as silk and animal bones have served as an inspiration for material scientists, because they demonstrate prominent toughness combined with strength and stiffness. In this regard, lots of one-component nano-composites have been created involving reinforcing colloidal nanorod cores with polymeric grafts bearing supramolecular motifs. In 2014, Ruokolainen and Ikkala

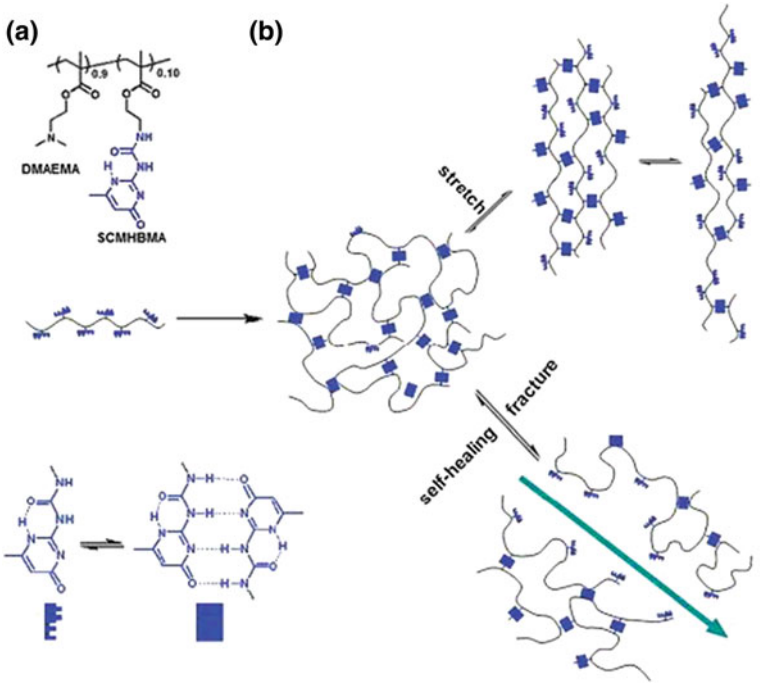

Fig. 10.12 **a** Chemical structure of the copolymer containing DMAEMA and SCMHBMA and **b** the schematic model of self-healing and stretching of the hydrogel formed by the copolymer. Reproduced from Ref. [32] by permission of The Royal Society of Chemistry

reported a one-component biomimetic nanocomposite which contains reinforcing colloidal cellulose nanocrystal (CNC) cores and acrylate polymer shells [33]. The polymer shells involve a set of hydrogen-bonding UPy moieties to form sacrificial bonds within the grafted brush architecture, and the interdigitation of the grafts and the UPy quadruple hydrogen bonds bind the nanocomposite network together. Under stress, UPy groups act as sacrificial bonds to dissipate fracture energy. This system demonstrated pronounced yields, noncatastropic growth of cracks, and dissipative deformation under tensile stress. The maximum in the stress–strain curve at 29.0 ± 3.0 MPa indicates pronounced yielding, with a Young's modulus of 1.5 ± 0.2 GPa. Moreover, they used TEM images of uniaxially elongate 500-nm-thick films to show the serrated crack surfaces, further emphasizing the reinforcing pull-out mechanisms of the colloidal CNCs. This architecture that involves supramolecular binding units within side chains of polymer grafts attached to colloidal reinforcements shows a novel approach for the construction of tough nanocomposites (Fig. 10.13).

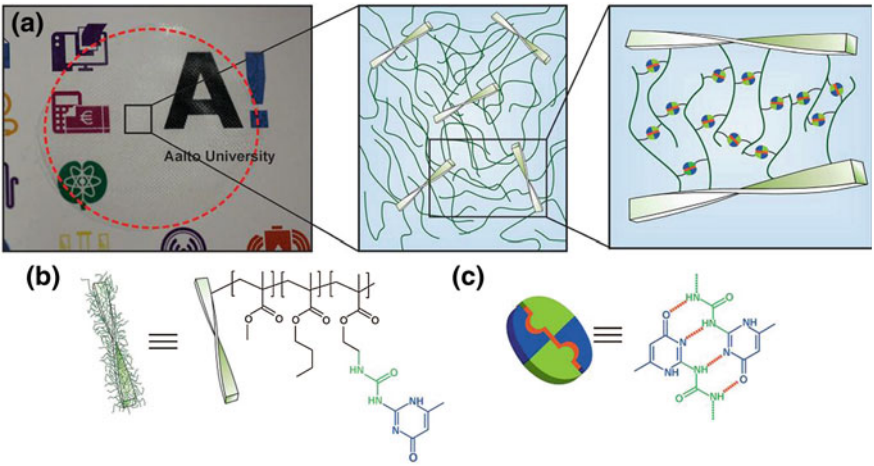

Fig. 10.13 **a** Transparency of a heat-pressed film of CNC-g-P(MMA-r-BMA-r-UPyMA). **b** Chemical composition of CNC-g-P(MMA-r-BMA-r-UPyMA). **c** The dimerization of UPy by four hydrogen bonds. Reproduced from Ref. [33] by permission of John Wiley & Sons Ltd

10.5 Supramolecular Polymers Constructed by Orthogonal Hydrogen Bonding-Driven Self-assembly and Other Non-covalent Interactions

In 1997, Reinhoudt and coworkers reported the first divergent nanostructure assembled by two different types of compatible noncovalent interactions, in which the importance of the orthogonality between the hydrogen bonding and metal–ligand coordination was explicitly recognized [34]. In 2005, Schubert and coworkers presented the highlights of the polymeric architectures with the combination of hydrogen bonding and other supramolecular interactions [35]. Since then, "orthogonal" was defined that different types of supramolecular interactions do not interact with each other. In 2012, Wang and coworkers published a tutorial review, where they summarized the reported supramolecular polymers constructed from the combination of multiple noncovalent binding interactions, mainly of two kinds, in the orthogonal way [13].

In 2013, Schmittel [12] and Zimmerman [11] further demonstrated the highly useful concept of orthogonality in organic chemistry, materials, and supramolecular chemistry. Without doubt, supramolecular polymers constructed by orthogonal self-assembly have already been an interesting topic in the area of supramolecular materials. It might be due to two reasons. First, the incorporation of selected orthogonal supramolecular moieties into one system could generate complicated, hierarchically-ordered materials with novel structures and new properties. Second, it can enhance the responsiveness of these supramolecular polymers to multiple external stimuli and open up a multitude of new chances. Therefore, in this section,

we would like to summarize the recent progress of supramolecular polymers that were orthogonally constructed by the combination of hydrogen bonding and other noncovalent interactions, such as metal–ion, host–guest, and π–π stacking interactions, and their emerging applications as "smart materials" are also briefly discussed.

Schubert and coworkers introduced two binding sites at two ends of a short linker with the ureidopyrimidinone (UPy) unit and terpyridine moieties, **16** and **17** (Fig. 10.14), which can orthogonally self-organize into linear polymers with the addition of metal ions in solution [36]. The ^{1}H NMR spectra and UV-Vis titration experiments indicated the successful dimerization of the hydrogen bonding units as well as the metal-tpy complexation with the addition of $FeCl_2$ in solution. Viscometry measurement of compound **16** with stepwise addition of $FeCl_2$ gave a direct proof of the formation of polymeric species. However, its vital drawback was the poor solubility in this case, which made it difficult to investigate the ring-chain equilibrium and determine the degree of polymerization. Then in 2005 Schubert and coworkers introduced covalent polymer assay poly(ε-caprolactone) as the linker between two binding sites to obtain the telechelic polymer, which showed very good solubility in the apolar solvent [37]. The coordination polymer exhibited a concentration-dependent ring-opening polymerization with a critical concentration of 0.25 mM. In the double-logarithmic plots of the viscosity versus the concentration, a slope of 2.2 at 'high' concentration was lower than the reported bis-ureidopyrimidinone compounds (2.8–4.2), which might be caused by impurities such as the small amount of non-UPy-functionalized precursor, ureidopyrimidinone starting material, or Fe(III) ions in the material acting as a chain stopper. In the

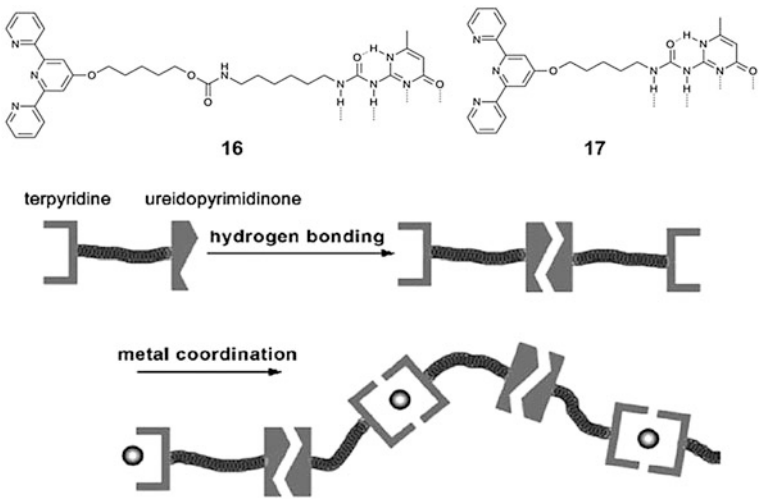

Fig. 10.14 Chemical structures of compound **16** and **17** and progress of the formation of the supramolecular polymers. Reproduced from Ref. [36] by permission of The Royal Society of Chemistry

native state, the coordinated polymer showed film-forming property and transparency at lower film thicknesses, much different from the opaque and brittle original polymers. In addition, the reversibility of the large polymeric complex formation was investigated by the addition of competing ligand HEEDTA (hydroxyethyl ethylenediaminetriacetic acid) or metal ions, opening a pathway toward new "switchable" functional polymers.

Ding and coworkers replaced the terpyridine moieties with a chiral Feringa's MonoPhos ligand to obtain a UPy-based bifunctional monomer **18** [38]. With the addition of $[Rh(cod)_2]BF_4$ to the solution of **18** in CH_2Cl_2, it could form a linear-assembled polymer with alternative orthogonal P-Rh coordination and UPy dimerization in the main chain (Scheme 10.5). The supramolecular coordination polymer **19** was insoluble in the apolar solvent such as toluene, which assured facile recovery and reusability of this catalyst. More importantly, this kind of heterogeneous catalyst showed excellent reactivity and enantioselectivity in the hydrogenation reaction.

The self-organized polymer **22** is composed of two monomers **20**, **21**, and one metal ion Fe(II). Monomer **20** is a heteroditopic building block with a terpyridine moiety and a Hamilton receptor at two ends of a hexanamido spacer, while monomer **21** is a homoditopic cyanurate derivative [39]. The supramolecular polymer **22** can be obtained when a 2:1 mixture of **20** and **21** in chloroform is titrated with 1.0 equiv. $FeCl_2$ in methanolic solution. Formation of the large polymeric aggregates was attested by the viscosity measurement and dynamic light scattering (DLS). DLS showed two processes in equilibrium in chloroform solution: one was the formation of particles with a hydrodynamic radius of R_H = 45 nm; the other was R_H = 5 μm (1–8 μm). Moreover, the reversibility of the supramolecular polymer could be modulated with competing ligands or variation of the pH value of the solution (Scheme 10.6).

Well-defined artificial supramolecular heterodimers with unique pseudo [2] rotaxane structures were prepared by Li and coworkers in orthogonal fashion based on the intermolecular quadruple hydrogen-bonding and host–guest interactions in

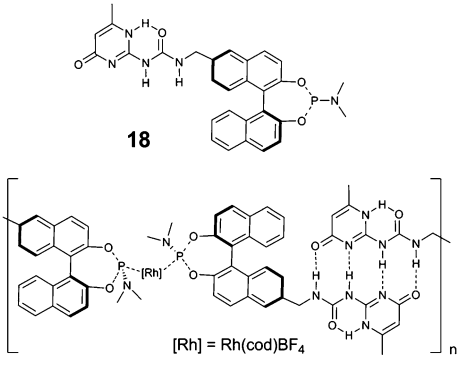

Scheme 10.5 Monomer **18** and the resulted polymeric catalyst **19**. Reproduced from Ref. [38] by permission of John Wiley & Sons Ltd

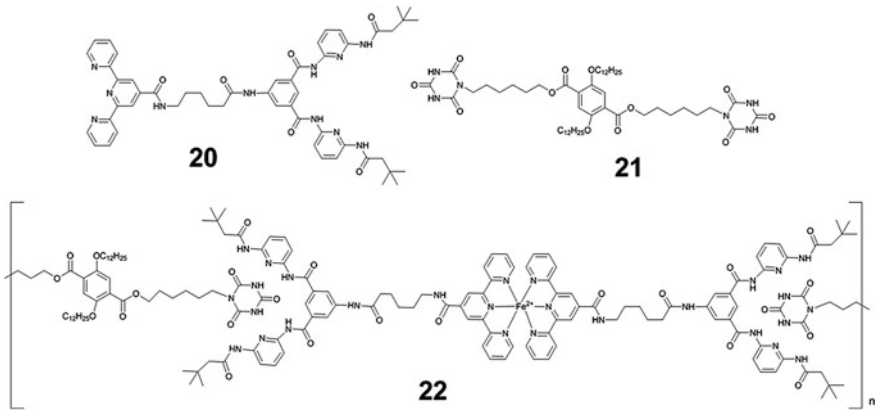

Scheme 10.6 Molecular structures of monomer **20**, **21** ,and the resulted polymer **22**. Reproduced from Ref. [39] by permission of John Wiley & Sons Ltd

2003 [20]. Recently, Wang and coworkers have designed and synthesized two heteroditopic monomers, one ureidopyrimidinone (UPy)-based monomer with paraquat moiety and the other UPy-based monomer with crown ether moiety, which were exploited to construct supramolecular aggregates by UPy dimerization and crown ether-paraquat recognition (Fig. 10.15) [40]. Dynamic light scattering (DLS) indicated that the resulting supramolecular aggregates with a hydrodynamic radius of 31 nm were observed with the equimolar of **M1** and **N1**. Finally, a novel type of crown ether-paraquat supramolecular polypseudorotaxane networks were developed with the hydrogen-bonded linear supramolecular polymer as the polymeric framework as well as crown ether-paraquat motif as a cross-linker [41].

Very recently, continuously following the above work and with the idea that bisparaquat derivative (**D1**) as an appropriate guest can form a [3]pseudorotaxane with two molecules of bifunctional UPy pillar[5]arene (**H1**), Wang and coworkers have fabricated a pillar[5]arene-based supramolecular polypseudorotaxane network, where a linear quadruple hydrogen-bonded supramolecular polymer backbones formed from **H1** bound with bisparaquat derivatives by the paraquat moiety threading into the cavity of the pillar[5]arene units as shown in Fig. 10.16 [42]. TEM observation showed that such supramolecular networks could further assemble to much bigger spherical aggregates, affording specific and tunable properties to form a translucent film with the combination of PEG-2000 as the polymer matrix.

Wang and coworkers further explored the fabrication of metal–ion-responsive dynamic linear supramolecular polymers constructed by orthogonal hydrogen bonding and crown ether-based host–guest interactions [43]. They designed and synthesized two monomers: the homoditopic building block **23**, which was comprised of two symmetrical dialkylammonium groups, and the heteroditopic building block **24**, which bore one B21C7 moiety and one UPy unit. As shown in Fig. 10.17, linear supramolecular polymers were achieved, in which a supramolecular dimer

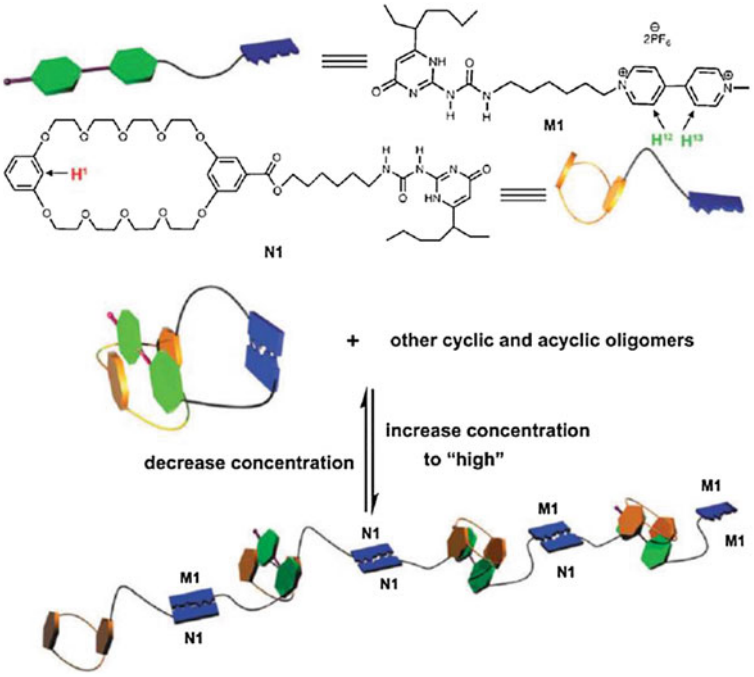

Fig. 10.15 Graphical representation of the construction of supramolecular polymers from monomers **M1** and **N1**

from **24** was initially obtained followed by polymerization upon addition of **23**. The disassembly/assembly of supramolecular polymers could be reversibly switched by addition/removal of K^+ without interfering with UPy dimerization due to the stronger binding of K^+ with B21C7 moiety than dialkylammonium moiety.

Hydrogen bonding interaction has been proved to be especially suitable as a noncovalent interaction for supramolecular self-assembly because of its fidelity and directionality. A very primitive synthetic DNA analogue, via the self-sorting of two competitive hydrogen-bonding pairs of side-chains, was introduced by Weck and coworkers (Scheme 10.7) [44]. In detail, they synthesized random and block copolymers **25** by ring-opening metathesis polymerization, which contained two kinds of hydrogen bonds side-chain thymine- and cyanuric acid-based recognition units. The pendant function groups exhibited orthogonal self-assembly behavior with the diamido pyridine units and Hamilton receptor moieties, respectively. The orthogonal self-assembly of these two kinds of hydrogen sites was confirmed by the titration experiments using both different recognition units in a one-pot procedure. And the stepwise titration experiment with the specific receptor showed a truly dynamic process of self-assembly.

Meijer and coworkers investigated the self-assembly behavior of ureidopyrimidinone (UPy) dimers substituted with additional urea (U) or urethane (T) functionality in various solvents (Fig. 10.18) [45]. Regarding the urea-substituted

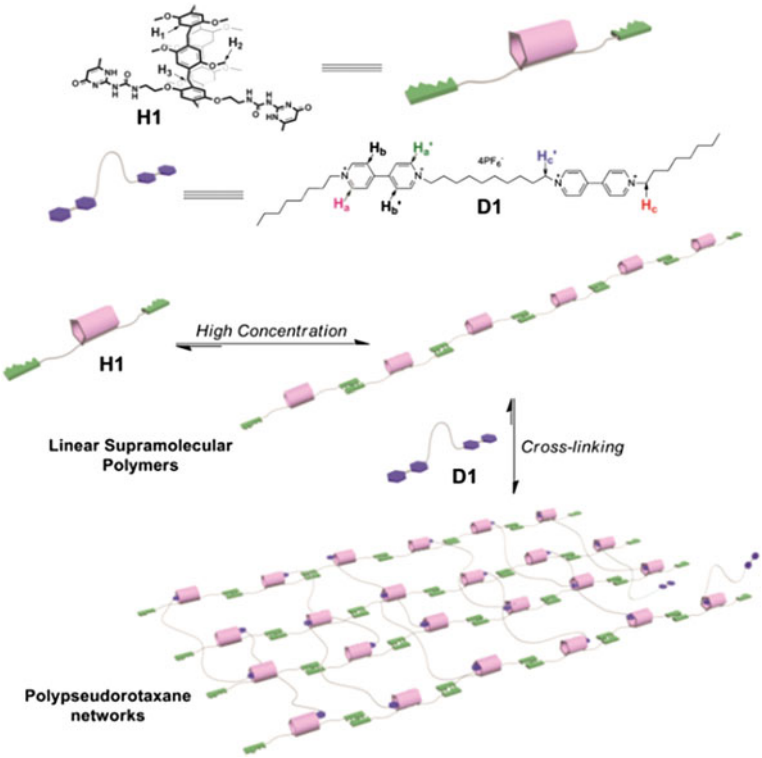

Fig. 10.16 Graphical representation of the construction of a polypseudorotaxane network from the monomer **H1** and cross-linker **D1**

molecule, the formation of the 1-D stacks was due to the lateral aggregation of urea–hydrogen bonding and their additional stabilization by the aromatic-aromatic π–π stacking confirmed by the concentration-dependent ^{1}H NMR and DOSY spectroscopy. And temperature-dependent CD spectroscopy showed the formation of larger helical stacks in the apolar solvent heptane. However, the urethane-substituted molecule only showed very weak lateral interactions.

Protein folding is a dynamic process of molecular self-assembly mainly based on the hydrogen bonding interactions, during which a single-stranded polypeptide chain folded to form a well-defined three-dimensional tertiary structure. Inspired by nature's way, several approaches for preparing synthetic analogues of folded proteins using, for example, helical polymers and dendrimers have been explored. For example, Meijer and coworkers reported a series of ABA triblock copolymers that contained two complementary association motifs and folded into single-chain polymeric nanoparticles (SCPNs) via orthogonal self-assembly (Fig. 10.19) [46]. The copolymers were prepared using atom-transfer radical polymerization (ATRP) and possessed different pendant functional groups in the A and B blocks. After postfunctionalization, the A block contained o-nitrobenzyl-protected 2-ureidopyrimidinone (UPy) moieties and the B

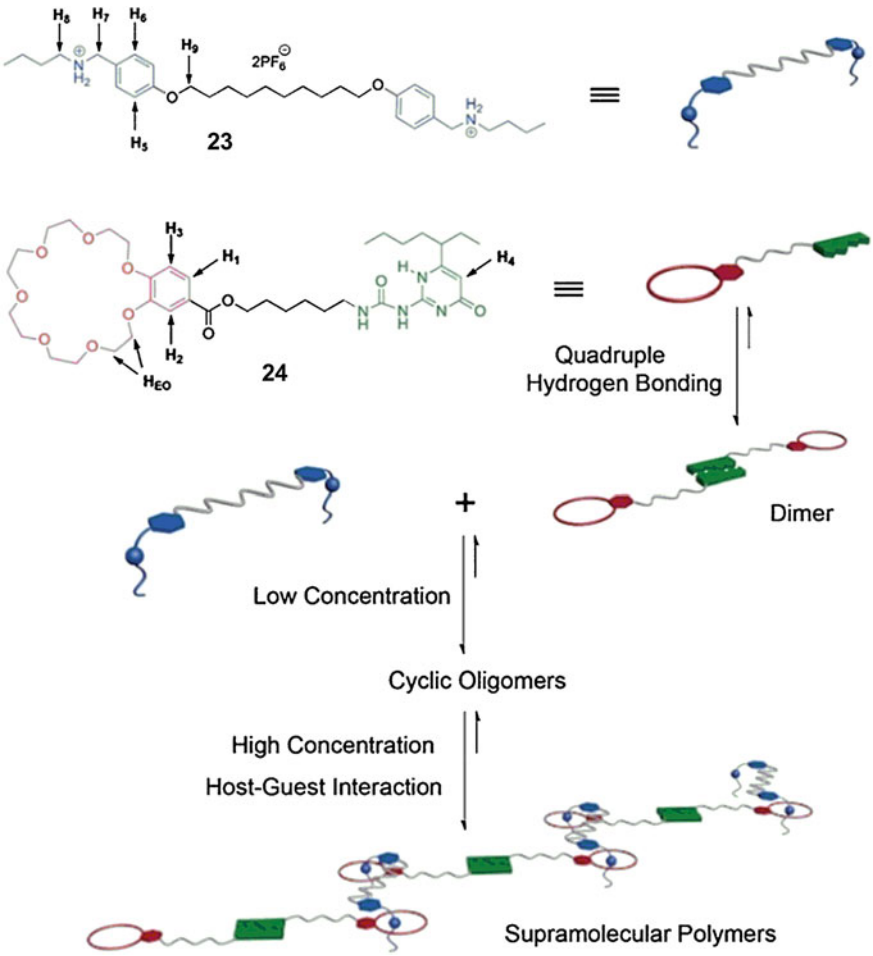

Fig. 10.17 Graphical representation of the supramolecular polymers constructed from monomers **23** and **24** by orthogonal self-assembly

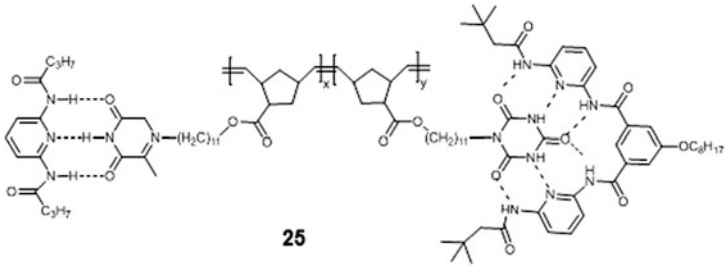

Scheme 10.7 Schematic representation of the resulted supramolecular polymer **25**. Reprinted with the permission from Ref. [44]. Copyright 2005 American Chemical Society

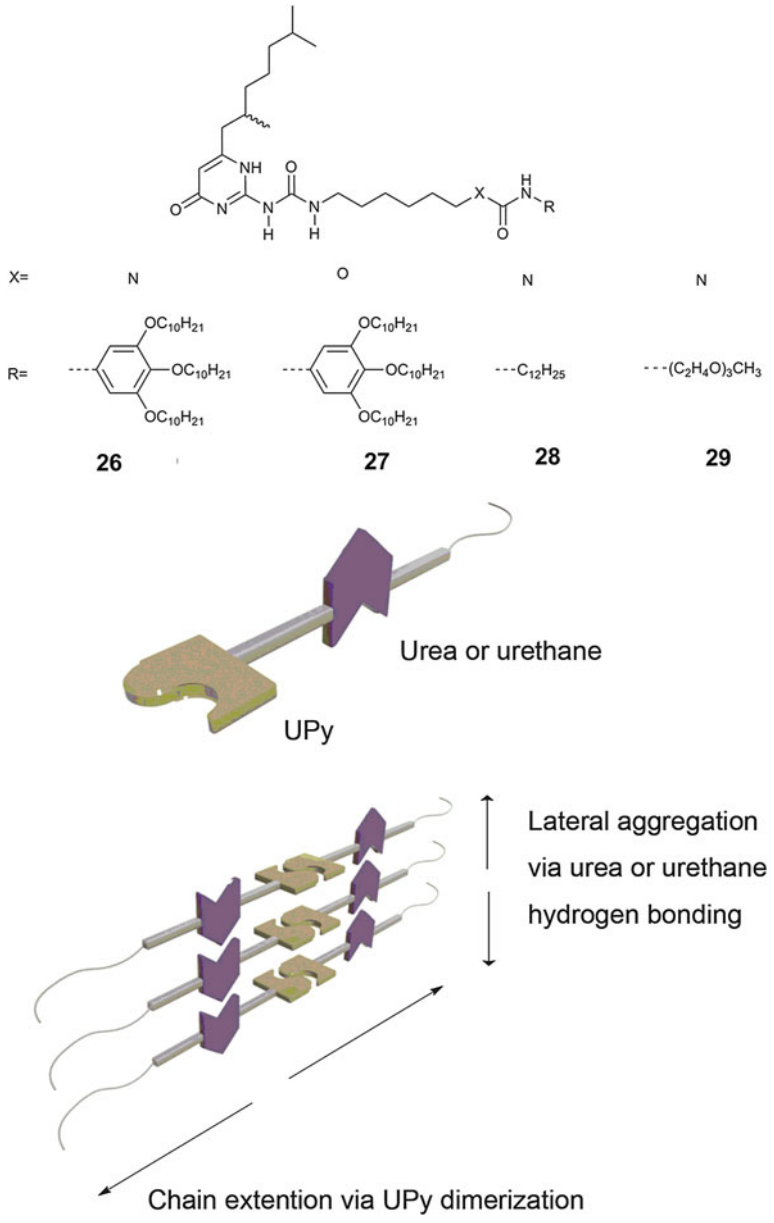

Fig. 10.18 Molecular structures of **26–29** and schematic representation of the resulted supramolecular polymer. Reproduced from Ref. [45] by permission of John Wiley & Sons Ltd

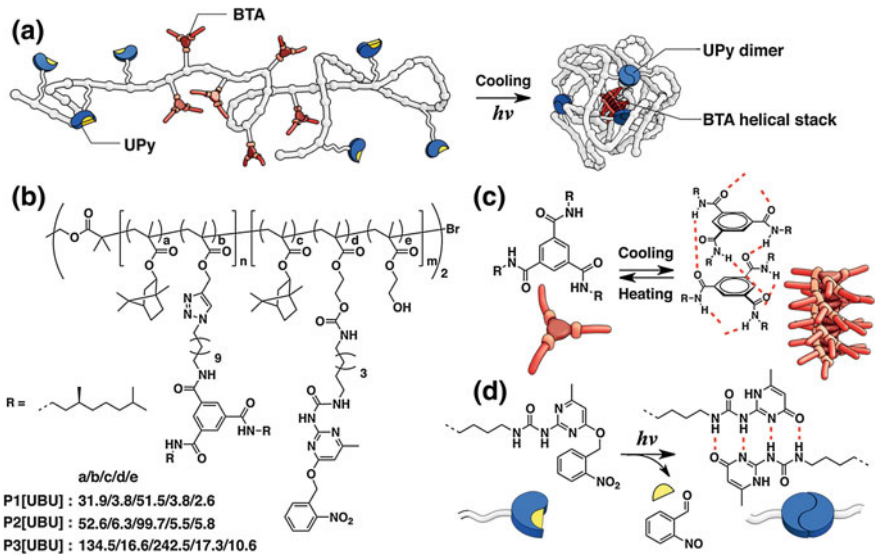

Fig. 10.19 **a** Design of a triblock copolymer with BTA and UPy moieties that folds into a single-chain polymeric nanoparticle cross-linked via orthogonal self-assembly. **b** Chemical structures of the triblock copolymers **P1[UBU]**, **P2[UBU]**, and **P3[UBU]**. **c** Helical self-assembly of chiral BTAs via threefold-symmetric hydrogen bonding. **d** Photoinduced dimerization of o-nitrobenzyl-protected UPys via quadruple hydrogen bonding. Reprinted with the permission from Ref. [46]. Copyright 2013 American Chemical Society

block contained benzene-1, 3, 5-tricarboxamide (BTA) moieties. The triblock copolymers could thermally fold into SCPNs through intramolecular self-assembly of the BTAs to form internal columnar helical stacks. UPy deprotection using UV light resulted in a further collapse of the polymers into more compact conformation via intramolecular UPy association. Well-defined single-chain nanoparticles with orthogonally self-assembling domains mimicking an α-helix and a β-sheet were successfully provided. This study provides a rational design approach for self-folding protein analogues and shows the broad applicability of orthogonal self-assembly within one polymer chain as a design principle for developing synthetic enzyme mimics with well-defined tertiary-folded structure.

10.6 Conclusions

Supramolecular polymers have been explored as smart materials because of their intrinsic reversibility of the bonds. In the past years, hydrogen bonding has been proven to be the most suitable candidate for applications in supramolecular chemistry. With increasing creation of hydrogen bonding motifs, the exploration of supramolecular polymers formed by multiple hydrogen bonds has been carried out

since the past decade. Thus more and more novel hydrogen-bonded supramolecular polymers have been constructed. On the one hand, supramolecular polymers with unique properties are constructed from small-molecular-weight monomers due to the high association constant. On the other hand, novel materials created from conventional polymers functionalized with hydrogen-bonding motif have been continuously explored to realize some special properties, such as self-healing and enhanced mechanical property. Inspired by biological systems, such as DNA and filaments of cytoskeleton in which different kinds of noncovalent interactions are involved to realize vital cell functions, scientists have been constructing novel supramolecular polymers with special functions through the combination of hydrogen bonding and other reversible interactions in orthogonal way in recent years. Fabrication of synthetic supramolecular polymers by orthogonal self-assembly is not only the necessary way chemists should go to reach the level of sophisticated natural systems but also the prospect of smart materials in areas ranging from environmental sustainability to information technology.

In spite of the great achievement, the study on supramolecular polymers incorporating more types of independent secondary interactions is still in its early stages. In this chapter, we have summarized some typical examples of the reported hydrogen-bonded supramolecular polymers. Most of these new materials are still winning with their novel structures, and only some of them exhibit potential applications, such as catalysis and biological functions. Nevertheless, the field of hydrogen-bonded supramolecular polymers, unquestionably, has a bright future.

References

1. Aida T, Meijer EW, Stupp SI (2012) Science 335:813
2. Greef TFAD, Smulders MMJ, Wolffs M, Schenning APHJ, Sijbesma RP, Meijer EW (2009) Chem Rev 109:5687
3. de Greef TFA, Meijer EW (2008) Nature 453:171
4. Brunsveld L, Folmer BJB, Sijbesma RP, Meijer EW (2001) Chem Rev 101:4071
5. Fouquey C, Lehn J-M, Levelut A-M (1990) Adv Mater 2:254
6. Sijbesma RP, Meijer EW (2003) Chem Commun 5
7. Steven CZ, Perry SC (2000) Struct Bond 96:64
8. Bandy TJ, Brewer A, Burns JR, Marth G, Nguyen T, Stulz E (2011) Chem Soc Rev 40:138
9. Watson JD, Crick FHC (1953) Nature 171:737
10. De Lucca Freitas LL, Stadler R (1987) Macromolecules 20:2478
11. Wong C-H, Zimmerman SC (2013) Chem Commun 49:1679
12. Saha ML, De S, Pramanik S, Schmittel M (2013) Chem Soc Rev 42:6860
13. Li S-L, Xiao T, Lin C, Wang L (2012) Chem Soc Rev 41:5950
14. Jorgensen WL, Pranata J (1990) J Am Chem Soc 112:2008
15. Murray TJ, Zimmerman SC (1992) J Am Chem Soc 114:4010
16. Beijer FH, Sijbesma RP, Kooijman H, Spek AL, Meijer EW (1998) J Am Chem Soc 120:6761
17. Sijbesma RP, Beijer FH, Brunsveld L, Folmer BJB, Hirschberg JHKK, Lange RFM, Lowe JKL, Meijer EW (1997) Science 278:1601
18. Chang SK, Hamilton AD (1988) J Am Chem Soc 110:1318
19. Beijer FH, Kooijman H, Spek AL, Sijbesma RP, Meijer EW (1998) Angew Chem Int Ed 37:75

20. Wang X-Z, Li X-Q, Shao X-B, Zhao X, Deng P, Jiang X-K, Li Z-T, Chen Y-Q (2003) Chem Eur J 9:2904
21. Corbin PS, Zimmerman SC (1998) J Am Chem Soc 120:9710
22. Blight BA, Hunter CA, Leigh DA, McNab H, Thomson PIT (2011) Nat Chem 3:244
23. Berl V, Schmutz M, Krische MJ, Khoury RG, Lehn J-M (2002) Chem Eur J 8:1227
24. Brunsveld L, Vekemans JAJM, Hirschberg JHKK, Sijbesma RP, Meijer EW (2002) Proc Natl Acad Sci USA 99:4977
25. Cate ATt, Sijbesma RP (2002) Macromol Rapid Commun 23:1094
26. Xiao T, Feng X, Ye S, Guan Y, Li S-L, Wang Q, Ji Y, Zhu D, Hu X, Lin C, Pan Y, Wang L (2012) Macromolecules 45:9585
27. Li S-L, Xiao T, Xia W, Ding X, Yu Y, Jiang J, Wang L (2011) Chem Eur J 17:10716
28. Xu J-F, Chen Y-Z, Wu D, Wu L-Z, Tung C-H, Yang Q-Z (2013) Angew Chem Int Ed 52:9738
29. Folmer BJB, Sijbesma RP, Versteegen RM, van der Rijt JAJ, Meijer EW (2000) Adv Mater 12:874
30. Dankers PYW, Harmsen MC, Brouwer LA, Van Luyn MJA, Meijer EW (2005) Nat Mater 4:568
31. Hentschel J, Kushner AM, Ziller J, Guan Z (2012) Angew Chem Int Ed 51:10561
32. Cui J, Campo Ad (2012) Chem Commun 48:9302
33. McKee JR, Huokuna J, Martikainen L, Karesoja M, Nykänen A, Kontturi E, Tenhu H, Ruokolainen J, Ikkala O (2014) Angew Chem Int Ed 53:5049
34. Huck WTS, Hulst R, Timmerman P, van Veggel FCJM, Reinhoudt DN (1997) Angew Chem Int Ed 36:1006
35. Hofmeier H, Schubert US (2005). Chem Commun 2423
36. Hofmeier H, El-ghayoury A, Schenning APHJ, Schubert US (2004). Chem Commun 318
37. Hofmeier H, Hoogenboom R, Wouters MEL, Schubert US (2005) J Am Chem Soc 127:2913
38. Shi L, Wang XW, Sandoval CA, Li MX, Qi QY, Li ZT, Ding KL (2006) Angew Chem Int Ed 45:4108
39. Grimm F, Ulm N, Gröhn F, Düring J, Hirsch A (2011) Chem Eur J 17:9478
40. Li S-L, Xiao T, Wu Y, Jiang J, Wang L (2011) Chem Commun 47:6903
41. Li S-L, Xiao T, Hu B, Zhang Y, Zhao F, Ji Y, Yu Y, Lin C, Wang L (2011) Chem Commun 47:10755
42. Hu X-Y, Wu X, Wang S, Chen D, Xia W, Lin C, Pan Y, Wang L (2013) Polm Chem 4:4292
43. Xiao T, Feng X, Wang Q, Lin C, Wang L, Pan Y (2013) Chem Commun 49:8329
44. Burd C, Weck M (2005) Macromolecules 38:7225
45. Nieuwenhuizen MML, de Greef TFA, van der Bruggen RLJ, Paulusse JMJ, Appel WPJ, Smulders MMJ, Sijbesma RP, Meijer EW (2010) Chem Eur J 16:1601
46. Hosono N, Gillissen MA, Li Y, Sheiko SS, Palmans AR, Meijer EW (2013) J Am Chem Soc 135:501